Università degli Studi di Ferrara

DOCTORAL COURSE IN PHYSICS
CYCLE XXXV

Coordinator: Prof. Eleonora LUPPI

Multiple stellar populations in globular clusters

Scientific-Disciplinary Sector: FIS/05

Author:
Michele SCALCO

Supervisor:
Prof. Piero ROSATI
Dr. Luigi BEDIN

Years: 2019/2024

Contents

List of Figures

List of Tables

Chapter 1

Introduction

Galactic globular clusters (GCs) are systems comprising metal-poor, coeval stars situated at the same distance from the Sun. Consisting of ancient stars (age $> 10\,\mathrm{Gyr}$) with a broad mass spectrum ($< 0.01 - 0.8\,\mathrm{M}_{\odot}$), GCs are some of the oldest stellar systems for which it is possible to measure the ages through the colour-magnitude diagrams (CMDs) of their resolved stellar populations. As among the oldest structures in the Milky Way, GCs serve as windows into the Universe's early stages, providing valuable insights into its formation history. For decades, they have been essential in testing predictions from stellar evolution models. The recent revelation that these stellar systems host multiple stellar populations (mPOPs) has profoundly altered our understanding of GCs, marking one of the most remarkable discoveries in the field of stellar populations.

This introductory chapter offers a concise overview of GCs and their mPOPs phenomenon, focusing on the two GCs subject of this thesis, ω Centauri and NGC 6752. The topics introduced here will be elaborated upon in subsequent chapters, establishing a foundational framework for the discussion that follows.

1.1 Multiple stellar populations in globular clusters

For a long time, GCs were regarded as the best examples of simple stellar populations, comprising stars with uniform distance, age, and chemical composition. However, this perspective was challenged following the discovery (Anderson, 1997) and subsequent confirmation (Bedin et al., 2004) of a split in the *unevolved* main sequence (MS) stars of ω Centauri (or NGC 5139, the most massive GC in the Milky Way, hereafter ω Cen). The split revealed two components, a blue and a red MS, with the blue MS being more metal-rich than the red one (Piotto et al., 2005). These findings highlighted a significant variation in helium content, with the blue MS exhibiting a strong helium enhancement up to Y$\sim$0.39 (Norris, 2004; King et al., 2012).

Subsequent investigations have shown that ω Cen represents an extreme case, and almost all studied GCs host distinct stellar populations, as evidenced by spectroscopic studies and photometric observations revealing multiple sequences. The number of identified populations ranges from two, as observed in NGC 6397 (Milone et al., 2012a), to more than fifteen, exemplified by ω Cen (Bellini et al., 2017d). Although each cluster displays unique patterns in the properties of its stellar populations, there are proprieties that are shared among multiple populations in all GCs. Generally, these populations can be categorized into two discrete groups of stars characterized by different chemical compositions, referred to as the first and second populations (1P and 2P).

While 1P stars possess a composition attributed to the proto-galactic interstellar matter from which they originated, 2P stars exhibit significant variations in helium and light elements, such as C, N, O, Na, Al, and, in some cases, Mg, Si, and K,

among cluster members. The occurrence and intricacy of the mPOPs phenomenon in GCs increase with cluster mass: more massive GCs feature larger helium variations and higher fractions of 2P stars (Piotto et al., 2015; Milone et al., 2017b). Certain clusters host 2P with a pronounced helium enhancement, approaching Y$\sim$0.40 (e.g., D'Antona and Caloi 2004; Norris 2004; Piotto et al. 2005; Piotto et al. 2007; King et al. 2012; Bellini et al. 2013), while in others, helium differences are measurable but relatively small (e.g., $\sim$0.01, as observed in NGC 6397, Milone et al. 2012a). 1P and 2P stars are characterized by anti-correlations in their light elements, such as Na-O, C-N, and Mg–Al, with 2P stars depleted in C and O, and enriched in N and Na (e.g., Carretta et al. 2009; Marino et al. 2008; Marino et al. 2010; Marino et al. 2011; Marino et al. 2012; Marino et al. 2015). Some massive clusters also display internal variations in heavy elements, including iron and *s*-process elements (e.g., Marino et al. 2015; Johnson et al. 2015). The relative proportion of 1P to 2P stars varies among GCs, and in most cases, 2P stars outnumber 1P stars.

Photometric studies have categorized GCs into two classes, namely Type I and Type II, with the latter constituting $\approx$17 per cent of the objects. Typically, Type I GCs host two main populations of 1P and 2P stars with similar metallicity but different abundances of some light elements. Type II GCs exhibit at least an additional sequence running on the red side of the CMD and display a more complex chemical pattern, including variations in Fe and heavy elements (e.g., Marino et al. 2015; Johnson et al. 2015).

Various scenarios have been proposed for the formation of mPOPs in GCs. According to some models, GCs have experienced multiple bursts of star formation where 2P stars formed from material polluted by more massive 1P stars that had previously evolved. In other scenarios, the formation of mPOPs is approximately coeval, and 2P stars would result from the accretion of gas onto 1P. Supermassive stars ($\sim 10^4$,$M_\odot$; Denissenkov and Hartwick 2014; Gieles et al. 2018), massive interacting binaries (de Mink et al., 2009; Bastian et al., 2013; Decressin et al., 2007), fast-rotating massive stars (e.g., Krause et al. 2013; Prantzos and Charbonnel 2006; Decressin et al. 2007), and asymptotic giant branch (AGB) and super-AGB stars (e.g., D'Ercole et al. 2010) may eject materials with a composition similar to that of 2P stars—somewhat helium-enriched and exposed to proton capture reactions at high temperatures. Recently, Renzini, Marino, and Milone (2022) and Renzini (2023) proposed that most GCs formed inside pre-galactic dwarfs, in an epoch when the main body of the Milky Way was not yet formed. However, all of these scenarios encounter many difficulties (Renzini et al. 2015a, for a review), making the occurrence of mPOPs in massive star clusters still an unsolved puzzle.

Understanding the chemical and dynamical properties of mPOPs is essential to constrain models for the key stellar and dynamical processes involved in the formation of GCs in the early Universe. The identification of a framework for the formation and evolution of GCs has major implications for numerous key topics, including the fundamental aspects of star formation, the collisional dynamical evolution of stellar systems, and the consequences for the origin of a variety of exotic objects (such as the binary black holes responsible for the emission of gravitational waves detected by the Laser Interferometer Gravitational-Wave Observatory (LIGO)), the mechanisms responsible for the assembly of the Galactic halo, and the role of GCs in the re-ionization of the early Universe.

1.2 Multiple stellar populations in the low-mass regime

The atmospheres of low-mass stars, characterized by high density and low effective temperatures, facilitate the formation of various oxygen-containing molecular species (e.g. CO, H_2O, OH, TiO, VO, ZrO). These molecules exhibit greater sensitivity to abundance variations, enabling an accurate identification of mPOPs. Indeed, low-mass stars proved to be effective probes for studying mPOPs, as demonstrated in various GCs through *Hubble Space Telescope* (*HST*) near-infrared (NIR) observations (Milone et al., 2012e; Milone et al., 2014; Milone et al., 2017a; Milone et al., 2019; Dondoglio et al., 2022) and *James Webb Space Telescope* (*JWST*) observations (see, e.g., Nardiello et al. 2022; Nardiello et al. 2023; Milone et al. 2023; Ziliotto et al. 2023; Cadelano et al. 2023).

Historically, investigations of mPOPs in GCs focused on combining ultra-violet (UV) and blue visual filters sensitive to chemical variations in stars more massive than $\sim$0.6 $M_\odot$. However, the faintest region of the MS remains inaccessible in the UV and blue visual, even for the closest GCs, due to limited signal-to-noise ratios in UV observations for lower-mass stars. Recent NIR *HST* photometry (Milone et al., 2012e; Milone et al., 2014; Milone et al., 2017a; Milone et al., 2019) has opened a new window for studying mPOPs by revealing multiple sequences of very-low mass stars. Identifying and separating mPOPs in lower-mass ranges, along with studying their chemical composition, is crucial for understanding the formation and dynamical history of GCs. Extending mass function (MF) determinations to lower masses and assessing the MF slopes of mPOPs across an extensive mass range (from $\sim$0.1 to $\sim$0.8 $M_\odot$) can provide invaluable insights, and help us to understand which formation scenario is the more plausible.

The discovery that mPOPs with different chemical compositions are present in fully convective M-dwarfs suggests that the chemical composition of mPOPs is not solely a product of stellar evolution. Notable examples include NGC 2808 (Milone et al., 2012e; Dondoglio et al., 2022) and M 4 (Milone et al., 2014; Dondoglio et al., 2022), which host two sequences of M-dwarf stars associated with the first and second generation stellar populations. The former exhibits primordial helium, O–C-rich/N-poor stars, while the latter is enriched in helium and N and depleted in C and O. In NGC 6752, Milone et al. (2019) identified three distinct sequences from the knee down to the bottom of the MS ($\sim$ 0.15 $M_\odot$), consistent with different oxygen abundances. The relative numbers of stars in these populations and their oxygen abundances resemble those among red giant branch (RGB) and more massive MS stars in M 4, suggesting that mPOP properties do not significantly depend on stellar mass in the $\sim$0.15-0.80 $M_\odot$ range. This insight provides fundamental constraints for theoretical studies on the formation of mPOPs. Additionally, the case of ω Cen presents an even more complex structure of M-dwarf populations (Milone et al., 2017a; Gerasimov et al., 2022a), with at least four stellar groups with different oxygen abundances below the MS knee, and two additional sequences visible on the red side of the MSs.

1.3 Spatial distribution of multiple stellar populations in globular clusters

The spatial distribution of stellar populations within GCs serves as valuable information, offering insights into their initial configurations and providing constraints on the formation scenarios for multiple populations (Vesperini et al., 2013).

In several GCs (e.g. 47 Tuc, NGC 2808, M 3, NGC 5927, ω Cen, M 22 and M 13) it has been observed that 2P stars exhibit a more pronounced concentration towards the cluster center compared to 1P stars (Milone et al., 2012c; Lee, 2017; Dondoglio et al., 2021; Cordero et al., 2014; Simioni et al., 2016; Sollima et al., 2007; Bellini et al., 2009; Bellini et al., 2013; Lardo et al., 2011; Johnson and Pilachowski, 2012). On the contrary, in other clusters (e.g. NGC 6752, NGC 6362, M 5, NGC 6366, and NGC 6838, among others) 1P and 2P stars display similar radial distributions (Lee, 2017; Dondoglio et al., 2021; Milone et al., 2019; Dalessandro et al., 2018).

These observations align with scenarios where 2P stars are born in the cluster's centre, resulting in a more centralized distribution compared to 1P stars at the time of formation. Clusters with centrally concentrated 2P stars retain the memory of the initial distribution of their multiple populations, while in other GCs, the mixing of 1P and 2P stars is more pronounced due to dynamic evolution (Vesperini et al., 2013).

1.4 The internal kinematics of the multiple stellar populations in globular clusters

Similar to the spatial distribution, the current kinematics of stars within a cluster, including rotation, velocity dispersion, anisotropy and level of energy equipartition, can provide valuable insights into the initial configuration of the GC (Vesperini et al., 2013; Mastrobuono-Battisti and Perets, 2013; Mastrobuono-Battisti and Perets, 2016).

The combined use of high-precision proper motions from *HST* multi-epoch images, *Gaia* data, and line-of-sight velocities obtained through extensive ground-based spectroscopic surveys has enabled a comprehensive exploration of the internal motions of distinct stellar populations within GCs. In some GCs, 2P stars exhibit velocity distributions that are more radially anisotropic than those of 1P stars (Cordoni et al., 2020a; Richer et al., 2013; Bellini et al., 2015; Milone et al., 2018a; Libralato et al., 2018a; Libralato et al., 2023). These observations align with a scenario where 2P stars are initially more centrally concentrated than 1P stars and subsequently diffuse towards the outskirts of the cluster. In contrast, in other clusters, both 1P and 2P stars exhibit isotropic velocity distributions (Cordoni et al., 2020a), suggesting that any initial differences in the kinematic properties between their 1P and 2P stars, if present, have been erased by dynamical processes.

1.5 Investigating the multiple stellar populations using *HST*

The *Hubble Space Telescope* has played a crucial role in advancing our understanding of mPOPs in GCs. Numerous studies have demonstrated the effectiveness of combining UV and optical filters to efficiently differentiate between distinct mPOPs.

The trio of *HST* filters – F275W, F336W, and F438W – of the ultraviolet and visible (UVIS) Wide Field Camera 3 (WFC3) is the most commonly used combination for studying and identifying mPOPs in GCs. The F275W and F336W passbands encompass OH and NH molecular bands, while F438W comprises CN and CH bands. Consequently, 1P stars, characterized as O-rich and C-rich but N-poor, appear relatively bright in F336W but fainter than 2P stars in F275W and F438W.

For the precise identification and characterization of mPOPs in a large sample of clusters, a photometric diagram maximizing the separation between stellar populations is required. Studies based on UV and optical *HST* photometry have

revealed that plots such as m_{F814W} versus $m_{F275W} - m_{F814W}$ or the pseudo-color $C_{F275W,F336W,F438W} = (m_{F275W} - m_{F336W}) - (m_{F336W} - m_{F438W})$ are highly effective in identifying mPOPs in GCs (Milone et al., 2015b; Milone et al., 2015a). The F275W filter, when combined with F814W, provides a wide colour baseline to detect helium variations among GC stars, while the pseudo-colour $C_{F275W,F336W,F438W}$ is mostly sensitive to the nitrogen abundance of multiple populations. Two-colour diagrams of MS, RGB, or asymptotic giant branch (AGB) stars derived from photometry in different filters that are sensitive to the specific chemical composition of GCs are referred to as ***chromosomic maps*** (ChMs, Milone et al., 2015b). ChMs have facilitated an unprecedented detailed analysis of multiple population patterns in GCs (Milone et al., 2017b; Milone et al., 2018b). One of the most commonly used ChMs is the two-pseudo-color diagram $C_{F275W,F336W,F438W}$ versus $m_{F275W} - m_{F814W}$, which maximizes the separation between stellar populations along the MS and the RGB. An example of the potential of this diagram is provided by Milone et al. (2015b) for NGC 2808, where it was used to identify and characterize at least five different stellar populations. Fig. 1.1 illustrates the procedure used to obtain the ChM, with upper-left and bottom-left panels showing the m_{814W} vs. $m_{F275W} - m_{F814W}$ CMDs in the region of the RGB and MS, respectively. The blue and red fiducial lines were used to verticalize the CMDs, as shown in the upper-right and bottom-right panels. In what follows, we define Δ_X^N as the abscissa of each star in the verticalized diagram for the colour X.

Right panel and middle panels of Fig. 1.2 are similar to Fig. 1.1 but for the m_{F814W} versus $C_{F275W,F336W,F438W}$ CMD. Finally, the right panels of Fig. 1.2 show the two color diagrams for the RGB and MS stars, obtained by combining the two verticalised CMDs. As can be seen, five different stellar populations can be identified. The five stellar populations are color-coded in Fig. 1.3.

While the *HST* filters F275W, F336W, F438W, and F814W (along with F606W) are commonly used to distinguish and identify mPOPs in the MS and RGB, the F110W and F160W filters of the WFC3 NIR camera aboard *HST* are extensively employed for characterizing multiple populations of M-dwarfs (Milone et al., 2012e; Milone et al., 2014; Milone et al., 2017a; Milone et al., 2019; Dondoglio et al., 2022). The F160W band is significantly influenced by absorption from various oxygen-containing molecules, including H_2O, while F110W photometry is minimally affected by oxygen abundance. Consequently, 2P stars, which exhibit reduced oxygen content compared to 1P stars, display brighter F160W magnitudes and redder F110W−F160W colours.

To illustrate the impact of light-element variations on the *HST* IR bands, the right panel of Fig. 1.4 displays two synthetic spectra from stars belonging to different populations: bMS (in azure) and rMS (in red), characterized by distinct helium and light-element content (Milone et al., 2012e). Specifically, bMS stars feature a helium content of Y = 0.25 and CNO abundances of [O/Fe]=0.4, [C/Fe]=−0.3, and [N/Fe]=0.5, while rMS stars have a helium content of Y = 0.38 and CNO abundances of [O/Fe]=−0.6, [C/Fe]=−0.7, and [N/Fe]=2.0. Both spectra assume T_{eff} = 4000K, log(g)=5.0, and a microturbulence of 1.0 km s^{-1}. The synthesis includes various molecules: CO, C_2, CN, OH, MgH, SiH, H_2O, TiO, VO, and ZrO. The resulting synthetic spectra (upper-right panel) were integrated over the transmission of the WFC3/IR F110W and F160W filters (lower-right panel) to generate synthetic magnitudes and colours. The middle-right panel of Fig. 1.4 illustrates the flux difference as a function of wavelength between the two spectra. H_2O molecules have the most significant impact on the synthetic spectra, causing a substantial reduction in flux for the rMS in the F160W filter.

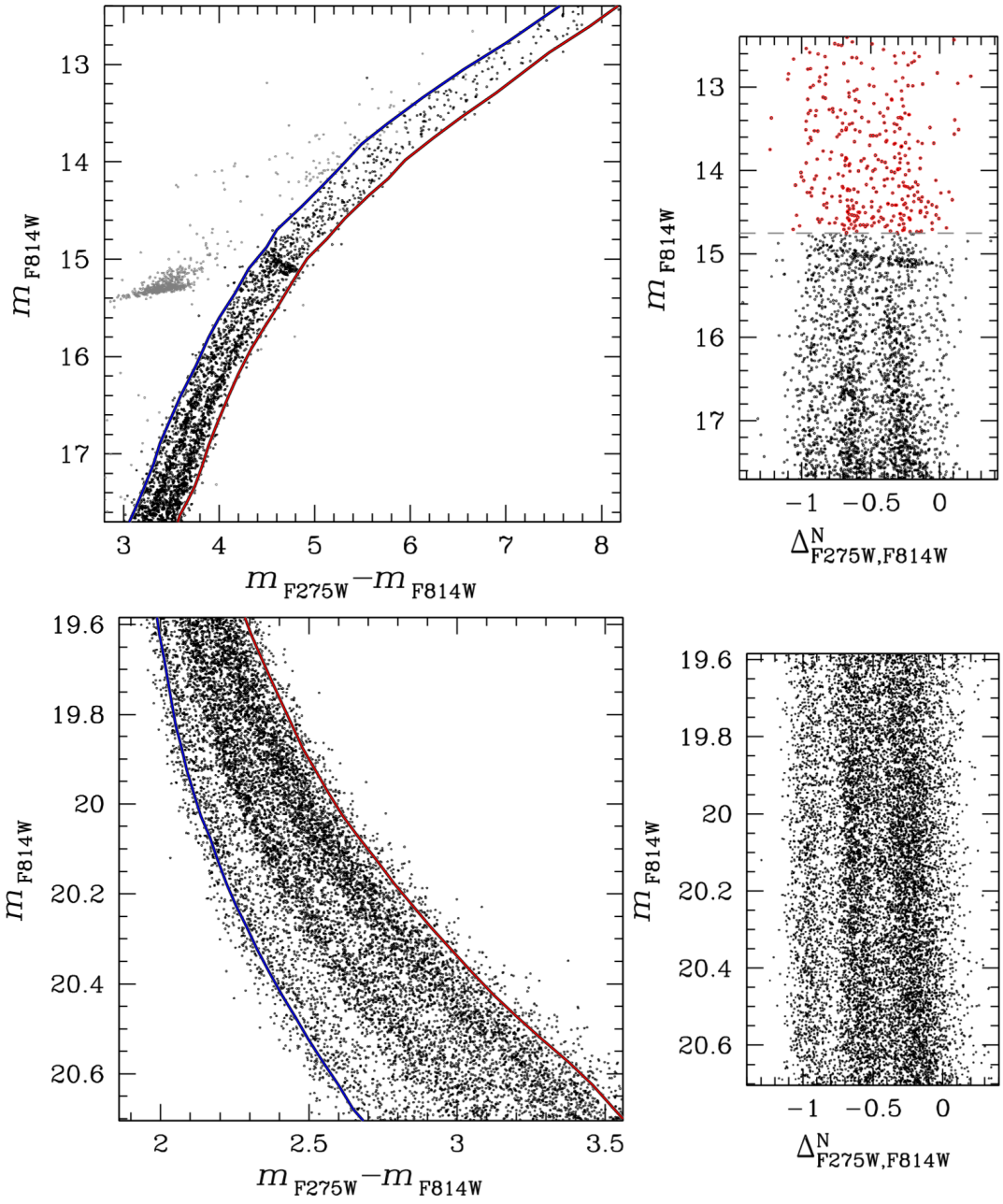

FIGURE 1.1: *Upper-left panel*: m_{F814W} vsersus $m_{F275W} - m_{F814W}$ CMD of NGC 2808 around the RGB. Red and blue lines are the fiducials adopted to verticalize the RGB. *Upper-right panel*: m_{F814W} versus $\Delta^{N}_{F275W,F814W}$ CMD. Red dots represent stars within the brightest part of the RGB with $m_{F814W} < 14.68$, as indicated by the location of the dashed line. *Bottom panels*: same as the upper panels but for the MS. Adapted from Fig. 2 and 4 of Milone et al. (2015b).

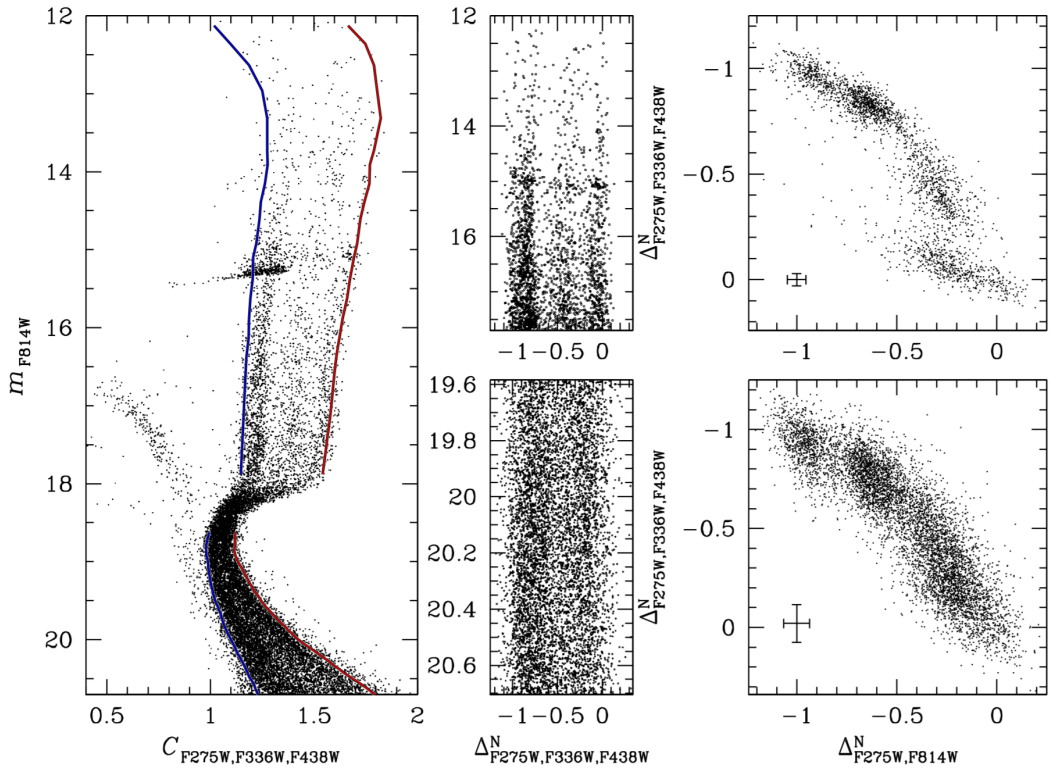

FIGURE 1.2: *Left panel*: m_{F814W} vs. $C_{F275W,F336W,F438W}$ CMD of NGC 2808. The red and blue lines represent the fiducial lines used to verticalize the MS and RGB. *Middle panels*: verticalized m_{F814W} versus $\Delta^N_{F275W,F336W,F438W}$ CMD for the MS (lower panel) and RGB (upper panel) stars. *Right panels*: $\Delta^N_{F275W,F336W,F438W}$ versus $\Delta^N_{F275W,F814W}$ ChM for the MS (lower panel) and RGB (upper panel) stars. Adapted from Fig. 5 of Milone et al. (2015b).

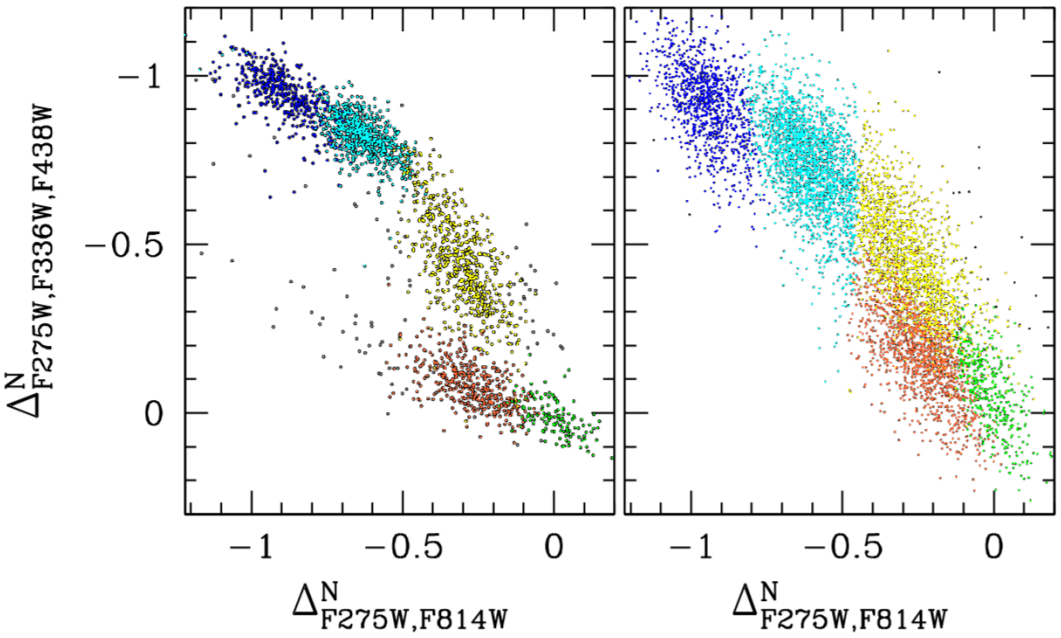

FIGURE 1.3: $\Delta^N_{F275W,F336W,F438W}$ versus $\Delta^N_{F275W,F814W}$ chromosomic map for the RGB and MS stars with the 5 identified stellar populations colour-coded. Adapted from Fig. 6 of Milone et al. (2015b).

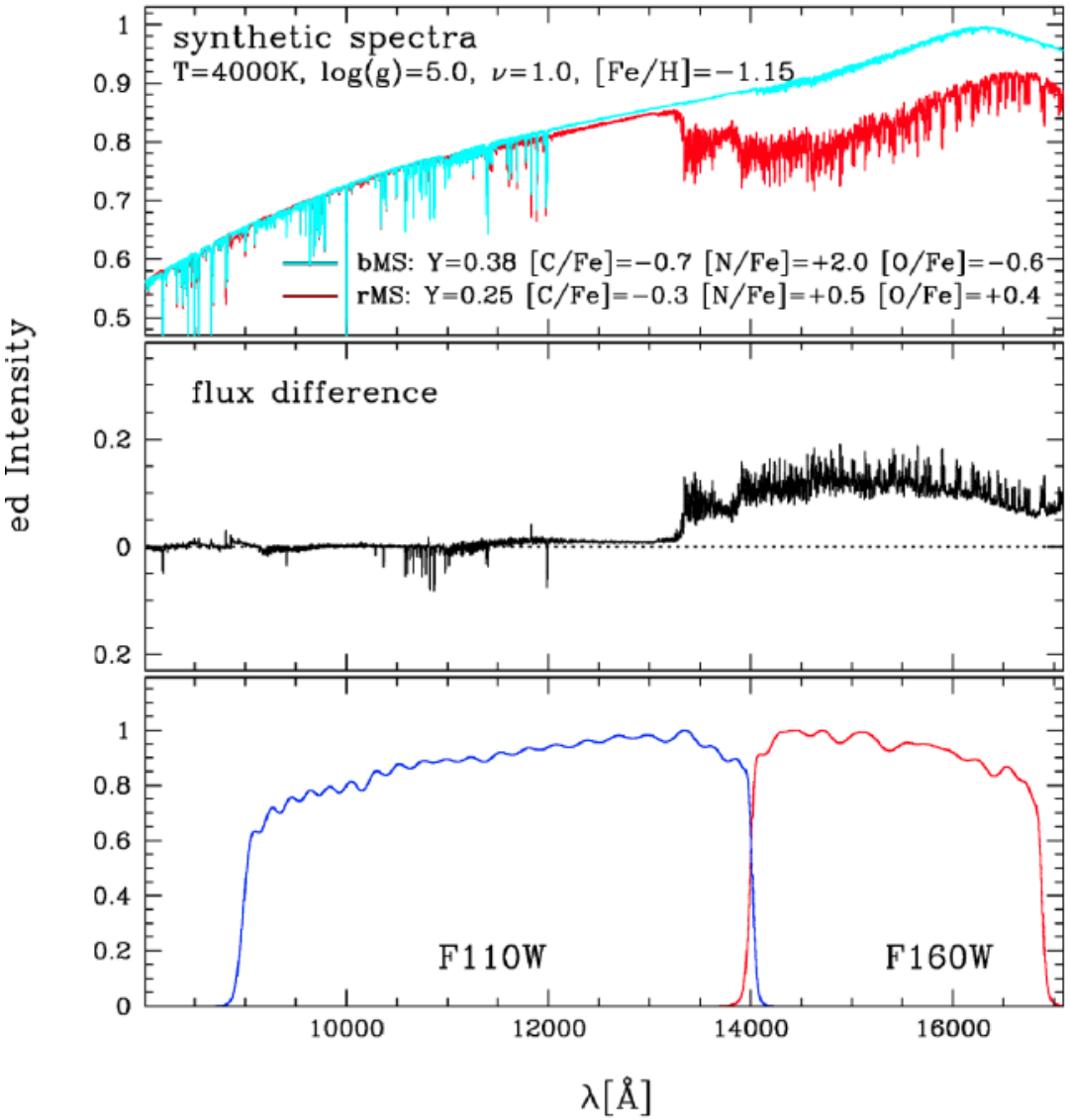

FIGURE 1.4: *Upper panel*: comparison of the synthetic spectra of a bMS star (cyan) and an rMS star (red, see text for more details). *Middle panel*: difference between the synthetic spectrum of a bMS and a rMS star. *Lower panel*: normalized responses of the F110W and F160W WFC3/NIR *HST* filters. Adapted from Fig. 4 of Milone et al. (2012e).

1.6 Main sequence multiple populations in ω Cen

The most massive GC of the Milky Way, ω Cen, is a low-reddening ($E(B-V) \sim 0.12$, Harris 1996; Harris 2010) GC that is relatively close ($\sim$5 kpc) to the Sun, making it an excellent target for a large variety of photometric and spectroscopic investigations. It hosts a very complex system of mPOPs that makes it one of the most enigmatic stellar systems of the Galaxy. In fact, it is populated by at least two main groups of stars with a large difference in their helium content (Y$\sim$0.40 for the He-rich component) and by a set of at least fifteen sub-populations (Bellini et al., 2017d). The complexity of mPOPs in this cluster is demonstrated by the multiple sub-giant branches and red-giant branches and by the presence of a double white dwarf cooling sequence (Bellini et al., 2013).

In contrast to the majority of monometallic GCs, stars in ω Cen span a wide range in metallicity with a primary component at $[Fe/H] \sim -1.7$ to -1.8, and a long tail extending up to $[Fe/H] \sim -0.6$ (e.g. Norris and Da Costa 1995; Pancino et al. 2002; Marino et al. 2010; Marino et al. 2011). It exhibits extreme star-to-star variation in several light elements, including C, N, O, Na, Mg, Al and Si and s-process elements (e.g. Brown and Wallerstein 1993; Norris and Da Costa 1995; Johnson and Pilachowski 2010; Stanford, Da Costa, and Norris 2010; Marino et al. 2012), and shows the typical abundance patterns among light elements that are observed in nearly all the Galactic GCs, such as the Na-O and C-N anti-correlations. Interestingly, in this extreme cluster distinct anti-correlations are present within stellar populations with different metallicity (Johnson and Pilachowski, 2010; Marino et al., 2010; Marino et al., 2011). The formation history behind the complex properties of the stellar populations of ω Cen is unknown. Some scenarios speculate that ω Cen is the nucleus of a dwarf galaxy accreted by the Milky Way or the result of the merger of two or more cluster (Norris et al., 1997; Jurcsik, 1998; Bekki and Freeman, 2003; Pancino et al., 2000; Bekki and Norris, 2006).

ω Cen may represent our best laboratory to shed light on many of the fundamental aspects of the origin of multiple populations. In particular, its long relaxation time (1.1 Gyr in the core and 10 Gyr at the half-mass radius, Harris 1996; Harris 2010) implies that the loss of memory due to the effects of two-body relaxation is likely to be negligible and the internal kinematic properties and spatial distribution of the multiple populations of this cluster can provide us with the best picture of the fingerprints of the formation process.

Bellini et al. (2009) conducted a comprehensive study on the radial distribution of the two principal groups of multiple populations identified in ω Cen. This investigation utilized a combination of space-based images obtained with the Wide Field Channel (WFC) of the Advanced Camera for Surveys (ACS) and the Wide Field and Planetary Camera 2 (WFPC2) mounted on *HST*, as well as ground-based images from the Focal Reducer and low dispersion Spectrograph 1 (FORS1) at the Very Large Telescope (VLT) and the Wide Field Imager (WFI) at the Cassegrain focus of the 2.2-m MPG/ESO telescope. The dataset covered a substantial portion of the cluster, extending from the inner core to the outskirts ($\approx$20 arcmin; refer to Fig. 1.5 for the position of the dataset in the plane of the sky).

In the left panel of Fig. 1.6, the CMD for different datasets is presented in the region of the MS, where the two most populated stellar populations, referred to as bMS and rMS, are distinctly separated. The dashed horizontal lines indicate the selected magnitude range for defining the bMS and rMS samples. Additionally, the fiducial lines (drawn manually) used to verticalise and separate the sequences are plotted in red. The right panel of Fig. 1.6 displays the verticalized CMDs using the

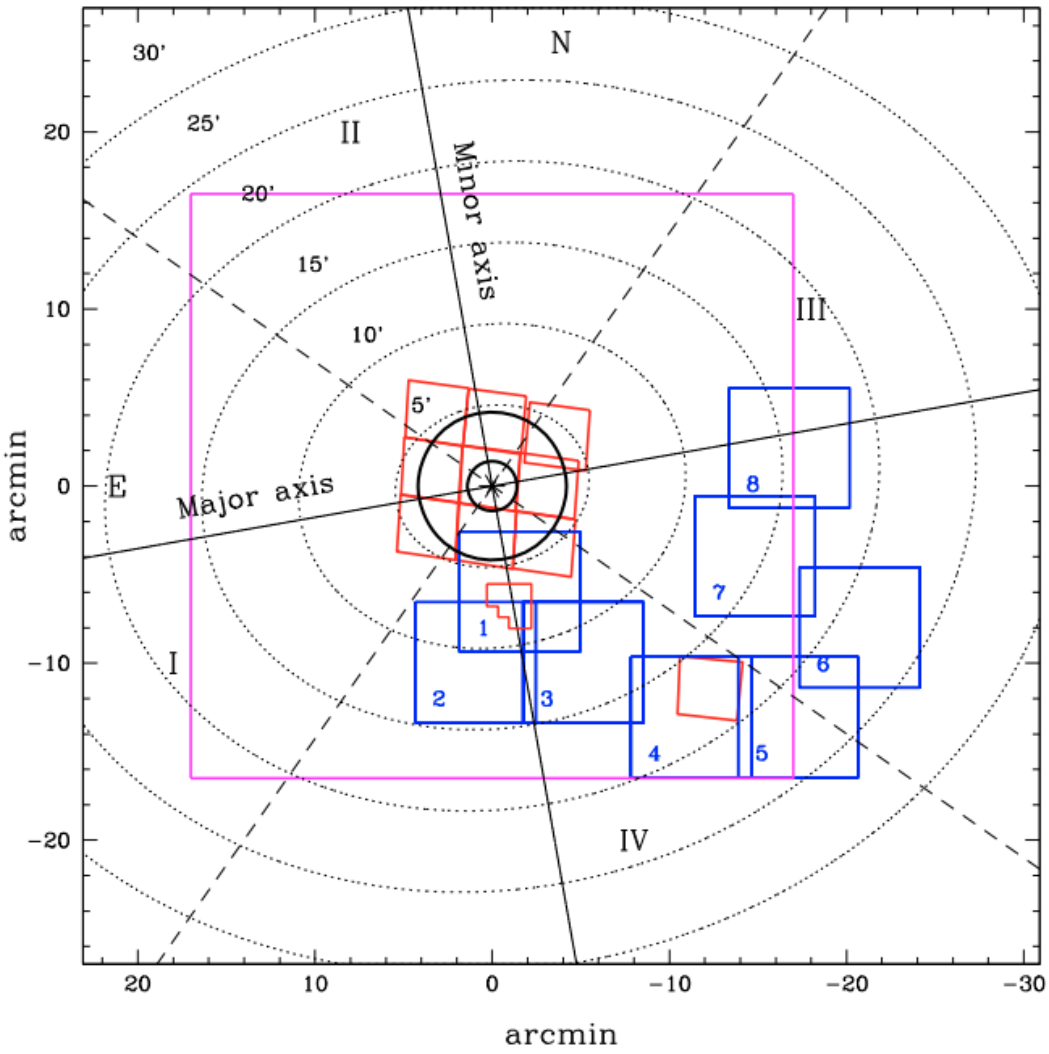

FIGURE 1.5: Footprints of the data sets used in Bellini et al. (2009), for the ACS/WFC and WFPC2 (in red), FORS1 (in blue) and WFI (in magenta). North is up, east to the left. The "∗" marks the cluster centre. Adapted from Fig. 1 of Bellini et al. (2009).

red fiducial lines. In each CMD, the bMS and rMS fractions were determined by simultaneously fitting the straightened colour distributions with two Gaussians, as illustrated in Fig. 1.7, with the area under each Gaussian serving as the estimate of the number of stars in each population. Finally, Fig. 1.8 illustrates the radial variation of the bMS to rMS ratio for the four datasets, where the inner ACS/WFC mosaic and the outer FORS1@VLT datasets were divided into five radial intervals each. Notably, the blue MS stars (bMS) exhibit a significantly higher spatial concentration than the red MS stars (rMS). Moreover, beyond ∼8 arcmin, the relative numbers of blue MS stars with respect to red MS stars experience a steep decline and then remain constant. A similar trend is observed in the relative number of intermediate-metallicity red-giant-branch stars (including the progeny of the bMS) concerning the metal-poor component (the progeny of the rMS).

A significant advancement in the exploration of the mPOPs of ω Cen was achieved by Bellini et al. (2017d). This study revealed that, within the core of the cluster,

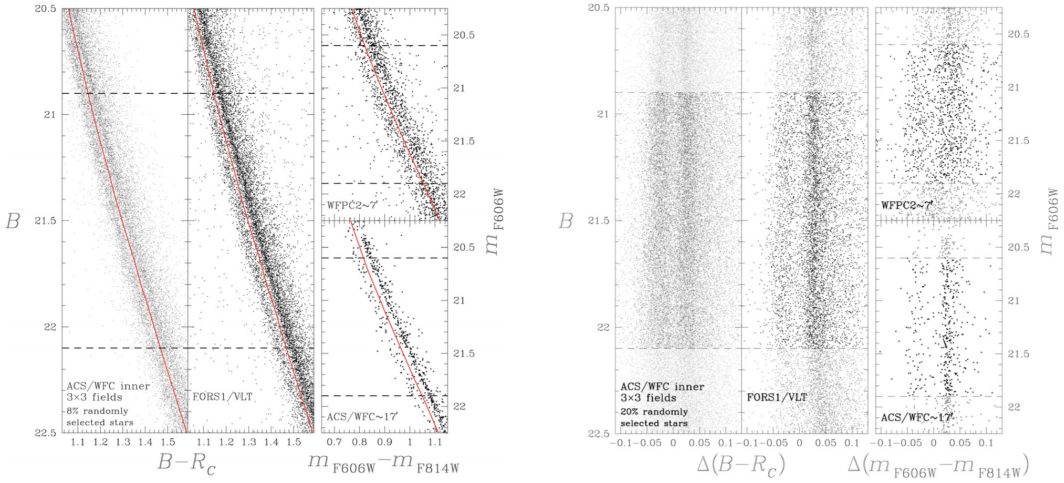

FIGURE 1.6: (*Left panel*): CMDs for different data sets in the region of the MS where the two most populated branches (bMS and rMS) are most separated in colour. The MS duality is clearly detected in all diagrams. The dashed horizontal lines mark the selected magnitude range for the definition of the bMS and rMS samples used in the derivation of their radial profiles. The fiducial lines (drawn by hand) that were used to straighten and separate the sequences are also plotted in red. (*Right panel*): same as the left panel but after subtraction, from the colour of each star, of the colour of the fiducial line at the same luminosity. Adapted from Fig. 6 and 7 of Bellini et al. (2009).

both the blue MS (bMS) and red MS (rMS) stars are further divided into three subcomponents each. The study identified a total of at least 15 sub-populations within ω Cen. By leveraging a combination of *HST* filters F275W, F336W, F438W, F606W, and F814W, along with the powerful tool of the ChM, the author discerned three subcomponents within both the bMS and the rMS groups. Additionally, Bellini et al. (2017d) uncovered three additional MS groups: MSa (with two subcomponents), MSd (with three subcomponents), sharing similar properties with the bMS, and MSe (with four subcomponents), exhibiting properties more similar to those of the rMS. In Fig. 1.9, the m_{F438W} versus $m_{F275W} - m_{F336W}$ CMD of ω Cen is presented, showcasing the fiducial lines of the 15 stellar subpopulations, color-coded accordingly. Furthermore, Fig. 1.10 displays the $\Delta^{N}_{CF275W,F336W,F438W}$ versus $\Delta^{N}_{F275W-F814W}$ ChM for the MS stars of ω Cen. This plot enables the identification of the 15 distinct stellar sub-populations, with colour-coding consistent with Fig. 1.9.

1.7 Main sequence multiple populations in NGC 6752

Using data acquired with the F110W and F160W filters of the WFC3/NIR camera on *HST*, Milone et al. (2019) identified three primary populations previously observed in the brightest portion of the CMD in the GC NGC 6752 (Milone et al. 2010; Milone et al. 2013; Milone et al. 2018b; Dotter et al. 2015, also see Dondoglio et al. 2022). These populations extend from the MS knee towards the lower end of the MS ($\approx$0.15 $M_{\odot}$). The left panel of Fig. 1.11 displays the m_{F160W} versus $m_{F110W} - m_{F160W}$ CMD of NGC 6752. As evident, three distinct sequences are identifiable, running from the MS knee towards the bottom of the MS. The redder sequence corresponds to MS-A, the bluer sequence to MS-C, and the intermediate sequence to MS-B. In the Hess diagram presented in the inset, these three sequences are even more apparent. The

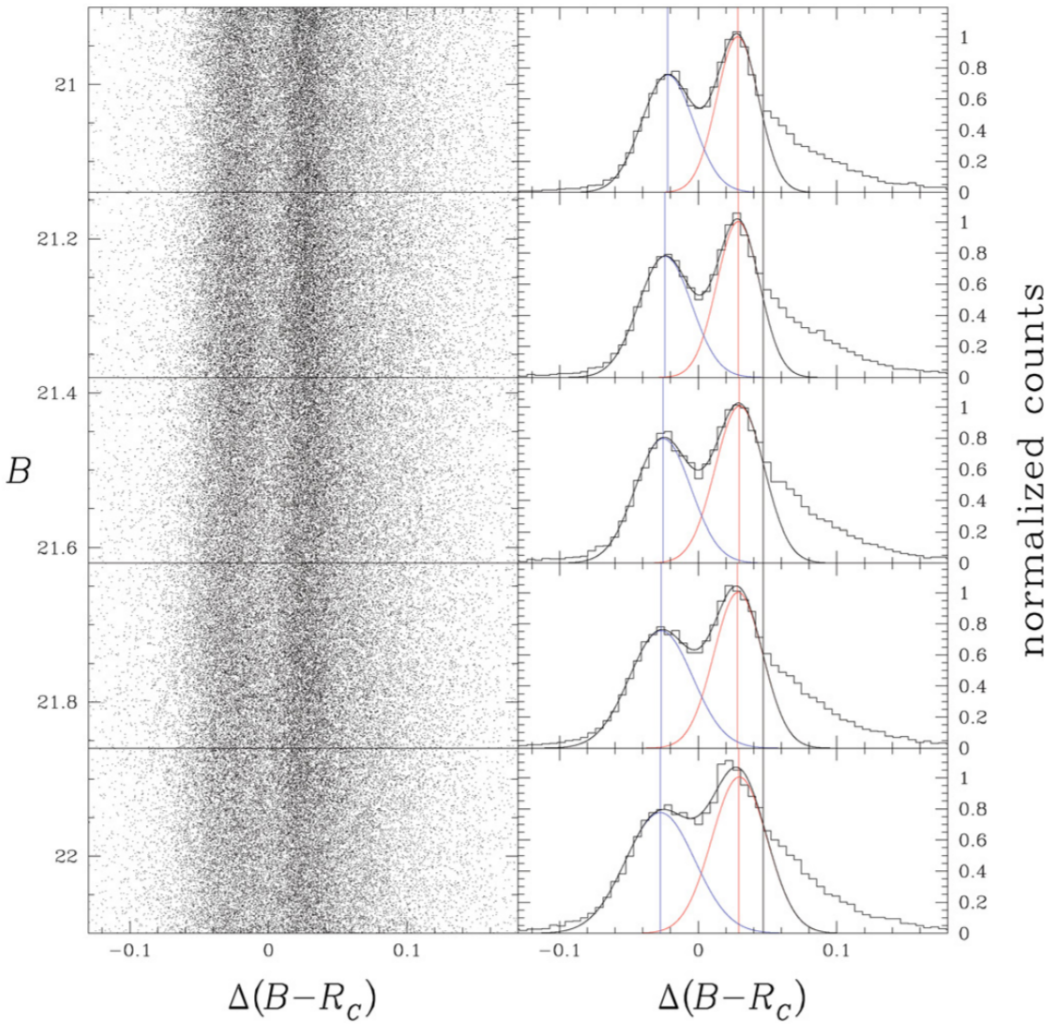

FIGURE 1.7: (B versus $\Delta(B-R_C)$ diagram verticalised for MS stars and divided into five magnitude intervals. On the right side is shown the $\Delta(B-R)$ histogram with the Gaussian best fit (see Bellini et al. 2009 for details). Adapted from Fig. 8 of Bellini et al. (2009).

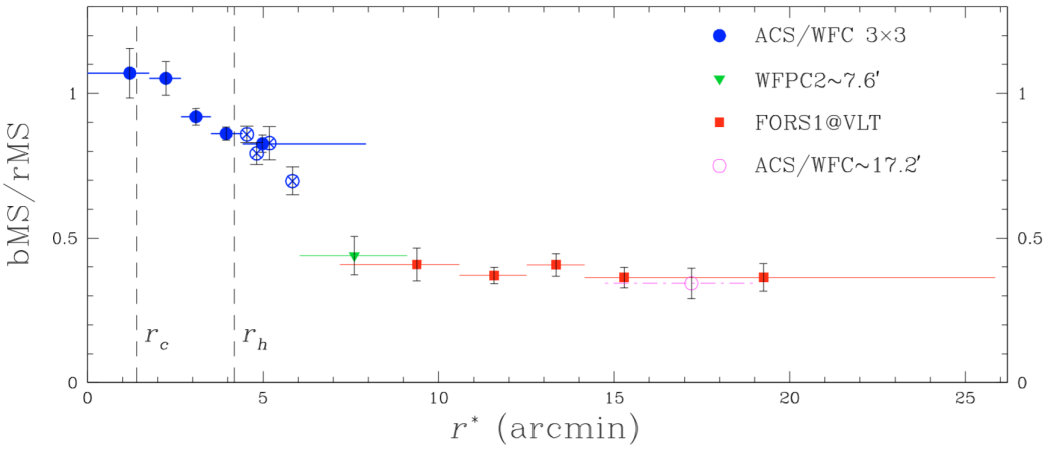

FIGURE 1.8: Number-count ratio of the two major groups of populations versus equivalent radius in ω Cen. Different colours and symbols refer to different data sets (see text for details). Dashed vertical lines mark the core radius and the half-mass radius. Adapted from Fig. 10 of Bellini et al. (2009).

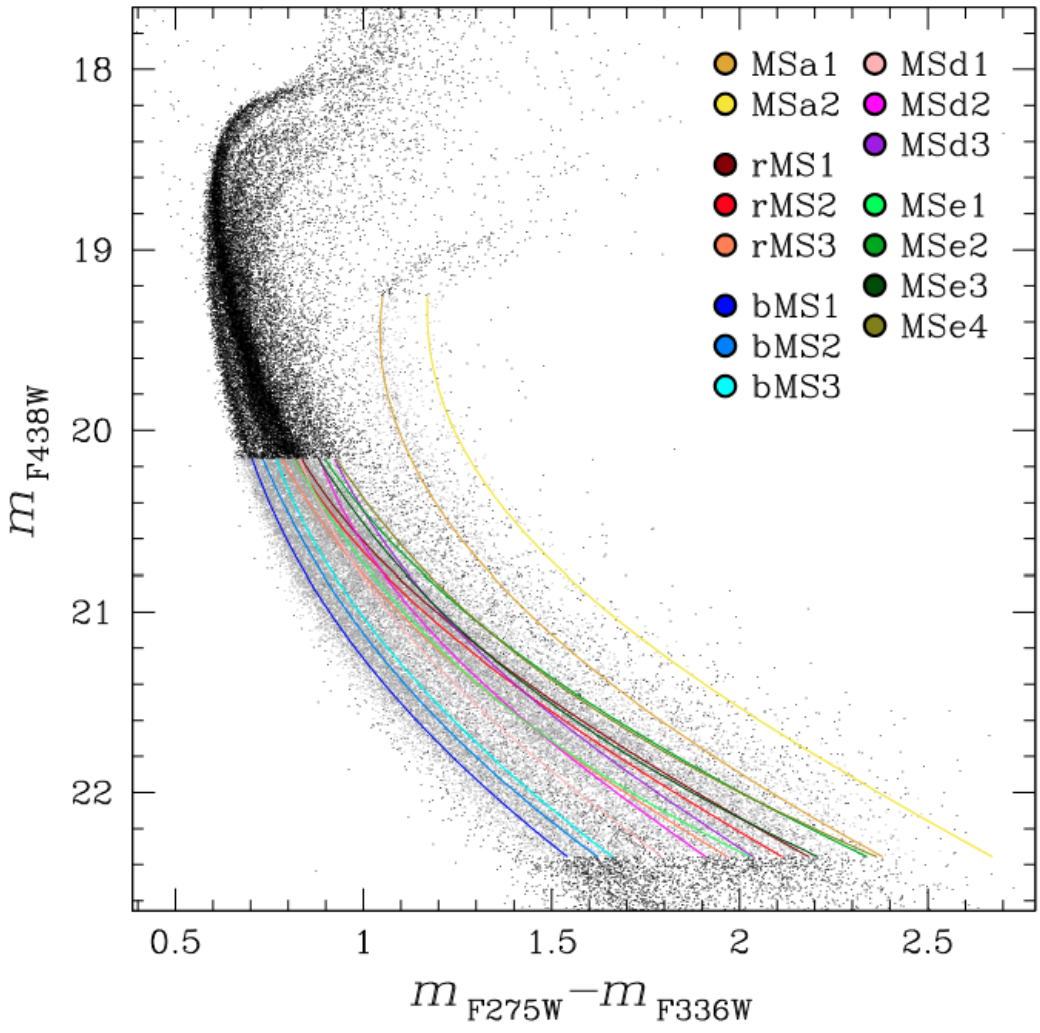

FIGURE 1.9: m_{F438W} versus $m_{F275W} - m_{F336W}$ CMD of ω Cen. Fiducial lines for each of the 15 subpopulations are color-coded accordingly. Adapted from Fig. 11 of Bellini et al. (2017d).

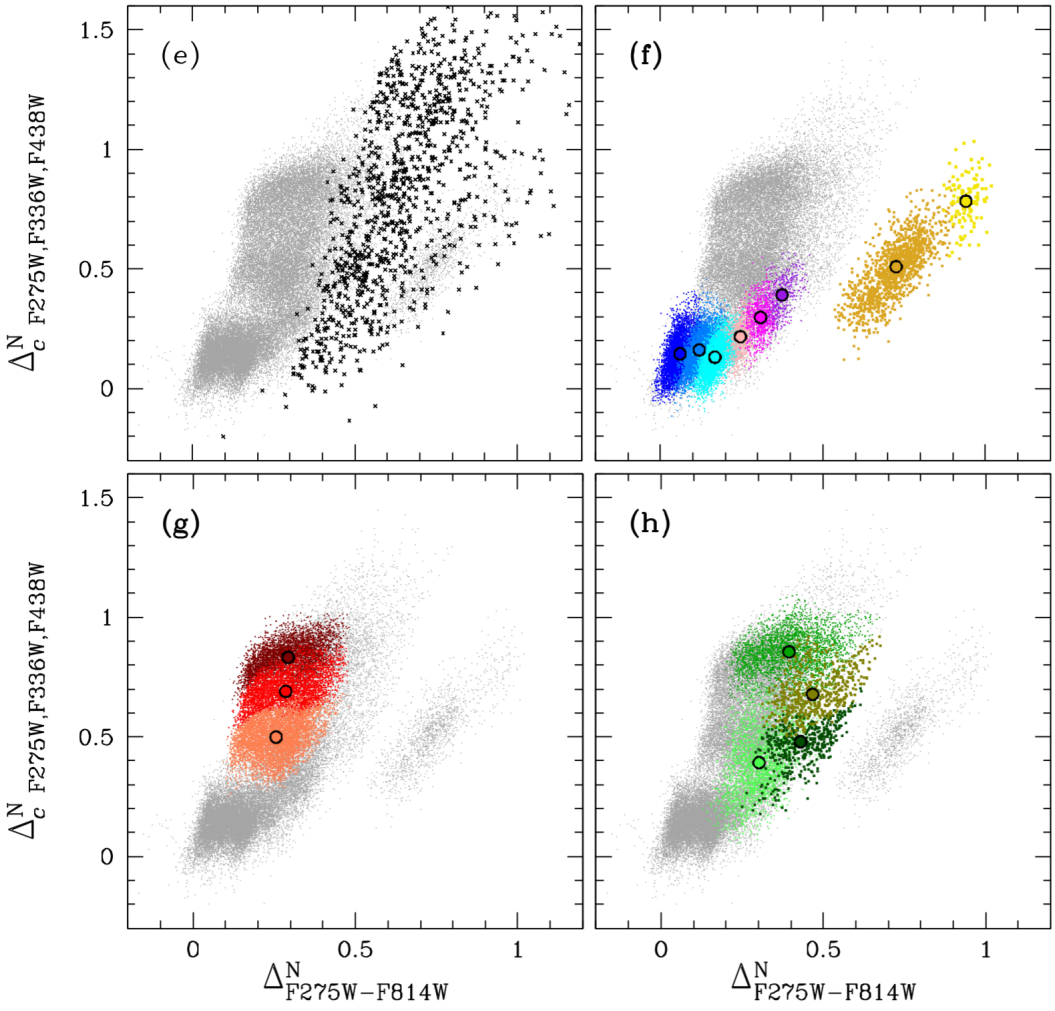

FIGURE 1.10: $\Delta^N_{CF275W,F336W,F438W}$ versus $\Delta^N_{F275W-F814W}$ ChM for the MS stars of ω Cen within $20.16 \leq m_{F438W} \leq 22.36$ (see Bellini et al. 2017d for details). In each panel, gray points represent MS single stars. Selected binary stars are only shown in black in the upper-right panel, for reference. Stars are colour-coded according to their sub-groups with the same colour-coded used in Fig. 1.9. The barycenter of each of the 15 known sub-populations is also marked with a solid circle. Adapted from Fig. 10 of Bellini et al. (2017d).

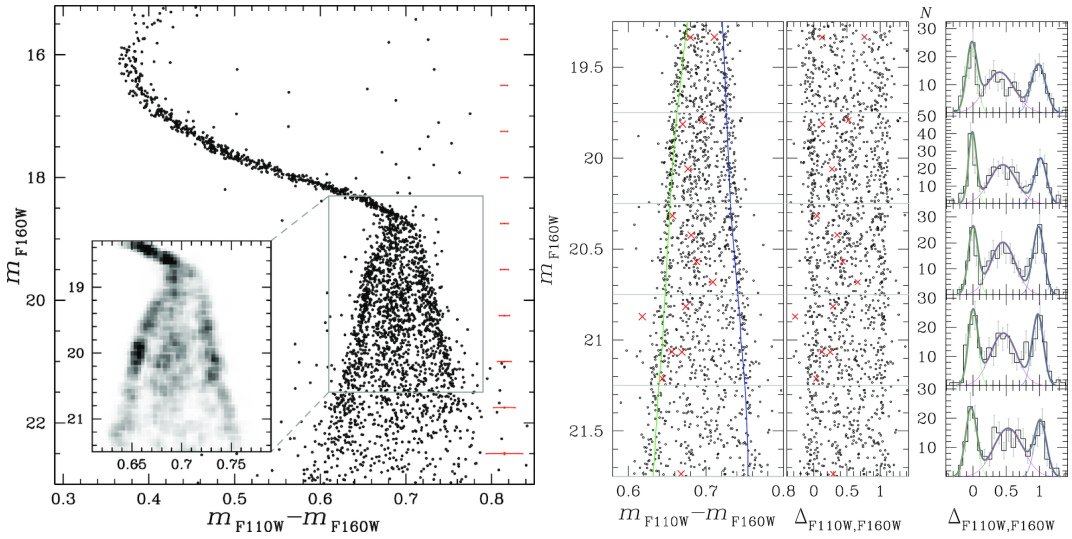

FIGURE 1.11: *Left panel*: NIR CMD of NGC 6752 from Milone et al. (2019). The Hess diagram highlights the region of the CMD where the three sequences are more evident. *Right panel*: procedure used in Milone et al. (2019) to estimate the fraction of MS-A, MS-B, and MS-C stars with respect to the total number of MS stars. The left sub-panel is a zoom of the CMD plotted in the *left panel* in the region where the three MSs are more clearly distinguishable. The green and blue lines are the fiducials of MS-A and MS-C, respectively, and are used to derive the verticalized m_{F160W} versus $m_{F110W} - m_{F160W}$ CMD plotted in the middle sub-panel. Right sub-panels show the $\Delta_{F110W,F160W}$ histogram distribution of cluster stars in the five luminosity intervals indicated by the grey lines plotted in the left and middle sub-panels. The grey tick lines overimposed on each histogram are the best-fitting three-Gaussian functions, whose components are represented with thin green, magenta, and blue lines. Adapted from Fig. 1 and 4 of Milone et al. (2019).

right panel of Fig. 1.11 outlines the procedure employed to estimate the fraction of MS-A, MS-B, and MS-C stars relative to the total number of MS stars. The left sub-panel provides a zoom of the CMD presented in the left panel of Fig. 1.11, focusing on the region where the three MSs are most distinguishable. The green and blue lines represent the fiducials of MS-A and MS-C, respectively, and are used to generate the verticalized m_{F160W} versus $m_{F110W} - m_{F160W}$ CMD shown in the middle sub-panel. The right sub-panel displays the $\Delta_{F110W,F160W}$ histogram distribution of cluster stars in the five luminosity intervals indicated by the grey lines in the left and middle sub-panels. The grey-tick lines overlaid on each histogram are the best-fitting three-Gaussian functions, with components represented by thin green, magenta, and blue lines. Clearly, the fractions of MS-A, MS-B, and MS-C stars are similar in the five magnitude intervals. Furthermore, MS-B exhibits greater broadening than MS-A and MS-C, indicating that its stars are not chemically homogeneous.

1.8 The role of this thesis

In this thesis, we expand the exploration of the mPOPs phenomenon by using *HST* photometry. Our investigation focused on two previously introduced GCs: ω Cen and NGC 6752. The thesis covers a broad spectrum of topics, ranging from the kinematic study within globular clusters and their multiple stellar populations to the examination of ultracool dwarf populations and the white dwarf sequence. Additionally, we focused on the investigation of the mass and luminosity functions of globular clusters and their multiple stellar populations, along with the study of Hα emitters in globular clusters.

A crucial and central aspect of this thesis is dedicated to studying the radial gradient of the mPOPs of ω Cen. For this project, I have obtained observational time with *HST* (PI: Scalco). As outlined earlier, the most comprehensive study of the radial distributions of multiple populations in ω Cen was conducted by Bellini et al. (2009), which identified a trend in the counts-number fraction of the two main populations (bMS/rMS), varying with the distance from the centre of the cluster. However, the investigation made by Bellini et al. (2009) is limited as they studied only the radial gradient of the two major population groups since they could not utilize CMDs to separate the (at least) 15 sub-populations identified by Bellini et al. (2017d). The resulting gradient is, therefore, just an average of the radial properties of the several sub-populations contained within each of the two major groups.

This thesis aims to extend the work initiated by Bellini et al. (2009), replacing CMDs with the powerful tool of the ChMs to separate and identify the sub-populations present within ω Cen. This work is a combination of data from my *HST* programme (PI: Scalco), archival *HST* data, and the results already published in Bellini et al. (2017d).

The radial variation of the ChMs needs to be studied continuously, particularly in the region where Bellini et al. (2009) found the strongest gradient, at least for some of the population components. In this context, the two fields observed under my *HST* programme are of fundamental importance as they are at a critical distance, where Bellini et al. (2009) identified the strongest gradient.

The results of this work promise to open a new window in the study of ω Cen and its mPOPs, offering crucial information for future theoretical investigations.

The structure of the thesis is outlined as follows:

the first part of the thesis is dedicated to ω Cen; Chapters 2 and 3 provide an overview of the data set and data reduction processes conducted on three external fields of ω Cen.

Chapter 4 discusses the data reduction of the observations from my *HST* program and investigates the radial gradient of the multiple stellar populations in ω Cen.

Chapter 5 presents a comprehensive analysis of the Hα emitters in ω Cen,

Chapter 6 delves into a study of rotation mass relation in globular clusters, focusing in three globular clusters, 47 Tuc, ω Cen and M 5.

The second part of the thesis is dedicated to NGC 6752; Chapter 7 offers a detailed kinematic study of NGC 6752 and its multiple stellar populations.

Chapter 8 explores the multiple stellar populations at low masses in NGC 6752, including their luminosity and mass function.

Chapter 9 focuses on examining the white dwarf (WD) cooling sequence (CS) of NGC 6752, while Chapter 10 conducts a thorough search for variable stars and transits in NGC 6752.

Finally, Chapter 11 offers concluding remarks and a brief summary of the findings obtained throughout this thesis.

Chapter 2

The *HST* large programme on ω Centauri – Catalogue of two external fields

In this chapter, we present the state-of-the-art catalogue and atlases for the two remaining parallel fields observed with the *Hubble Space Telescope* for the large programme on ω Centauri. These two fields are located at $\sim$12′ from the centre of the globular cluster (in the West and South-West directions) and were imaged in filters from the ultraviolet to the infrared. Both fields were observed at two epochs separated by about 2 years that were used to derive proper motions and to compute membership probabilities. The material discussed in this Chapter has been published in Monthly Notices of the Royal Astronomical Society (MNRAS; Scalco et al. 2021).

2.1 Introduction

The "*Hubble Space Telescope* (*HST*) large program of ω Centauri" (GO-14118 + GO-14662, PI: Bedin, L. R.) aims at observing the white dwarf (WD) cooling sequence (CS) for the stars of this Galactic globular cluster (GC) down to the faintest WDs. These observations aim to better characterize the multiple WD CSs discovered within this cluster (Bellini et al., 2013) and to investigate the connection between the WD CSs with the well-known main sequence (MS) multiple populations (mPOPs) (Bedin et al. 2004, Villanova et al. 2007, Bellini et al. 2009; Bellini et al. 2010; Bellini et al. 2017d; Bellini et al. 2018, Marino et al. 2011, Milone et al. 2017a) and the cluster Helium enhancement (Norris 2004, King et al. 2012).

The primary data-set of the program includes observations of a primary field (hereafter, field F0) obtained with the Wide-Field Channel (WFC) of the Advanced Camera for Surveys (ACS), located about 12′ from the cluster's centre. F0 is the only field that is sufficiently deep to reach the faintest theoretically detectable WDs in the cluster. In order to de-contaminate the fields from background and foreground objects, the pair of programs (GO-14118 and GO-14662) was designed to obtain observations at two epochs. For each epoch, the main field F0 was observed in 66 orbits and at 3 different orientations (22 orbits each), with the aim of minimizing the impact of imperfect Charge Transfer Efficiency (CTE) correction, imperfect calibrations, and systematic errors.

Given that specific orientations are available only at different epochs of the year, *de facto*, each of the three orientations is a sub-epoch for the main F0 field, but it also

places the parallel observations in three additional and different fields. These parallel fields were taken with the Wide-Field-Camera 3 (WFC3) in both the Ultraviolet-Visible (UVIS) channel (8 orbits per epoch per field) and in the Infrared (IR) channel (14 orbits per epoch per field).

These three parallel fields (hereafter referred to as F1, F2, and F3) were collected with the purpose of studying, through different approaches, the mPOPs in stars at different evolutionary phases and at different radial distances from the cluster centre. Parallel fields were observed with different filters in order to have a wider colour baseline to identify and better separate the different mPOPs within ω Centauri (hereafter, ω Cen).

The exposures from the parallel field F1 were reduced and presented in the three publications: the mPOPs at very faint magnitudes were analysed by Milone et al. (2017a) (Paper I). Bellini et al. (2018) (Paper II) analysed the internal kinematics of the mPOPs, complementing our GO14118 + GO-14662 data with archival images collected more than 10 yrs earlier under *HST* programs GO-9444 and GO-10101 (on both PI: King). Finally, Libralato et al. (2018b) (Paper III) presented the absolute proper motion estimate for ω Cen in our field F1.

In this Chapter, we present the catalogue and the atlases for the two remaining WFC3 parallel fields, F2 and F3. Our new catalogue provides multi-band photometry, proper motions (PMs), and membership probabilities for all sources detected in our fields; the atlases are high-resolution FITS images, with headers containing the astrometric solutions with keywords in the World Coordinate System (WCS).

This Chapter is organised as follows: Section 2.2 is dedicated to the description of the data; Section 2.3 briefly outlines the data reduction process; Section 2.4 presents some of the colour-magnitude diagrams obtained; Section 2.5 describes the PM measurements and the methodology to estimate membership probability; in Section 2.6, we describe in detail the content of the data released tables. Finally, in Section 2.7 we briefly summarize the key results, indicating potential immediate future uses of this catalogue and also identify our own upcoming scientific investigations that will make use of it.

2.2 Data set

Fields F2 and F3 were observed in 2016 (GO-14118) and 2018 (GO-14662), using both channels of the WFC3. In each epoch, data were collected with the UVIS channel in five filters (F275W, F336W, F438W, F606W, and F814W) and with the IR channel in two filters (F110W and F160W). Table 2.1 reports the complete list of *HST* observations of fields F2 and F3 for each epoch.

Figure 2.1 shows the locations of the GO-14118 and GO-14662 fields (F0 to F3), superimposed on an image from the Digital Sky Survey (DSS)[1]. The primary ACS/WFC field (F0) is shown in azure, while the three parallel WFC3 fields (F1 to F3) are plotted in pink. For reference, we also show the central field (in yellow) analysed in Bellini et al. (2017b), Bellini et al. (2017c), and Bellini et al. (2017d). The GO-14118 and GO-14662 fields cover a radial extent from $\sim 2\,r_{\rm h}$ to $\sim 4\,r_{\rm h}$ (being $r_{\rm h} = 5\farcm00$ the half-light radius, Harris 1996). In this chapter, we consider only data for fields F2 and F3 (both circled in green).

[1] https://archive.eso.org/dss/dss

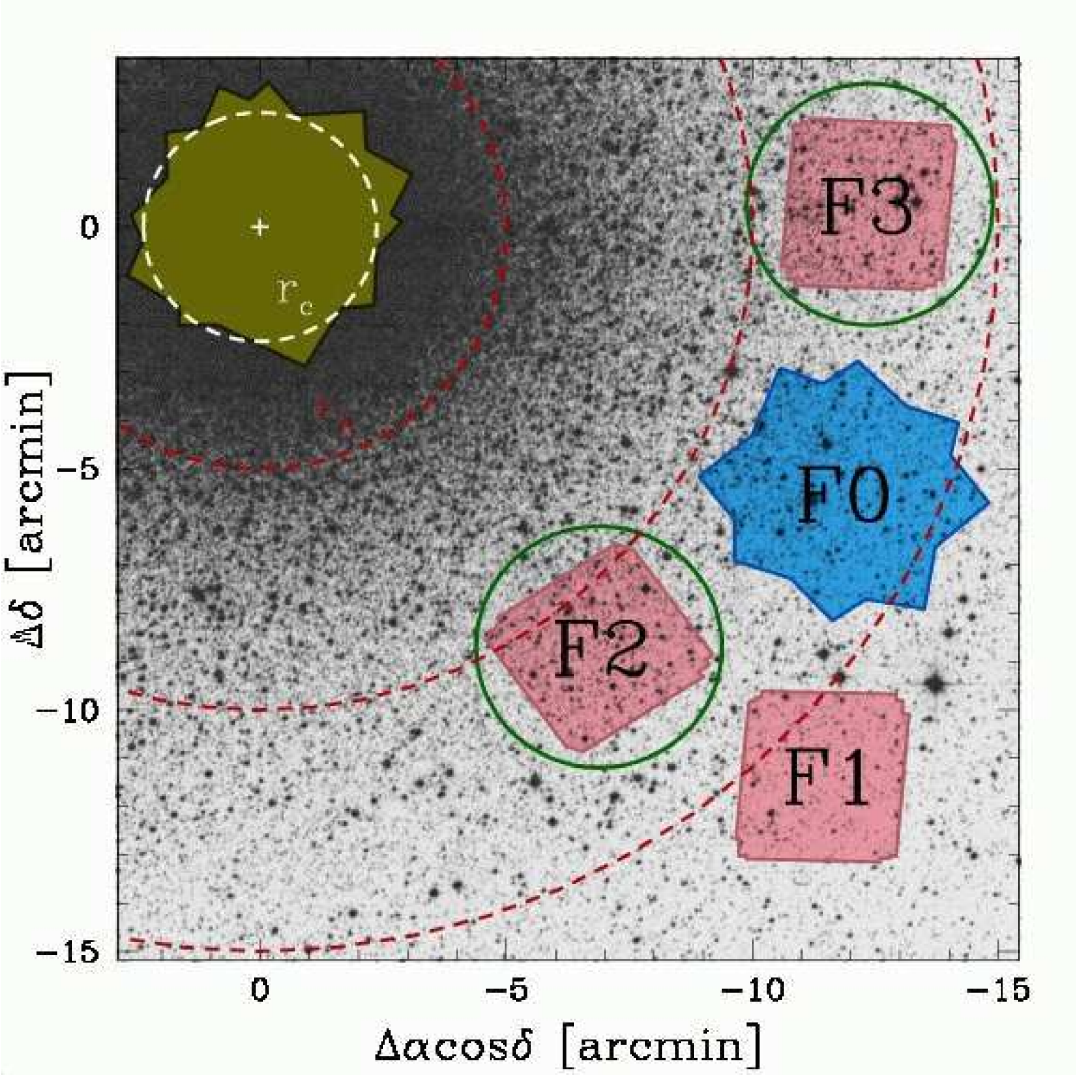

FIGURE 2.1: Outlines of the fields observed in *HST* programs GO-14118 + GO-14662, superimposed on a DSS image of ω Cen. The primary ACS/WFC field (F0) is in azure, while the three parallel WFC3 fields are shown in pink. We also show, in yellow, the central field presented in Bellini et al. (2017b), Bellini et al. (2017c), and Bellini et al. (2017d). Units are in arcmin measured from the cluster centre. The data discussed in this chapter come from fields F2 and F3, which are marked with green circles. The white and red dashed circles mark the cluster's core radius ($r_c = 2'.37$), the half-light radius ($r_h = 5'.00$), at $2\,r_h$ and $3\,r_h$, respectively, from the centre.

TABLE 2.1: List of *HST* Observations of Fields F2 and F3.

Field F2		
Filter	Exposures	Epoch
	Epoch 1 (GO-14118)	
	WFC3/UVIS	
F275W	4×1328 s	2016/07/01-05
F336W	4×1230 s	2016/07/01-05
F438W	4×98 s	2016/07/01-05
F606W	2×99 s + 2×1255 s + 2×1347 s	2016/06/30-07/04
F814W	2×98 s + 2×1253 s + 2×1345 s	2016/06/27-07/04
	WFC3/IR	
F110W	7×143 s + 14×1303 s	2016/06/24-07/04
F160W	7×143 s + 14×1303 s	2016/06/27-07/05
	Epoch 2 (GO-14662)	
	WFC3/UVIS	
F275W	1×1240 s + 3×1243 s	2018/06/30-/07/01
F336W	4×1157 s	2018/06/30-/07/01
F438W	4×104 s	2018/06/30-/07/01
F606W	2×104 s + 2×1186 s + 2×1266 s	2018/06/30
F814W	2×104 s + 2×1186 s + 2×1266 s	2018/06/28
	WFC3/IR	
F110W	7×143 s + 14×1203 s	2018/06/24-07/01
F160W	7×143 s + 14×1203 s	2018/06/27-30
Field F3		
Filter	Exposures	Epoch
	Epoch 1 (GO-14118)	
	WFC3/UVIS	
F275W	4×1328 s	2016/01/31
F336W	4×1230 s	2016/01/31
F438W	4×98 s	2016/01/31
F606W	2×99 s + 2×1255 s + 2×1347 s	2016/01/30
F814W	2×98 s + 2×1253 s + 2×1345 s	2016/01/30-31
	WFC3/IR	
F110W	7×143 s + 14×1303 s	2016/01/30-02/04
F160W	7×143 s + 14×1303 s	2016/02/04-05
	Epoch 2 (GO-14662)	
	WFC3/UVIS	
F275W	4×1229 s	2018/01/30-31
F336W	4×1143 s	2018/01/30-31
F438W	4×104 s	2018/01/30-31
F606W	1×95 + 1×104 s + 2×1172 s + 2×1252 s	2018/01/30
F814W	2×104 s + 2×1172 s + 2×1252 s	2018/01/30-31
	WFC3/IR	
F110W	7×143 s + 14×1203 s	2018/02/09-24
F160W	7×143 s + 14×1203 s	2018/02/20-25

2.3 Data Reduction

In this analysis, we used only `_flc`-type images (in units of e^-) for WFC3/UVIS, and `_flt`-type images (in units of e^-/s) for WFC3/IR, as they preserve the pixel data with its original sampling for stellar-profile fitting.

These `_flc`-type and `_flt`-type images are both corrected via standard calibrations (bias, flat field and dark); in addition, the `_flc`-type images are also corrected for CTE defects following the empirical approach described in Anderson and Bedin (2010).

2.3.1 First-Pass Photometry

We measure the stellar positions and fluxes in each exposure using the `FORTRAN` code `hst1pass`, which is a generalised version of the `img2xym_WFC` software package (Anderson and King, 2006). Starting from spatially-variable –but time-averaged– empirical Point Spread Function (PSF) libraries (e.g., Anderson and King 2006), the routine `hst1pass` runs a single pass of source finding for each exposure without performing neighbour subtraction. We perturbed the empirical PSF in order to find the best spatially variable PSF for each image. Stellar positions and fluxes are obtained by fitting each source with the obtained PSF. Stellar positions in each single-exposure catalogue are corrected for geometric distortion by using the state-of-the-art geometric-distortion corrections of Bellini, Anderson, and Bedin (2011) for WCF3/UVIS, and the publicly available WFC3/IR correction developed by J. Anderson (Anderson 2016, Instrument Science Report WFC3 2016-12, Appendix A) [2].

2.3.2 The Master Frame

For each field, we defined a common, pixel-based reference coordinate system, based on a WFC3/UVIS F814W single-exposure catalogue. Then, for the images taken in each filter, we used only bright, unsaturated, and well-measured stars to derive general six-parameter linear transformations to transform stellar positions – as measured in each individual exposure – onto the common reference frame system. The photometry of these preliminary catalogues was zero-pointed to the first long exposure taken in each filter/epoch.

2.3.3 Second-Pass Photometry

The second-pass photometry is performed through the `FORTRAN` software package `KS2`, which is based on `kitchen_sync`, originally designed to reduce specific ACS/WFC data (Anderson et al., 2008). The code `KS2`, also developed by J. Anderson, takes images, perturbed PSF arrays, and transformations obtained during the "first-pass photometry" stage to simultaneously find and measure stars in all of the individual exposures and for the entire set of filters. By relying on multiple exposures, `KS2` finds and measures faint stars that would be otherwise lost in the noise of individual exposures. A detailed description of Anderson's code is given in Bellini et al. (2017b) and Nardiello et al. (2018).

The star-finding procedure is accomplished through different passes of finding, moving progressively from the brightest to the faintest stars. During the initial star-finding pass, the software starts from a list of bright stars, available from the first-pass photometry, and constructs weighted masks around the bright stars, which

[2] Available at https://www.stsci.edu/ jayander/STDGDCs/

helps the software avoid PSF-related artefacts. Then, KS2 subtracts the bright stars. In the following pass, the routine searches for stars that are fainter than the stars from previous iteration, and then measures and subtracts them. In each successive iteration of finding, KS2 identifies stars that satisfy increasingly relaxed search criteria.

For this project, we chose to execute nine iterations of finding. To make the catalogue as similar as possible to that of the F1 field released by Bellini et al. (2018), we performed the star-finding using the F606W and F814W filters. In the first four iterations, we required that a star be present in the F606W and F814W long exposures. In the last pass, we focused on the short exposures to get KS2-derived photometry for the brighter stars.

KS2 has three approaches for measuring stars, each of which is best suited for stars in different magnitude regimes. The first method gives the best results for stars that are bright enough to generate a high signal-to-noise peak within its local 5×5 pixel, neighbour-subtracted raster. When that happens, the routine measures, in each image, the flux and the position of the source using an appropriate local PSF, after subtracting the neighbour stars. The local sky value is computed using the surrounding pixels in an annulus (between 5 and 8 pixels in radius), with the contributions of the neighbours and the star itself subtracted.

Methods two and three work best for faint stars and in crowded environments. In method two, starting from the position obtained during the finding stage, KS2 uses the PSF to determine a best-fit flux from the inner 3×3 pixels. Method three is similar, but it uses the brightest 4 pixels and weights them by the expected fraction of the PSF in those pixels. For a detailed description of the three methods, we refer to Bellini et al. (2017b) and Nardiello et al. (2018). We have verified that the photometry of the three methods for stars near the overlap magnitude regions is consistent.

Saturated stars are not measured by KS2. However, their position and fluxes are recovered from the first-pass photometry and supplemented in output. Our final photometric catalogue contains a total of 42,551 sources in both fields.

In addition to the astro-photometric catalogue, KS2 outputs stacked images obtained from the `_flc` and `_flt` exposures. For each field, we generated 11 different stacked images: one for the filters F275W, F336W, and F438W, and two for the filters F606W, F814W, F110W, and F160W, separating short- and long-exposure images. We make these stacked image pairs available with 1×1 and 2×2 pixel super-sampling.

Figure 2.2 shows the upper part of the m_{F814W} vs. $m_{\mathrm{F606W}} - m_{\mathrm{F814W}}$ colour-magnitude diagram (CMD). Black dots are unsaturated stars in both the F606W and F814W long exposures, while red crosses mark stars that are saturated in the long exposure in at least one filter and were not found in the short exposures. Finally, stars marked with blue circles are saturated in the long exposures but are found unsaturated in the short ones. Stars marked with green dots are stars saturated in at least one filter in the short exposures. Black dots and blue circles are stars deemed best-measured by method one in KS2, while the positions and the fluxes of the stars marked with red crosses and green dots are available through the first-pass photometry since saturated stars are not measured by KS2.

2.3.4 Photometric calibration

The photometry has been zero-pointed into the Vega magnitude system by following the recipe of Bedin et al. (2005a), Bellini et al. (2017b) and Nardiello et al. (2018). The process of zero-pointing *HST*'s photometry is based on the comparison between

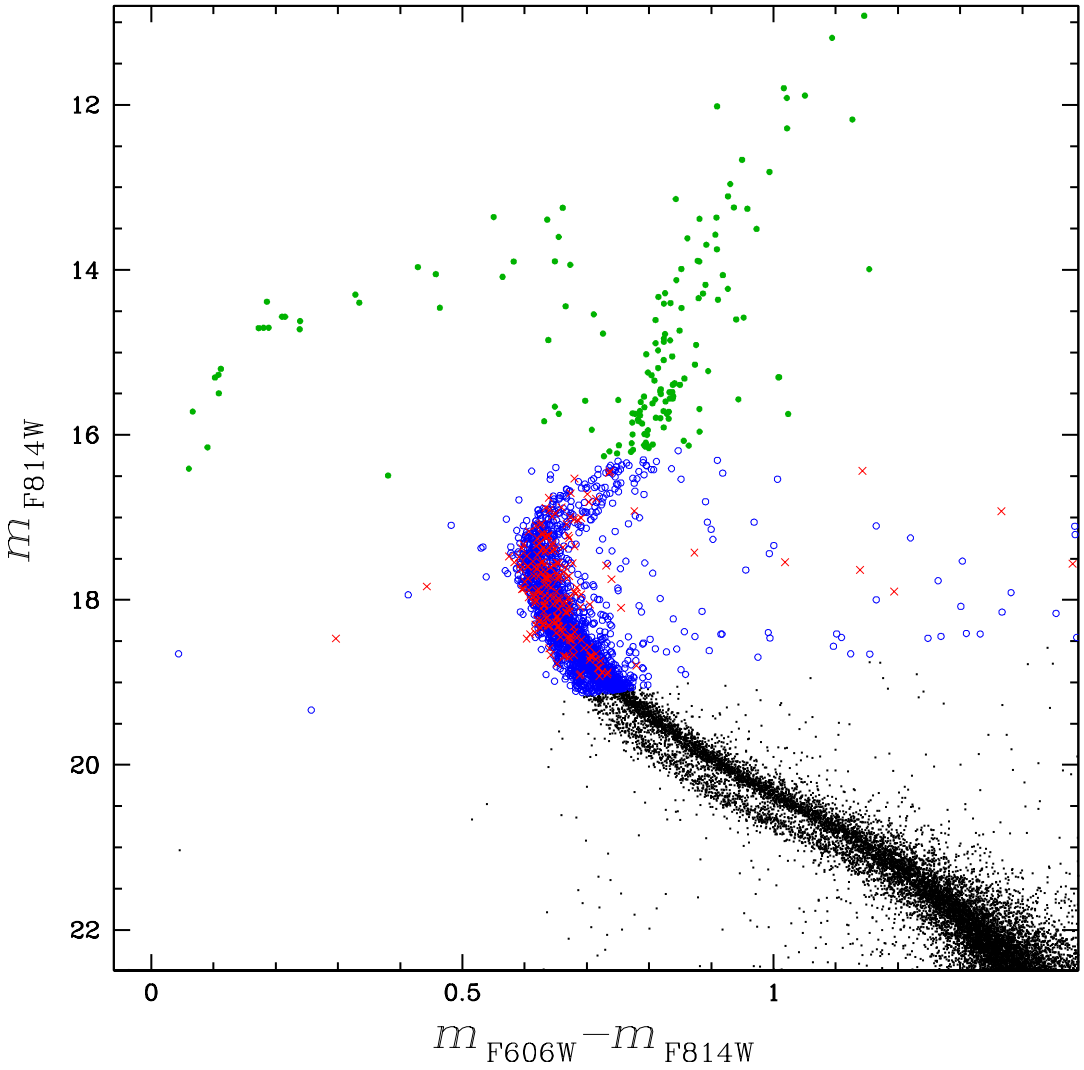

FIGURE 2.2: Bright part of the m_{F814W} vs. $m_{\mathrm{F606W}} - m_{\mathrm{F814W}}$ CMD. The unsaturated stars in the long exposures for both filters (black dots) and stars saturated in the long exposure but not in the short ones (blue circles) are directly measured by KS2. Red crosses represent stars that are saturated in at least one filter-long exposure and not measured in the short ones. Finally, green dots represent stars that are saturated in at least one filter short exposure. The fluxes of those stars are measured in the first-pass photometry.

TABLE 2.2: Photometric-calibration Zero Points

Filter	$< \delta m >$ (mag)	ZP(Vegamag) (mag)
	WFC3/UVIS	
F275W	$+7.5965 \pm 0.04$	$+22.737$
F336W	$+7.5371 \pm 0.04$	$+23.554$
F438W	$+4.8644 \pm 0.03$	$+24.999$
F606W	$+7.6494 \pm 0.07$	$+25.995$
F814W	$+7.6288 \pm 0.06$	$+24.684$
	WFC3/IR	
F110W	-0.0833 ± 0.01	$+26.042$
F160W	-0.0916 ± 0.02	$+24.662$

our PSF-based instrumental magnitudes and the aperture-photometry on `_drc` exposures (calibrated and resampled images normalized to 1 s exposure time). The calibrated magnitude $m_{\mathrm{CAL,X}}$ of a star in the filter X is given by:

$$m_{\mathrm{CAL,X}} = m^{\mathrm{flc}}_{\mathrm{PSF,X}} + \mathrm{ZP_X} + < \delta m >$$

where $m^{\mathrm{flc}}_{\mathrm{PSF,X}}$ is our instrumental PSF-based magnitude as measured on `_flc` (or `_flt` for the IR channel) exposures, $\mathrm{ZP_X}$ is the filter Vega-mag zero point and $< \delta m >$ is the median magnitude difference between $m^{\mathrm{drc}}_{\mathrm{AP(r,\infty)}}$, the aperture photometry measured on `_drc` (or `_drz`) exposures within a finite-aperture radius r but corrected to account for an infinite-aperture radius and our PSF-based instrumental magnitudes. $\mathrm{ZP_X}$ and the encircled energy fractions as a function of r can be found on the WFC3 webpage[3] for tabulated wavelengths.

Since the two fields are crowded, we used only bright, unsaturated stars for the photometric calibration. For this reason, we made use of the photometry obtained with the method one, which is best suited for bright stars.

We measured the `_drc` (`_drz`) aperture photometry of bright, relatively isolated, and unsaturated stars by using an aperture value of 10 and 3 pixels (0.4 arcsec) for UVIS and IR, respectively. Each of these measurements was then corrected for the finite aperture. For each filter, we cross-identified stars in common between the `_drc`-based aperture photometry and our `KS2` method-one photometry. For each measurement, we then computed the 2.5σ-clipped median values $< \delta m > = m^{\mathrm{drc}}_{\mathrm{AP(r,\infty)}}$ - $m^{\mathrm{flc}}_{\mathrm{PSF,X}}$.

Finally, we verified that the photometric zero-points evaluated by using methods 2 and 3 are consistent with the values obtained with method 1. Therefore, we apply the calibration correction obtained for method one to the other two methods. Table 2.2 summarizes the aperture-correction $< \delta m >$ values obtained for each filter, together with the respective Vega-mag zero points from the STScI website.

2.3.5 Astrometry

We cross-reference the stars in our catalogue with the stars in the Gaia early Data Release 3 (Gaia eDR3; Gaia Collaboration et al. 2021). Gaia's positions were evolved to the observed epochs. We found about 3,200 sources in common, which were used to anchor our positions (X,Y) to the Gaia eDR3 absolute astrometric system. As such,

[3] https://www.stsci.edu/hst/instrumentation/wfc3/data-analysis/photometric-calibration

the positions are referred to the reference epoch of Gaia catalogue, 2016.0, which is in the International Celestial Reference System (ICRS).

2.3.6 Quality parameters

In addition to positions and fluxes, KS2 provides other diagnostic parameters, such as the RMS of the individual-exposure photometry measurements. This latter is useful when selecting the best-measured stars in investigations that require high-precision stellar evolutionary sequences in CMDs.

The quality-of-fit (QFIT) parameter informs about the accuracy of the PSF-fitting during the measurements of the position and the flux of a star. The closer to unity the QFIT is, the more a source resembles the adopted PSF model. This parameter allows us to distinguish between stars that are isolated and/or well-measured and other sources for which the light profiles are not accurately fit by the PSF (cosmic rays, hot pixels, extended sources, blends, etc).

The "o" parameter is defined as the initial (i.e., before neighbour subtraction) ratio of the light within the fitting radius due to nearby neighbours to the light of the star. Since neighbour subtraction is never perfect, and it is hard to measure faint stars surrounded by much brighter sources, the photometry of sources with large values of the "o" parameter is likely less accurate.

The parameter RADXS (Bedin et al., 2008) is a shape parameter that measures how much the deviation of the PSF shape is from the predictions by comparing the source flux just outside the PSF core and the flux expected from the PSF model. Galaxies have large positive values of RADXS, while objects sharper than the PSF, e.g. cosmic rays or hot pixels, have large negative values of RADXS.

Finally, KS2 also reports the number of images in which a star was found (N_f), and the number of good measurements of the star used to compute its average position and flux (N_g) (those consistent with the average, see Anderson et al. (2008) for further details).

2.4 Colour-magnitude diagrams

In Figure 2.3, we show an example of selection of well-measured stars using the quality parameters provided by KS2. Top and middle panels of Figure 2.3 show, respectively from the left to the right, the photometric errors σ, defined as the RMS divided by the square root of N_g, QFIT and RADXS as a function of F814W and F606W magnitudes obtained with method 1 (see Sect. 3). Similar plots can be made using method-2 and method-3 outputs. In this example, the selection criteria for parameters σ and QFIT are made by eye, arbitrarily defining a line (indicated in red) that separates the bulk of well-measured stars from the outliers. For the RADXS parameter, we selected all stars that satisfy the condition: $-0.05 <$RADXS$< +0.05$ (panels (c) and (f) of Figure 2.3).

The bottom panels of Figure 2.3 show the $m_{\rm F606W}$ vs. $m_{\rm F606W} - m_{\rm F814W}$ colour-magnitude diagram for the stars that pass the selection criteria in both filters (panel (g)) and for the stars that were rejected in at least one filter (panel (h)). From the CMDs, it is clear that many stars ($\sim 39\%$) with poor photometric quality are rejected with these tight selections.

Panel (a) of Figure 2.4 shows the full $m_{\rm F606W}$ vs. $m_{\rm F606W} - m_{\rm F814W}$ CMD obtained combining the best-measured stars of the three different photometric methods, selected using the selection procedure described above. No selection cuts were applied

to saturated stars. The three red lines define the regions within which stars are saturated in at least one filter, or for which photometry is obtained with one of the three methods. In panels (b)-(f), we show in detail the five regions that are outlined in panel (a) to provide an overview of specific evolutionary sequences. Clockwise from panel (b) to (f) we show the horizontal branch (HB), the red-giant branch (RGB), the sub-giant branch (SGB), the main sequence (MS) and the WD cooling sequences.

2.5 Proper motions

We computed the PMs using the technique developed by Bellini et al. (2014) and improved in Bellini et al. (2018) and Libralato et al. (2018b). This is an iterative procedure that treats each image as a stand-alone epoch and can be summarised in two main steps: (1) transforms the stellar positions of each exposure into a common reference frame by means of a six-parameter linear transformation; (2) fit these transformed positions as a function of the epoch with a least-square straight line. The slope of this line, computed after several outlier-rejection stages, is a direct measurement of the PM.

Following Bellini et al. (2018), we excluded from the PM analysis the UVIS F275W[4] and IR F110W and F160W exposures. This choice of excluding IR images from the PM analysis is motivated by three reasons. First, our finding is done in filters F814W and F606W of UVIS (see Sect. 3.3), which proved to have the greatest signals for both WDs and low MS stars, and most importantly because UVIS has the highest angular resolution to avoid blends. Second, the higher resolving power and pixel size of UVIS, with respect to IR (39.75 mas vs. 121mas), directly translates into a higher astrometric precision ($\sim$0.4 mas, Bellini, Anderson, and Bedin 2011 for UVIS, vs. $\sim$1.2 mas for IR, Anderson 2016). Third, as IR and UVIS images essentially map the very same epochs, IR would only have added noise to PM measurements, mainly due to its lower resolving power, exposing to blends in these relatively high crowded fields.

We made use of stellar positions as measured by `KS2`'s method 1, which is best suited to high-precision PM analyses. As a common reference frame, we used star positions from the Gaia eDR3 catalogue, around 3 arcmin centred on the two fields F2 and F3. We transformed the `KS2` method-1 stellar positions, which are based on a reference frame that was obtained from the catalogue of a single WFC3/UVIS F814W exposure, by means of a six-parameter linear transformation. We defined an initial set of unsaturated reference stars, using the parameters described in section 2.3.6 to remove the poorly-measured stars, and we selected the likely cluster members on the basis of their positions in the CMD. The PM fitting and data rejection was performed exactly as described in Bellini et al. (2014), which provides a detailed description of the PM extraction and outlier rejection.

We iterated the procedure a few times in order to refine the reference-star list and the PM measurements. At the end of each iteration, we improved the reference-star list by removing all objects that have a large PM error or for which the PM is not consistent with the cluster's mean motion. The outlier-rejecting iterations stop when the number of reference stars differs by less than 2 from one iteration to the next.

[4]Filters bluer than F336W are affected by large colour-dependent positional residuals with respect to the UVIS distortion solution (Bellini, Anderson, and Bedin, 2011), and they are not suitable for high-precision astrometry.

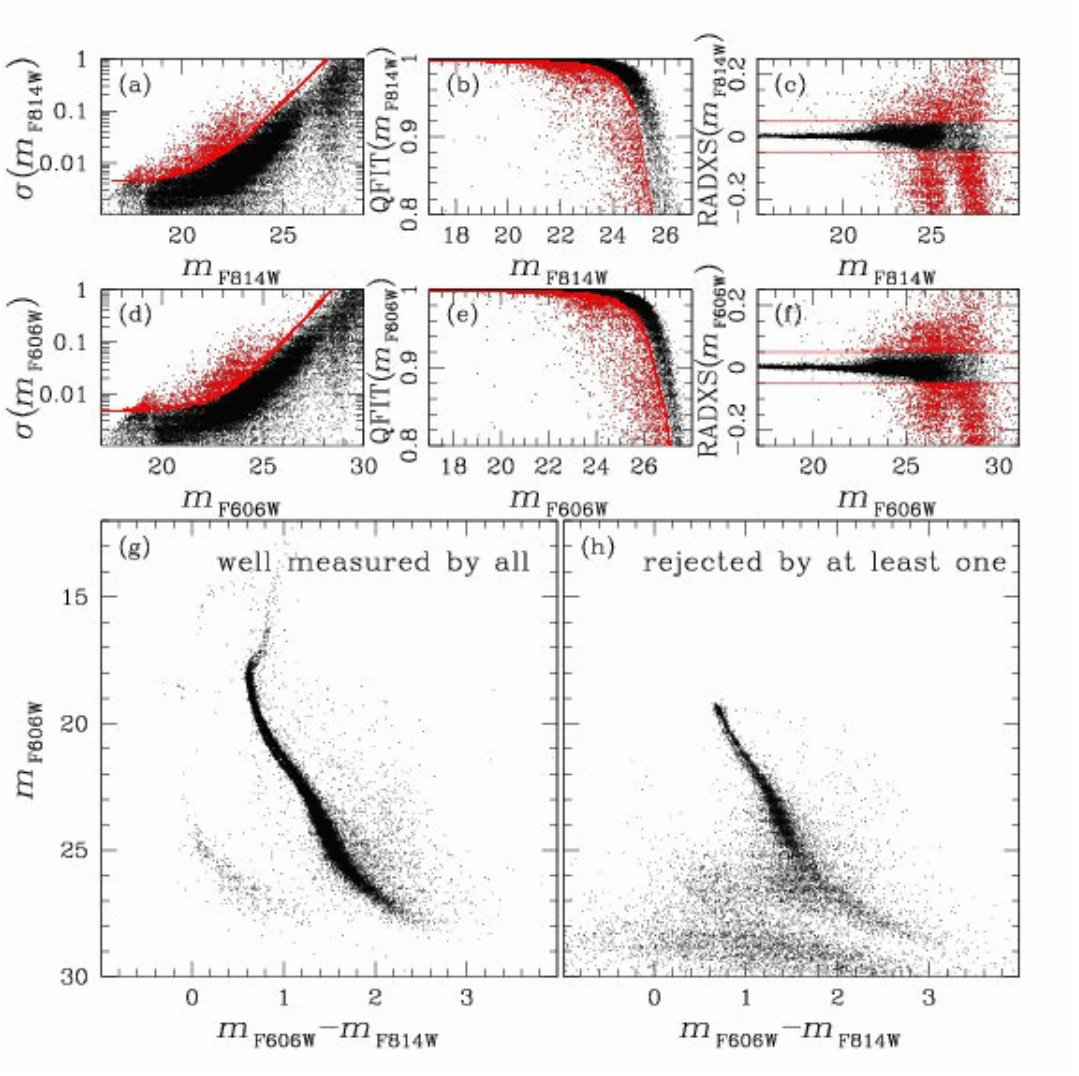

FIGURE 2.3: Effect of simple stellar selections based on σ, QFIT and RADXS. (a)-(c) Selection of the stars based on σ, QFIT and RADXS in function of the F814W magnitude. The red lines separate the bulk of those defined as well-measured stars from the outliers. The rejected stars are represented in red. (d)-(f) Analogues to (a)-(c) but for F606W photometry. (g) m_{F606W} vs. $m_{F606W} - m_{F814W}$ CMD of stars that are well measured according to all the 6 parameters. (h) Same CMD of (g) but of stars that are rejected by at least one filter.

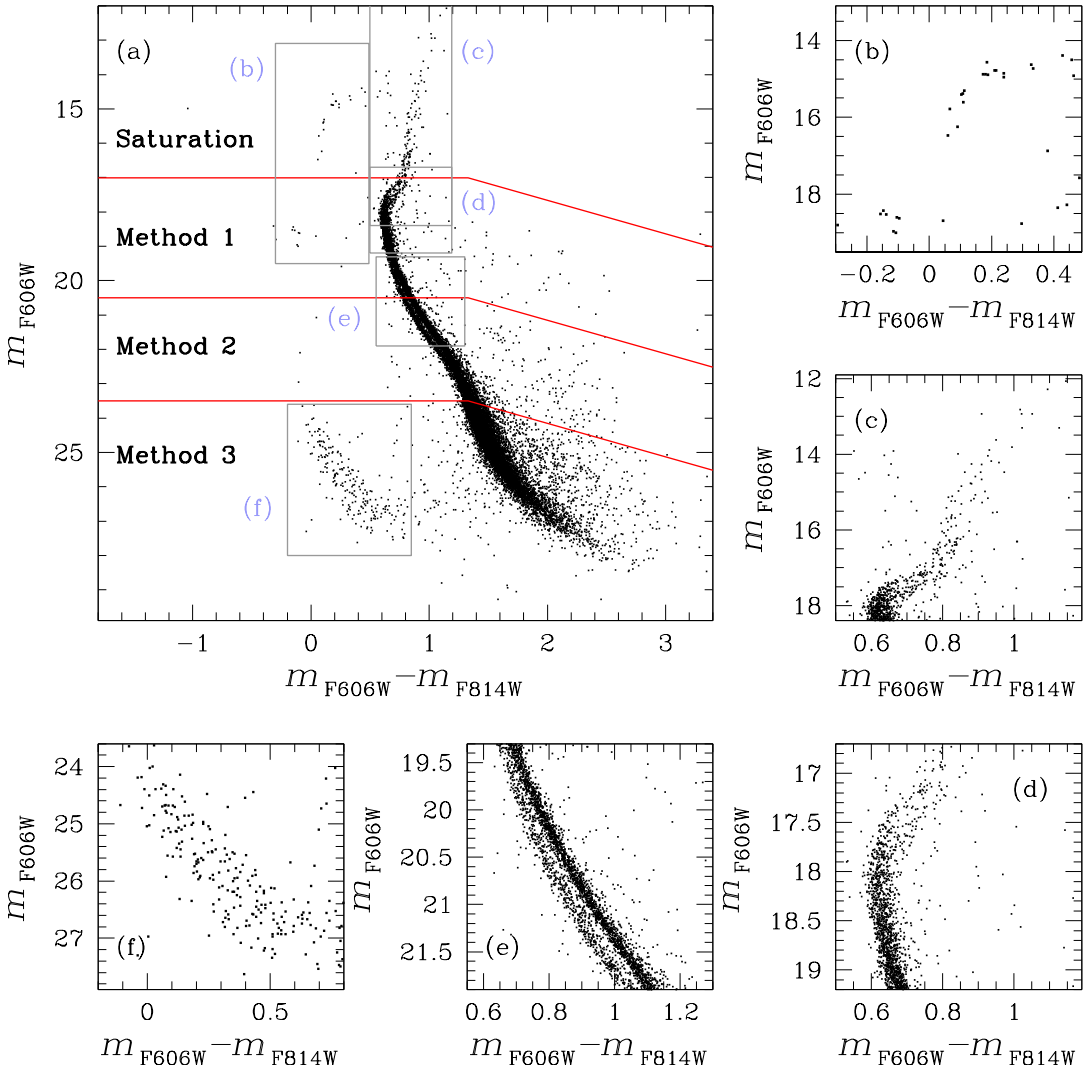

FIGURE 2.4: (a) Full m_{F606W} vs. $m_{F606W} - m_{F814W}$ CMD of ω Cen obtained by combining the best stars measured in the three photometric methods (see section 2.3.3). The transition between each photometric method is highlighted by red lines. All saturated stars are shown, with no selection. (b)-(f) Detail of the five regions that are outlined in (a). Moving clockwise, the panels show: (b) the HB, (c) the RGB, (d) the SGB, (e) the MS and (f) the WD cooling sequence.

While for field F1 Bellini et al. (2018) made also use of archival data collected several years earlier within *HST* programs GO-9444 (PI: King, I. R.) and GO-10101 (PI: King, I. R.), here for fields F2 and F3, we have only the two epochs of GO14118 and GO14662, just ∼2 years apart. Therefore our considerably shorter time-baseline (∼2 yr vs. ∼15 yr) directly translates into a proportionally inferior PM precision as compared with Bellini et al. (2018).

The initial master list contained 42551 sources, 27885 (∼65%) of which had high-precision PMs. The missing 14666 sources were rejected at different iteration stages. Our final catalogue is provided with the same set of quality and diagnostic parameters described in Bellini et al. (2014).

Systematic errors in the PMs were corrected following the prescription of Bellini et al. (2014) and Bellini et al. (2018). Figure 2.5 and 2.6 illustrate the correction procedure for fields F2 and F3 respectively.

We started by selecting likely cluster members on the basis of their position on the PM diagram (within 1.5 mas yr^{-1} from the bulk distribution) and rejecting all sources with a large PM error. Local PM corrections were applied as described in Section 7.4 of Bellini et al. (2014). In brief, systematic errors were mitigated "*a posteriori*", locally correcting the PM of each star according to the 2.5σ-clipped median value of the closest likely cluster members and within 0.5 $m_{\rm F606W}$ magnitudes from the target star (excluding the target star itself).

Panels (e) and (f) show the maps of the local median values obtained with the uncorrected (raw) components of the motion: $\Delta\mu_\alpha \cos\delta$ in panels (e) and $\Delta\mu_\delta$ in panels (f). Each point is a source, colour-coded according to its locally averaged PM value, as shown on the colour bar on the right-hand side of panels (e). Panels (g) and (h) show similar maps after the high-frequency variations are corrected. Points are colour-coded using the same colour scheme as panels (e) and (f).

We verified that after the correction, neither component of the corrected PM suffers from systematic effects due to stellar colour (panels (a) and (b)) and luminosity (panels (c) and (d)), dividing the stars into bins of fixed size in colour and magnitude, and evaluating the 3σ-clipped median value of the motion along $\Delta\mu_\alpha \cos\delta$ and $\Delta\mu_\delta$. The lack of systematic effect is clearly visible in panels (a), (b), (c) and (d), where the computed median values are shown as a red filled circles, with error bars.

The quantities $\Delta\mu_\alpha \cos\delta$ and $\Delta\mu_\delta$ are in units of mas yr^{-1} in all the panels. The associated errors of the mean are typically smaller than the size of the red circles. As a reference, the red horizontal line shows the lack of systematic effects.

Panel (i) shows the PM diagram after the *a posteriori* correction. Since our reference list consists of cluster members, our PMs are relative to the cluster mean motion, and cluster members are represented by the bulk in the centre of the PM diagram. All other sources are foreground and background field sources. Finally, panel (j) shows PM errors as a function of the $m_{\rm F606W}$ magnitude.

2.5.1 Membership probability

To derive the membership probability, we followed a method based on PMs described by Balaguer-Núnez, Tian, and Zhao (1998), Bellini et al. (2009) and Nardiello et al. (2018). The density function of cluster and field stars is modelled with an axisymmetric 2D Gaussian distribution centred respectively on the origin of the vector-point diagram (VPD; since PMs are computed relative to the cluster's bulk motion) and on the field proper motion centre. Cluster and field stars were selected on the basis of their position on the VPD. For each target star, the membership probability

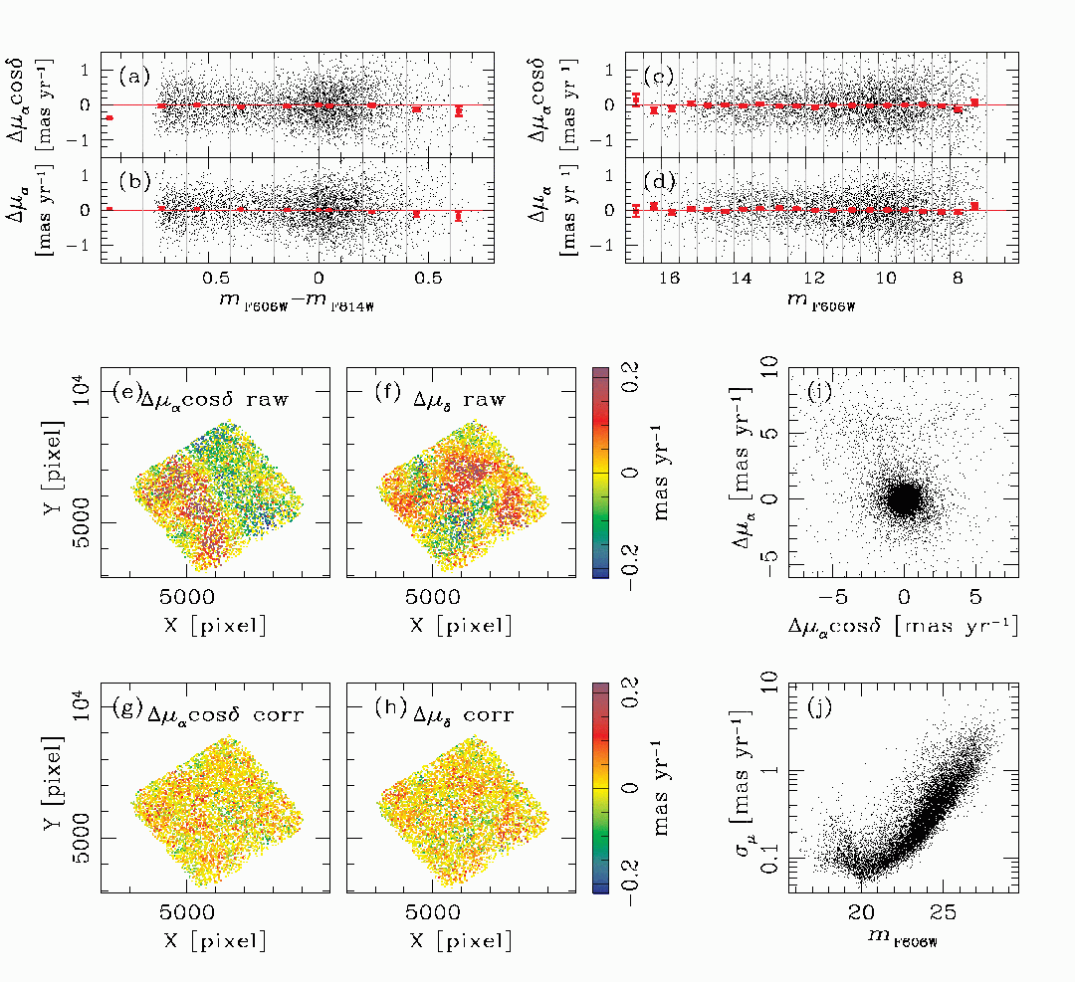

FIGURE 2.5: This figure illustrates the *a posteriori* procedure applied to the raw PM measurement for field F2. Panels (a) and (b) show that corrected PMs (in units of mas yr^{-1}) do not suffer from systematic effects as a function of stellar colour. Similarly, panels (c) and (d) show that corrected PMs do not suffer from systematic effects as a function of stellar magnitude. In panels (e) and (f) we report the maps of the locally measured mean raw PM components of cluster members. Specifically, the deviation along $\mu_\alpha \cos\delta$ is in panel (e), and the deviation along μ_δ is in panel (f). Each star is colour-coded according as shown by the vertical bar on the immediate right of panel (f). Panels (g) and (h) show the maps of the locally measured mean corrected PM of cluster members. We applied the same colour scheme as in panels (e) and (f). Panel (i) shows the corrected proper motion diagram. Finally, panel (j) shows the corrected proper motion error in function of the F606W magnitude.

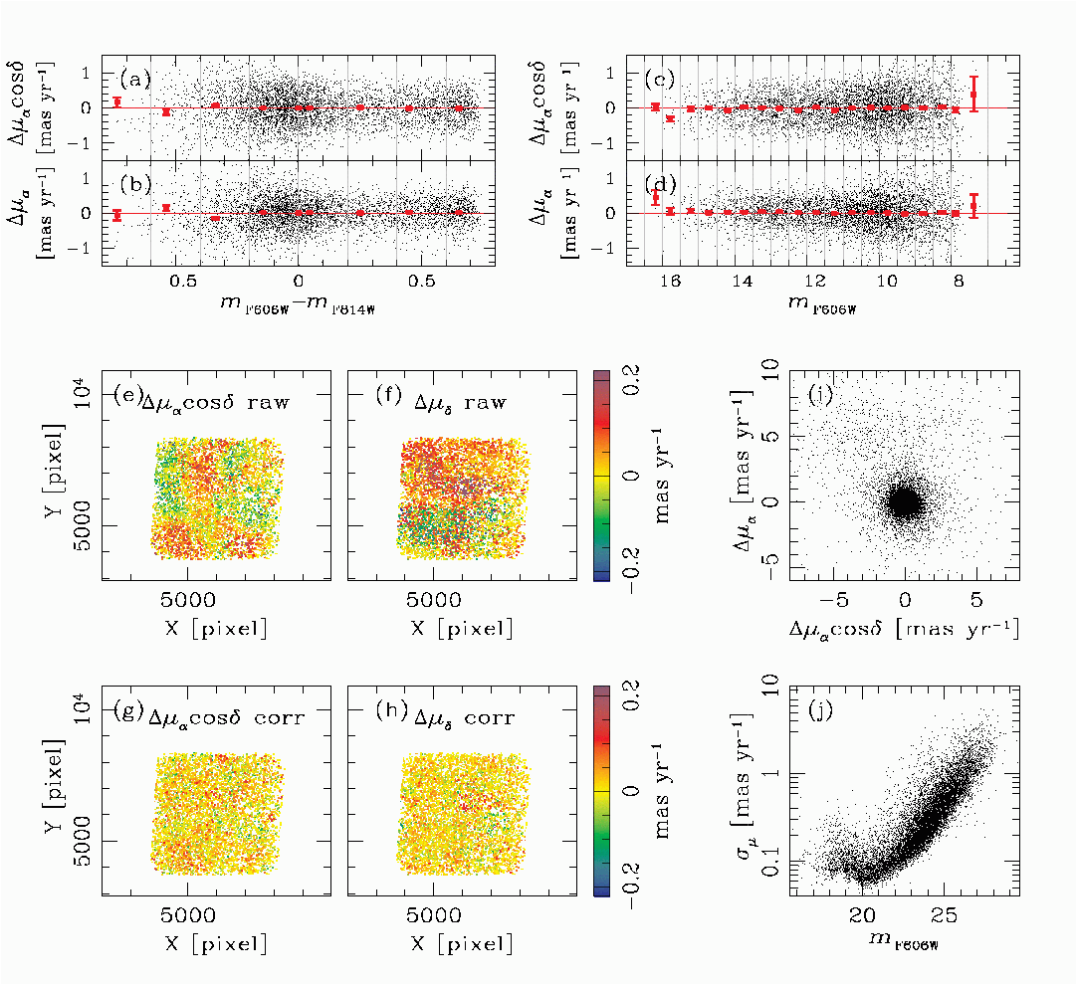

FIGURE 2.6: As in Figure 2.5 but for field F3.

was estimated using a sub-sample of reference stars having a magnitude similar to those of the target. The frequency function for the i-th star of a cluster is:

$$\Phi_c^{\nu} = \frac{\exp\left\{-\frac{1}{2}\left[\frac{(\mu_{xi}-\mu_{xc})^2}{\sigma_{xc}^2+\epsilon_{xi}^2}+\frac{(\mu_{yi}-\mu_{yc})^2}{\sigma_{yc}^2+\epsilon_{yi}^2}\right]\right\}}{2\pi(\sigma_c^2+\epsilon_{xi}^2)^{1/2}(\sigma_c^2+\epsilon_{yi}^2)^{1/2}}$$

where (μ_{xi}, μ_{yi}) are the proper motion of the i-th stars, (μ_{xc}, μ_{yc}) the cluster proper motion centre, $(\sigma_{xc}, \sigma_{yc})$ the intrinsic proper motion dispersion of member stars, defined as the 68.27^{th} percentile of the μ_{xi} and μ_{yi} distribution, and $(\epsilon_{xi}, \epsilon_{yi})$ the observed errors of the proper-motion component of the i-th star. Similar for the field:

$$\Phi_f^{\nu} = \frac{\exp\left\{-\frac{1}{2(1-\gamma^2)}\left[\frac{(\mu_{xi}-\mu_{xf})^2}{\sigma_{xf}^2+\epsilon_{xi}^2}-\frac{2\gamma(\mu_{xi}-\mu_{xf})(\mu_{yi}-\mu_{yf})}{(\sigma_{xf}^2+\epsilon_{xi}^2)^{1/2}(\sigma_{yf}^2+\epsilon_{yi}^2)^{1/2}}+\frac{(\mu_{yi}-\mu_{yf})^2}{\sigma_{xf}^2+\epsilon_{yi}^2}\right]\right\}}{2\pi(1-\gamma^2)^{1/2}(\sigma_{xf}^2+\epsilon_{xi}^2)^{1/2}(\sigma_{yf}^2+\epsilon_{yi}^2)^{1/2}}$$

where (μ_{xf}, μ_{yf}) is the field proper motion centre, $(\sigma_{xf}, \sigma_{yf})$ the field intrinsic proper motion dispersion, defined as the 68.27^{th} percentile of the μ_{xi} and μ_{yi} distribution, and γ the correlation coefficient:

$$\gamma = \frac{(\mu_{xi}-\mu_{xf})(\mu_{yi}-\mu_{yf})}{\sigma_{xf}\sigma_{yf}}$$

The distribution function of all the stars can be computed as follows:

$$\Phi = \Phi_c + \Phi_f = (n_c \cdot \Phi_c^{\nu}) + (n_f \cdot \Phi_f^{\nu})$$

where n_c and n_f are the normalized number of stars for cluster and field ($n_c + n_f = 1$). Therefore, for the i-th star the resulting membership probability is

$$P_c(i) = \frac{\Phi_c(i)}{\Phi(i)}$$

Our evaluation of the membership probability does not consider the sources' spatial distribution, since our apertures are small enough to treat the member/field ratio as constant.

Figure 2.7 shows an example of field-star decontamination based on membership probabilities. Poorly measured stars were removed using the parameters described in section 2.3.6, using a tighter selection than that in Figure 2.3. No quality-selection cuts are applied for saturated stars. Panel (a) shows the $m_{\rm F606W}$ vs. $m_{\rm F606W} - m_{\rm F814W}$ CMD while panel (b) illustrates the membership distribution. The red line, drawn by hand, separates cluster members from field stars, which are represented in black and in red respectively in all the panels. We highlight in blue the stars that are saturated in at least one filter. Finally, saturated stars with no proper motion measurements and for which it is not possible to estimate the membership probability are represented in green.

2.6 The catalogue

The catalogue consists of an astrometric- and several photometric files. Each file contains a description of the data and has the same number of lines, one for each source in the same order.

The astrometric file (ID_XY_RD.dat) contains the star ID, an identifier number associated to the field containing the star, stellar position both in X, Y (pixels) and R.A., DEC. (decimal degrees), followed by PM information and PM diagnostic as described in Bellini et al. (2014); the last 5 columns contain the proper motion and the

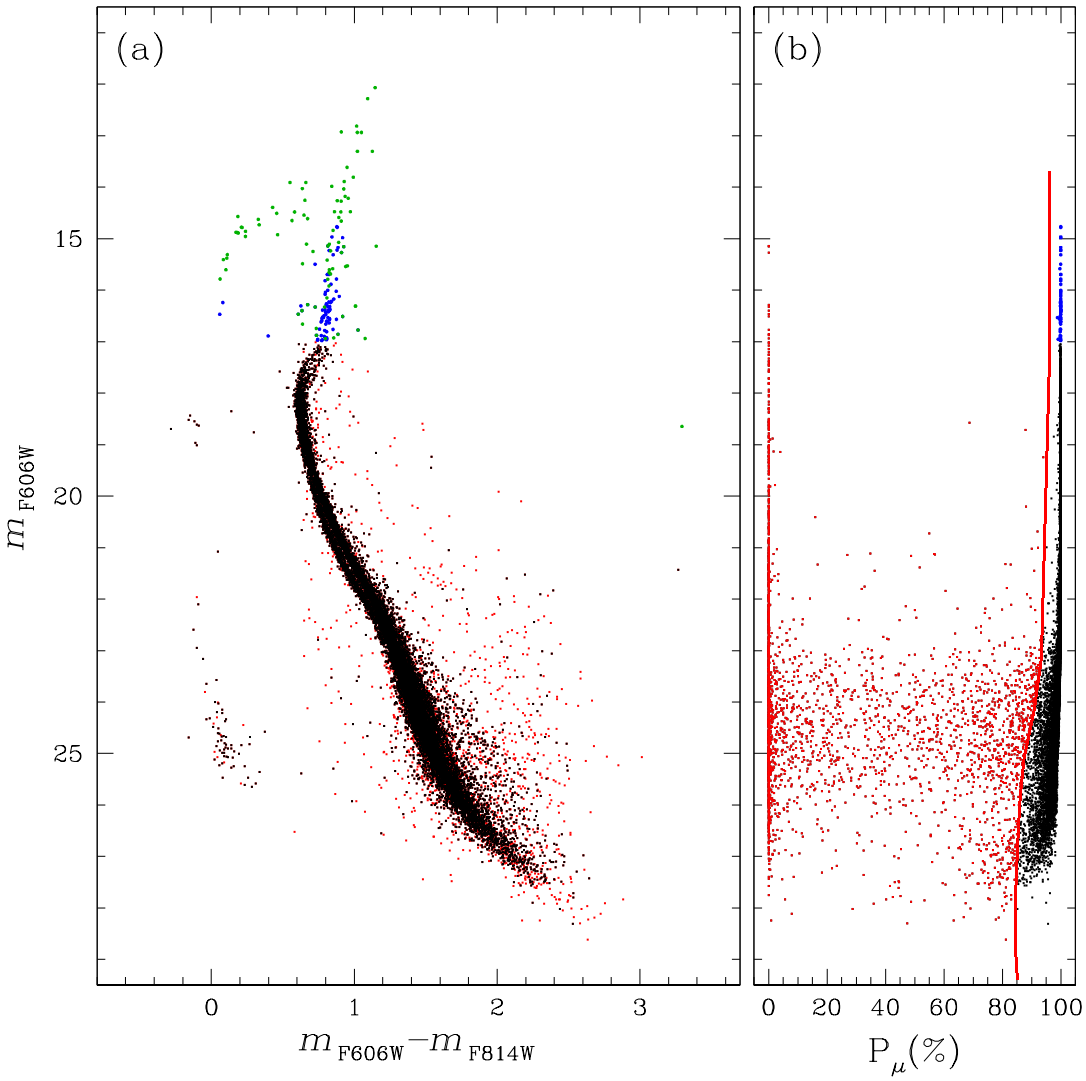

FIGURE 2.7: Probable-member selection. Only well-measured stars are shown. No quality selection cuts are applied to saturated stars. Panel (a) shows the m_{F606W} vs $m_{F606W} - m_{F814W}$ CMD. Saturated stars with no proper motion measurements and for which is impossible to estimate the membership probability are shown in green. Panel (b) presents the membership probability as a function of m_{F606W} magnitude, and the selection drawn by hand. In all panels, we highlight in red field stars and in black likely cluster members. Stars that are saturated in at least one filter are shown in blue.

TABLE 2.3: Extract of the Method-one F814W Photometry File

m_{F814W}	RMS	QFIT	o	RADXS	N_f	N_g	Sky (e^-)	rms Sky (e^-)	Sat flag
...	...	...	...	...	...	...	...	...	...
19.9181	0.0101	1.000	0.00	−0.0030	6	6	522.7	289.4	0
19.0149	0.0047	1.000	0.00	0.0001	8	8	1102.3	634.0	0
21.1528	0.0390	0.996	0.00	−0.0062	8	8	245.4	138.7	0
20.8745	0.0072	1.000	0.00	−0.0043	6	6	252.3	131.0	0
20.2702	0.0080	1.000	0.00	−0.0010	8	8	397.2	206.7	0
22.3625	0.0286	0.998	0.00	0.0081	7	7	91.2	31.4	0
21.4836	0.0095	0.999	0.00	−0.0030	8	6	161.1	71.0	0
22.8419	0.0127	0.997	0.00	0.0092	7	6	77.5	22.7	0
22.2140	0.0201	0.999	21.37	0.0021	8	8	104.8	35.2	0
22.5099	0.1260	0.978	257.83	0.0294	8	8	110.4	46.9	0
...	...	...	...	...	...	...	...	...	...

associated errors along R.A. and DEC. after the *a posteriori* correction, and the membership probability. Stars with no PM measurements have a flag value of −999.999 for all PM-related columns except for U_{ref} (a flag value that tells if a star was used as reference cluster member for the six-parameter linear transformation in the PMs evaluation), N_{found} and N_{used}, which are instead flagged to −999.

For each filter, we provide a different file for each photometric method (e.g., F336W.m1.dat, F336W.m2.dat, or F336W.m3.dat for methods one, two and three, respectively) containing VEGAMAG magnitudes, quality parameters (RMS, QFIT, o, RADXS, N_f and N_g) for each measured star. In addition, the method-one files also contain information about the local sky background, as well as a saturation flag to distinguish between unsaturated and saturated stars. For F606W and F814W filters, when a star is saturated or not found in the long exposures, its photometry is recovered from the short exposures. The photometry of saturated stars comes from the first-pass reduction.

While for UVIS filters the saturation limit is fixed, establishing the saturation limit for IR filters, where final numbers are the results of multiple readings, can be a hard task. For this reason, for IR filters we provide two different catalogues for each method, separating short and long exposures (e.g., F110W.m1.short.dat, F110W.m1.long.dat for short and long exposures respectively).

If a star is not found in a given filter the VEGAMAG magnitude is flagged to −99.999 and the QFIT, o and RADXS parameters are flagged to 0. For stars measured in only one image, it is not possible to compute the RMS parameter, so its value is flagged to −99.999. Finally, saturated stars have a flagged value of −99.999 for RMS and 0 for the other parameters. Tables 3-6 show an extract of the astrometric file and the three photometric files for the F814W filter.

A visual summary of the catalogue is given in Figure 2.8 for three different CMDs, obtained using filters that span different intervals of wavelength: m_{F336W} vs. $m_{F275W} - m_{F438W}$ (ultraviolet filters) in panel (a), m_{F606W} vs. $m_{F606W} - m_{F814W}$ (optical filters) in panel (b) and m_{F110W} vs. $m_{F110W} - m_{F160W}$ (near-infrared filters) in panel (c). Poorly measured stars are removed using the photometric parameters described in section 2.3.6 and following the selection illustrated in Figure 2.3. Probable cluster members and background sources are separated using the membership probability and are represented respectively with black and grey dots in panels (a), (b) and (c) of Figure 2.8. We corrected the photometry for differential reddening

TABLE 2.4: Extract of the Method-two F814W Photometry File

m_{F814W}	RMS	QFIT	o	RADXS	N_f	N_g
...	...	...	...	...	...	...
19.9194	0.0097	0.986	0.00	0.0031	6	6
19.0131	0.0056	1.000	0.00	−0.0009	8	8
21.1541	0.0378	0.995	0.00	−0.0040	8	8
20.8739	0.0074	0.999	0.00	−0.0044	6	6
20.2685	0.0070	1.000	0.00	−0.0019	8	8
22.3556	0.0351	0.996	0.00	0.0064	7	7
21.4100	0.1351	0.987	0.00	0.0038	8	8
22.8274	0.0241	0.995	0.00	0.0076	7	6
22.1978	0.0226	0.994	14.96	0.0031	8	8
22.4234	0.1975	0.971	130.68	0.0066	8	8
...	...	...	...	...	...	...

TABLE 2.5: Extract of the Method-three F814W Photometry File

m_{F814W}	RMS	QFIT	o	RADXS	N_f	N_g
...	...	...	...	...	...	...
19.9477	0.0189	0.993	0.00	0.0154	6	6
19.0156	0.0122	1.000	0.00	0.0022	8	8
21.1912	0.0092	1.000	0.00	0.0100	8	8
20.8616	0.0109	1.000	0.00	0.0182	8	8
20.2678	0.0077	1.000	0.00	−0.0008	8	8
22.4082	0.0372	0.999	0.00	0.0260	8	8
21.4870	0.0502	0.999	0.00	0.0231	8	7
22.8921	0.0433	1.000	0.00	0.0572	8	8
22.2390	0.0410	0.998	3.32	0.0162	8	8
22.6223	0.0556	0.999	20.22	0.0608	8	8
...	...	...	...	...	...	...

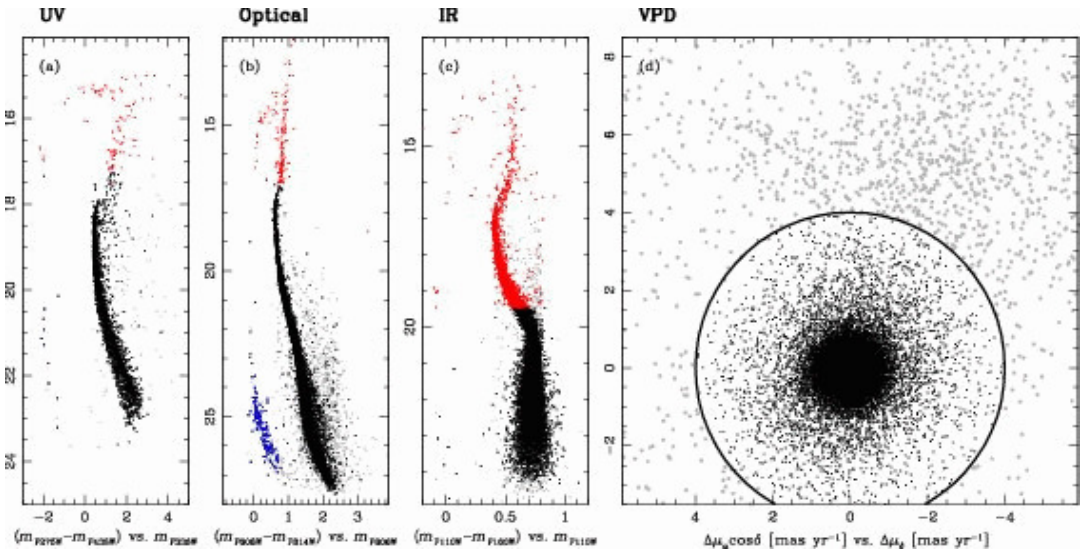

FIGURE 2.8: CMD for different interval of wavelength obtained after removing the poorly measured stars and correcting for differential reddening as in Bellini et al. (2017c). (a) $m_{\rm F336W}$ vs. $m_{\rm F275W} - m_{\rm F438W}$ ultraviolet CMD. (b) $m_{\rm F606W}$ vs. $m_{\rm F606W} - m_{\rm F814W}$ optical CMD. (c) $m_{\rm F110W}$ vs. $m_{\rm F110W} - m_{\rm F160W}$ near-infrared CMD. For panels (a), (b) and (c) saturated stars are in red while WDs are in blue and likely cluster members are represented in black while probable foreground and background field objects are in grey. Panel (d) shows the VPD of the relative PMs of the best-measured stars in the two analysed fields, where we set a 4 mas yr^{-1} limit from the bulk distribution of the most probable cluster-members (black dots), and indicate background and foreground field sources with grey filled dots.

following the method described in Bellini et al. (2017c), which is an evolution of procedures described in Sarajedini et al. (2007). Saturated stars are represented in red while WDs are in blue. Panel (d) shows the VPD of the relative PMs, after the *a posteriori* correction, of the two analysed fields. Likely cluster-members, within 4 mas yr^{-1} from the bulk distribution, are represented with black dots, while background and foreground field sources are represented with grey filled dots.

Together with the astro-photmetric catalogue, we also release for each of the two fields the atlases, i.e., a view of the field through stacked images. We produce those in two versions: sampled at 1×- and at 2×-supersampled pixels. These stacked images are in standard `fits` format and contain in their headers the astrometric WCS solution linked to Gaia eDR3. For each field, we provide one single stack image each for filters F275W, F336W and F438W, and two stack images for each of F606W, F814W, F110W and F160W, separating short- and long-exposure images.

To give a visual sense of the stacks, we show in Figure 2.9 three-colour images for fields F2 (left) and F3 (middle). An ICRS grid is overimposed in each image for reference. In the right panel, we show a zoomed region, at a scale that shows the individual pixels, of the field F3.

2.7 Summary and Conclusions

As part of the delivery of our large programme on ω Cen we are committed to releasing astro-photometric catalogues of all our studied fields. Along with this chapter, we present and publicly release *(i)* the astro-photometric catalogue, and *(ii)* the

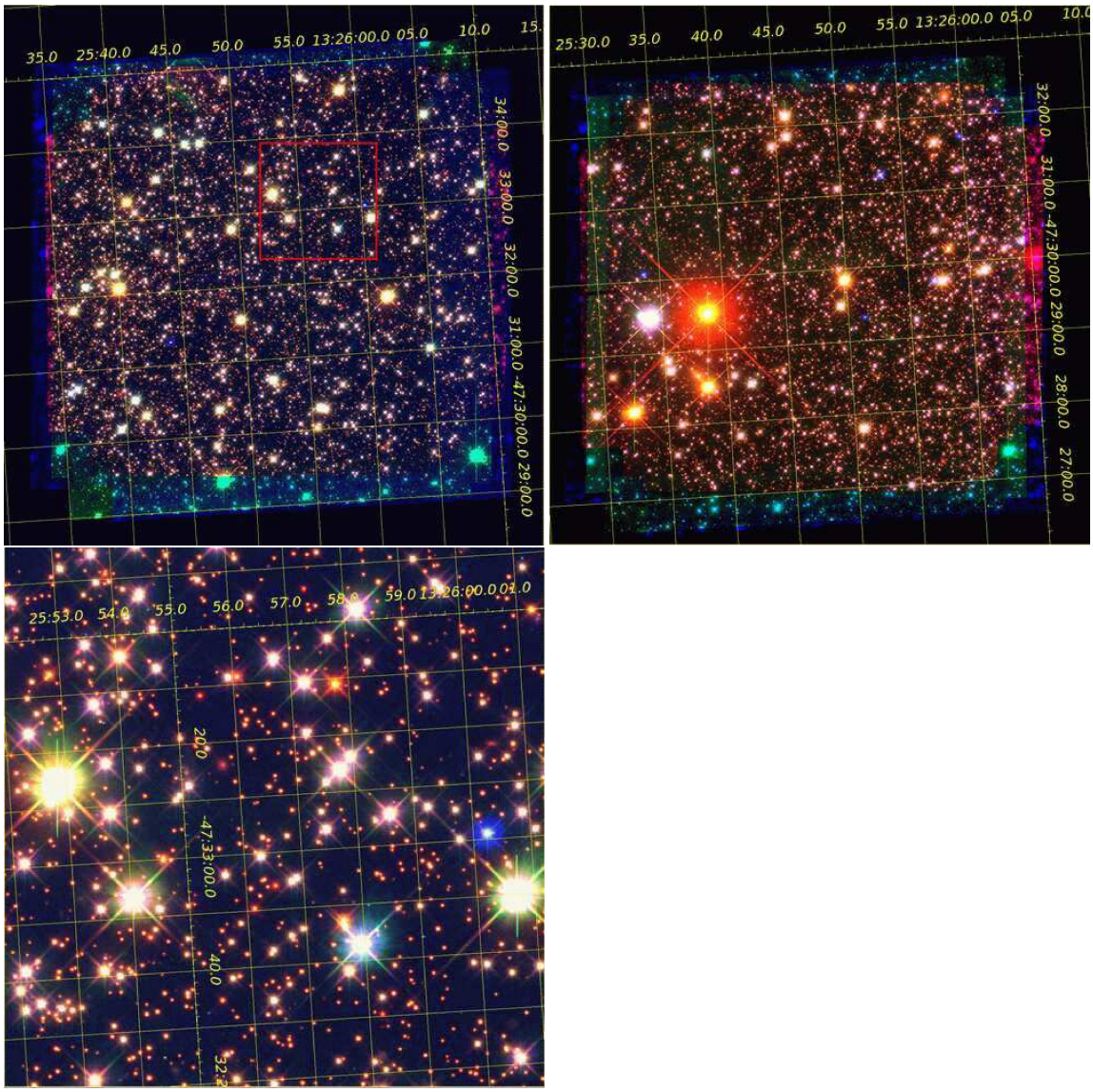

FIGURE 2.9: Three-colour images for field F2 (left) and F3 (middle) with an ICRS grid over-imposed for reference (in yellow). In the right panel, we show the zoom-in indicated with the red box in field F2. The red, green, and blue channels are filled by F110W, F606W and F336W, respectively.

multi-band atlases for the remaining two (out of three) WFC3 parallel fields F2 and F3 (indicated in Figure 2.1), which were not previously released (field F1 is the only one that has been released so far, Bellini et al. 2018).

The catalogues provide stellar positions, PMs and PM diagnostic quantities, magnitudes and quality parameters. Each file contains a header with a short description of the data it contains. Together with the catalogue, we release atlases in each filter. These are stacked images available in two versions: one in original pixel size, and a version super-sampled by a factor 2. Both versions have headers containing the astrometric solutions with keywords in the WCS. We make images publicly available on our `url`[5] and as supplementary electronic online material of this journal. Upon reasonable request, we could also provide light curves for each filter of individual sources.

The scientific exploitation of the present catalogue has great potential. The most immediate and simple application would be to select interesting proper-motion members in any of the identified mPOPs sequences or in the binary sequence for detailed spectroscopic follow-up investigation. The catalogue is an *HST* legacy and can provide an early epoch for future and astrometric campaigns, which can extend the time-baseline and therefore enable more accurate differential internal kinematic investigations among the different mPOPs of ω Cen, as well as many other unforeseeable uses.

[5] https://web.oapd.inaf.it/bedin/files/PAPERs_eMATERIALs/wCen_HST_LargeProgram/P04/

Chapter 3

The *HST* large programme on ω Cen – Exploring the Ultracool Dwarf Population with Stellar Atmosphere and Evolutionary Modelling

Observations of brown dwarfs in globular clusters can provide important information concerning the evolutionary and chemical history of the Milky Way due to their continuous cooling and high sensitivity of spectra to composition. However, the detection of these sources is been prevented by their faint luminosities and the large distances of the globular clusters. Upcoming instruments like the James Webb Space Telescope are expected to improve our ability to observe brown dwarfs in globular clusters. In this chapter, we present data from the Hubble Space Telescope that were used to make predictions for forthcoming data from the James Webb Space Telescope for ω Cen, one of the largest and most well-studied globular clusters in the Milky Way. The cluster contains distinct populations with different chemical compositions and helium content. Those data were used to calculate new interior and atmosphere models and determine the physical properties of the cluster members to make predictions for brown dwarfs in the cluster. The material discussed in this Chapter has been published in the Astrophysical Journal (ApJ; Gerasimov et al. 2022a). This study combines observational data and theoretical modelling to provide insights into the stellar and substellar population of ω Cen.

3.1 Introduction

Brown dwarfs are substellar objects with masses below the threshold for sustaining hydrogen fusion ($\sim 0.08 M_{\odot}$). Unlike hydrogen-burning stars, these objects do not achieve energy equilibrium and begin cooling shortly after formation, resulting in a gradual decrease in effective temperature and luminosity. The low effective temperatures of brown dwarfs facilitate complex molecular chemistry in their atmospheres, leading to the formation of clouds with various compositions. Due to their spectra's high sensitivity to elemental abundances and their continuous cooling process, these objects serve as ideal chemical tracers for studying the Milky Way's evolutionary history.

Observing brown dwarfs presents challenges due to their faint luminosities and low temperatures, which restricts the study to the closest and youngest objects in the Milky Way. Consequently, research on brown dwarfs has primarily focused on

isolated sources with near-solar metallicities and chemical compositions that do not adequately represent the early evolutionary history of our galaxy and lack secondary indicators of their origins and physical properties.

In this context, we turn our attention to brown dwarfs in globular clusters. A typical globular cluster contains tens of thousands of coeval members, each individually observable, with similar ages and chemical compositions that can be deduced photometrically from the colour-magnitude diagram (CMD). Importantly, unlike field stars in the solar neighbourhood, members of globular clusters exhibit chemical abundances characteristic of the Milky Way's early, metal-poor phases of formation. Therefore, globular clusters provide unique laboratories for studying brown dwarfs with non-solar abundances and old ages. Parameters that can be independently constrained by examining the overall cluster population.

Gerasimov et al. (2022a) presented new models to analyze the interior and atmosphere of the brown dwarfs in ω Cen, the most massive globular cluster in the Milky Way. By comparing synthetic colour-magnitude diagrams (CMDs) generated from these models with new observations taken by the Hubble Space Telescope (HST) of the low-mass main sequence of ω Cen, Gerasimov et al. (2022a) were are able to determine the most accurate physical properties of the cluster and calibrate for interstellar reddening. Additionally, the models are extended to the substellar regime, enabling predictions of the expected colours, magnitudes, and colour-magnitude space densities of brown dwarfs within ω Cen, even at effective temperatures as low as $\approx$ 1000 K.

In the following, we present the observational data presented in Gerasimov et al. (2022a).

3.2 Observations

To determine the best-fit isochrone for ω Cen, Gerasimov et al. 2022a compared each population isochrone to photometric data acquired with *HST ACS/WFC* in the `F606W` and `F814W` bands (programmes *GO-9444* and *GO-10101*; PI: King), and *HST WFC3/IR* in the `F110W` and `F160W` bands (programmes *GO-14118* and *GO-14662* for *WFC3*; PI: Bedin). Observations were carried out in a $3' \times 3'$ field situated $\sim$ 3 half-light radii ($\approx 7'$) southwest of the cluster centre (see field F1 in Figure 1a of Bellini et al. 2018). This is the deepest observed field for ω Cen for which both optical and near-infrared *HST* observations are available.

The primary data reduction followed the procedure described in Scalco et al. (2021) for two other *HST* ω Cen fields, and is analogous to methods adopted in numerous previous works (Bellini et al., 2017b; Bellini et al., 2018; Milone et al., 2017a; Milone et al., 2017a; Bedin et al., 2019c). In brief, positions, fluxes and multiple diagnostic quality parameters were extracted using the point spread function (PSF) fitting software package `KS2` (Anderson and King, 2006; Anderson et al., 2008); see Scalco et al. (2021) and references therein. The photometric zero-point onto the `VEGAMAG` system was determined using the approach of Bedin et al. (2005a). The sample was filtered by quality parameters σ (photometric error), `QFIT` (correlation between pixel values and model PSF), and `RADXS` (flux outside the core in excess of PSF prediction; Bellini et al. 2017b; Bedin et al. 2008), as described in Scalco et al. (2021, Section 4).

We used the relative proper motions of sources in the observed region to separate field stars from cluster members. Proper motions were obtained by comparing the extracted positions of stars measured in the earliest and latest programmes

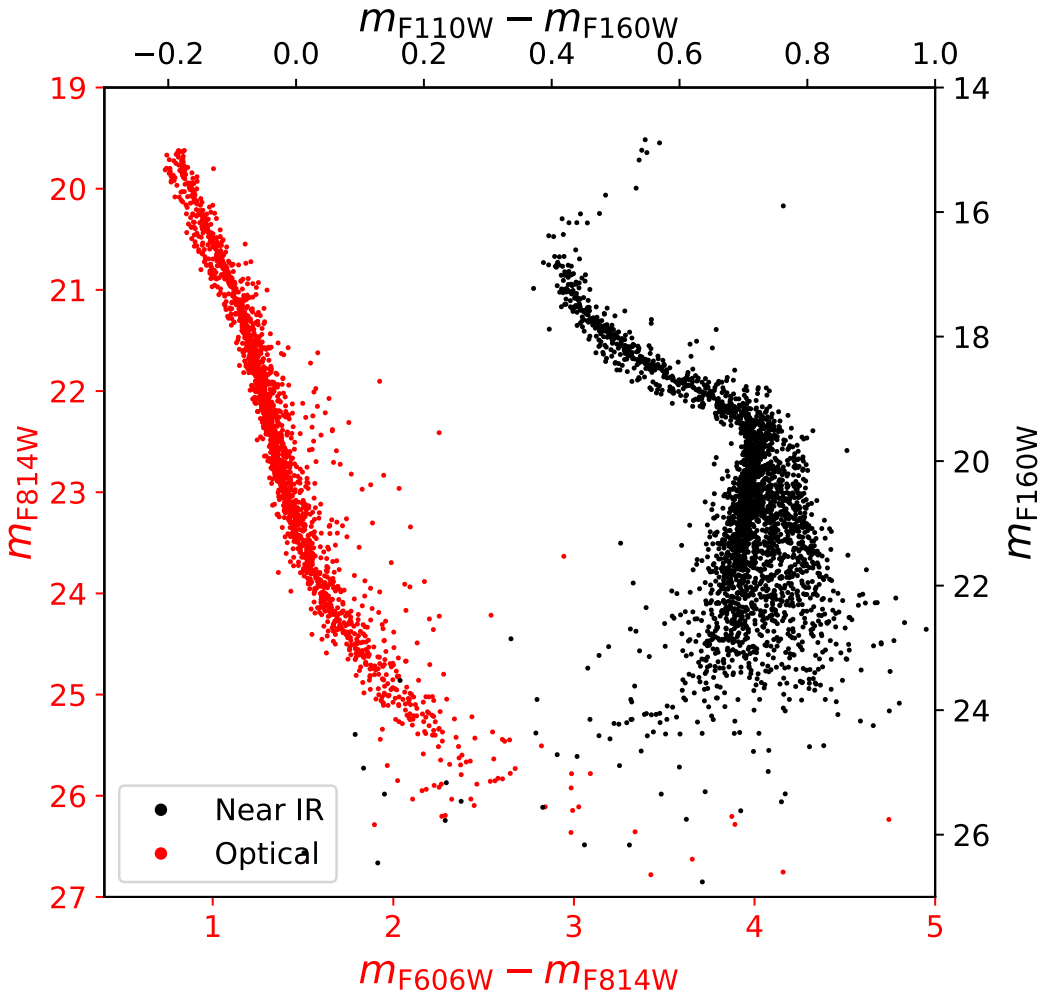

FIGURE 3.1: Proper motion-selected zero-pointed differential reddening-corrected photometry of the Main Sequence of ω Cen. Optical photometry was acquired with *HST ACS/WFC* and near-infrared photometry with *HST WFC3/IR*. Only unsaturated stars are shown for the optical photometry. The Main Sequence bifurcation can be seen in both datasets.

(*GO-9444* and *GO-14662*, respectively), providing epoch baselines of up to 15 years. Photometry in each filter was corrected for systematic photometric offsets following Bedin et al. (2009a). A general correction for differential reddening was also applied following the method described in Bellini et al. (2017c, Section 3).

Measurement of the LF requires quantification of source completeness as a function of colour and magnitude, for which we followed the approach described in Bedin et al. (2009a). We generated a total of 2.5×10^5 artificial stars (AS) with random positions. For each AS, a `F606W` magnitude was drawn from a uniform distribution. The remaining three magnitudes (`F814W`, `F110W`, `F160W`) were then chosen to place the AS along the approximate ridgeline of the Main Sequence in various colour-magnitude spaces. AS were introduced in each exposure and measured one at a time to avoid over-crowding, making the process independent of the LF. A star was considered recovered when the difference between the generated and measured star position was less than 0.1 pixels and the magnitude difference was less than 0.4 mag. Finally, the stars were divided into half-magnitude bins and the photometric errors

and completeness for each bin were computed.

The near-infrared and optical colour-magnitude diagrams based on our observations are shown in Figure 3.1.

We include with this chapter an astro-photometric catalogue of measured sources in the *HST* imaged fields and multi-band atlases for each filter. The main catalogue (filename: `Catalog`) includes right ascensions and declinations in units of decimal degrees; as well as `VEGAMAG` magnitudes in `F606W`, `F814W`, `F110W` and `F160W` before zero-pointing and differential reddening corrections. The last three columns contain flags to differentiate unsaturated and saturated stars for `F606W` and `F814W` filters and a proper motion-based flag to distinguish between field stars and cluster members.

Four additional catalogues `R-I_vs_I.dat`, `J-H_vs_H.dat`, `C_RIH_vs_H.dat` and `I-H_vs_J.dat` contain differential reddening-corrected, zero-pointed colours and magnitudes diagrams in the $m_{\mathrm{F606W}} - m_{\mathrm{F814W}}$ vs m_{F814W}, $m_{\mathrm{F110W}} - m_{\mathrm{F160W}}$ vs m_{F160W}, $(m_{\mathrm{F606W}} - m_{\mathrm{F814W}}) - (m_{\mathrm{F814W}} - m_{\mathrm{F160W}})$ vs m_{F160W}, and $m_{\mathrm{F814W}} - m_{\mathrm{F160W}}$ vs m_{F110W} observational planes. All four files have the same number of entries and ordering as the main catalogue with one-to-one correspondence.

Finally, for each filter we provide two additional files containing the estimated photometric errors (`F606W_err.dat`, `F814W_err.dat`, `F110W_err.dat` and `F160W_err.dat`) and completeness (`F606W_comp.dat`, `F814W_comp.dat`, `F110W_comp.dat` and `F160W_comp.dat`) computed in each half-magnitude bin.

We also release with this chapter atlases of the imaged field in each of the four filters. These atlases consist of stacked images produced with two sampling versions: one atlas sampled at the nominal pixel resolution and one atlas sampled at 2×-supersampled pixel resolution. The stacked images adhere to standard *FITS* format and contain headers with astrometric *WCS* (*World Coordinate System*) solutions tied to *Gaia* Early Data Release 3 astrometry (Gaia Collaboration et al., 2021). We provide a single stacked view for each of `F606W` and `F814W` fields, and two stacked views for each of `F110W` and `F160W` fields separated into short and long exposure images.

The catalogues and atlases are included with this chapter as supplementary electronic material and are available online[1].

[1] https://web.oapd.inaf.it/bedin/files/PAPERs_eMATERIALs/wCen_HST_LargeProgram/P05/

Chapter 4

The *HST* large programme on ω Centauri – The radial gradient of the stellar populations.

We present a study examining the radial gradient of the fifteen multiple stellar populations within the globular cluster Omega Centauri. This investigation extends beyond the central region of the cluster and encompasses a broader portion of its expanse. Our analysis combines previously published Hubble Space Telescope data from an earlier chapter of this thesis with newly collected data obtained under the Hubble Space Telescope program GO-16247 (P.I.: Scalco). Our findings reveal variations in the number of stars within the two most populous stellar populations, referred to as bMS and rMS, as a function of radial distance from the cluster centre. Additionally, we observe fluctuations in the number of stars for less populous stellar populations, denoted as MSa and MSd, across the radial gradient. In contrast, the populations MSe exhibit relatively consistent numbers of stars across varying radial distances.

4.1 Introduction

Omega Centauri (or NGC 5139, hereafter ω Cen) is known to host a very complex system of multiple stellar populations that makes it one of the most enigmatic stellar systems of the Galaxy. It is populated by at least two main groups of stars with a large difference in their helium content (Y$\sim$0.40 for the He-rich component) and by a set of at least fifteen sub-populations (Bellini et al., 2017d). The complexity of multiple stellar populations in this cluster is demonstrated by the multiple sub-giant branches and red-giant branches and by the presence of a double white dwarf cooling sequence (see Bellini et al., 2013).

The *Hubble Space Telescope* (*HST*) GO-16247 programme (P.I. Scalco), as a part of a larger investigation made up of archival material (of $\sim$hundred of orbits), aims – for the first time – to study the complete radial coverage of the multiple stellar-populations distributions along (essentially) the entire globular cluster ω Cen.

Schematically, the existing HST radial coverage of the cluster can be divided into three *parts*. Fig. 4.1 shows the locations of the three *parts*, superimposed on an image from the Digital Sky Survey (DSS)[1]. The *part (i)* of the radial coverage, maps the cluster from the centre out to $\sim$1 r_c (where r_c=2.37 arcmin is the core radius, Harris 1996; Harris 2010) and is represented in yellow in Fig. 4.1. The entire photometric catalogues for this field have been published by Bellini et al. (2017b).

[1] https://archive.eso.org/dss/dss

The *part (ii)* of the radial coverage, maps the outskirts of the cluster and consists of three *HST* fields, mapping between $\sim$10 arcmin and $\sim$20 arcmin from the centre of ω Cen, and collected under the multi-cycle programme GO-14118+14662 (P.I. Bedin). Those fields are represented in pink in Fig. 4.1 (fields F1, F2 and F3). We also show in blu the primary field of the programme GO-14118+14662 (field F0).

The exposures from the parallel field F1, F2 and F3 were reduced and presented in the four previous publications of this series: the multiple stellar populations (mPOPs) at very faint magnitudes in the field F1 were analysed by Milone et al. (2017a, hereafter Paper I). Bellini et al. (2018, hereafter Paper II) analysed the internal kinematics of the mPOPs in the field F1, complementing the GO14118 + GO-14662 data with archival images collected more than 10 yrs earlier under *HST* programmes GO-9444 and GO-10101 (on both PI: King). Libralato et al. (2018b, hereafter Paper III) presented the absolute proper motion estimate for ω Cen in the field F1. Finally, Scalco et al. (2021, hereafter Paper IV) released the astro-photometric catalogue for the fields F2 and F3.

The *Part (iii)* maps the radial distance between $\sim$3 arcmin and $\sim$10 arcmin from the cluster centre. Those fields are represented in green in Fig. 4.1 (fields F4 and F5). Those fields were observed under programmes GO-12580 (PI: A. Renzini) and GO-14759 (PI: T. M. Brown) and, more recently, under the GO-16247 programme (P.I. Scalco).

This part of the cluster covers a crucial radial range for the study of the radial distribution of the multiple stellar populations in ω Cen. So far, the most detailed study of the radial distributions of multiple populations in ω Cen was made by (Bellini et al., 2009), who used both space-based images and ground-based images to map the cluster from the inner core to the outskirts ($\sim$20 arcmin). (Bellini et al., 2009) found a trend in the counts-number fraction of the two main populations (bMS/rMS), varying with the distance from the centre of the cluster. In particular, they found that the gradient of the two populations is essentially flat in the core $r \lesssim 3$ arcmin and in the outskirt $r \gtrsim 10$ arcmin, while it is maximum between $3 \lesssim r \lesssim 10$ arcmin.

In this chapter, we present the analysis of the two intermediate fields F4 and F5, providing a study of the multiple stellar populations of ω Cen at this fundamental radial distance. Together with the analysis, we also release the catalogue and atlases of the analysed fields. The catalogue and the atlases for the two fields F4 and F5. Our new catalogue are consistent with the catalogue providede in the Paper IV for the fields F2 and F3 and provides multi-band photometry, proper motions (PMs), and membership probabilities for all sources detected in our fields; the atlases are high-resolution FITS images, with headers containing the astrometric solutions with keywords in the World Coordinate System (WCS).

Finally, we combine the photometry obtained from fields F4 and F5 with that from fields F2 and F3 (see Scalco et al., 2021) to differentiate and identify the fifteen stellar populations found in the core of the cluster (see Bellini et al., 2017d) in the external part of the cluster. This allowed us, for the first time, to investigate the radial gradient of these multiple stellar populations along almost the entire extent of the cluster.

This Chapter is organised as follows: Section 4.2 is dedicated to the description of the data; Section 4.3 briefly outlines the data reduction process; Section 4.4 presents some of the colour-magnitude diagrams obtained; Section 4.5 describes the PM measurements and the methodology to estimate membership probability; in Section 4.6, we describe in details the content of the data released tables. In Section 4.7, we detail the sample selection and differential reddening correction applied to our data, while Section 4.8 provides a brief description of the process used to identify and separate

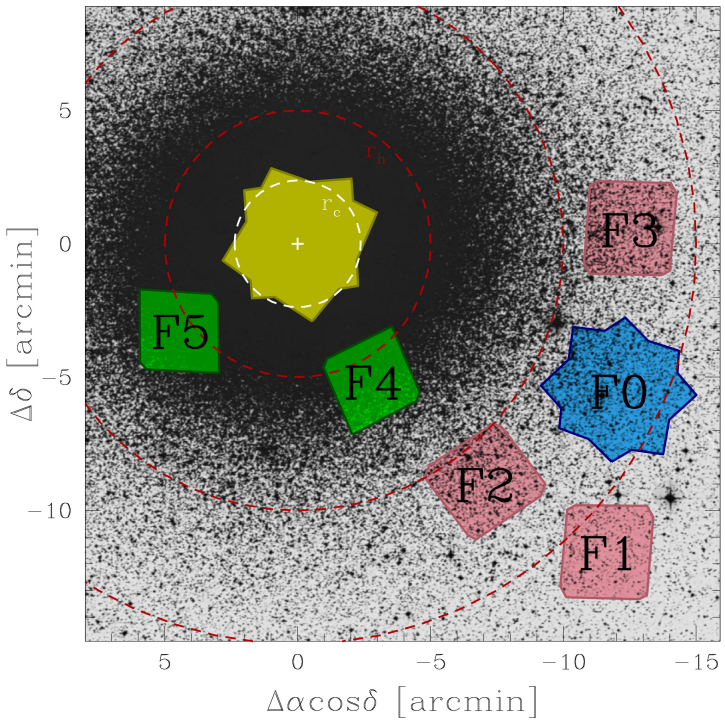

FIGURE 4.1: Outlines of the fields observed in *HST* programs GO-14118 + GO-14662 (P.I. Bedin) and GO-16427 (P.I. Scalco), superimposed on a DSS image of ω Cen. The primary GO-14118 + GO-14662 ACS/WFC field (F0) is in azure, while the three GO-14118 + GO-14662 parallel WFC3 fields are shown in pink. The two GO-16427 fields (discussed in this chapter) are shown in green. We also show, in yellow, the central field presented in Bellini et al. (2017b), Bellini et al. (2017c), and Bellini et al. (2017d). Units are in arcmin measured from the cluster centre. The white and red dashed circles mark the cluster's core radius ($r_c = 2'.37$), the half-light radius ($r_h = 5'.00$), at $2\,r_h$ and $3\,r_h$, respectively, from the centre.

all stellar populations and their subpopulations. In Section 4.9, we provide a summary of the main findings, emphasizing the radial gradients observed within the stellar populations and their respective subpopulations. Finally, in Section 4.10, we offer a concise overview of the obtained results, accompanied by a comparison to the theoretical framework.

4.2 Data set

Fields F4 and F5 were observed in 2012, 2016, 2017 and 2022 using the UVIS channel of the WFC3. In each field, data were collected with five filters (F275W, F336W, F438W, F606W and F814W). Table 1 reports the complete list of *HST* observations of fields F4 and F5.

TABLE 4.1: List of *HST* Observations of Fields F4 and F5.

Field F4		
Filter	Exposures	Epoch
	Epoch 1 (GO-12580)	
	WFC3/UVIS	
F275W	2×909 s + 2×914 s + 2×1028 s + 2×1030 s + 2×1267 s	2012/03/09-04/29
F336W	2×562 s + 2×565 s + 1×945 s + 1×953	2012/03/09-04/29
F438W	2×200 s + 2×210 s	2012/03/09-04/29
	Epoch 2 (GO-14759)	
	WFC3/UVIS	
F275W	1×765 s + 1×850 s	2017/04/13
F336W	1×630 s + 1×765 s	2017/04/13
F438W	1×630 s + 1×1025 s	2017/04/13
	Epoch 3 (GO-16247)	
	WFC3/UVIS	
F606W	1×325 s + 1×348 s	2022/03/12
F814W	1×13 s + 4×348 s	2022/03/12
Field F5		
Filter	Exposures	Epoch
	Epoch 1 (GO-14759)	
	WFC3/UVIS	
F275W	2×765 s + 2×850 s	2016/12/10-14
F336W	2×630 s + 2×765 s	2016/12/10-14
F438W	2×630 s + 2×1025 s	2016/12/10-14
	Epoch 2 (GO-16247)	
	WFC3/UVIS	
F606W	1×325 s + 1×348 s	2022/04/27
F814W	1×13 s + 4×348 s	2022/04/27

4.3 Data Reduction

In this analysis, we used only `_flc`-type images as they preserve the pixel data with its original sampling for stellar-profile fitting. The data reduction was done following the procedure described in Scalco et al. (2021) for the fields F2 and F3 (see figure 4.1). Brielfy, the reduction process can be divided in two main steps: first and second pass photometry. In the first pass photometry, we measured the stellar positions and fluxes in each exposure using the `FORTRAN` code `hst1pass`, which is a generalised version of the `img2xym_WFC` software package (Anderson and King, 2006). Stellar positions and fluxes are obtained by fitting each source with a spatially variable PSF tailorated for each image. Stellar positions in each single-exposure catalogue are corrected for geometric distortion by using the state-of-the-art geometric-distortion corrections of Bellini, Anderson, and Bedin (2011).
For each field, we defined a common, pixel-based reference coordinate system, based on a WFC3/UVIS F814W single-exposure catalogue. Then, for the images taken in each filter, we used only bright, unsaturated, and well-measured stars to derive general six-parameter linear transformations to transform stellar positions – as measured in each individual exposure – onto the common reference frame system. The photometry of these preliminary catalogues was zero-pointed to the first long exposure taken in each filter/epoch.
The second-pass photometry is performed through the `FORTRAN` software package `KS2`, which is based on `kitchen_sync`, originally designed to reduce specific ACS/WFC data (Anderson et al., 2008). The code `KS2` takes images, PSFs , and transformations obtained during the "first-pass photometry" stage to simultaneously find and measure stars in all of the individual exposures and for the entire set of filters. A detailed description of the software is given in Bellini et al. (2017b), Nardiello et al. (2018) and Scalco et al. (2021).
Figure 4.2 shows the upper part of the m_{F814W} vs. $m_{\mathrm{F606W}} - m_{\mathrm{F814W}}$ colour-magnitude diagram (CMD). Black dots are unsaturated stars in the F814W long exposures, while red crosses mark stars that are saturated in the F814W long exposure and were not found in the short exposures. Finally, stars marked with blue circles are saturated in the F814W long exposures but are found unsaturated in the short ones. Stars represented with black dots and blue circles are directly measured by `KS2`, while the positions and the fluxes of the stars marked with red crosses are available through the first-pass photometry, since saturated stars are not measured by `KS2`.

The photometry has been zero-pointed into the Vega magnitude system by following the recipe of Bedin et al. (2005a). In brief, the process of zero-pointing *HST*'s photometry is based on the comparison between our PSF-based instrumental magnitudes and the aperture-photometry on `_drc` exposures (calibrated and resampled images normalized to 1 s exposure time). We refer to Scalco et al. (2021) for a complete description of the photometric-calibration process. Table 4.2 reports the photometric-calibration zero points for each filter.

We cross-reference the stars in our catalogue with the stars in the Gaia Data Release 3 (Gaia DR3; Gaia Collaboration et al. 2021). Gaia's positions were evolved to the observed epochs. We found about 416 sources in common, which were used to anchor our positions (X,Y) to the Gaia eDR3 absolute astrometric system. As such, the positions are referred to the reference epoch of Gaia catalogue, 2016.0, which are in the International Celestial Reference System (ICRS).

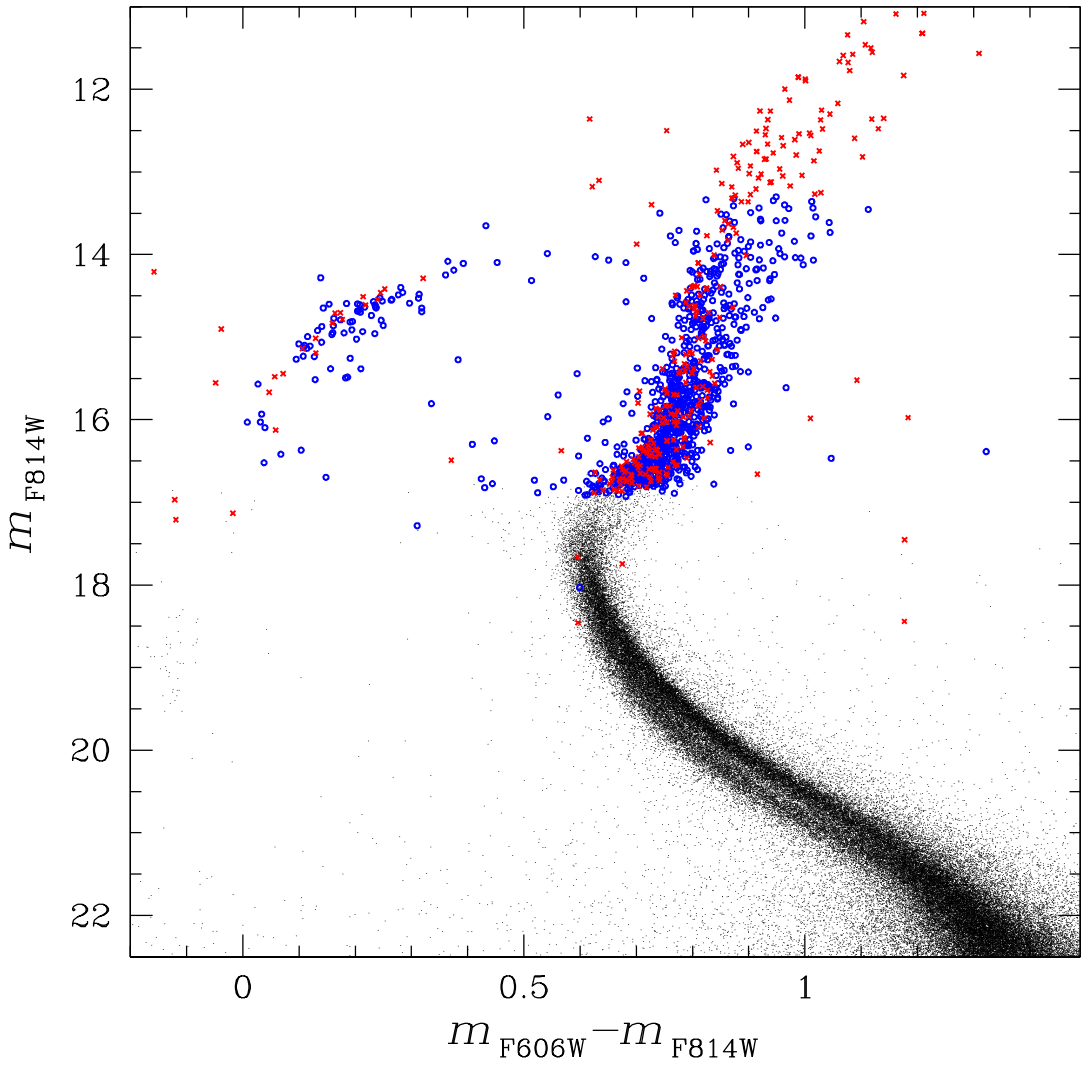

FIGURE 4.2: Bright part of the m_{F814W} vs. $m_{\mathrm{F606W}} - m_{\mathrm{F814W}}$ CMD. The unsaturated stars in the long exposures for the F814W filter are shown with black dots while stars saturated in the long exposures but not in the short one for the F814W filter are shown with blue circles. Those stars are directly measured by KS2. Red crosses represent stars that are saturated in the F814W filter long exposure and not measured in the short ones.

TABLE 4.2: Photometric-calibration Zero Points

Filter	ZP(Vegamag) (mag)
WFC3/UVIS	
F275W	+30.322
F336W	+30.865
F438W	+32.403
F606W	+32.178
F814W	+30.895

4.4 Colour-magnitude diagrams

In addition to positions and fluxes, KS2 provides a series of diagnostic parameters useful to identify the best-measured sources. Those paremeters are: the RMS of the individual-exposure photometry measurements, the quality-of-fit (QFIT) parameter (a parameter that informs about the accuracy of the PSF-fitting), the "o" parameter (defined as the initial ratio of the light within the fitting radius due to nearby neighbors to the light of the star) and the RADXS parameter (a shape parameter that measures how much the deviation of the PSF shape is from the predictions Bedin et al. 2008). We refer to Scalco et al. (2021) for an accurate description of the KS2 dignostic parameters.

In Figure 4.3, we show an example of selection of well-measured stars using the quality parameters provided by KS2. Top and middle panels of Figure 4.3 show, respectively from the left to the right, the photometric errors σ, defined as the RMS divided by the square root of N_g, QFIT and RADXS as a function of F814W and F606W magnitudes obtained with method 1 (see Sect. 3). Similar plots can be made using method-2 and method-3 outputs. In this example, the selection criteria for parameters σ and QFIT are made by eye, arbitrarily defining a line (indicated in red) that separate the bulk of well-measured stars from the outliers. We also rejected all the start with RMS>0.25 and QFIT<0.75. For the RADXS parameter, we selected all stars that satisfy the condition: $-0.15 <$RADXS$< +0.15$ (panels (c) and (f) of Figure 4.3).

The bottom panels of Figure 4.3 show the $m_{\rm F606W}$ vs. $m_{\rm F606W} - m_{\rm F814W}$ colour-magnitude diagram for the stars that pass the selection criteria in both filters (panel (g)) and for the stars that were rejected in at least one filter (panel (h)). From the CMDs, it is clear that many stars ($\sim$ 39%) with poor photometric quality are rejected with these tight selections.

Panel (a) of Figure 4.4 shows the full $m_{\rm F606W}$ vs. $m_{\rm F606W} - m_{\rm F814W}$ CMD obtained combining the best measured stars of the three different photometric methods, selected using the selection procedure described above. No selection cuts were applied to saturated stars. The three red lines define the regions within which stars are saturated in at least one filter, or for which photometry is obtained with one of the three methods. In panels (b)-(f), we show in detail the five regions that are outlined in panel (a) to provide an overview of specific evolutionary sequences. Clockwise from panel (b) to (f) we show the horizontal branch (HB), the red-giant branch (RGB), the sub-giant branch (SGB), the main sequence (MS) and the WD cooling sequences.

4.5 Proper motions

We computed the PMs using the technique described in Scalco et al. (2021). This method, developed by Bellini et al. (2014) and improved in Bellini et al. (2018) and Libralato et al. (2018b), is an iterative procedure that treats each image as a stand-alone epoch and can be summarised in two main steps: (1) transforms the stellar positions of each exposure into a common reference frame by means of a six-parameters linear transformation; (2) fit these transformed positions as a function of the epoch with a least-square straight line. The slope of this line, computed after several outlier-rejection stages, is a direct measurement of the PM. We refer to Scalco et al. (2021) for a complete description of the process.

Our catalogue contains 262,746 sources and we were able to obtain high-precision PMs for 66,824 sources. Our final catalogue is provided with the same set of quality

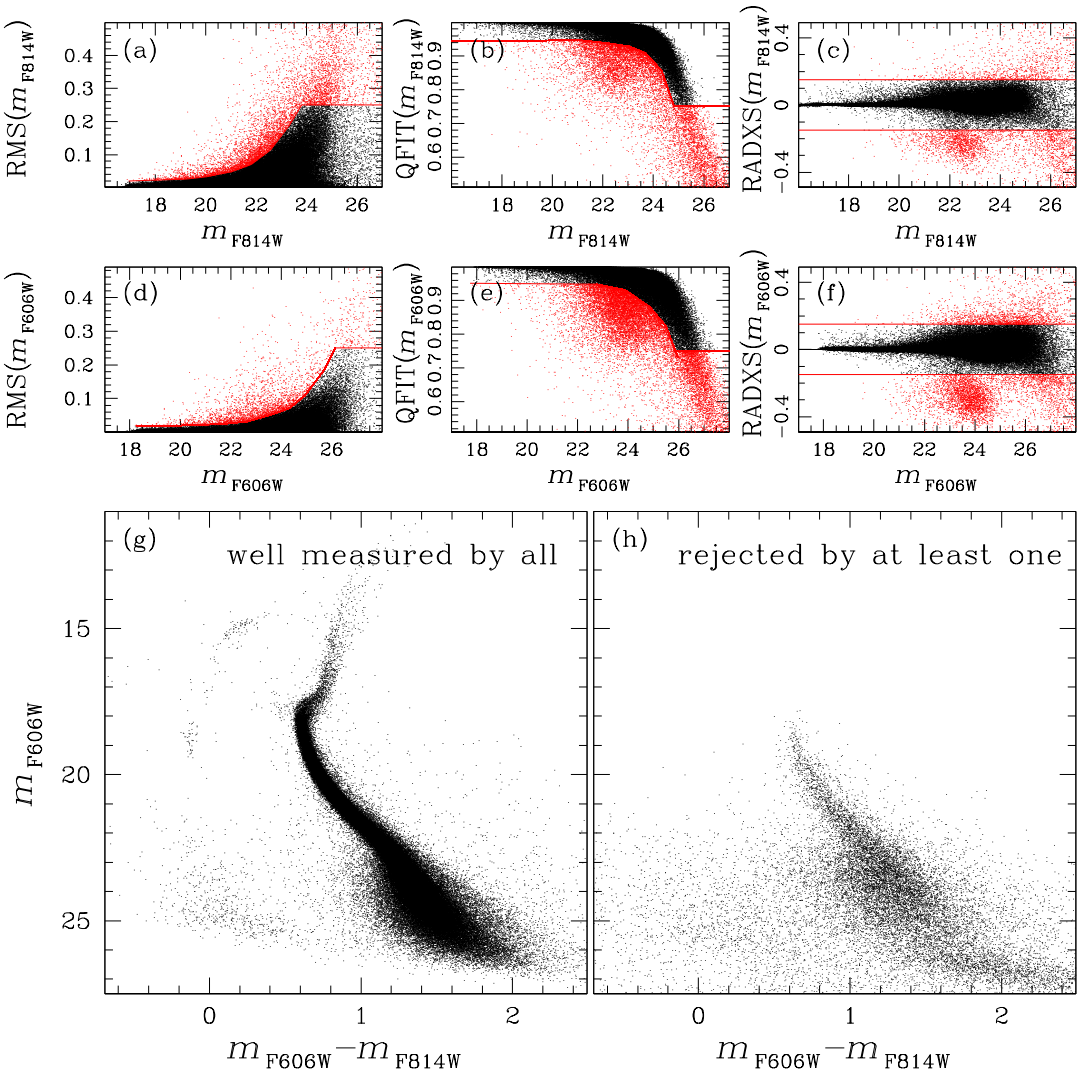

FIGURE 4.3: Effect of simple stellar selections based on σ, QFIT and RADXS. (a)-(c) Selection of the stars based on σ, QFIT and RADXS in function of the F814W magnitude. The red lines separate the bulk of those defined as well-measured stars from the outliers. The rejected stars are represented in red. (d)-(f) Analogues to (a)-(c) but for F606W photometry. (g) $m_{\rm F606W}$ vs. $m_{\rm F606W} - m_{\rm F814W}$ CMD of stars that are well measured according to all the 6 parameters. (h) Same CMD of (g) but of stars that are rejected by at least one filter.

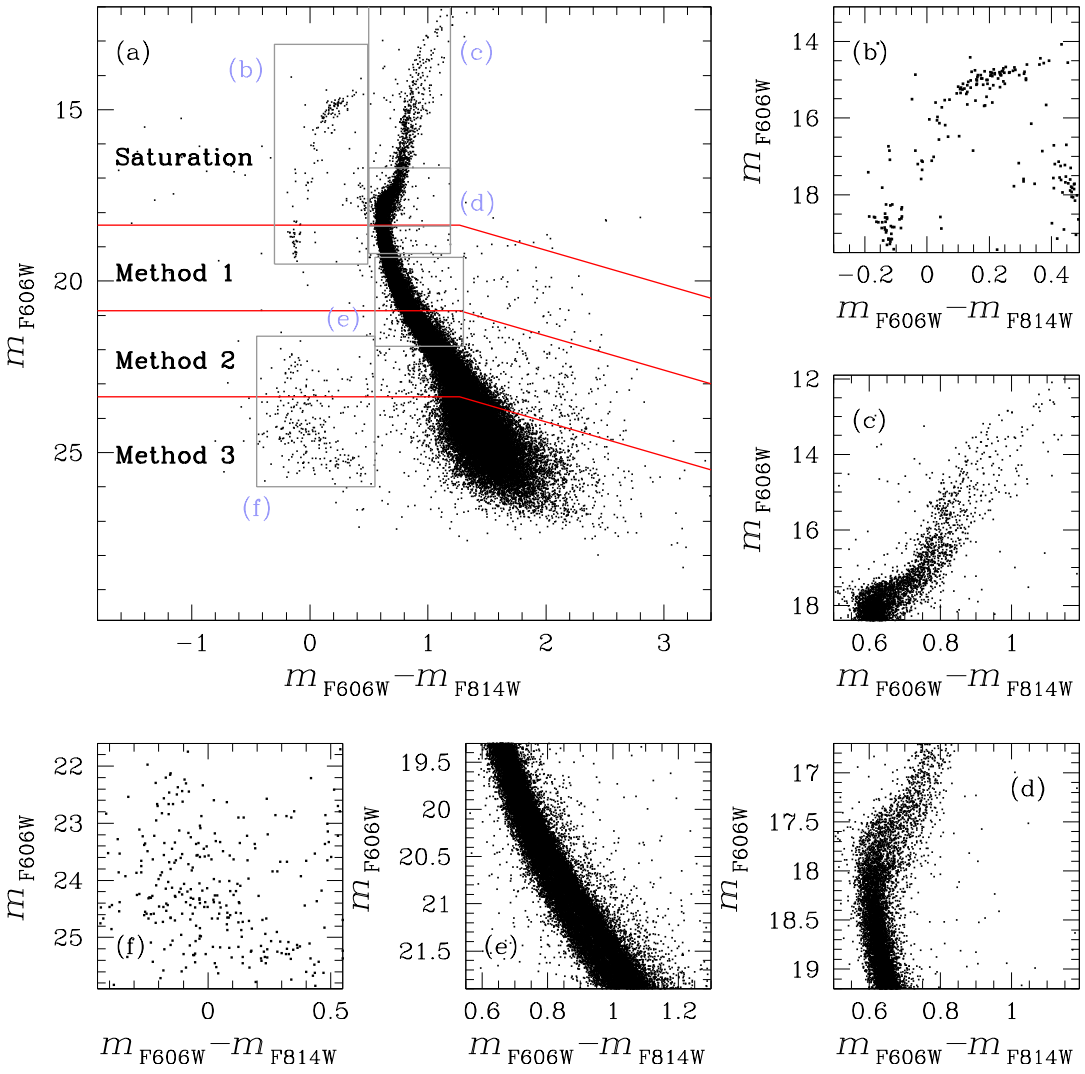

FIGURE 4.4: (a) Full m_{F606W} vs. $m_{F606W} - m_{F814W}$ CMD of ω Cen obtained by combining the best stars measured in the three photometric methods (see section 4.3). The transition between each photometric method is highlighted by red lines. All saturated stars are shown, with no selection. (b)-(f) Detail of the five regions that are outlined in (a). Moving clockwise, the panels show: (b) the HB, (c) the RGB, (d) the SGB, (e) the MS and (f) the WD cooling sequence.

and diagnostic parameters described in Bellini et al. (2014).
Systematic errors in the PMs were corrected "*a posteriori*" following the prescription of Bellini et al. (2014) and Bellini et al. (2018). Figure 4.5 and 4.6 illustrate the correction procedure for field F4 and F5 respectively. In brief, the PM of each star were locally corrected according to the 2.5σ-clipped median value of the closest likely cluster members and within 0.5 $m_{\rm F606W}$ magnitudes from the target star (excluding the target star itself).

Panels (e) and (f) show the maps of the local median values obtained with the uncorrected (raw) components of the motion: $\Delta\mu_\alpha \cos\delta$ in panels (e) and $\Delta\mu_\delta$ in panels (f). Each point is a source, colour-coded according its locally-averaged PM value, as shown on the colour bar on the right-hand side of panels (e). Panels (g) and (h) show similar maps after the high-frequency variations are corrected. Points are colour-coded using the same colour scheme as panels (e) and (f).

We verified that after the correction, neither component of the corrected PM suffers from systematic effects due to stellar colour (panels (a) and (b)) and luminosity (panels (c) and (d)), dividing the stars into bins of fixed size in colour and magnitude, and evaluating the 3σ-clipped median value of the motion along $\Delta\mu_\alpha \cos\delta$ and $\Delta\mu_\delta$. The lack of systematic effect is clearly visible from panels (a), (b), (c) and (d), where the computed median values are shown as a red filled circles, with error bars.

The quantities $\Delta\mu_\alpha \cos\delta$ and $\Delta\mu_\delta$ are in units of mas yr^{-1} in all the panels. The associated errors of the mean are typically smaller than the size of the red circles. As a reference the red horizontal line shows the lack of systematic effects.

Panel (i) shows the PM diagram after the *a posteriori* correction. Since our reference list consists of cluster members, our PMs are relative to the cluster mean motion, and cluster members are represented by the bulk in the centre of the PM diagram. All other sources are foreground and background field sources. Finally, panel (j) shows PM errors as a function of the $m_{\rm F606W}$ magnitude.

4.5.1 Membership probability

To derive the membership probability, we followed a method based on PMs described by Balaguer-Núnez, Tian, and Zhao (1998), Bellini et al. (2009) and Nardiello et al. (2018). The density function of cluster and field stars is modelled with an axisymmetric 2D Gaussian distribution centered respectively on the origin of the vector-point diagram (VPD; since PMs are computed relative to the cluster's bulk motion) and on the field proper motion centre. Cluster and field stars were selected on the basis of their position on the VPD. For each target star, the membership probability was estimated using a sub-sample of reference stars having a magnitude similar to those of the target. We refer to Scalco et al. (2021) for a detaliated description of the method.
Figure 4.7 shows an example of field-star decontamination based on membership probabilities. Poorly measured stars were removed using the parameters described in section 4.4. No quality-selection cuts are applied for saturated stars. Panel (a) shows the $m_{\rm F606W}$ vs. $m_{\rm F606W} - m_{\rm F814W}$ CMD while panel (b) illustrates the membership distribution. The red line, drawn by hand, separates cluster members from field stars, which are represented in black and in red respectively in all the panels. We highlight in blue the stars that are saturated in at least one filter. Finally, saturated stars with no proper motion measurements and for which it is not possible to estimate the membership probability are represented in green.

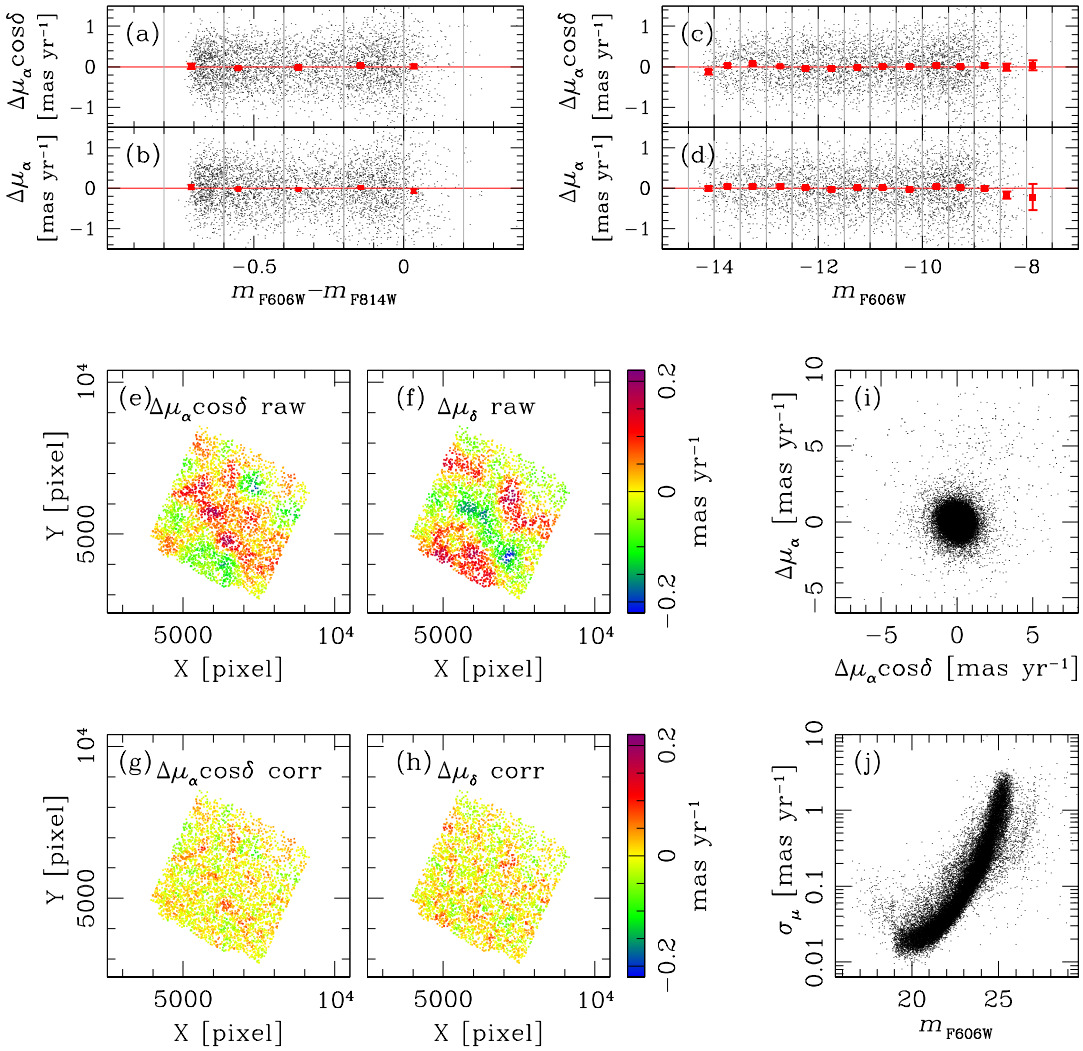

FIGURE 4.5: This figure illustrates the *a posteriori* procedure applied to the raw PM measurement for field F4. Panels (a) and (b) show that corrected PMs (in units of mas yr^{-1}) do not suffer from systematic effects as a function of stellar colour. Similarly, panels (c) and (d) show that corrected PMs do not suffer from systematic effects as a function of stellar magnitude. In panels (e) and (f) we report the maps of the locally measured mean raw PM components of cluster members. Specifically, the deviation along $\mu_\alpha \cos\delta$ is in panel (e), and the deviation along μ_δ is in panels (f). Each star is colour-coded as shown by the vertical bar the immediate right of panel (f). Panels (g) and (h) show the maps of the locally-measured mean corrected PM of cluster members. We applied the same colour-scheme as in panels (e) and (f). Panel (i) shows the corrected proper motion diagram. Finally, panel (j) shows the corrected proper motion error in function of the F606W magnitude.

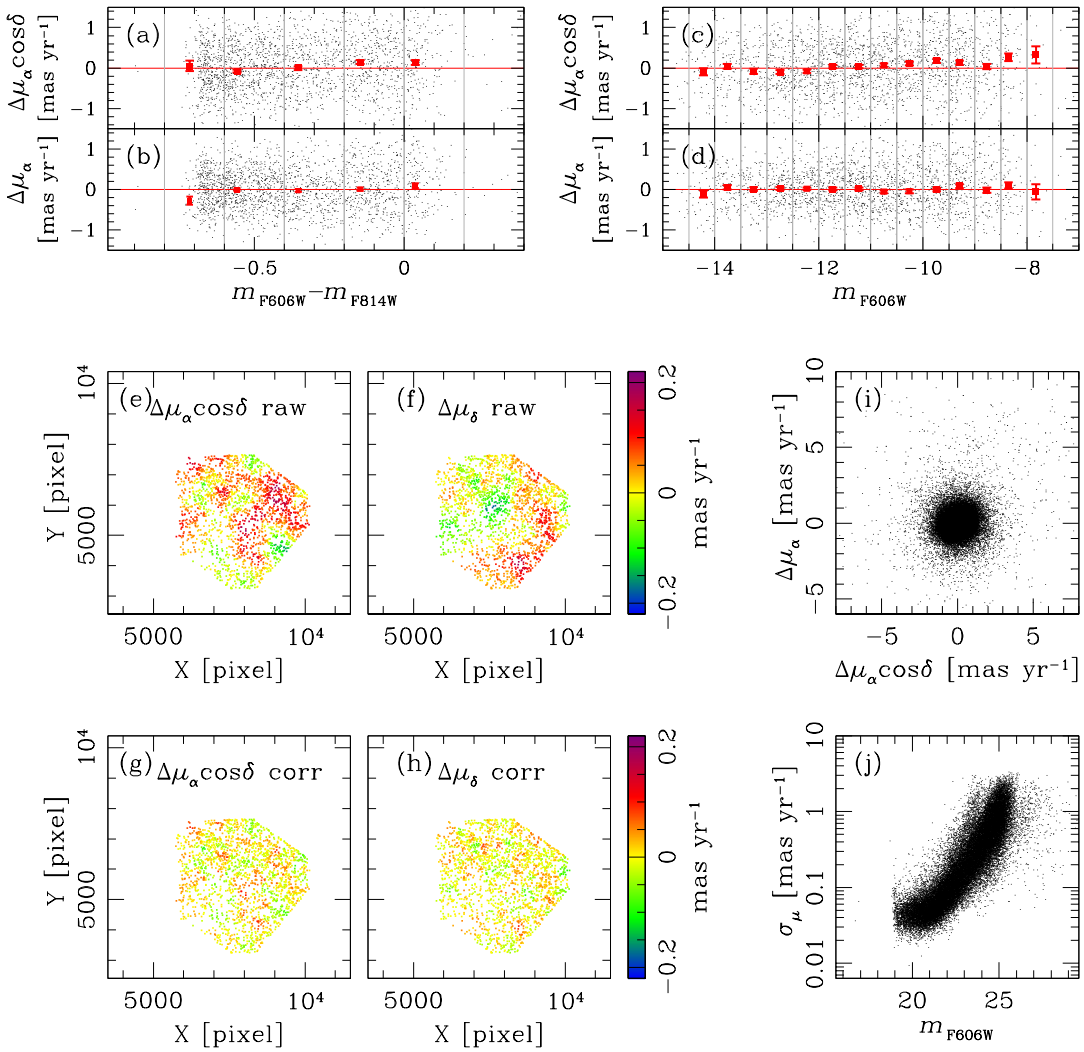

FIGURE 4.6: As in Figure 4.5 but for field F5.

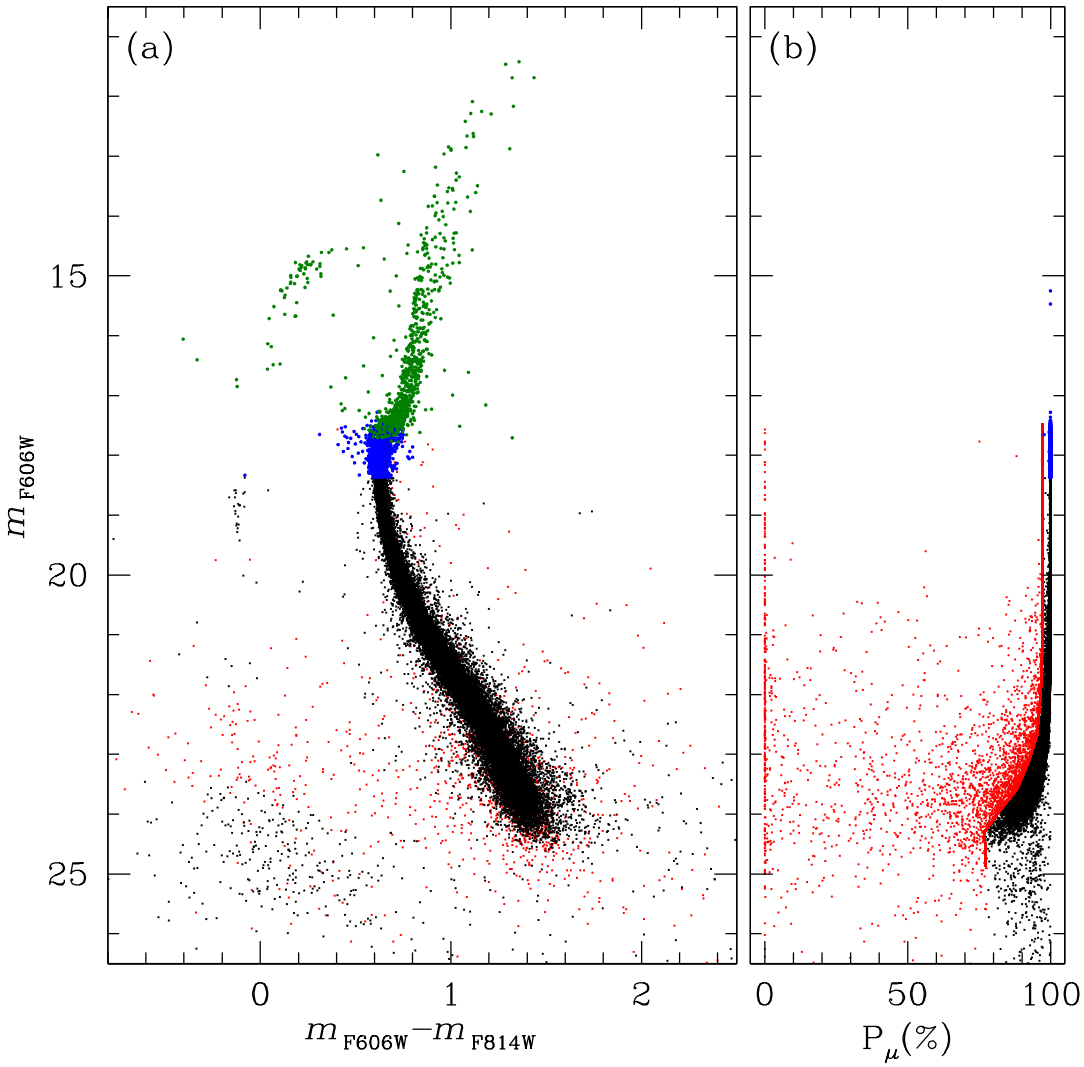

FIGURE 4.7: Probable-member selection.Only well-measured stars are shown. No quality selection cuts are applied to saturated stars. Panel (a) shows the m_{F606W} vs $m_{F606W} - m_{F814W}$ CMD. Saturated stars with no proper motion measurements and for which is impossible to estimate the membership probability are shown in green. Panel (b) presents the membership probability as a function of m_{F606W} magnitude, and the selection drawn by hand. In all panels, we highlight in red field stars and in black likely cluster member. Stars that are saturated in at least one filter are shown in blue.

TABLE 4.3: Extract of the Method-one F814W Photometry File

m_{F814W}	RMS	QFIT	o	RADXS	N_f	N_g	Sky (e^-)	rms Sky (e^-)	Sat flag
...	...	...	...	...	...	...	...	...	...
24.1816	0.0485	0.932	9.18	0.1156	2	2	34.8	7.4	0
21.8427	0.0022	0.995	54.15	0.0011	2	2	60.8	15.5	0
21.9605	0.0056	0.997	347.01	0.0129	2	2	0.0	0.0	0
23.4890	0.0148	0.969	101.74	−0.0154	2	2	44.6	11.6	0
22.4107	0.0141	0.992	0.39	−0.0144	2	2	45.8	10.2	0
24.1861	0.0472	0.928	0.38	−0.0100	2	2	44.3	6.7	0
22.3460	0.0080	0.994	0.46	0.0055	2	2	41.6	10.0	0
21.7213	0.0065	0.998	6.60	0.0069	2	2	58.6	12.9	0
22.4028	0.0020	0.994	191.56	0.0038	2	2	66.2	21.7	0
23.5722	0.0240	0.970	79.53	0.0454	2	2	43.9	7.6	0
...	...	...	...	...	...	...	...	...	...

4.6 The catalogue

The catalogue consists of an astrometric- and several photometric files. Each file contains a description of the data and has the same number of lines, one for each source in the same order.
The astrometric file (ID_XY_RD.dat) contains the star ID, an identifier number associated to the field containing the star, stellar position both in X, Y (pixels) and R.A., DEC. (decimal degrees), followed by PM information and PM diagnostic as described in Bellini et al. (2014); the last 5 columns contain the proper motion and the associated errors along R.A. and DEC. after the *a posteriori* correction, and the membership probability. Stars with no PM measurements, have a flag value of −999.999 for all PM related columns except for U_{ref} (a flag value that tells if a star was used as reference cluster member for the six-parameter linear transformation in the PMs evaluation), N_{found} and N_{used}, which are instead flagged to −999.
For each filter, we provide a different file for each photometric method (e.g., F336W.m1.dat, F336W.m2.dat, or F336W.m3.dat for methods one, two and three, respectively) containing VEGAMAG magnitudes, quality parameters (RMS, QFIT, o, RADXS, N_f and N_g) for each measured star. In addition, the method-one files also contain information about the local sky background, as well as a saturation flag to distinguish between unsaturated and saturated stars. For F606W and F814W filters, when a star is saturated or not found in the long exposures, its photometry is recovered from the short exposures. The photometry of saturated stars comes from the first-pass reduction.
If a star is not found in a given filter the VEGAMAG magnitude is flagged to −99.999 and the QFIT, o and RADXS parameters are flagged to 0. For stars measured in only one image, it is not possible to compute the RMS parameter, so its value is flagged to −99.999. Finally saturated stars have a flagged value of −99.999 for RMS and 0 for the other parameters. Tables 3-6 show an extract of the astrometric file and the three photometric files for the F814W filter.

A visual summary of the catalogue is given in Figure 4.8 for two different CMDs, obtained using filters that span different intervals of wavelength: m_{F336W} vs. $m_{F275W} - m_{F438W}$ (ultraviolet filters) in panel (a) and m_{F606W} vs. $m_{F606W} - m_{F814W}$ (optical filters) in panel (b). Poorly measured stars are removed using the photometric parameters described in section 4.4 and following the selection illustrated in Figure 4.3.

TABLE 4.4: Extract of the Method-two F814W Photometry File

m_{F814W}	RMS	QFIT	o	RADXS	N_f	N_g
...	...	...	...	...	...	...
24.3164	0.1257	0.920	2.10	0.1397	2	2
21.8407	0.0499	0.994	31.58	−0.0027	2	2
21.9785	0.0160	0.995	49.63	0.0143	2	2
23.4789	0.0933	0.955	21.61	0.0013	2	2
22.4051	0.0428	0.991	0.08	−0.0273	2	2
24.2631	0.2656	0.923	0.00	0.0406	2	2
22.3610	0.0344	0.993	0.20	0.0039	2	2
21.7218	0.0583	0.997	2.57	0.0099	2	2
22.4545	0.0207	0.991	45.59	0.0258	2	2
23.6672	0.0150	0.967	15.33	0.0926	2	2
...	...	...	...	...	...	...

TABLE 4.5: Extract of the Method-three F814W Photometry File

m_{F814W}	RMS	QFIT	o	RADXS	N_f	N_g
...	...	...	...	...	...	...
24.4484	0.2428	1.000	1.25	0.1783	2	2
21.8588	0.2563	1.000	5.82	0.0022	2	2
22.0078	0.1014	0.993	32.32	0.0083	2	2
23.4459	0.1602	0.967	11.25	−0.0227	2	2
22.3593	0.0175	0.999	0.01	−0.0360	2	2
24.1225	0.4952	0.990	0.00	−0.0271	2	2
22.3395	0.0179	0.998	0.03	−0.0014	2	2
21.7377	0.0137	1.000	1.08	0.0043	2	2
22.4470	0.0121	1.000	42.52	−0.0053	2	2
23.8316	0.0319	0.998	9.27	0.1131	2	2
...	...	...	...	...	...	...

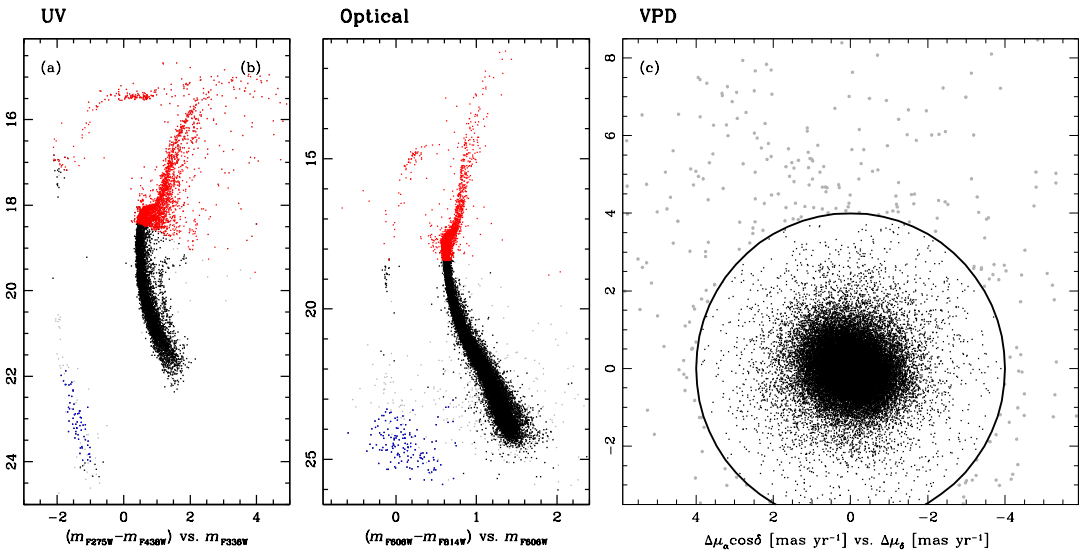

FIGURE 4.8: CMD for different interval of wavelength obtained after removing the poorly measured stars and correcting for differential reddening as in Bellini et al. (2017c). (a) m_{F336W} vs. $m_{F275W} - m_{F438W}$ ultraviolet CMD. (b) m_{F606W} vs. $m_{F606W} - m_{F814W}$ optical CMD. For panels (a) and (b) saturated stars are in red while WDs are in blue and likely cluster members are represented in black while probable foreground and background field objects are in gray. Panel (c) shows the VPD of the relative PMs of the best measured stars in the two analysed fields, where we set a 4 mas yr^{-1} limit from the bulk distribution of the most probable cluster-members (black dots), and indicate background and foreground field sources with gray filled dots.

Probable cluster members and background sources are separated using the membership probability, and are represented respectively with black and gray dots in panels (a) and (b) of Figure 4.8. We corrected the photometry for differential reddening following the method described in Bellini et al. (2017c), which is an evolution of procedures described in Sarajedini et al. (2007). Saturated stars are represented in red while WDs are in blue. Panel (c) shows the VPD of the relative PMs, after the *a posteriori* correction, of the two analysed fields. Likely cluster-member, within 4 mas yr^{-1} from the bulk distribution, are represented with black dots, while background and foreground field sources are represented with gray filled dots.
Together with the astro-photmetric catalogue, we also release for each of the two fields the atlases, i.e., a view of the field through stacked images. We produce those in two versions: sampled at 1×- and at 2×-supersampled pixels. These stacked images are in standard `fits` format and contain in their headers the astrometric WCS solution linked to Gaia eDR3.

4.7 The main sequence multiple stellar populations

In what follows we provide a study of the multiple stellar populations along the MS of ω Cen. The study presented here, follow precisely the method presented in Bellini et al. (2017b), Bellini et al. (2017c), and Bellini et al. (2017d), and its described in the following.

4.7.1 Sample selection and differential-redening correction

In addition to the catalogue obtained for fields F4 and F5, we retrieved the catalogue for fields F2 and F3 as published in Scalco et al. (2021). Our combined catalogue encompasses a substantial number of sources across a wide range of radial distances from the cluster centre. The intermediate fields F4 and F5 exhibit higher population densities and a higher number of stars compared to the external fields F2 and F3, offering robust statistical significance. Notably, the photometry in field F4, with its extensive observations in F438W, F336W, and F275W, demonstrates greater precision and accuracy than that of field F5.

As outlined in the preceding section, the photometric measurements of stars within our catalogue were conducted using three distinct methods, each designed for specific magnitude ranges (refer to Bellini et al. 2017b; Nardiello et al. 2018; Scalco et al. 2021 for details). For our analysis, we opted to utilize the photometry obtained through the first method, as it yields the most accurate photometry within the magnitude range under consideration.

In what follows we describe the selection process applied to identify a sample of well-measured stars and the subsequent differential reddening correction performed on the selected sample for each field.

Sample selection

To ensure a well-measured sample of stars, we implemented a selection process using a set of quality parameters provided by `KS2`, following a similar approach as described in Scalco et al. (2021); Bellini et al. (2017b) and Bellini et al. (2017c). The quality parameters employed include the photometric error ($\sigma_{\rm PHO}$), the quality-of-fit (QFIT) parameter, which quantifies the PSF-fitting residuals, and the RADXS parameter, a shape parameter that allows for differentiation between stellar sources, galactic sources, and cosmic ray/hot pixels introduced in Bedin et al. (2008). Further details regarding these parameters can be found in Bellini et al. (2017b), Nardiello et al. (2018), and Scalco et al. (2021).

The selection process is described in the following and it has been applied to each field separately. For each filter, we divided the stars into 0.5 magnitude bins and evaluated for each bin the 2.5σ-clipped median value and dispersion (σ) of each photometric parameter. We then defined a series of points by adding (for $\sigma_{\rm PHO}$ and RADXS parameters) or subtracting (for the QFIT parameter) 2.5σ from the median values of each magnitude bin and interpolated the points with a spline. Stars with $\sigma_{\rm PHO}$ or |RADXS| values above or QFIT values below the interpolating spline are considered bad-measured stars and excluded from the analysis. However, we set two hard constraints: stars are always considered well-measured and included in the analysis if their QFIT values are above 0.95, and if their |RADXS| values are below 0.1. Finally, we required selected stars to be cluster members by excluding all the sources with MP<90%.

Differential-reddening correction

We corrected our photometry for the effects of differential reddening on zero-point variations with location in the field following the procedure described by Bellini et al. (2017c) (see also Sarajedini et al. 2007; Milone et al. 2012d). The differential-reddening correction is been applied for each field separately. Briefly, for each field, we started by selecting a sample of reference stars by choosing all objects likely belonging to the most populated sequence in the $m_{\rm F814W}$ versus $m_{\rm F275W} - m_{\rm F814W}$

and $m_{\rm F814W}$ versus $m_{\rm F336W} - m_{\rm F438W}$ CMDs, in close analogy of what was done in Bellini et al. (2017c). We limited our reference stars to be within the magnitude range $16.5 < m_{\rm F814W} < 18.8$. We evaluated a separate differential-reddening correction for each of the CMDs utilised in this chapter. For each CMD, we derived the fiducial line of our sample of reference stars in the CMD and measured the residual in colour between our sample of reference stars and the fiducial along the reddening directions. For each star, we considered the median of the residual values from the 75 or 50 neighbouring reference stars as the best estimate of the differential reddening.

4.8 The stellar populations

We employed the methodology outlined in Bellini et al. (2017d), to discern and characterize the distinct stellar populations within our selected star sample. The procedure involves several steps and can be summarized as follows: we initiate the process with a preliminary selection of a specific population on the CMD where its features are most prominent. We then plot these preliminarily selected stars on various CMDs, in which outliers are easily discernible and can be excluded. We employed rectified and parallelized two-colour diagrams, namely chromosomic maps (ChMs, for additional details, see Milone et al., 2015a; Milone et al., 2015b) to highlight finer population structures. Once stars belonging to a particular population are identified and isolated, they are removed from consideration, and the process is reiterated for other populations. This iterative approach continues until no further distinct sequences can be reliably identified. We refer to Bellini et al. (2017d) for a complete description of the procedure.

For consistency and comparability with the findings presented in Bellini et al. (2017d), we meticulously followed the same procedures, utilized identical CMDs, and employed the same fiducial lines (with small adjustments in colour and magnitude to align with our photometry). This approach ensured that our selections on the CMDs and the verticalization process remained consistent (we refer to Bellini et al., 2017d, for a comprehensive description of the CMDs and fiducials used). However, the envelopes used to define the subpopulations in ChMs are not identical to those used in Bellini et al. (2017d). Instead, they are defined manually for each field separately in this work due to potential significant differences in ChMs at various radial distances. The entire procedure was repeated independently for each field and it is briefly presented below for field F4. The corresponding figures for the other fields can be found in the end of the Section.

All CMDs feature $m_{\rm F438W}$ on the y-axis, with varying colours. Following the convention in Bellini et al. (2017d), we will henceforth identify a CMD solely by its colour.

4.8.1 MSa

One of the most distinguishable populations is the MSa (where the *a* stands for *anomalous*, see Pancino et al., 2000), characterized by a narrow sequence that is notably redder and more curved compared to the majority of MS stars. Panel (a) of Fig. 4.9 illustrates the $m_{\rm F336W} - m_{\rm F438W}$ CMD of stars within our selected sample for field F4. In this CMD, stars attributed to the MSa are distinctly separated from the remaining MS population, with the colour boundaries delineated by red lines. The magnitude range for selection is confined between $19.26 < m_{\rm F438W} < 22.36$, as indicated by two horizontal red lines in panel (a) (note that the bright limit will be

set to a fainter level for the analysis of the other populations). Subsequently, the initially selected MSa stars are plotted on the $m_{\rm F438W} - m_{\rm F606W}$ CMD (black dots in panel (b)), while the remaining unidentified MS stars are shown in grey. Our MSa selection is restricted to stars within the two red lines (hereafter, red lines will always indicate our selection boundaries, black points will denote selected stars from the previous panel, while all other stars will be in grey). Panel (c) shows the $m_{\rm F275W} - m_{\rm F438W}$ CMD of the surviving MSa stars that passed both selections in panels (a) and (b). A few additional outliers from our MSa candidates (black points outside the two red lines) were subsequently removed. Finally, the $m_{\rm F336W} - m_{\rm F438W}$ and $m_{\rm F275W} - m_{\rm F336W}$ CMDs of the stars that passed all selections are shown in black in panels (d) and (f), respectively, while the excluded stars are shown in grey. In each panel, we used two fiducial lines (represented in green) enclosing the MSa population to rectify and parallelize the population sequence (hereafter, the fiducial used to verticalize the CMDs will be represented in green to differentiate it from the fiducials used for making selections). To do this, we defined for each star the quantity $\Delta^{\rm N}_X = [(X - X_{\rm blue\,fiducial})/(X_{\rm red\,fiducial} - X_{\rm blue\,fiducial})]$ where $X = (m_{\rm F336W} - m_{\rm F438W})$, $(m_{\rm F275W} - m_{\rm F336W})$ and $X_{\rm blue\,fiducial}$ and $X_{\rm red\,fiducial}$ are the colour of the blue and red fiducial at the F438W magnitude of the corresponding star. The verticalised $\Delta^{\rm N}_{\rm F336W-F438W}$ and $\Delta^{\rm N}_{\rm F275W-F336W}$ CMDs of only selected stars are represented in panels (e) and (g). The ChM obtained from the combination of the two verticalised diagrams is shown in panel (h), while the Hess diagram of the ChM is shown in panel (i). The colour mapping of this and the following Hess diagrams goes from blue (lowest density), green (average density), yellow, and red (highest density). The shape of the ChMs shown in panels (h) and (i) closely resembles the one reported in Bellini et al. (2017d, see Fig. 1), where a similar distribution was observed. Bellini et al. (2017d) identified a primary clump at the ChM centre, extending into a tail towards the lower-left region, alongside a secondary, less populated clump in the upper-right area. This closely resembles what we observe here: there is a prominent main clump centred around coordinates (0.5, 0.5) with a tail extending towards (0.1, 0.1). A secondary, less populated clump positioned approximately at (0.75, 0.9) seems to emerge, although the statistical significance of this second clump is very low due to the limited number of sources available. Following Bellini et al. (2017d) two subpopulations of MSa are defined in panel (l): the MSa1 (dark yellow) and the MSa2 (light yellow), within the black envelopes. All the sources outside these envelopes are rejected.

The corresponding procedures for fields F5, F3, and F2 are shown in Fig. 4.16, 4.22, and 4.28, respectively. The ChM obtained for field F5 closely resembles that of field F4, albeit with a slightly more blurred appearance due to the lower photometric quality of field F5. Similarly, the ChMs obtained for fields F2 and F3 exhibit a similar pattern, but the limited number of stars in these fields, particularly belonging to the MSa populations, results in low statistical significance. As a result, a reliable separation of the two stellar populations is not feasible in these fields, and therefore, only the total number of MSa stars in these two fields was considered. The final sample of MSa stars in fields F2 and F3 consist of those falling inside the black envelope in panel (l) of Fig. 4.28 and Fig. 4.22, respectively, represented by black dots.

4.8.2 bMS

The blue MS (bMS, see Bellini et al., 2009) stands out distinctly on the blue side of the MS, rendering it easily distinguishable. This is evident in panel (a) of Fig. 4.10, which illustrates the $m_{\rm F438W} - m_{\rm F814W}$ CMD. In this and the following panels of

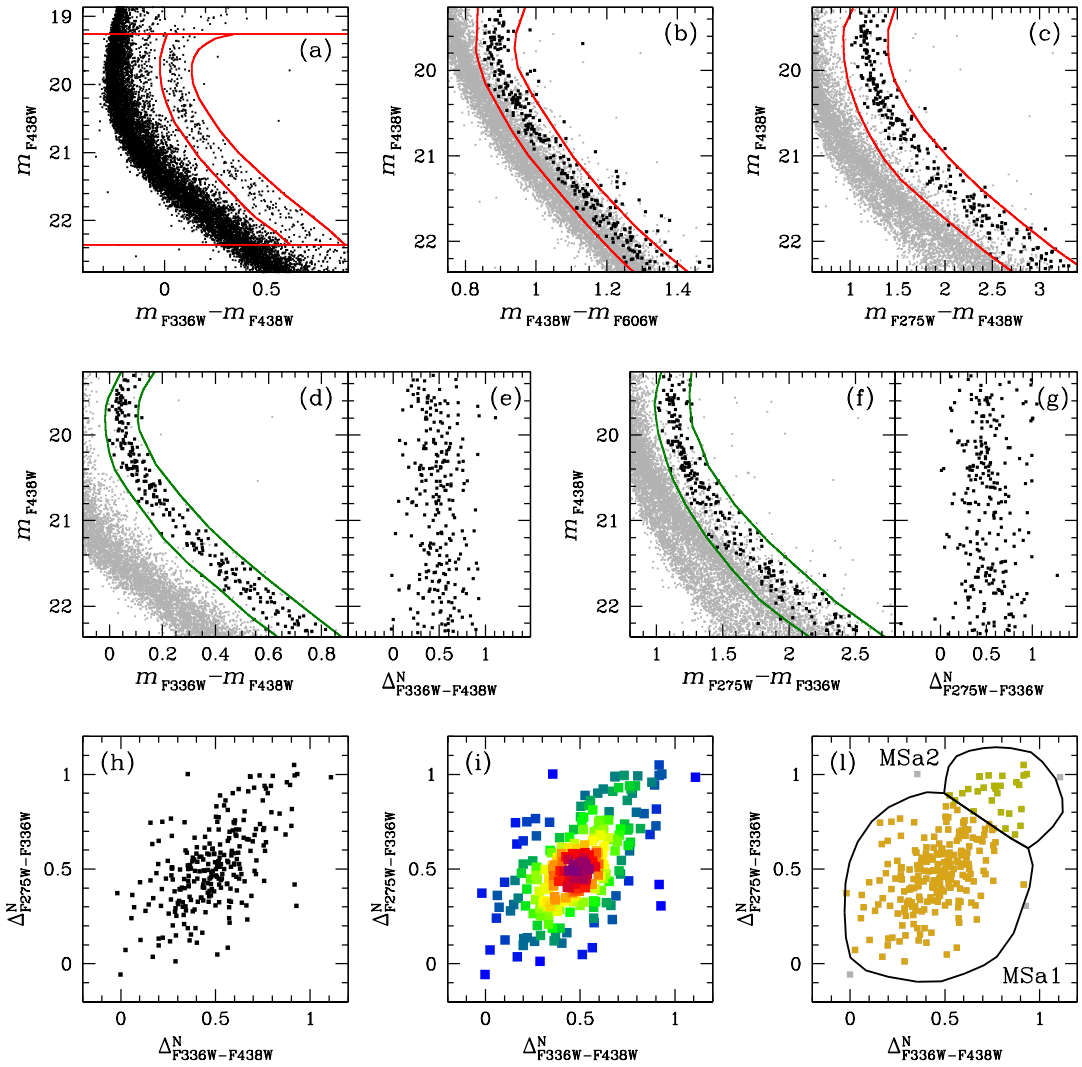

FIGURE 4.9: Illustration of the selection procedures we applied to isolate MSa stars. (a) Preliminary selection of MSa candidates on the $m_{F336W} - m_{F438W}$ CMD (within the red lines). (b)-(c) Selection refinements using two CMDs of different colours. In black we show MSa stars selected from the previous panel, in grey the rest of the MS. Rejected stars are those outside the two red lines. (d) Fiducial lines (in green) used to verticalize the MSa in the $m_{F336W} - m_{F438W}$ CMD. Stars that survived the selections from panels (a)+(b)+(c) are represented in black, while other stars are in grey. (e) Verticalized $\Delta_{m_{F336W}-m_{F438W}}$ CMD. (f)-(g) Same as panels (d) and (e) but for the $m_{F275W} - m_{F336W}$ CMD. (h) $\Delta_{m_{F275W}-m_{F336W}}$ versus $\Delta_{m_{F336W}-m_{F438W}}$ ChM of MSa stars. (e) Hess diagram of the ChM. (f) The two defined MSa subpopulations: MSa1 (in dark yellow) and MSa2 (in light yellow).

the figure, all previously identified stars (in this case, MSa1 and MSa2 stars) have been removed. The two red lines delineate the colour boundaries of our preliminarily selected bMS stars. The selection is confined to the magnitude range $20.16 < m_{\rm F438W} < 22.36$, as indicated by the two horizontal red lines. In panel (b) we show the $m_{\rm F336W} - m_{\rm F438W}$ CMD of preliminarily selected bMS stars from panel (a). Stars rejected in panel (a) are in grey. We removed a few outliers using the two red lines. A further selection refinement is applied on the $m_{\rm F275W} - m_{\rm F438W}$ CMD (panel (c)). The $m_{\rm F336W} - m_{\rm F438W}$ and $m_{\rm F275W} - m_{\rm F336W}$ CMDs of the stars surviving all the selections are represented in black in panel (d) and (f), respectively, while the excluded stars are shown in grey. The green fiducial lines are used to verticalise the sequences of bMS stars following the same procedure used above for the MSa. The two verticalised $\Delta^{\rm N}_{\rm F336W-F438W}$ and $\Delta^{\rm N}_{\rm F275W-F814W}$ CMDs are shown in panels (e) and (g). Panel (h) shows he $\Delta^{\rm N}_{\rm F336W-F438W}$ versus $\Delta^{\rm N}_{\rm F275W-F814W}$ ChM of the bMS stars, while the Hess diagram of the ChM is presented in panel (i). The shape of the ChMs presented in panels (h) and (i) closely resemble those illustrated in Bellini et al. (2017d, see Fig. 2). Consistent with the findings in Bellini et al. (2017d), we can distinctly identify three stellar populations, each characterized by clumps located at coordinates (0.3, 0.3), (0.5, 0.6), and (0.8, 0.8). It's worth noting that the clump situated at (0.5, 0.6) appears to be more prominent and visually discernible compared to the findings reported in Bellini et al. (2017d), suggesting a possible radial gradient within the bMS subpopulations. However, it's evident that all clumps display varying degrees of overlap and contamination with each other, and their structure appears highly fragmented. Following the same approach of Bellini et al. (2017d), we defined three subpopulations of the bMS in panel (l): the bMS1 (blue), the bMS2 (azure), and the bMS3 (cyan), each defined as all stars within the respective black envelope.

The procedures for identifying the bMS population in fields F5, F3, and F2 are outlined in Fig. 4.17, 4.23, and 4.29, respectively. Despite variations in photometric accuracy and statistical limitations, the general shape of the ChMs remains consistent across all fields. In field F5, the ChM resembles that of field F4, albeit slightly more blurred due to lower photometric accuracy. Given this limitation, we opted not to separate the three subpopulations but to consider only the total number of bMS stars for this field.

In fields F2 and F3, the visibility of the three clusters on the ChM is reduced due to limited statistics. Nevertheless, in the ChM in field F2, we can recognize a pattern similar to the ChM in field F4, with three distinct clumps located around coordinates (0.3, 0.3), (0.55, 0.55), and (0.85, 0.85). Notably, the central clump appears even more prominent compared to field F4, which aligns with the earlier anticipation of a potential radial gradient within the bMS subpopulations.

The field F3 presents a challenging scenario in the ChM analysis. The bMS1 populations appear to be absent, while there is a suggestion of an increase in the populations of bMS2 and bMS3. However, the positions of the three subpopulations in the ChM are not clearly defined, making reliable separation unfeasible. In spite of these considerations, we attempted to identify the three bMS subpopulations in field F2 (see panel (l) of Fig. 4.29), while we only considered the total number of bMS stars for field F3. The final sample of bMS stars in fields F5 and F3 consist of those falling inside the black envelope in panel (l) of Fig. 4.17 and Fig. 4.23, respectively, represented by black dots.

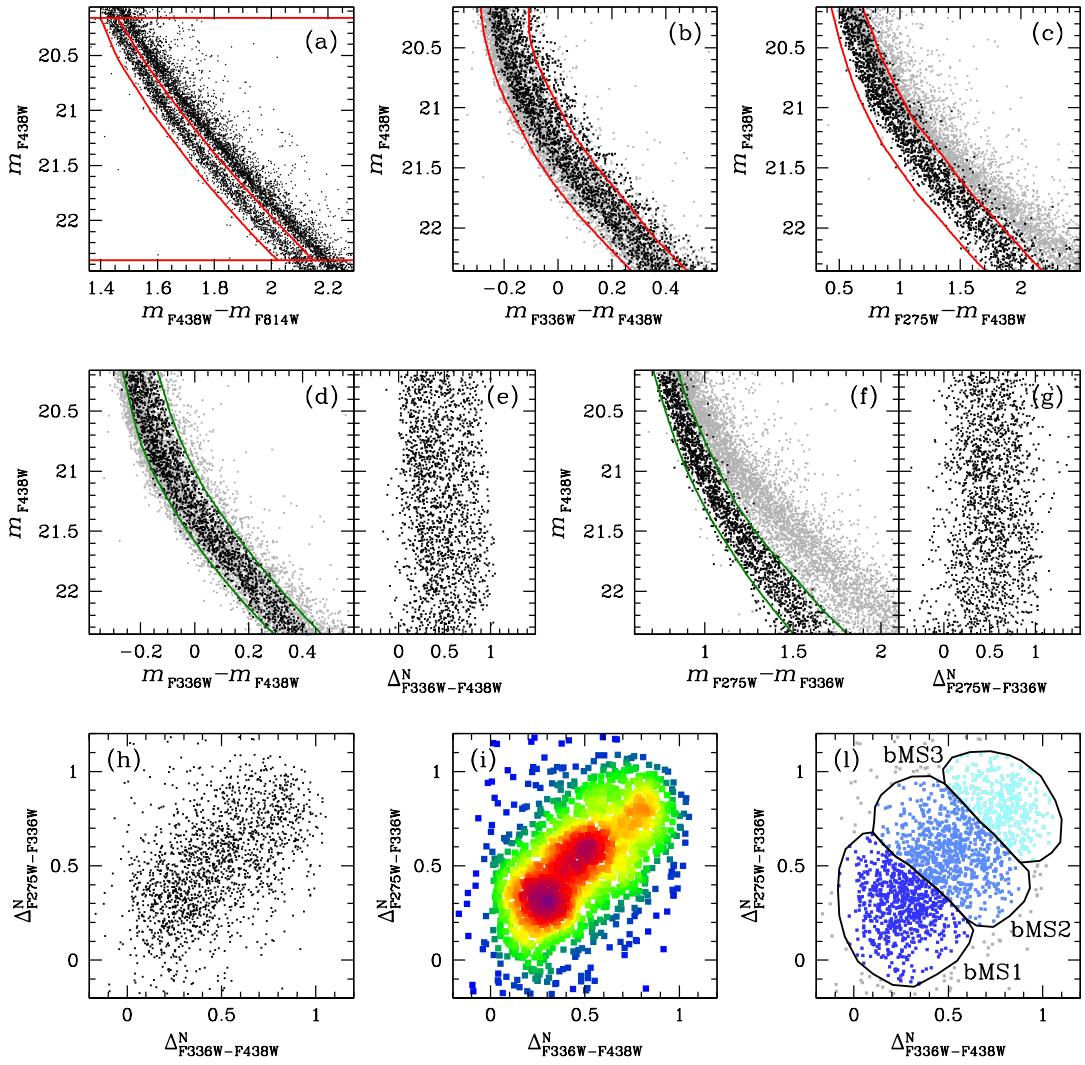

FIGURE 4.10: Similar to Fig. 4.9 but for the bMS stars. (a) Preliminary selection of bMS stars on the $m_{F438W} - m_{F814W}$ CMD (within the red lines). Already identified MSa1 and MSa2 stars have been removed from the CMD. (b)-(c) Preliminarily selected bMS stars are further refined using the $m_{F336W} - m_{F438W}$ and $m_{F275W} - m_{F438W}$ CMDs. As for Fig. 4.9, stars surviving from the previous panel are in black, while rejected stars are in grey. (d)-(f) Fiducial lines (in green) used to verticalize the MSa in the $m_{F336W} - m_{F438W}$ and $m_{F275W} - m_{F336W}$ CMDs. (e)-(g) Verticalized $\Delta_{m_{F336W}-m_{F438W}}$ and $\Delta_{m_{F336W}-m_{F438W}}$ CMDs. (h) $\Delta_{m_{F336W}-m_{F438W}}$ versus $\Delta_{m_{F275W}-m_{F814W}}$. (i) Hess diagram of the ChM. (l) The three main subcomponents of the bMS, namely bMS1 (dark blue), bMS2 (azure), and bMS3 (light blue).

4.8.3 rMS

Another straightforward population to isolate is the red MS (rMS, see Bellini et al., 2009). This population becomes apparent in the $m_{\rm F275W} - m_{\rm F814W}$ CMD shown in panel (a) of Fig. 4.11, after the removal of MSa and bMS stars. We kept the same magnitude limits as for the bMS, and preliminarily selected rMS stars on this panel by means of the two red lines. Selected stars are then plotted in black in the $m_{\rm F606W} - m_{\rm F814W}$ CMD of panel (b), where we remove a few outliers. An additional rejection of likely outliers is performed on the $m_{\rm F336W} - m_{\rm F438W}$ CMD of panel (c). We verticalised the sequencies of rMS stars on the $m_{\rm F336W} - m_{\rm F438W}$ and $m_{\rm F275W} - m_{\rm F336W}$ CMDs by means of the green iducials shown in panels (d) and (f). The two verticalised $\Delta^{\rm N}_{\rm F336W-F438W}$ and $\Delta^{\rm N}_{\rm F275W-F814W}$ CMDs are shown in panels (e) and (g). Panel (h) shows the $\Delta^{\rm N}_{\rm F275W-F336W}$ versus $\Delta^{\rm N}_{\rm F336W-F438W}$ ChM of selected rMS stars (in black). The corresponding Hess diagram is in panel (i). The shape of the ChMs presented in panels (h) and (i) resembles those reported by Bellini et al. (2017d, see Fig. 3). Similar to the findings in Bellini et al. (2017d), we can distinguish three distinct stellar populations, characterized by clumps located at coordinates (0.35, 0.65), (0.65, 0.45), and (0.8, 0.3). However, it is important to note that all clumps exhibit a higher degree of overlap and contamination compared to the results reported by Bellini et al. (2017d). The shape of these clumps and the relative abundance of their populations appear slightly different from the findings in Bellini et al. (2017d). Specifically, the leftmost clumps appear more prominent than those observed in the previous study. This variation could be attributed to contamination by other populations, such as the populations MSe (discussed in Section 4.8.5), or it could indicate intrinsic variations in the number of stars within the rMS subpopulations as a function of radial distance from the cluster centre. Following the approach of Bellini et al. (2017d) we defined three rMS subpopulations in panel (l): rMS1 (brown), rMS2 (red), and rMS3 (orange).

Corresponding figures for the other fields are presented in Fig. 4.18, 4.24, and 4.30. Across all fields, the general shape of the ChMs remains consistent. In field F5, the ChM resembles that of field F4, yet it is significantly blurred, hindering accurate identification of the three subpopulations. In fields F2 and F3, only the leftmost clump is clearly visible, appearing more prominent compared to fields F4 and F5, particularly in field F3. The other two clumps are barely discernible, posing challenges for identification. Similar to fields F4 and F5, the dominance of the leftmost clump in fields F2 and F3 might stem from contamination by other populations or intrinsic radial variations in the number of stars within the three rMS subpopulations. As a result, we opted not to estimate any subpopulations for these fields but we only consider the total number of rMS stars. The final sample of rMS stars in these fields consists of those falling inside the black envelope in panel (l) of Fig. 4.18, 4.24 and 4.30, represented by black dots.

4.8.4 MSd

Here, we turn our focus to the MSd population (see Bellini et al., 2017d). In panel (a) of Fig. 4.12, we present the $m_{\rm F336W} - m_{\rm F814W}$ CMD for stars not categorized under populations MSa, bMS, and rMS. We selected all stars falling between the two red diagonal lines and kept the same magnitude limits used for the bMS and rMS stars (red horizontal lines). Panel (b) shows the $m_{\rm F606W} - m_{\rm F814W}$ CMD of these selected stars in black, where two distinct sequences are evident. The MSd stars, situated in the blue component, are preliminarily selected (red lines) in panel (b). Further refinement

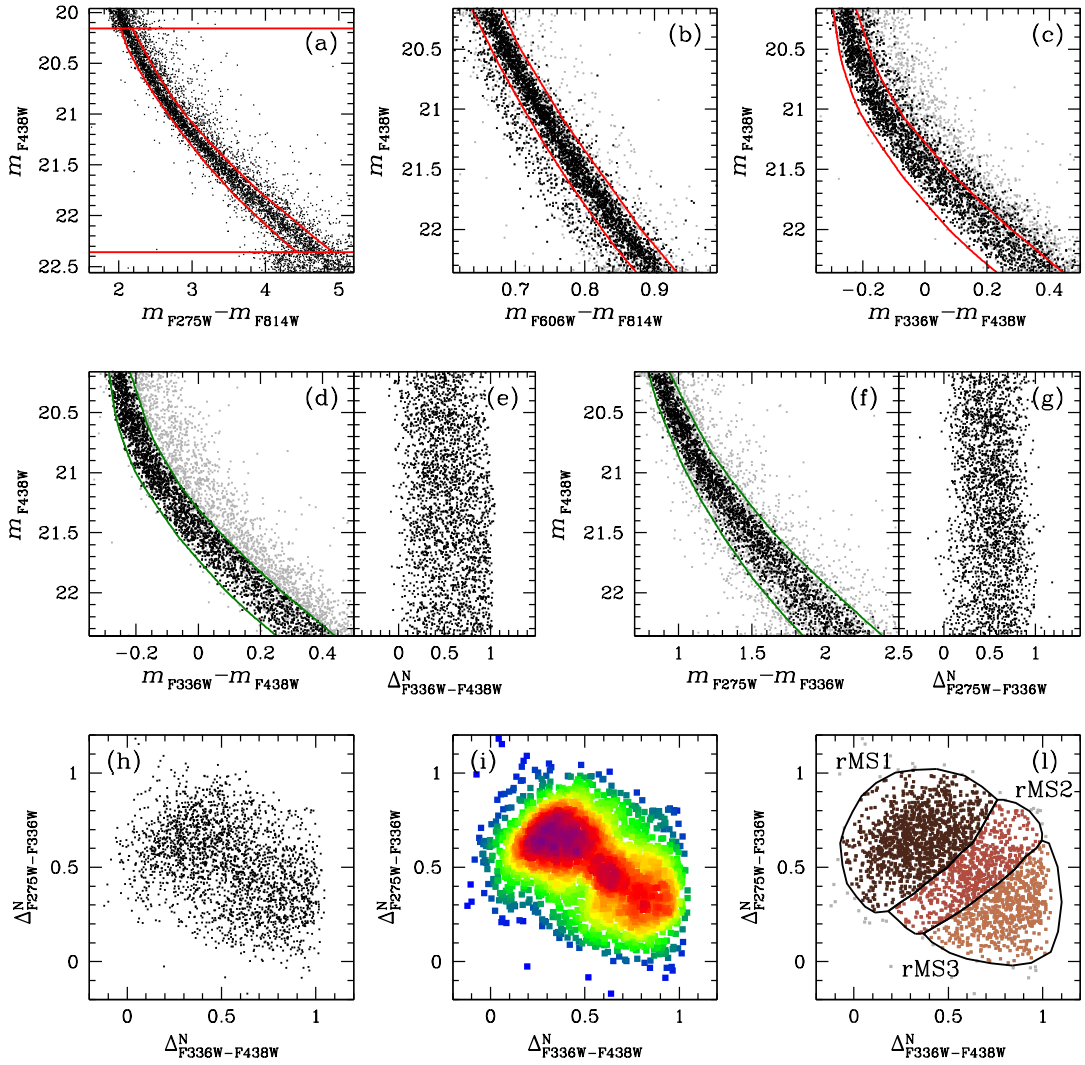

FIGURE 4.11: Similar to Fig. 4.9 and 4.10 but for the rMs stars. The Hess diagram in panel (i) reveals three main subcomponents, labelled as rMS1 (brown), rMS2 (red), and rMS3 (orange) in panel (l).

of the MSd sample involved removing a few outliers using the $m_{\rm F275W} - m_{\rm F814W}$ and $m_{\rm F336W} - m_{\rm F438W}$ CMDs (panels (c) and (d), respectively). The fiducials used to verticalised the MSd sequence in the $m_{\rm F336W} - m_{\rm F438W}$ and $m_{\rm F275W} - m_{\rm F336W}$ CMDs are shown in green in panels (e) and (g), while the verticalised $\Delta^{\rm N}_{\rm F336W-F438W}$ and $\Delta^{\rm N}_{\rm F275W-F814W}$ CMDs are shown in panels (f) and (h). The ChM and Hess diagrams of selected MSd stars are shown in panels (i) and (l), respectively. The ChM shape resembles that presented in Bellini et al. (2017d, see Fig. 5), where three clumps were identified: two primary clumps situated in the lower-left and centre sections of the plot, and a less populated clump positioned in the upper-right section. Similarly, we observe two main clumps at coordinates (0.25, 0.3) and (0.6, 0.65), along with a less populated clump at (0.8, 0.85). However, the two main clumps exhibit significant overlap and contamination, posing challenges in clear subpopulation separation. The border between these clumps appears higher and more towards the right than what was presented in Bellini et al. (2017d), with the (0.25, 0.3) clump appearing more prominent compared to the findings reported therein. The three subpopulations are defined in panel (m), labelled as MSd1 (pink), MSd2 (magenta), and MSd3 (purple).

The ChM for field F5 (see Fig. 4.19) presents a challenging scenario for the identification of the three subpopulations, displaying a different structure compared to what was obtained for field F4. Additionally, the ChMs for fields F3 and F2 (see Fig. 4.25 and 4.31, respectively) are characterized by a low number of stars and poor statistics, making it very difficult to identify the three clumps. Due to these limitations, we decided not to apply any subpopulation selection for these fields, but to only consider the total number of MSd stars. The final sample of MSd stars in these fields consists of those falling inside the black envelope in panel (m) of Fig. 4.19, 4.25, and 4.31, represented by black dots.

4.8.5 MSe

Here, we focus our attention to the red component, constituting the MSe population (see Bellini et al., 2017d), which was excluded in panel (b) of Fig. 4.12. Panel (a) of Fig. 4.13 is similar to panel (b) of Fig. 4.12, but without MSd stars. Within this panel, we initially selected MSe stars as those enclosed by the two red lines. Subsequently, we refined the MSe sample as shown in panels (b) and (c). Panels (d) and (f) of Fig. 4.13 shows the fiducials utilized to verticalize the MSe sequence, while panels (e) and (g) exhibit the verticalized CMDs. Panels (h) and (i) shows the ChM of the selected MSe stars and the corresponding Hess diagram. The ChM presented here closely resembles that illustrated in Bellini et al. (2017d, see Fig. 6): two prominent clumps are clearly discernible, situated approximately at (0.45, 0.3) and (0.25, 0.75). However, due to lower statistics, the identification of the additional two less populated clumps introduced by Bellini et al. (2017d) is not feasible. Therefore, we concentrate our attention solely on the two main clumps. In panel (l), we consequently delineate the following two MSe subpopulations: MSe1 (lime) and MSe2 (green).

The corresponding figures for fields F5, F3, and F2 are presented in Fig. 4.20, 4.26, and 4.32, respectively. For field F5, the obtained ChM closely resembles that of field F4, albeit more blurred. In fields F2 and F3, despite lower statistics, we are still able to identify the two subpopulations.

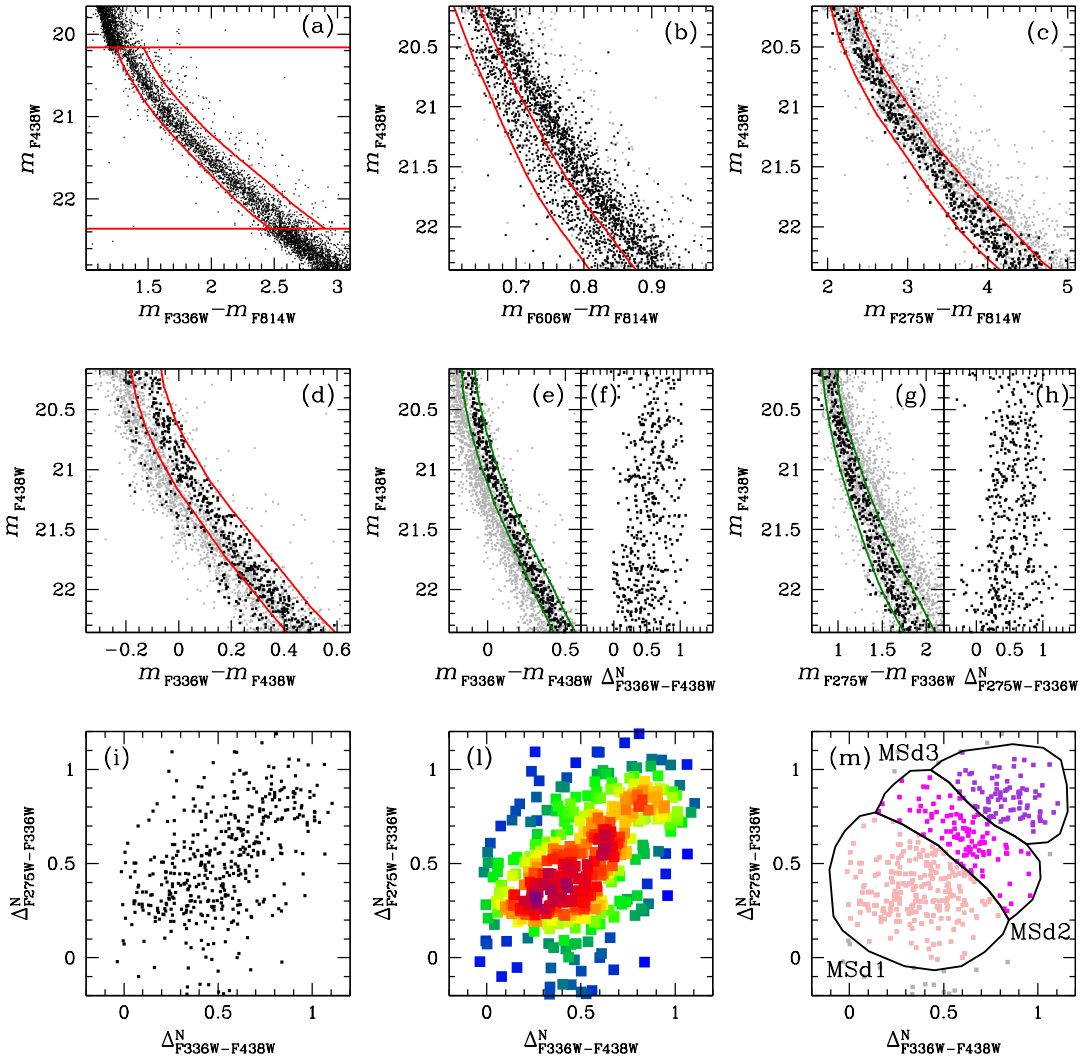

FIGURE 4.12: (a) $m_{F336W} - m_{F814W}$ CMD of the MS stars not belonging to MSa, bMs and rMS. We selected all stars falling between the two red diagonal lines. (b) $m_{F606W} - m_{F814W}$ CMD of the stars selected in (a), where they clearly split into two components. The MSd stars, situated in the blue component, are preliminarily selected. (c)-(d) Selection refinements for MSd stars. (e)-(g) Fiducials (in green) used to verticalise the MSd sequence in the $m_{F336W} - m_{F438W}$ and $m_{F275W} - m_{F336W}$ CMDs. (f)-(h) Verticalised $\Delta^{N}_{F336W-F438W}$ and $\Delta^{N}_{F275W-F814W}$ CMDs. The ChM (i) and Hess diagram (l) of MSd stars reveal three main subpopulations, which we define in panel (m) as MSd1 (pink), MSd2 (magenta), and MSd3 (purple).

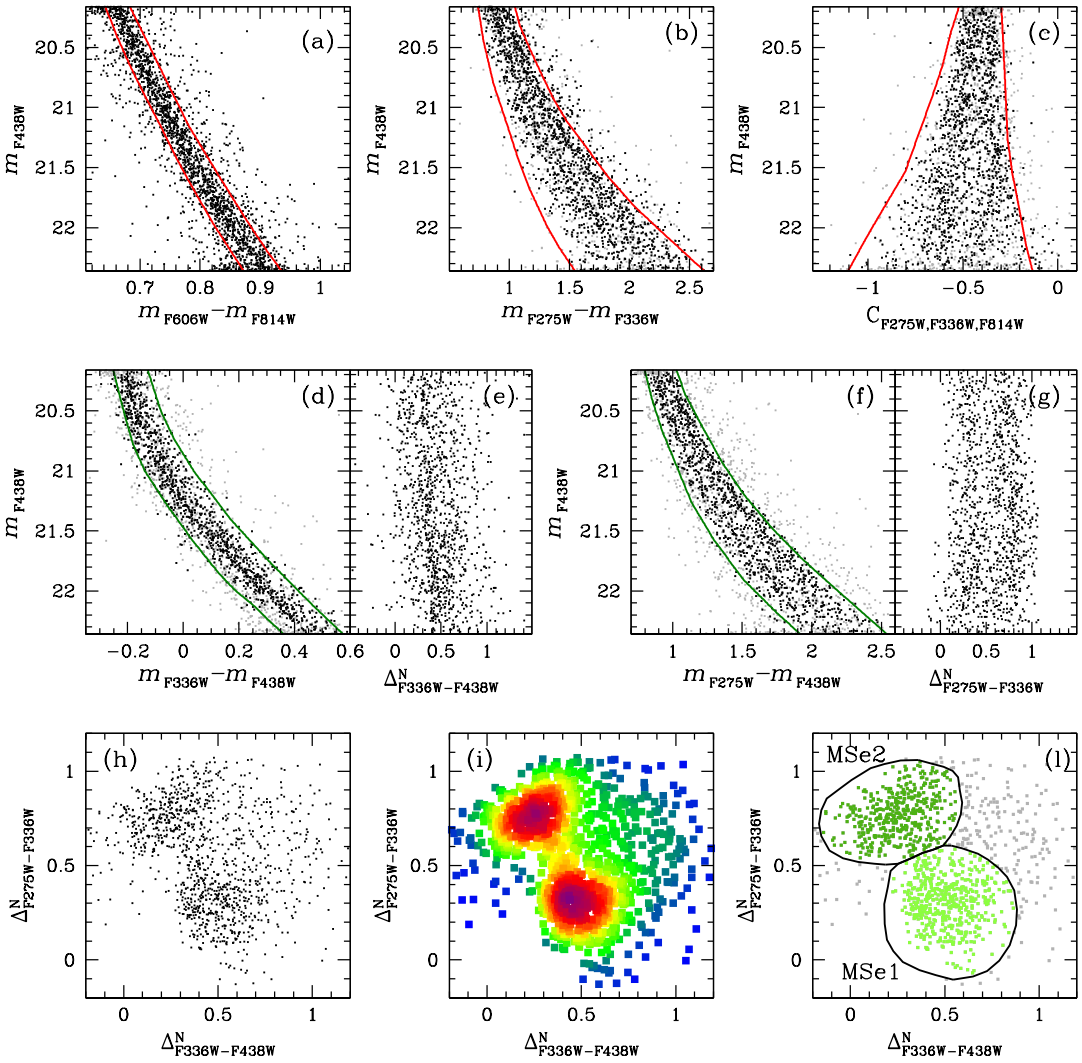

FIGURE 4.13: (a) Same as panel (b) of Fig. 4.12, in which we also removed MSd stars. The remaining stars, constituting the MSe population, form a well-defined sequence on this plane, which we select and further refine in panels (b) and (c). (d)-(f) fiducials (in green) used to verticalise the MSe sequences. (e)-(g) verticalised CMDs. (h)-(i) ChM and the Hess diagram of MSe stars. (l) We identified the two MSe populations as MSe1 (lime) and MSe2 (green).

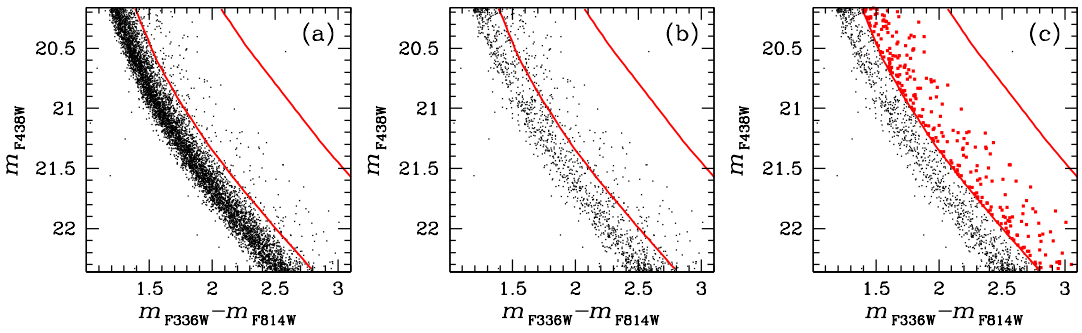

FIGURE 4.14: (a) $m_{F336W} - m_{F814W}$ CMD of ω Cen within the interval 20.35< m_{F438W} <22.55. (b) Same as (a) but with MSa1 and MSa2 stars removed. (c) Same as (b) but colour-coded to highlight the MSe3 and MSe4 subpopulations. (d) Same as (c) but with MSe3 and MSe4 stars also removed. The two red fiducial lines (taken from Bellini et al., 2017d) delineate the red and blue limits where binaries are expected. (e) Same as (b) but for unidentified stars only. Binary stars are identified as those between the two red lines and are depicted in red in panel (f), while the remaining unidentified stars are shown in black.

4.8.6 Estimate of the binary fraction

We determine the binary fraction within our sample of unidentified MS stars using the approach outlined in Bellini et al. (2017d). Panel (a) of Fig. 4.14 shows the $m_{F336W} - m_{F814W}$ CMD, where the stars form the subpopulations MSa1 and MSa2 were removed for clearer identification of binaries stars. The two red fiducial lines (taken from Bellini et al., 2017d) delineate the red and blue limits where binaries are expected. Panel (b) shows the same CMD as the preceding panel, but this time, we excluded all stars belonging to the previously identified subpopulations. Unidentified stars between the two red lines are potential binaries (represented in red in panel (c)). The relative plots for the fields F5, F3 and F2 are shown in Fig. 4.21, 4.27 and 4.33, respectively.

4.9 Radial variation among stellar populations

Table 4.6 presents the count and relative percentage of stars in the magnitude range $20.16 < m_{F438W} < 22.36$, across the five identified multiple stellar populations and their subpopulations, alongside the estimated number of binaries and unidentified stars in fields F2, F3, F4, and F5. Additionally, the corresponding values from the central field reported by Bellini et al. (2017d) are included. Each field's distance interval from the cluster centre is provided, with the fields listed in order from the closest to the farthest.

The separation and identification of multiple stellar populations, particularly their subpopulations, have proven to be more challenging than outlined in Bellini et al. (2017d). This difficulty stems from lower photometric accuracy and precision, attributed to fewer exposures (especially in field F5) and limited star counts and statistics, particularly evident in the two external fields, F2 and F3. Notably, the proportion of unidentified stars in our fields exceeds that reported for the central field (7.64% ± 0.14%), with the highest proportion observed in field F5 (23.94% ± 0.59%). This discrepancy is primarily due to the reduced photometric accuracy in this field.

In all fields analyzed, the two most populous stellar populations observed are the rMS and the bMS populations, except for field F3, where the MSe populations outnumber the bMS population.

The count of MSa stars shows a nearly consistent trend with radial distance from the cluster centre, although there is a subtle indication of a slight decrease. This trend is observed from a central value of 3.53% $\pm$ 0.10% to $\sim$2.4% in the intermediate (F4 and F5) and $\sim$1.7% in the external (F2 and F3) fields. The ratio between the two MSa subpopulations, MSa2/MSa1, in the two intermediate fields (the only ones where separation was feasible) aligns with the ratio found in the cluster centre (MSa2/MSa1 $\sim$0.09 $\pm$ 0.01, $\sim$0.08 $\pm$ 0.02 and $\sim$0.13 $\pm$ 0.03, for the central, F5 and F4 field, respectively), indicating no significant radial gradient between the two subpopulations.

A clear trend is observed in the bMS population with radial distance from the cluster centre, with bMS populations decreasing from the centre to the outskirts. Specifically, there is a central value of 32.32% $\pm$ 0.33%, dropping to $\sim$23-24% in the two intermediate fields (F4 and F5), and further to $\sim$15-16% in the two external fields (F2 and F3). Regarding the bMS subpopulations, as discussed in Section 8.4.2, the prominence of the central clump in the ChM of the two intermediate fields (F4 and F5, see Fig. 4.10 and 4.17) and in the two external fields (F2 and F3, see Fig. 4.29 and 4.23) compared to the ChM of the central field (see Fig. 2 of Bellini et al., 2017d) suggests a possible radial gradient within the three bMS subpopulations. A reliable division of the three bMS subpopulations was feasible only in the central field and fields F4 and F2. The number counts reveal that while the ratio between the number of bMS1 stars and the total number of bMS stars, bMS1/bMS, remains relatively constant (bMS1/bMS$\sim$0.38-0.40) within the three fields, the relative ratio for bMS2 shows an increase. It goes from a value of bMS2/bMS$\sim$0.29 $\pm$ 0.01 in the central field to a value of bMS2/bMS$\sim$0.42 $\pm$ 0.02 (an increase of $\sim$45%) in field F4 and bMS2/bMS$\sim$0.48 $\pm$ 0.06 (an increase of $\sim$60% compared to the central value) in field F2. At the same time, the relative ratio for the population bMS3 shows a decrease. It goes from a value of bMS3/bMS$\sim$0.31 $\pm$ 0.01 in the central field to a value of bMS3/bMS$\sim$0.20 $\pm$ 0.01 (a decrease of $\sim$37%) in field F4 and bMS3/bMS$\sim$0.14 $\pm$ 0.03 (a decrease of $\sim$56% compared to the central value) in field F2.

The number of rMS stars in the intermediate fields (29.98% $\pm$ 0.67% and 33.62% $\pm$ 0.79%, for F5 and F4, respectively) aligns with the central field value (33.20% $\pm$ 0.33%). However, an increase is noted in the number of rMS stars in the two external fields (45.64% $\pm$ 2.33% and 46.14% $\pm$ 2.25%, for F2 and F3, respectively). As anticipated in Section 4.8.3, the leftmost clump in the ChMs for the fields F5, F4, F3 and F2 present a prominence more evident with respect to what was found in the central field (see Fig. 3 of Bellini et al., 2017d). This can be due to contamination from other populations, especially the MSe populations, which partially overlap the rMS population in most CMDs, or can indicate a radial gradient within the rMS subpopulations. The only field in which we were able to separate the rMS subpopulations with sufficient accuracy was the F4 field. Analysis of the number counts reveals a notable trend: the rMS1/rMS ratio displays a significant increase. Specifically, it rises from rMS1/rMS$\sim$0.29 $\pm$ 0.01 in the central field to rMS1/rMS$\sim$0.49 $\pm$ 0.02 (an increase of $\sim$70%) in field F4. Conversely, the relative ratios for the rMS3 population exhibit a decrease. From the central field to field F4, the rMS3/rMS ratio decreases from rMS3/rMS$\sim$0.43 $\pm$ 0.01 to rMS3/rMS$\sim$0.27 $\pm$ 0.01 (a decrease of $\sim$37%). Finally, the rMS2/rMS ratio maintains a relatively constant value for the central field and field F4 ($\sim$0.25-0.29). Although we couldn't estimate the number counts of the rMS subpopulations in the two external fields (F2 and F3), their ChMs suggest a trend

similar to what was observed in field F4, with an increase in the rMS1 subpopulation and a decrease in the rMS3 subpopulation, with the population rMs2 remaining constant.

For the MSd population, the number of MSd stars in the two intermediate fields (4.68% $\pm$ 0.24% and 5.80% $\pm$ 0.29% for F5 and F4, respectively) aligns closely with the central field value (5.10% $\pm$ 0.12%), but slightly decreases in the two external fields (3.50% $\pm$ 0.54% and 3.23% $\pm$ 0.50% for F2 and F3, respectively). Among these fields, only field F4 allowed for the separation of the MSd subpopulations, although with considerable uncertainties due to the envelope positions in the ChM. Nonetheless, the number counts suggest a potential trend among the MSd subpopulations. While the MSd3/MSd ratio remains relatively constant in the central field and field F4 ($\sim$0.20-0.22), the relative ratios for the MSd1 and MSd2 subpopulations exhibit a radial gradient. Specifically, from the central field to field F4, the MSd1/MSd ratio increases from MSd1/MSd$\sim$0.38 $\pm$ 0.02 to MSd1/MSd$\sim$0.56 $\pm$ 0.05 (an increase of $\sim$68%), while the MSd2/MSd ratio decreases from MSd2/MSd$\sim$0.41 $\pm$ 0.02 to MSd2/MSd$\sim$0.24 $\pm$ 0.03 (a decrease of $\sim$60%). However, it's important to note that these numbers are affected by uncertainties stemming from the envelope positions on the ChM, as mentioned earlier.

For the MSe population, the number of stars remains relatively stable across varying radial distances from the cluster centre, ranging between $\sim$13.8% to 17.2%. Although we were unable to separate the smallest MSe subpopulations (MSe3 and MSe4) due to low statistics, we achieved accurate separation of the two main MSe subpopulations (MSe1 and MSe2) in all fields. The relative number of the two subpopulations, MSe1 and MSe2, maintains a constant ratio in the central field and in the intermediate fields (F4 and F5), with MSe2/MSe1 $\sim$1, while it shows a notable increase in the two external fields (F2 and F3), with a value of MSe2/MSe1 $\sim$2.2.

Concerning the number of binaries, there is an observed trend with radial distance, with an increase from 2.70% $\pm$ 0.08% in the central field to $\sim$4% in the intermediate fields and $\sim$6% in the external fields.

4.9.1 The bMS/rMS radial trend

As outlined in Section 8.1, Bellini et al. (2009) conducted an extensive examination of the radial distribution of the two primary stellar populations in ω Cen (rMs and bMS), identifying a radial gradient in their counts-number fraction (bMS/rMS). In Fig. 10.1, we show a comparison with the radial profile presented in Bellini et al. (2009, black points) alongside the ratios derived from the data presented in this study (red points), revealing a notable agreement between the two datasets.

4.10 Summary

In this chapter, we focused into the reduction process of HST data acquired through the GO-16247 programme (P.I. Scalco). We provided an overview of the dataset and the process of data reduction. Subsequently, we amalgamated the newly obtained data with previously processed data (as discussed in Chapter 2) to extend the analysis initiated by Bellini et al. (2017d), thus presenting, for the first time, a comprehensive examination of the radial gradient of the multiple stellar populations within ω Cen spanning a significant portion of the cluster.

Our analysis revealed significant trends within the stellar populations of ω Cen and their subpopulations. We observed a consistency in the radial distribution patterns of the two predominant stellar populations (bMS/rMS), aligning with findings reported by Bellini et al. (2009).

Globular cluster stars are typically divided into two distinct groups based on their chemical composition. The first population (1P) stars exhibit a composition similar to that of stars in the Galactic field, while the second population (2P) stars show depletion in certain light elements like carbon, oxygen, and magnesium, and enrichment in elements such as helium, nitrogen, aluminum, and sodium compared to 1P stars (see reviews by Smith, 1987; Bastian and Lardo, 2018b; Gratton et al., 2019).

According to various formation scenarios (D'Ercole et al., 2008a; Calura et al., 2019), 2P stars are expected to form more centrally concentrated in the cluster's inner regions and gradually mix with 1P stars during the cluster's evolution driven by two-body relaxation. Additionally, ω Cen is known to have a long relaxation time ($\sim$1.1 Gyr in the core and $\sim$10 Gyr at the half-mass radius, Harris 1996; Harris 2010), suggesting that the loss of memory due to two-body relaxation effects is likely negligible, and the stellar populations have maintained the same spatial distribution they had when they originated. This aligns with our observations: the 2P population (represented by the bMS population) is more centrally concentrated compared to the 1P population (represented by the rMS population).

Regarding the radial variations of the subgroups of 2P (i.e. bMS), in a recent pubblication (Bekki and Tsujimoto, 2019) was found that the most extreme 2P (i.e., the one with higher helium content) appears to be initially somewhat more concentrated than the 2G with lower helium content. The radial differences in the gradient of the bMS subpopulations, as observed in this study, appear to align with this notion. However, we stress the need for caution when interpreting subpopulations, as they require careful consideration. Spectroscopic follow-ups are essential for classifying the chemical properties of these stellar populations to gain a deeper understanding of their characteristics. Additionally, the complex formation history and intricate system of stellar populations in ω Centauri further underscore the need for future theoretical simulations involving multiple stellar populations, beyond just 1P and 2P, to enhance our comprehension of the presented results.

Furthermore, we note that the weaker radial variation observed in the MSa and MSd populations may be in line with findings from simulations presented in Lacchin, Calura, and Vesperini (2021). However, we approach this comparison with caution, recognizing the necessity for further observational efforts to characterize the chemical properties of MSd before drawing definitive conclusions.

Wide-field missions recently approved by NASA (such as UVEX) and ongoing (such as Euclid) will contribute to statistical analysis and spatial distribution of these stellar populations.

TABLE 4.6: The distribution of stars in the magnitude range $20.16 < m_{F438W} < 22.36$ among various populations in the two intermediate fields (F4 and F5) and the two external fields (F2 and F3) examined in this chapter, along with the central field analyzed in Bellini et al. (2017d).

		Central field[1] $r/r_h \lesssim 0.64$		Field F5 $0.74 \lesssim r/r_h \lesssim 1.36$	
Main Group	Subgroup	NStars	Fraction	NStars	Fraction
Entire MS		39,526	100%	8635	100%
MSa		1394	3.53% ± 0.10%	194	2.25% ± 0.16%
	MSa1	1283	3.25% ± 0.09%	180	2.09% ± 0.16%
	MSa2	111	0.28% ± 0.03%	14	0.16% ± 0.04%
bMS		12,776	32.32% ± 0.33%	2017	23.36% ± 0.58%
	bMS1	5141	13.01% ± 0.19%	-	-
	bMS2	3683	9.32% ± 0.16%	-	-
	bMS3	3952	10.00% ± 0.17%	-	-
rMS		13,124	33.20% ± 0.33%	2589	29.98% ± 0.67%
	rMS1	3739	9.46% ± 0.16%	-	-
	rMS2	3838	9.71% ± 0.16%	-	-
	rMS3	5547	14.03% ± 0.20%	-	-
MSd		2016	5.10% ± 0.12%	404	4.68% ± 0.24%
	MSd1	757	1.92% ± 0.07%	-	-
	MSd2	819	2.07% ± 0.07%	-	-
	MSd3	440	1.11% ± 0.05%	-	-
MSe		6129	15.51% ± 0.21%	1027	11.89% ± 0.39%
	MSe1	2555	6.46% ± 0.13%	519	6.01% ± 0.27%
	MSe2	2591	6.56% ± 0.13%	508	5.88% ± 0.27%
	MSe3	463	1.17% ± 0.05%	-	-
	MSe4	520	1.32% ± 0.06%	-	-

Field F4 $0.87 \lesssim r/r_h \lesssim 1.48$		Field F2 $1.97 \lesssim r/r_h \lesssim 2.59$		Field F3 $2.20 \lesssim r/r_h \lesssim 2.84$	
N_{Stars}	Fraction	N_{Stars}	Fraction	N_{Stars}	Fraction
7174	100%	1227	100%	1333	100%
187	2.61% ± 0.19%	17	1.39% ± 0.34%	28	2.10% ± 0.40%
166	2.32% ± 0.18%	-	-	-	-
21	0.29% ± 0.06%	-	-	-	-
1727	24.07% ± 0.65%	204	16.63% ± 1.26%	203	15.23% ± 1.15%
669	9.32% ± 0.38%	79	6.44% ± 0.75%	-	-
721	10.05% ± 0.39%	97	7.91% ± 0.83%	-	-
337	4.70% ± 0.26%	28	2.28% ± 0.52%	-	-
2412	33.62% ± 0.79%	560	45.64% ± 2.33%	615	46.14% ± 2.25%
1171	16.32% ± 0.51%	-	-	-	-
602	8.39% ± 0.36%	-	-	-	-
639	8.91% ± 0.37%	-	-	-	-
416	5.80%± 0.29%	43	3.50% ± 0.54%	43	3.23% ± 0.50%
231	3.22% ± 0.22%	-	-	-	-
101	1.41% ± 0.14%	-	-	-	-
84	1.17% ± 0.13%	-	-	-	-
952	13.27% ± 0.46%	158	12.87% ± 1.09%	229	17.18% ± 1.23%
501	6.98% ± 0.32%	48	3.91% ± 0.58%	72	5.40% ± 0.65%
451	6.29% ± 0.31%	110	8.96% ± 0.89%	157	11.78% ± 0.99%
-	-	-	-	-	-
-	-	-	-	-	-
286	3.99% ± 0.24%	78	6.36% ± 0.74%	89	6.68% ± 0.73%
1194	16.64% ± 0.52%	167	13.61% ± 1.12%	126	9.45% ± 0.88%

[1] From Bellini et al. (2017d).

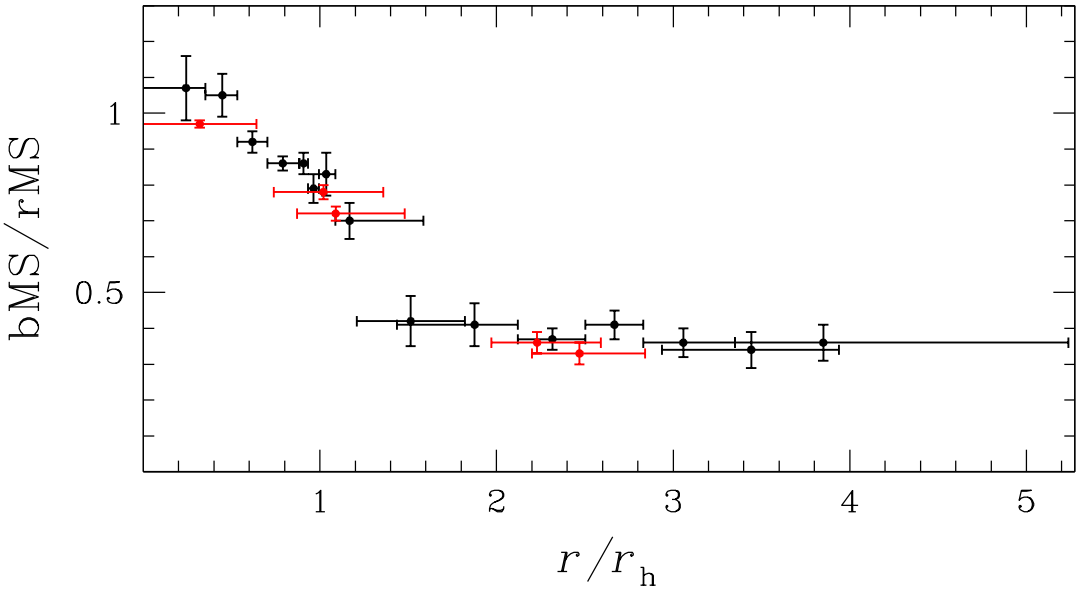

FIGURE 4.15: bMS/rMS as a function of the radial distance. Black points are from Bellini et al. (2009) while red points are from this study.

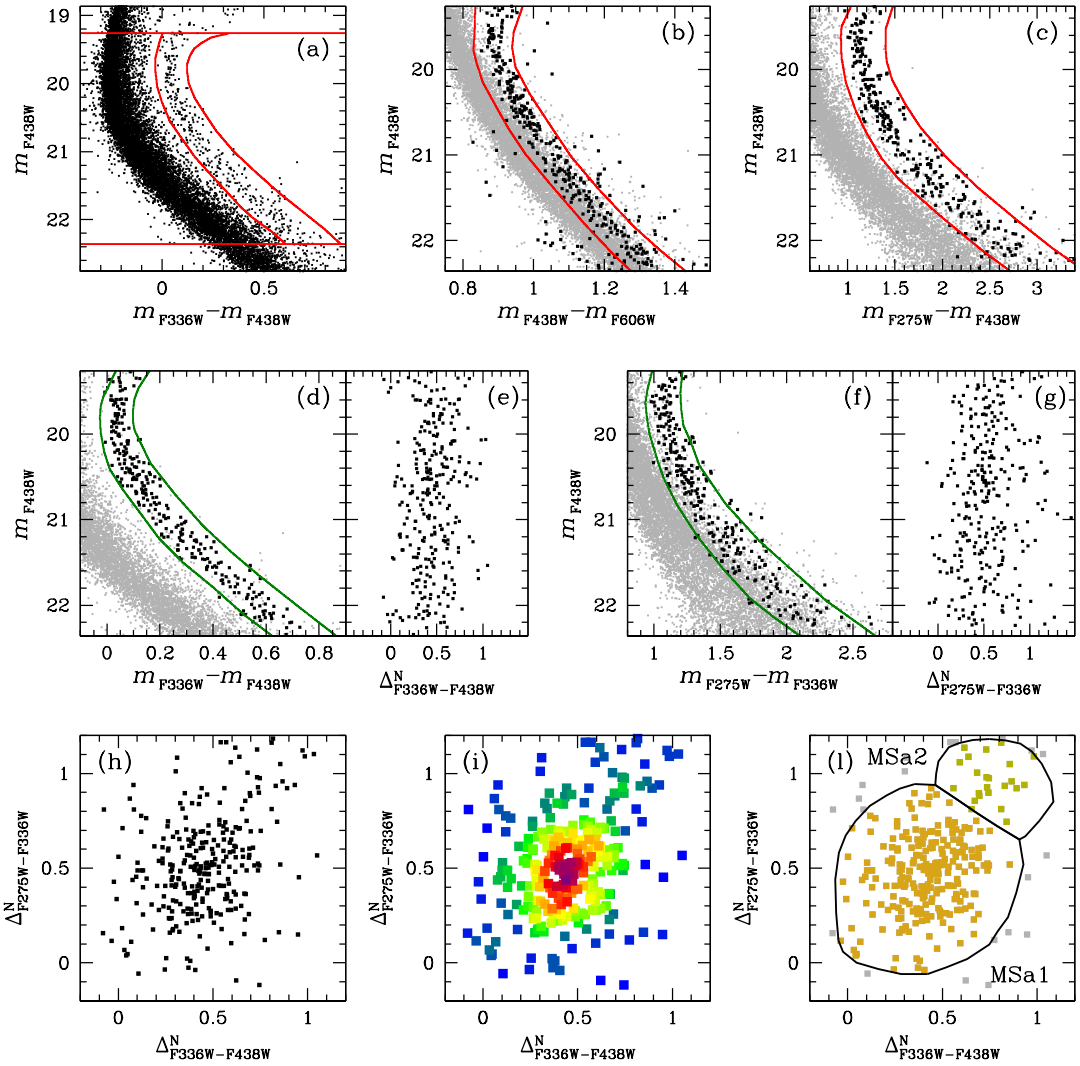

FIGURE 4.16: Same as Fig. 4.9 but for the F5 fields.

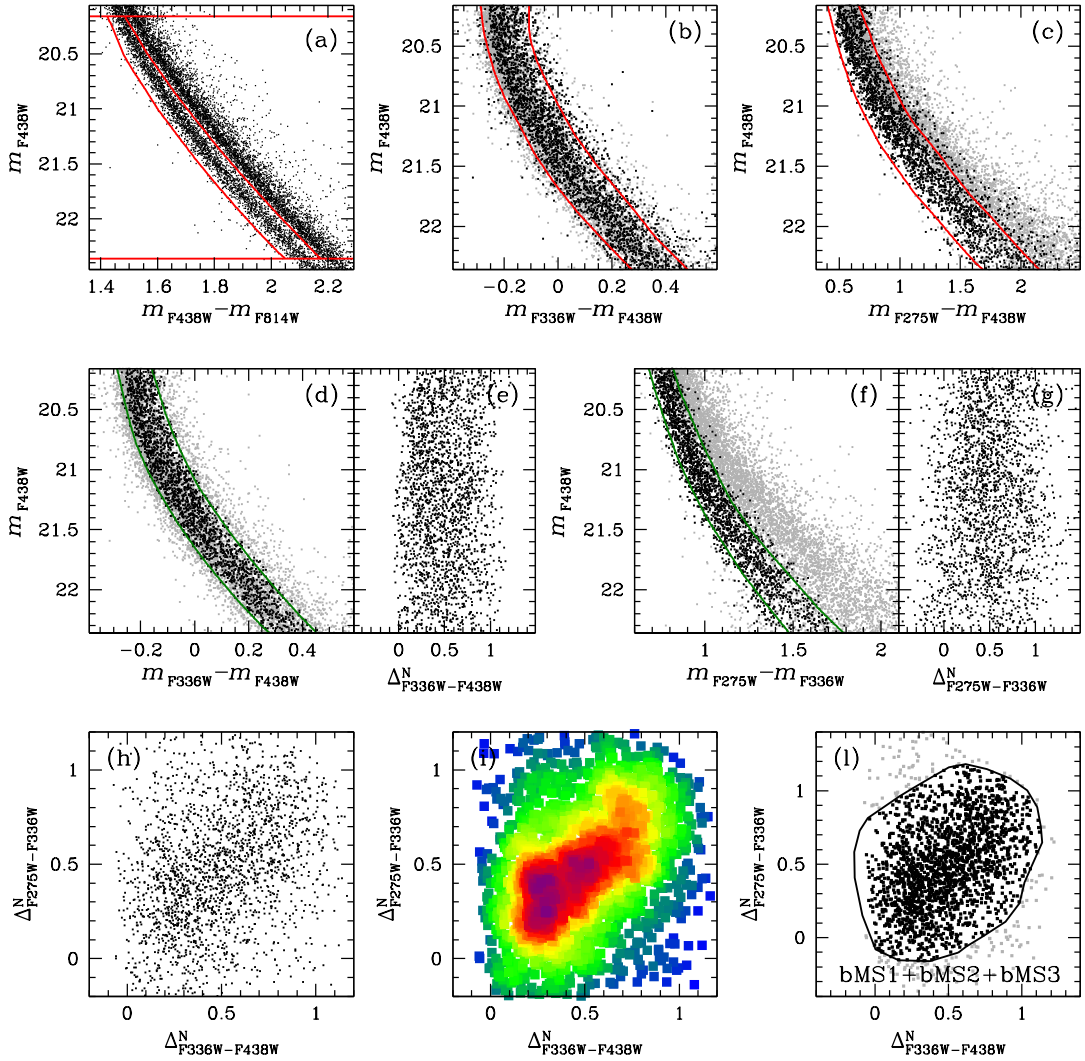

FIGURE 4.17: Same as Fig. 4.10 but for the F5 fields.

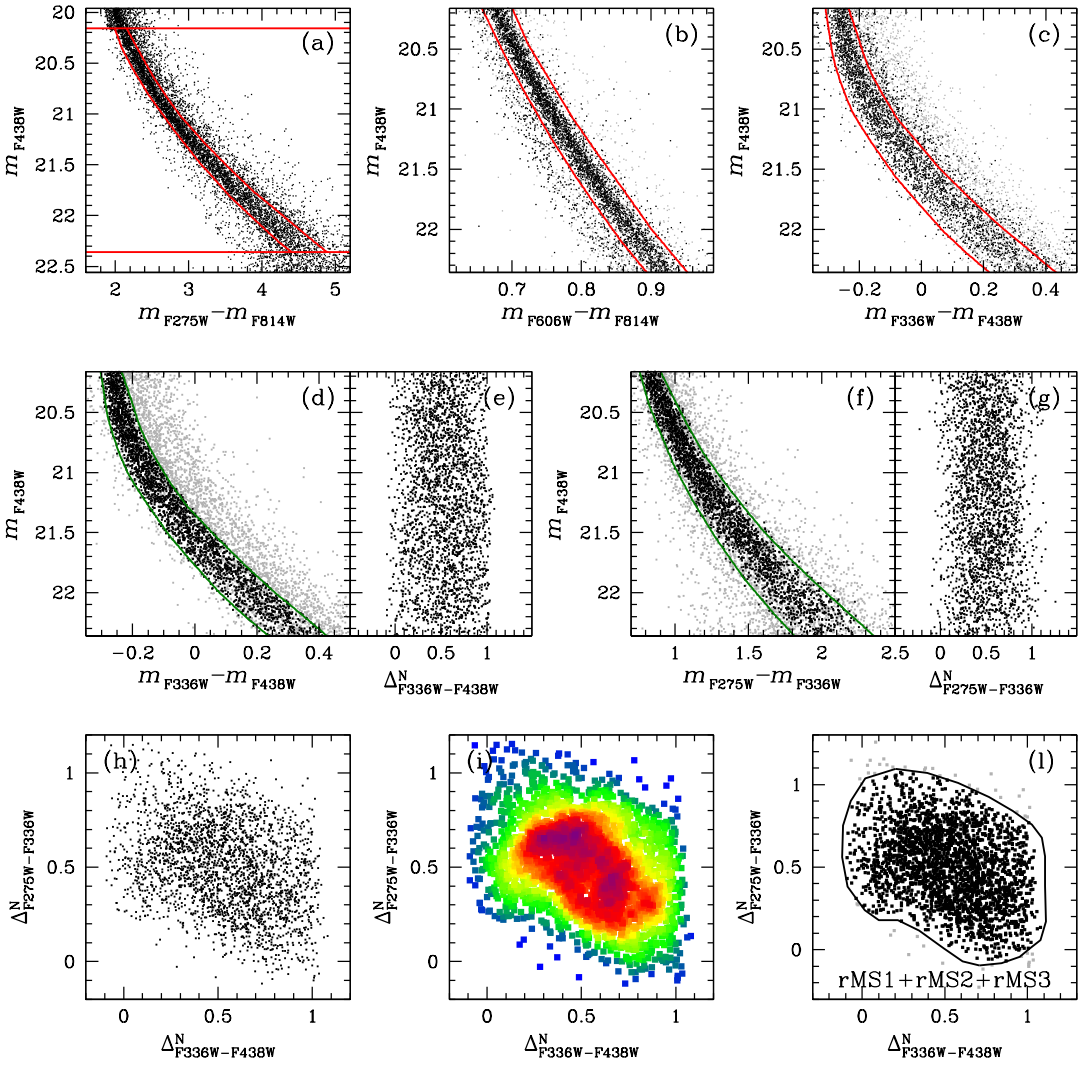

FIGURE 4.18: Same as Fig. 4.11 but for the F5 fields.

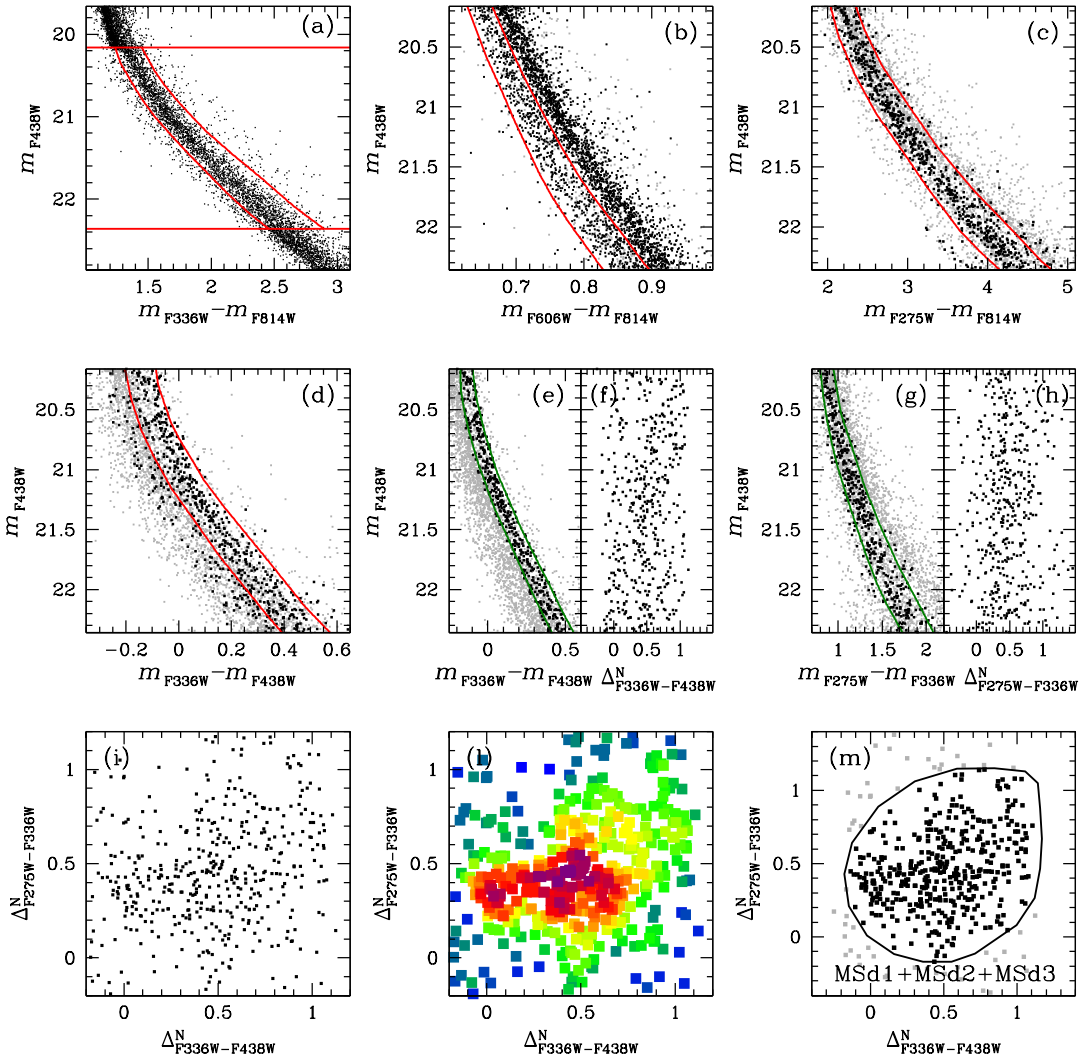

FIGURE 4.19: Same as Fig. 4.12 but for the F5 fields.

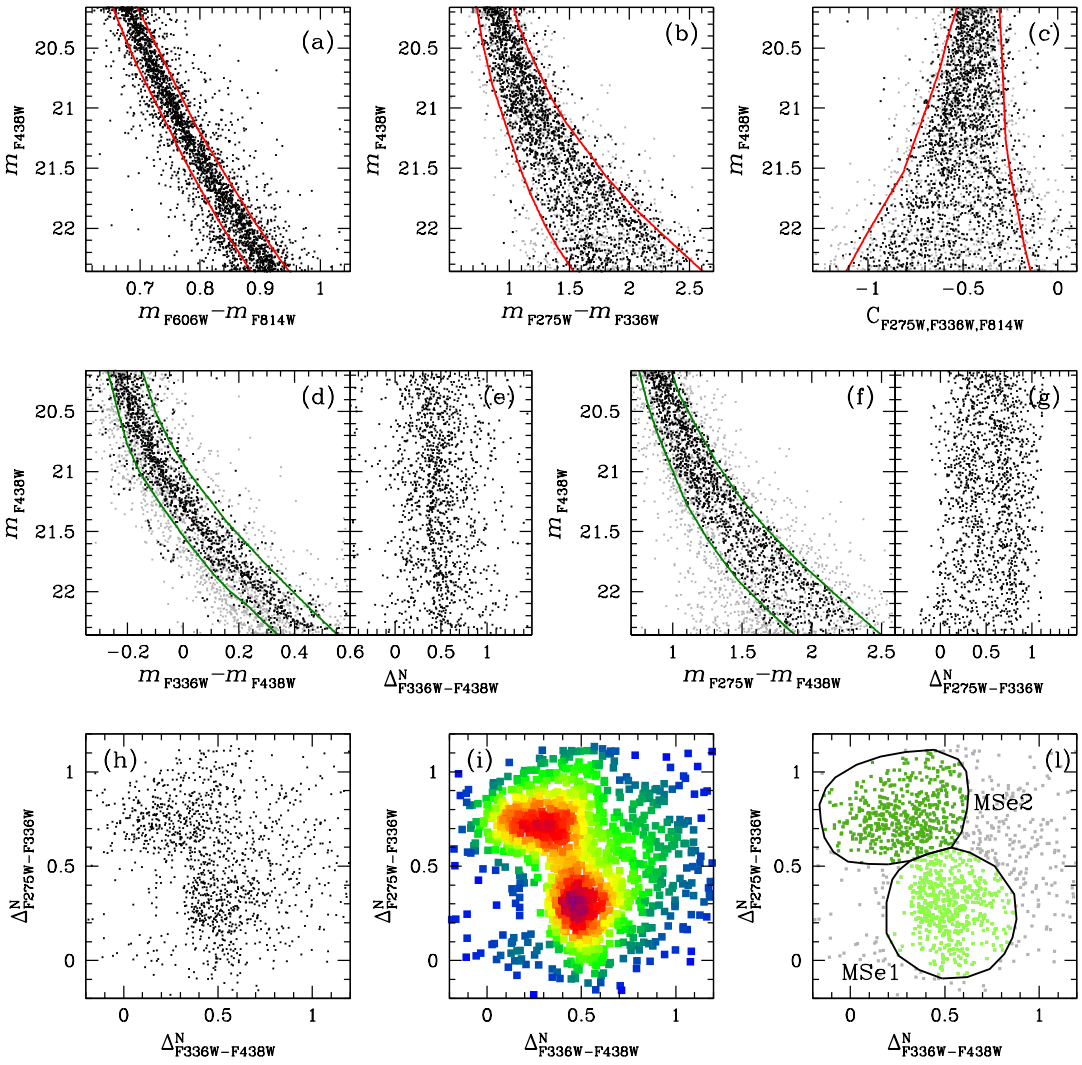

FIGURE 4.20: Same as Fig. 4.13 but for the F5 fields.

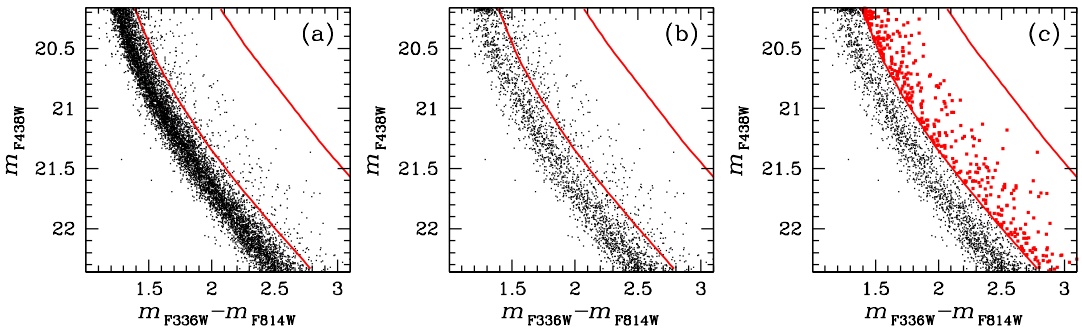

FIGURE 4.21: Same as Fig. 4.14 but for the F5 fields.

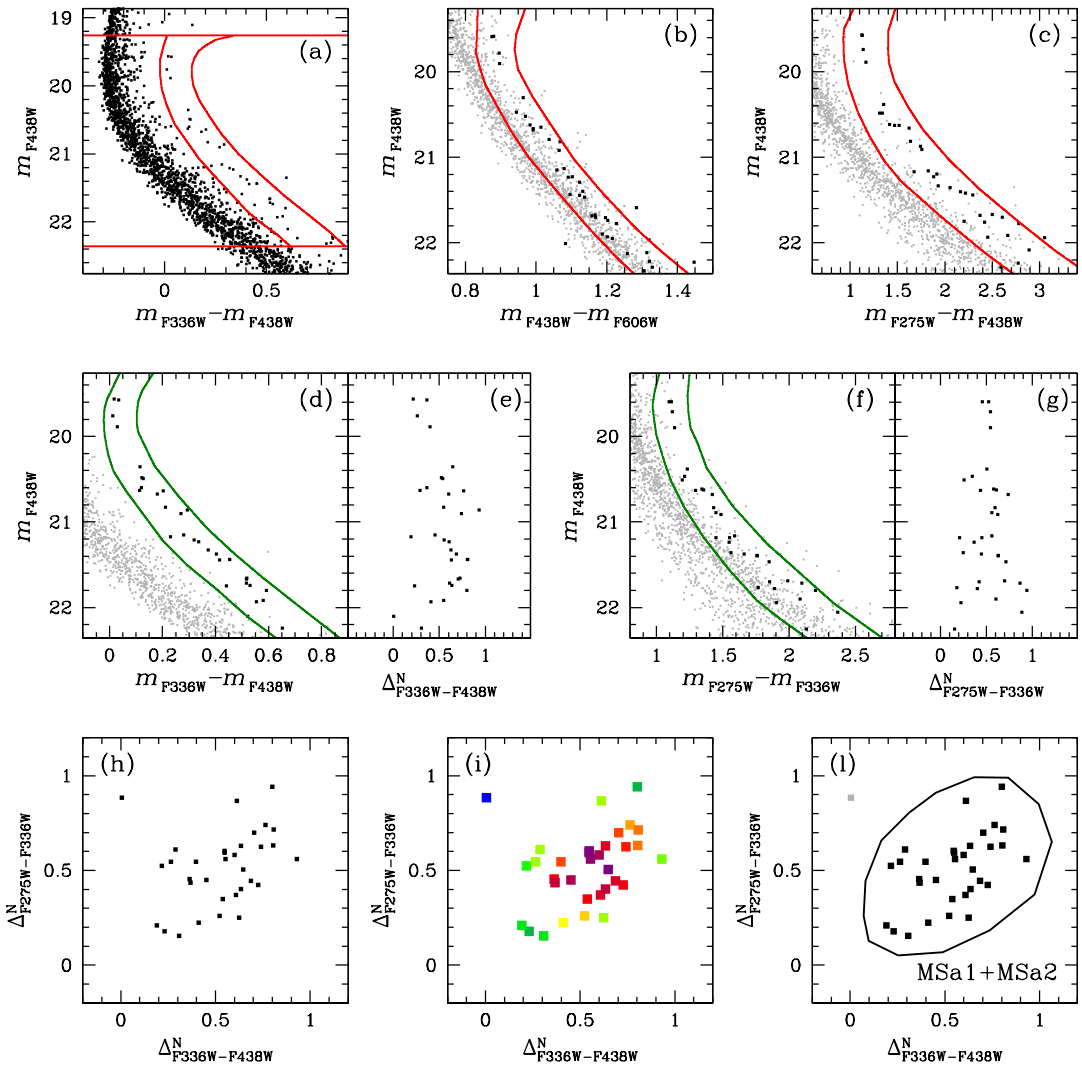

FIGURE 4.22: Same as Fig. 4.9 but for the F3 fields.

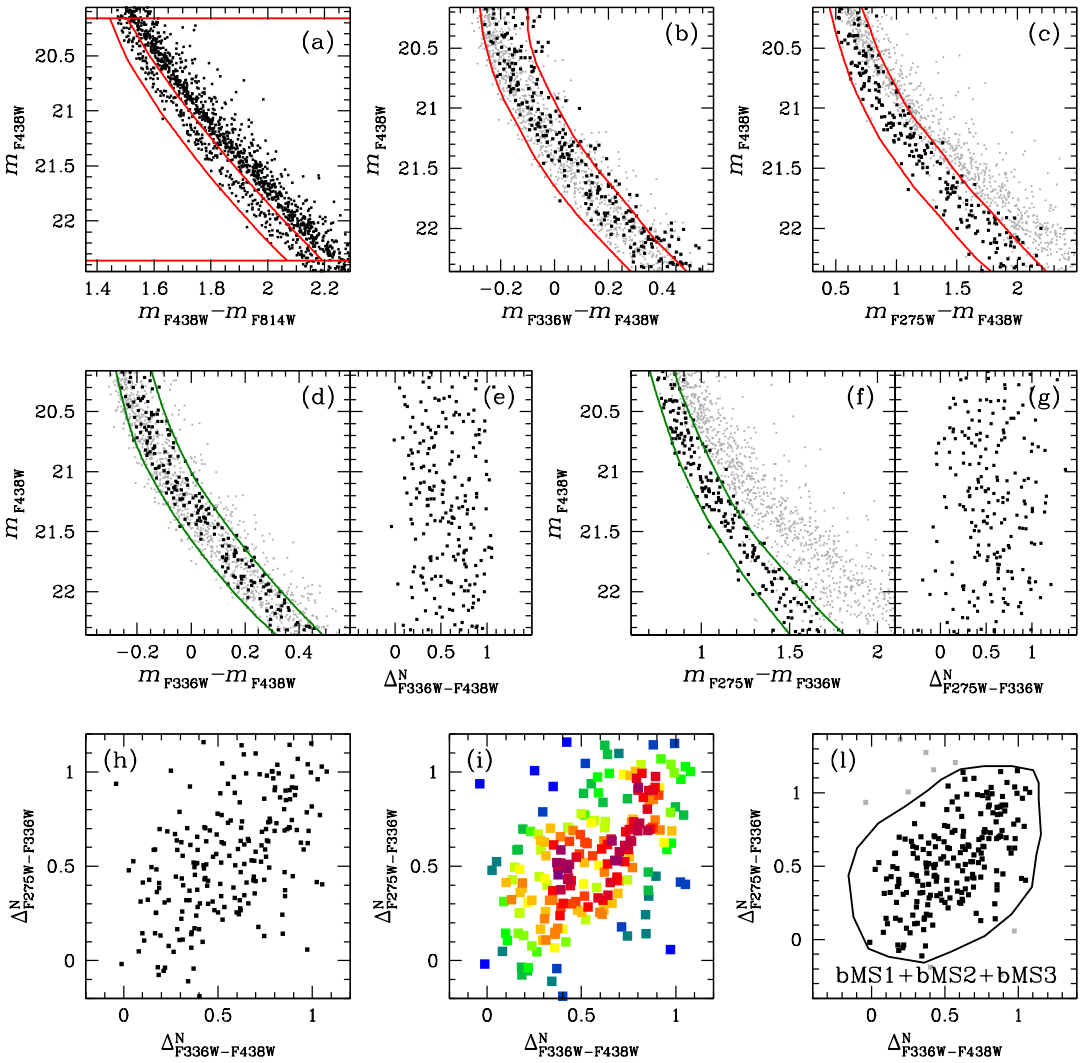

FIGURE 4.23: Same as Fig. 4.10 but for the F3 fields.

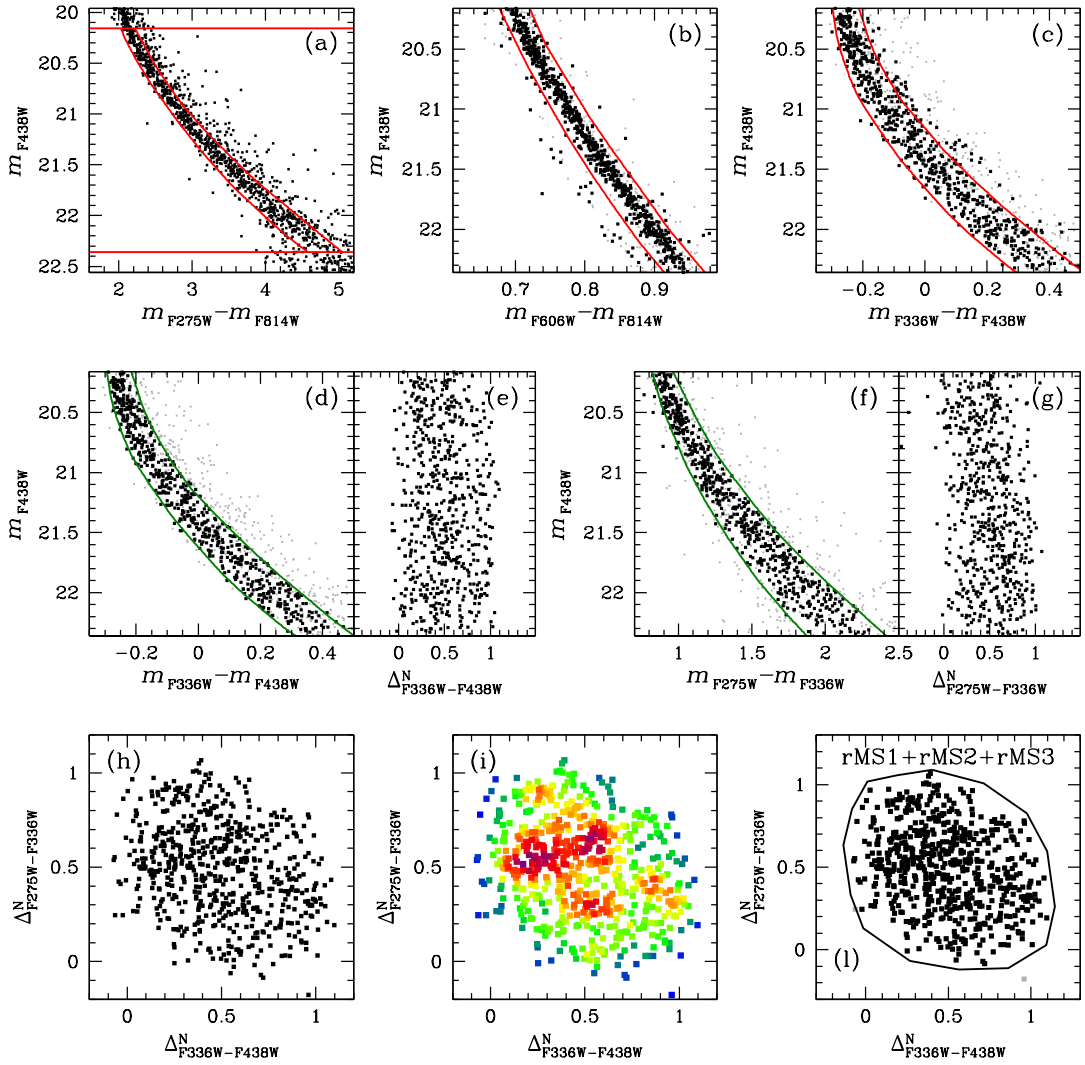

FIGURE 4.24: Same as Fig. 4.11 but for the F3 fields.

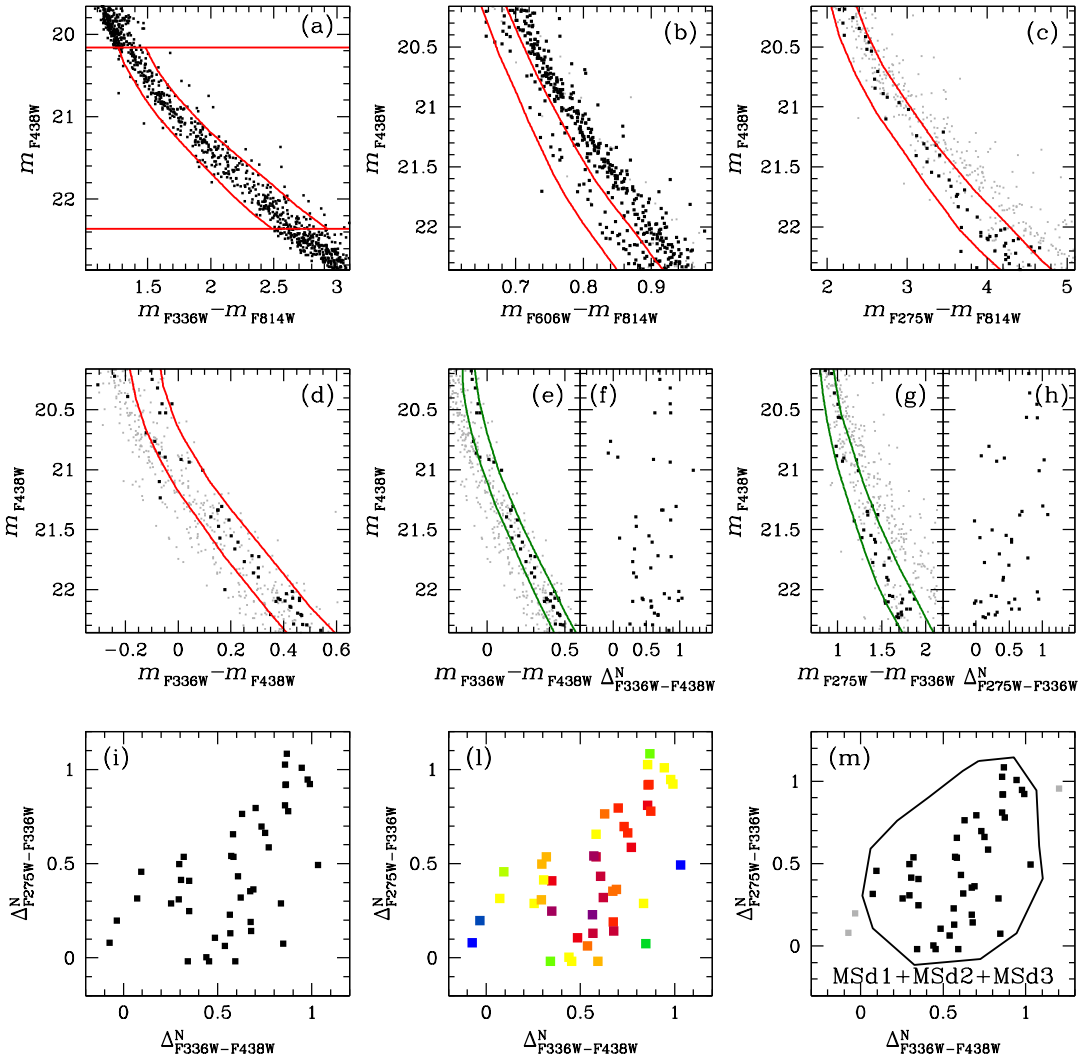

FIGURE 4.25: Same as Fig. 4.12 but for the F3 fields.

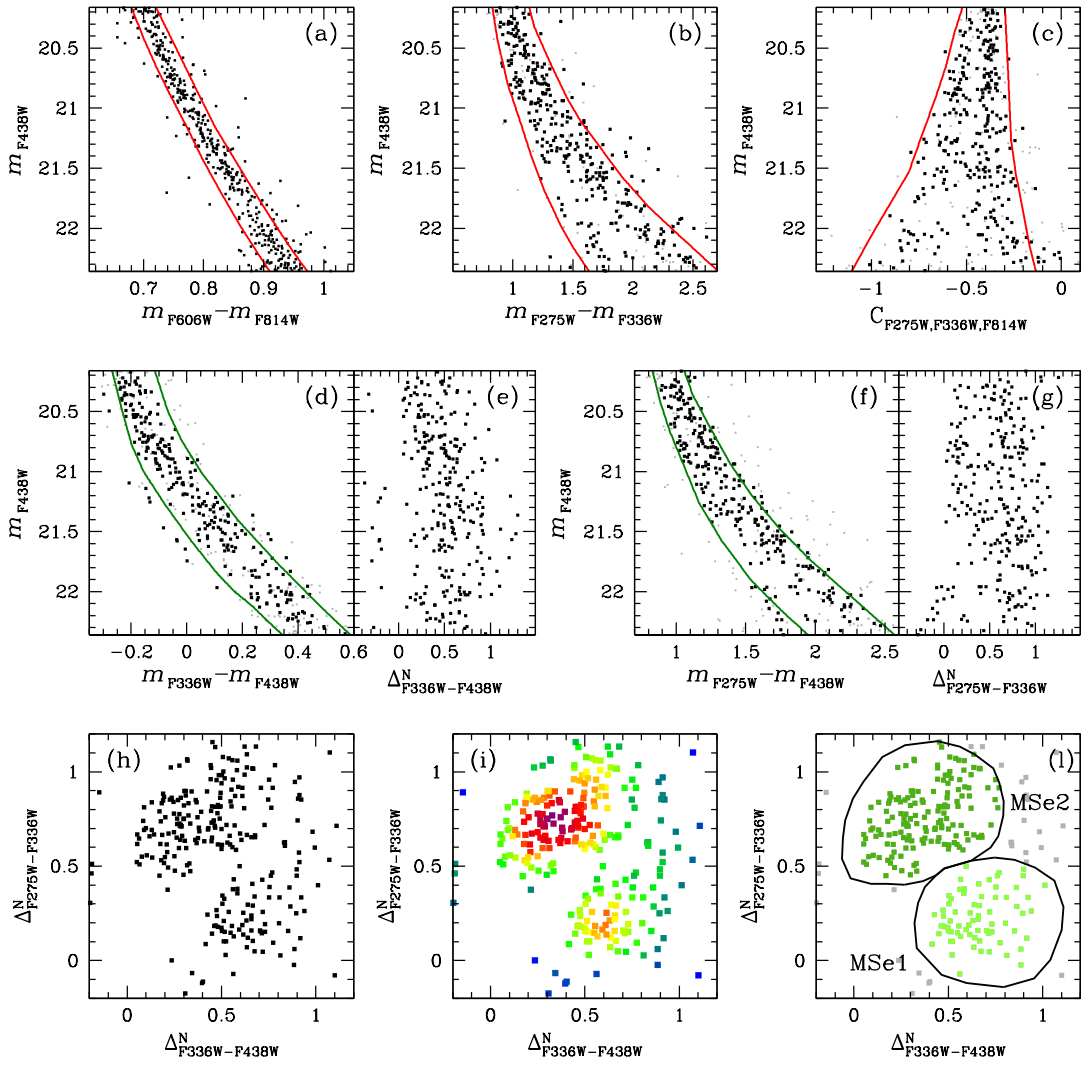

FIGURE 4.26: Same as Fig. 4.13 but for the F3 fields.

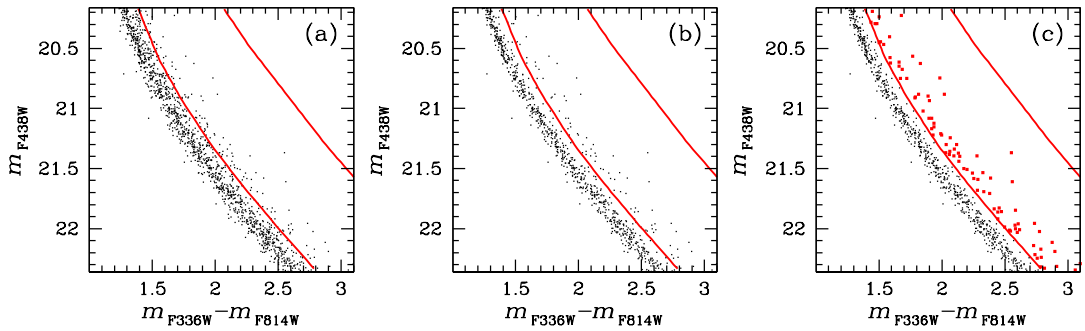

FIGURE 4.27: Same as Fig. 4.14 but for the F3 fields.

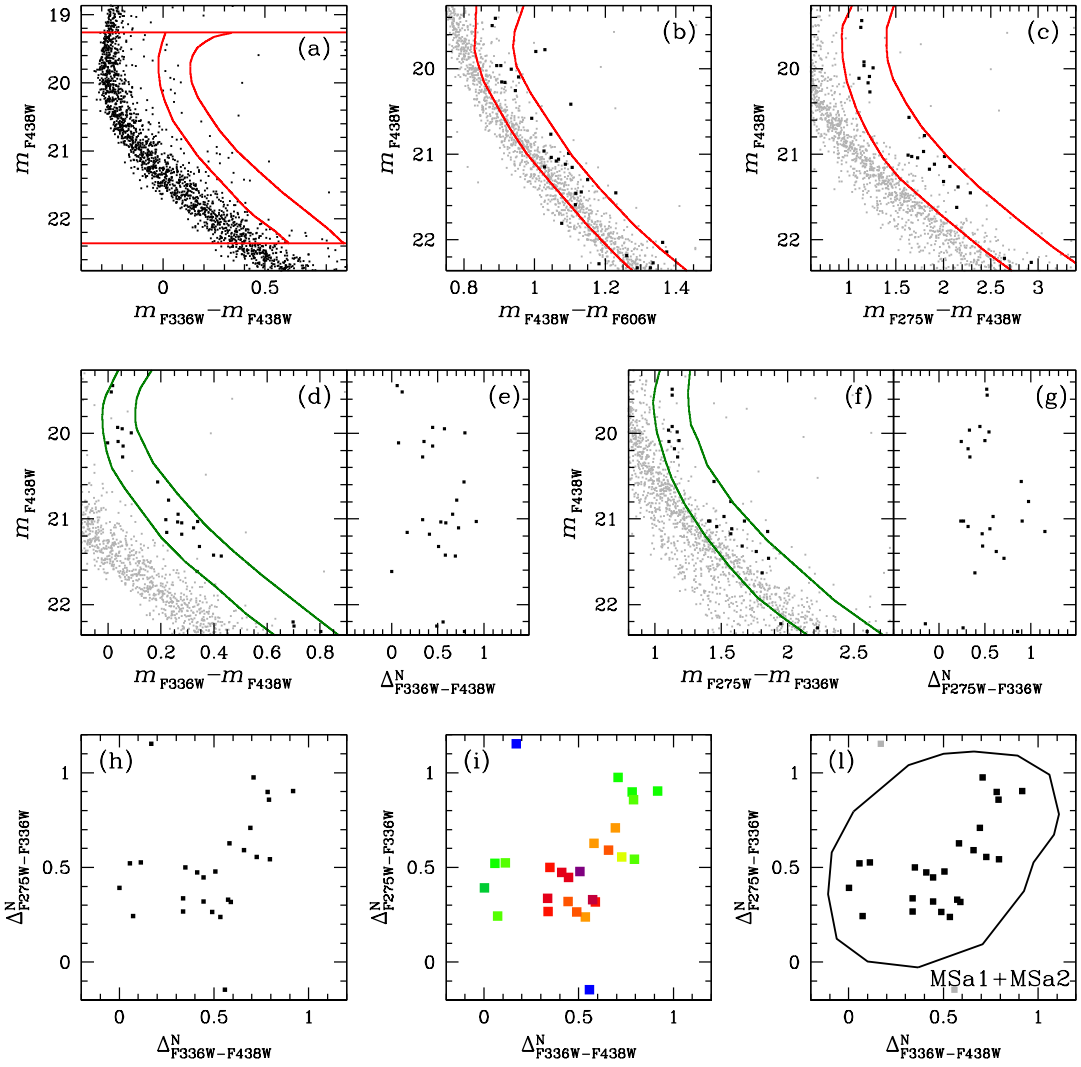

FIGURE 4.28: Same as Fig. 4.9 but for the F2 fields.

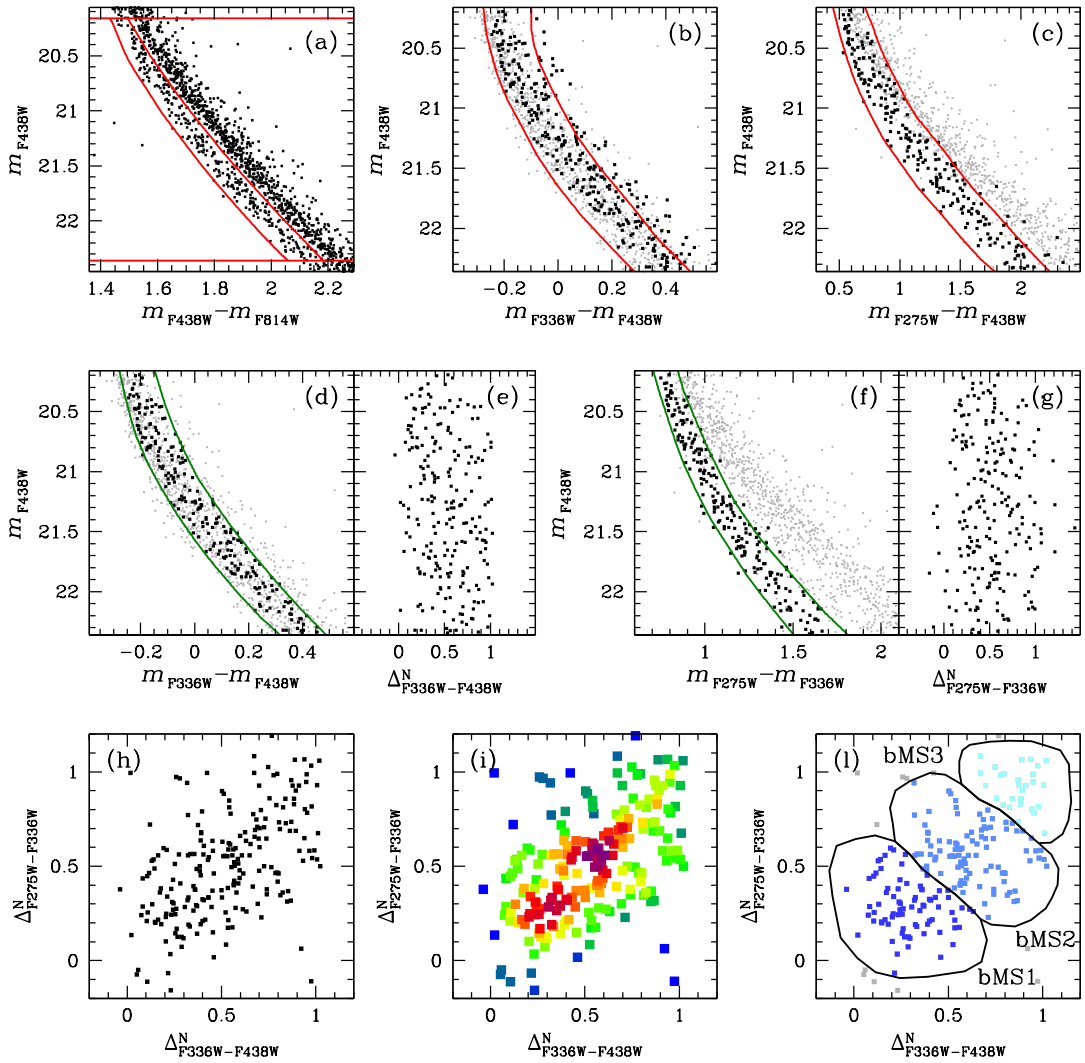

FIGURE 4.29: Same as Fig. 4.10 but for the F2 fields.

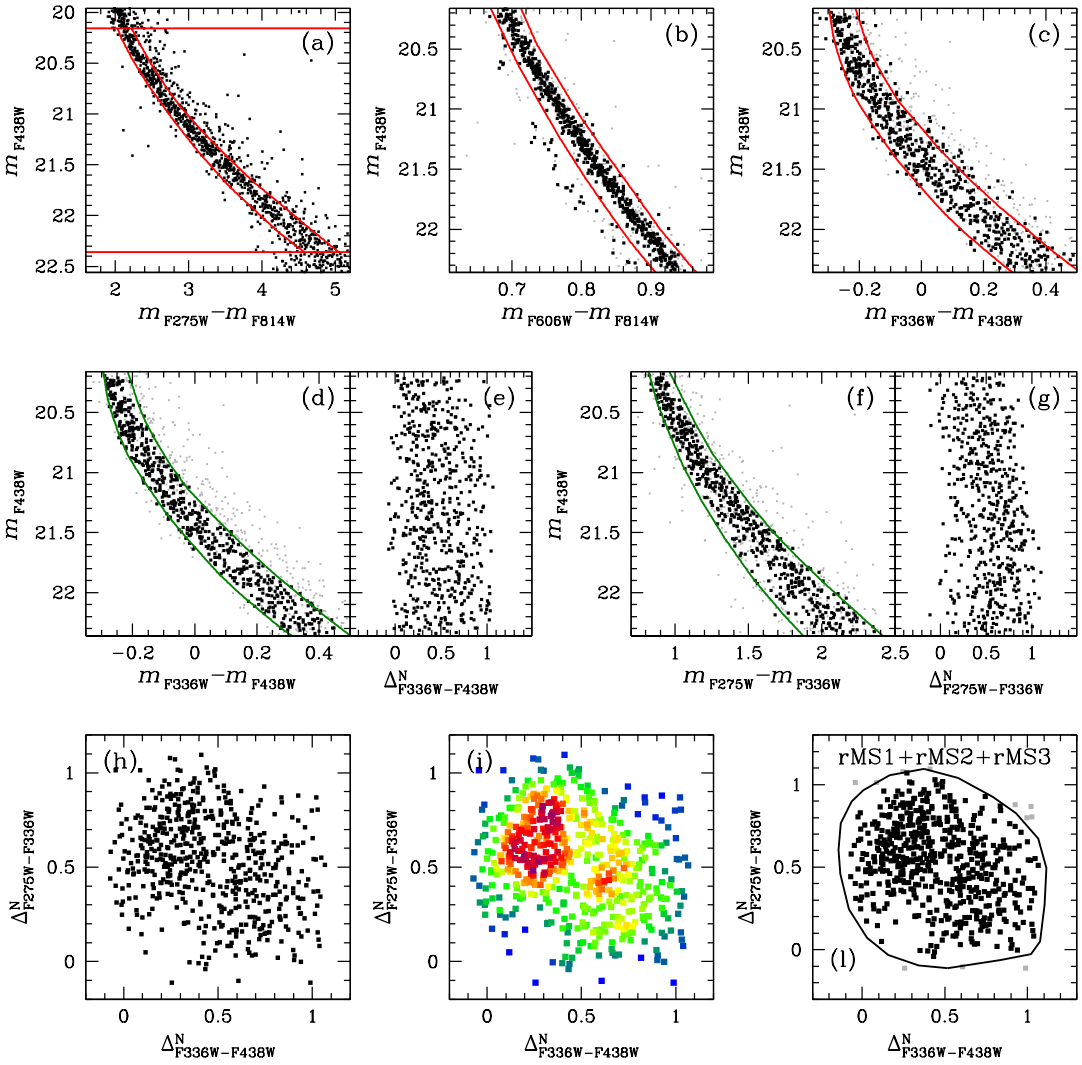

FIGURE 4.30: Same as Fig. 4.11 but for the F2 fields.

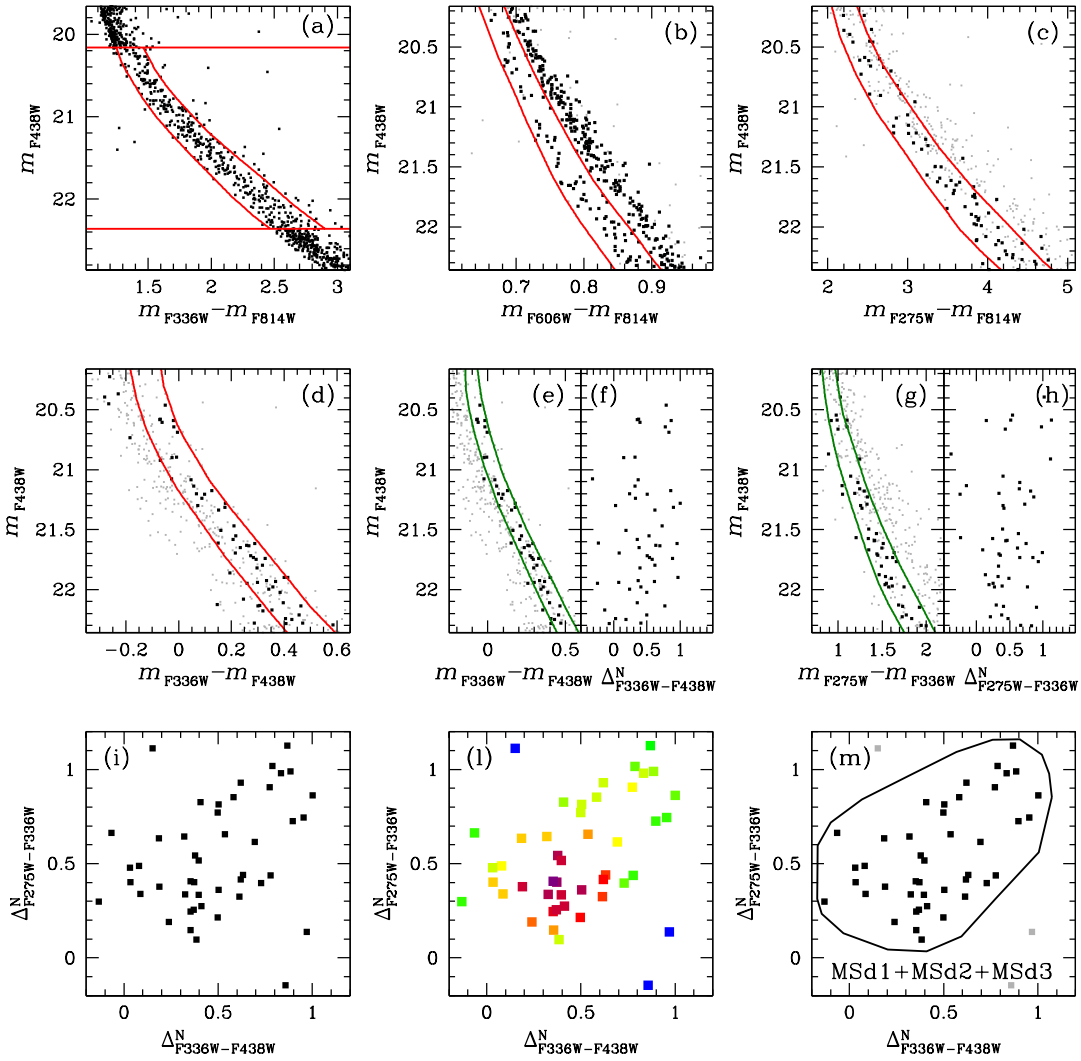

FIGURE 4.31: Same as Fig. 4.12 but for the F2 fields.

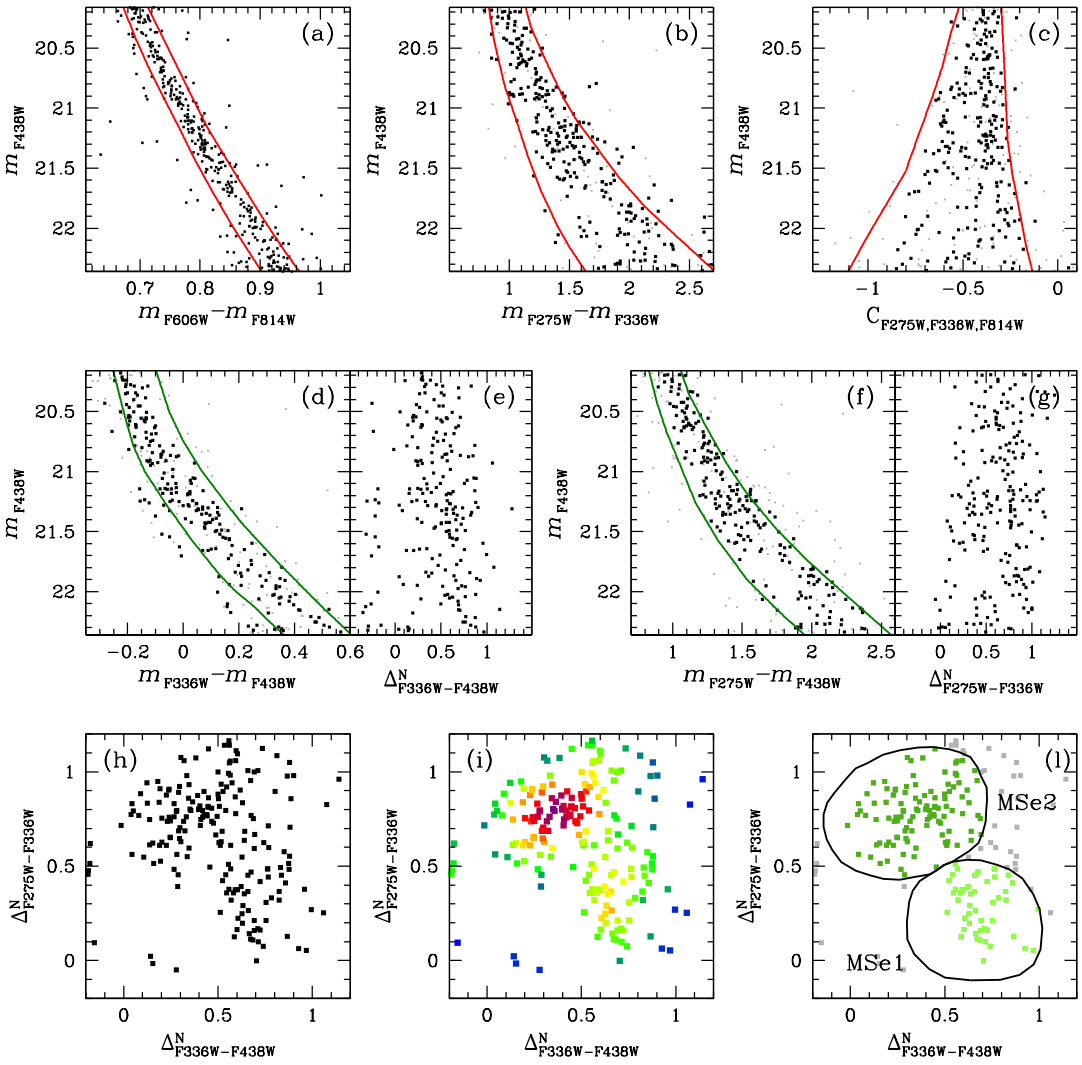

FIGURE 4.32: Same as Fig. 4.13 but for the F2 fields.

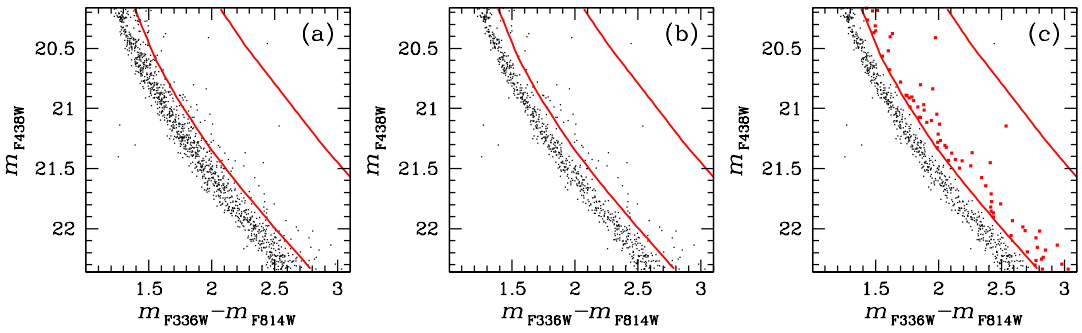

FIGURE 4.33: Same as Fig. 4.14 but for the F2 fields.

Chapter 5

Hα emitters in ω Centauri

We present a census of Hα emitters in the globular cluster Omega Centauri, using a set of Hubble Space Telescope images obtained with the the broad F435W and F625W filters and with the narrow-band F658N filter. This combination of filters offers a powerful tool to identify sources characterised by a strong Hα emission. We used the $m_{\rm F435W} - m_{\rm F625W}$ vs. $m_{\rm F625W} - m_{\rm F658N}$ color–color diagram as photometric diagnostic. In the analysed field, we identified 38 Hα emitters. For each source, we provide a photometric estimate of the equivalent width of the Hα emission.

5.1 Introduction

Globular clusters (GCs) are highly efficient environments for the formation of exotic objects such as low-mass X-ray binaries (LMXBs), cataclysmic variables (CVs), millisecond pulsars (MSPs), and blue straggler stars (BSSs). These objects originate from binary systems and interactions within the dense cores of GCs and prove insights into the dynamical evolution of these clusters.

CVs are binary systems consisting of a white dwarf accreting material from a main-sequence or sub-giant star while LMXBs and MSPs, contain a compact object (a stellar black hole or a neutron star). The accretion process in these objects leaves distinct signatures in their spectra. For instance, CVs often exhibit emission lines from Balmer recombination (e.g., Hα, Hβ) or excess in the ultraviolet continuum. These emissions are attributed to accretion disks and accretion coronae. In the case of magnetic CVs, optical and UV emissions arise from accreted material flowing along magnetic field lines and accreting directly onto the white dwarf without forming a viscous disk. Non-magnetic or weakly magnetic CVs show emissions from various parts of the accretion disk.

Emission lines in the spectra of main-sequence stars can also be attributed to chromospheric activity (CA) resulting from non-radiative heating mechanisms powered by convection and magnetic fields. The presence of Hα emission from CA is expected in low-mass stars, and the study of the equivalent width (EW(Hα)) produced by CA is essential for identifying Hα emission signatures from accreting stars of different ages.

By following a method proposed by De Marchi, Panagia, and Romaniello (2010), which identifies stars with Hα excess emission in star-forming regions, here we used archival Hubble Space Telescope observations to conduct an Hα survey of main-sequence stars in ω Cen. The method combines broad-band F435W and F625W photometry with narrow-band Hα imaging to measure the EW(Hα) of stars showing Hα excess emission, enabling the identification and characterization of accreting stars in this GC. The chapter is organized as follows: in Section 5.2 we present the data set used in his work and the data reduction; in Section 5.3 we describe the method used

TABLE 5.1: List of *HST* Observations of ω Cen.

Filter	Exposures	Epoch
	ACS/WFC	
F435W	12×12 + 24×340 s	2002/06/27-30
F625W	12×8 + 24×340 s	2002/06/27-30
F658N	36×440 s	2002/06/27-30

to identify the Hα emitters in ω Cen while in Section 5.4 we briefly summarize the results.

5.2 Observations and data reduction

The data used in this work come from the HST program 9442 (P.I. Cool) and consist of a series of ACS/WFC images obtained through the broad F435W and F625W filters and with the narrow-band F658N filter. The images cover a total field of view (FoV) of $\sim 6 \times 6$ arcmin. Details on exposure time for each filter are given in Table 5.1 (see also Cool et al., 2013).

The data reduction was done following the procedure described in Scalco et al. (2021). In brief, the reduction process consists of two steps. In the first step, we performed the "first pass photometry", by measuring the stellar positions and fluxes in each exposure through point-spread function (PSF) fitting and using the `FORTRAN` code `hst1pass`. To do this, we used a set of spatially variable PSFs obtained by perturbing the publicly available HST "library" PSF. Stellar positions in each single-exposure catalogue were corrected for geometric distortion by using the state-of-the-art geometric-distortion corrections of Bellini, Anderson, and Bedin (2011).

We then defined a common reference-frame system based on a Gaia Data Release 3 (Gaia DR3) catalogue. The master frame was set with a pixel scale of 50 mas pixel^{-1}. We derived general six-parameter linear transformations to transform stellar positions of each individual image onto the common reference frame system.

The second-pass photometry was performed through the `FORTRAN` software package `KS2`. The code `KS2` takes images, PSFs, and transformations obtained during the "first-pass photometry" stage to simultaneously find and measure stars in all of the individual exposures and for the entire set of filters. A detailed description of the software is given in Bellini et al. (2017b), Nardiello et al. (2018) and Scalco et al. (2021).

The photometry has been zero-pointed into the Vega magnitude system by following the recipe of Bedin et al. (2005a). We removed the poorly measured stars using a set of quality parameter produced by our software, following the prescriptions of Scalco et al. (2021). Finally, the photometry was corrected for zero-point spatial variations following the recipes in Milone et al. (2012d).

Figure 5.1 shows the $m_{\rm F435W} - m_{\rm F625W}$ vs. $m_{\rm F435W}$ CMD (grey dots) for the stars that survived the photometric quality selections. We compared the observed CMD with isochrones from the Dartmouth database (black line; Dotter et al. (2008)). We assumed [Fe/H] = -1.53, [α/Fe] = 0.2 and adopted the age, t = 11.5 Gyr, distance modulus $(m - M)_0$ = 13.94, and reddening $E(B - V)$ = 0.12.

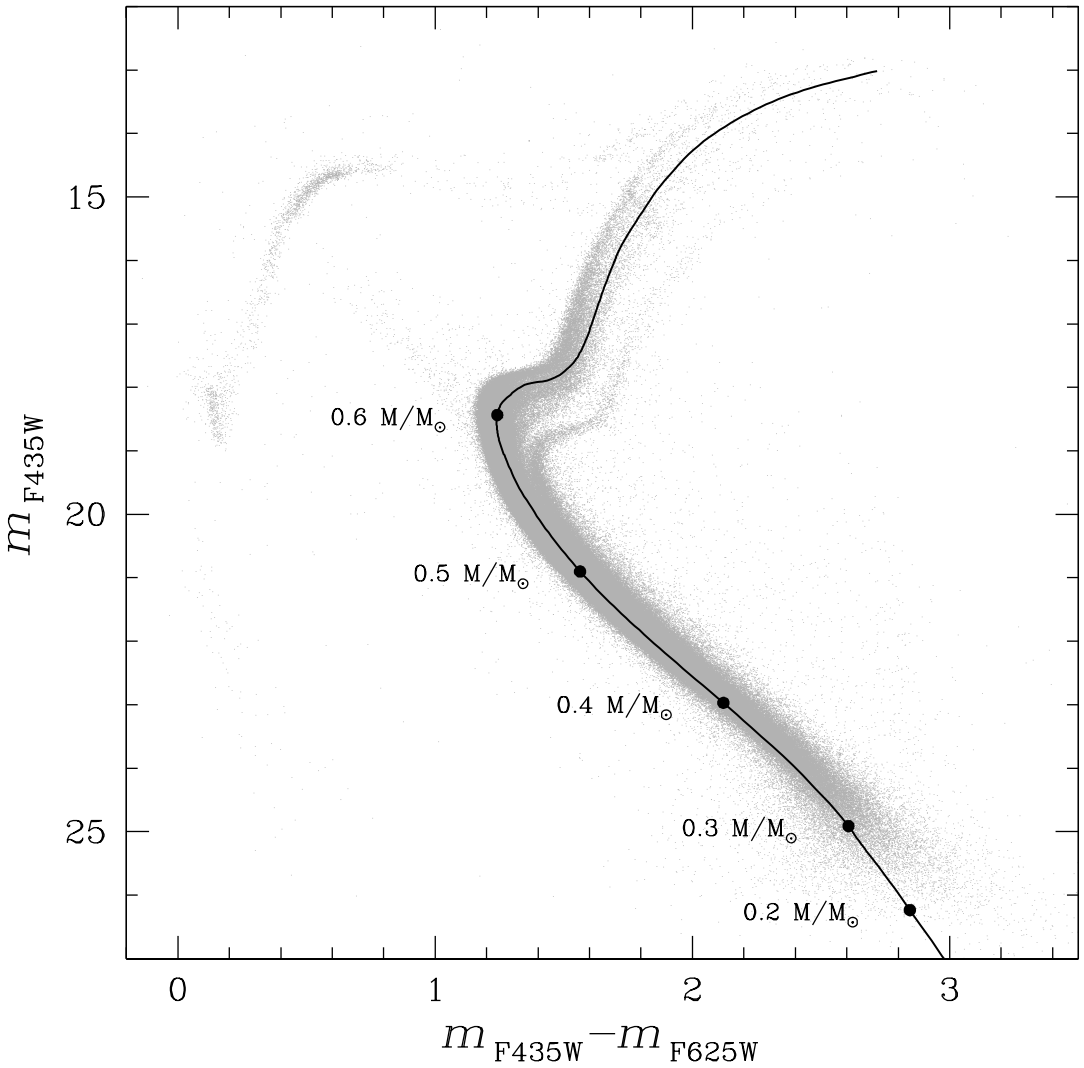

FIGURE 5.1: $m_{\rm F435W} - m_{\rm F625W}$ vs. $m_{\rm F435W}$ CMD (grey dots) for the stars that survived the photometric quality selections. For comparison, we also show the best-fitting isochrones from the Dartmouth database (black line; Dotter et al. 2008).

5.3 Selection of objects with Hα emission

We used the method described in De Marchi, Panagia, and Romaniello (2010) and recently applied to GCs by Beccari et al. (2014), Pallanca et al. (2013), and Pallanca et al. (2017) to identify all of the objects showing Hα excess in our field. This approach is based on the use of the R-band magnitude as an indicator of the level of the photospheric continuum near the Hα line so that stars with strong Hα emission will have a large $R - H\alpha$ colour.

Here we made use of the combination of $m_{\rm F435W}$, $m_{\rm F625W}$ and $m_{\rm F658N}$ filters to identify all of the objects showing Hα excess. This combination of filters can provide both an accurate determination of the continuum and a good estimate of the Hα emission, being the Hα line contribution to the $m_{\rm F435W}$ and $m_{\rm F625W}$ filters negligible.

Figure 5.2 shows the position of all of the stars with magnitude $m_{\rm F435W} > 17$ in the $m_{\rm F435W} - m_{\rm F625W}$ vs. $m_{\rm F625W} - m_{\rm F658N}$ color–color diagram. As expected, the vast majority of MS stars show very low Hα excess emission. As a consequence, in the $m_{\rm F435W} - m_{\rm F625W}$ vs. $m_{\rm F625W} - m_{\rm F658N}$ plane they define a very narrow sequence, which empirically indicates the locus of stars with no Hα emission. To identify all the sources showing Hα emission, we calculated a reference line for the stars not showing Hα excess that is defined as the median $m_{\rm F625W} - m_{\rm F658N}$ colour of stars with magnitude $17 < m_{\rm F435W} < 24$ (black line in figure 5.2). For each source, we measured the difference between the observed $m_{\rm F625W} - m_{\rm F658N}$ colour and the value of $m_{\rm F625W} - m_{\rm F658N}$ measured along the reference line for source with no Hα emission. We then selected as candidate Hα emitters those objects with a colour difference that is at least five times larger than the source intrinsic photometric error. For all of the candidate Hα emitters, we derived an estimation of the Hα emission line following Equation (4) in De Marchi, Panagia, and Romaniello (2010): pEW $= RW \times [1 - 10^{(-0.4 \times \Delta H\alpha)}]$, where RW is the rectangular width of the filter in units, which depends on the specific characteristics of the filter (see Table 4 in De Marchi, Panagia, and Romaniello 2010). We then refined our Hα souces selections by requiring $pEW > 20$. We found a total of 38 sources. All the selected Hα emitters are represented with black dots in figure 5.2. Figure 5.3 shows the position of the selected source in the $m_{\rm F435W} - m_{\rm F625W}$ vs. $m_{\rm F435W}$ CMD. As can be seen, all the Hα emitter are located on the blue side of the MS. Finally, figure 5.4 shows the position of the selected sources in the pEW vs. $m_{\rm F435W} - m_{\rm F625W}$ diagram.

5.4 Conclusion

GCs are known to be the perfect environment for the formation of exotic objects such as low-mass X-ray binaries (LMXBs), cataclysmic variables (CVs), millisecond pulsars (MSPs), and blue straggler stars (BSSs). The dynamical study of these sources can provide important information on the dynamical history of the parent cluster. Most of these exotic objects are expected to Hα emitters.

Here we presented a study of Hα emitters in the globular cluster Omega Centauri, using a set of HST images obtained with the the broad F435W and F625W filters and with the narrow-band F658N filter. We made use of the $m_{\rm F435W} - m_{\rm F625W}$ vs. $m_{\rm F625W} - m_{\rm F658N}$ color-color diagram to obtain an estimate of the $m_{\rm F435W} - m_{\rm F625W}$ photometric continum. We then selected all the sources with a $m_{\rm F625W} - m_{\rm F658N}$ colour difference with respect to the photometric continuum that is at least five times

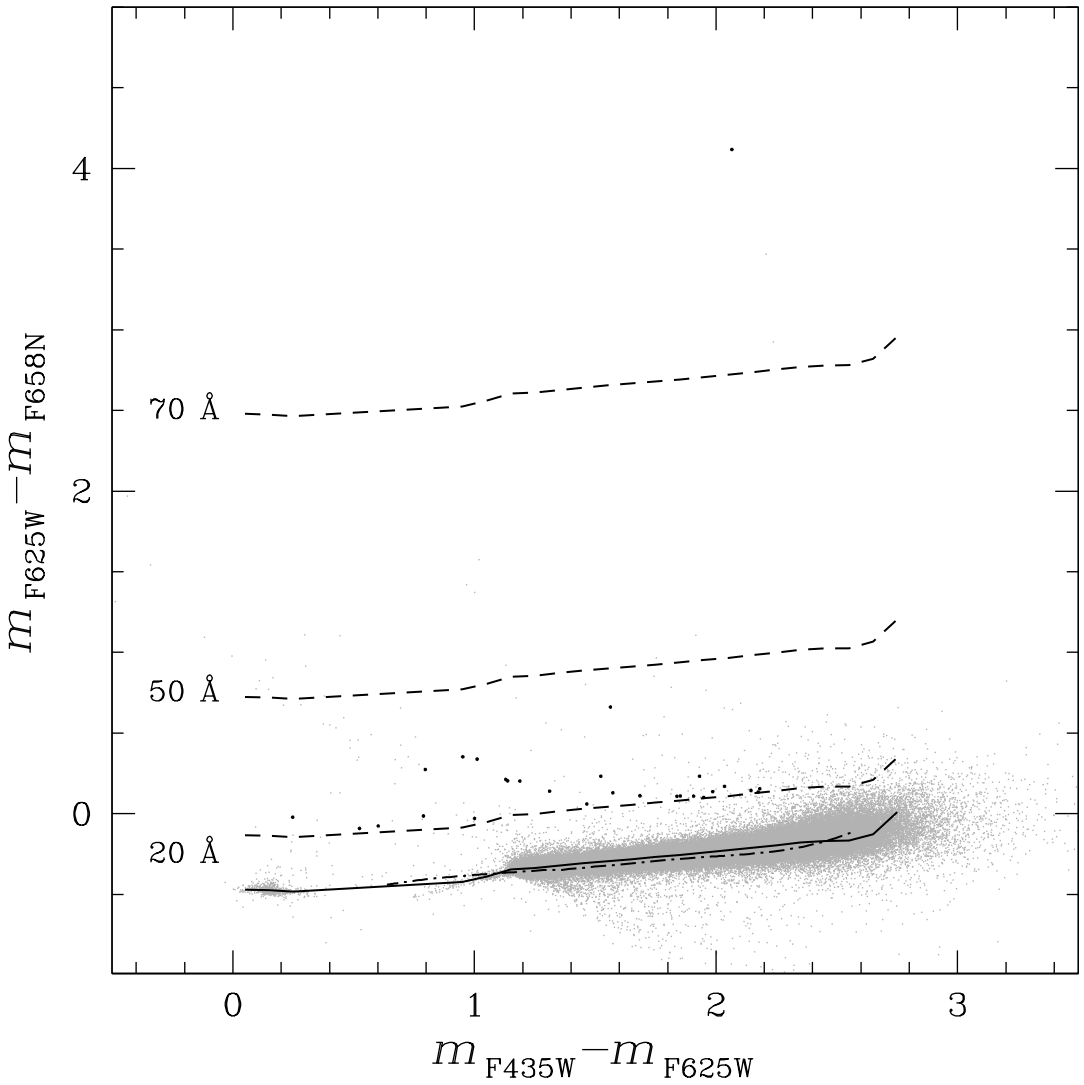

FIGURE 5.2: Selection of stars with Hα excess emission in a colour–colour diagram. The figure shows the position of all of the stars with magnitude $m_{F435W} > 17$ in the $m_{F435W} - m_{F625W}$ vs. $m_{F625W} - m_{F658N}$ colour–colour diagram. The solid line represents the median $m_{F435W} - m_{F625W}$ colour of stars, and is defined as the locus of stars without Hα excess emission and hence the location of stars with EW(Hα) = 0. The dashed lines show the position of stars at increasing levels of Hα emission. All the objects with Hα excess emission at least five times larger than the photometric uncertainty on their $m_{F435W} - m_{F625W}$ colours and pEW>20 are shown in black. The dot-dashed line shows the location of the colour relationship derived for these bands using the Bessell, Castelli, and Plez (1998) atmospheric models.

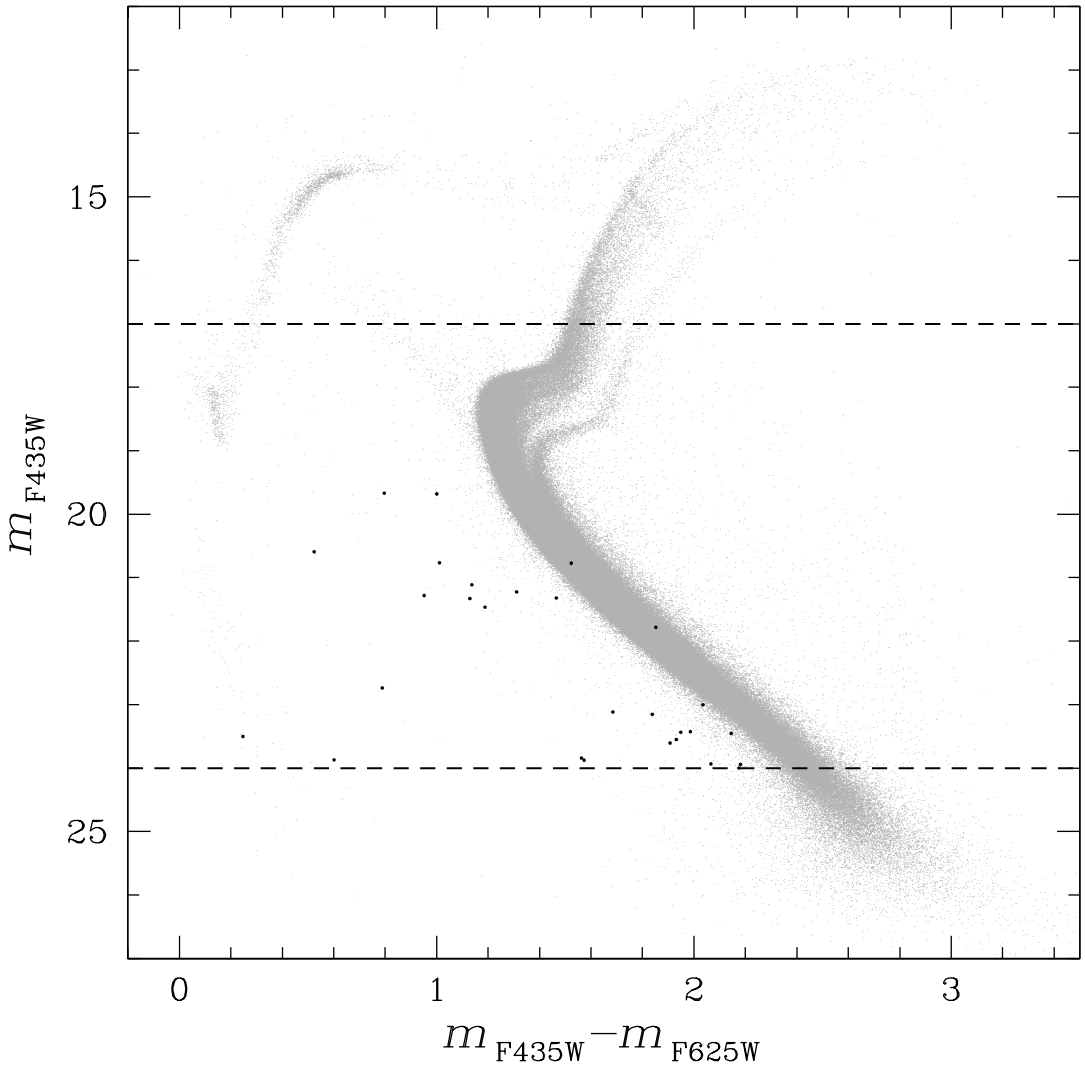

FIGURE 5.3: Position of the selected source (black dots) in the $m_{\mathrm{F435W}} - m_{\mathrm{F625W}}$ vs. m_{F435W} CMD.

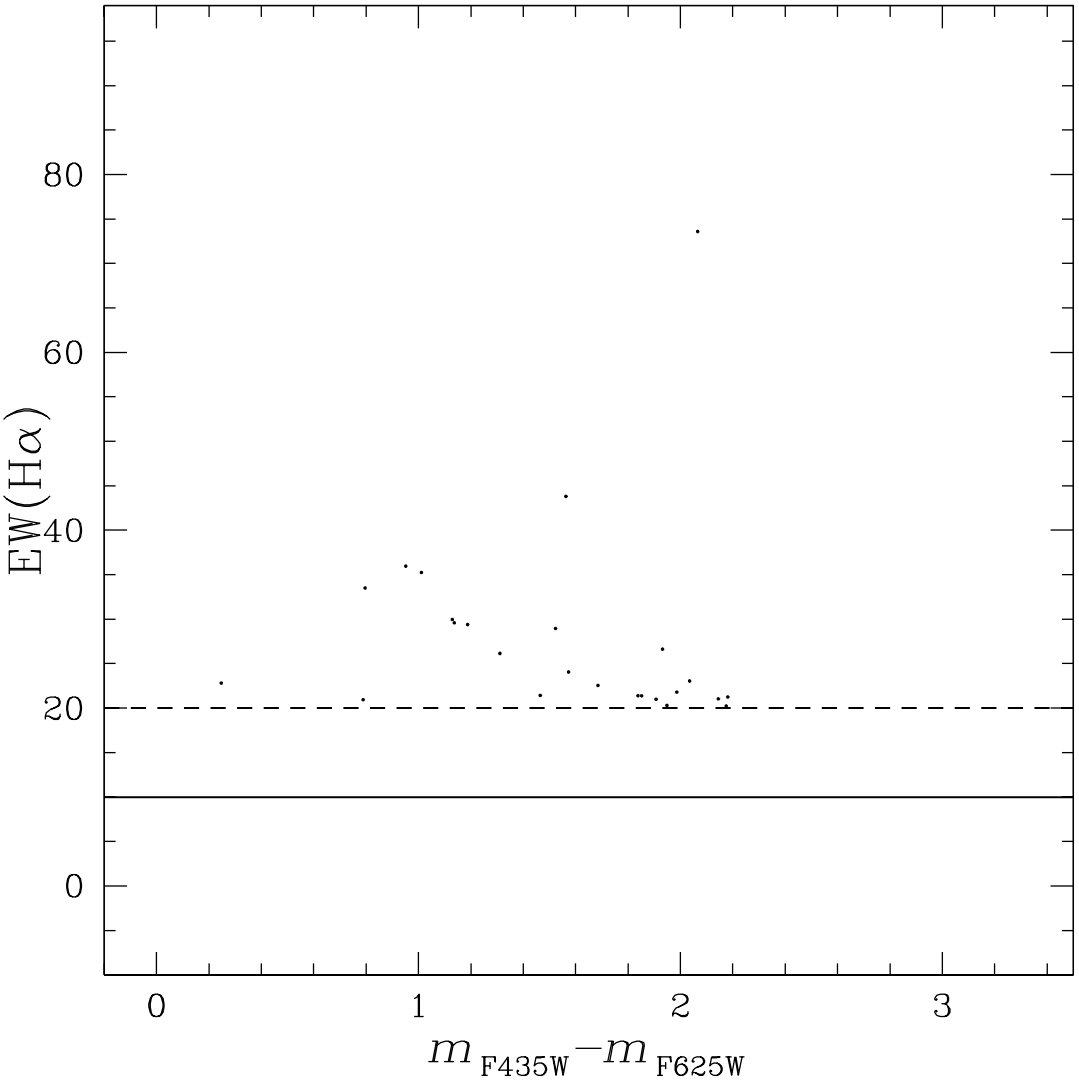

FIGURE 5.4: Position of the selected sources in the pEW vs. $m_{\mathrm{F435W}} - m_{\mathrm{F625W}}$ diagramm.

larger than the source intrinsic photometric error. For all of the candidate Hα emitters, we derived an estimation of the Hα emission width pEW and selected all the sources with pEW>20. We found in total 38 sources.

Chapter 6

First observational evidence of a relation between globular clusters' internal rotation and stellar masses

Several observational studies have shown that many Galactic globular clusters (GCs) are characterised by internal rotation. Theoretical studies of the dynamical evolution of rotating clusters have predicted that, during their long-term evolution, these stellar systems should develop a dependence of the rotational velocity around the cluster's centre on the mass of stars, with the internal rotation increasing for more massive stars. In this Chapter, we present the first observational evidence of the predicted rotation-mass trend. In our investigation, we exploited the *Gaia* Data Release 3 catalogue of three GCs: NGC 104 (47 Tuc), NGC 5139 (ω Cen) and NGC 5904 (M 5). We found clear evidence of a cluster rotation-mass relation in 47 Tuc and M 5, while in ω Cen, the dynamically youngest system among the three clusters studied here, no such trend was detected. The material discussed in this Chapter has been published as a Letter in Monthly Notices of the Royal Astronomical Society (MNRAS; Scalco et al. 2023).

6.1 Introduction

High-precision proper-motion (PM) studies enabled by space-based facilities such as *Hubble Space Telescope* (*HST*) and *Gaia*, and line-of-sight velocities produced by large ground-based spectroscopic surveys are providing key insights into the internal kinematic properties of GCs and have opened a new important window in the study of these systems. The results emerging from these observational investigations reveal a dynamical picture that differs significantly from the traditional view of GCs as isotropic, non-rotating systems.

Numerous studies have now found that internal rotation is a common feature in GCs (e.g., Bellini et al. 2017a, Bianchini et al. 2018, Ferraro et al. 2018, Lanzoni et al. 2018, Kamann et al. 2018, Vasiliev and Baumgardt 2021) and several clusters for which observations allowed to investigate the kinematic properties in a broad range of radial distances from the clusters' centres have often revealed an anisotropic velocity distribution in the clusters' outer regions (e.g., Bellini et al. 2014, Watkins et al. 2015, Jindal, Webb, and Bovy 2019, Libralato et al. 2022).

The discovery of multiple stellar populations in GCs (see e.g. Gratton et al. 2019 for a recent review) has provided evidence of further complexities in various aspects of the study of these systems and a few early studies have shown differences in the rotation and anisotropy of different stellar populations (e.g., Richer et al. 2013,

Cordero et al. 2017, Bellini et al. 2018, Cordoni et al. 2020b; Cordoni et al. 2020a, Kamann et al. 2020, Dalessandro et al. 2021, Libralato et al. 2023).

The present-day dynamical properties of GCs provide important information both on the initial conditions imprinted at the time of the cluster's formation and on the effects of long-term evolutionary processes such as internal two-body relaxation and the interactions with the external tidal field of the Galaxy. Effects of dynamical evolution on the internal kinematics include, for example: the gradual development of a dependence of the velocity dispersion on the stellar mass as clusters evolve towards energy equipartition (Trenti and van der Marel 2013), a radial anisotropy in the cluster's velocity distribution — which may be imprinted in various evolutionary phases and whose variation with the clustercentric distance is subsequently affected by internal relaxation, stellar escape, and the external tidal field (see e.g. Trenti, Bertin, and van Albada 2005, Vesperini et al. 2014, Tiongco, Vesperini, and Varri 2022).

As mentioned above, many GCs are characterised by internal rotation. Numerical simulations (see e.g. Einsel and Spurzem 1999, Ernst et al. 2007, Tiongco, Vesperini, and Varri 2017, Kamlah et al. 2022) have shown that internal relaxation and stellar escape lead to redistribution and loss of angular momentum so that the strength of the present-day rotation is expected to be smaller than the primordial one emerging at the end of the formation phase.

As shown in a number of theoretical studies, the presence of internal rotation has several implications for the long-term dynamical evolution of clusters and the rotational properties of clusters may shed light on a number of fundamental aspects of the dynamics of GCs. Internal rotation may affect the rate of stellar escape and the cluster's evolution towards core collapse (see e.g. Kamlah et al. 2022 and references therein), the coupling between internal rotation and the cluster's orbital motion can lead to a variation of the orientation of the internal rotation axis with the clustercentric distance (Tiongco, Vesperini, and Varri, 2018; Tiongco, Vesperini, and Varri, 2022). Numerical simulations have also shown that internal rotation has a significant impact on the fundamental effects of two-body relaxation; specifically, a number of studies have found that rotating star clusters are characterised by anisotropic mass segregation (see e.g. Szölgyén, Meiron, and Kocsis 2019, Livernois et al. 2021; Livernois et al. 2022, Tiongco, Collier, and Varri 2021) and a difference between the degree of energy equipartition in the tangential and radial components of the velocity dispersion (see e.g. Livernois et al. 2022).

Numerical simulations have also predicted that, during a cluster's evolution, the rotational velocity develops a dependence on the stellar mass with more massive stars tending to rotate more rapidly than low-mass stars (see Kim, Lee, and Spurzem 2004, Hong et al. 2013, Livernois et al. 2021; Livernois et al. 2022). In this Chapter, we focus our attention on this prediction and present an analysis, based on *Gaia* Data Release 3 (*Gaia* DR3, Gaia Collaboration et al. 2016; Gaia Collaboration et al. 2023) data of three GCs (47 Tuc, ω Cen and M 5), providing the first observational evidence of the predicted trend between rotational velocity and stellar mass.

6.2 Gaia DR3 data: selections and cluster membership

Our analysis is specifically focused on three GCs (47 Tuc, ω Cen, and M 5). These three clusters have been selected since they are among those with the strongest internal rotation and their distance from the Sun is such that the range of stellar magnitudes available from the *Gaia* data corresponds to a stellar mass range sufficient

TABLE 6.1: Proprieties of the three studied clusters. For each cluster, the table provides: name of the cluster, position and half-light radius, r_h, from Harris (1996) and Harris (2010), mean PM ($\langle \mu_\alpha cos\delta \rangle$,$\langle \mu_\delta \rangle$) and central velocity dispersion, σ_0, from Vasiliev and Baumgardt (2021), radius used in this work for the data extraction from the *Gaia* DR3 catalogue, r_{ext}, number of stars passing the astrometric and photometric quality selections, N_s, and number of selected member stars, N_m.

ID	R.A. (J2000) [h m s]	Decl. (J2000) [° ′ ″]	r_h [arcmin]	$\langle \mu_\alpha cos\delta \rangle$ [mas/yr]
NGC 104	00 24 05.67	−72 04 52.6	3.17	5.252 ± 0.021
NGC 5139	13 26 47.24	−47 28 46.5	5.00	-3.250 ± 0.022
NGC 5904	15 18 33.22	+02 04 51.7	1.77	4.086 ± 0.023

$\langle \mu_\delta \rangle$ [mas/yr]	σ_0 [mas/yr]	r_{ext} [arcmin]	N_s	N_m
-2.551 ± 0.021	0.5462	40	61257	36608
-6.746 ± 0.022	0.5609	40	92603	45665
-9.870 ± 0.023	0.2340	25	10613	6344

($\sim$0.6–0.85 $M_\odot$) to explore the dependence of rotation on the stellar mass.

For each of the clusters analysed in our study, we retrieved astrometry, photometry, parallaxes (π), and PMs of all sources from the *Gaia* DR3 archive that are located within a given radius from the nominal cluster centre (the exact value of this radius and the central coordinate for each cluster are reported in Table 6.1). We defined a sample of stars with reliable photometry and astrometry by following the recommendations of Fabricius et al. (2021), Lindegren et al. (2021) and Riello et al. (2021), but with tighter selections on some parameters. Specifically, for each of the three clusters we retained all sources from the *Gaia* DR3 catalogue with:

$$\begin{cases} 13 < G < 20, \\ \texttt{RUWE} < 1.15, \\ \texttt{astrometric\_excess\_noise\_sig} \leqslant 2, \\ \texttt{ipd\_gof\_harmonic\_amplitude} < 0.1, \\ \texttt{ipd\_frac\_multi\_peak} \leqslant 2, \\ \texttt{visibility\_periods\_used} \geqslant 10, \\ \texttt{duplicated\_source} = 0, \\ \texttt{astrometric\_gof\_al} < 4 \text{ and} \\ C - f(G_{BP} - G_{RP}) < 3\sigma_C, \end{cases}$$

where C is the `phot_bp_rp_excess_factor`, $f(x) = \sum_i a_i x^i$, with the polynomial coefficients a_i taken from Table 2 of Riello et al. (2021) and σ_C given by Equation (18) of Riello et al. (2021).

These selections are particularly severe for the very central regions of the clusters due to the limited capabilities of *Gaia* in crowded and dense environments. As an example of the result of the selection procedure, we show in Fig. 6.1 the distribution of selected sources in the plane of the sky for 47 Tuc. Due to the selections, the inner part of the cluster is strongly underpopulated, with essentially no stars inside the cluster's half-light radius, r_h. A similar central depletion is present in the data selected for the analysis of ω Cen and M 5.

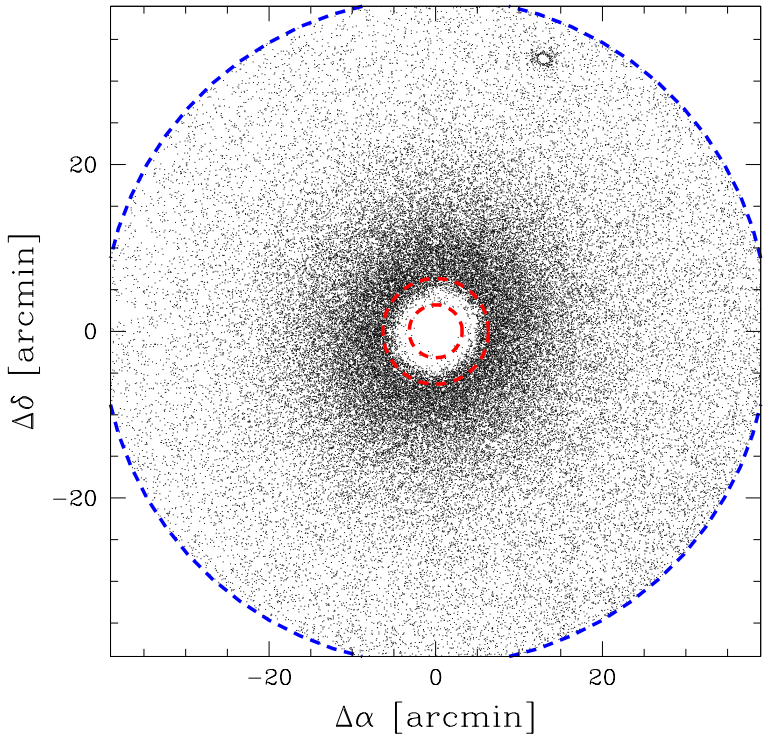

FIGURE 6.1: Spatial distribution of the selected sources for 47 Tuc. The red dashed circles represent the cluster's half-light radius (r_h = 3.17 arcmin Harris 1996; Harris 2010) and $2r_h$, while the blue dashed circle represents the extraction radius (r_{ext} = 40 arcmin).

The number of stars passing the photometric and astrometric quality selections is reported in Table 6.1 for each cluster.

6.2.1 Selection of cluster members

To derive the clusters rotation from the *Gaia* DR3 catalogue, we first need to select the most probable cluster members for each cluster. To do this, we used a procedure based on stellar PMs, π and positions in the colour-magnitude diagram (CMD). The procedure is illustrated in Fig. 6.2 for 47 Tuc and summarised in the following:

1. We initially applied the orthographic projection of the celestial coordinates and converted PMs using Equation (2) from Gaia Collaboration et al. (2018). We plotted G as a function of the PM relative to the mean PM of the cluster (from Vasiliev and Baumgardt, 2021, see also Table 6.1), μ_R, (panel a of Fig. 6.2) for each source in the sample. We drew by hand a line that separates cluster stars (μ_R close to 0) from field stars, and defined a sample of probable cluster members.

2. We plotted G as a function of π for the probable cluster members and drawn by hand two lines that enclose all the stars with likely cluster π (panel b of Fig. 6.2). All the stars that lie outside these two lines were excluded from the sample of probable cluster members.

3. We plotted the G versus $G_{BP} - G_{RP}$ CMD for the probable cluster members (panel c of Fig. 6.2). We identified in the cleaned CMD the sequence of stars associated with the cluster and defined by hand lines that follow the red and

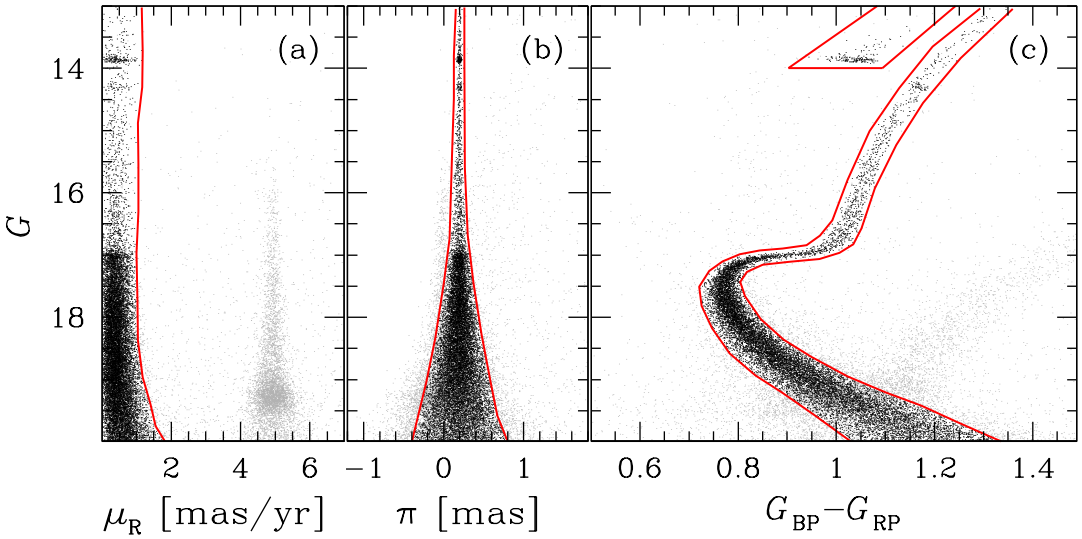

FIGURE 6.2: This figure illustrates the procedure used to select probable members of 47 Tuc. (a) G versus μ_R; (b) G versus π; (c) G versus $G_{BP} - G_{RP}$ CMD. The red lines in all panels are used to separate cluster members from field stars. Selected cluster members are in black, while field stars are in grey. Only 60% of the sample is shown for clarity.

blue edges of the sequence profiles. We then removed from the sample of probable cluster members all the stars that lie outside of these boundaries.

We iterate this procedure a few times to improve our membership selection. The number of cluster members for each GC and other physical parameters are reported in Table 6.1.

6.3 Globular clusters rotation

In this section, we briefly review the theoretical predictions about the dependence of the cluster's internal rotational velocity on the stellar mass and then present the observational results obtained from the analysis of the *Gaia* DR3 catalogue.

6.3.1 Theoretical predictions

A few theoretical studies on the dynamics of rotating star clusters (Kim, Lee, and Spurzem, 2004; Hong et al., 2013; Livernois et al., 2021; Livernois et al., 2022) have found that one of the fundamental effects of dynamical evolution of rotating star clusters is the development of a dependence of the internal rotation on the mass of the stars, where the rotational velocity increases with the stellar mass. We refer to those papers for a complete description of the evolutionary path of the various models explored. Here we focus our attention on the N-body models discussed in Livernois et al. (2022).

Although these models are not aimed at a direct comparison with observational data of any specific GC, in order to establish a closer connection with the analysis presented in this Chapter, we quantify the development and the strength of the dependence of the rotational velocity on the stellar mass found in the Livernois et al's models using the same parameters adopted in our observational analysis.

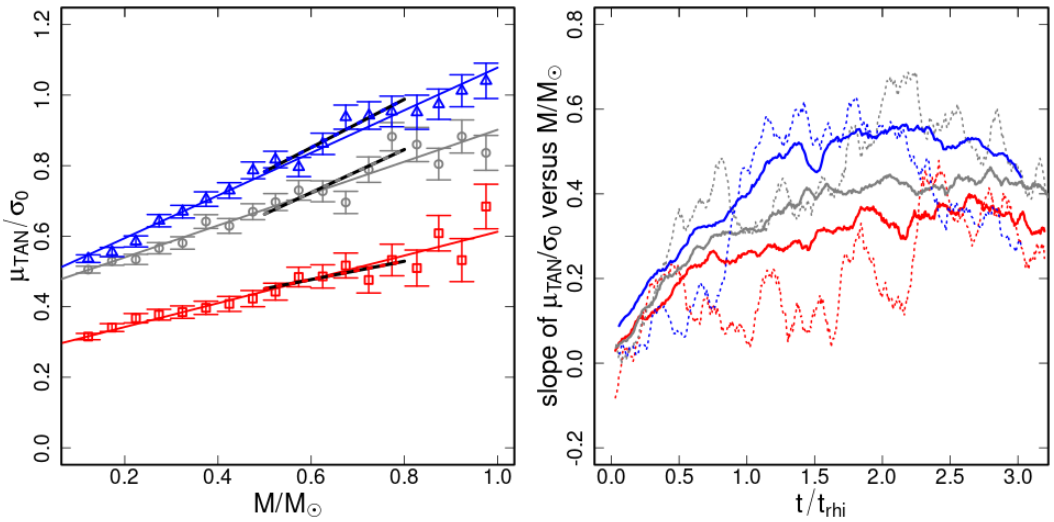

FIGURE 6.3: *Left panel*: μ_{TAN}/σ_0 versus mass measured at $t/t_{rhi} = 2$ for the low (red), moderate (grey), and high (blue) rotation models studied in Livernois et al. (2022). Thin (thick) lines show the best linear fit using the 0.1–1 $M_\odot$ (0.5–0.8 $M_\odot$) mass range. *Right panel*: slope of the μ_{TAN}/σ_0-mass relationship as a function of time (normalised to t_{rhi}) for all the three models. The continuous lines represent the running average of the slope calculated using the full mass range available in the simulation (0.1–1 $M_\odot$), while the dashed lines represent the running average of the slope calculated using a narrower mass range closer to that available in the observational analysis (0.5–0.8 $M_\odot$).

Livernois et al. (2022) studied the dynamical evolution of three multi-mass, rotating star cluster models characterised by low-, moderate-, and high-rotation; in the left panel of Fig. 6.3, we plot μ_{TAN}/σ_0 (where μ_{TAN} is the tangential component of the velocity and σ_0 is the central velocity dispersion of all stars, evaluated on the plane perpendicular to the rotation axis) versus mass measured at $t/t_{rhi} = 2$ (where t_{rhi} is the initial half-mass relaxation time) for those three models. It is interesting to point out that the models predict a linear relationship between μ_{TAN}/σ_0 and stellar mass and its strength is thus properly quantified by the slope shown in this panel. In the right panel, we plot the time evolution of the slope of the μ_{TAN}/σ_0-mass relationship as a function of time, for all three models.

As shown in this figure, all models develop a mass-dependent rotation curve that is characterised by a rotation increasing with the stellar mass. The slope of the μ_{TAN}/σ_0-mass relationship depends on the strength of the initial rotation and is slightly steeper for models with more rapid initial rotation. In this figure, we show both the slope calculated using the full mass range available in the simulation (0.1–1 $M_\odot$) and the same slope calculated using a narrower mass range closer to that available in the observational analysis (0.5–0.8 $M_\odot$; see Section 6.3.2). As expected, the calculation using a broader mass range results in a more robust and less noisy estimate of the slope of the μ_{TAN}/σ_0-mass relationship but both estimates follow a similar time evolution.

6.3.2 Observational results

In light of the results presented in Livernois et al. (2022) and shown in Fig. 6.3 we made use of our *Gaia* DR3 catalogue to investigate the presence of a rotation-mass

relation in our three GCs, 47 Tuc, ω Cen and M 5.

We initially decomposed the PMs into radial and tangential components ($\mu_{\rm RAD}$, $\mu_{\rm TAN}$) and propagated the velocity uncertainties. For each cluster, we divided the sample of member stars into equally populated radial bins. Then, for each bin, we evaluated the median value of $\mu_{\rm TAN}$, using a maximum likelihood approach. The top panels of Fig. 6.4, show the obtained rotation profiles, in absolute value, for each cluster (black points). The profiles are normalised by the central velocity dispersion value, σ_0, provided by Vasiliev and Baumgardt (2021) and reported in Table 6.1. The rotation curves are compared with those published in Vasiliev and Baumgardt (2021) (blue solid line), showing a quite good agreement.

We converted magnitudes into stellar masses via isochrone fitting, for which we used isochrones from the Dartmouth Stellar Evolution Database (Dotter et al., 2008). We adopted cluster metallicities [Fe/H] from Harris (1996) and Harris (2010) and assumed primordial helium abundance ($Y = 0.246$). We assumed $[\alpha/{\rm Fe}] = +0.2$ for 47 Tuc and M 5 (Dotter et al., 2010), and $[\alpha/{\rm Fe}] = +0.4$ for ω Cen (Milone et al., 2020), and adopted age, distance modulus and reddening that best fit the data. We then associated to each star the corresponding mass in the interpolating isochrone[1]. The reddening has been converted into absorption using the extinction coefficient provided in Casagrande and VandenBerg (2018). Following Watkins et al. (2022), we identified in the CMD all the stars belonging to the AGB and HB and reassigned their masses to be equal to the maximum in the sample. We limited our analysis to stars located at a distance $r > 2r_{\rm h}$ so as to remove the inner radial regions affected by a significant incompleteness in the *Gaia* data after the selections (see Appendix in the online material).

Finally, for each cluster, we divided the sample of member stars equally populated mass bins. Then, for each bin, we evaluated the median value of $\mu_{\rm TAN}$, again with a maximum likelihood method. The absolute values of the median rotational velocities, normalised by σ_0, are shown in the bottom panels of Fig. 6.4 as a function of the stellar mass, along with the least square linear fit (red lines). As shown by this Figure, there is a clear trend of rotational velocity increasing with the stellar mass.

It is important to point out that such a trend could also result from the combined effect of mass segregation (massive stars preferentially populating the inner regions) and the increase of the rotational velocity at smaller distances from the cluster's centre. In order to estimate the extent of this effect we have assigned to each star a value of rotational velocity depending only on the star's radial position (and calculated from the rotational velocity profile calculated in our analysis and shown in the top panels of Fig. 6.4). In this test, all stars at a given distance from the cluster's centre have the same rotational velocity regardless of their stellar mass: by construction, we have completely removed the specific mass-dependence of $\mu_{\rm TAN}$ predicted by simulations and on which our study is focused. With these data, we have then calculated the $\mu_{\rm TAN}/\sigma_0$-mass slope which, in this case, is entirely due to the combined effect of mass segregation and radial variation of $\mu_{\rm TAN}$. The slope of the $\mu_{\rm TAN}$-mass trend obtained in this test is 0.13 ± 0.01 for 47 Tuc and 0.19 ± 0.02 for M 5; in both cases the slope is significantly weaker than that found in the full analysis and confirms that trend found in our study for these two clusters is due to the effect predicted by theoretical studies. For ω Cen, on the other hand, the slope found with this test is equal to 0.24 ± 0.03 and is consistent with that obtained in the full analysis showing

[1]We neglected the presence of multiple stellar-populations since their effect is likely to be small, as shown in Libralato et al. (2019).

that for this cluster no significant $\mu_{\rm TAN}$-mass trend (other than that simply due to mass segregation and radial variation of $\mu_{\rm TAN}$) is detected.

It is interesting to point out that the lack of a significant $\mu_{\rm TAN}$-mass trend in ω Cen might be due to the fact that this cluster is the dynamically youngest system among the three clusters studied (the half-mass relaxation time is $\log(t_{\rm rh}/{\rm yr}) = 10.39$, 9.58, and 9.45 for ω Cen, 47 Tuc, and M 5, respectively; Baumgardt and Hilker 2018) and such a trend might not have developed yet (or still be very weak).

As for the slopes found in 47 Tuc and M 5, we notice that the slope for 47 Tuc is consistent with those found in our simulations while the slope for M 5 is a bit larger than those in our models. As pointed out in section 6.3.1, the goal of these simulations is not a close comparison with observational data but rather that of illustrating the fundamental effects of dynamical evolution on the development of a $\mu_{\rm TAN}$-mass trend. Simulations spanning a broader range of initial structural and kinematic initial conditions would be necessary for a full exploration of the possible range of values of the $\mu_{\rm TAN}$-mass slopes.

6.4 Conclusion

At odds with the traditional dynamical picture according to which GCs would be isotropic and non-rotating stellar systems, several recent observational studies have shown that many GCs are instead characterised by the presence of internal rotation. A few theoretical studies have focused their attention on the dynamics of rotating clusters and explored the effects of various dynamical processes on the evolution of a cluster's internal rotation. One of the predictions of these theoretical studies is that, during their long-term dynamical evolution, GCs develop a dependence of their internal rotational velocity on the stellar mass where more massive stars tend to rotate around the cluster's centre more rapidly than low-mass stars.

In this Chapter, after reviewing the theoretical predictions using the simulations of rotating clusters of Livernois et al. (2022), we have exploited data from the *Gaia* DR3 catalogue to carry out an analysis of the rotational properties of three GCs (47 Tuc, ω Cen, and M 5) aimed at validating the predicted relation between internal rotation about the cluster's centre and stellar mass.

Our study reveals that 47 Tuc and M 5 are characterized by a trend between rotation and stellar mass, where the rotational velocity increases with the stellar mass and provides the first observational evidence of the predicted rotation-mass relation. The trend between rotational velocity and mass found in ω Cen, on the other hand, is consistent with being simply due to the combined effect of mass segregation and radial variation of the rotational velocity; ω Cen is a dynamically young cluster, and the lack of a significant $\mu_{\rm TAN}$-mass (or the presence of a weaker one undetected in our analysis) trend is generally consistent with the expected development of this relation during a cluster's long term-evolution.

Due to the faint magnitude limit of *Gaia*, we focused our analysis only on nearby and rapidly rotating GCs, in order to have a sufficient mass interval and rotation signal to properly characterise the $\mu_{\rm TAN}/\sigma_0$-mass slope. Future observational investigations, possibly based on *HST*, *JWST*)and *Roman Space Telescope* PM measurements, extending the mass range down to lower masses than those currently available, and out to the tidal radius, would significantly strengthen the investigation of the $\mu_{\rm TAN}/\sigma_0$-mass relationship and provide the opportunity to carry out a comprehensive investigation of this trend, explore the possible dependence of its strength on other clusters' dynamical properties and evolutionary history.

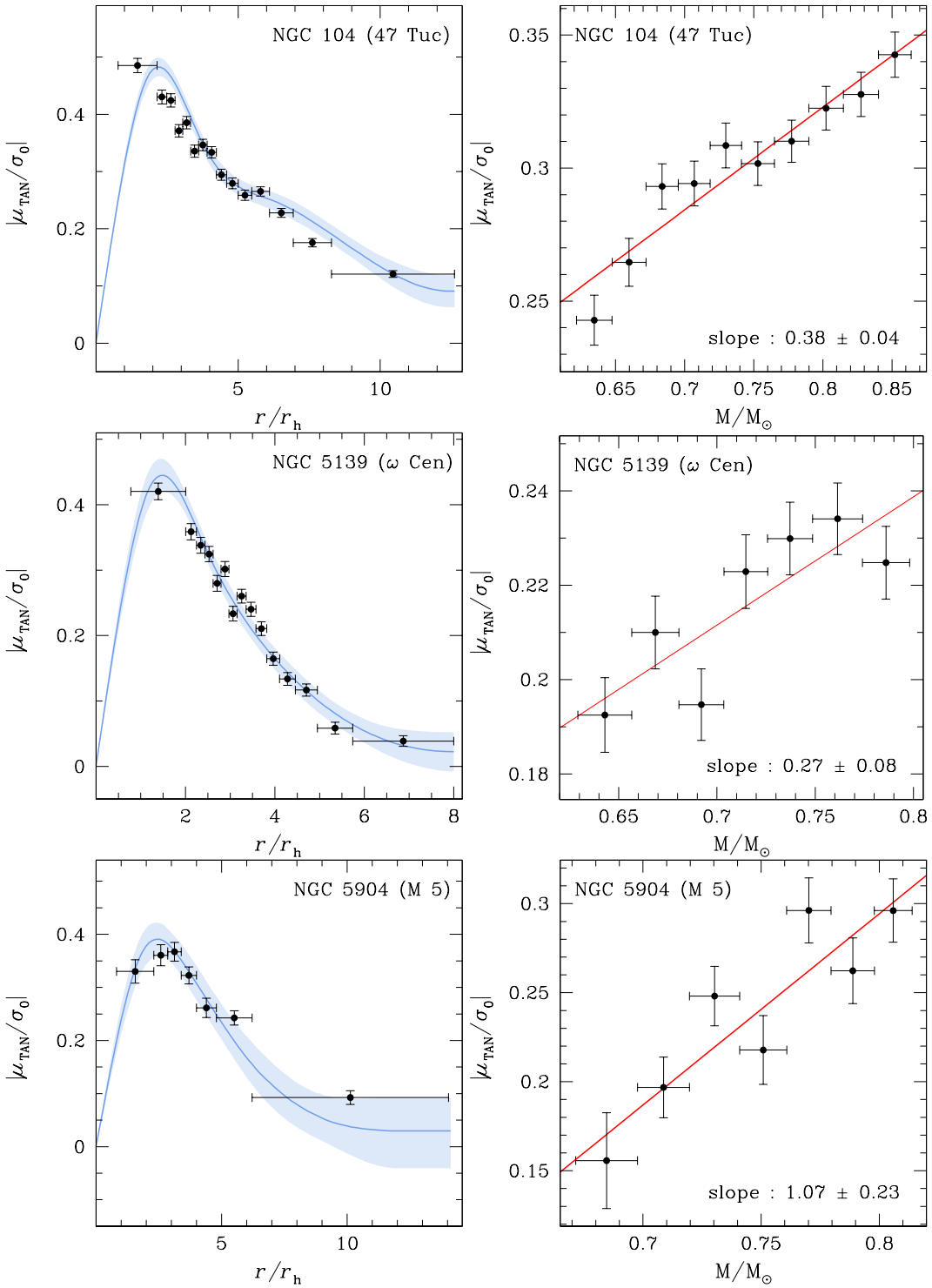

FIGURE 6.4: *Left panels*: absolute value of the rotation profile in the plane of the sky obtained with the sample of cluster members selected in this work from the *Gaia* DR3 catalogue (black points), for the three clusters. The rotation curves are normalised by the central velocity dispersion value, σ_0, provided by Vasiliev and Baumgardt (2021). r_h is the half-light radius of the cluster from Harris (1996) and Harris (2010). The values of σ_0 and r_h are reported in Table 8.1, for each cluster. The solid blue lines and shaded areas represent the rotation profiles presented in Vasiliev and Baumgardt (2021) and their 68% confidence intervals, respectively. *Right panels*: $|\mu_{TAN}/\sigma_0|$ as a function of the stellar mass (black points). The red lines represent the least square fits of the bins. The slopes of the red lines are also reported.

Chapter 7

The *HST* Large Programme on NGC6752 - Internal Kinematics

According to N-body simulations, the present-day kinematic proprieties of multiple stellar populations in globular clusters are the results of different initial conditions of the system. The study of the internal motions of stars in globular clusters offers a unique opportunity to investigate the formations and evolution process that lead to the formation of these objects and their multiple stellar populations. Here we provide a detailed study of the internal kinematics and structure of the globular cluster NGC 6752. In this work, we combined the proper motion data from Gaia early Data Release 3 with HST photometry in the core of the cluster, where the Gaia resolving power is limited by crowding, and in two external fields. Using HST data we were able to disentangle the multiple stellar populations in NGC 6752 in the faint magnitude regime inaccessible by Gaia. We also made use of ESO/VLT and Keck archival data to study the line of sight velocity of the stars in NGC 6752.

7.1 Introduction

Galactic globular clusters (GCs) are known to be composed of two main groups of stars usually referred to as first and second generation (1G, 2G, Tiongco, Vesperini, and Varri 2017; Milone et al. 2018c), with different helium enhancement and chemical compositions (e.g. Marino et al. 2019). Various formation scenarios have been proposed for their origin, but none of them seems to be satisfactory (see Renzini et al. 2015b for a review).

According to some scenarios, GCs have experienced multiple star-formation episodes and the 2G stars are formed from the processed material of intermediate- to high-mass stars formed during the first burst (e.g., Ventura et al. 2001; Decressin, Charbonnel, and Meynet 2007; de Mink et al. 2009; D'Ercole et al. 2010; Krause et al. 2013; Denissenkov and Hartwick 2014; D'Antona et al. 2016; Calura et al. 2019).

Another scenario proposes a single star-formation episode, where 2G stars have accreted material ejected by supermassive stars (Denissenkov and Hartwick, 2014) on forming protostars (see e.g., Gieles et al. 2018) during the early stage of their formation.

Observational studies have revealed that 1G and 2G stars differ not only in their chemical abundance but also in their kinematic proprieties, with the 2G population characterized by a more rapid rotation and a more radially anisotropic velocity distribution than 1G stars (see e.g. Richer et al. 2013; Bellini et al. 2015; Bellini et al. 2018; Cordero et al. 2017; Milone et al. 2018c; Libralato et al. 2019; Cordoni et al. 2020b; Cordoni et al. 2020a). These differences reveal the existence of a tight link

between the origin of multiple stellar populations and their different chemical composition and the cluster's formation and dynamical history.

According to N-body simulations, the present-day kinematic proprieties of the 1G and 2G stars are the results of their different initial conditions (e.g. Tiongco, Vesperini, and Varri 2016; Tiongco, Vesperini, and Varri 2019; Vesperini et al. 2013; Vesperini et al. 2021). Thus, the study of the internal motions of the multiple stellar populations, such as rotation and velocity-dispersion and anisotropy radial profile, offers an important tool to study the formation and evolution of GC and can help to disentangle between the different formation scenarios.

In this sense, the high-precision proper motions provided by the Gaia mission have revitalised the study of the internal kinematic proprieties of GCs. However, given the difficulty of Gaia in crowded environments and its faintness limits, these studies are focused only on bright stars outside the inner regions. The high resolving power of the Hubble Space Telescope (HST) provides a powerful tool to study the proper motions of stars in crowded and faint regimes inaccessible to Gaia.

NGC 6752 is known to host different stellar populations as revealed by its complex colour–magnitude diagrams obtained by combining optical and ultraviolet photometry. This cluster is known to host three different stellar populations, namely A, composed of stars with primordial helium abundance (Y$\sim$0.246), B and C, enhanced in helium by Y$\sim$0.01 and 0.03, respectively (Milone et al., 2010; Milone et al., 2013; Milone et al., 2018c; Dotter et al., 2015). These three stellar populations have been identified and separated through the entire CMD, from the RGB and the upper MS to the M-dwarf regime (Milone et al., 2019). Spectroscopic studies have demonstrated that population-C stars are enhanced in N, Al, Si, and Na and depleted in C, O, and Mg, with respect to population A, while population-B stars have intermediate chemical composition.

Here we present a detailed kinematic and structural study of NGC 6752 using Hubble Space Telescope (HST) and Gaia early Data Release 3 (Gaia eDR3) data. The Chapter is organised as follows: Section 7.2 is dedicated to the description of the data; Section 7.3 provides an estimate of the absolute proper motion (PM) and parallax of NGC 6752; Section 7.4 provide an estimate of the line of sight (LOS) velocity of NGC 6752; Section 7.5 describes the methodology to estimate membership probability (MP); Section 7.6 describes the structural parameters of NGC 6752; Section 7.7 analysed the rotation of NGC 6752 both in the plane of sky and in the LOS direction; Section 7.8 shows the velocity-dispersion and anisotropy radial profile of the stars in NGC 6752; Section 7.9 present the mass function of NGC 6752 and it multiple stellar populations; Filanny, Section 7.10 provides a brief summary of the results obtained in this chapter.

7.2 Data set

To investigate the internal kinematics of NGC 6752, we combined proper motions from Gaia eDR3, HST photometry and high-precision radial velocities provided by Baumgardt and Hilker (2018) and derived from archival ESO/Very Large Telescope (VLT) and Keck spectra together with published radial velocities from the literature. In this section, we provide a brief description of the data set.

7.2.1 Gaia eDR3

We used a box of 10×5 degrees centered in the nominal cluster center (RA = 287.717, $\delta = -59.984554$; Harris 1996) for our initial extraction. We selected stars from the Gaia archive [1] using the following search:

```
FROM gaiaedr3.gaia_source
WHERE CONTAINS(POINT('ICRS',gaiaedr3.gaia_source.ra,
gaiaedr3.gaia_source.dec),
BOX('ICRS',287.717,−59.984554,10,5)
)=1
```

We found a total of 741,931 sources. Following Soltis, Casertano, and Riess (2021) we applied a series of quality cuts on the data:

```
AND astrometric_excess_noise_sig <=8
AND astrometric_excess_noise <4
AND astrometric_params_solved >3
AND phot_bp_rp_excess_factor <2.5
AND phot_proc_mode =0
AND astrometric_gof_al <4)
```

After these quality cuts, our starting sample includes 582,754 stars. Figure 10.1 shows the distribution on the sky of the sources. The yellow and red circles mark the cluster's half-light radius ($r_c = 1\farcm91$), and the tidal radius ($r_h = 53\farcm76$, Harris 1996) respectively, from the centre. After our eDR3 quality cuts, the central $\sim 3'$ radius of the cluster is essentially un-populated. This is due to the relatively crowding of the central region of NGC 6752, which affects the quality of the Gaia measurements. Panel (a) of Figure 10.2 shows the Gaia G vs. Gaia $G_{BP} - G_{RP}$ CMD of the sources. Panels (b),(c),(d) and (e) show the proper motion distribution of the stars in the four regions defined by the grey dashed lines of panel (a). The proper motions for the stars in our sample fall into two separate components; the narrower component centred around (−3.17,−4.01) is due to cluster stars, while the much broader component roughly centred at (−5, 0) is due to field stars. The absolute proper motion of NGC 6752 (μ_α, μ_δ) = (−3.17±0.01, −4.01±0.01) mas/yr, reported by Baumgardt et al. (2019) for Gaia Data Release 2 (Gaia DR2), is shown as red dots. A red circle centred in (−3.17,−4.01) of radius 1 mas/yr is used to separate likely cluster members (black dots) to field stars (grey dots).

7.2.2 HST

To study the kinematics of NGC 6752 we used a wide range of HST fields in order to cover an extensive part of the cluster. Figure 7.3 shows the locations of the HST fields used in this work, superimposed on an image from the Digital Sky Survey (DSS)[2]. The dataset is composed of a central field (represented in yellow in Fig. 7.3), two external fields from the HST multi-epoch program GO-15096+GO-15491 (PI: Bedin; fields F0 and F1, represented in blue and magenta in Figure 7.3, respectively) and another two external fields from the HST programs GO-12254 (PI: Cool), GO-12311

[1] https://gea.esac.esa.int/archive/
[2] https://archive.eso.org/dss/dss

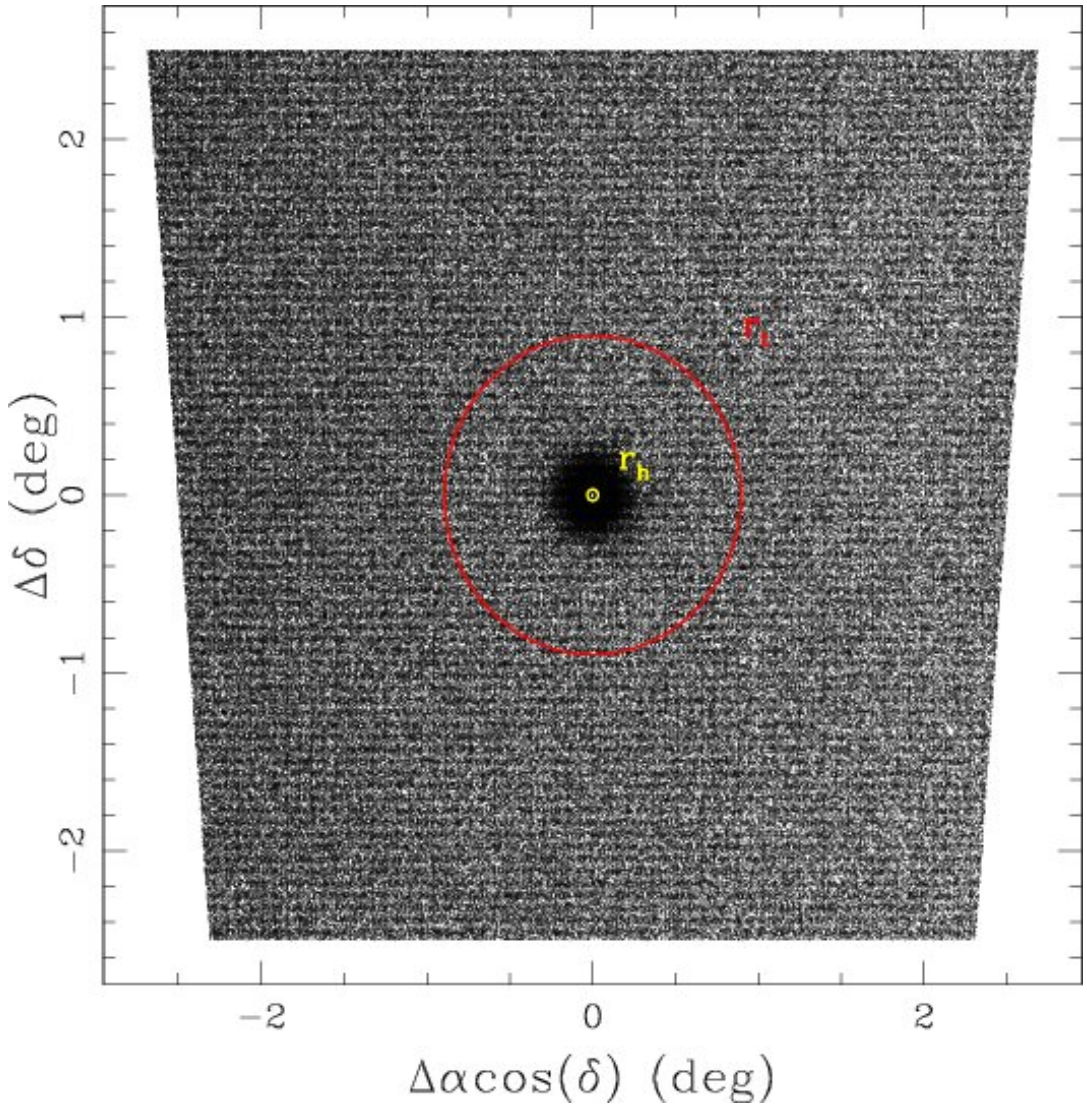

FIGURE 7.1: Distribution on the sky of the sources that survived our eDR3 quality cuts. Units are in degrees measured from the cluster centre. The yellow and red circles mark the cluster's half-light radius ($r_c = 1'.91$), and the tidal radius ($r_h = 53'.76$) respectively, from the centre.

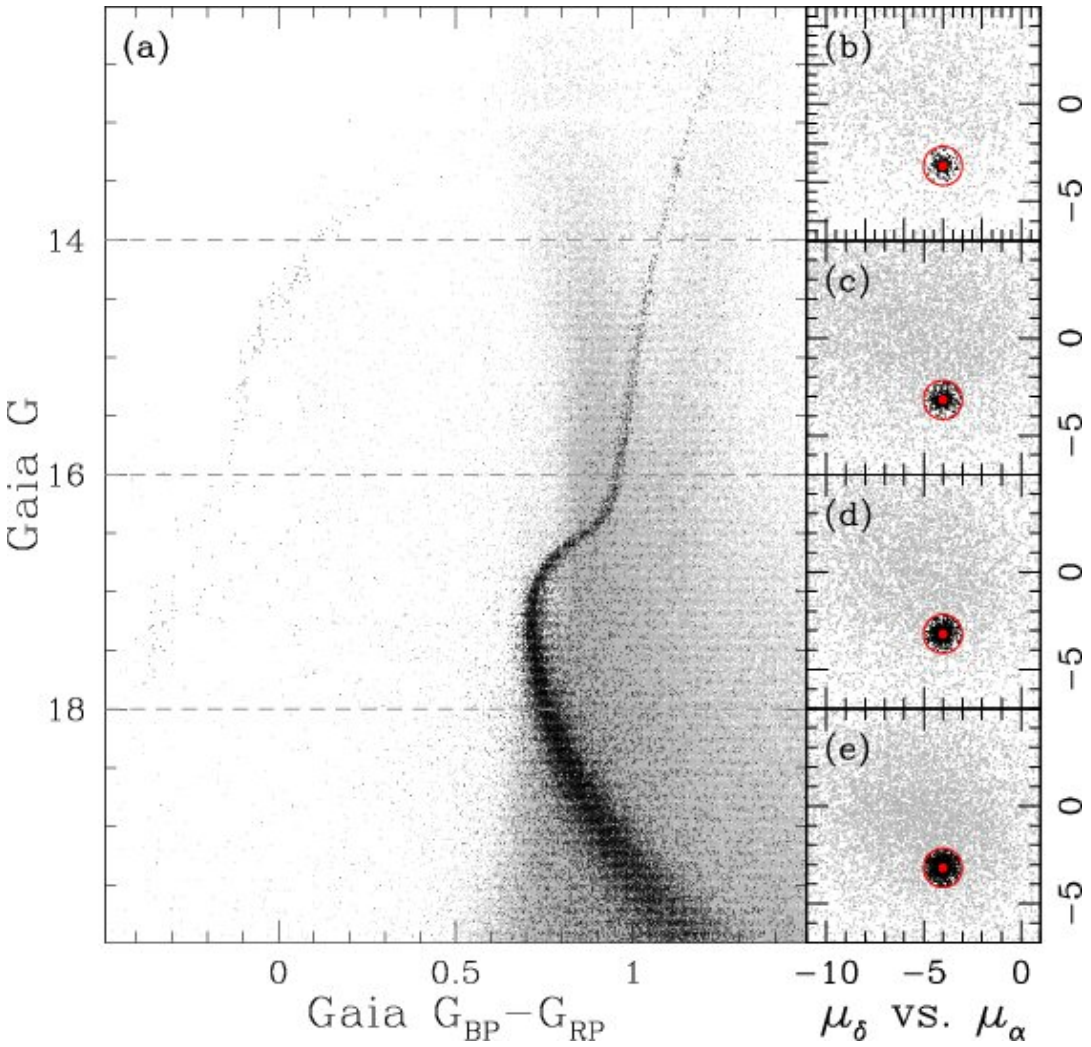

FIGURE 7.2: (a) Gaia G vs. Gaia $G_{BP} - G_{RP}$ CMD. The dashed gray lines divide the CMD in four regions. (b)-(c)-(d)-(e) proper motion distribution of the stars in the four regions defined in panel (a). For convenience, we show only the 95%, 90% and 50% of the stars in panels (c), (d) and (e), respectively. The red dots represent the absolute proper motion of NGC 6752 (μ_α, μ_δ) = (-3.17 ± 0.01, -4.01 ± 0.01) mas/yr, as reported in Baumgardt et al. (2019). The red circles centered in (-3.17,-4.01) and with radius 1 mas/yr are used to separate likely cluster members to field stars. In all panels, sources that fall outside the red circles are shown in gray, while stars that fall inside the circle are shown in black.

(PI: Piotto) and GO-15857 (PI: Bellini; fields F2 and F3, represented in green in Figure 7.3). Table 7.1 reports the complete list of NGC 6752 HST observations used in this work. The photometry and positions of stars in the HST images were extracted following the prescriptions of Scalco et al. (2021). In a nutshell, the reduction can be divided in two steps, first and second pass photometry. In the first pass photometry, we used the `FORTRAN` code `hst1pass` Anderson and King (2006) to find the best spatially variable PSF for each image, and then we used this PSF to measure the stellar positions and fluxes of each star. The second pass photometry, which is mostly based on the software described in Anderson and King (2006)), takes images and perturbed PSF arrays obtained during the 'firstpass photometry' stage to simultaneously find and measure stars in all of the individual exposures and for the entire set of filters. The photometry was calibrated onto the Vega-mag system following the procedures given in Bedin et al. (2005a). Star positions were corrected for geometric distortion using the solutions given in Bellini, Anderson, and Bedin (2011) for WCF3/UVIS, and the publicly available WFC3/IR correction developed by Anderson (2016).

We removed the poorly measured stars using a set of quality parameters produced by our software, in close analogy of what was done in Scalco et al. (2021). Finally, the photometry was corrected for zero-point spatial variations following the recipes in Milone et al. (2012a).

We cross-matched the photometry obtained in the central field with the proper motions (PMs) catalogue provided by Libralato et al. (2022). The PMs for the fields F0, F1, F2 and F3 were computed using the technique described in Milone et al. (2012a) (see also Bellini et al. (2014), Bellini et al. (2018), and Libralato et al. (2018b). This is an iterative procedure that treats each image as a stand-alone epoch and can be summarized in two main steps: (1) transforms the stellar positions of each exposure into a common reference frame by means of a six-parameter linear transformation; (2) fit these transformed positions as a function of the epoch with a least-square straight line. The slope of this line, computed after several outlier-rejection stages, is a direct measurement of the PM. We verified that neither component of the PM suffers from systematic effects due to stellar colour and luminosity.

High-frequency-variation systematic effects were corrected as described in Bellini et al. (2018), i.e. according to the median value of the closest 100 likely cluster members (excluding the target star itself).

7.2.3 Radial velocities

The line of sight (LOS) velocities used in our analysis are provided by Baumgardt and Hilker (2018), which used a combination of more than 15000 high-precision radial velocities derived from archival ESO/VLT and Keck spectra together with ∼20000 published radial velocities from the literature. For NGC 6752 we found a total of 2.018 sources for which LOS velocities are provided.

7.3 Absolute proper motion and parallax estimate

In this section, we provide an estimate of the absolute proper motion and parallax of NGC 6752 using Gaia EDR3 data.

Starting from the absolute proper motion of NGC 6752 ($\mu_{\alpha,DR2}$, $\mu_{\delta,DR2}$) = (-3.17 ± 0.01, -4.01 ± 0.01) mas/yr, reported by Baumgardt et al. (2019) for Gaia Data Release 2, we estimated the median values of μ_α and μ_δ for the stars that fall inside a radius of 1 mas/yr centred in ($\mu_{\alpha,DR2}$, $\mu_{\delta,DR2}$). We obtained a value of ($\mu_{\alpha,0}$, $\mu_{\delta,0}$) =

TABLE 7.1: List of *HST* observations of NGC 6752 used in this work.

Filter	Instrument	Proposal ID	Exposures	Epoch
		Central field		
F275W	WFC3/UVIS	12311	12×369 s	2011/03/23-04/03
F336W	WFC3/UVIS	11729	2×500 s	2010/05/05
F435W	ACS/WFC	12254	5×10 + 10×380 s	2011/05/19-11/14
F606W	ACS/WFC	9453	1×1 + 1×4 + 1×40 s	2002/09/15
		10775	1×2 + 4×35 s	2006/05/24
F814W	ACS/WFC	9453	1×1 + 1×4 + 1×45 s	2002/09/15
		10775	1×2 + 4×40 s	2006/05/24
		Field F0		
F606W	ACS/WFC	15096	27×45 + 56×1270 s	2018/09/09-18
		15491	28×45 + 56×1270 s	2021/09/02-11
F814W	ACS/WFC	15096	10×45 + 19×1270 s	2018/09/07-09
		15096	5×45 + 10×1270 s	2019/08/01-15
		15491	12×143 + 24×1270 s	2021/09/02-12
		15491	2×45 + 4×1270 s	2022/02/14
		Field F1		
F110W	WFC3/IR	15096	28×143 + 56×1303 s	2018/09/09-18
		15491	28×143 + 56×1303 s	2021/09/02-11
F160W	WFC3/IR	15096	12×143 + 24×1303 s	2018/09/07-09
		15096	5×143 + 10×1303 s	2019/08/01-16
		15491	12×143 + 24×1303 s	2021/09/02-12
		Field F2		
F275W	WFC3/UVIS	15857	2×960 + 2×962 + 1×1082 s	2020/07/03-05
F336W	WFC3/UVIS	15857	1×469 + 1×471 + 2×617 s	2020/07/03-05
F438W	WFC3/UVIS	15857	1×204 + 1×206 + 1×258 s	2020/07/03-05
		12254	1×732 + 1×737 + 1×743 + 1×790 s	2011/08/30-09/07
F475W	ACS/WFC	12311	2×265 s	2011/03/23-04/03
F606W	ACS/WFC	15857	1×320 + 5×337 s	2020/07/03
F625W	WFC3/UVIS	12254	3×569 + 9×660 s	2011/08/30-09/07
F814W	ACS/WFC	15857	1×319 + 5×338 s	2020/07/03
		Field F3		
F435W	ACS/WFC	15857	2×870 + 1×925 + 1×933 + 1×1055 s	2020/07/03-05
F438W	WFC3/UVIS	12254	1×732 + 1×737 + 1×743 + 1×790 s	2011/11/14
F606W	ACS/WFC	12193	1×500 s	2011/05/21
F625W	WFC3/UVIS	12254	1×569 + 3×660 s	2011/11/14
F814W	ACS/WFC	12193	1×15 + 1×200 s	2011/05/21
		15857	1×344 + 1×346 + 1×492 + 1×529 s	2020/07/03-05

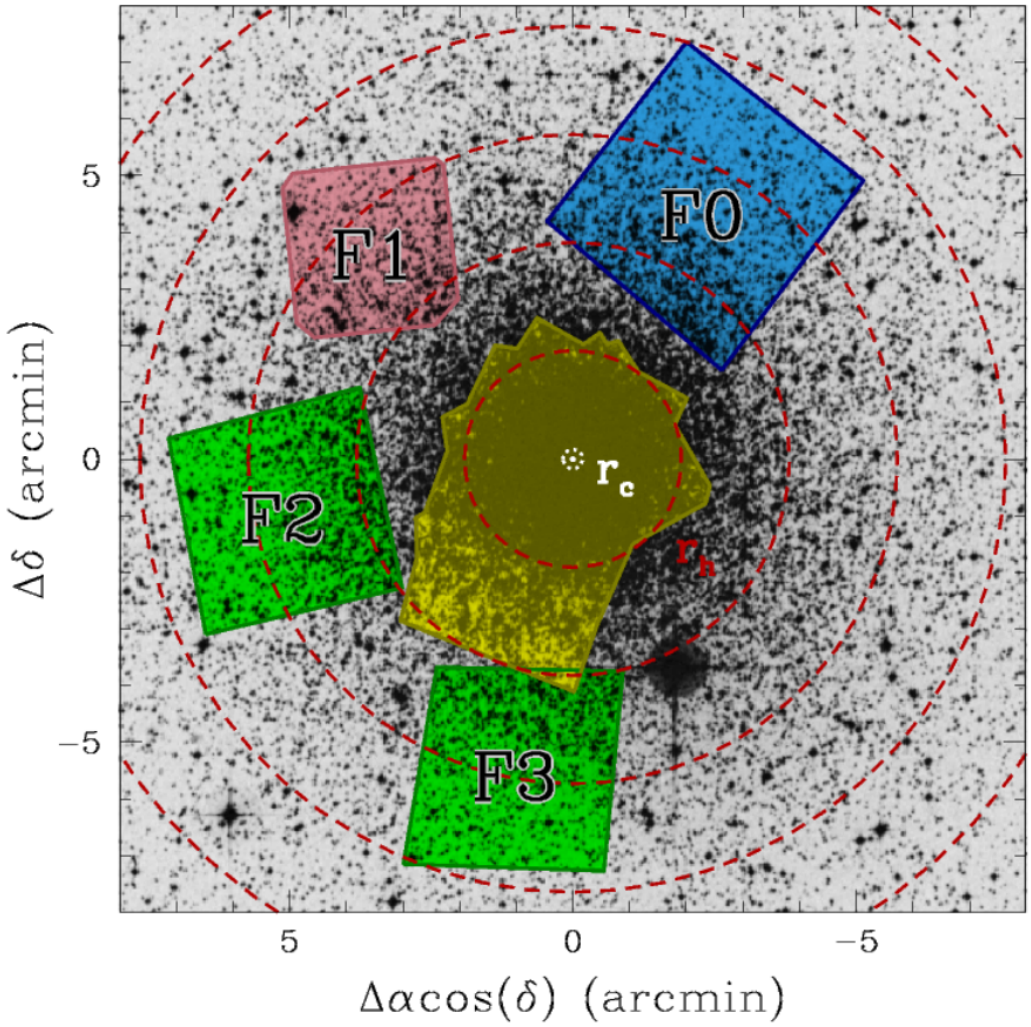

FIGURE 7.3: Outlines of the fields observed in HST programs GO-115096 + GO-15419 + GO-15857, superimposed on a DSS image of NGC 6752. The primary GO-115096 + GO-15419 ACS/WFC field F0 is in azure, while the parallel WFC3/IR field, F1, is shown in pink. The two GO-15857 fields are shown in green. We also show, in yellow, the central field presented in Libralato et al. (2022). Units are in arcmin measured from the cluster centre. The white dotted circle marks the core radius (r_c = 0.17 arcmin) from the centre. The red dashed circles mark the cluster's half-light radius (r_h = 1.91 arcmin), at nr_h, where n=1,..,7, from the centre.

(-3.1380 ± 0.0013,-4.0332 ± 0.0013). We removed from the sample all the stars outside 1 mas/yr from ($\mu_{\alpha,0}$,$\mu_{\delta,0}$), leaving a total of 37,122 sources. We adopt a cluster membership criterion based on the combination of position and proper motion, to remove the field stars. Panel (a) of Figure 8.4 shows the distribution of the angular distance $\Delta\sigma$ of each star from the nominal cluster center (RA = 287.717, δ = -59.984554; Goldsbury et al. 2010; Harris 1996), and the proper motion difference $\Delta\mu$ of each star from $\mu_{\alpha,0}$ and $\mu_{\delta,0}$. A clear clustering of sources can be seen on the left of the plot. We divided the stars with $\Delta\sigma$<1 in bins of 0.1 $\Delta\mu$ and evaluated for each bin the 68th percentile of the distribution, after a few iterations. The red line in panel (a) of Figure 8.4 represent the 3σ value of the bins. We removed all the sources at the right of the red line, leaving a total of 23,142 sources. Panel (b) of Figure 8.4 shows the Gaia G vs. Gaia $G_{\rm BP} - G_{\rm RP}$ color-magnitude diagram (CMD) of the stars that survived the proper motion selection. As we can see the typical features of a globular cluster in color-magnitude space, namely main sequence, red giant branch, and horizontal branch are clearly visible. However, we can see in the plot a small number of apparent outliers in magnitude and colour distribution. These stars could be foreground or background stars, or stars with anomalous properties or Gaia eDR3 measurements. Therefore, we further restrict cluster membership using the color-magnitude diagram. First, we divide the colour-magnitude diagram into 7 regions, as shown in panel (b) of Figure 8.4. We then divided into intervals of 0.1 Gaia G mag the stars belonging to the MS, SGB, RGB and RGB-tip regions and in intervals of 0.5 Gaia G mag the stars belonging to the AGB, BHB and EHB regions. For each interval, we determined the 32nd and the 68th percentiles of the Gaia $G_{\rm BP} - G_{\rm RP}$ distribution. The points corresponding to the 32nd and 68th percentile have been interpolated with a cubic spline and the two derived lines were used to verticalise the diagrams of each region. We divided the verticalised diagrams into bins of 0.5 Gaia G magnitude and calculated the σ-clipped median of each bin, where σ is defined as the 68th percentile of the distribution. Stars that do not pass the σ-clipping are represented with red dots in panel (b) of Figure 8.4. We removed these sources from the sample, leaving a total of 15,765 objects. As can be seen, the faint part of the main sequence (MS) is characterized by a great dispersion in colour, and the σ-clipped selection does not seem to follow the sequence profile. We then refined by hand the selection at the end of the MS (see Figure 8.4), leaving a total of 15,175 sources.

We divided the 15,058 stars belonging to the MS, SGB, RGB and RGB-tip regions in bins of 0.5 Gaia G magnitude. We then evaluated for each bin the 3σ-clipped median of the μ_α and μ_δ components. The error associated with each bin is defined as $\sigma/\sqrt{N-1}$, where N is the number of stars contained in the considered bin. The median values and their relative uncertainties are reported in Table 7.2, along with the weighted mean of the bin values and its associate's error.

The values reported in Table 7.2 are plotted in Figure 10.3, for the μ_α (panel (a)) and μ_δ (panel (b)) components. The points are color-coded and labelled as in panel (b) of Figure 8.4. The σ and 3σ errors are represented with continue and dotted error bars, respectively. The weighted mean of the bins is represented with a dashed horizontal black line, in both panels. The light and dark gray area, represent the σ and 3σ errors of the weighted mean, respectively. As can be seen, there is a good correlation between the bins. Of 18 bins, in the μ_α component, 9 correlate within 1σ and 4 correlate within 3σ with the weighted mean, while in the μ_δ component 14 correlate within 1σ, 4 correlate within 3σ and 1 do not correlate with the weighted mean. The bins belonging to the RGB-tip are characterised by the larger errors given the small numbers of stars they contain. Moreover, the last bin of the MS is characterised

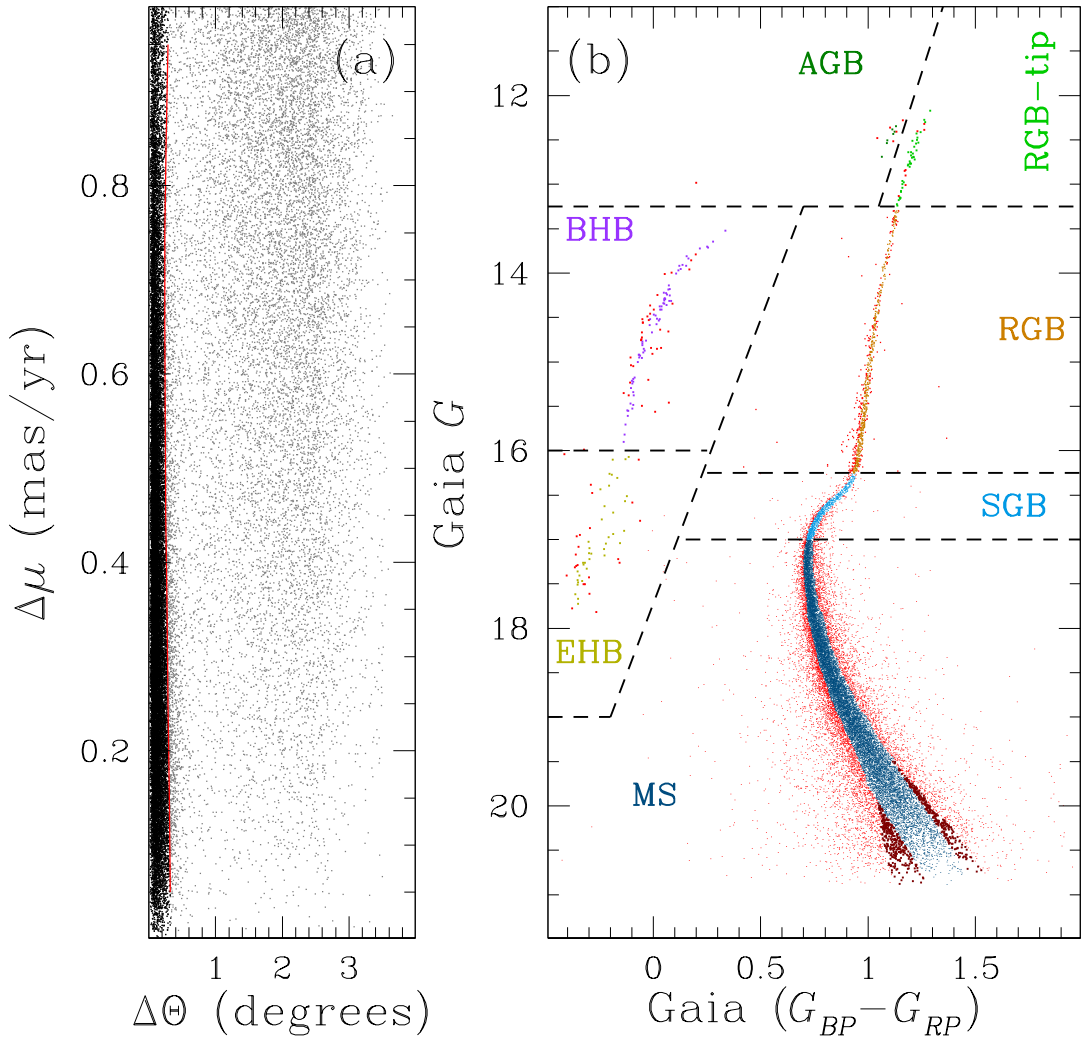

FIGURE 7.4: (a) Angular separation vs. proper motion difference of the stars from nominal. A clear clustering can be seen on the left of the plot. All stars at the left of the red line are considered cluster members (see text for details). (b) Gaia G vs. Gaia $G_{BP} - G_{RP}$ CMD of the stars that survived the proper motion selection. We used the CMD to remove the outliers, represented with red dots (see text for details). The selection in the faint part of the MS was refined by hand. The sources removed by hand are represented with dark red dots.

TABLE 7.2: Values for μ_α and μ_δ and their errors σ_{μ_α} and σ_{μ_δ} binned by G magnitude. f_{μ_α} and f_{μ_δ} are the fraction of stars that survive the 3σ-clipping. The weighted mean of the bins and its associated error are also reported.

Bin range	N stars	f_{μ_α}	μ_α (mas/yr)	σ_{μ_α}	f_{μ_δ}	μ_δ (mas/yr)	σ_{μ_δ}
12.0 - 12.5	7	1.0000	−3.4167	0.1524	1.0000	−4.0684	0.0745
12.5 - 13.0	23	1.0000	−3.1046	0.0400	1.0000	−4.0723	0.0486
13.0 - 13.5	36	1.0000	−3.1661	0.0367	0.9722	−4.0499	0.0404
13.5 - 14.0	29	1.0000	−3.0895	0.0510	1.0000	−4.0306	0.0363
14.0 - 14.5	43	1.0000	−3.1970	0.0296	1.0000	−4.0290	0.0377
14.5 - 15.0	65	1.0000	−3.1634	0.0269	1.0000	−4.0469	0.0304
15.0 - 15.5	78	1.0000	−3.2038	0.0300	1.0000	−4.0213	0.0316
15.5 - 16.0	131	1.0000	−3.1471	0.0206	1.0000	−4.0175	0.0227
16.0 - 16.5	241	1.0000	−3.1433	0.0168	0.9917	−3.9985	0.0153
16.5 - 17.0	693	0.9899	−3.1758	0.0091	0.9971	−4.0266	0.0089
17.0 - 17.5	1231	0.9976	−3.1623	0.0072	0.9992	−4.0194	0.0070
17.5 - 18.0	1747	0.9977	−3.1601	0.0059	0.9983	−4.0434	0.0060
18.0 - 18.5	2260	0.9987	−3.1618	0.0056	0.9973	−4.0316	0.0057
18.5 - 19.0	2489	0.9992	−3.1645	0.0060	0.9988	−4.0419	0.0057
19.0 - 19.5	2501	1.0000	−3.1785	0.0067	0.9996	−4.0512	0.0064
19.5 - 20.0	2203	1.0000	−3.1591	0.0086	1.0000	−4.0441	0.0082
20.0 - 20.5	1129	1.0000	−3.1433	0.0144	1.0000	−4.0420	0.0143
20.5 - 21.0	152	1.0000	−3.0960	0.0434	1.0000	−4.1821	0.0419
Result			−3.1639	0.0024		−4.0372	0.0024

by strong bias due to the limits of Gaia at faint magnitudes. We then repeat the weighted mean excluding the first and the last two bins. We obtain a value of (μ_α, μ_δ) = (-3.1648 ± 0.0025, -4.0365 ± 0.0024) mas/yr, very close to the value obtained using all the bins. This means that the first and last two bins do not particularly affect the result.

As a reference, Figure 10.10 shows the binned μ_α (panel (a)) and μ_δ (panel (b)) components, as a function of the Gaia G magnitude for the 117 stars belonging to the AGB, BHB and EHB regions defined in Figure 8.4. As in Figure 10.3 the continue and dotted error bars represent the σ and 3σ errors of the bins. The dashed black lines represent the proper motion weighted mean obtained using the MS+SGB+RGB+RGB-tip sample and reported in Table 7.2. As we can see, the points are more widespread than in Figure 10.3 and the error bars are much larger. Most of the points appear to lie below the black dashed line.

The 14,984 stars from the MS, SGB, RGB and RGB-tip regions that survived the proper motions 3σ-clipping, were used to estimate the parallax of NGC 6752. Figure 10.4 shows the parallax of the stars in the sample as a function of the Gaia G magnitude. As we can see, most of the sources are clustered around a parallax value $\varpi \sim 0.25$. We divide the sample into bins of 0.5 Gaia G magnitude and estimated for each bin the 3σ-clipped median of the parallax. As above, we considered as σ the 68th percentile of the distribution. The error associated at each bin is defined as $\sigma/\sqrt{N-1}$, where N is the number of stars contained in the considered bin. Following Soltis, Casertano, and Riess (2021) we add a parallax uncertainty floor of 4 μas. The red line in Figure 10.4 separates the stars that survived the σ-clipping (colour-coded as in n panel (b) of Figure 8.4) from the outliers (represented in grey). The values of the bins and their associated errors are reported in Table 7.3. The weighted

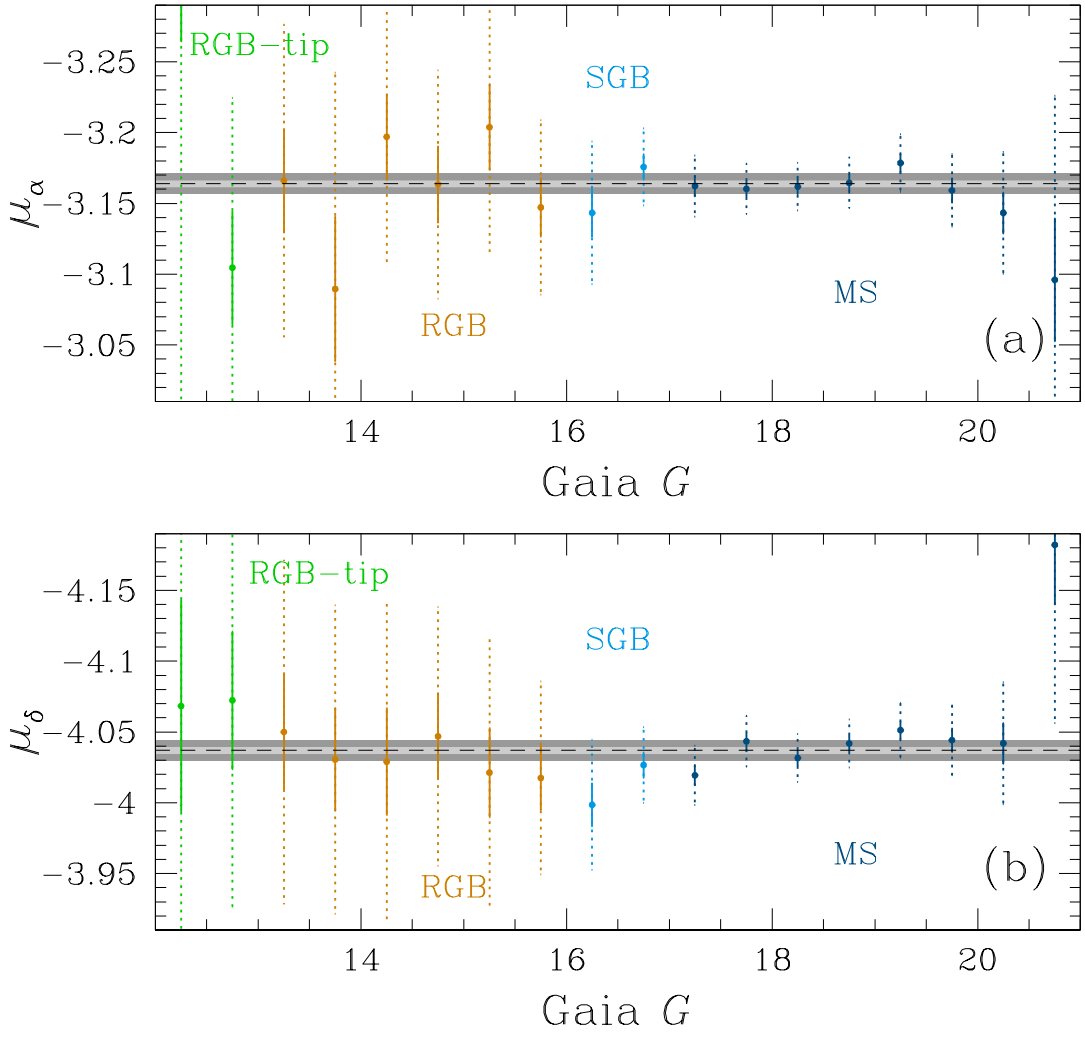

FIGURE 7.5: (a) μ_α binned as a function of magnitude. The continue and dashed error bars represent the σ and 3σ errors, respectively. The weighted median value of the bins is represented by a dashed line. The light and dark gray area represent the σ and 3σ errors of the weighted mean, respectively. The bins are color-coded and labelled as in Figure 8.4. (b) same of (a) but for the δ component.

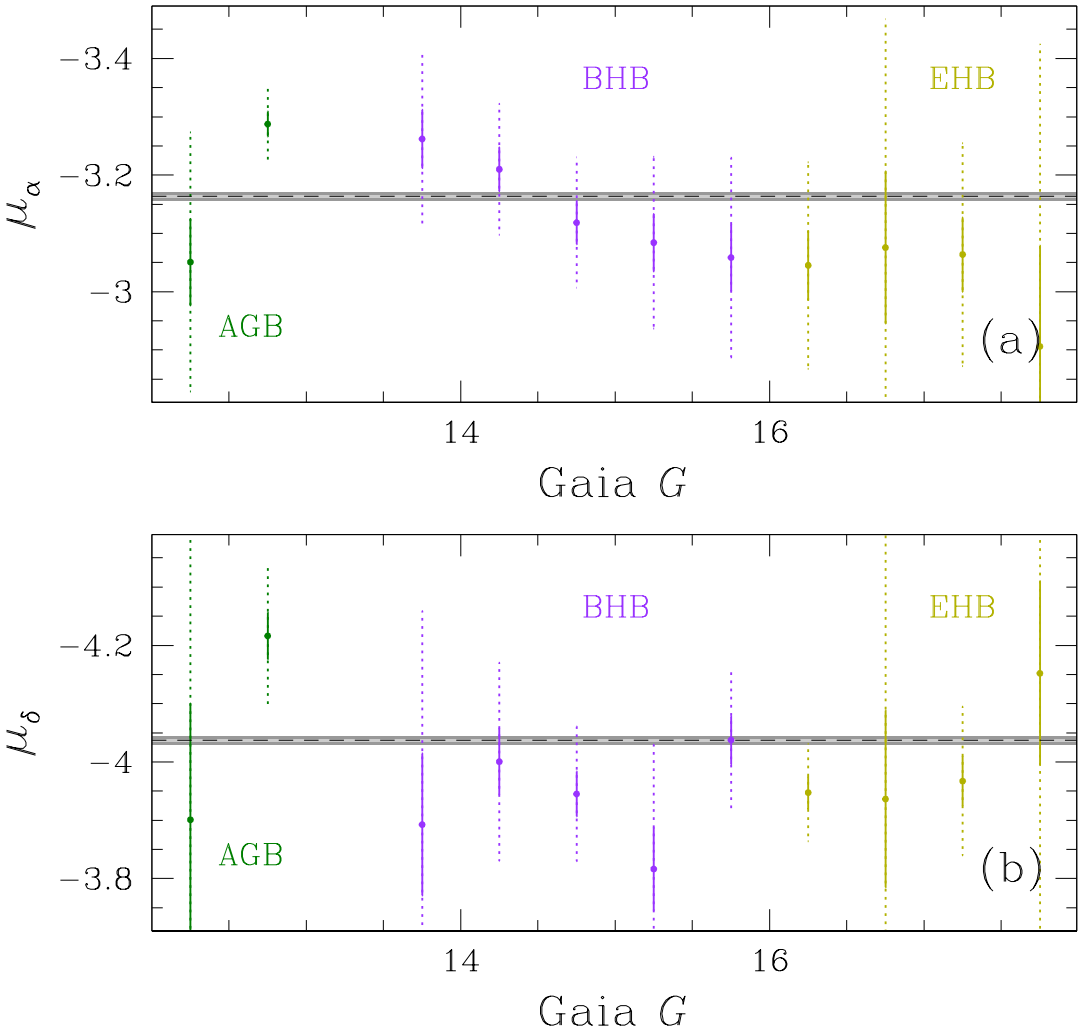

FIGURE 7.6: As in Figure 10.3 but for the AGB, BHB and EHB regions. The black dashed lines represent the value estimated using the stars from the MS+SGB+RGB+RGB-tip regions and reported in Table 7.2.

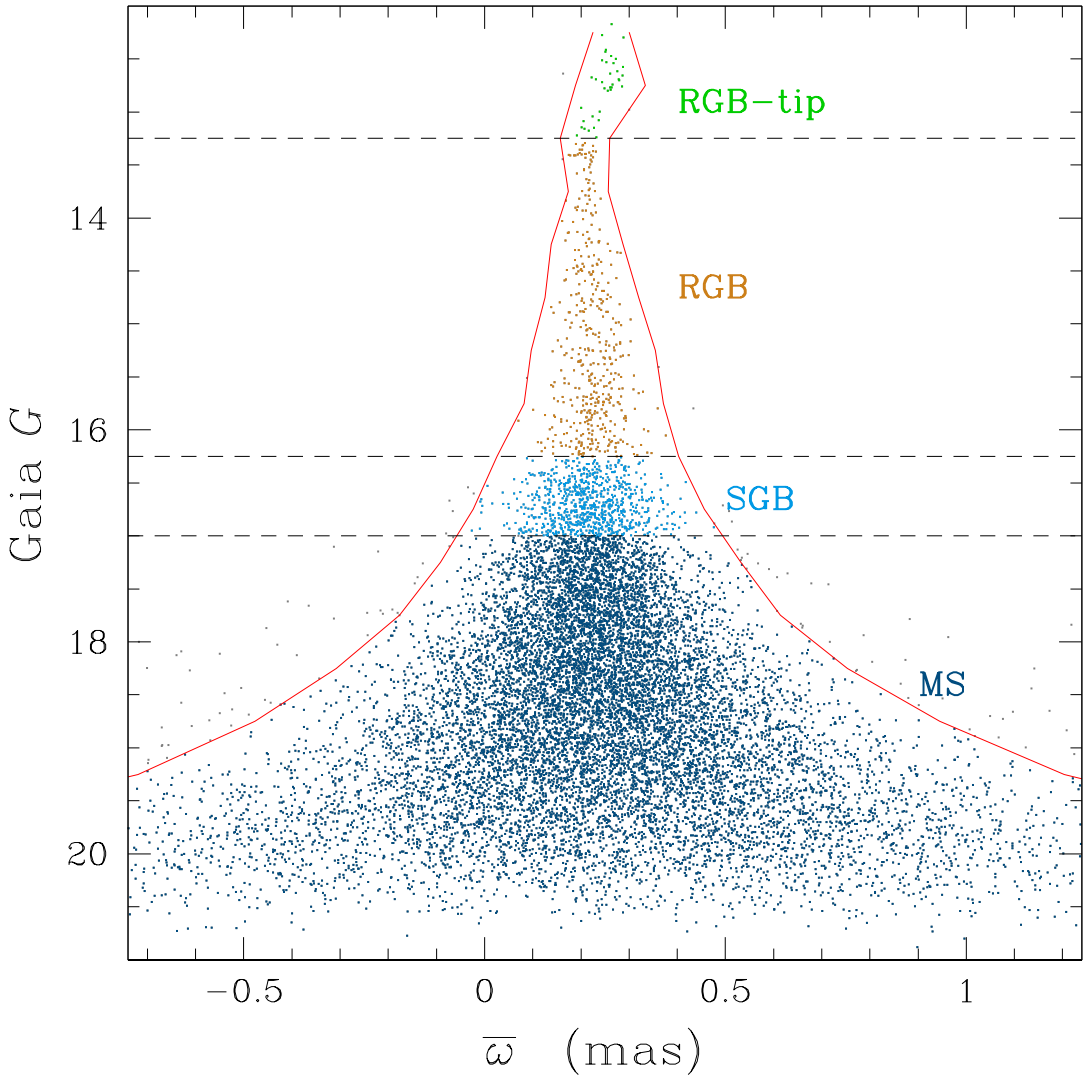

FIGURE 7.7: Parallax of the stars in the sample as a function of the Gaia G magnitude. The red lines separate the stars that survived the σ-clipping, from the outliers (grey dots). The stars are color-coded and labelled as in Figure 8.4.

mean of the bins and its associated error are also reported in Table 7.3. As can be seen, the red lines start to be discontinuous above a Gaia G magnitude $\sim$ 16.5, indicating that stars belonging to the RGB and RGB-tip regions are not suitable for a precise estimate of the NGC 6752 nominal parallax.

The values reported in Table 7.3 are plotted in panel (a) of Figure 10.5. As a reference, panel (b) of Figure 10.5 shows the binned parallax as a function of the Gaia G magnitude for the stars belonging to the AGB, BHB and EHB regions. As for Figure 10.3 and 10.10 the points are color-coded and labelled as in Figure 8.4. The continue and dotted error bars represent the σ and 3σ errors of the bins, in both panels. The dashed black lines represent the parallax weighted mean obtained using the MS+SGB+RGB+RGB-tip sample and reported in Table 7.3. The light and dark gray area, represent the σ and 3σ errors of the weighted mean, respectively.

We can see from panel (a) that all the points appear to be in a good correlation. Of 18 bins, 7 correlate within 1σ, 8 correlate within 3σ and 3 (the two belonging to the RGB-tip and the first belonging to the RGB) do not correlate with the weighted mean.

TABLE 7.3: Values for parallax binned by G magnitude. f is the fraction of stars that survive the 3σ-clipping. σ is the parallax statistical error.

Bin range	N stars	f	ϖ (mas)	σ
12.0 - 12.5	7	1.0000	0.2751	0.0047
12.5 - 13.0	23	1.0000	0.2779	0.0051
13.0 - 13.5	35	1.0000	0.2477	0.0029
13.5 - 14.0	29	1.0000	0.2550	0.0026
14.0 - 14.5	43	1.0000	0.2531	0.0039
14.5 - 15.0	64	1.0000	0.2634	0.0041
15.0 - 15.5	78	0.9872	0.2664	0.0049
15.5 - 16.0	130	0.9923	0.2683	0.0043
16.0 - 16.5	239	0.9958	0.2472	0.0041
16.5 - 17.0	678	0.9926	0.2476	0.0031
17.0 - 17.5	1221	0.9894	0.2505	0.0030
17.5 - 18.0	1731	0.9942	0.2468	0.0032
18.0 - 18.5	2243	0.9960	0.2471	0.0038
18.5 - 19.0	2480	0.9927	0.2578	0.0048
19.0 - 19.5	2499	0.9960	0.2606	0.0064
19.5 - 20.0	2203	0.9950	0.2564	0.0101
20.0 - 20.5	1129	0.9973	0.2805	0.0197
20.5 - 21.0	152	0.9934	0.3042	0.0891
Result			0.2220	0.0327 ± 0.0010

The last two bins of the MS are characterised by large errors due to the difficulty of Gaia at the faint regimes. We then exclude the first and the last two bins from the sample and evaluate again the parallax weighted mean of the bins. We obtain a parallax ϖ=0.2189 ± 0.0010, very similar to the value obtained above. We conclude that the last and first two bins do not strongly influence the weighted mean value.

Panel (b) of Figure 10.5 shows the binned parallax as a function of the Gaia G magnitude for the stars belonging to the AGB, BHB and EHB regions. While the stars belonging to the AGB and BHB stars seem to correlate with the mean parallax value of NGC 6752 reported in Table 7.3, EHB stars appear to be far below the black dotted line and show a trend with the Gaia G magnitude.

As pointed out in Lindegren et al. (2021), parallaxes provided by Gaia EDR3 can be subject to systematic errors due to imperfections in the instrument and data processing methods. We applied the parallax correction described in Lindegren et al. (2021) to our sample, and evaluated the binned parallax as a function of the Gaia G magnitude as in Figure 10.5, using the corrected values. The results are shown in Figure 10.6. As can be seen, the external bins (the bins from the RGB-tip region, the three brighter bins from the RGB region and five lower bins from the MS region) appear to better correlate after the Lindegren et al. (2021) correction. However, the eight central bins (the three lower bins from the RGB region, the bins from the SGB region and the three brighter bins from the MS region) appear more widespread than in Figure 10.5. The stars belonging to these bins are characterised by small errors in proper motions (as can be seen in Figure 10.3) and their parallax errors show some linearity (Figure 10.5). For this reason, these stars are best suited for a precise estimate of the parallax of NGC 6752 and we decided to not use the Lindegren et al. (2021) correction in this work. We adopted the difference between the weighted mean parallax estimated with the Lindegren et al. (2021) correction, $\varpi_{LIN} = 0.2547$,

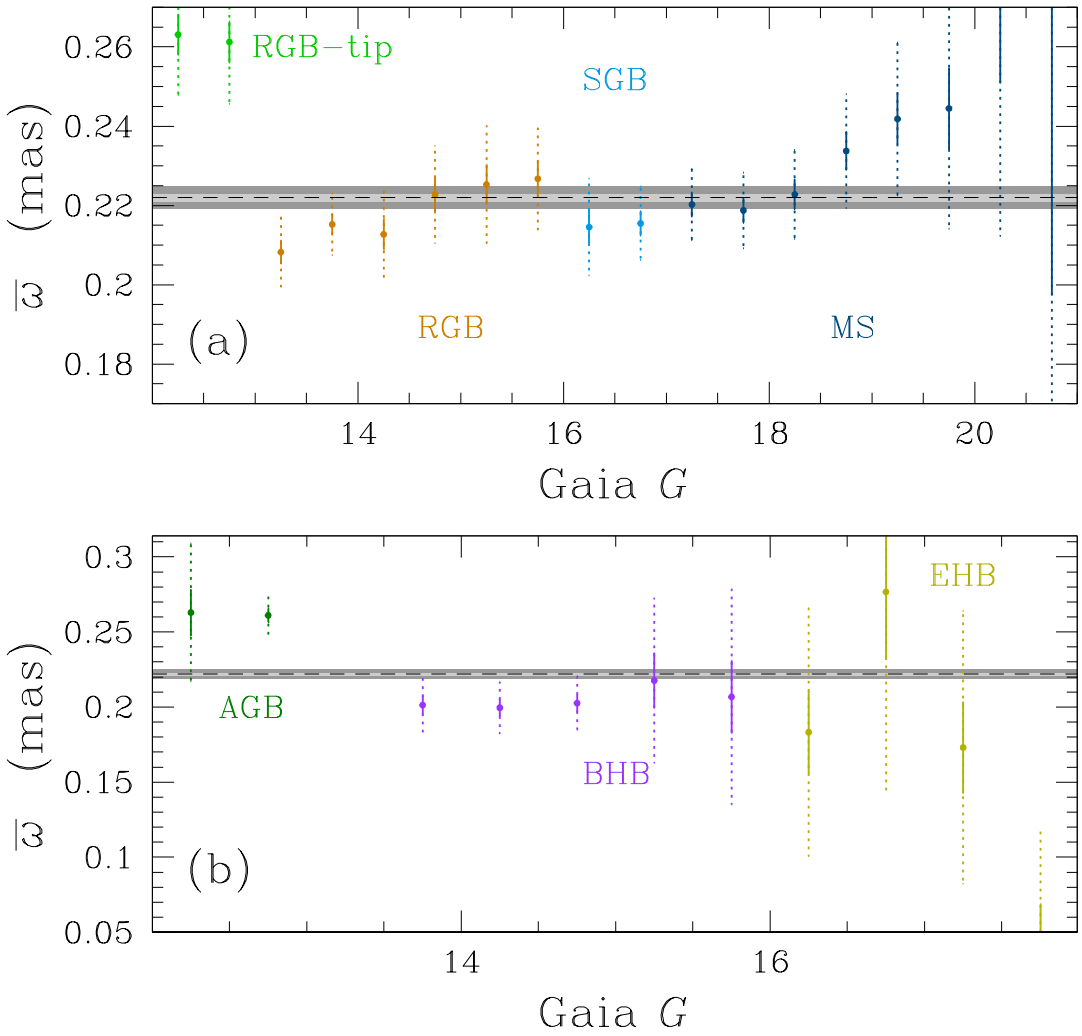

FIGURE 7.8: (a) Parallax binned as a function of magnitude for stars in the MS, SGB, RGB and RGB-tip regions defined in Figure 8.4. The continue and dashed error bars represent the σ and 3σ errors, respectively. The weighted median value of the bins is represented by a dashed line. The light and dark gray area represent the σ and 3σ errors of the weighted mean, respectively. The bins are colour-coded and labelled as in Figure 8.4. (b) same of (a) but for the stars belonging to the AGB, BHB and EHB regions.

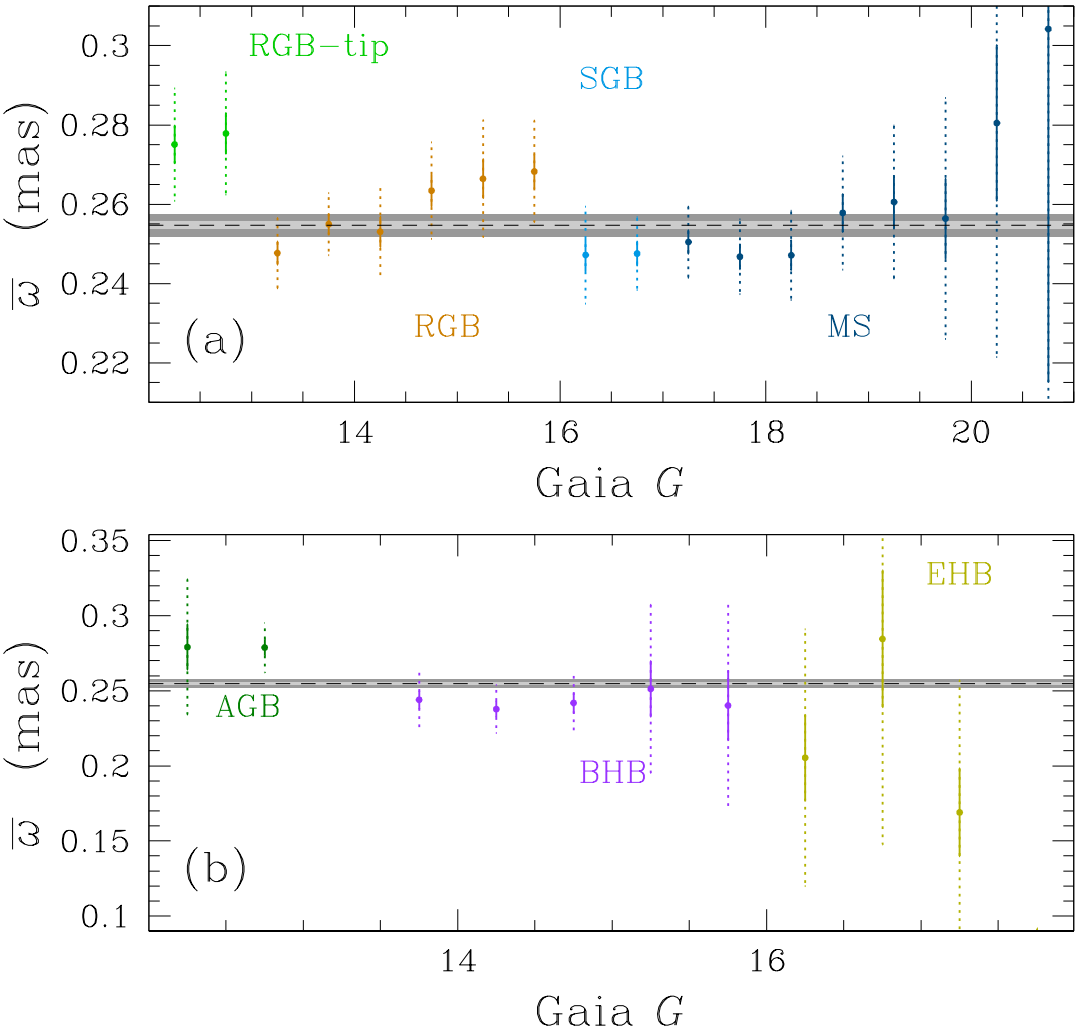

FIGURE 7.9: Same of Figure 10.5 but with the Lindegren et al. (2021) correction.

and without the Lindegren et al. (2021) correction, $\varpi = 0.2220$, as our parallax error, $\varpi_{LIN} - \varpi = 0.0327$.

To obtain a robust estimate of the absolute proper motion and parallax of NGC 6752, we took only the stars belonging to the SGB and MS regions with a Gaia G magnitude $16.5 < G < 19.5$. As can be seen from Figure 10.3 and 10.5 the main source of error in the evaluation of the proper motion and parallax weighted mean are due to stars belonging to the RGB-tip, RGB regions and the fainter part of the MS region. These bins have large errors and they hardly correlate with the other bins. Moreover, Figure 10.4 shows that the distribution of the parallax as a function of the Gaia G magnitude stars to become discontinue above $G \sim 16.5$. This implies that stars belonging to the RGB-tip and RGB regions are not suitable for a precise parallax estimate. We then select all the stars that passed all the previously done selections and with a Gaia G magnitude $16.5 < G < 19.5$, for a total of 10,736 stars, and we performed the same procedure used in Figure 10.3 and Figure 10.5. The values of the bins are reported in Table 7.4.

The weighted mean of the proper motion component gives $(\mu_\alpha, \mu_\delta) = (-3.1663 \pm 0.0026, -4.0365 \pm 0.0026)$ mas/yr. We adopt this value as the nominal absolute proper motion of NGC 6752.
We adopt the weighted mean of the parallaxes and its associated error $(\varpi) = (0.2225 \pm 0.0281)$

TABLE 7.4: Values for μ_α, μ_δ and parallax binned by G magnitude magnitude $16.5 < G < 19.5$.

Bin range	N stars	f_{μ_α}	μ_α (mas/yr)	σ_{μ_α}	f_{μ_δ}
16.5 - 17.0	670	1.0000	-3.1758	0.0089	1.0000
17.0 - 17.5	1200	1.0000	-3.1634	0.0073	1.0000
17.5 - 18.0	1707	1.0000	-3.1601	0.0059	1.0000
18.0 - 18.5	2223	0.9996	-3.1620	0.0056	1.0000
18.5 - 19.0	2438	1.0000	-3.1640	0.0060	1.0000
19.0 - 19.5	2468	1.0000	-3.1786	0.0067	1.0000
Result			-3.1663	0.0026	
μ_δ (mas/yr)	σ_{μ_δ}	f_ϖ	ϖ (mas)	σ_ϖ	
-4.0233	0.0089	0.9970	0.2165	0.0031	
-4.0178	0.0070	0.9983	0.2206	0.0029	
-4.0453	0.0059	0.9994	0.2191	0.0031	
-4.0305	0.0056	0.9996	0.2231	0.0037	
-4.0395	0.0057	0.9996	0.2360	0.0047	
-4.0514	0.0064	0.9996	0.2438	0.0064	
-4.0365	0.0026		0.2225	0.0281 ± 0.0015	

TABLE 7.5: Final estimates of the absolute proper motion, $\mu_{\alpha,NGC\,6752}$, $\mu_{\delta,NGC\,6752}$, parallax $\varpi_{NGC\,6752}$ and LOS velocity of NGC 6752 along with the cluster position (RA,δ) from Goldsbury et al. (2010).

Parameter	Value	Uncertainty
RA (deg)	287.717^a	2.7×10^{-5} [a]
δ (deg)	-59.984554^a	2.7×10^{-5} [a]
$\mu_{\alpha,NGC\,6752}$	-3.1663^b	0.0026^b
$\mu_{\delta,NGC\,6752}$	-4.0365^b	0.0026^b
$\varpi_{NGC\,6752}$	0.2225^b	0.0015^b
V_{LOS}	-26.0482	0.1383^b

[a] Goldsbury et al. (2010)
[b] This work

mas, as the absolute Gaia eDR3 parallax for NGC 6752, corresponding to a distance of d$\sim$4.5$\pm$0.03 kpc and a distance modulus of μ = 13.2633 mag.

Table 7.5 reports our final estimates of the absolute proper motion, $\mu_{\alpha,NGC\,6752}$, $\mu_{\delta,NGC\,6752}$ and parallax $\varpi_{NGC\,6752}$ of NGC 6752 along with the cluster position (RA,δ) from Goldsbury et al. (2010). We highlight here that, in this work, we did not provide an estimate of the position of the cluster due to Gaia's difficulty in operating in crowded environments. NGC 6752 is a core-collapsed globular cluster, and the relatively crowding of the central region of NGC 6752, affects the quality of the Gaia measurements. For this reason, we decide to take the cluster position given by Goldsbury et al. (2010) as our best estimate of the position of NGC 6752.

As mentioned above, Baumgardt et al. (2019) obtained an absolute proper motion of NGC 6752 of ($\mu_{\alpha,DR2}$, $\mu_{\delta,DR2}$) = (-3.17 ± 0.01, -4.01 ± 0.01) mas/yr, using data from Gaia DR2. The estimate obtained in this work, using Gaia EDR3 ($\mu_{\alpha,EDR3}$, $\mu_{\delta,EDR3}$) = (-3.1663 ± 0.0026, -4.0365 ± 0.0026) mas/yr, is in agreement within 1σ. Souza et al. (2020) reported a distance for NGC 6752 of 4.11 ± 0.08 kpc using data from Hubble Space Telescope (HST). Our estimate of d$\sim$4.5$\pm$0.03 kpc is in agreement with 5σ.

TABLE 7.6: Values for the LOS velocity binned by G magnitude. f is the fraction of stars that survive the 3σ-clipping. σ is the LOS velocity statistical error.

Bin range	N stars	f	V_{LOS} (km/s)	σ (km/s)
10.0 - 10.5	8	1.0000	-25.1700	0.9714
10.5 - 11.0	7	1.0000	-25.9600	1.3227
11.0 - 11.5	12	1.0000	-22.3100	0.8442
11.5 - 12.0	18	1.0000	-24.5800	1.2175
12.0 - 12.5	21	1.0000	-27.2100	1.0979
12.5 - 13.0	29	1.0000	-26.4600	0.9563
13.0 - 13.5	64	0.9688	-26.6600	0.5864
13.5 - 14.0	46	0.9783	-26.4700	0.5744
14.0 - 14.5	56	0.9821	-27.0400	0.5634
14.5 - 15.0	68	1.0000	-26.1000	0.5632
15.0 - 15.5	48	1.0000	-26.5900	0.7585
15.5 - 16.0	102	0.9902	-25.6300	0.3990
16.0 - 16.5	213	1.0000	-25.5500	0.2685
16.5 - 17.0	367	0.9973	-26.1000	0.2486
17.0 - 17.5	84	1.0000	-26.9300	0.4895
Result			-25.9894	0.1290

7.4 Line of sight velocity

In what follows we provide an estimate of the absolute LOS velocity of NGC 6752.

We make use of the membership probability provided by Baumgardt and Hilker (2018) to remove the field stars from the catalogue, cutting all the stars with a membership probability equal to zero. Panel (a) of Figure 7.10 shows the Gaia G vs. Gaia $G_{BP} - G_{RP}$ CMD of the 1,592 stars that survived the membership probability selection. We further restrict cluster membership using the color-magnitude diagram, in close analogy of what was done in the previous section (see Figure 8.4). Briefly, we divide the colour-magnitude diagram into 6 regions, as shown in panel (a) of Figure 7.10. We then divided in intervals of 0.1 Gaia G mag the stars belonging to the SGB,RGB and RGB-tip regions and in intervals of 0.5 Gaia G mag the stars belonging to the AGB,BHB and EHB regions. For each interval, we determined the 32nd and the 68th percentiles of the Gaia $G_{BP} - G_{RP}$ distribution. The points corresponding to the 32nd and 68th percentile have been interpolated with a cubic spline and the two derived lines were used to verticalise the diagrams of each region. We divided the verticalised diagrams into bins of 0.5 Gaia G magnitude and calculated the 2σ-clipped median of each bin. Stars that do not pass the σ-clipping are represented with red dots in panel (a) of Figure 7.10. We removed these sources from the sample, leaving a total of 1,308 objects.

We divided the 1,308 stars belonging to the SGB, RGB and RGB-tip regions in bins of 0.5 Gaia G magnitude. We then evaluated for each bin the 3σ-clipped median of the LOS velocity component. The bin values and their relative uncertainties are reported in Table 7.6, along with the weighted mean of the bin values and its associate's error.

The values reported in Table 7.6 are plotted in panel (b) of Figure 7.10. The points are colour-coded and labelled as in panel (a) of Figure 7.10. The σ and 3σ errors of the bins are represented with continue and dotted error bars, respectively. The weighted

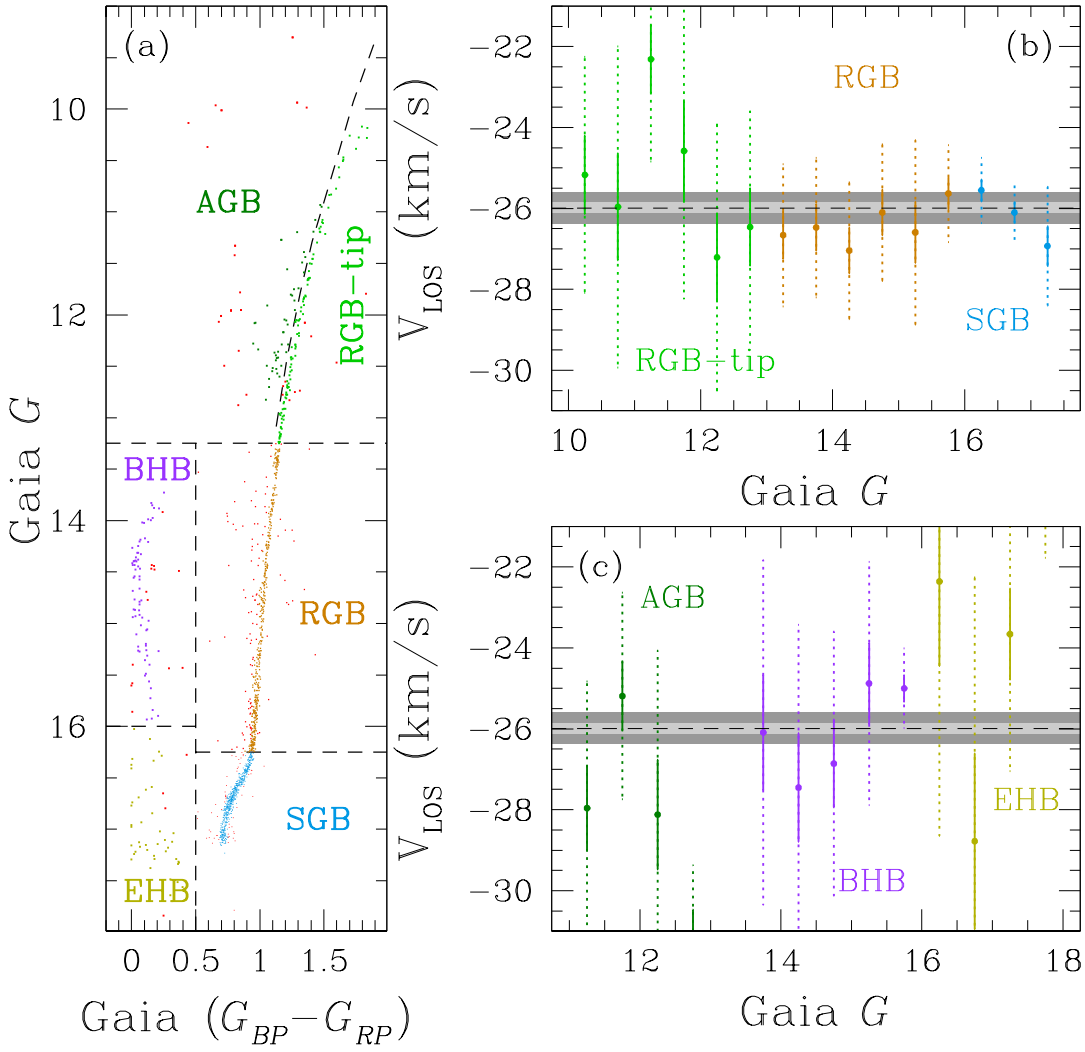

FIGURE 7.10: LOS velocity of NGC 6752. (a) Gaia G vs. Gaia $G_{BP} - G_{RP}$ CMD of the stars that survived the membership probability selection. We define 6 different regions, represented with different colours and labels. We used the positions of the stars in the CMD to remove the outliers, represented with red dots (see text for details). (b) LOS velocity binned as a function of magnitude for the stars belonging to the SGB, RGB and RGB-tip regions that survived the selections. The continue and dashed error bars represent the σ and 3σ errors, respectively. The weighted mean value of the bins is represented by a dashed line. The light and dark gray area represent the σ and 3σ errors of the weighted mean, respectively. The bins are colour coded and labelled as in panel (a). (c) LOS velocity binned as a function of magnitude for the stars belonging to the AGB, EHB and BHB regions that survived the selections. The black dashed line and the light and dark gray area are the same as panel (b).

mean of the bins is represented with a dashed horizontal black line. The light and dark gray area, represent the σ and 3σ errors of the weighted mean, respectively.

As can be seen, there is a good correlation between the bins and the weighted mean. Of 15 bins, 10 correlate within 1σ, 4 correlate within 3σ and 1 do not correlate with the weighted mean. The bins belonging to the RGB-tip contain a small number of stars ($N < 30$). As a consequence, they are characterised by large errors and their contribution to the estimate of the weighted mean is small. We then cut all the bins with less than 30 sources and estimated the weighted mean of the remaining bins. We obtain a value of $V_{LOS} = -26.0482 \pm 0.1383$, which is in agreement with the value obtained using all bins and reported in Table 7.6. We adopted this value as the absolute LOS velocity of NGC 6752. We reported this value in Table 7.5.

The absolute LOV velocity estimated in this work is in excellent agreement with the value reported in the literature. Baumgardt and Hilker (2018), using a large set of N-body simulations obtained a value of $V_{LOS} = -26.2 \pm 0.1$, while Lardo et al. (2015) used a sample of radial velocity measurements extracted from the *Gaia-ESO* spectroscopic survey and obtain a value of $V_{LOS} = -26.9 \pm 0.2$. Finally, Lane et al. (2010), using *AAOmega* observations obtain a value of $V_{LOS} = -26.1 \pm 0.2$.

For comparison, panel (c) of Figure 7.10 shows the binned LOS velocity for the stars belonging to the AGB, BHB and EHB regions. The weighted mean and its σ and 3σ errors are the same as panel (b) of Figure 7.10 and reported in Table 7.6. As can be seen, the bins appear more widespread with respect to panel (b). Of 13 bins, only 5 correlated within 1σ, 6 correlated within 3σ and 2 did not correlate with the weighted mean.

7.5 Membership probability

We derived the membership probability (MP), following a method based on PMs and parallax described by Griggio and Bedin (2022) which is an evolution of the method described in Balaguer-Núnez, Tian, and Zhao (1998), Bellini et al. (2009), Nardiello et al. (2018), and Scalco et al. (2021).

Panel (a) of Figure 7.11 shows the MP of the stars in our catalogue as a function of the Gaia G magnitude. We impose a cut to separate likely cluster members from field stars. We binned all the stars with MP$>$ 95% in intervals of Gaia G magnitude, in such a way that each bin contains the $\sim$ 10% of the stars in the sample. We evaluated for each bin the 68th percentile of the distribution. The red line in panel (a) of Figure 7.11 connects the obtained values. All the stars at the left of the red line are considered as probable cluster members, while all the stars at the right of the red line are considered as field stars. Panel (b) shows the Gaia G vs. Gaia $G_{\rm BP} - G_{\rm RP}$ CMD of the sources. The dashed grey lines divide panels (a) and (b) into three regions. The distribution on the sky of the sources in the three regions defined in panels (a) and (b) are shown in panels (c)-(d)-(e). In each panel, cluster members and field stars are represented with black and grey dots. The 10 most distant sources from the cluster centre that survived the MP selection are shown as red-filled dots in all the panels. The astro-photometric parameters of the 10 sources, along with their distance from the cluster centre are reported in Table 7.7.

We evaluated the proper motion and parallax weighted mean of the stars with MP$>$ 99% and Gaia G magnitude $16.5 < G < 19.5$ as in the previous section. We obtain a value of (μ_α,μ_δ) = (-3.1697 ± 0.0020,-4.0355 ± 0.0020) mas/yr and ϖ = (0.2251 ± 0.0015) mas, very similar to the value obtained in the previous section.

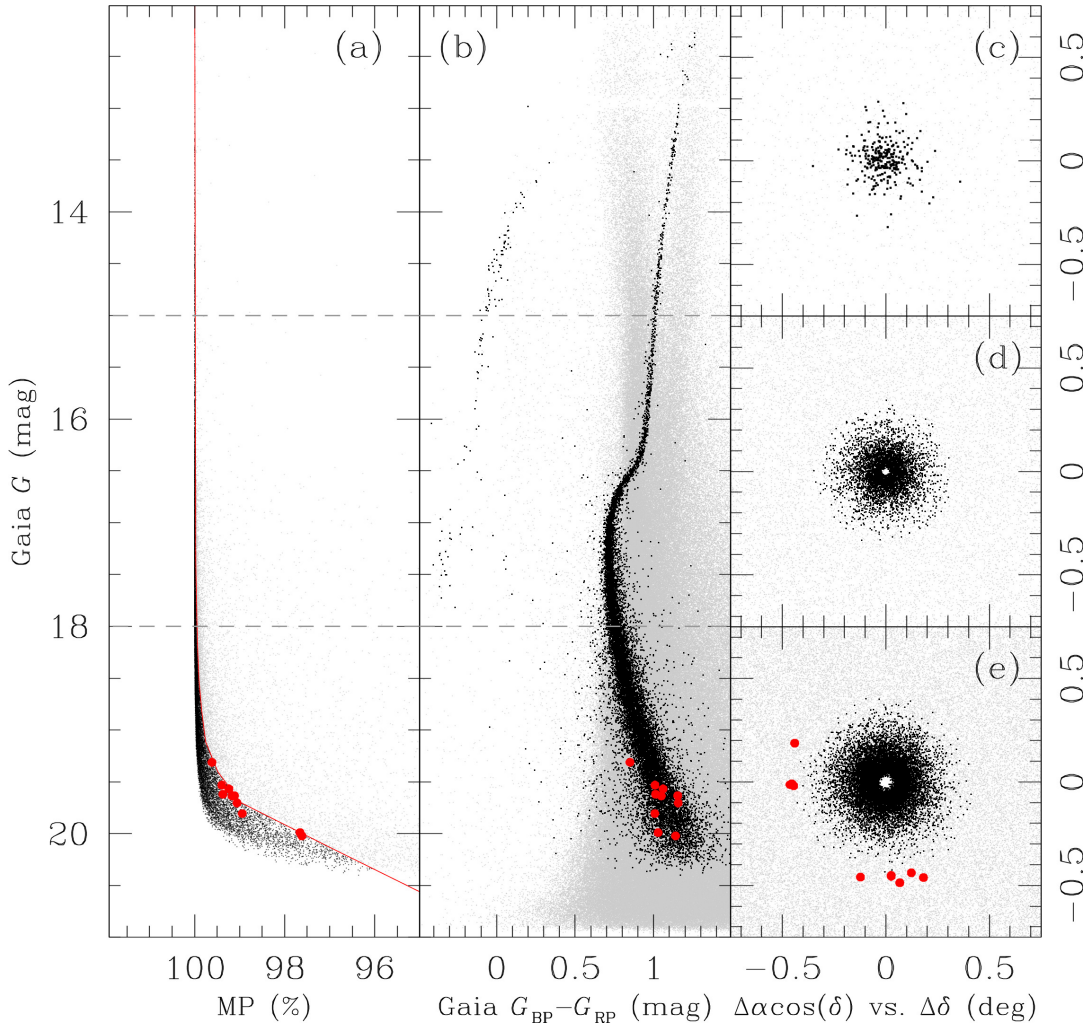

FIGURE 7.11: Example of cluster member selection based on MP. (a) MP as a function of the Gaia G magnitude. The red line separates likely cluster members from field stars. (b) Gaia G vs. Gaia $G_{BP} - G_{RP}$ CMD. The dashed grey lines divide panels (a) and (b) into three regions. (c)-(d)-(e) Distribution on the sky of the sources in the three regions defined in panels (a) and (b). In each panel, cluster members and field stars are represented with black and grey dots. The 10 most distant sources from the cluster centre that survived the MP selection are represented with red-filled circles.

TABLE 7.7: Values of $\Delta\alpha cos\delta$, $\Delta\delta$, Gaia G, G_{BP} and G_{RP} magnitude, MP, and PM in the radial and tangential direction for the 10 most distant sources from the centre of the cluster that survived the MP selection.

N	DR (arcmin)	$\Delta\alpha cos\delta$ (deg)	$\Delta\delta$ (deg)	G	G_{BP}	G_{RP}	MP
1	29.7704	0.1818	-0.4617	19.7041	20.2225	19.0659	99.0585
2	29.5033	0.0674	-0.4871	19.5682	20.0139	18.9532	99.2366
3	28.7027	-0.4400	0.1878	20.0224	20.5442	19.4039	97.6194
4	28.5514	-0.1226	-0.4598	19.6337	20.1680	19.0145	99.1163
5	27.7551	-0.4624	-0.0128	19.6365	20.0794	19.0302	99.1687
6	27.3746	0.0257	-0.4555	19.5320	19.9865	18.9776	99.3966
7	27.3370	0.1236	-0.4385	19.6198	20.1238	19.1104	99.3710
8	27.2611	-0.4543	-0.0084	19.3116	19.6237	18.7737	99.6139
9	27.1086	0.0261	-0.4511	19.9908	20.3118	19.2825	97.6577
10	26.7214	-0.4450	-0.0187	19.8063	20.2405	19.2321	98.9418

7.6 Structural parameters of NGC 6752

In the following, we analyse the structural parameters ellipticity and position angle of NGC 6752. We define the ellipticity $e = b/a$ where a and b are respectively the semimajor and semi-minor axes of the interpolated ellipses. We, first of all, estimated the 2D binned kernel density of all the stars belonging to the MS+SGB+RGB+RGB-tip sequence, that survived the MP selection in panel (a) of Figure 7.11 and with a Gaia G magnitude $16.5 < G < 19.5$. The 2D binned kernel density is shown in panel (a) of Figure 8.14 where the levels of red are indicative of the density of the stars. A visual inspection of panel (a) suggests that NGC 6752 is not subjected to a strong elongation. Starting from a radial distance of $R = 5'$, we calculated 11 isodensity contour lines and used the algorithm by Halir and Flusser () to fit each contour line with an ellipse by means of least-squares. The ellipticity and position angle profiles are presented in panels (b) and (c) of Figure 8.14, respectively. The uncertainty associated with each measurement is determined by means of bootstrapping 1000 times with replacement. The black dashed line in panel (b) of figure 8.14 represents the weighted mean of the bins for the ellipticity, $e = 0.0254 \pm 0.0010$. Similarly, the black dashed line in panel (c) of figure 8.14 represents the weighted mean of the bins for the position angle, $PA = (329.34 \pm 1.16)^{\circ}$.

7.7 Rotation of NGC 6752

In the following, we investigate the rotation in the plane of the sky and along the LOS for NGC 6752.

7.7.1 Rotation on the plane of the sky

We studied the rotation of NGC 6752 in the plane of the sky by following the method presented in Scalco et al. (2023). In brief, we retrieved all sources from the *Gaia* DR3 archive that are located within a given radius from the nominal cluster centre. We then defined a sample of stars with reliable photometry and astrometry by following the recommendations of Fabricius et al. (2021), Lindegren et al. (2021) and Riello et al. (2021), but with tighter selections on some parameters. Finally, we defined a sample of probable cluster members by following a procedure based on stellar

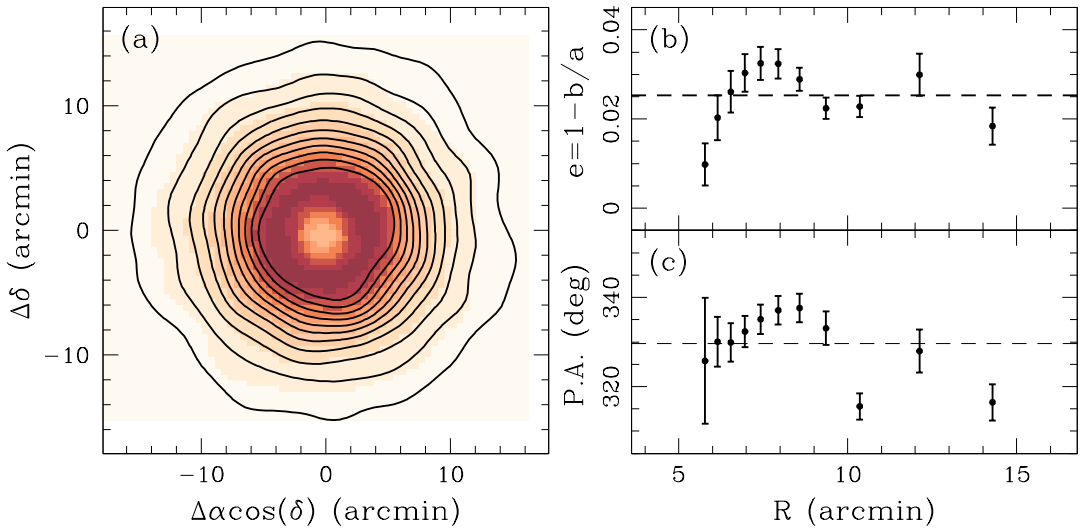

FIGURE 7.12: Estimate of the structural parameters of NGC 6752. (a) 2D binned kernel density estimate of the stars that survived the membership probability selection of Figure 7.11 and the 11 isodensity contour lines. (b) Ellipticity, e, as a function of the radial distance from the cluster centre, R. The black dashed line represents the weighted mean of the bins $e = 0.0254 \pm 0.0010$. (c) Position angle, PS, as a function of the radial distance from the cluster centre, R. The black dashed line represents the weighted mean of the bins $PA = (329.34 \pm 1.16)^{\circ}$.

proper motions, parallax and positions in the colour-magnitude diagram (CMD): We plotted G as a function of the PM relative to the mean PM of the cluster, and we define by hand a line that separate cluster stars from field stars. We then repeated the same procedure for the parallax. Finally, we refine our selection using the G vs. $B - R$ CMD by defining lines that enclose the sequences of stars associated with the cluster (see Fig. 2 of Scalco et al. 2023). The 15,587 sources that survived the selections were used to estimate the rotation of the cluster as follows: we started by dividing the field of view into 32 circular sectors with arc lengths of 11.25°. We then calculated the median proper motions of stars in each circular sector by using a maximum likelihood approach. The results are shown in panels (a) and (b) of Figure 8.15 for the μ_α and μ_δ components, respectively. A visual inspection of these two panels reveals a clear sinusoidal trend of the bins in the two directions. To quantify the rotation of NGC 6752 we perform a last-square fitting to the points using the sinusoidal function

$$\Delta V = A_{rot} sin(PA + \phi) + c \tag{7.1}$$

We obtain a value of $A_{rot,\alpha} = 25.3186 \pm 2.7136$ μas/yr, $\phi_\alpha = (21.4383 \pm 0.1096)^{\circ}$ and $c_\alpha = 5.4038 \pm 1.9410$ μas/yr, and $A_{rot,\delta} = 31.2802 \pm 4.0493$ μas/yr, $\phi_\delta = (7.7593 \pm 0.1270)^{\circ}$ and $c_\delta = 5.8191 \pm 2.8408$ μas/yr, for the μ_α and μ_δ components, respectively. We exploit the r^2 parameter (Glantz and Slinker 1990, Cordoni et al. 2020b) to estimate the statistical significance of the fit. We obtain a value of $r^2_\alpha \simeq 0.75$ and $r^2_\delta \simeq 0.68$ for the two components, respectively.

We studied the rotation of NGC 6752 in the plane of the sky as a function of the radial distance from the cluster centre as done in Scalco et al. (2023). We initially decomposed the PMs into radial and tangential components ($\mu_{\rm RAD}$, $\mu_{\rm TAN}$) and propagated the velocity uncertainties. We divided the 15,587 member stars into 10 equally populated radial bins. Then, for each bin, we evaluated the median value of $\mu_{\rm TAN}$,

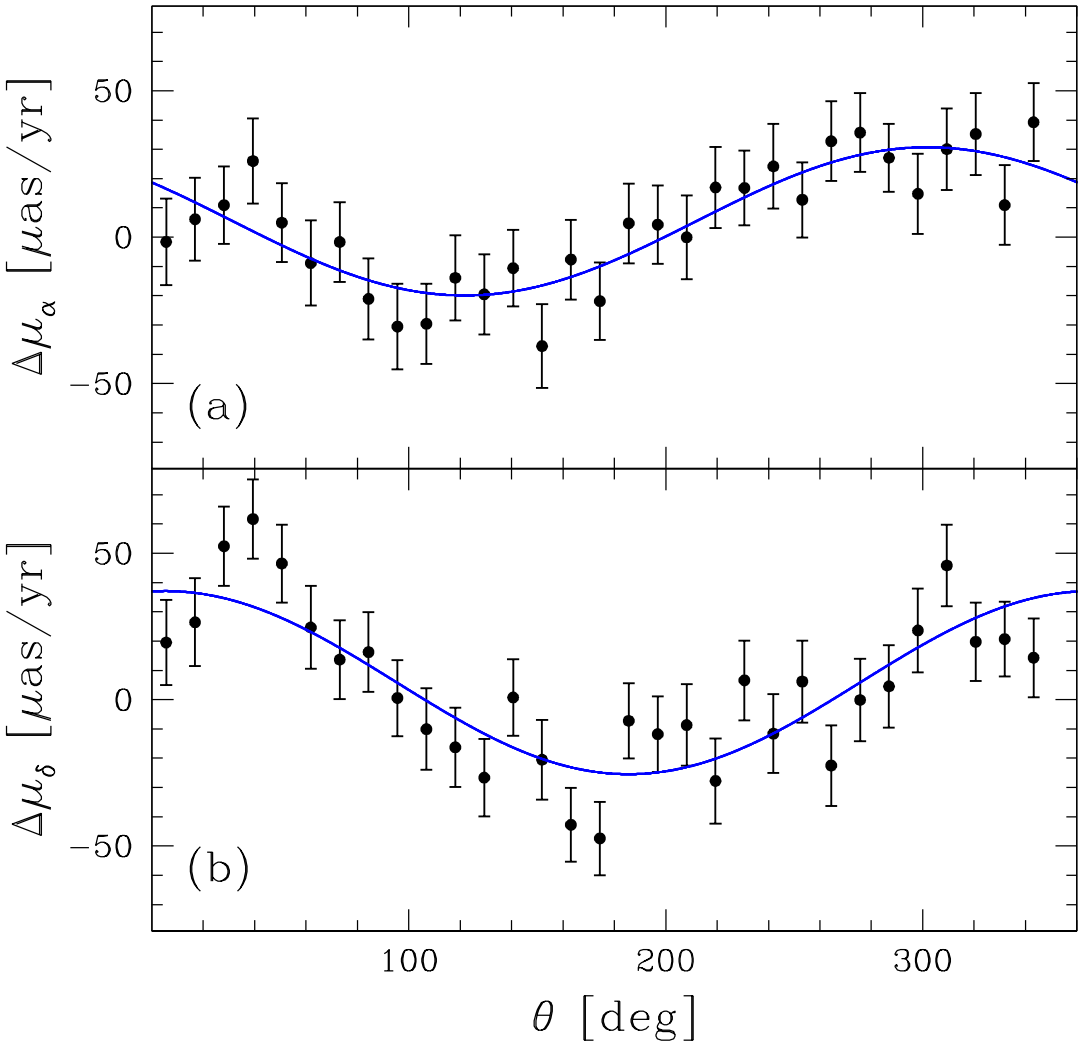

FIGURE 7.13: Estimate of the rotation on the plane of the sky of NGC 6752. (a)-(b) $\Delta\mu_\alpha$ and $\Delta\mu_\delta$ as a function of the position angle θ. The blue lines represent the best-fit function.

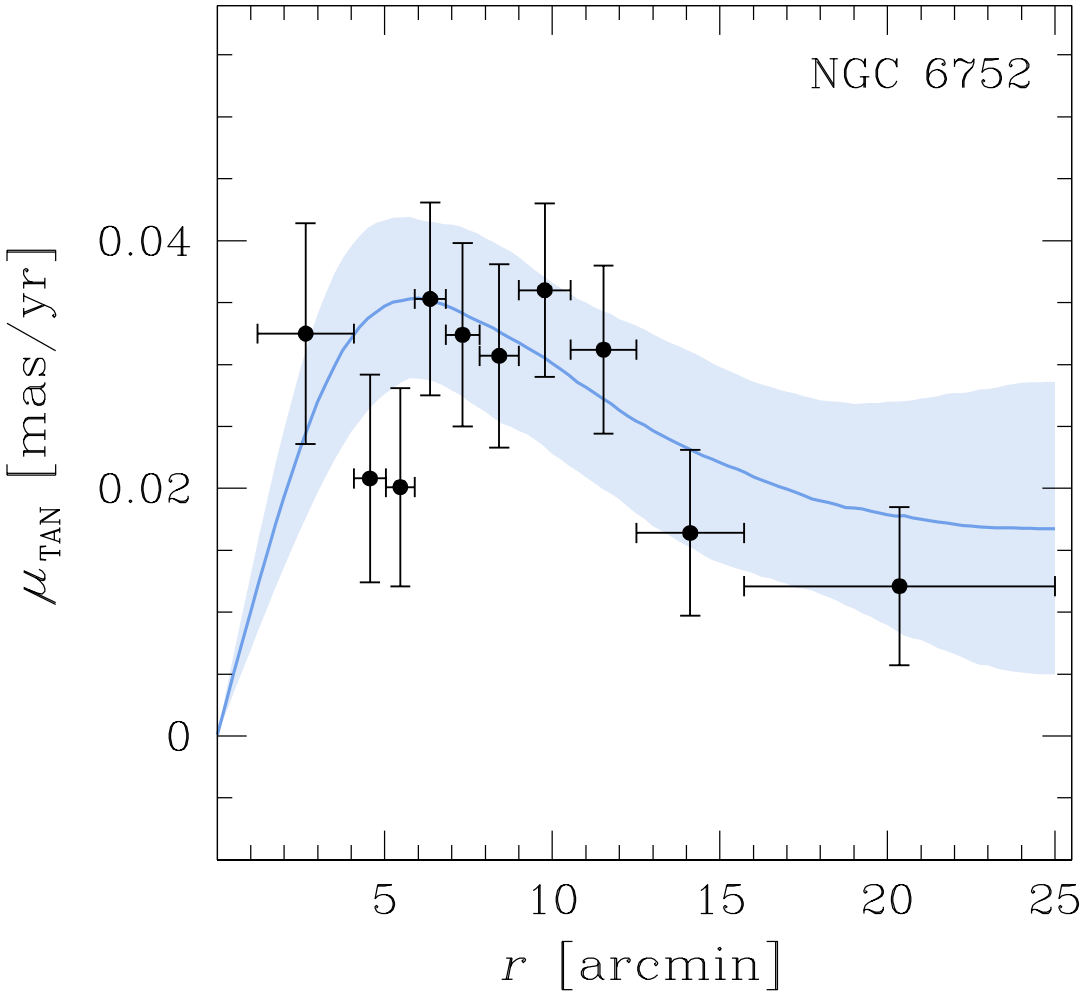

FIGURE 7.14: Rotation profile of NGC 6752 in the plane of the sky (black points). The solid blue line and shaded area represent the rotation profile presented in Vasiliev and Baumgardt (2021) for NGC 6752 and their 68% confidence intervals, respectively.

again with a maximum likelihood approach. Figure 7.14 shows the obtained rotation profile (black points). The curve is compared with those published in Vasiliev and Baumgardt (2021) (blue solid line), showing a quite good agreement.

We make use of the LOS velocity catalogue provided by Baumgardt and Hilker (2018) to search for a rotational signal in the LOS direction. We initially selected all the stars, belonging to the SGB+RGB+RGB-tip sequence, that survived the selection in panel (a) of Figure 7.10 and with a Gaia G magnitude $12<G<17$. We left a total of 1.014 stars. We divided the field of view into 16 circular sectors with arc lengths of 22.5° and separated by steps of 11.25°. We then calculated the median proper motions of stars in each circular sector. The results are shown in Figure 7.15.

To quantify the LOS rotation of NGC 6752 we performed least-squares fitting using the function in equation 1. We obtain a value of $A_{rot} = -0.7983 \pm 0.0002$ mas/yr, $\phi = (1.5250 \pm 0.0002)^\circ$ and $c = 0.1469 \pm 0.0001$ mas/yr. We exploit the r^2 parameter (Cordoni et al. (2020b)) to estimate the statistical significance of the fit. We obtain a value of $r^2 \simeq 0.41$. The best-fit function is represented by a blue line in Figure 7.15.

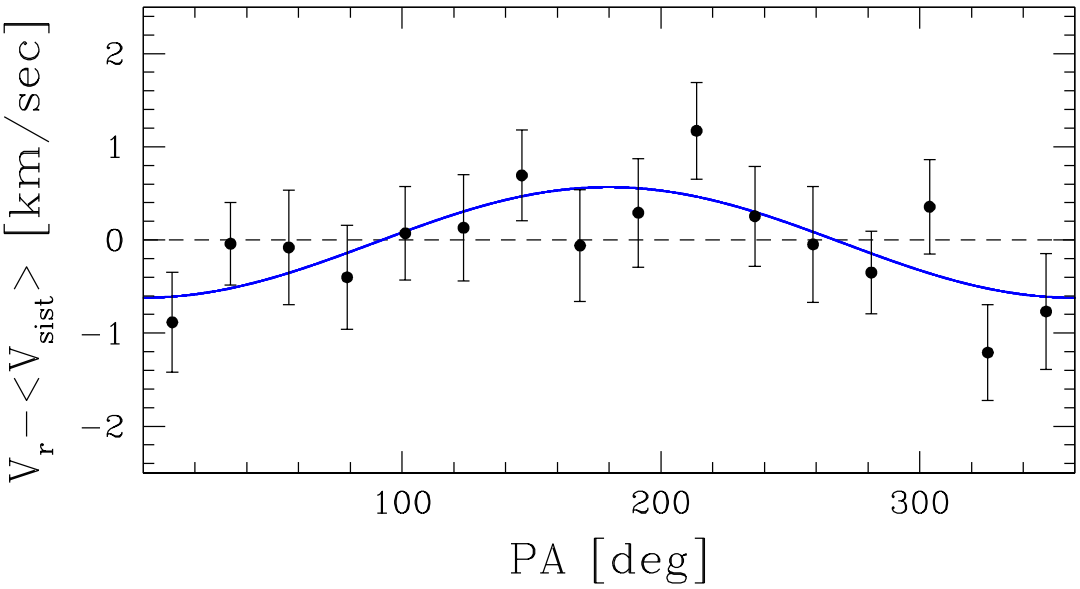

FIGURE 7.15: LOS velocity as a function of the position angle. The blue line represents the best-fit function.

7.8 Velocity dispersion

The present-day kinematic proprieties of globular clusters, such as velocity dispersion profile and anisotropy, offer a unique opportunity to investigate the initial configurations of the system. While most globular clusters are considered completely relaxed in the core, the outer regions, characterised by longer relaxation times, can still retain some memory of their initial kinematic conditions. In order to obtain a better understanding of the formation and kinematic history of globular clusters, is necessary to extend the observational studies to cover a wider radial range of distances from clusters' centres to include the outer regions. Here we provide a detailed study of the velocity dispersion profile of NGC 6752 along an extensive part of the cluster, by combining our Gaia DR3, HST and LOS velocities catalogues.

7.8.1 Gaia DR3

Vasiliev and Baumgardt (2021) used Gaia eDR3 data to study the kinematic properties of the Milky Way globular cluster and determine the PM dispersion profiles for more than 100 clusters. Here, we briefly describe the method (more details in Vasiliev and Baumgardt (2021).

For each cluster, a probabilistic mixture modelling in the 3d astrometric space (parallax and two PM components) is applied to the stars. The distribution of all sources is represented by two or three Gaussian components and an Extreme Deconvolution approach is used to determine their mean values and covariance matrices. Then a Markov chain Monte Carlo is run, where the angular distance from the cluster centre is used as an additional property of each star. A Plummer profile is used to fit the cluster surface density profile, for which the scale radius of the Plummer profile is allowed to be adjusted during the simulation. The intrinsic PM dispersion is represented by a cubic spline in radius with 2-5 nodes, with amplitudes that are also varied during the fit. Finally, the membership probability of the stars is evaluated at the end of the simulation. Figure 7.16 shows the comparison between the

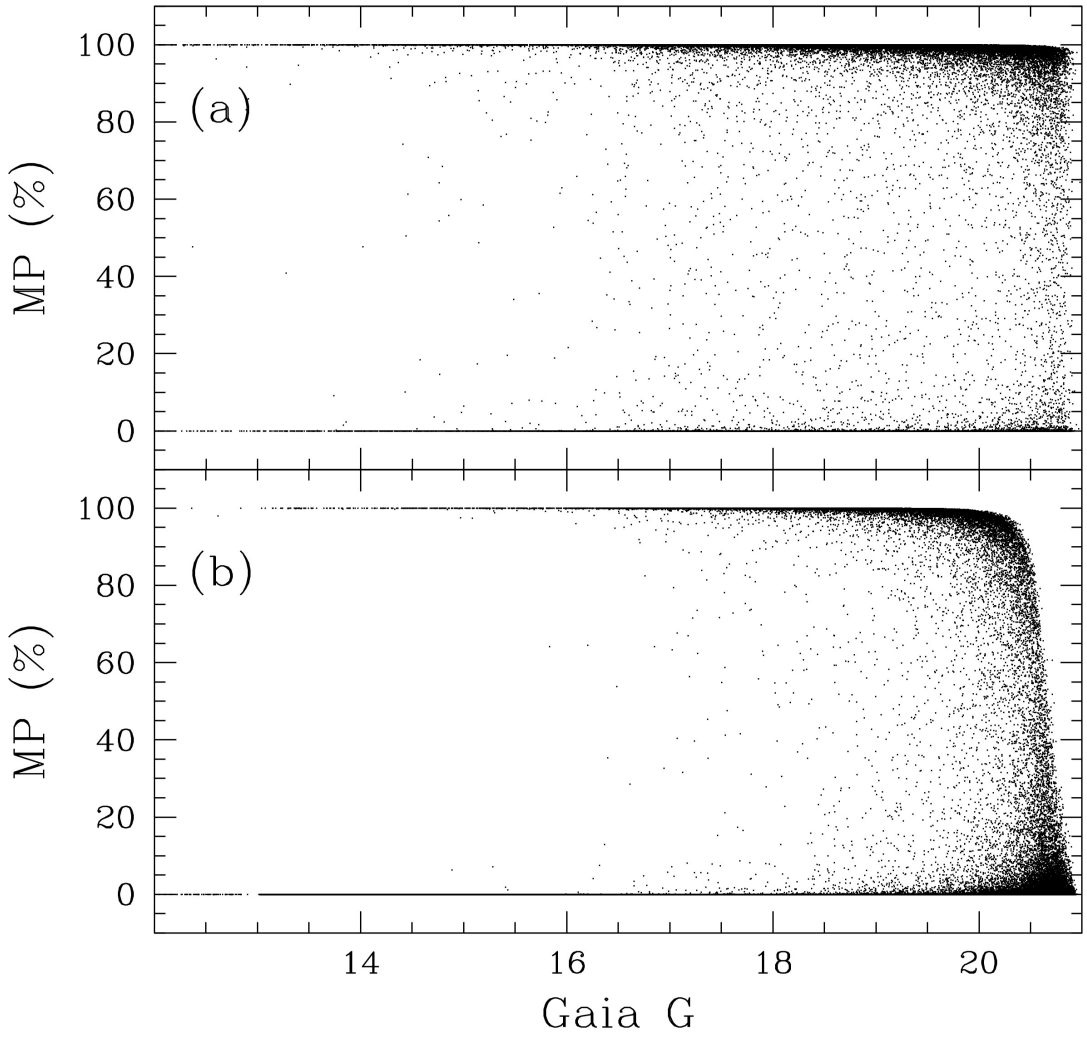

FIGURE 7.16: (a)-(b) Membership probability as a function of the Gaia G magnitude from Vasiliev and Baumgardt (2021) and this work, respectively.

membership probability, as a function of the Gaia G magnitude, obtained in Vasiliev and Baumgardt (2021) (panel (a)) and in this work (panel (b)).

In this section, we present the velocity dispersion profile of NGC 6752 using our Gaia DR3 data. We divided the sample of probable cluster members defined in the previous section into 10 equally populated radial bins. To derive the velocity dispersion of in each bin we considered the negative log-likelihood function:

$$\lambda = \prod_{i=0}^{N} p(v_i, \epsilon_i), \tag{7.2}$$

with the probability of finding a star with velocity v_i and uncertainty ϵ_i given by

$$p(v_i, \epsilon_i) = \frac{1}{2\pi\sqrt{\sigma^2 + \epsilon_i^2}} exp\left(-\frac{(v_i - v)^2}{2(\sigma^2 + \epsilon_i^2)}\right). \tag{7.3}$$

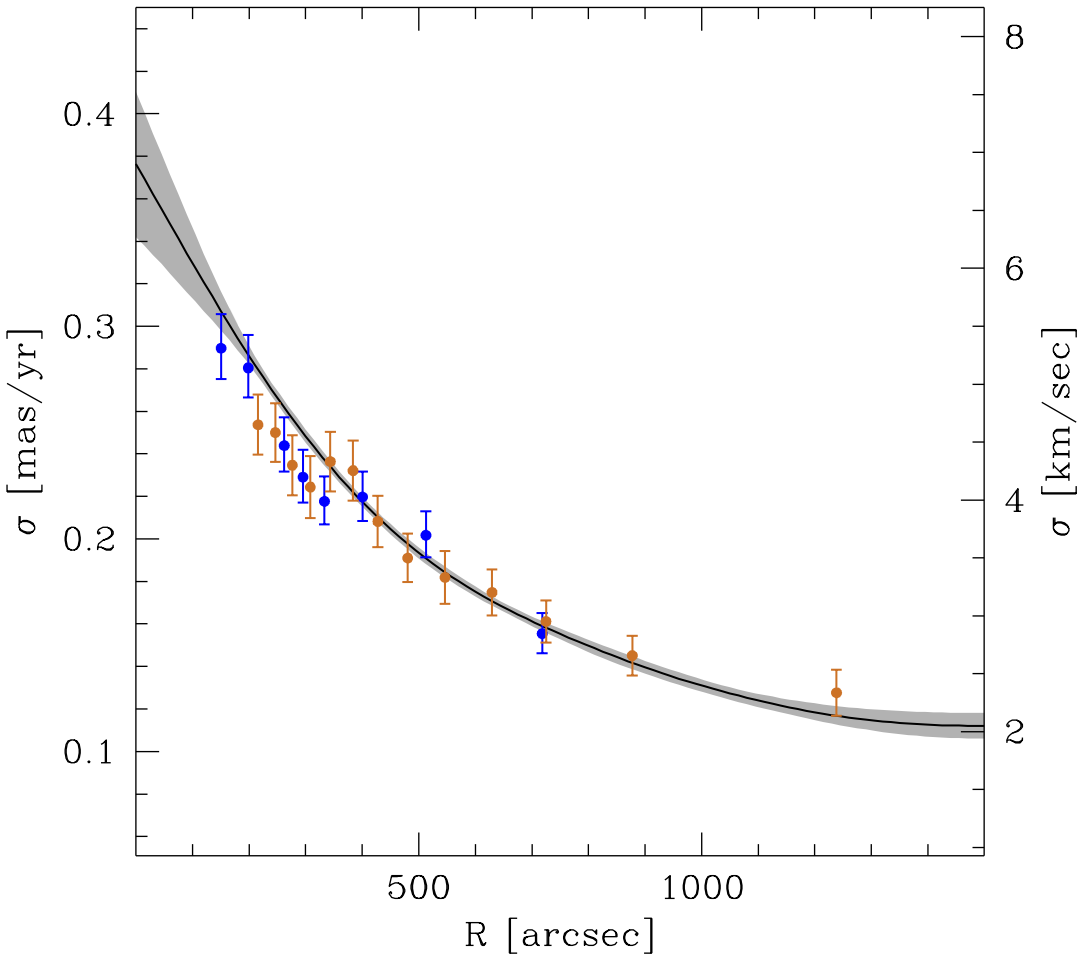

FIGURE 7.17: Velocity dispersion profile of NGC 6752 using our Gaia DR3 catalogue (ocher points). The PM dispersion profile presented in Vasiliev and Baumgardt (2021) is marked for comparison by the black solid line, with a shaded gray area representing its 68% confidence interval. The blue points represent the velocity dispersion values reported in the article and accessible in the online database.

The best fitting (ν,σ) are those that maximise the likelihood function. The uncertainties associated with each point are determined by bootstrapping with replacements performed 1000 times.

Figure 7.17 shows the obtained values (ocher points). For comparison, we also show the profile obtained by Vasiliev and Baumgardt (2021) (black solid line with shaded gray area representing its 68% confidence interval) and the velocity dispersion values reported in the online database [3] (blue points; we adopted a cluster distance of d=4.1 kpc as reported by Vasiliev and Baumgardt (2021).

7.8.2 The central field and field F2 of NGC 6752

Studies based on ultraviolet and optical HST photometry have shown that two-colour diagrams obtained by combining F275W, F336W and F438W (the so-called "magic trio") and F814W offer a powerful way to identify populations of stars with different helium and light-element abundances (Milone et al., 2012a; Milone et al., 2015b). These two-color diagrams, also referred to as 'chromosomic maps' (ChM),

[3] https://people.smp.uq.edu.au/HolgerBaumgardt/globular/

TABLE 7.8: Fractions of MSa, MSb and MSc stars with respect to the total number of MS stars for different magnitude intervals.

m_{F814W}	MSa	MSb	MSc
18.2 - 18.4	23.3%	46.5%	30.2%
18.4 - 18.6	24.7%	47.2%	28.1%
18.6 - 18.8	19.3%	46.6%	34.1%
18.8 - 19.0	17.1%	47.5%	35.4%

have provided an unprecedented detailed analysis of the MP pattern in Milky Way GCs (Milone et al., 2017a; Milone et al., 2018c). Here we make use of the $m_{F275W} - m_{F814W}$ colour, which is mostly sensitive to stellar populations with different helium abundances, and the $C_{F275W,F336W,F438W} = (m_{F275W} - m_{F336W}) - (m_{F336W} - m_{F438W})$ pseudo-colour, which maximizes the separation among stellar populations with different nitrogen contents, to identify and separate the three multiple stellar populations of NGC 6752 (Milone et al., 2013; Milone et al., 2019).

Panel (a) of Figure 7.18 shows the $m_{F275W} - m_{F814W}$ vs. m_{F814W} CMD for MS stars with 18<m_{F814W}<19, while panel (c) shows the $C_{F275W,F336W,F438W}$ vs. m_{F275W} CMD for MS stars with 20<m_{F275W}<23. For each CMD, we drew by hand two fiducial lines, as shown in panels (a) and (c) of Figure 7.18, that were used to verticalise the CMDs. The verticalised CMD are shown in panels (b) and (d) of Figure 7.18. Panels (e), (f) and (g) show the ChM obtained form the combination of the two verticalised diagrams. As can be seen from the Hess diagram shown in panel (f), we can clearly identify three different stellar populations. In panel (g) of Figure 7.18 we separated and colour-coded the three stellar populations; hereafter we will refer to these three MS stellar populations as MSa (green), MSb (magenta) and MSc (blue). These three components contain 914 ($\sim$ 25%), 1609 ($\sim$ 45%) and 1177 ($\sim$ 30%) stars, respectively. These values are similar to those obtained in (Milone et al., 2013; Milone et al., 2019).

We divided all the stars with a magnitude 18.2< m_{F814W} <19 in bins of 0.2 mag. For each bin, we fitted with a 2D-Gaussian function the distribution of the three stellar populations in the Δ_1 vs. Δ_2 plane. Table 7.8 reports, for each bin, the fractions of MSa, MSb and MSc stars with respect to the total number of MS stars, estimated from the areas of the corresponding 2D-Gaussians. As we can see, the number of stars belonging to the MSa and MSc populations changes with the m_{F814W} magnitude, with the MSa becoming less populated for faint magnitude and vice versa for the MSc, while the MSb remains constant.

We repeated the procedure to identify and separate the three multiple stellar populations in the field F2. Figure 7.19 shows the obtained ChM and the relative separation of the three stellar populations.

We analysed the radial distribution of the velocity dispersion profile of the three stellar populations following the method described in Libralato et al. (2022) and Watkins et al. (2015). Briefly, we cut all the stars with $N_{found}/N_{used} < 0.9$, where N_{found} is the number of data points found for each star and N_{used} is the number of data points used for the final calculations of the proper motions. We also cut all the stars with $\chi^2_x > 1.5$ and $\chi^2_y > 1.5$ and PM error larger than 0.1 mas yr^{-1}. We evaluated the membership probability of the sources following a method based on PM described in Balaguer-Núnez, Tian, and Zhao (1998), Bellini et al. (2009), Nardiello et al. (2018), and Scalco et al. (2021). We then removed all the sources with a membership probability less than 80%.

After the quality selection, we found a total of 848 MSa, 1.486 MSb and 1.090 MSc

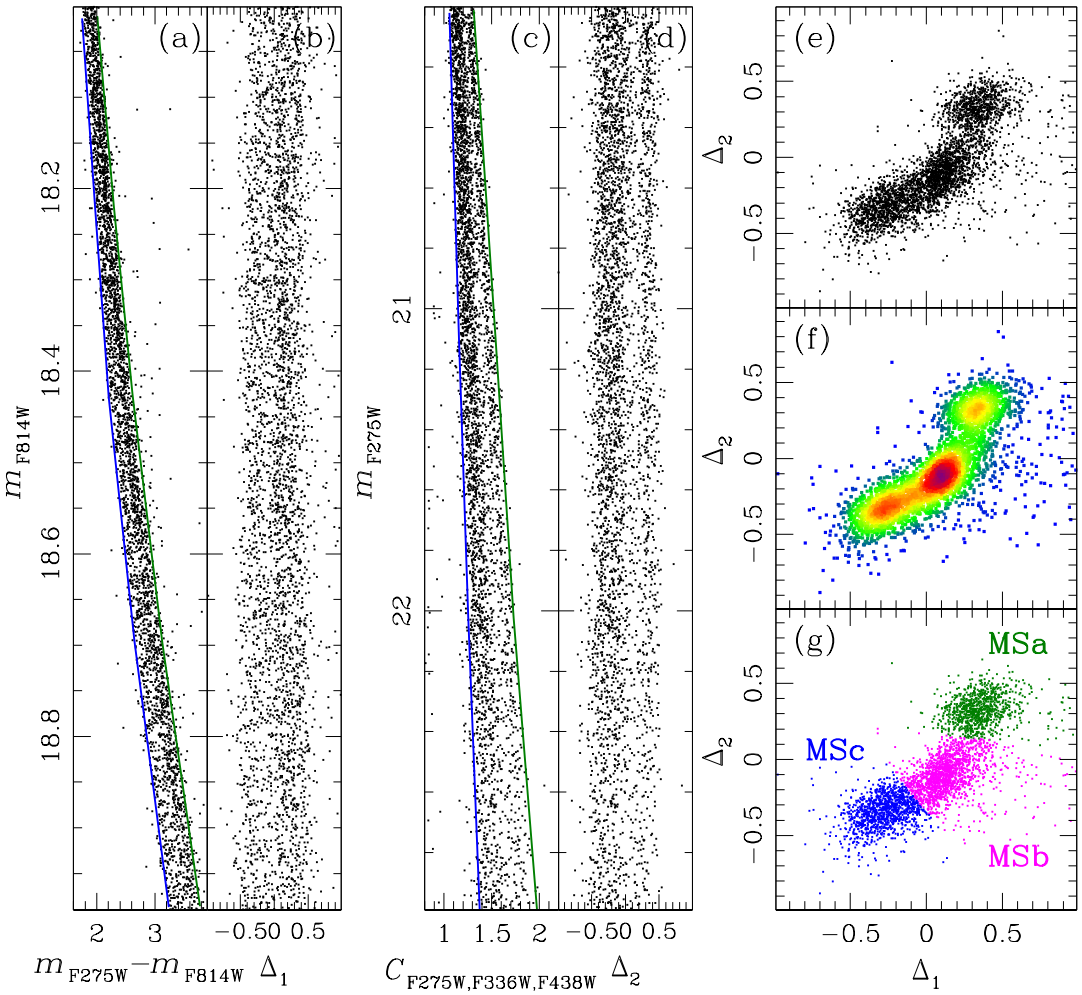

FIGURE 7.18: Procedure to separate and identify the three stellar populations in NGC 6752 in the MS. (a) $m_{F275W} - m_{F814W}$ vs. m_{F814W} CMD for MS stars with 18<m_{F814W}<19. The two fiducial lines, drawn by hand are used to verticalise the diagram (b) $m_{F275W} - m_{F814W}$ vs. m_{F814W} verticalised CMD. (c) $C_{F275W,F336W,F438W}$ vs. m_{F275W} CMD for MS stars with 20<m_{F275W}<23. (d) $C_{F275W,F336W,F438W}$ vs. m_{F275W} verticalised CMD. (e) ChM was obtained by combining the two verticalised diagrams. (f) Hess diagram. Three different stellar populations are clearly visible. (g) The three different stellar populations are colour-coded in green (MSa), magenta (MSb) and blue (MSc).

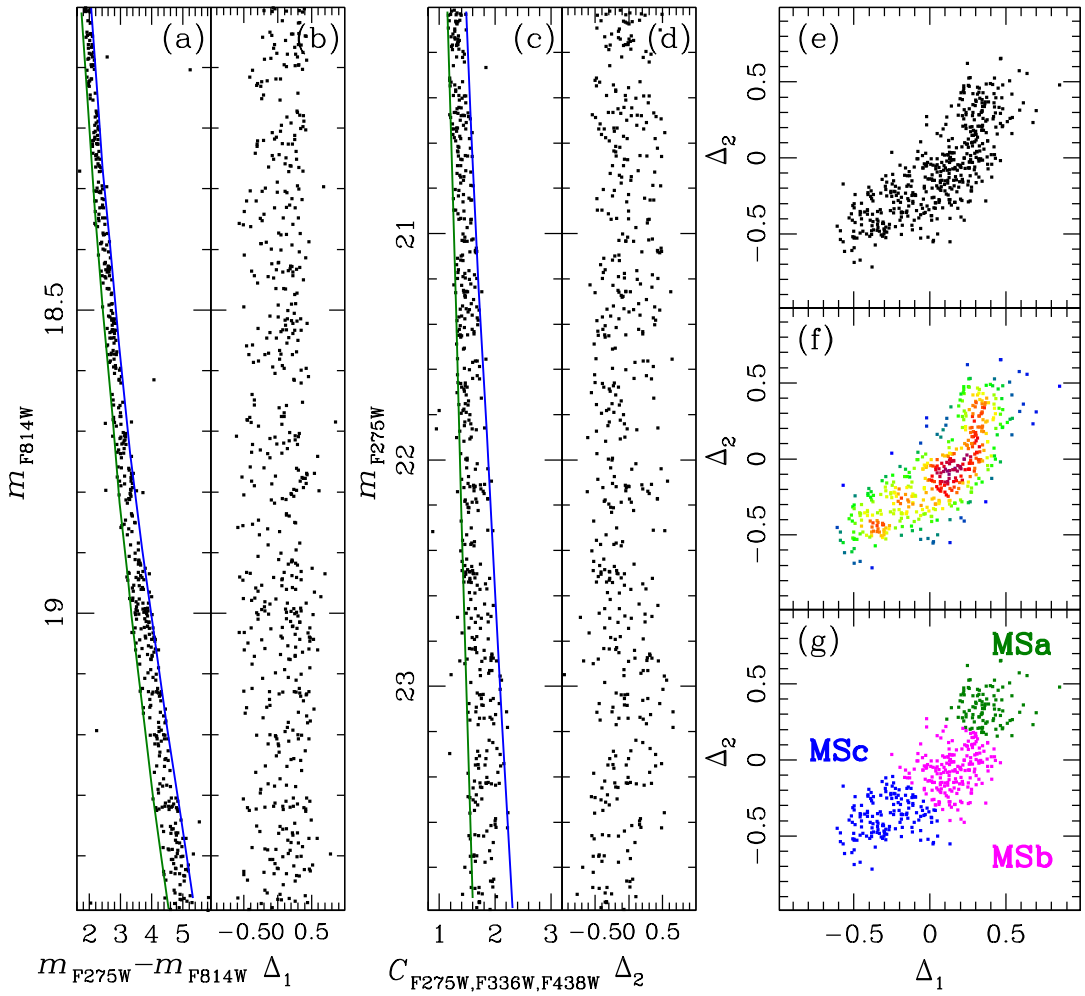

FIGURE 7.19: As in figure 7.18 but for the field F2.

TABLE 7.9: Values of σ_0 for the radial and tangential components and anisotropy for each stellar population.

	MSa	MSb	MSc
$\sigma_{0,rad}$	0.408±0.013	0.408±0.010	0.399±0.012
$\sigma_{0,tan}$	0.424±0.009	0.401±0.008	0.414±0.008
$< \sigma_{rad}/\sigma_{tan} - 1 >$	0.031±0.047	-0.019±0.034	0.027±0.042
RGBa	RGBb		RGBc
0.382±0.031	0.332±0.048		0.353±0.012
0.395±0.027	0.371±0.034		0.369±0.006
0.013±0.126	0.114±0.146		0.047±0.180

stars. We divided the stars that survived the selections into 5, 9 and 6 equally populated bins for MSa, MSb and MSc, respectively. We derived the velocity dispersion of each group of stars in each bin using equations 2 and 3. The velocity dispersion profile, for the three stellar populations, is shown in Figure 7.20 for the radial (panel (a)) and tangential (panel (b)) component, σ_{rad} and σ_{tan}. The points are colour-coded for each stellar population as in panel (g) of Figure 7.18. The velocity dispersion profiles are over-plotted with the best-fitting Plummer (1911) model

$$\sigma^2(R) = \frac{\sigma_0^2}{\sqrt{(1 + R^2/r_h^2)}} \tag{7.4}$$

where σ_0^2 is the central velocity dispersion and r_h is the half-light radius ($r_h = 1.91'$, Harris 1996). The values of σ_0 for each population are reported in Table 7.9 for both radial and tangential components.

As we can see, the three stellar populations are characterised by similar velocity dispersion profiles. This result is not surprising: given the shot relaxation time of NGC 6752 ($\sim 7.6 \times 10^6$ at the core radius and $\sim 6 \times 10^9$ at the half-light radius) the different stellar populations have had time to dynamically conform to each other. Finally, panel (c) of Figure 7.20 shows the $\sigma_{tan}/\sigma_{rad} - 1$ as a function of the radial distance for the three components. The three horizontal lines represent the weighted mean of the bins, for each stellar group. The weighted mean of the bins is reported in Table 7.9. As we can see, none of the three populations shows any sign of anisotropy.

To extend our multi-wavelength study of the different stellar populations of NGC 6752, we attempted to identify and separate the three stellar populations along different parts of the CMD. We repeated the procedure illustrated in Figure 7.18 for the stars along the RGB. Panel (a) of Figure 7.21 shows the obtained ChM. We separate and colour-coded the three stellar populations, hereafter RGBa (green), RGBb (magenta) and RGBc (blue). These three components contain 184, 183 and 123 stars, respectively. Panel (b) of Figure 7.21 shows the locations of these three different stellar populations along the $C_{F275W,F336W,F438W}$ vs. m_{F275W} CMD.

We studied the velocity dispersion profile of the three components by following the same procedure adopted above. Again, we cut all the stars with $N_{found}/N_{used} < 0.9$, $\chi^2_x > 1.5$ and $\chi^2_y > 1.5$, PM error larger than 0.1 mas yr^{-1} and removed all the sources with a membership probability less than 80%. After the selection criteria, we found a total of 89 RGBa, 98 RGBb and 67 RGBc stars. We divided the stars of each sample that survived the selections in 3 equally populated bins. We used equations 2 and 3 to estimate the velocity dispersion of each bin. Figure 7.22 shows the radial distribution of the velocity dispersion profile in the radial (panel (a)) and tangential

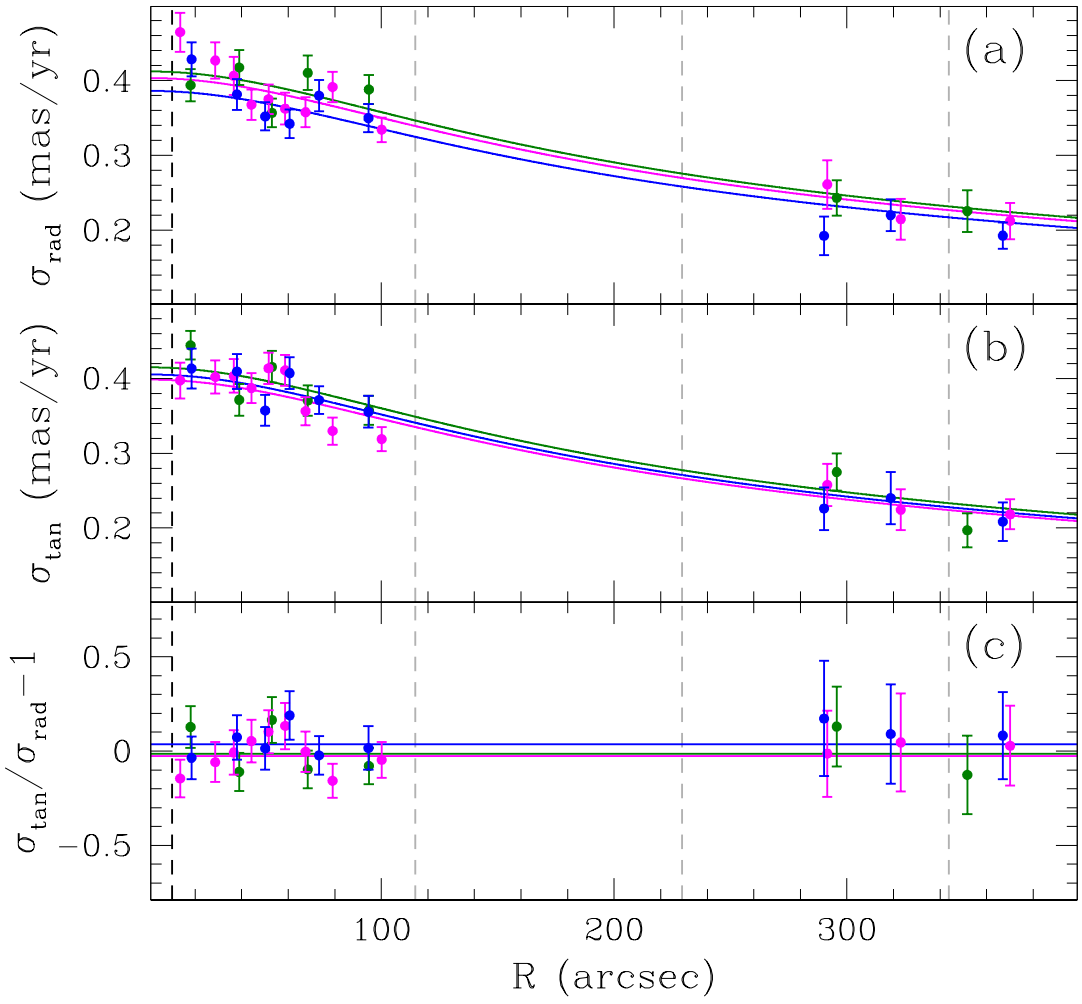

FIGURE 7.20: Radial distribution of the velocity dispersion profile of the three MS stellar populations in the central field and field F2, for the radial (a) and tangential (b) components, σ_{rad} and σ_{tan}. The three stellar populations are color-coded as in panel (g) of Figure 7.18 and 7.19. The bins are over-plotted with the best-fitting Plummer (1911) model. (c) $\sigma_{tan}/\sigma_{rad} - 1$ as a function of the radial distance for the three components. The black and grey dashed vertical lines represent the core and half-light radius, respectively.

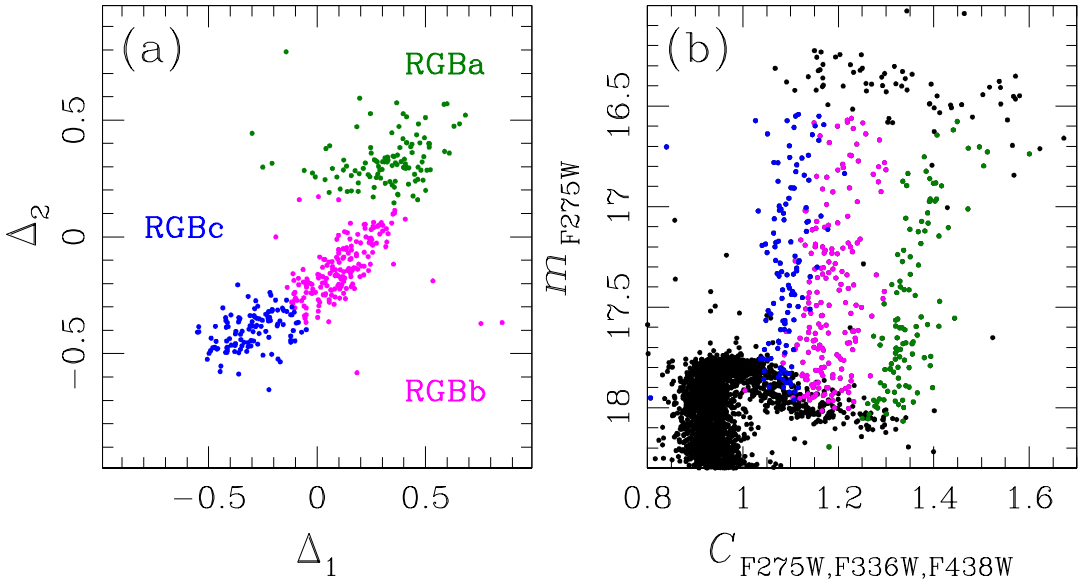

FIGURE 7.21: (a) ChM for the RGB stars obtained following the procedure illustrated in Figure 7.18. The three different stellar populations are colour-coded in green (RGBa), magenta (RGBb) and blue (RGBc). (b) locations of the three stellar populations along the $C_{F275W,F336W,F438W}$ vs. m_{F275W} CMD.

(panel (b)) direction for the three RGB stellar populations. The bins are over-plotted with the best-fitting Plummer model (see equation 4). The values of σ_0 for each population are reported in Table 7.9 for both radial and tangential components. As we can see, the velocity dispersion are comparable with that obtained for the MS stars (see Figure 7.20). As for the MS, the three stellar populations are characterised by similar velocity dispersion profiles.Panel (c) of Figure show the $\sigma_{tan}/\sigma_{rad} - 1$ as a function of the radial distance for the three components. As in Figure 7.20 the three horizontal lines represent the weighted mean of the bins, for each stellar group. The weighted mean of the bins is reported in Table 7.9.

Equipartition radial profile

GCs are collisional systems, meaning that the stars inside them undergo a lot of interactions with each other during the life of the cluster. During these interactions, the energy is typically transferred from the star with higher energy to the star with lower energy, in a process called two-body relaxation. A state of hypothetical equilibrium is reached when all the stars share the same kinetic energy $\frac{1}{2}m\sigma^2$, where m is the stellar mass and σ is the velocity dispersion. As a consequence, after enough iterations, we would observe that low-mass stars move faster than high-mass stars. This is known as energy equipartition.

Encouraged by the results obtained in Watkins et al. (2022) we investigated the equipartition radial profile of NGC6752 using the Libralato et al. (2022) data set. We began by applying the selections described in Libralato et al. (2022). We then removed a few outliers based on their proper motions following the prescription of Watkins et al. (2022) (see Section 3.4). We then divided the sample into 6 radial bins. We divided the stars in each radial bin into 10 mass bins and calculated for each bin the velocity dispersion, σ, of the stars. Here we used only stars with a mass, M, between 0.3 and 0.55 solar masses. We then evaluated the value of the

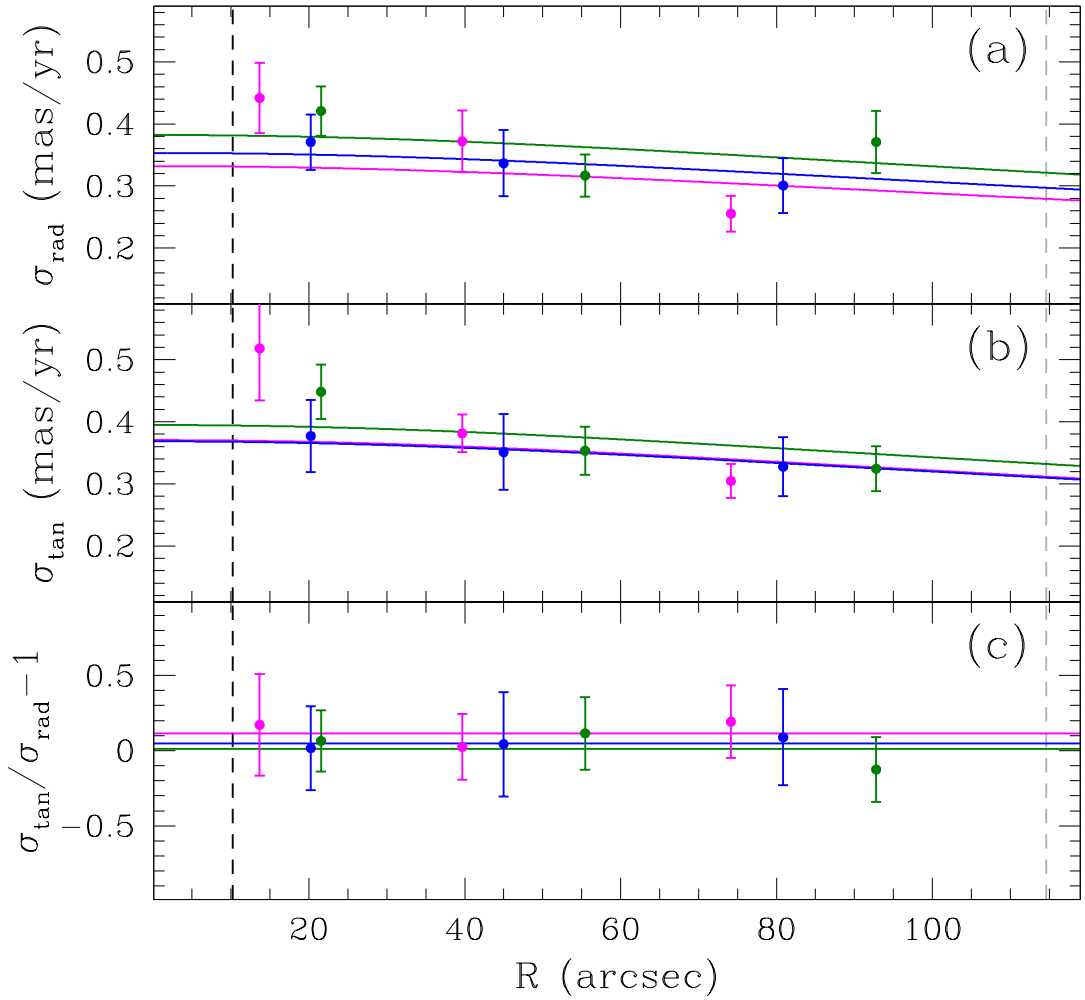

FIGURE 7.22: As in Figure 7.20 but for the RGB stars.

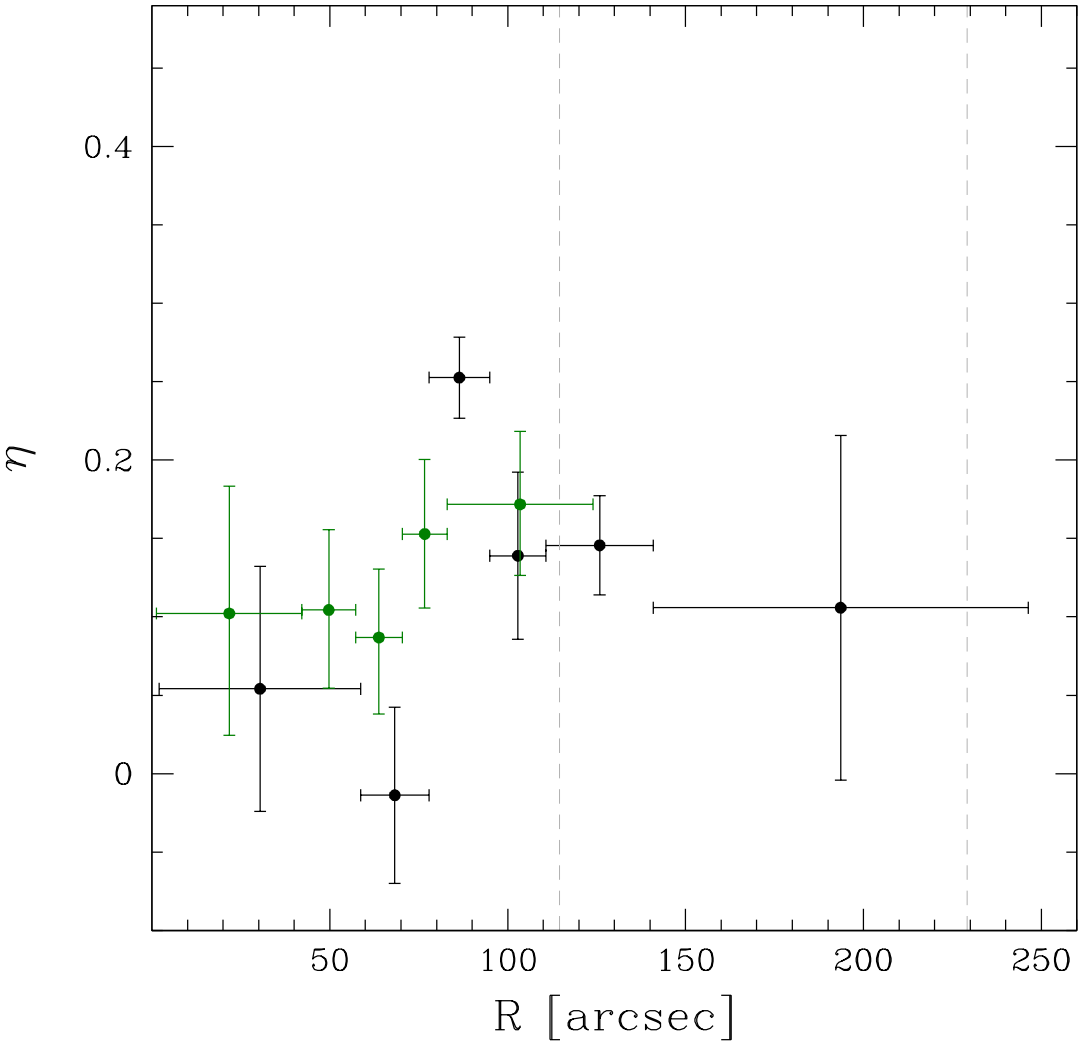

FIGURE 7.23: Radial profile of the energy equipatition η for the central field (black points). For comparison, we also show in green the profile obtained by Watkins et al. (2022).

equipartition, η, in each radial bin, by fitting the values of the velocity dispersion as a function of the stellar mass with a line in the $log(\sigma) - log(m)$ plane. The slope of the interpolations line is a direct estimate of η. The obtained values for η are shown with black points in Figure 7.23. For comparison, we also show, in green, the values reported by Watkins et al. (2022). As can be seen, in both figures the general trend found in Watkins et al. (2022) is confirmed also for the region of the cluster between r_h and $2 \times r_h$.

7.8.3 The field F0

The field F0 of NGC 6752 was observed by HST as a part of a large *Hubble Space Telescope* investigation aiming at reaching the faintest stars in this globular cluster and studying its white dwarf cooling sequence. As can be seen from Table 7.1, this field was heavily observed in optics with the HST WFC/ACS F606W and F814W filters, in four epochs and for a total of 80 orbits. Bedin et al. (2019c) presented the discovery of a serendipitous dwarf galaxy in this field, while Bedin et al. (2019c)

focused on the study of the white dwarf cooling sequence of NGC 6752. Here we present a kinematical study of the stars in this field.

We derived the PM of the stars in the field F0 following the procedure described in Libralato et al. (2022), which is based on the technique developed by Bellini et al. (2014) and improved in Bellini et al. (2018) and Libralato et al. (2018b). This is an iterative procedure that treats each image as a stand-alone epoch and can be summarized in two main steps: (1) transforms the stellar positions of each exposure into a common reference frame by means of a six-parameter linear transformation; (2) fit these transformed positions as a function of the epoch with a least-square straight line. The slope of this line, computed after several outlier-rejection stages, is a direct measurement of the PM. We verified that neither component of the PM suffers from systematic effects due to stellar colour and luminosity. High-frequency-variation systematic effects were corrected as described in Bellini et al. (2018), where the proper motion of each star is corrected according to the median value of the closest 100 likely cluster members (excluding the target star itself).

Panel (b) of Figure 7.24 shows the vector-point diagram (VPD) of the 33.959 sources for which we were able to measure PMs. Three groups of objects are clearly distinguishable in the VPD: (1) clusters stars (black dots), centred in the origin of the VPD; (2) field objects (grey dots), characterized by a broad distribution and (3) a broader component roughly centred around (3.17, 4.04) mostly due to stars belonging to the dwarf galaxy *Bedin-I* (blue filled dots; see Bedin et al. (2019c). Panel (a) of Figure 7.24 shows the $m_{F606W} - m_{F814W}$ vs. m_{F606W} CMD for the three components. As can be seen, the stars belonging to the dwarf galaxy *Bedin-I* occupy a specific region of the CMD. Panel (c) of Figure 7.24 shows the X-Y pixel-based position of the stars, for the three components, with the blue-filled dots that mostly fall in the region where the dwarf galaxy *Bedin-I* is located. Finally, panel (d) of Figure 7.24 shows the PM errors as a function of the m_{F606W} magnitude.

GCs are assumed to evolve toward a state of energy equipartition, for which the velocity dispersion scales with stellar mass as $\sigma_\mu \propto m^{-\eta}$, with η varying with the radial distance from the centre, reaching a maximum value $\eta_{max} \approx 0.15$ in the core, and evolving from $\eta \sim 0.08$ to zero in the outskirts (Trenti and van der Marel, 2013).

To measure the state of energy equipartition in the field F0 we follow the method described in Bellini et al. (2018). We started by removing all badly measured stars using a set of photometric quality parameters in close analogy of what was done in Scalco et al. (2021). Following Libralato et al. (2022) we removed all the stars with $N_{found}/N_{used} < 0.9$, $\chi^2_x > 1.5$ and $\chi^2_y > 1.5$. We plotted the PM errors of the sources, in both directions, as a function of the m_{F606W} magnitude and verified that most of the stars follow a clear trend. We divided the sample into bins of 0.5 m_{F606W} magnitude and evaluated for each bin the 68th percentile of the distribution. We then interpolated the points corresponding to the 68th percentile with a spline and removed all the sources above the interpolating line. We applied this procedure to both directions, separately. Finally, we used the CMD to remove a few outliers, defining by hand two fiducial lines (see panel (a) of Figure 7.25) and removed all the sources with a membership probability less than 80%. After these quality selections our sample contains a total of 3.771 sources.

We divided the MS of the cluster into 20 equally populated magnitude bins in m_{F606W} (panel (a) of Figure 7.25). We color-coded each bin from blue to yellow to purple moving from the brighter to the fainter bin. We used equations 2 and 3 to estimate the velocity dispersion of each bin. To convert magnitudes into stellar masses, we fitted the same Dotter et al. (2008) isochrone applied in Milone et al. (2019). We assumed [Fe/H] = -1.61, [α/Fe] = 0.4, helium abundance $Y = 0.246$ and adopted

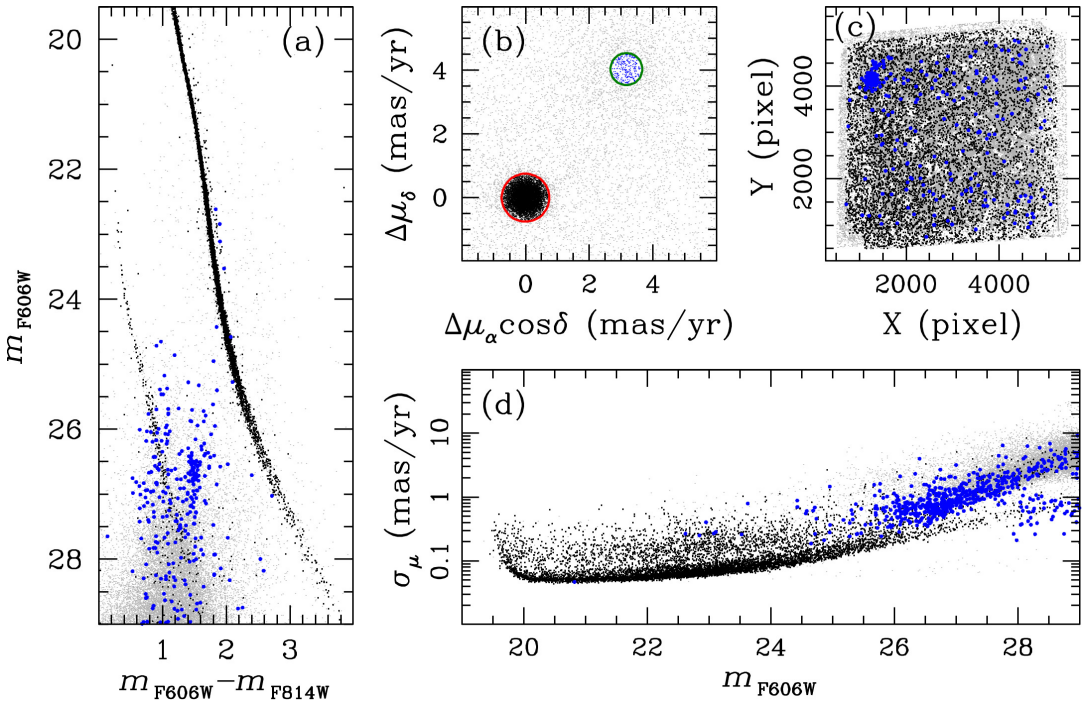

FIGURE 7.24: This figure illustrates the astro-photometric data of the stars in the field F0 for which we were able to measure PMs. (a) $m_{F606W} - m_{F814W}$ vs. m_{F606W} CMD. (b) vector-point diagram. (c) X-Y pixel-based position of the stars. (d) PM errors as a function of the m_{F606W} magnitude. In each panel, cluster stars are represented with black dots, field stars are represented with grey dots and stars likely belonging to the dwarf galaxy *Bedin-I* are represented with blue-filled dots.

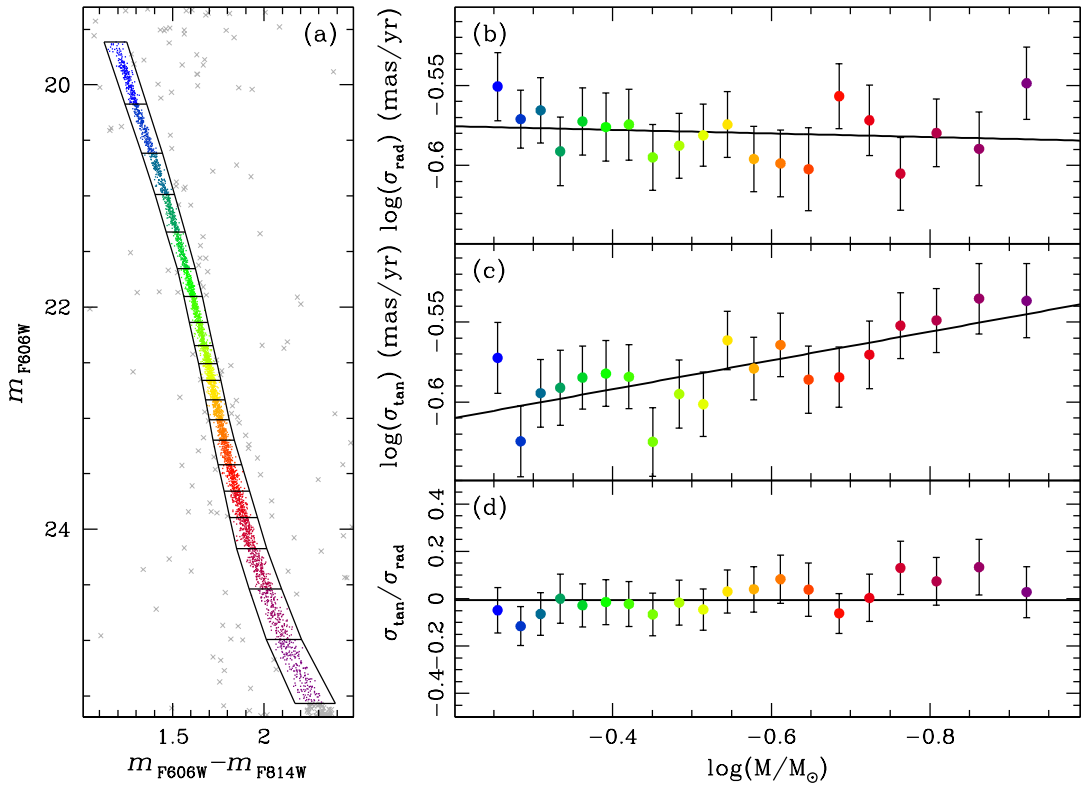

FIGURE 7.25: Energy equipartition in the field F0 of NGC 6752. (a) $m_{F606W} - m_{F814W}$ vs. m_{F606W} CMD of the MS divided into 20 equally populated bins, coloured from blue to purple moving toward fainter bins. We used the same Dotter et al. (2008) isochrone applied in Milone et al. (2019) to transform stellar magnitudes into solar masses. (b)-(c) velocity dispersion profile of the bins as a function of stellar mass in a log–log plane for the radial and tangential components, respectively. The black lines represent the least-square fit of the bins. (d) $(\sigma_{tan}/\sigma_{rad} - 1)$ as a function of the stellar mass. The black horizontal line represents the weighted mean of the bins.

the age, $t = 12.5$ Gyr, distance modulus, $(m - M)_0 = 12.95$, and reddening $E(B - V) = 0.07$. We converted the reddening into absorption in the F606W and F814W bands by using the relations: $A_{F606W} = 0.90328 \times E(B - V)$ and $A_{F814W} = 0.59696 \times E(B - V)$.

Panel (b) and (c) of Figure 7.25 show the velocity dispersion profile of each bin as a function of the stellar mass for the radial and tangential components, respectively. The black line is the least-square fit of the bins. While for the radial component, the stars are consistent with being in nearly no energy equipartition, in the tangential direction the stars show some sign of equipartition, with a slope of $\eta_{tan} = 0.09 \pm 0.02$. Panel (d) of Figure 7.25 shows the $(\sigma_{tan}/\sigma_{rad} - 1)$ as a function of the stellar mass. The black horizontal line at $(\sigma_{tan}/\sigma_{rad} - 1) \sim 0$ represents the weighted mean of the bins. As can be seen, the anisotropy between the two components is negligible. We combined together the two components and found a value of $\eta = 0.04 \pm 0.02$. We then conclude that MS stars in field F0 are consistent with being in nearly *no energy equipartition*.

7.8.4 The field F1

As can be seen from Table 7.1, the field F1 was observed by HST for a total of 3 epochs. The first epoch was analysed in Milone et al. (2019) which found that the three main populations (A, B, and C), previously observed in the brightest part of the color-magnitude diagram (Milone et al., 2013; Milone et al., 2017a; Nardiello et al., 2015a), define three distinct sequences that run from the main-sequence (MS) knee towards the bottom of the MS ($\sim$0.15 $M_{\odot}$).

Here we made use of all three epochs to provide a kinematic study of the stars in the field F1. We estimate the proper motions of the stars following a method similar to that described in Bellini et al. (2014) and Bellini et al. (2018). We fit the positions of the stars in each image as a function of the epoch with a least-square straight line. The slope of this line, computed after a few iterations, gives a direct measurement of the PM. We then plotted the combined PM value of each star as a function of the $m_{\rm F160W}$ magnitude and defined by hand a line to remove field stars.

We initially removed a few outliers using a set of photometric quality parameters in close analogy of what was done in Scalco et al. (2021). The photometry was corrected for zero-point spatial variations following the recipes of Milone et al. (2012a). Panel (a) of Figure 7.26 shows the $m_{F110W} - m_{F160W}$ vs. m_{F110W} CMD of the 3.105 selected sources. As can be seen, we can clearly identify three different sequences, corresponding to the three different stellar populations of NGC 6752 found in Milone et al. (2013), Milone et al. (2017a), and Nardiello et al. (2015a)) and in Figure 7.18. We define by hand two fiducial lines to verticalise the diagram. Panel (b) of Figure 7.26 shows the $m_{F110W} - m_{F160W}$ vs. m_{F110W} verticalised CMD. We define two vertical lines at $\Delta_{F110W,F160W} = -0.25$ and $\Delta_{F110W,F160W} = 0.3$ to separate the three different stellar populations, MSa (green), MSb (magenta) and MSc (blue). We found a total of 663 MSa ($\sim$ 33%), 891 MSb ($\sim$ 44%) and 458 MSc ($\sim$ 23%) stars. These values are similar to that obtained in Milone et al. (2019).

We evaluated the velocity dispersion profile of the three components using a procedure similar to that in previous sections. We initially removed all the stars with large PM errors and χ^2 values. We plotted the PM errors and χ^2 values of the sources, in both directions, as a function of the m_{F160W} magnitude and verified that most of the stars follow a clear trend. We divided the sample into bins of 0.5 m_{F160W} magnitude and evaluated for each bin the 68th percentile of the distribution. We then interpolated the the points corresponding to the 68th percentile with a spline and removed all the sources above the interpolating line. We applied this procedure to both directions, separately.

We evaluated the membership probability of the sources following the method described in Balaguer-Núnez, Tian, and Zhao (1998), Bellini et al. (2009), Nardiello et al. (2018), and Scalco et al. (2021). We then removed all the sources with a membership probability of less than 80%.

After this cleaning, we found a total of 197 MSa, 288 MSb and 163 MSc stars. We divided the stars that survived the selection in 6, 9 and 5 equally populated bins for MSa, MSb and MSc, respectively. We used equations 2 and 3 to estimate the velocity dispersion of each bin. Figure 7.27 shows the radial distribution of the velocity dispersion profile in the radial (panel (a)) and tangential (panel (b)) direction for the three populations. The bins are over-plotted with the best-fitting Plummer model (see equation 4). The values of σ_0 for each population are reported in Table 7.10 for both radial and tangential components.

Following the procedure described in the previous subsection, we studied the state of the energy equipartition for the three different stellar populations. Figure

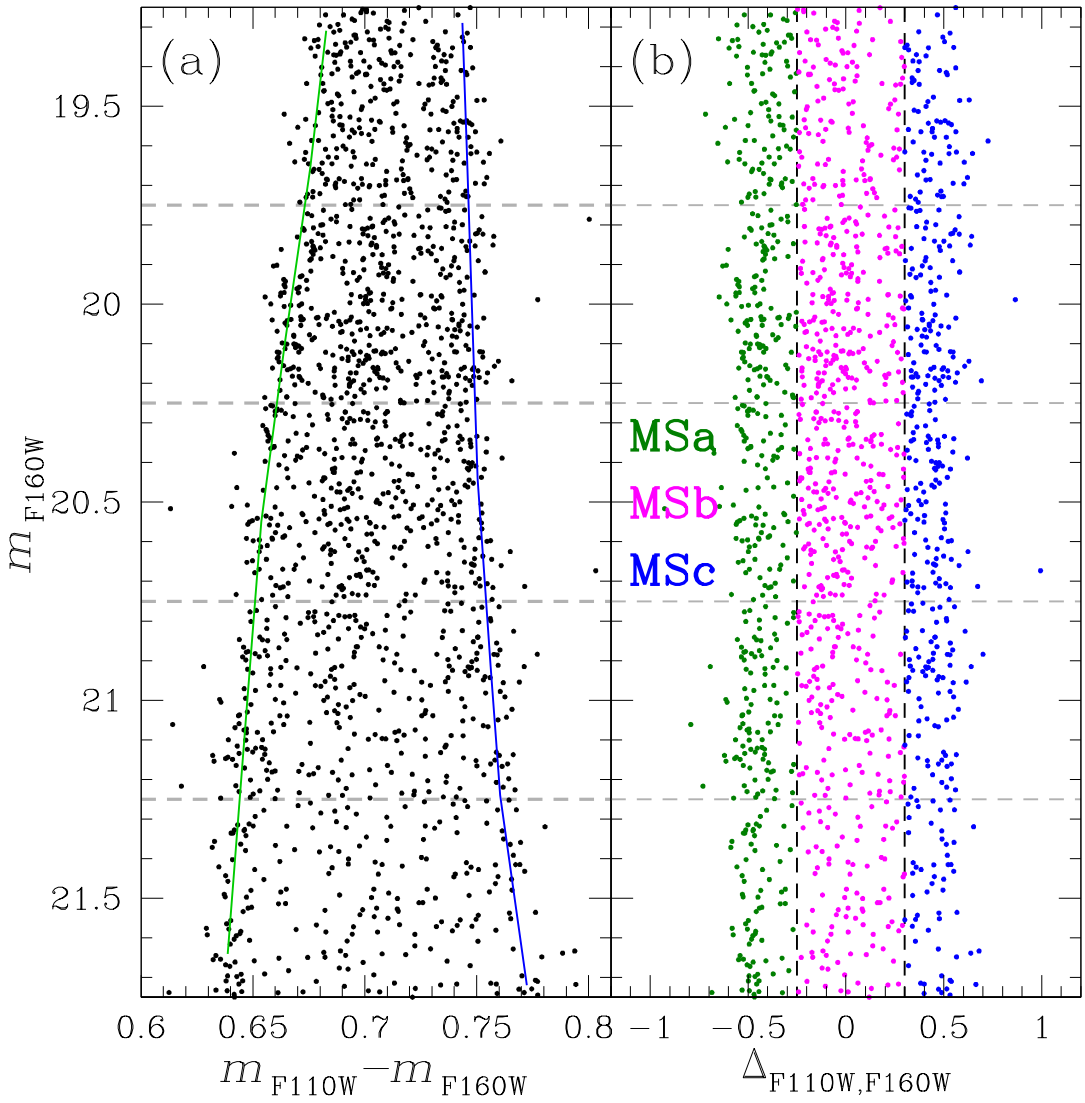

FIGURE 7.26: (a) $m_{F110W} - m_{F160W}$ vs. m_{F110W} CMD of NGC 6752. We drew by hand two fiducial lines to verticalise the diagram. (b) $m_{F110W} - m_{F160W}$ vs. m_{F110W} verticalised CMD.

TABLE 7.10: Values of σ_0 for the radial and tangential components and anisotropy for each stellar population of Figure 7.26 and 7.27.

Values of σ_0 for the radial and tangential components and anisotropy for each stellar population of Figure 7.26 and 7.27.

	MSa	MSb	MSc
$\sigma_{0,rad}$	0.483±0.021	0.462±0.019	0.457±0.035
$\sigma_{0,tan}$	0.483±0.029	0.454±0.018	0.487±0.029
$< \sigma_{rad}/\sigma_{tan} - 1 >$	-0.079±0.094	-0.003±0.080	-0.052±0.096

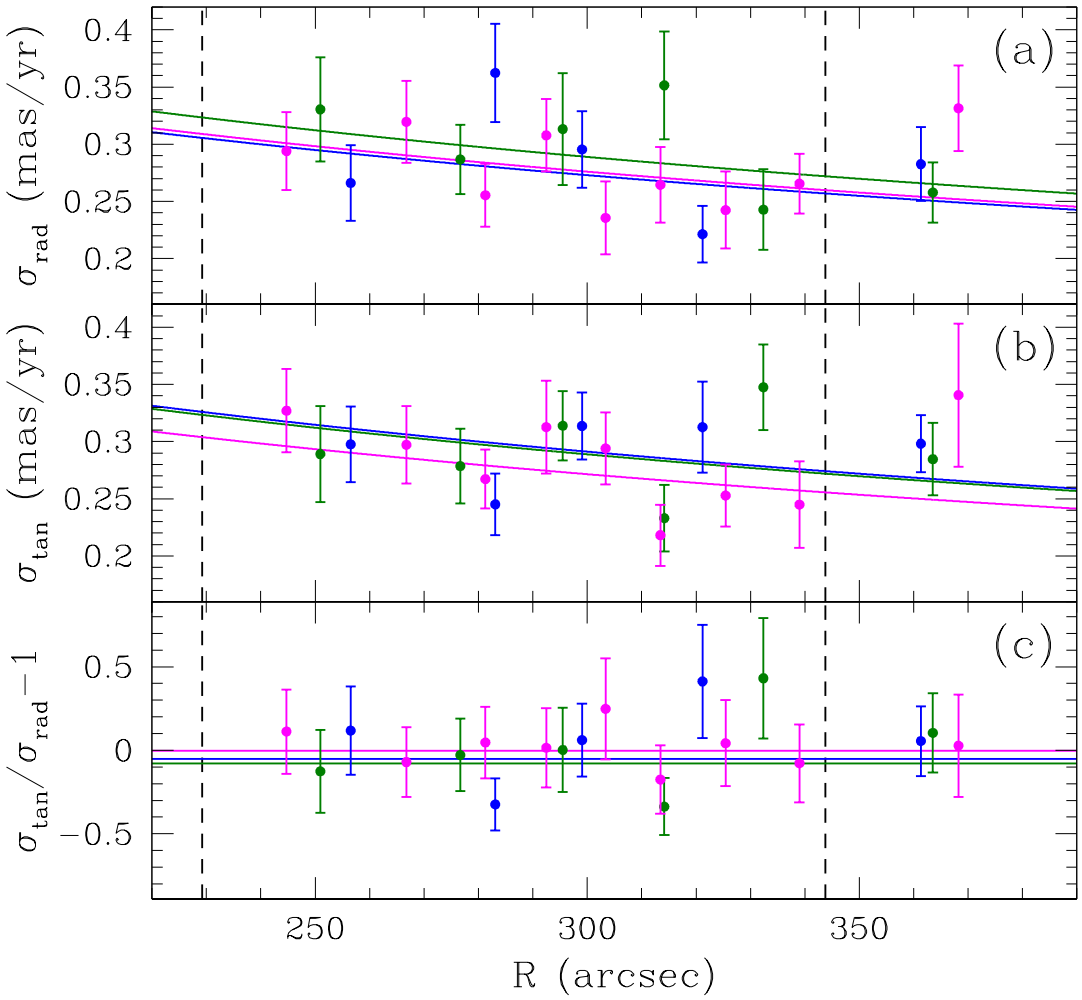

FIGURE 7.27: As in Figure 7.20 and 7.22 but for the stars shown in Figure 7.26.

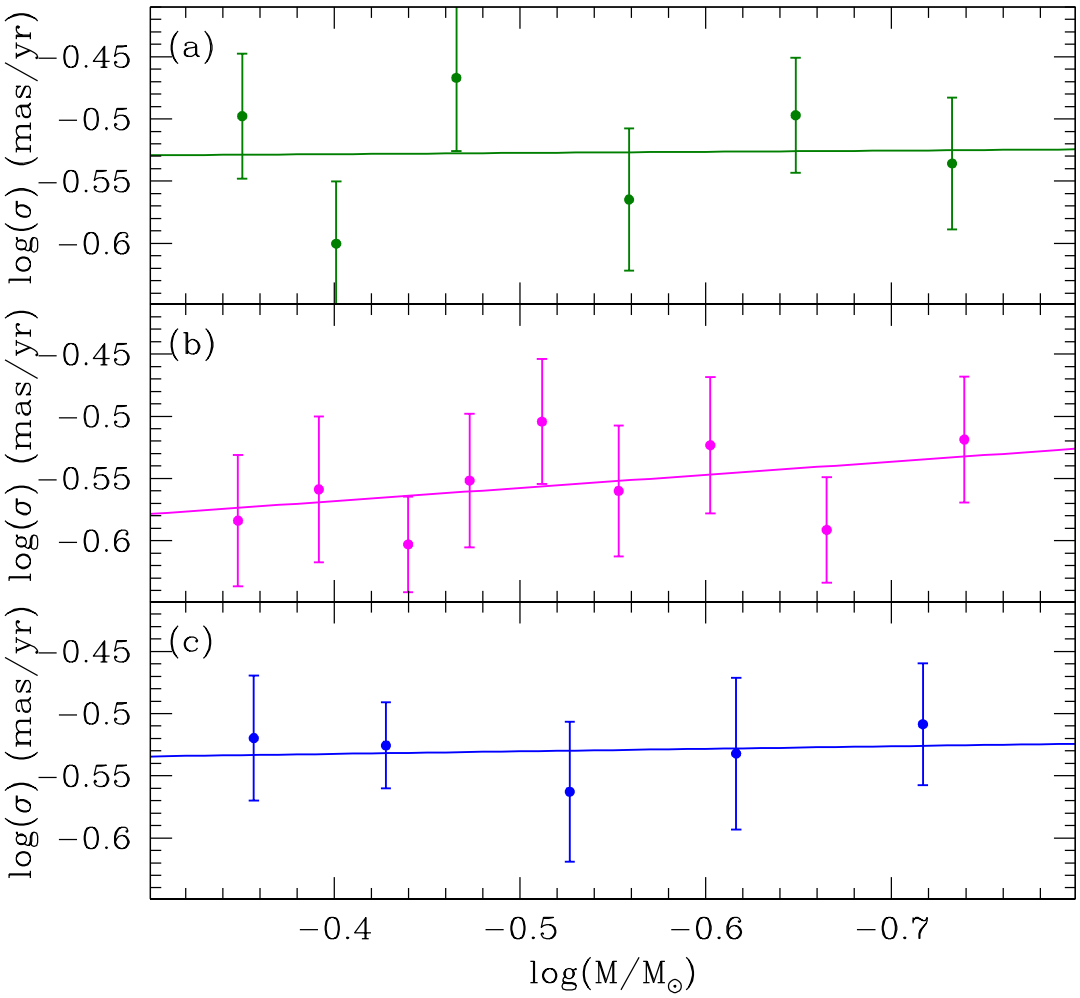

FIGURE 7.28: Energy equipartition for the three stellar populations MSa, MSb and MSc in the infrared field. a-b-c velocity dispersion as a function of the stellar mass for MSa, MSb and MSc stars, respectively.

7.28 shows the velocity dispersion as a function of the stellar mass for MSa (panel (a)), MSb (panel (b)) and MSc (panel (c)) stars. While populations MSa and MSc do not show any significant trend with the stellar mass ($\eta_{MSa} = 0.009 \pm 0.167$ and $\eta_{MSc} = 0.02 \pm 0.08$), population MSb shows a certain degree of energy equipartition, with a value of $\eta_{MSa} = 0.10 \pm 0.09$.

7.8.5 LOS velocity dispersion

We make use of the LOS velocity catalogue provided by Baumgardt and Hilker (2018) to study the velocity dispersion of NGC 6752 in the LOS direction. We selected all the stars, belonging to the SGB+RGB+RGB-tip sequence, that survived the selection in panel (a) of Figure 7.10 and with a Gaia G magnitude 12<G<17. Panel (a) of Figure 7.29 shows the LOS velocity of the 1.014 stars that survived the selections as a function of the radial distance from the cluster centre. The values are scaled by the absolute LOS velocity $< V_{sist} >= -26.0482$ found in section 4. We binned the stars in intervals of Gaia G magnitude, in such a way that each bin contain the $\sim$ 10% of the sources in the sample. For each bin, we derived the velocity dispersion using equations 2 and 3. The LOS velocity dispersion profile is shown in panel (b) of Figure 7.29. The LOS velocity dispersion profile is over-plotted with the best-fitting

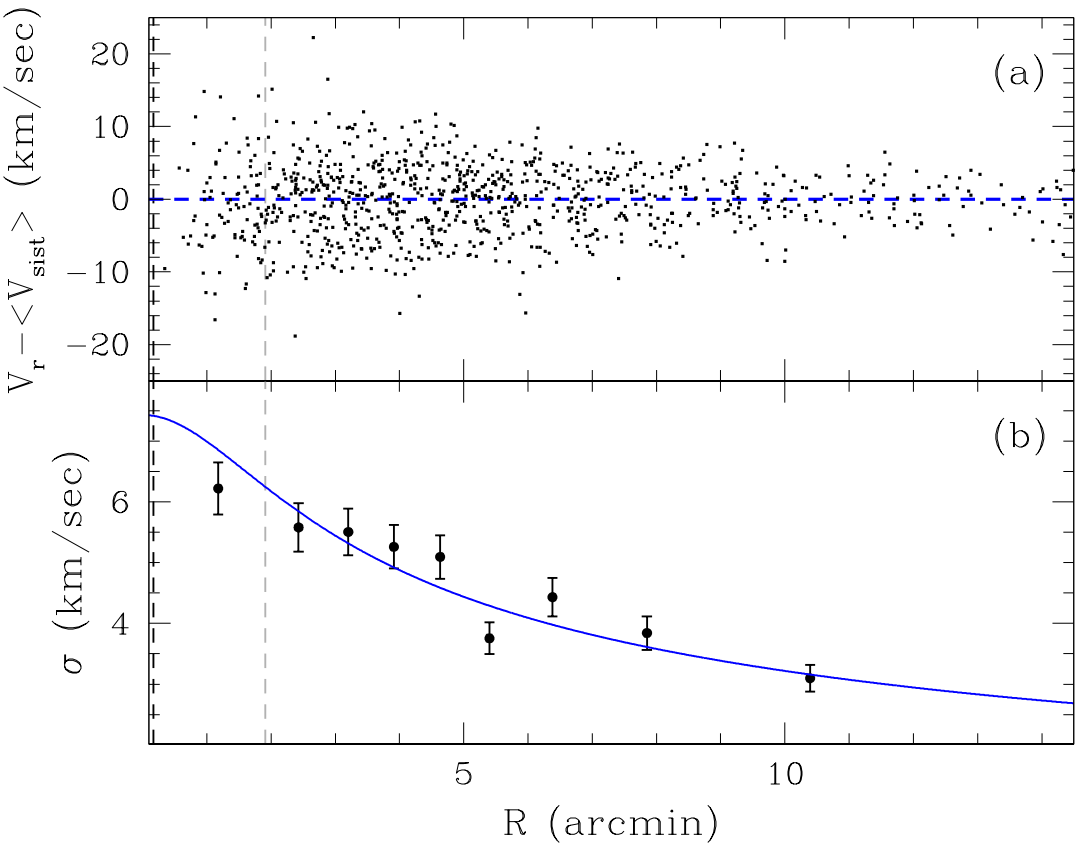

FIGURE 7.29: (a) LOS velocity, scaled by $< V_{sist} >= -26.0482$, of the stars that survived the selections as a function of the radial distance from the cluster centre. The blue horizontal dashed line represents a LOS velocity equal to 0. (b) LOS velocity dispersion profile. The bins are over-plotted with the best-fitting Plummer model.

Plummer (1911) model (see equation 4). We obtain a value of the central dispersion $\sigma_0 = 7.44 \pm 0.04$ (km/sec) which is in agreement within 1.3σ with the value reported by Lardo et al. (2015).

7.8.6 The velocity dispersion profile of NGC 6752

In section 8.1 we presented the velocity dispersion profile of NGC 6752 using Gaia EDR3 data. Here we provide the velocity dispersion profile of the cluster by combining Gaia eDR3 and HST data.

We made use of the proper motion catalogue provided by Libralato et al. (2022) and the proper motion of the field F0, as derived in section 8.3, to derive the velocity dispersion profile of the central and F0 fields. Again, we followed the method described in Libralato et al. (2022) and Watkins et al. (2015). We cut all the stars with $N_{found}/N_{used} < 0.9$, $\chi^2_x > 1.5$ and $\chi^2_y > 1.5$, PM error larger than 0.1 mas yr^{-1}. We then removed all the sources with a membership probability less than 80% and restricted our analysis to stars with a magnitude $m_{F606W} < 18.7$ and $22.7 < m_{F606W} < 19.7$ for the central and F0 fields, respectively. Finally, we removed a few outliers using the CMD, following the procedure described in Section 3 (see panel (b) of Figure 8.4). After these quality selections, we found a total of 9.424 and 2.323 for the central and F0 fields, respectively. We divided the two samples into 20 and 10 equally

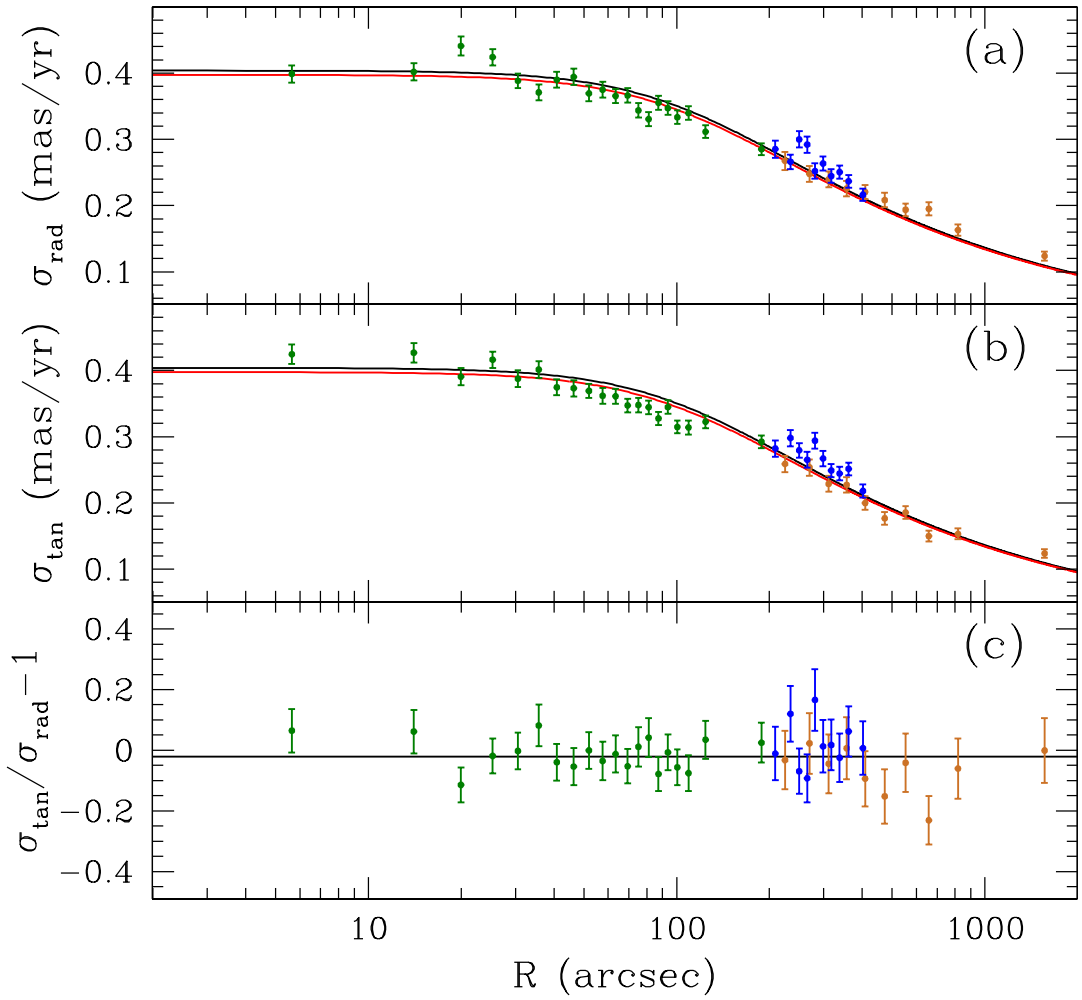

FIGURE 7.30: Velocity dispersion profile of NGC 6752 obtained combining Gaia EDR3 data (ocher dots), HST central field data (green dots) and HST filed F0 data (blue dots). (a)-(b) velocity dispersion profile for the radial and tangential components, respectively. The black and red lines represent the best-fitting Plummer model for the radial and tangential components, respectively. (c) $\sigma_{tan}/\sigma_{rad} - 1$ as a function of the radial distance. The black horizontal line represents the weighted mean of the bins.

populated bins, respectively, and derived the velocity dispersion of each bin using equations 2 and 3.

Figure 7.30 shows the velocity dispersion profile of NGC 6752, for both the radial (panel (a)) and tangential (panel (b)) components. The ocher, green and blue points represent the velocity dispersion values obtained using the Gaia EDR3, central field and field F0 stars, respectively. The velocity dispersion profiles are over-plotted with the best-fitting Plummer (1911) model (see equation 4). We obtained a central value of $\sigma_{0,rad} = 0.404 \pm 0.004$ and $\sigma_{0,tan} = 0.397 \pm 0.004$ for the radial and tangential components, respectively. Panel (c) of Figure 7.30 shows the $\sigma_{tan}/\sigma_{rad} - 1$ as a function of the radial distance. The horizontal line at $\sigma_{tan}/\sigma_{rad} - 1 = -0.021 \pm 0.011$ represents the weighted mean of the bins.

7.8.7 Kinematic distance

In this subsection, we provide an estimate of the distance of NGC 6752 through kinematic measurements. For an isotropic GC, the relation between the velocity dispersion along the LOS and in the plane of the sky is:

$$\sigma_{LOS} = 4.74 d \sigma_{\mu} \tag{7.5}$$

where d is the distance in kpc, σ_{LOS} and σ_{μ} are the velocity dispersion along the LOS (km s^{-1}) and in the plane of the sky (mas yr^{-1}), respectively, and 4.7404 (km yr kpc^{-1} mas^{-1} s^{-1}) is the conversion factor. From the value of the central LOS velocity dispersion $\sigma_{LOS} = 7.44 \pm 0.04$ (km/sec) obtained above and the combined value of the radial and tangential component of the central velocity dispersion in the plane of the sky $\sigma_{\mu} = 0.401 \pm 0.02$ (mas/yr) we obtain a distance of $d = 3.91 \pm 0.41$ kpc.

7.9 Mass function

Here we used our HST catalogue to study the mass function of NGC 6752 both globally and separately for the three different stellar populations, and at a different radial distance from the cluster centre.

7.9.1 Central field

In this section, we investigate the MF for the central field (field in yellow in figure 7.3). The list of observations for the central field is provided in Table 7.1.

We used artificial stars (ASs) to determine the completeness level of the analysed sample. To perform the AS test we generated a catalog of 200,000 stars with fixed positions and magnitudes. Stars are randomly distributed within each FoV with the criterion of mimicking the radial distribution of the observed stars. The magnitude of ASs is derived so that stars are placed on the fiducial lines that reproduce the average distribution of cluster stars in the observed CMDs.

We initially examined the mass function of the central field of NGC 6752 as a whole, without distinguishing between the three multiple stellar populations. To achieve this, we exclusively utilized the F606W and F814W filters that cover the entire field.

To identify a reliable sample of stars, we made use of various photometric and astrometric quality parameters provided by KS2, following a similar approach to Scalco et al. (2021). These parameters include the random mean scatter of photometric measurements, the QFIT parameter and the RADXS parameter. We then selected stars based on their position in the CMD. Finally, we selected a sample of probable cluster members using the position of the stars in the vector point diagram.

We determine the completeness level of the sample at different m_{F606W} magnitude bins using the AS. We considered a star recovered if the distance between the input and output position and magnitude is less than 1 pixel and 0.75 mag, respectively, and if it passes the criteria of selection adopted for real stars. Completeness is calculated as the fraction of recovered stars on the input stars in different magnitude bins. Figure 7.31 shows the completeness level as a function of the m_{F606W} and m_{F814W}.

We converted magnitudes into stellar masses via isochrone fitting, for which we used isochrones from the Dartmouth Stellar Evolution Database (Dotter et al., 2008). We adopted cluster metallicities [Fe/H] from Harris (1996) and assumed primordial

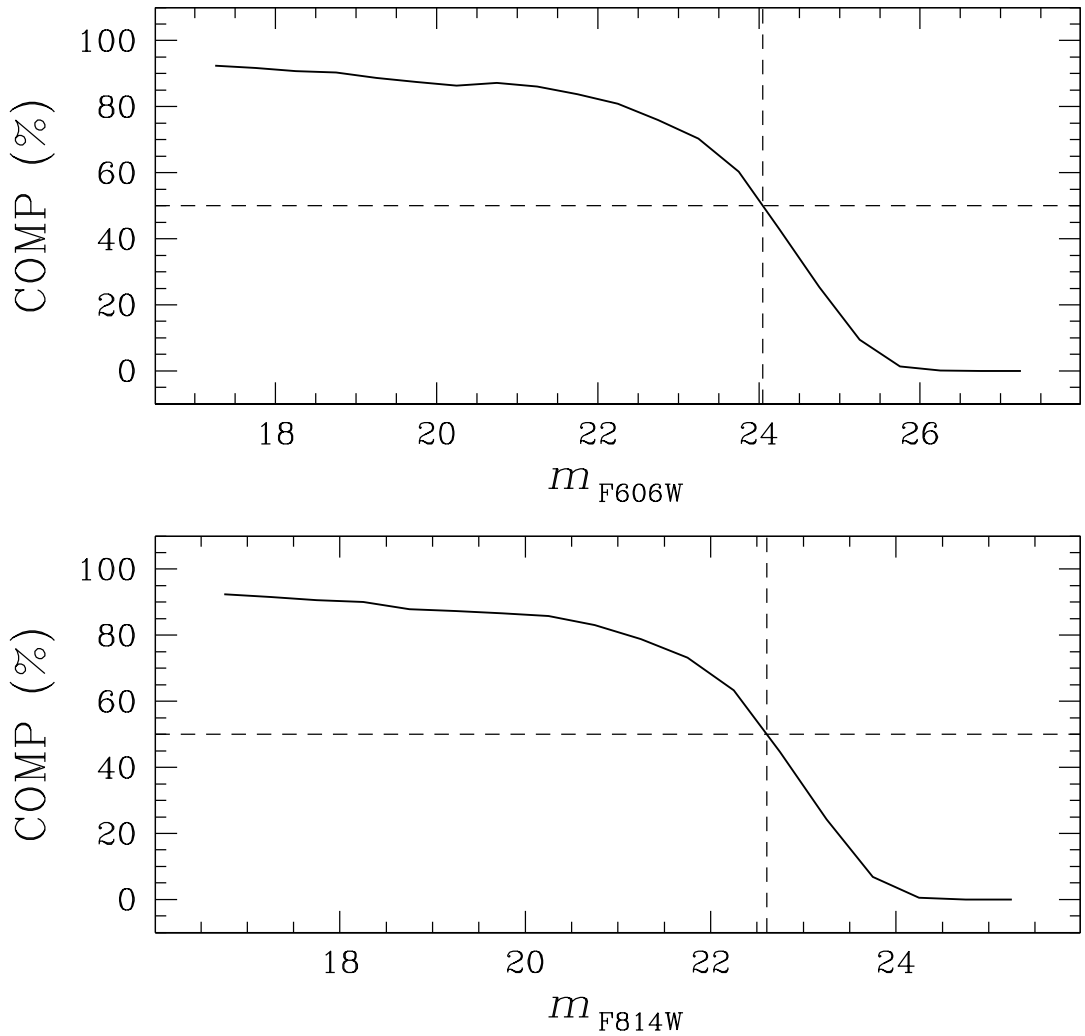

FIGURE 7.31: Completeness based on AS test for the F606W and F814W filter, for the central field.

helium abundance (Y = 0.246). We assumed [α/Fe] = + 0.2 (Dotter et al., 2010) and adopted age, distance modulus, and reddening that best fit the data. We then associated with each star the corresponding mass in the interpolating isochrone. The left panel of figure 7.32 shows the $m_{\rm F606W} - m_{\rm F606W}$ vs. $m_{\rm F606W}$ CMD for the stars that survived the selections, while the red line represents the interpolating isochrone. The central and right panels represent the number count of stars as a function of the $m_{\rm F606W}$ magnitude and mass (black points), and the number cont of stars corrected for completeness (green points). Finally, figure 7.33 shows the mass function for the central field.

We made use of the chromosomic map presented in figure 7.18 and 7.21 to separate and identify the three stellar populations in the central field but with a larger magnitude extend (17.5<m_{F814W}<19.5) for the stars in the MS, in order to extend as much as possible the MF.

Figure 7.34 shows the MF of the three different stellar populations. As can be seen, population A is characterised by a slope of the mass function, $\alpha_A = 2.338 \pm 0.269$, much higher than populations B and C ($\alpha_B = 1.805 \pm 0.267$ and $\alpha_C = 0.91 \pm 0.206$). We divide the sample of stars into two radial bins ($0 < r/r_h < 0.5$ and $0.5 < r/r_h < 1$), and evaluated for each bin the mass function of the three stellar populations following the process used above. The results are shown in figure 7.35 and 7.36 for the inner and outer bins, respectively. As one can expect the slope of the mass function for the three stellar populations is much lower in the external bin, which is in agreement with the results presented in figure 7.33 for the global mass function.

7.9.2 Field F1 and F2

As we saw in the previous section, fields F1 and F2 (together with the central field) contain sufficient filter coverage to separate and identify the multiple stellar populations in NGC 6752. Multiple stellar populations are identifiable in the low MS for field F1 and in the MF for field F2. Given that the two fields are located at a similar radial distance from the cluster centre we can combine together the information from the two fields to obtain a unique and extended MF for the three stellar populations.

We studied the MF for the fields F1 and F2 following the same procedure illustrated in the previous subsection for the central field. Figure 7.37 and 7.38 show the obtained global MF for the fields F1 and F2, respectively.

We made use of the separation done in figure 7.26 and 7.19 to study the MF of the three stellar populations in the two fields. Figure 7.39 shows the mass function for the three stellar populations identified in the fields F1 and F2. The lower part of the MF (0.1<$M/M_\odot$<0.5) is given by the field F1 while the upper part (0.55<$M/M_\odot$<0.75) is given by the field F2.

In figure 7.40 and 7.41 are shown the MF for the three stellar populations, separated for the two fields F1 and F2 and their relative slope, represented with a dashed line. The slope of the MF for the three stellar populations are $\alpha_A = -0.523 \pm 0.098$, $\alpha_B = -0.327 \pm 0.164$ and $\alpha_C = -0.404 \pm 0.027$, respectively, for the field F1; while for the field F2 we obtain values of $\alpha_A = -2.504 \pm 3.177$, $\alpha_B = -1.763 \pm 1.435$ and $\alpha_C = -2.835 \pm 1.423$.

7.9.3 Fields F0 and F3

Since fields F0 and F3 don't provide the filter baseline necessary to separate and identify the different stellar populations, here we provide the global mass function

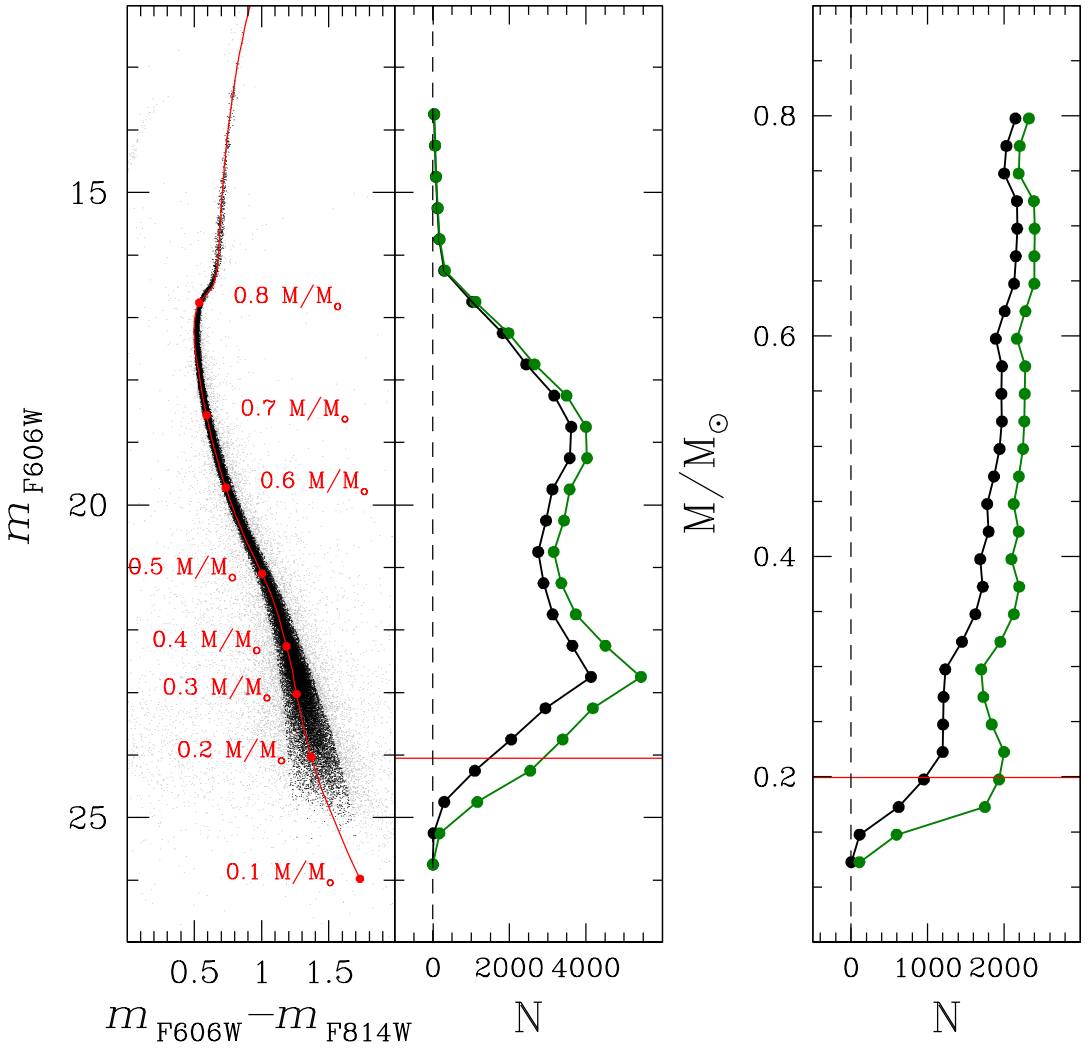

FIGURE 7.32: *Left panel*: $m_{F606W} - m_{F606W}$ vs. m_{F606W} CMD of the central field. Selected stars are represented in black while rejected stars are represented in grey. The red line represents the interpolating isochrone. *Middle panel*: Count number of stars (black points) and count number of stars corrected for completeness (green dots) as a function of the m_{F606W} magnitude. *Right panel*: Count number of stars (black points) and count number of stars corrected for completeness (green dots) as a function of mass. The red lines represent the 50% in completeness.

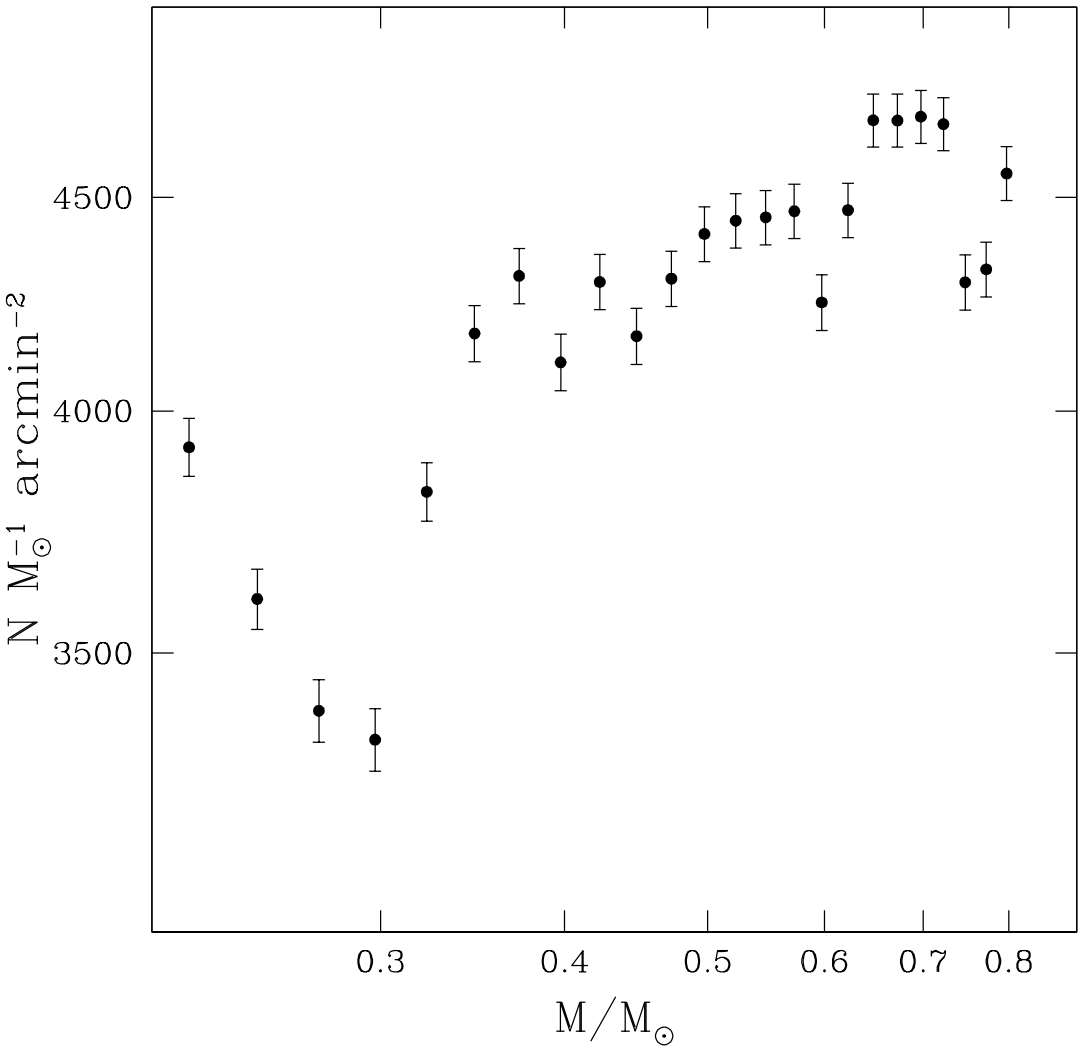

FIGURE 7.33: Mass function of the central field of NGC 6752.

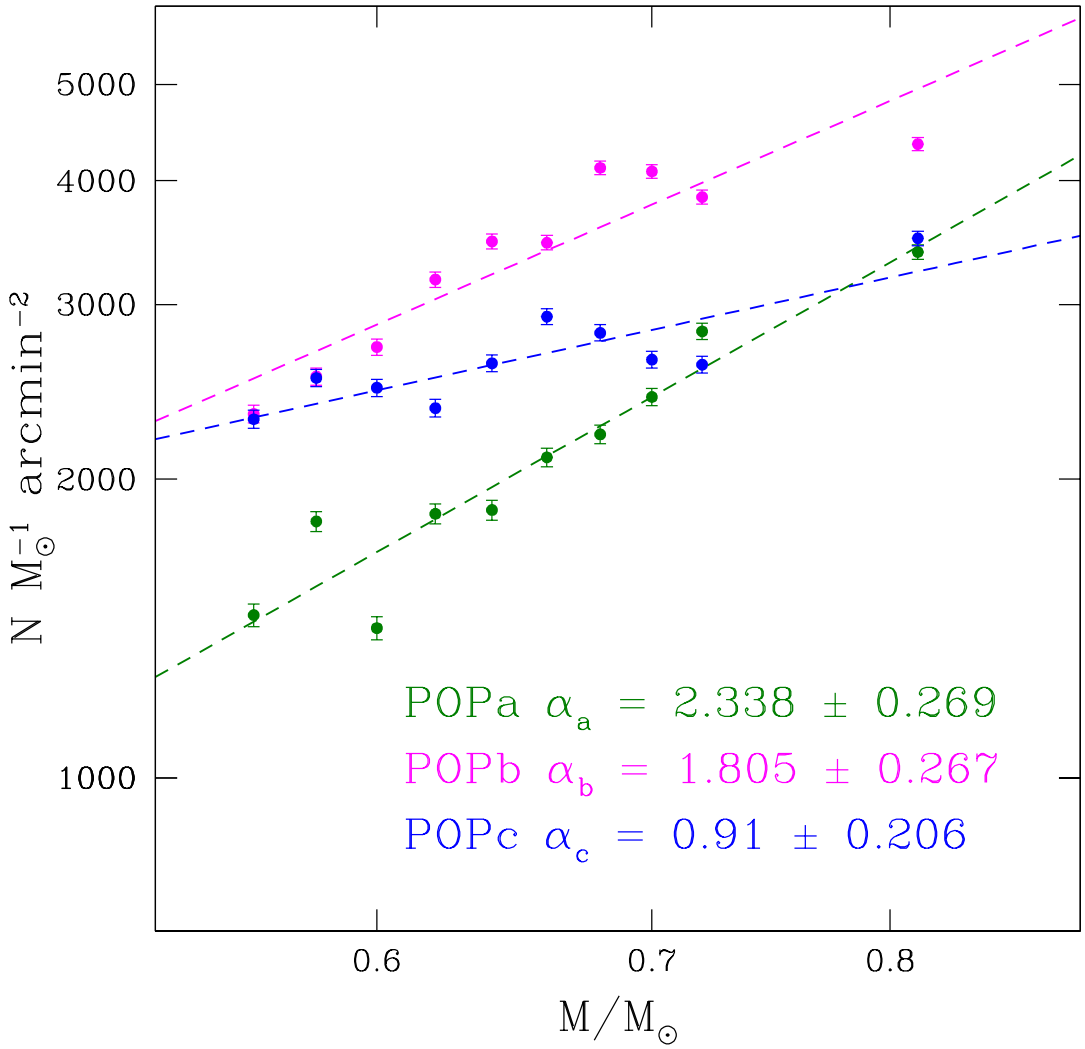

FIGURE 7.34: Mass function of the three different stellar populations for the central field (radial range $0 < r/r_h < 1$).

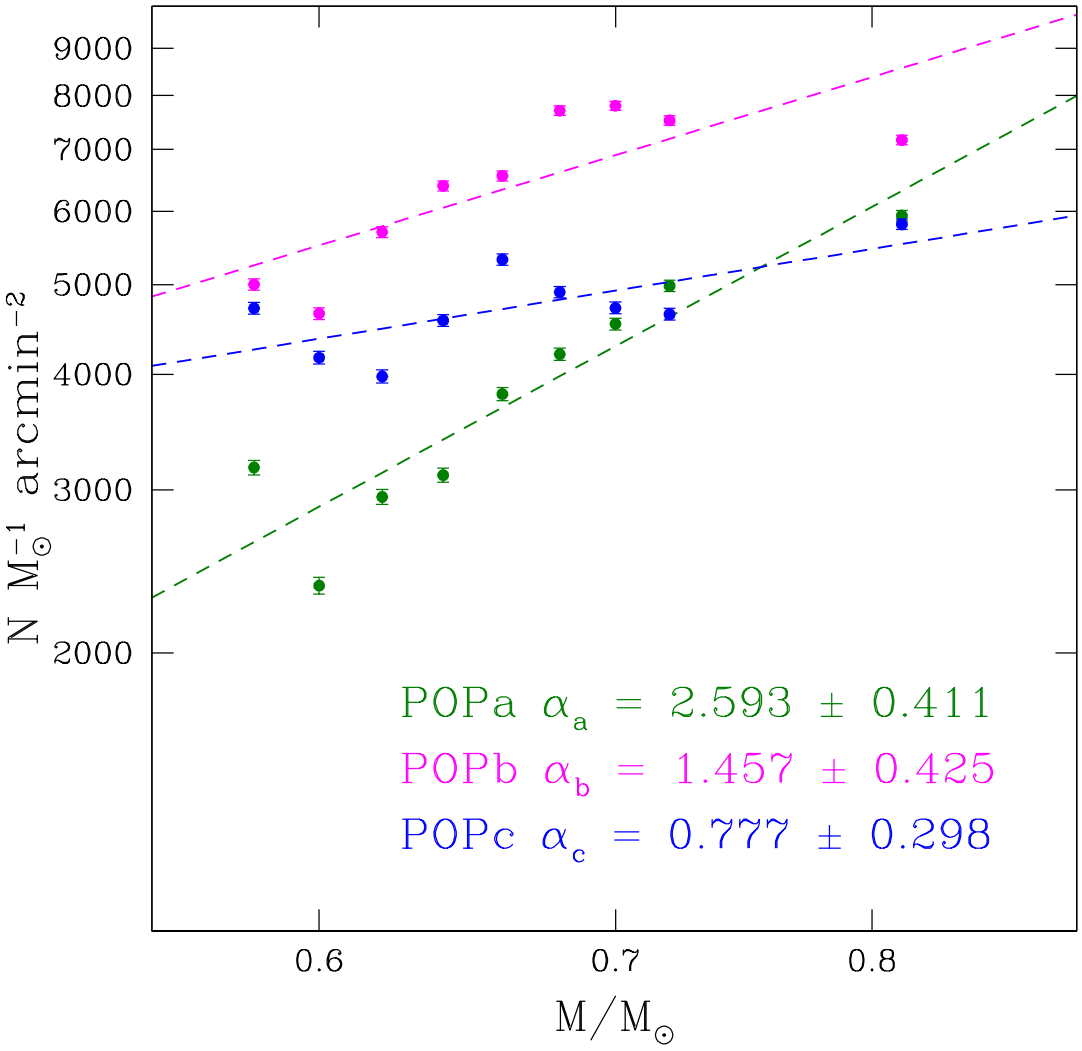

FIGURE 7.35: As for figure 10.10 but for the stars located at a distance from the cluster centre $0 < r/r_h < 0.5$.

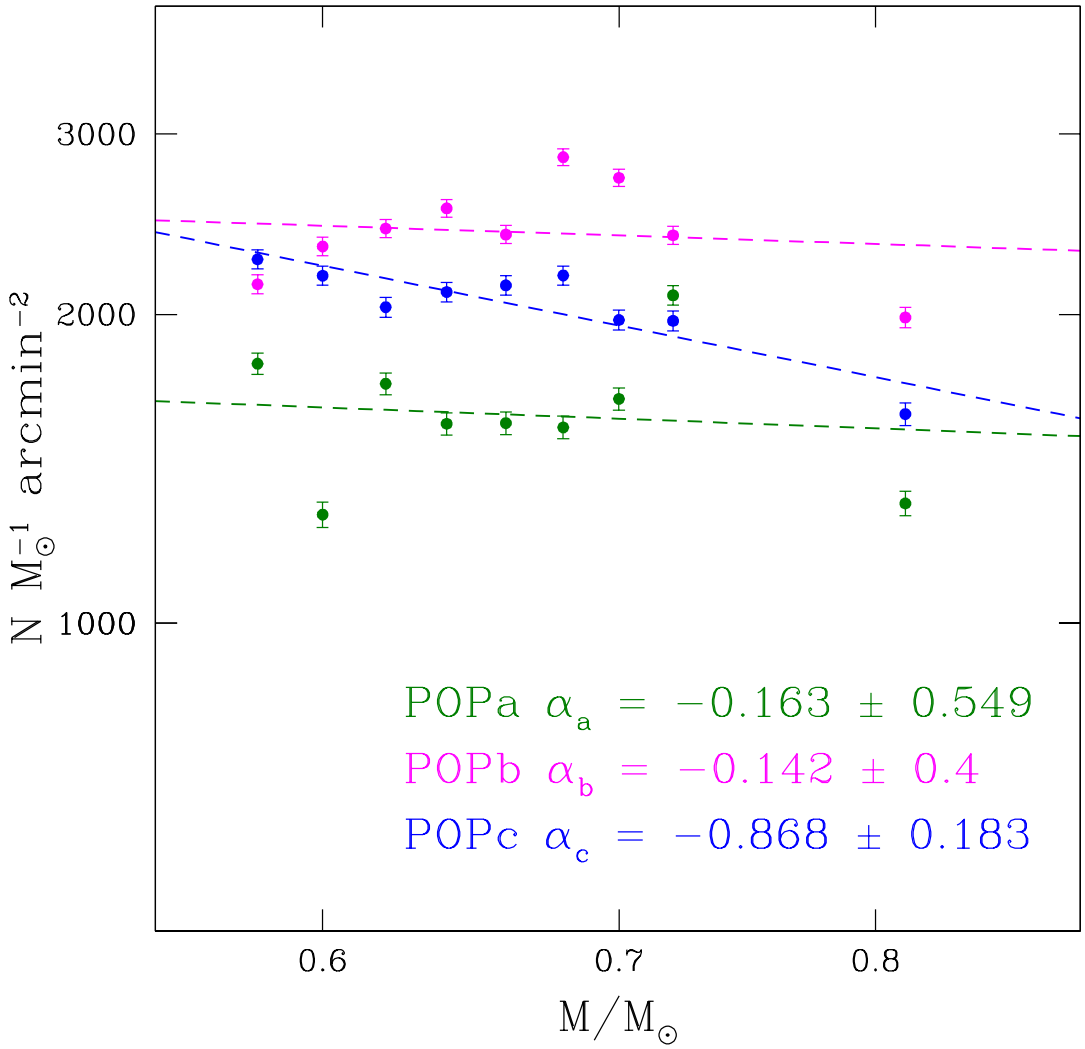

FIGURE 7.36: As for figure 10.10 but for the stars located at a distance from the cluster centre $0.5 < r/r_h < 1$.

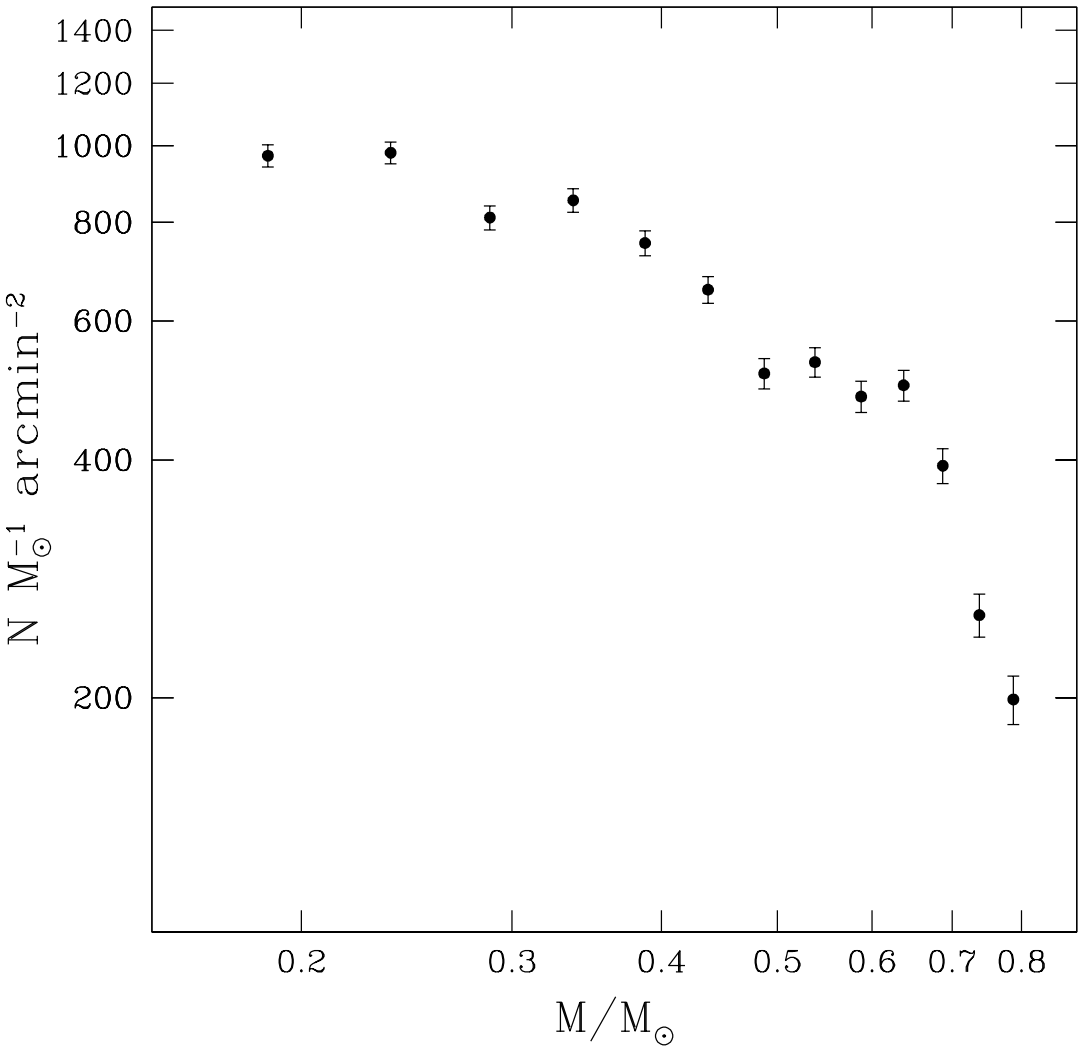

FIGURE 7.37: Mass function of the field F1.

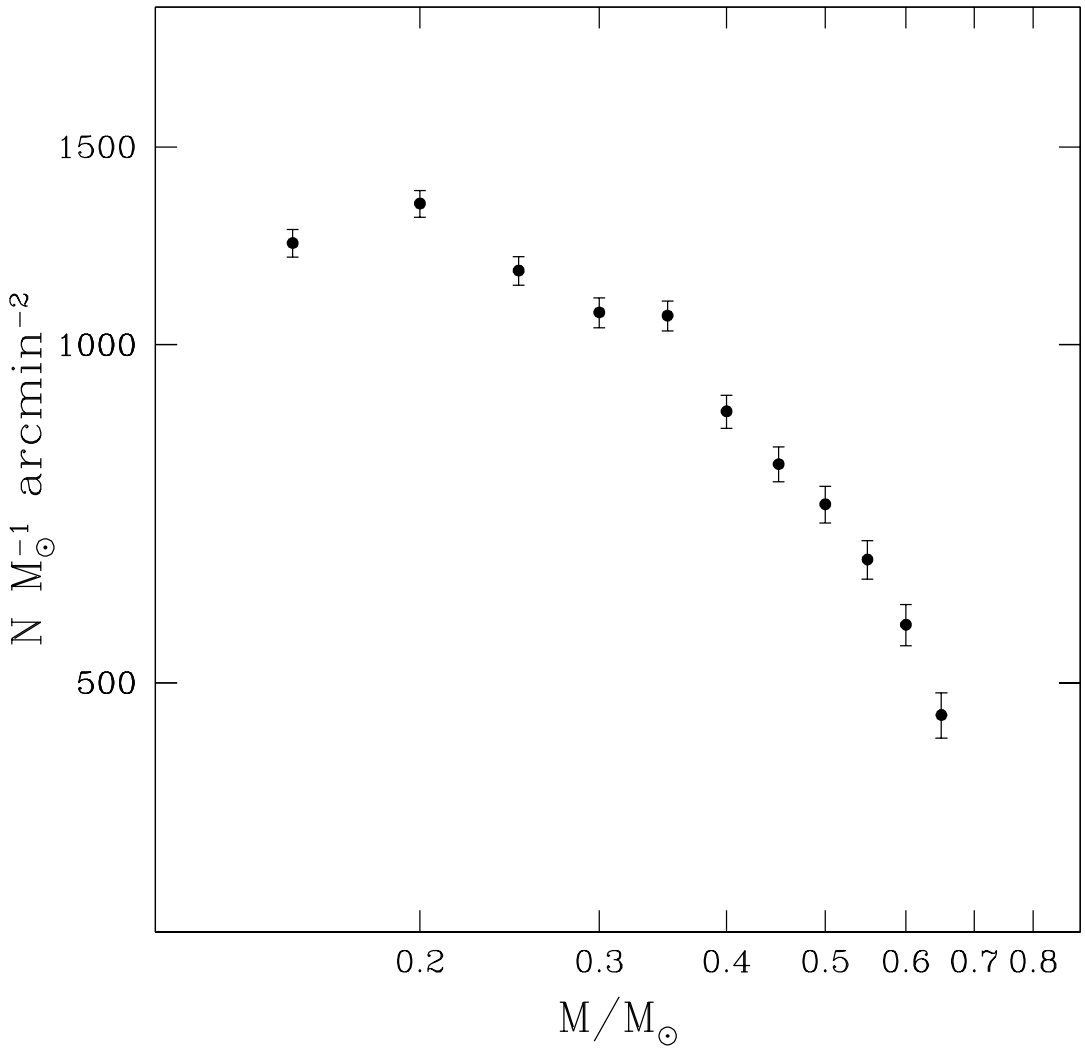

FIGURE 7.38: Mass function of the field F2.

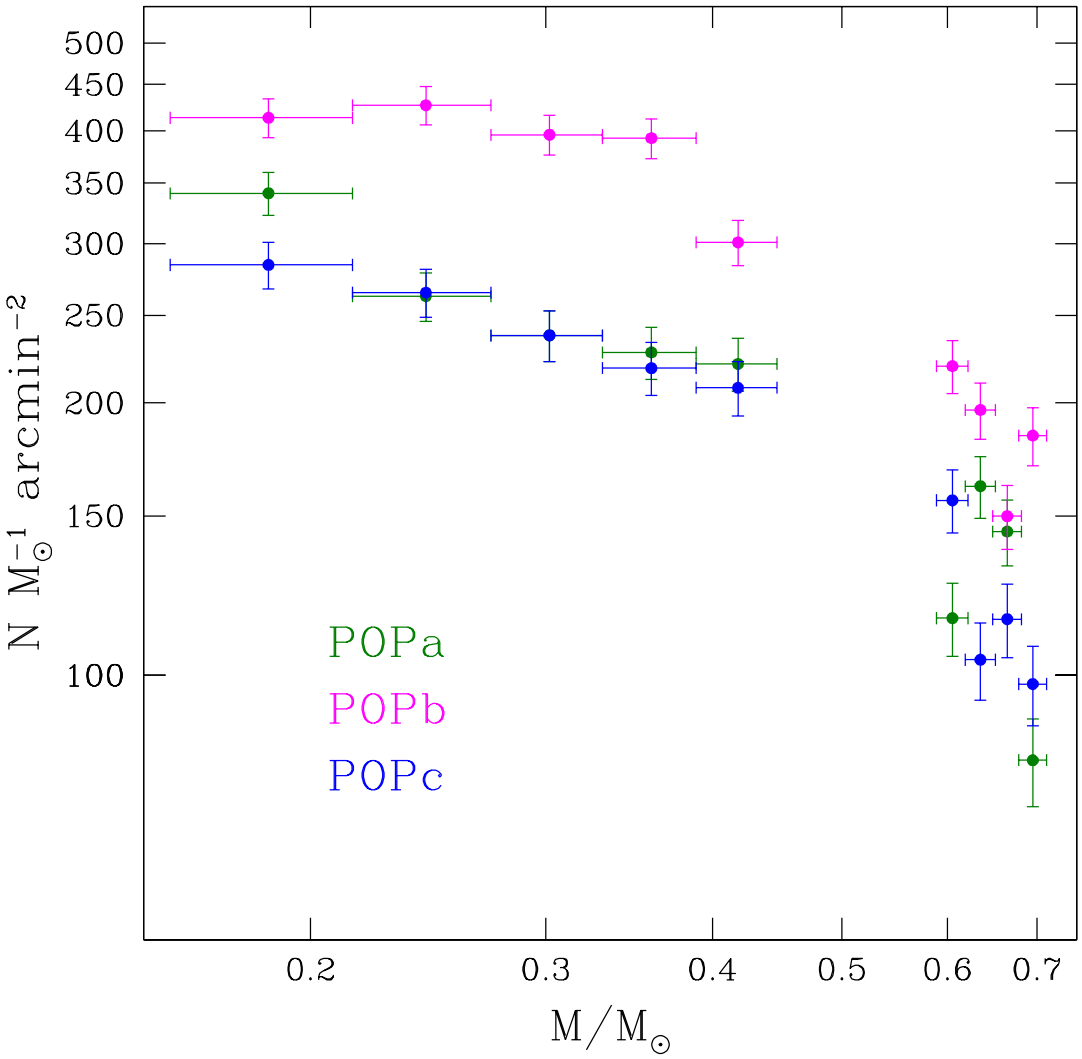

FIGURE 7.39: Mass function of the three stellar populations identified in figure 7.26 and 7.19 for the fields F1 and F2, combined together.

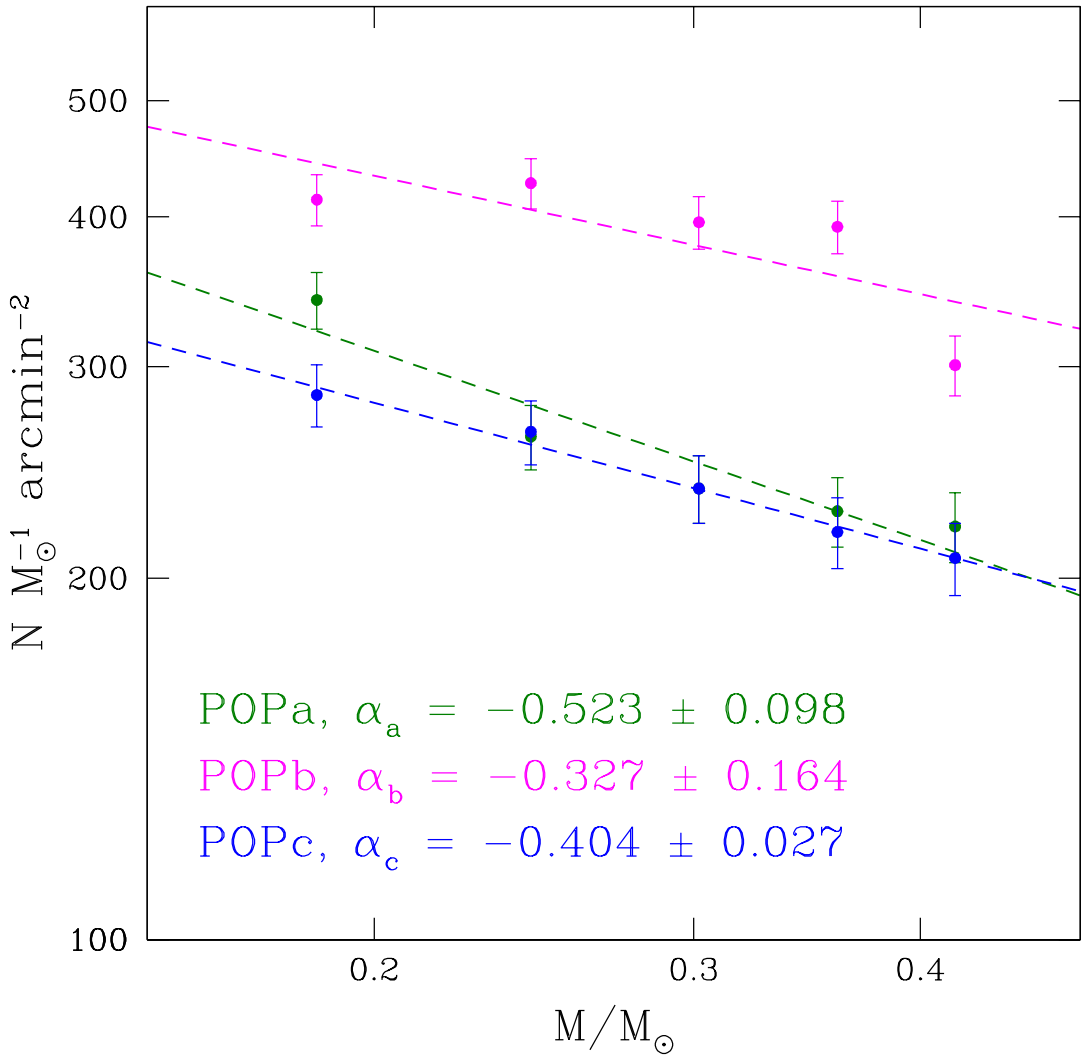

FIGURE 7.40: Mass function of the three different stellar populations identified in figure 7.26 for the field F1.

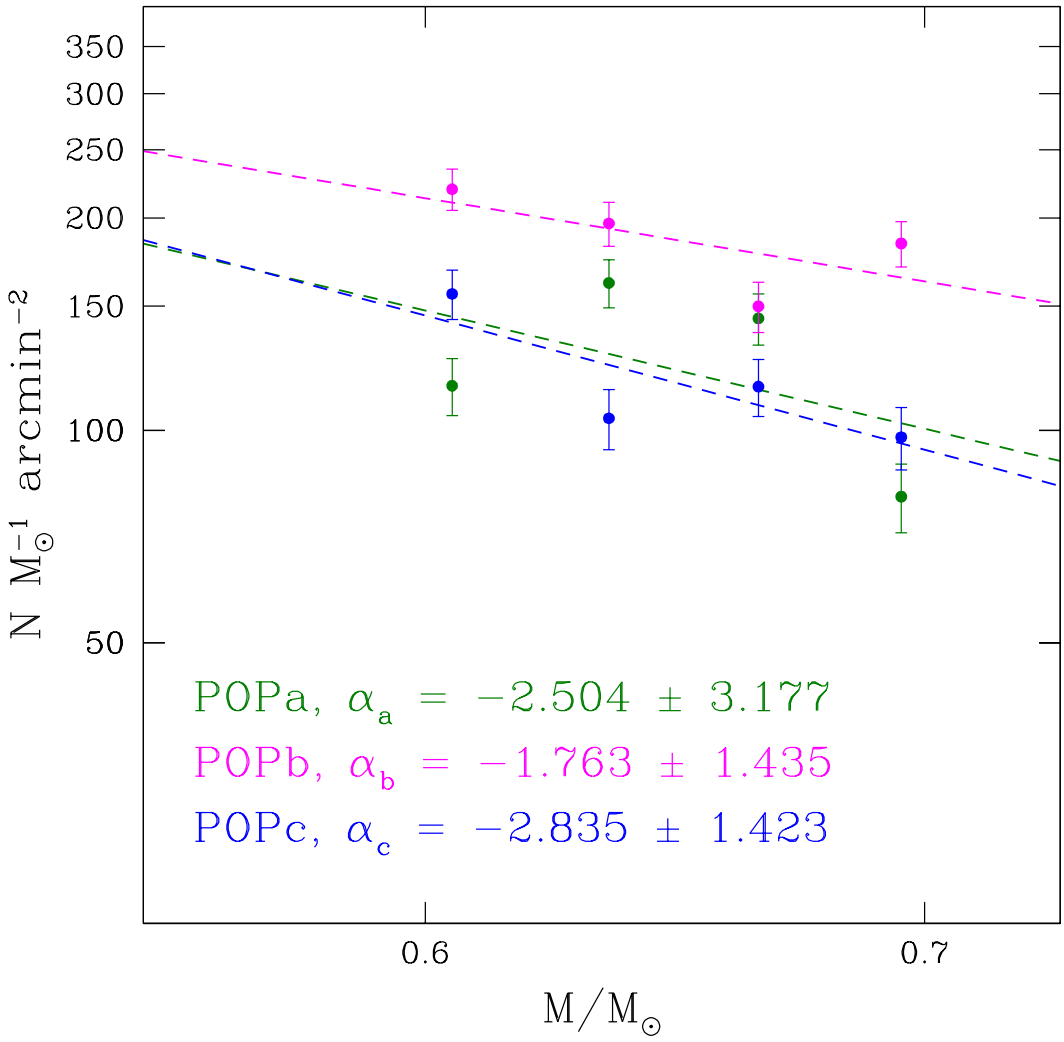

FIGURE 7.41: Mass function of the three stellar populations identified in figure 7.19 for the field F2.

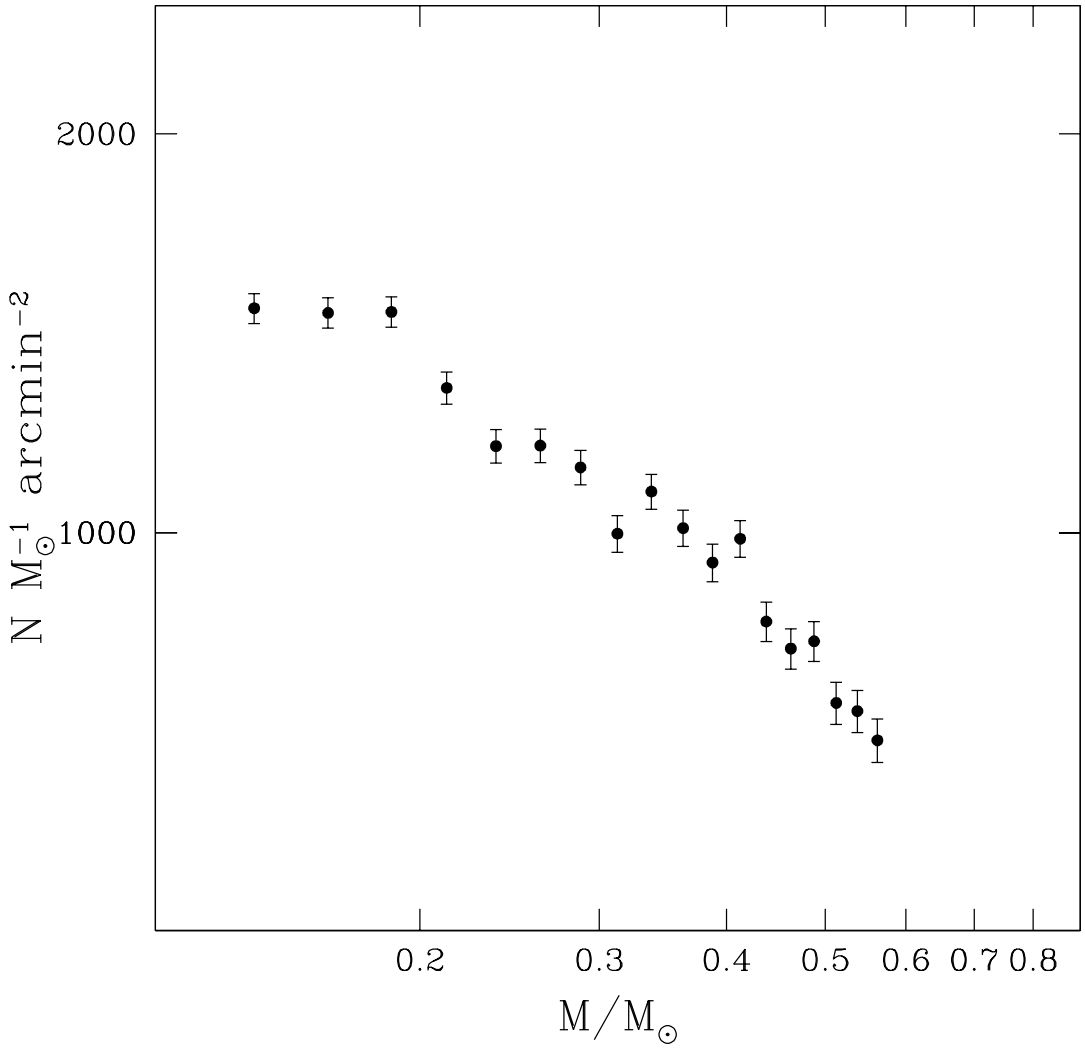

FIGURE 7.42: Mass function of the field F0.

for the stars in those fields. The mass function for the fields F0 and F3, obtained following the procedure described above, are shown in figure 7.42 and 7.43.

7.10 Summary

In this chapter, we presented a complete kinematic study of the globular cluster NGC 6752 using a wide range of data obtained with HST, Gaia and ESO/VLT-Keck. Together with the kinematics we also provided a study of the LF and MF of NGC 6752.

NGC 6752 is known to host three different stellar populations, namely A, composed of stars with primordial helium abundance (Y∼0.246), B and C, enhanced in helium by Y∼0.01 and 0.03, respectively (Milone et al., 2010; Milone et al., 2013; Milone et al., 2018c; Dotter et al., 2015). These three stellar populations have been identified and separated through the entire CMD, from the RGB and the upper MS to the M-dwarf regime (Milone et al., 2019).

We first of all estimated the absolute proper motion and parallax of NGC 6752 using data from the Gaia space telescope. We selected a sample of well-measured sources following the criteria applied by Soltis, Casertano, and Riess (2021). We selected a sample of cluster members by following a membership criterion based on

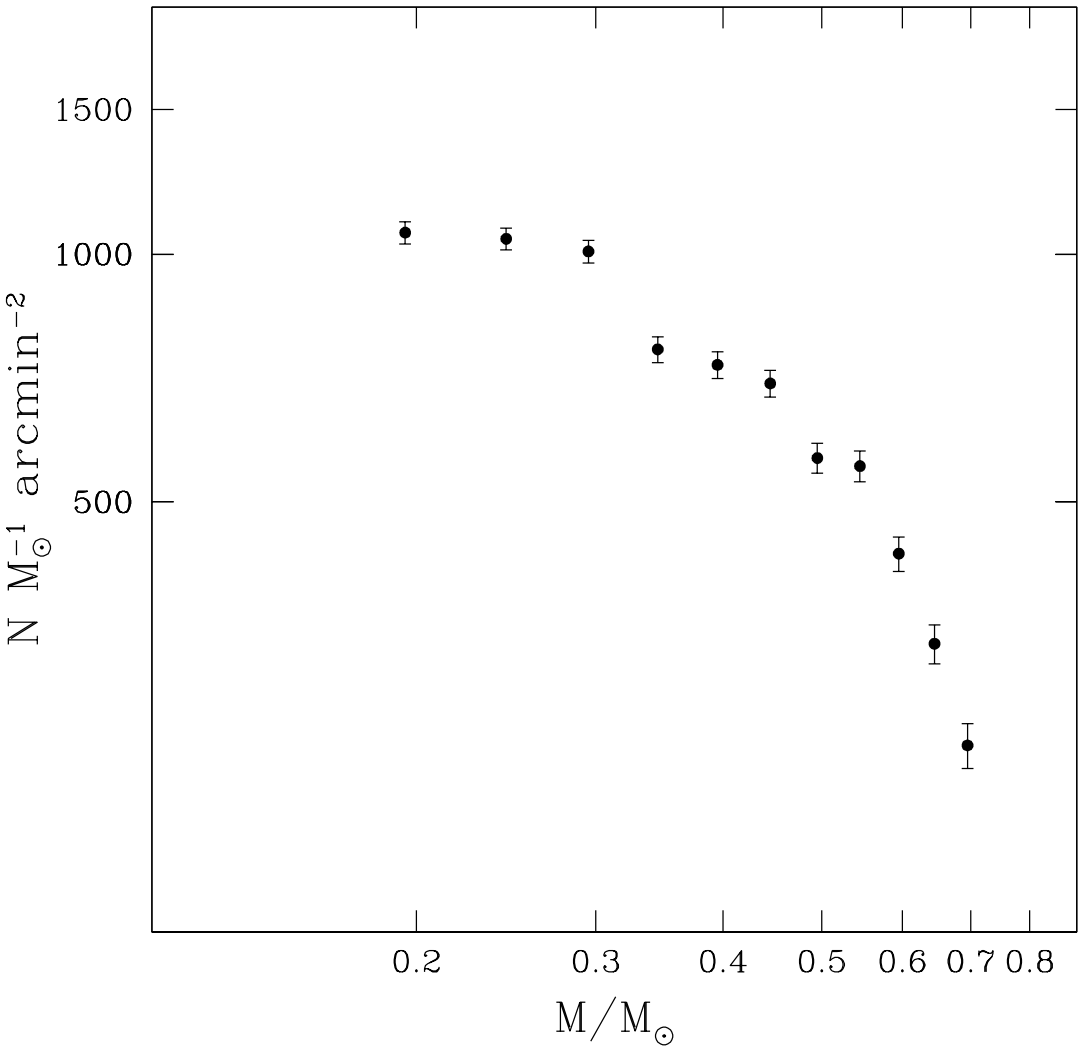

FIGURE 7.43: Mass function of the field F3.

the combination of position and proper motions. We then used the color-magnitude diagrams to refine our selection. We divided the stars belonging to the MS+SGB sequence with a magnitude $16.5 < G < 19.5$ in bins of 0.5 magnitudes and evaluated for each bin the 3σ-clipped median of the μ_α and μ_δ components. We defined as the absolute proper motion of NGC 6752 as the weighted mean of the bins.

We then used the sources that survived the 3σ-clipping to estimate the parallax of the cluster. Again, we divided the sources into bins of 0.5 magnitudes and evaluated for each bin the 3σ-clipped median value of the parallax. The absolute parallax of NGC 6752 is defined as the weighted mean of the bins.

We obtained a value of (μ_α,μ_δ) = (-3.1663 ± 0.0026,-4.0365 ± 0.0026) for the absolute proper motion and (ϖ) = (0.2225 ± 0.0281) mas, for the parallax corresponding to a distance of d$\sim$4.5$\pm$0.03 kpc and a distance modulus of μ = 13.2633 mag. These values are in agreement with the values reported by Baumgardt et al. (2019) and Souza et al. (2020).

We made use of the radial velocities catalogue of NGC 6752 provided by Baumgardt and Hilker (2018) to provide an estimate of the absolute radial velocity of the cluster. We initially made use of the membership probability provided with the catalogue to remove a few outliers. We then refine our selection using the colour-magnitude diagrams. We divided all the stars belonging to the SGB, RGB and RGB-tip regions in bins of 0.5 Gaia G magnitude and evaluated for each bin the 3σ-clipped median of the LOS velocity component. We defined the weighted mean of the bins $V_{LOS} = -26.0482 \pm 0.1383$, as the absolute radial velocity of the cluster. The value is in agreement with the value reported by Baumgardt and Hilker (2018), Lardo et al. (2015), and Lane et al. (2010).

We derived the membership probability (MP), following a method based on PMs and parallax described by Griggio and Bedin (2022) and defined a sample of cluster members by using a selection on the membership probability. We then re-estimate the absolute proper motion and parallax of the cluster using the newly selected sample of stars. We obtained a value of μ_α,μ_δ) = (-3.1697 ± 0.0020,-4.0355 ± 0.0020) mas/yr and ϖ = (0.2251 ± 0.0015) mas, very similar to the value obtained before.

We made use of the data from Gaia to estimate some structural parameters of the cluster, such as ellipticity and position angle. We estimated the 2D binned kernel density of all the stars that survived the MP selection with a Gaia G magnitude $16.5 < G < 19.5$. Starting from a radial distance of $R = 5'$, we calculated 11 isodensity contour lines and used the algorithm by Halir and Flusser () to fit each contour line with an ellipse by means of least-square. We evaluated the weighted mean of the ellipticity and position angle of each bin obtaining a value of $e = 0.0254 \pm 0.0010$ and $PA = (329.34 \pm 1.16)^\circ$, respectively.

We studied the rotation of NGC 6752 in the plane of the sky by following the method presented in Scalco et al. (2023). We defined a sample of stars with reliable photometry and astrometry by following the recommendations of Fabricius et al. (2021), Lindegren et al. (2021) and Riello et al. (2021), but with tighter selections on some parameters. Finally, we defined a sample of probable cluster members by following a procedure based on stellar proper motions, parallax and positions in the colour-magnitude diagram (CMD). The rotation profile obtained in this work is in quite agreement with the profile obtained by Vasiliev and Baumgardt (2021). Finally, we used the radial velocity catalogue to quantify the radial velocity of NGC 6752. We obtained a value of $v_{LOS} = 0.7983 \pm 0.0002$ mas/yr.

We used a combination of data from Gaia and HST (from several fields located

at different radial distances and directions from the cluster centre) to study the velocity dispersion profile of NGC 6752, both globally and divided for the three different mPOPs. We initially used our Gaia DR3 catalogue to estimate the velocity dispersion profile of the cluster from 200 to 1500 arcmin. The profile is in agreement with the profile reported by Vasiliev and Baumgardt (2021). We then used the $m_{F275W} - m_{F814W}$ vs. $C_{F275W,F336W,F438W}$ pseudo-colour diagram, or chromosomic map, to separate the three stellar populations in the MS (MSa, MSb and MSc) in two HST fields (one central field and one external field). We made use of the PMs catalogue provided by Libralato et al. (2022) for the central field and the PMs obtained in this work in the external field, to study the velocity dispersion profile separately for the three stellar populations. To do this, we followed the same procedure described in Libralato et al. (2022). As expected the three stellar populations share the same kinematic, both in the radial and tangential direction. We repeated the procedure for the stars in the RGB of the central field. Also in this case, we found no evidence of a different kinematic for the three stellar populations.

We investigated the equipartition profile of NGC 6752 using the PM catalogue provided by Libralato et al. (2022). We begin by dividing the sample into 6 radial bins. We divided the stars in each radial bin into 10 mass bins and calculated for each bin the velocity dispersion, σ, of the stars. We then evaluated the value of the equipartition, η, in each radial bin, by fitting the values of the velocity dispersion as a function of the stellar mass with a line in the $log(\sigma) - log(m)$ plane. The slope of the interpolations line is a direct estimate of η. The equipartition profile obtained in this work is in agreement with the profile obtained by Watkins et al. (2022).

We made use of an HST external field of NGC 6752 observed only in infrared to study the kinematics of the M-dwarfs of the cluster. We identified in the lower part of the $m_{F110W} - m_{F160W}$ vs. m_{F110W} the three sequences of stars associated with the three stellar populations of NGC 6752. We then studied the velocity dispersion profile of the stars for the three separated populations following the same method used above. As for the stars in the MS and RGB, we do not find a clear difference in the kinematics of the three stellar populations.

We made use of the LOS velocity catalogue provided by Baumgardt and Hilker (2018) to study the velocity dispersion of NGC 6752 in the LOS direction. We obtain a value of the central dispersion $\sigma_0 = 7.44 \pm 0.04$ (km/sec) which is in agreement within 1.3σ with the value reported by Lardo et al. (2015).

Finally, we used our HST catalogue to study the mass function of NGC 6752 both globally and separately for the three different stellar populations, and at a different radial distance from the cluster centre. To do this, we used artificial stars (ASs) to determine the completeness level of the analysed sample. We initially examined the mass function of the central field of NGC 6752 as a whole, without distinguishing between the three multiple stellar populations. The total MF is shown in figure 7.33. We then used the $m_{F275W} - m_{F814W}$ vs. $C_{F275W,F336W,F438W}$ chromosomic map to separate the three stellar populations in the MS and to study the MF of the three stellar populations separately. We noticed that population A is characterised by a slope of the mass function, $\alpha_A = 2.338 \pm 0.269$, much higher than populations B and C ($\alpha_B = 1.805 \pm 0.267$ and $\alpha_C = 0.91 \pm 0.206$). We then repeated the procedure for the fields F1 and F2. Multiple stellar populations are identifiable in the low MS for field F1 and in the MF for field F2. Given the fact that the two fields are located at a similar radial distance from the cluster centre, we combined together the information from the two fields to obtain a unique and extended MF for the three stellar populations. Figure 7.39 shows the mass function for the three stellar populations identified in the fields F1 and F2. The lower part of the MF ($0.1<M/M_{\odot}<0.5$) is given by the field F1

while the upper part ($0.55<M/M_{\odot}<0.75$) is given by the field F2. In Figure 7.40 and 7.41 are shown the MF for the three stellar populations, separated by the two fields F1 and F2 and their relative slope, represented with a dashed line. The slope of the MF for the three stellar populations are $\alpha_A = -0.523 \pm 0.098$, $\alpha_B = -0.327 \pm 0.164$ and $\alpha_C = -0.404 \pm 0.027$, respectively, for the field F1; while for the field F2 we obtain values of $\alpha_A = -2.504 \pm 3.177$, $\alpha_B = -1.763 \pm 1.435$ and $\alpha_C = -2.835 \pm 1.423$.

Chapter 8

The *HST* Large Programme on NGC 6752 - V. Differences in Luminosity and Mass Functions among Multiple Stellar Populations.

Here we exploit the astro-photometric dataset of the multi-epoch infrared parallel field of a *Hubble Space Telescope* Large Programme aimed at studying the faintest stars of the globular cluster NGC 6752 to determine the luminosity and mass functions of the multiple stellar populations of this cluster. Thanks to the measurement of proper motions and deeper completeness, the results presented in this chapter represent a significant improvement over those of previous studies. We successfully derived membership probabilities reaching stars as faint as $m_{\rm F160W} \sim 25$, allowing us to reliably distinguish the three main stellar populations detected within this cluster. We employed a new set of model isochrones that have been individually fit to the colour-magnitude diagram of each population. We present a comprehensive analysis of the luminosity and mass functions for three stellar populations within NGC 6752. Notably, our findings reveal differences in the present-day luminosity and mass functions of first-generation and second-generation stars; these differences are consistent with the manifestation of the effects of dynamical processes acting on populations with different initial spatial distributions. Finally, we publicly release the catalogues with positions, photometry, proper motions, and memberships probabilities, as well as the stacked-image atlases and all newly calculated stellar models. The material discussed in this Chapter has been submitted in Astronomische Nachrichten (AN).

8.1 Introduction

Globular-cluster (GC) stars are commonly categorised into two distinct main groups based on their chemical composition. The first-population (1P) stars exhibit a Galactic-field-like composition, while the second-population (2P) stars are characterised by depletion in specific light elements, such as carbon, oxygen, and magnesium, and enrichment in helium, nitrogen, aluminium, and sodium compared to the 1P stars. Both 1P and 2P stars can host sub-populations of stars (see reviews by Smith, 1987; Bastian and Lardo, 2018b; Gratton et al., 2019).

Various formation scenarios have been proposed to explain the origin of multiple stellar populations (mPOPs) in GCs. These scenarios can be divided into two categories. The first category of scenarios involves multiple star-formation episodes,

where intermediate- to high-mass stars formed during the first burst eject winds of processed material, contributing to the formation of the 2P stars. Gas from massive interacting binaries (de Mink et al., 2009; Renzini, Marino, and Milone, 2022; Renzini, 2023), fast-rotating massive stars (Decressin et al., 2007; Krause et al., 2013), stellar mergers (Wang et al., 2020), and asymptotic-giant-branch (AGB) and super-AGB stars (e.g. Ventura et al. 2001; D'Ercole et al. 2008b; D'Antona et al. 2016) have been suggested as possible contributors (see also Renzini et al., 2015a, for a review).

The second category of formation scenarios proposes the early accretion of material ejected by supermassive stars or massive interacting binaries by a fraction of stars of the same generation, leading to the formation of all stars in a single star-formation episode (e.g. Bastian et al. 2013; Denissenkov and Hartwick 2014; Gieles et al. 2018; Winter and Clarke 2023).

In the past, the study of mPOPs in GCs focused mainly on stars with masses greater than $\sim$0.6 $M_{\odot}$, utilising ultraviolet (UV) and visual filters, mainly because of the limited signal-to-noise ratio of the UV observations for stars with lower masses. However, the identification and separation of mPOPs at lower-mass ranges, along with the investigation of their chemical composition, is of fundamental importance to understanding the formation and dynamical history of GCs. Specifically, extending determinations of their mass function (MF) to lower masses and determining the MF slopes of mPOPs across an extensive mass range (from $\sim$0.1 to $\sim$0.8 solar masses) can offer invaluable insights to allow discrimination among various proposed formation scenarios. As outlined in Vesperini et al. (2018), utilizing N-body simulations, substantial distinctions can arise between the local MFs of the 1P and the 2P when assuming both populations form with the same initial MF. Specifically, within the outer regions of a cluster, the local MF of the 2P tends to exhibit a steeper slope compared to the 1P MF. This phenomenon is a result of the combined effects of mass segregation and the outward migration of low-mass stars, within a system where the 2P was initially more centrally concentrated and populated the outer regions preferentially with low-mass stars.

Very low-mass (VLM) stars are characterised by high-density and low-effective temperature atmospheres. Their spectral peak occurs in the near-infrared (NIR) region, where several oxygen-containing molecules (e.g. CO, H_2O, OH, TiO, VO, ZrO), significantly impact opacity (Allard and Hauschildt, 1995). Consequently, variations in chemical composition are easy to see in the spectra of these stars.

The recent breakthrough in studying mPOPs at lower masses has been made possible by the NIR channel of the Wide Field Camera 3 (WFC3/NIR) on board the *Hubble Space Telescope* (*HST*, Milone et al. 2012e; Milone et al. 2014; Milone et al. 2017a; Milone et al. 2019). The WFC3/NIR F160W band is significantly affected by absorption from various oxygen-containing molecules, including H_2O and CO, while WFC3/NIR F110W photometry remains mostly unaffected by the oxygen abundance. As a result, 2P stars, which are depleted in oxygen compared to 1P stars, exhibit brighter F160W magnitudes and redder F110W-F160W colours than the 1P stars. Observations in these filters have proven highly effective in distinguishing and characterising M-dwarf mPOPs in several GCs, including NGC 2808 (Milone et al., 2012e; Dondoglio et al., 2022), NGC 6121 (M4, Milone et al. 2014; Dondoglio et al. 2022), ω Centauri (Milone et al., 2017a; Gerasimov et al., 2022a), NGC 6752 (Milone et al., 2019), and 47 Tucanae (Gerasimov et al., 2023). Recent *James Webb Space Telescope* (*JWST*) observations have further enriched the observational characterization of multiple populations by revealing distinct populations in M-dwarf stars of a few clusters (see e.g. Nardiello et al. 2022; Nardiello et al. 2023; Milone et al. 2023; Ziliotto et al. 2023; Cadelano et al. 2023).

Here we present the reduction and analysis of NIR images from *HST* observations of a deep field of the nearby (∼4 kpc) GC NGC 6752. The data presented here were collected under the *HST Large Programme on NGC 6752* (GO-15096 + GO-15491; P.I.: L. R. Bedin).

NGC 6752 is known to host three different stellar populations (A, B, and C), which are clearly identifiable along an extensive part of the CMD, from the red-giant branch (RGB) to the low main sequence (MS). Population A is traditional 1P, with abundances similar to those of field stars with the same metallicity. Populations B and C are the 2Ps and are characterized by enhanced abundances of helium, nitrogen, sodium, and a depletion of carbon, and oxygen; the enhancement/depletion is stronger in population C and milder in population B (see Milone et al. 2013).

The primary data set of the programme includes observations of a primary field obtained with the Wide Field Channel (WFC) of the Advanced Camera for Surveys (ACS) with the aim of examining the white dwarf (WD) cooling sequence (CS) within NGC 6752. This investigation has been addressed in two earlier papers from this series (Bedin et al. 2019a, and Bedin et al. 2023). To effectively remove background and foreground objects from the observed fields, these programmes were devised to acquire observations at distinct epochs. For each epoch, images of a parallel field were taken with the WFC3/NIR. This parallel field was collected to investigate the mPOPs of NGC 6752 at the bottom of the MS.

The first epoch of the parallel NIR field was analysed in the second publication of this series (Milone et al., 2019). In that study, it was found that the three main populations (the aforementioned A, B, and C) — previously observed in the brightest part of the CMD (Milone et al., 2013) — define three distinct sequences in the IR CMD. These sequences extend from the MS knee, a typical feature found in the NIR CMD and occurring at the lower mass end of the MS. The MS knee is a result of absorption processes involving molecular hydrogen within the atmospheres of cooler, low-mass MS stars, leading to a shift of these stars towards bluer colours (Linsky, 1969; Mould and Hyland, 1976). The distinct sequences extend all the way to the bottom of the MS (∼0.1 $M_\odot$).

In this analysis, we provide a more comprehensive reduction and analysis of the parallel NIR field discussed in Milone et al. (2019), utilising the complete data set gathered through the combined GO-15096 + GO-15491 programmes. The inclusion of additional observations has led to significant improvements upon Milone et al. (2019). With a temporal baseline of approximately three years, we can now accurately distinguish between cluster members and background/foreground sources using proper motion (PM) measurements. Additionally, the number of available images has doubled since Milone et al. (2019). This expanded photometric data set enables us to further distinguish and analyse the three distinct stellar populations with greater precision.

The chapter is organised as follows: the observations and data reduction are presented in Section 8.2. In Section 8.3 we present the NIR CMD, while Section 8.4 and Section 8.5 present the results of our determination of the luminosity functions (LFs) and MFs for the three different mPOPs. Finally, Section 8.6 provides a brief summary and discussion of our results.

8.2 Observations and data reduction

A total of 255 images were acquired in three different epochs for a total duration of 85 *HST* orbits, specifically in 2018 (40 orbits), 2019 (5 orbits), and 2021 (40 orbits).

TABLE 8.1: List of *HST* observations of NGC 6752.

Filter	Exposures	Epoch
	WFC3/NIR	
Epoch 1: 2018.7	(GO-15096)	(40 *HST* orbits)
F110W	28×143 + 56×1303 s	2018/09/09-18
F160W	12×143 + 24×1303 s	2018/09/07-09
Epoch 2: 2019.6	(GO-15096)	(5 *HST* orbits)
F160W	5×143 + 10×1303 s	2019/08/01-16
Epoch 3: 2021.7	(GO-15491)	(40 *HST* orbits)
F110W	28×143 + 56×1303 s	2021/09/02-11
F160W	12×143 + 24×1303 s	2021/09/02-12

During the first and third epochs, data were collected using two filters, F110W and F160W. Only the F160W filter was used during the second epoch. During each orbit, *HST* collected one short exposure of 143 s and two long exposures of 1303 s each. All images were acquired in MULTIACCUM mode with SAMPSEQ=SPARS10 and NSAMP=15 for the short exposures and SAMPSEQ=SPARS100 and NSAMP=14 for the long exposures. Table 8.1 reports the complete list of *HST* WFC3/NIR observations for the observed outer field of NGC 6752.

Figure 8.1 shows the locations of the primary and parallel fields, superposed on an image from the Digital Sky Survey (DSS)[1]. The primary ACS/WFC field (F0) is shown in azure, while the parallel WFC3/NIR field (F1) is plotted in pink. In this chapter, we consider only data from field F1.

The data were reduced following the procedure outlined in Scalco et al. (2021). In summary, this procedure involves two main steps: the *first-pass* and *second-pass* photometry. During the *first-pass* photometry, we perturbed a set of"libary" WFC3/IR effective Point Spread Functions (ePSFs) (see Anderson and King 2000; Anderson and King 2006 and Anderson 2016) to determine the optimal spatially variable PSF for each image. Then, using these PSFs, we extracted the positions and fluxes of the stars within each image. This extraction was carried out using the `FORTRAN` code `hst1pass` (see Anderson 2022 WFC3/ISR 2022-05). To account for geometric distortion, the stellar positions in each individual exposure catalogue were corrected using the publicly available WFC3/IR correction (Anderson, 2016). For each of the two filters, the positions and magnitudes were transformed to a common reference frame using six-parameter linear transformations and photometric zero points.

Subsequently, we performed the *second-pass* photometry using the `FORTRAN` software package `KS2`, which is based on the software `kitchen_sync` presented in Anderson et al. 2008. This software routine makes use of the results obtained from the *first-pass* stage to simultaneously identify and measure stars across all individual exposures and filters. By relying on multiple exposures, `KS2` effectively detects and measures faint stars that would be otherwise lost in the noise of individual exposures. The star-finding process is executed through a series of passes, gradually moving from the brightest to the faintest stars. In each iteration, the routine identifies stars that are fainter than those found in the previous iteration, subsequently measuring and subtracting them. This iterative approach ensures that progressively fainter stars are detected and accounted for, enhancing the overall accuracy of the photometric measurements. `KS2` employs three distinct methods for measuring stars, with each approach specifically tailored for different magnitude ranges. We refer

[1] https://archive.eso.org/dss/dss

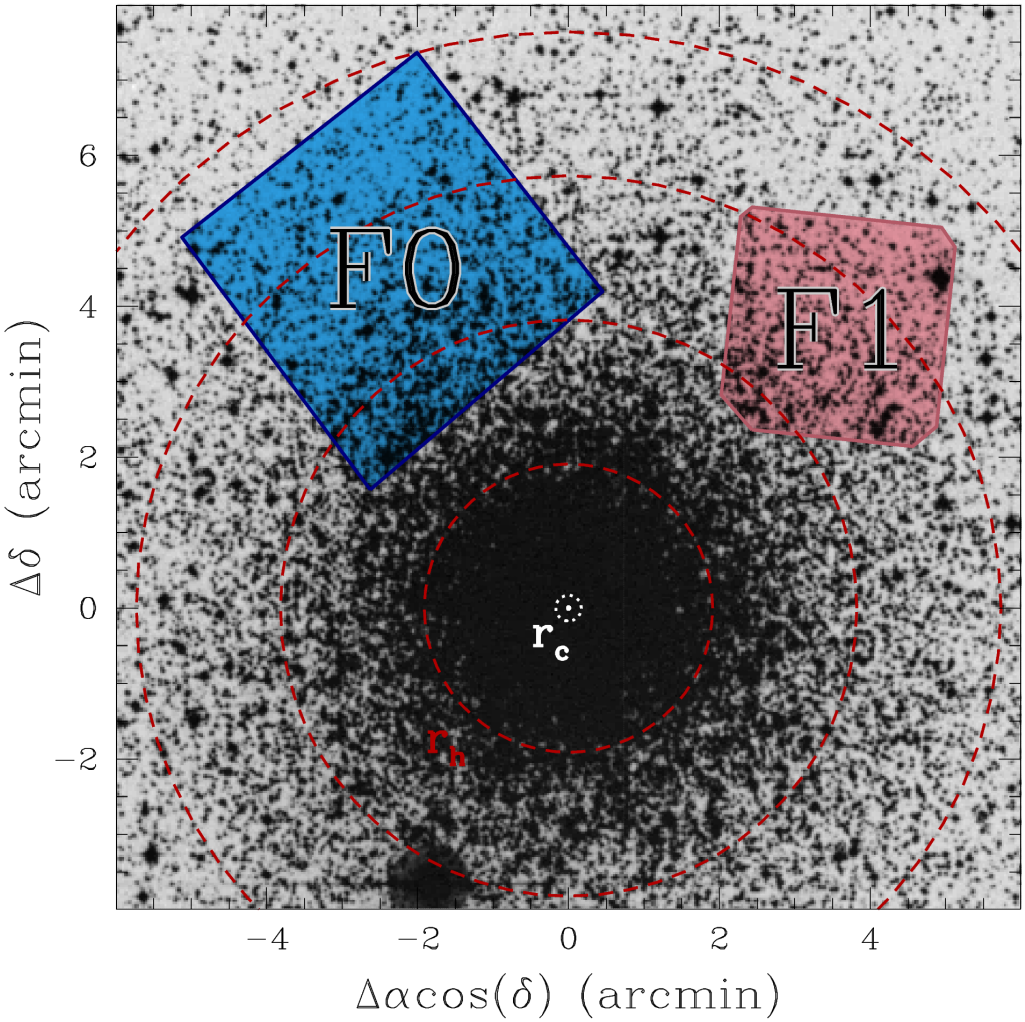

FIGURE 8.1: Outlines of the fields observed in *HST* programme GO-15096 + GO-15491, superimposed on a DSS image of NGC 6752. The primary ACS/WFC field (F0) is in azure, while the parallel WFC3/NIR field is shown in pink (F1). Units are in arcmin measured from the cluster centre. The data discussed in this chapter come from field F1. The white dashed circle marks the cluster's core radius ($r_c = 0'.17$; Harris 1996; Harris 2010); the red dashed circles mark the half-light radius ($r_h = 1'.91$; Harris 1996; Harris 2010), and $2\,r_h$, $3\,r_h$ and $4\,r_h$ from the centre.

to Bellini et al. (2017b), Nardiello et al. (2018), and Scalco et al. (2021) for a detailed description of the methods and procedures.

The photometry has been zero-pointed into the Vega magnitude system by following the recipe of Bedin et al. (2005a) and adopting the photometric zero-points provided by STScI web page for WFC3/NIR[2]. We cross-referenced the stars in our catalogue with the stars in the *Gaia* Data Release 3 (*Gaia* DR3, Gaia Collaboration et al. 2016; Gaia Collaboration et al. 2023). The sources found in common were used to anchor our positions (X, Y) to the *Gaia* DR3 absolute astrometric system.

To ensure a well-measured sample of stars measured in *HST* images, we implemented a selection process using a set of quality parameters provided by `KS2`, following a similar approach as described in Scalco et al. (2021). The quality parameters employed include the photometric error (σ), the quality-of-fit (QFIT) parameter, which quantifies the PSF-fitting residuals, and the RADXS parameter, a shape parameter that allows for differentiation between stellar sources, galactic sources, and cosmic ray/hot pixels introduced in Bedin et al. (2008). Further details regarding these parameters can be found in Bellini et al. (2017b), Nardiello et al. (2018), and Scalco et al. (2021).

Panels (a)-(f) of Fig. 10.1 illustrate the selection process for the photometry derived from the short exposures using the first method of `KS2`. We plotted each parameter as a function of the stellar magnitude. For the σ and QFIT parameters, we drew by hand fiducial lines to separate the bulk of well-measured stars from the outliers (panels (a), (b), (d) and (e) of Fig. 10.1). For the RADXS parameter, we selected stars that satisfy the condition: $-0.05 < \mathrm{RADXS} < +0.1$ (panels (d) and (f) of Fig 10.1). Finally, panels (g), (h) and (i) of Fig. 10.1 show the m_{F160W} versus $m_{\mathrm{F110W}} - m_{\mathrm{F160W}}$ CMD for all the detected sources, the sources rejected by the selection criteria, and the sources that passed the criteria, respectively. We performed the same procedure for the photometry obtained from the long exposures and for all the extraction methods utilised by `KS2`. We combined the most accurately measured stars from the three different photometric methods of `KS2` to obtain a single final catalogue, incorporating photometry obtained from both long and short exposures.

PMs were computed using the technique described in Scalco et al. (2021) (see also Bellini et al. 2014; Bellini et al. 2018; Libralato et al. 2018b; Libralato et al. 2022). This iterative procedure treats each image as an independent epoch and can be summarised in two main steps: first, it transforms the stellar positions from each exposure into a common reference frame through a six-parameter linear transformation. Then, it fits these transformed positions as a function of the epoch using a least-square straight line. The slope of this line, determined after multiple outlier-rejection stages, provides a direct measurement of the PM. High-frequency-variation systematic effects were corrected as described in Bellini et al. (2018), i.e. according to the median value of the closest 100 likely cluster members (excluding the target star itself).

We computed the membership probability (MP) of each star, by following a method based on PMs described by Balaguer-Núnez, Tian, and Zhao (1998) (see also Bellini et al. 2009; Nardiello et al. 2018; Scalco et al. 2021). Figure 10.2 illustrates the selection of cluster members based on MP. We defined as cluster members all the sources with MP>90% (as represented in panel (d) of Fig. 10.2). Relative PMs as a function of the $m_{\mathrm{F110W}} - m_{\mathrm{F160W}}$ colour are shown in panel (a) while the vector-point diagram (VPD) is shown in panel (b). panel (c) shows the m_{F160W} versus $m_{\mathrm{F110W}} - m_{\mathrm{F160W}}$ CMD.

[2] https://www.stsci.edu/hst/instrumentation/wfc3/data-analysis/photometric-calibration

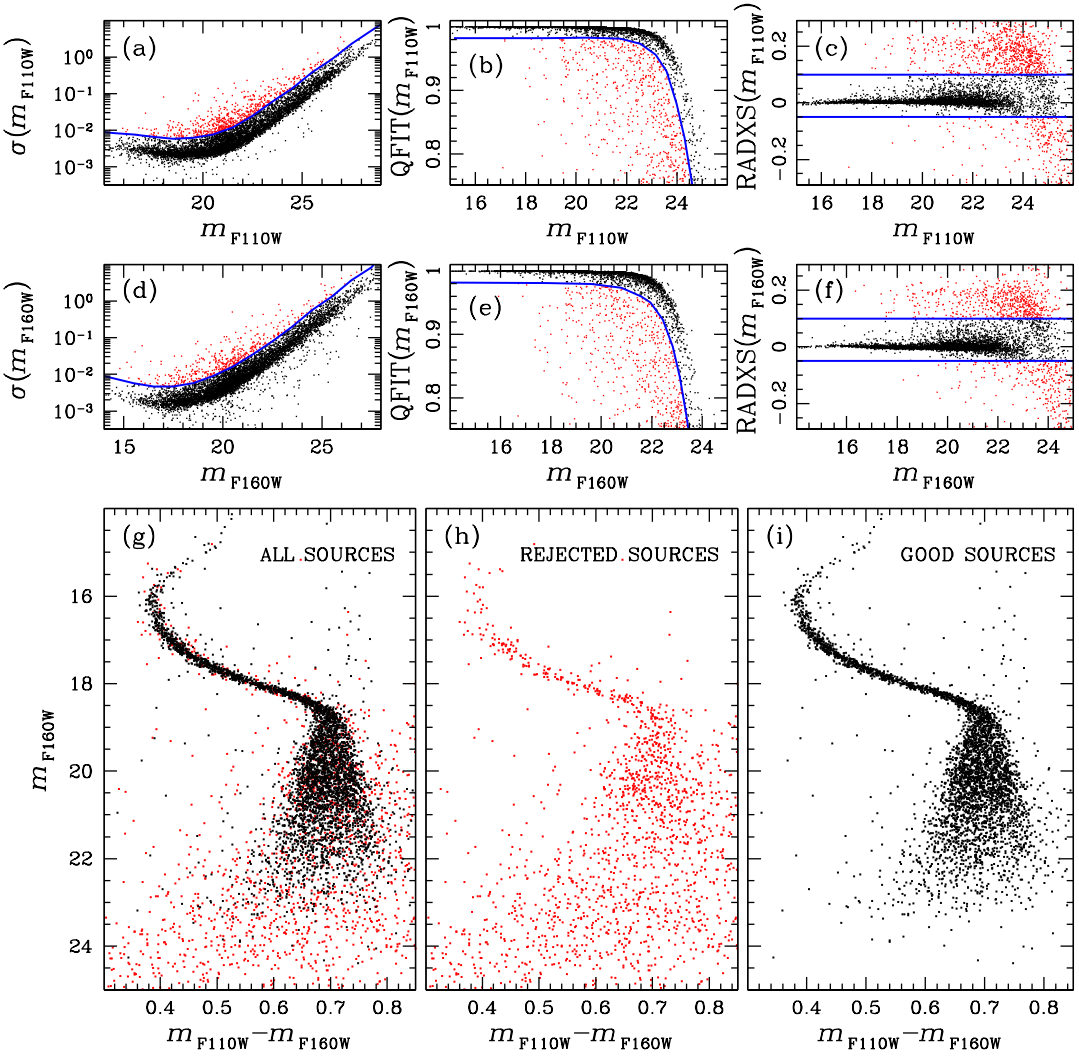

FIGURE 8.2: Procedure used to distinguish well-measured stars from outliers. (a)-(c) distributions of the photometric error (σ), quality-of-fit (QFIT), and RADXS as a function of the F110W magnitude. The blue lines separate well-measured stars from outliers. (d)-(f) same as (a)-(c) but for the F160W filter. (g)-(i) m_{F160W} versus $m_{F110W} - m_{F160W}$ CMD for all the detected sources, the sources rejected by the selections, and the sources that passed the selections, respectively. In all panels, well-measured sources are represented in black, while rejected sources are shown in red.

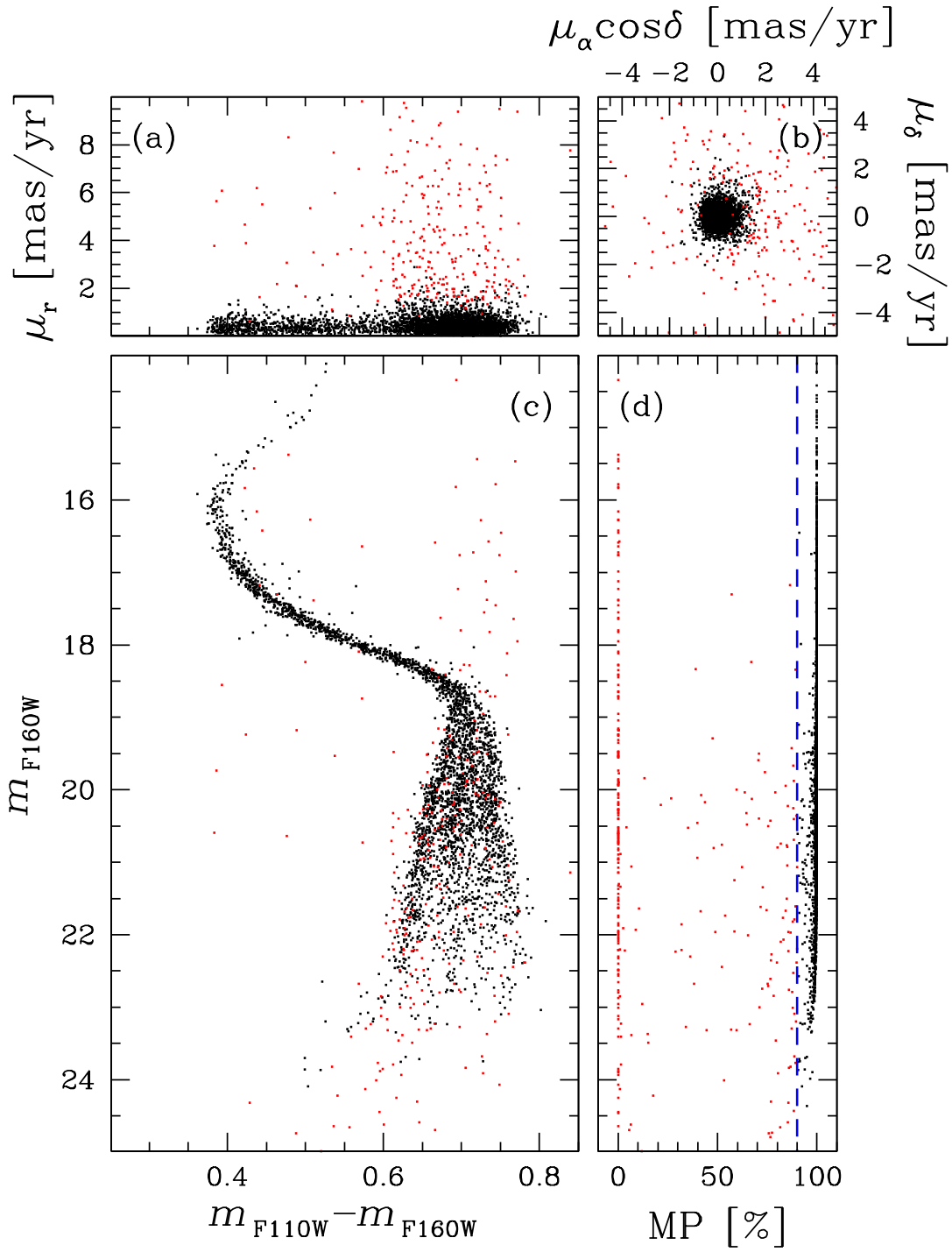

FIGURE 8.3: Cluster membership selection. (a) relative PMs as a function of the $m_{F110W} - m_{F160W}$ colour. (b) Vector point diagram. (c) m_{F160W} versus $m_{F110W} - m_{F160W}$ CMD. (d) Membership probability (MP) as a function of the m_{F160W} magnitude. The red line at MP=90% denotes the MP threshold used in this study. In all panels, cluster members are represented in black, while field stars are shown in red.

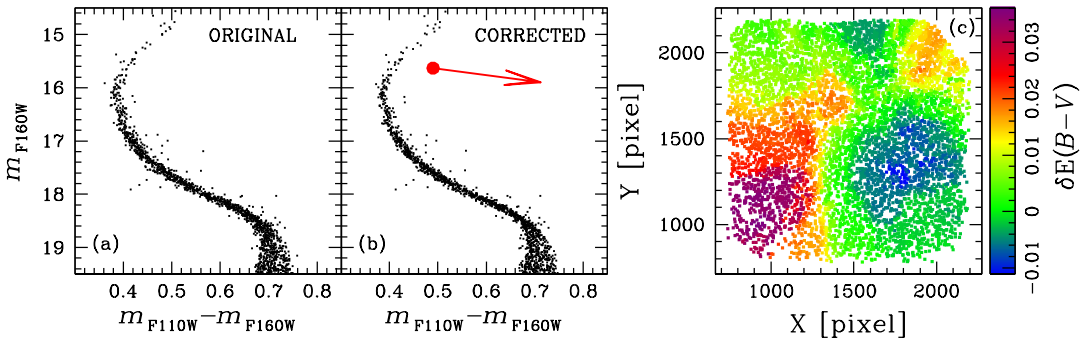

FIGURE 8.4: Comparison between the original m_{F160W} versus $m_{F110W} - m_{F160W}$ CMD (a) and the same CMD corrected for differential reddening (b). The red arrow in (b) shows the reddening direction. (c) Differential reddening map, color-coded using the color-mapping scheme shown on the right.

Next, we corrected our photometry for the effects of differential reddening on zero-point variations with location in the field following the procedure described by Milone et al. (2012d) (see also Sarajedini et al. 2007; Bellini et al. 2017c). In brief, we derived the fiducial MS line and measured the residual between a sample of bright MS stars and the fiducial along the reddening directions. For each star, we considered the median of the residual values from the 50 neighbouring bright MS stars as the best estimate of the differential reddening. Panels (a) and (b) of Fig. 8.4 provide a comparison of the m_{F160W} versus $m_{F110W} - m_{F160W}$ CMD in the upper part of the MS, where the effects of differential reddening are more pronounced, thanks to the negligible random errors. The figure illustrates the CMD before and after applying the differential-reddening correction. The values in magnitudes of the applied differential reddening (δE($B - V$)) of each star as a function of the (X, Y) stellar position can be used to construct the two-dimensional map of the differential reddening across the field of view (FoV). This map is shown in panel (c) of Fig. 8.4, color-coded using the color-mapping scheme shown on the right of the figure.

We cross-matched the stars that survived our photometric and membership selections with the catalogue presented in Milone et al. (2019). Figure 10.3 shows the comparison between the two data sets, showing a significant improvement in the new catalogue. Notably, not only has the number of sources increased due to the expanded observational area, but stars in common with Milone et al. (2019) now benefit from twice the exposure time and a considerably larger time baseline. This has allowed us to derive improved PMs and, consequently, more accurate MPs for these stars.

As part of this publication, we are making publicly available the astro-photometric catalogue and atlases we have constructed here. These resources are provided in a format identical to the catalogue and atlases made available by Scalco et al. (2021). For a comprehensive description of these resources, we refer to Scalco et al. (2021). When available, we also provide for sources in our catalogue the corresponding *Gaia* DR3 identification numbers. The supplementary electronic material through this journal will also be available at our website[3].

[3] https://web.oapd.inaf.it/bedin/files/PAPERs_eMATERIALs/NGC6752_V/

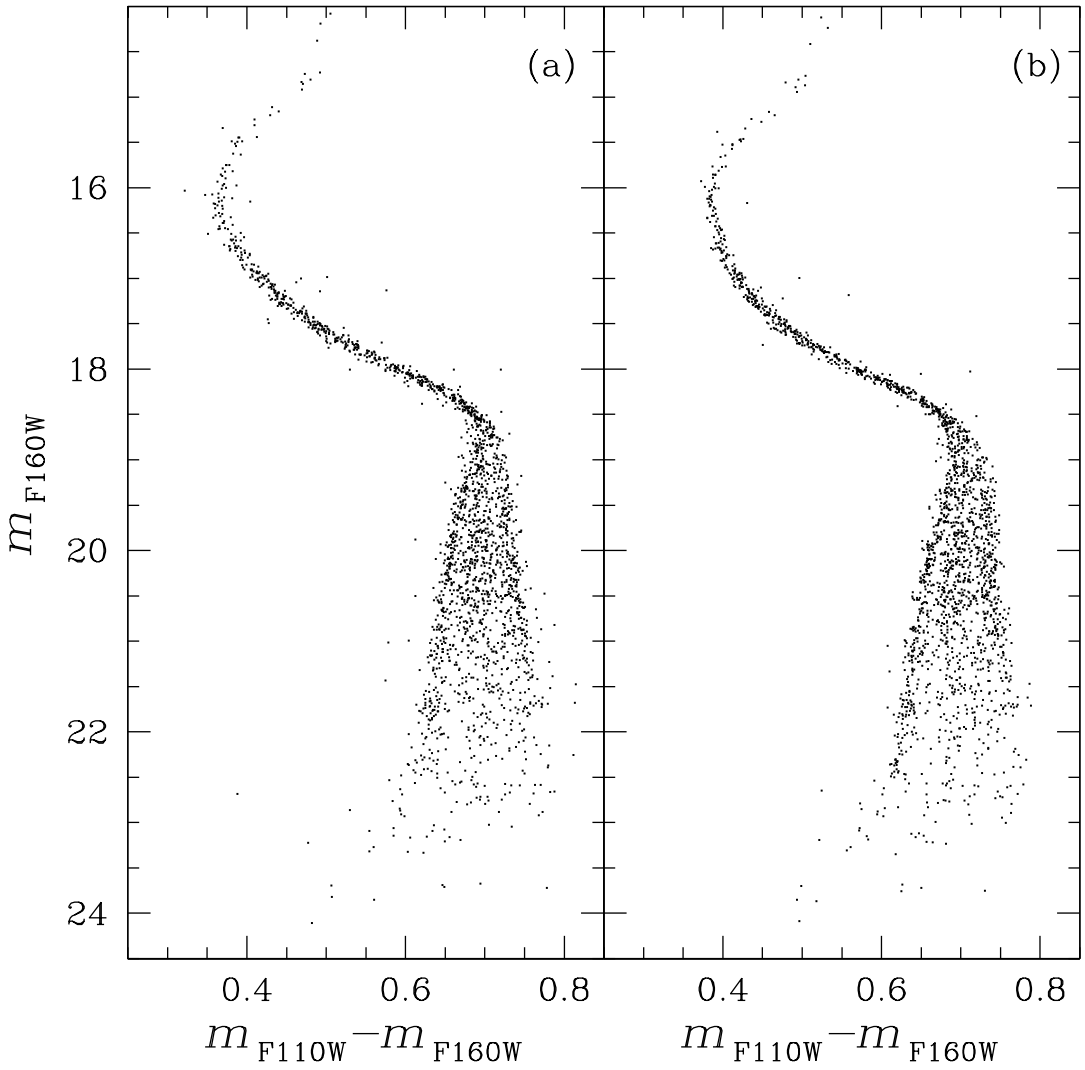

FIGURE 8.5: Comparison between two CMDs made using the catalogue presented in Milone et al. (2019) (panel a) and our new reduction (panel b).

8.3 The Infrared CMD of NGC 6752

Figure 10.6 shows the $m_{\rm F160W}$ versus $m_{\rm F110W} - m_{\rm F160W}$ CMD of our catalogue. The grey dots represent stars that passed the photometric quality selections, while the black dots represent stars that survived both the photometric and MP selections.

Upon visual examination of this figure, it becomes evident that the MS is narrow and well-defined in the magnitude range between the MS turn-off ($m_{\rm F160W} \sim 16$) and the MS knee ($m_{\rm F160W} \sim 18.5$). However, as we move from the knee towards the lower end of the MS ($m_{\rm F160W} \sim 24$), the MS becomes wider, and at this point, it becomes possible to distinguish the presence of three MS sequences of low-mass stars. The split of the MS is a direct outcome of the distinct oxygen abundance in the three populations (Milone et al., 2019). As discussed in Section 8.1, the $m_{\rm F110W} - m_{\rm F160W}$ colour is sensitive to the absorption bands of H_2O molecules, making it effective in distinguishing stars with different oxygen content. Following the nomenclature defined in Milone et al. (2019)), we label stars along the bluest sequence as MS-A, those along the reddest sequence (displaying the most significant oxygen depletion) as MS-C, and stars along the intermediate sequence as MS-B (showing an intermediate chemical composition). MS-A corresponds with the 1P stars, whereas MS-B and MS-C correspond to the 2Ps stars.

In what follows, we present an overview of our procedures for assessing the completeness of our sample, as well as our methodology for evaluating the isochrones of each population.

8.3.1 Artificial stars

Artificial stars (ASs) were used to estimate photometric errors and to derive the completeness level of our sample by following the procedure by Bedin et al. (2008) and Bedin et al. (2009a). We generated a catalogue including the X and Y positions and the F110W and F160W magnitudes of 90,000 stars (30,000 for each sequence) randomly distributed around the FoV. The ASs have instrumental magnitudes ranging from -6.5 to 1.5 (which correspond to $\sim$ 18 to $\sim$ 26 in calibrated magnitude) in the F160W band, while the corresponding F110W magnitudes are derived from the fiducial lines of the three sequences. These fiducial lines were established by manually setting a series of fiducial points along the three sequences in the $m_{\rm F160W}$ versus $m_{\rm F110W} - m_{\rm F160W}$ CMD and connecting them through straight lines (see panel (a) of Fig. 10.10). The ASs were generated and reduced using the same software used for real stars, `KS2`.

To track potential systematic errors, panels (b) and (c) of Fig. 10.10 show the difference between input and output (I/O) magnitudes versus input magnitude for ASs found within 0.5 pixels of the input coordinates, in the F110W and F160W filter, respectively. For each filter, we divided the magnitude range covered by our AS photometry into bins of half magnitude and calculated the 2.5 σ-clipped median of the differences per magnitude bin. The obtained values are plotted in Fig. 10.10 as red points with the corresponding standard deviation as error bars. Upon visual examination of this figure, it becomes evident that the mean differences are negligible. Consequently, based on the small magnitude of these differences, we have opted not to apply any input-output photometric correction.

As pointed out in Bedin et al. (2008), our ability to find a given faint star depends strongly on its environment. Extremely bright stars create a mottled background, making it hard to find faint sources in their vicinity. For this reason, Bedin et al. (2008) introduced a new parameter, rmsSKY, which can be used to determine which

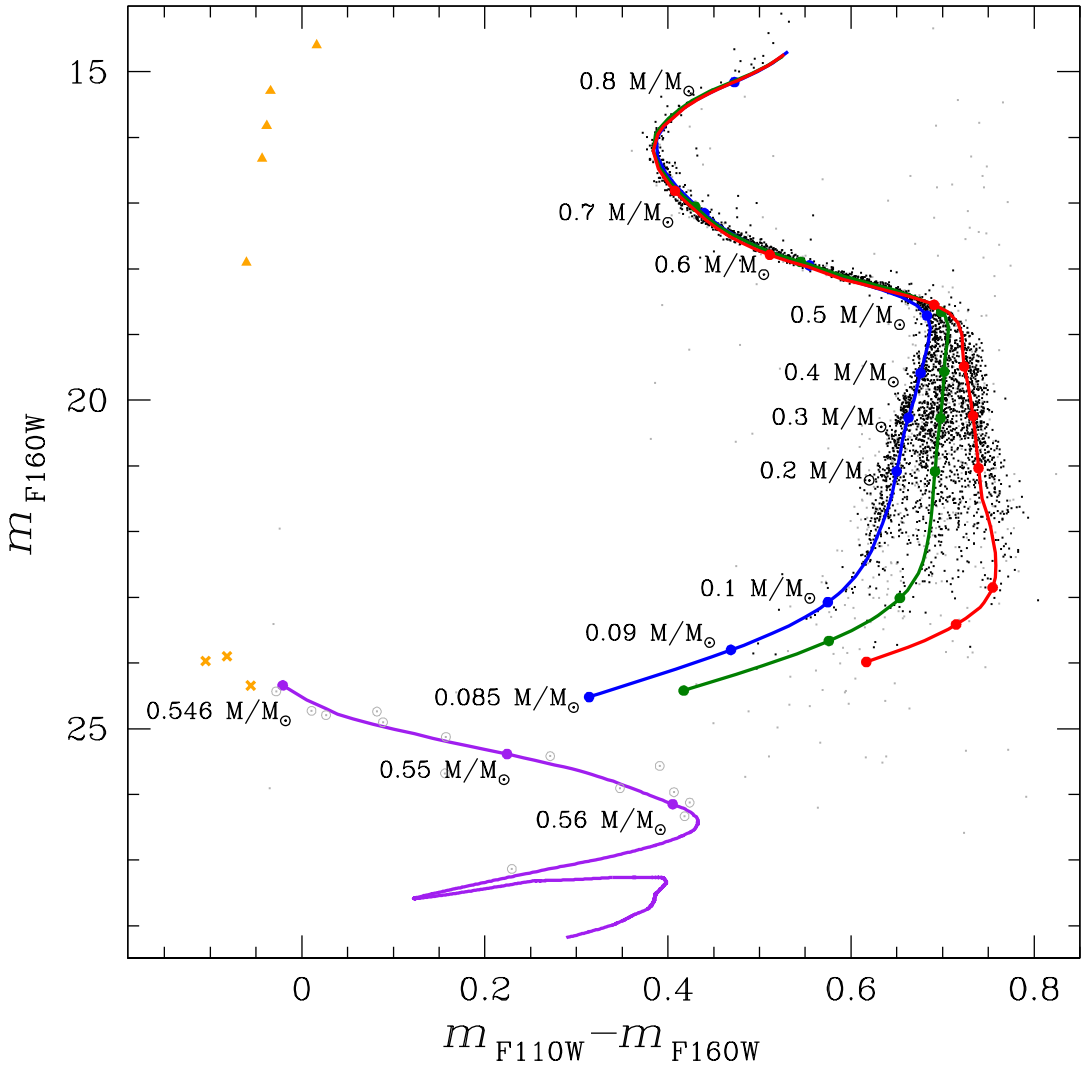

FIGURE 8.6: The three isochrones described in Section 8.3.2 corresponding to MS-A (in blue), MS-B (in green), and MS-C (in red) super-imposed on the m_{F160W} versus $m_{F110W} - m_{F160W}$ CMD. The diagram includes stars that have passed photometric quality selection (depicted as grey dots) and stars that have passed both the photometric and MP selections (depicted as black dots). The corresponding isochrone for the WD is shown in purple in the lower-left part of the plot, with the three WD candidates shown as orange crosses. Other stars that only passed the photometric selections and are situated along the WD isochrone are enclosed by a grey circle. We also show, as orange triangles, stars belonging to the horizontal branch (HB). For each isochrone, we've marked specific mass values, with their labels displayed on the plot.

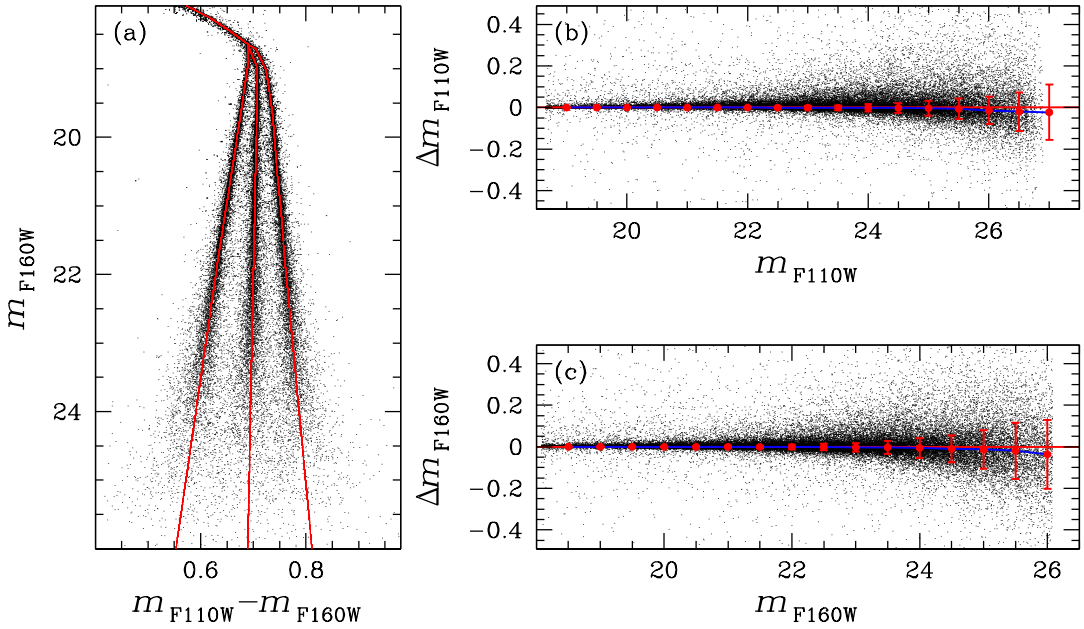

FIGURE 8.7: (a) Simulated CMD derived from ASs. Red dots are the input ASs, while the measured ASs are coloured black. (b)-(c) Difference between inserted and recovered ASs magnitudes for F110W and F160W filter, respectively. We considered only stars found within a 0.5-pixel tolerance radius of the input coordinates. The red horizontal lines indicate the position of a null difference, while the blue lines are the splines through the median values obtained in each magnitude interval, represented with red points, with the corresponding standard deviation as red bars.

locations in the field have a favourable background. We then can define two types of completeness: an "overall completeness", c, defined as the fraction of stars recovered, and a "local completeness" defined as $c_g = c/f_g$, where f_g is the fraction of the image where a source is searchable. To estimate f_g, we followed the procedure outlined in Bedin et al. (2008). We plotted the rmsSKY parameter as a function of magnitude and defined by hand a line that separates well-measured stars from poorly measured ones. f_g is defined as the fraction of stars that survived the rmsSKY selection criteria as a function of magnitude.

Figure 10.4 shows the "overall" and "local" completeness level of our field, for the F110W (panel (a)) and F160W filter (panel (b)). For each filter, we divided the magnitude range covered by our AS photometry into bins of half magnitude and evaluated the percentage of AS sources recovered. An AS is considered recovered if the difference between the input and output position and magnitude is less than 1.0 pixel and 0.75 mag. respectively, and if it passes the criteria of selection adopted for real stars (see Fig. 10.1). To assess the impact of the MP selection (as illustrated in Fig. 10.2) on completeness, we replicated the procedure for evaluating PMs and MPs, as applied to real stars, to the ASs. Specifically, we utilized the position of the ASs in each epoch, extracted through our ASs test, to assess the PMs of each AS by applying the same methodology used for the real stars. Subsequently, we computed the MP for the ASs using the obtained PMs, following the procedure described above for real stars. We applied identical MP selection criteria to the ASs as those used for the real stars.

The "overall" and "local" completeness estimates are represented with black and blue dots respectively in both panels. For comparison, we also show the "overall" completeness obtained without considering the MP selection, represented by red dots in both panels. As expected, completeness is higher in the absence of MP selection, particularly at lower magnitudes where obtaining reliable PM estimates can be challenging. The incorporation of PMs in the completeness evaluation represents a significant improvement compared to Milone et al. (2019). We want to highlight that, in the upcoming analysis, we will rely solely on the "overall" completeness obtained with all the selections.

We followed a similar procedure to assess the completeness of stars along the WD CS. Specifically, we generated a sample comprising 15,000 stars with instrumental magnitudes spanning from -0.5 to 1.5 (which correspond to ~ 24 to ~ 26 in calibrated magnitude) in the F160W band. The corresponding F110W magnitudes were derived from the fiducial line of the WD CS in the $m_{\rm F160W}$ versus $m_{\rm F110W} - m_{\rm F160W}$ CMD (refer to panel (a) of Fig. 8.9). In Fig. 8.9, panels (b) and (c) illustrate the completeness levels for stars along the WD CS. The "overall" completeness level, with MP selection, is represented by black dots, while completeness without MP selection is indicated by red dots. Additionally, the "local" completeness levels are depicted as blue dots. It's worth noting that the completeness level remains below 50% across the entire magnitude range under consideration.

The completeness values for both the "overall" and "local" completeness of our sample in the two filters, as well as for both the MS and the WD CS, can be accessed online, on our website and as supplementary electronic material within this journal (alongside the catalogue and the atlases).

8.3.2 Isochrone fits

Model isochrones were calculated and fit to the observed CMD of NGC 6752, following the approach in Gerasimov et al. (2023). This approach allows the abundances

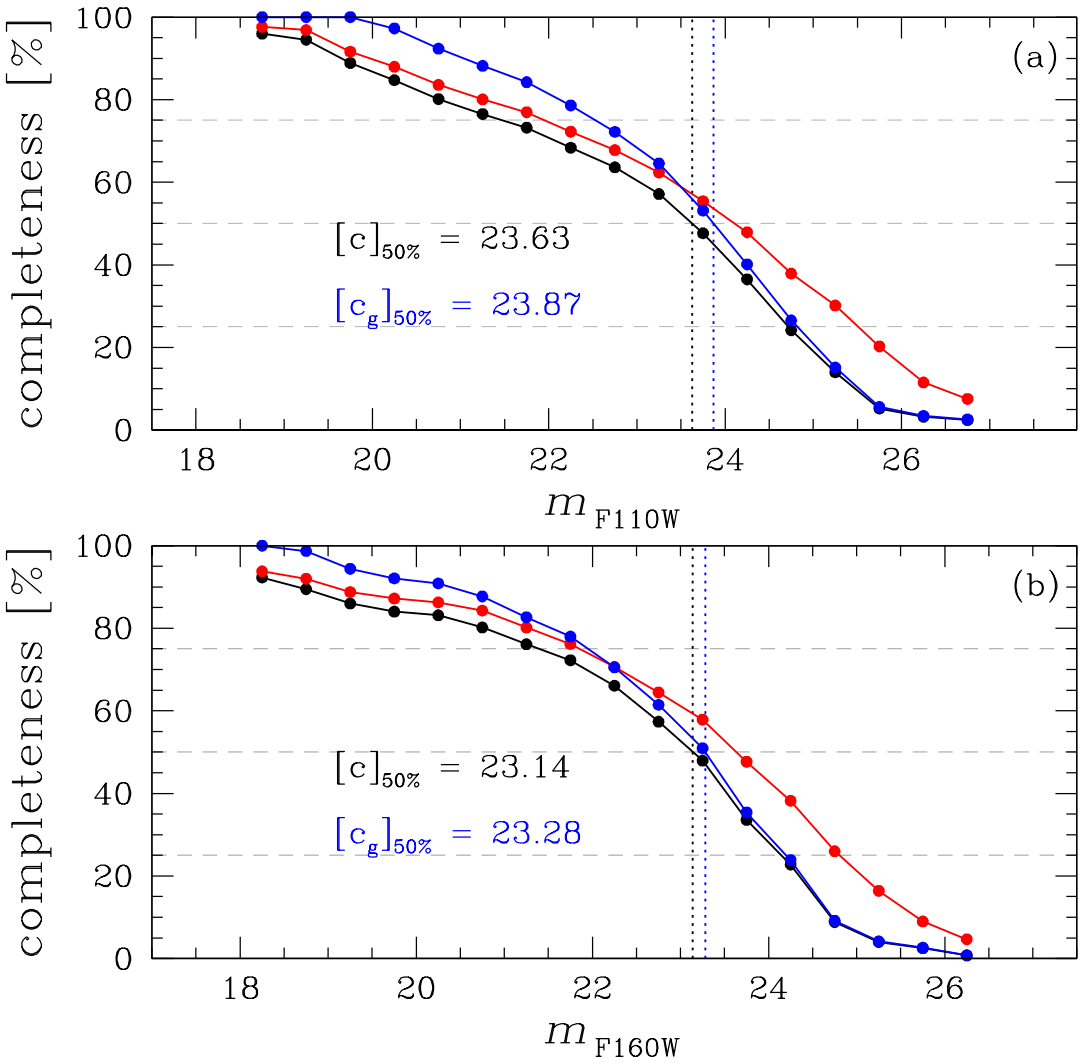

FIGURE 8.8: Completeness based on AS tests for the F110W (a) and F160W (b) filter. Black points show the conventional completeness c, while the blue points are the low-rmsSKY completeness c_g. We also report, for each filter, the magnitude where c and c_g are equal to 50% ($[c]_{50\%}$ and $[c_g]_{50\%}$). For comparison, we also show the conventional completeness obtained without considering the MP selection, represented with red points.

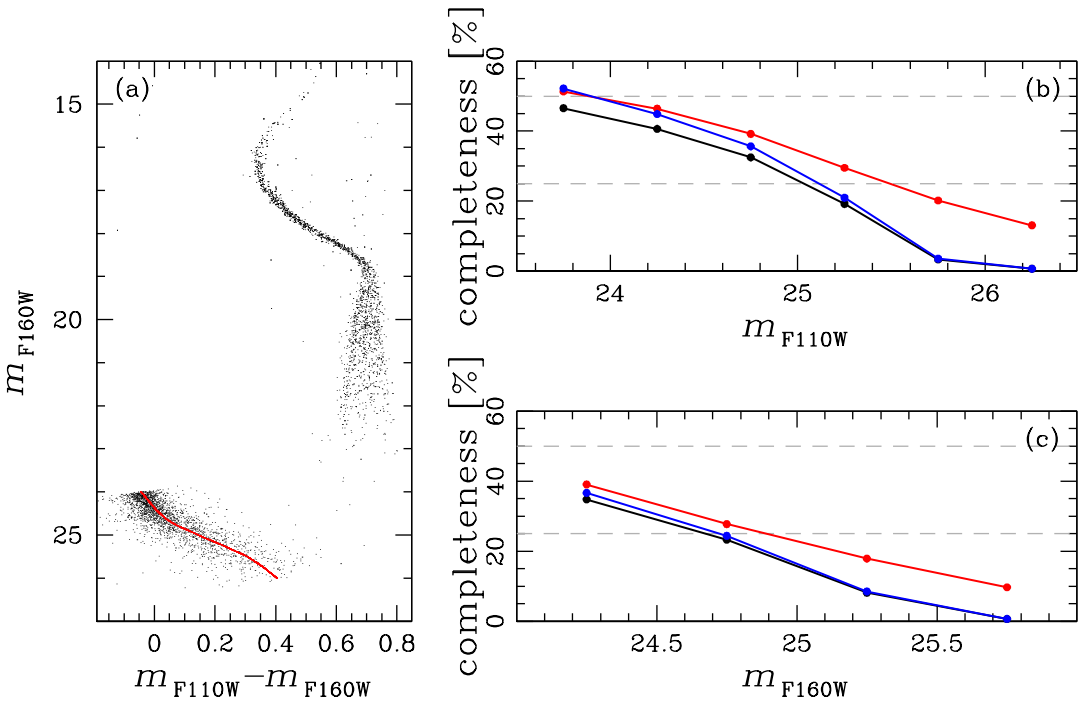

FIGURE 8.9: Same as panel (a) of Fig. 10.10 and panels (a) and (b) of Fig. 10.4 but for the WD CS.

of individual elements to be adjusted to match observations as well as possible. The effect of non-solar element abundances is thoroughly accounted for in stellar interiors and atmospheres, as well as the boundary conditions connecting them. The isochrones are based on new evolutionary models, calculated using the `MESA` code (Paxton et al., 2011; Paxton et al., 2013; Paxton et al., 2015; Paxton et al., 2018; Paxton et al., 2019), and new model atmospheres, calculated using `PHOENIX 15` (Hauschildt, Baron, and Allard, 1997; Allard, Homeier, and Freytag, 2011; Allard, Homeier, and Freytag, 2012; Gerasimov et al., 2020) and `BasicATLAS / ATLAS 9` (Kurucz, 1970; Kurucz, 2005; Kurucz, 2014; Larkin, Gerasimov, and Burgasser, 2023).

The parameters of our isochrones are summarised in Table 8.2. Among the spectroscopic abundances in Milone et al. (2013) and Yong et al. (2005) and Yong et al. (2008) that were used as the initial guesses in our analysis, [O/Fe], [Na/Fe], [Al/Fe] needed to be adjusted to reconcile our model isochrones with the lower MS photometry. Additionally, non-solar [C/Fe] values needed to be adopted for MS-A and MS-B. The adjusted photometric abundances retain the key features of GC chemistry, specifically the Na – O and N – C anti-correlations; however, we find that the difference between 1P and 2P abundances that were required to reproduce the photometric scatter is smaller than the spectroscopic abundance spread of red giants by $0.2-0.3$ dex. Our photometric estimate of [Al/Fe] appears to consistently exceed the spectroscopic counterpart in all three populations by up to 0.4 dex. Significant discrepancies between photometric and spectroscopic abundances are not unexpected, since both methods are affected by distinct systematic errors. The offset between spectroscopic and photometric estimates of [O/Fe] of order 0.15 dex shown in Table 8.2 is consistent with previous work (Gerasimov et al., 2023). The large offset in [Al/Fe] is likely a combination of systematic errors in both photometric and spectroscopic estimates due to the poorer isochrone fit in the vicinity of the MS knee, where the photometric constraints on [Al/Fe] are strictest, and strong non-local thermodynamic equilibrium effects on the spectral features of aluminium (Andrievsky et al.,

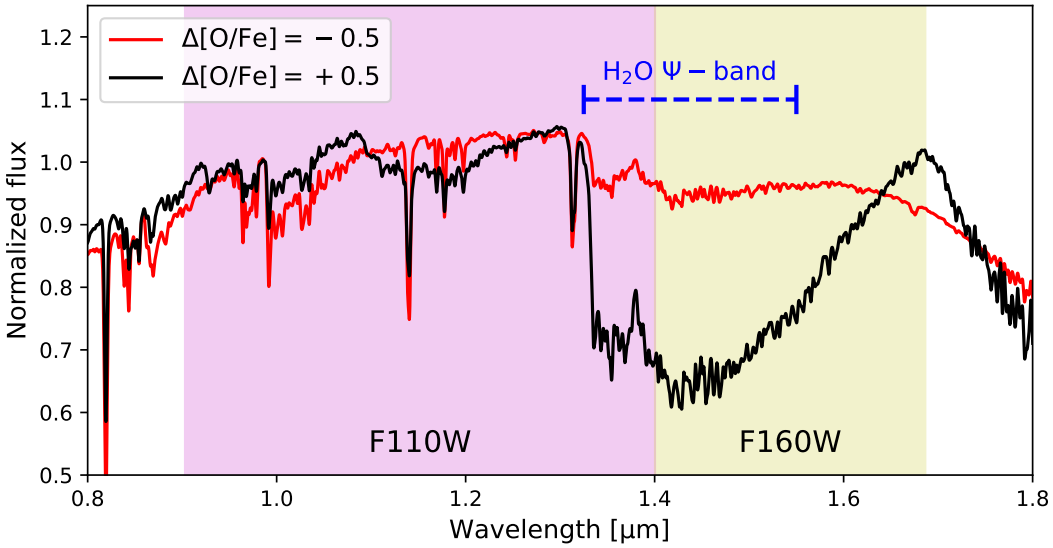

FIGURE 8.10: Synthetic spectra for two stars from MS-B and with stellar mass $0.095\,M_{\odot}$, characterised by different content of [O/Fe]. The wavelength windows of the WFC3/NIR F110W and F160W filter bands are highlighted in magenta and yellow colours, respectively. We also denote the H_2O absorption band.

2008). In general, small offsets between spectroscopic and photometric abundances indicate that the quoted values are particularly reliable, while larger offsets require a follow-up investigation of associated systematic errors. In particular, more robust photometric abundances may be derived by considering the colours in additional photometric bands.

All model atmospheres, evolutionary models, and isochrones employed in this study are available online[4].

The final fits of three isochrones corresponding to MS-A, MS-B, and MS-C are represented in Fig. 10.6, in blue, green, and red, respectively. In addition to the isochrones, we've marked specific mass values with their corresponding labels on the plot.

To illustrate the impact of oxygen variations on the *HST* NIR bands, Fig. 8.10 shows two synthetic spectra representing stars from MS-B and stellar mass $0.095\,M_{\odot}$. These two spectra are characterised by different content of [O/Fe], specifically $\Delta[O/Fe] = -0.5$ (in red) and $\Delta[O/Fe] = 0.5$ (in black), with respect to the [O/Fe] value reported in Table 8.2. The figure focuses on the wavelength range covered by the WFC3/NIR F110W and F160W filter bands, highlighted by magenta and yellow colours, respectively. The H_2O absorption band is also indicated. The H_2O molecules have a strong effect on the two synthetic spectra, resulting in a notably lower flux in the F160W filter.

The WD CS of NGC 6752 in the infrared

A representative 12.5 Gyr WD isochrone is shown in the lower-left part of Fig. 10.6. It has been computed using the WD models by Salaris et al. (2022) calculated for metal-poor progenitors employing the Cassisi et al. (2007a) electron conduction opacities

[4] http://romanger.com/models.html

TABLE 8.2: Parameters of new NGC 6752 isochrones calculated in this study. $\alpha_{\rm MLT}$ is the assumed convective mixing length in the interior in terms of pressure scale heights. $(m-M)_0$ and $E(B-V)$ are the distance modulus and optical reddening in mag, respectively. Y is the helium mass fraction. All abundances are given in dex with respect to the solar standard used in Gerasimov et al. (2022a). The values estimated from isochrone fitting are highlighted in bold; the rest of the parameters were adopted from the literature. In the "Ref." columns, "M19" refers to Milone et al. (2019); "M13" to the compilation of spectroscopic abundances in Table 2 of Milone et al. (2013), derived from Yong et al. (2005) and Yong et al. (2008); "M13Y" to the best-fit Y values for the three populations from Milone et al. (2013); "C10" to the recommended solar abundance of carbon from Caffau et al. (2010), "TO" to the isochrone best fit around the MS turn-off point and the subgiant branch; and "LMS" to the isochrone best fit near the end of the MS below the MS knee. The "Offset" columns show the difference between the photometric best fit and the spectroscopic value from Milone et al. (2013), where applicable. Age, $\alpha_{\rm MLT}$, $(m-M)_0$ and $E(B-V)$ were assumed to be identical for all three populations. The errors in "TO" parameters are taken directly from the covariance matrix of the fit. The errors in "LMS" parameters are taken as the weighted standard deviation of the best-fit value along the lower MS.

	MS-A			MS-B			MS-C		
Parameter	Value	Offset	Ref.	Value	Offset	Ref.	Value	Offset	Ref.
$\alpha_{\rm MLT}$	1.57 ±0.05	–	TO	1.57 ±0.05	–	TO	1.57 ±0.05	–	TO
Age [Gyr]	12.63 ±0.40	–	TO	12.63 ±0.40	–	TO	12.63 ±0.40	–	TO
$(m-M)_0$	13.10 ±0.01	–	TO	13.10 ±0.01	–	TO	13.10 ±0.01	–	TO
$E(B-V)$	+0.07	–	M19	+0.07	–	M19	+0.07	–	M19
Y	0.246	–	M13Y	0.254	–	M13Y	0.275	–	M13Y
[Fe/H]	−1.65	–	M13	−1.61	–	M13	−1.61	–	M13
[C/Fe]	+0.20 ±0.19	–	LMS	−0.30 ±0.19	–	LMS	+0.00	–	C10
[N/Fe]	−0.11	–	M13	+0.92	–	M13	+1.35	–	M13
[O/Fe]	+0.67 ±0.03	+0.02	LMS	+0.50 ±0.04	+0.07	LMS	+0.23 ±0.02	+0.20	LMS
[Na/Fe]	−0.03	–	M13	+0.26	–	M13	+0.31 ±0.05	−0.30	LMS
[Mg/Fe]	+0.51	–	M13	+0.49	–	M13	+0.40	–	M13
[Al/Fe]	+0.65 ±0.13	+0.37	LMS	+1.10 ±0.04	+0.40	LMS	+1.34 ±0.03	+0.20	LMS
[Si/Fe]	+0.27	–	M13	+0.33	–	M13	+0.35	–	M13
[Ca/Fe]	+0.21	–	M13	+0.24	–	M13	+0.27	–	M13
[Sc/Fe]	−0.05	–	M13	−0.04	–	M13	−0.04	–	M13
[Ti/Fe]	+0.10	–	M13	+0.14	–	M13	+0.15	–	M13
[V/Fe]	−0.34	–	M13	−0.29	–	M13	−0.25	–	M13
[Mn/Fe]	−0.50	–	M13	−0.44	–	M13	−0.45	–	M13
[Co/Fe]	−0.03	–	M13	−0.00	–	M13	−0.06	–	M13
[Ni/Fe]	−0.06	–	M13	−0.06	–	M13	−0.03	–	M13
[Cu/Fe]	−0.66	–	M13	−0.59	–	M13	−0.60	–	M13
[Y/Fe]	−0.09	–	M13	−0.01	–	M13	+0.01	–	M13
[Zr/Fe]	+0.07	–	M13	+0.20	–	M13	+0.21	–	M13
[Ba/Fe]	−0.09	–	M13	−0.12	–	M13	+0.05	–	M13
[La/Fe]	+0.12	–	M13	+0.10	–	M13	+0.13	–	M13
[Ce/Fe]	+0.28	–	M13	+0.25	–	M13	+0.28	–	M13
[Nd/Fe]	+0.23	–	M13	+0.22	–	M13	+0.23	–	M13
[Eu/Fe]	+0.31	–	M13	+0.30	–	M13	+0.34	–	M13

(see Salaris et al., 2022, for more details), the WD initial-final mass relation by Cummings et al. (2018), and progenitor lifetimes taken from the α-enhanced models by Pietrinferni et al. (2021).

Notably, in the upper part of the WD isochrone, we observe three sources that survived both the photometric and MP selections (shown as orange crosses) and lie very close to the isochrone. Other stars that passed only the photometric selections are situated along the WD isochrone (marked by a grey circle around them), making them potential WD candidates. However, due to the limited depth of our data, we cannot ensure a sufficient level of PM accuracy to distinguish reliably between cluster members and field stars in this faint region of the CMD. Consequently, more data will be necessary to confirm the presence of an extended WD sequence.

We employed the WD isochrone shown in the plot to determine the effective temperature ($T_{\rm eff}$) and gravity (g) values for the three surviving WDs, which passed both the photometric and MP selection criteria. The resulting values are as follows, ordered from the brightest to the faintest source: $T_{\rm eff} = (2.510 \pm 0.223) \times 10^4$ K, $(2.379 \pm 0.212) \times 10^4$ K and $(1.782 \pm 0.159) \times 10^4$ K, and $\log(g)$ = 7.824, 7.829 and 7.857, in cgs units.

8.4 Luminosity Function of sub-populations

In this Section, we present the LFs for the three MSs within the magnitude range of $19 < m_{\rm F160W} < 23.5$. Two different methods were used to assess the LFs, which are described in the following.

8.4.1 Luminosity Function using regions in the verticalised CMD

The initial procedure follows a method similar to the one outlined in Milone et al. (2012b). In panel (a) of Fig. 10.5, we present a zoomed region of the $m_{\rm F160W}$ versus $m_{\rm F110W} - m_{\rm F160W}$ CMD shown in Fig. 10.6, where the triple MS sequence is most evident.

The fiducial lines, constructed by connecting manually drawn fiducial points on the CMD with straight lines, appear as blue and red lines for MS-A and MS-C, respectively, on the CMD. These fiducial lines were used to create the diagram shown in panel (b) of Fig. 10.5, with the abscissa calculated using equation (1) from Milone et al. (2019). In this diagram, we established three distinct regions, denoted as R_1, R_2, and R_3, each corresponding to the three MS populations, MS-A, MS-B, and MS-C. These defined regions are visually represented by blue, green, and red colours, respectively, in panel (b) of Fig. 10.5.

It is important to note that not all the single MS-A(B,C) stars are confined solely within $R_{1(2,3)}$, as a fraction of them may migrate to nearby regions due to a combination of measurement errors and overlapping distributions of the chemical abundances within each MS. We will evaluate this latter effect in the following section. In this section, we're focusing solely on the impacts stemming from measurement errors. To account for this contamination effect and estimate the actual number of stars in each population we utilised the following procedure:

The total numbers $N_{i=1,2,3}$ (corrected for completeness) of stars within each region $R_{i=1,2,3}$ can be expressed as the sum of three terms:

$$N_i = N_{\rm A} f_i^{\rm A} + N_{\rm B} f_i^{\rm B} + N_{\rm C} f_i^{\rm C}. \tag{8.1}$$

TABLE 8.3: Number of stars for each MS (N_A, N_B and N_C) in nine magnitude bins and for the two methods.

Δm_{F160W}	Regions			Gaussian		
	N_A	N_B	N_C	N_A	N_B	N_C
19.0-19.5	129±11	121±11	73±9	124±11	68±8	126±11
19.5-20.0	138±12	169±13	118±11	112±11	180±13	128±11
20.0-20.5	141±12	236±15	167±13	100±10	288±17	156±12
20.5-21.0	118±11	202±14	139±12	97±10	215±15	146±12
21.0-21.5	133±12	108±10	94±10	100±10	177±13	59±8
21.5-22.0	107±10	101±10	59±8	63±8	189±14	17±4
22.0-22.5	77±9	61±8	30±5	58±8	81±9	25±5
22.5-23.0	33±6	50±7	18±4	31±6	38±6	31±6
23.0-23.5	20±4	17±4	8±3	19±4	11±3	15±4

where N_A, N_B, and N_C represent the total number of stars in the three populations, and f_i^A, f_i^B, and f_i^C are the fractions of stars from the three populations that fall within the i-th region[5].

To estimate the quantities f_i^A, f_i^B, and f_i^C, we employed ASs (see Section 8.3.1). For each real star in our catalogue, we identified the five closest ASs in terms of position and magnitude and defined a sample of ASs. We then verticalized the obtained ASs sample using the same procedure and fiducial lines shown in Fig. 10.5. The values of f_i^A, f_i^B, and f_i^C were evaluated as the fraction of ASs associated with MS-A, MS-B, and MS-C stars that fall in each region R_1, R_2, and R_3.

We solved Eq. 8.1 for the nine magnitude bins defined by the grey horizontal lines in Fig. 10.5, obtaining estimates of N_A, N_B, and N_C for each bin. The corresponding values are reported in Table 8.3, while the three LFs for the three individual MSs are displayed in panel (a) of Fig. 8.12, with the associated errors represented as Poisson errors. Within the magnitude interval $19 < m_{F160W} < 21.25$, MS-B exhibits the highest number of stars, while populations MS-A and MS-C have a smaller and similar number of stars. Moving to the magnitude interval $21.25 < m_{F160W} < 23.5$, MS-B and MS-A are the most populated, with nearly the same number of stars, while MS-C shows a lower number of stars. An examination of this figure seems to reveal that MS-B and MS-C LFs follow a comparable trend with magnitude. They exhibit an increase up to approximately $m_{F160W} \sim 20.25$, followed by a gradual decrease for faint magnitudes. In contrast, the LF for MS-A remains relatively constant in the brighter region and only starts to decrease at magnitudes fainter than $m_{F160W} \sim 21.5$, with a behaviour similar to those of the LFs of MS-B and MS-C.

These distinctions become even more pronounced in panel (b) of Fig. 8.12, where the LFs for the three individual MSs are normalised by the value of the first bin for each respective MS. Notably, within the magnitude interval of $19 < m_{F160W} < 21.25$, the three MSs manifest distinct trends, with MS-B and MS-C displaying a pronounced increase with respect to MS-A. In the magnitude range of $21.25 < m_{F160W} < 23.5$, the three MSs share a similar trend.

Finally, panel (c) of Fig. 8.12 presents the ratio of N_A, N_B, and N_C to the total number of stars, N. The values are reported in Table 8.4.

[5]In the analysed region of the m_{F160W} versus $m_{F110W} - m_{F160W}$ CMD, the MSs exhibit a nearly vertical orientation, causing binary stars to be closely mixed with single stars. As a result, in this analysis, we did not consider the presence of binaries. However, we emphasise, that the observed binary fraction in this cluster is rather low anyway (∼0.7%, see Milone et al., 2010).

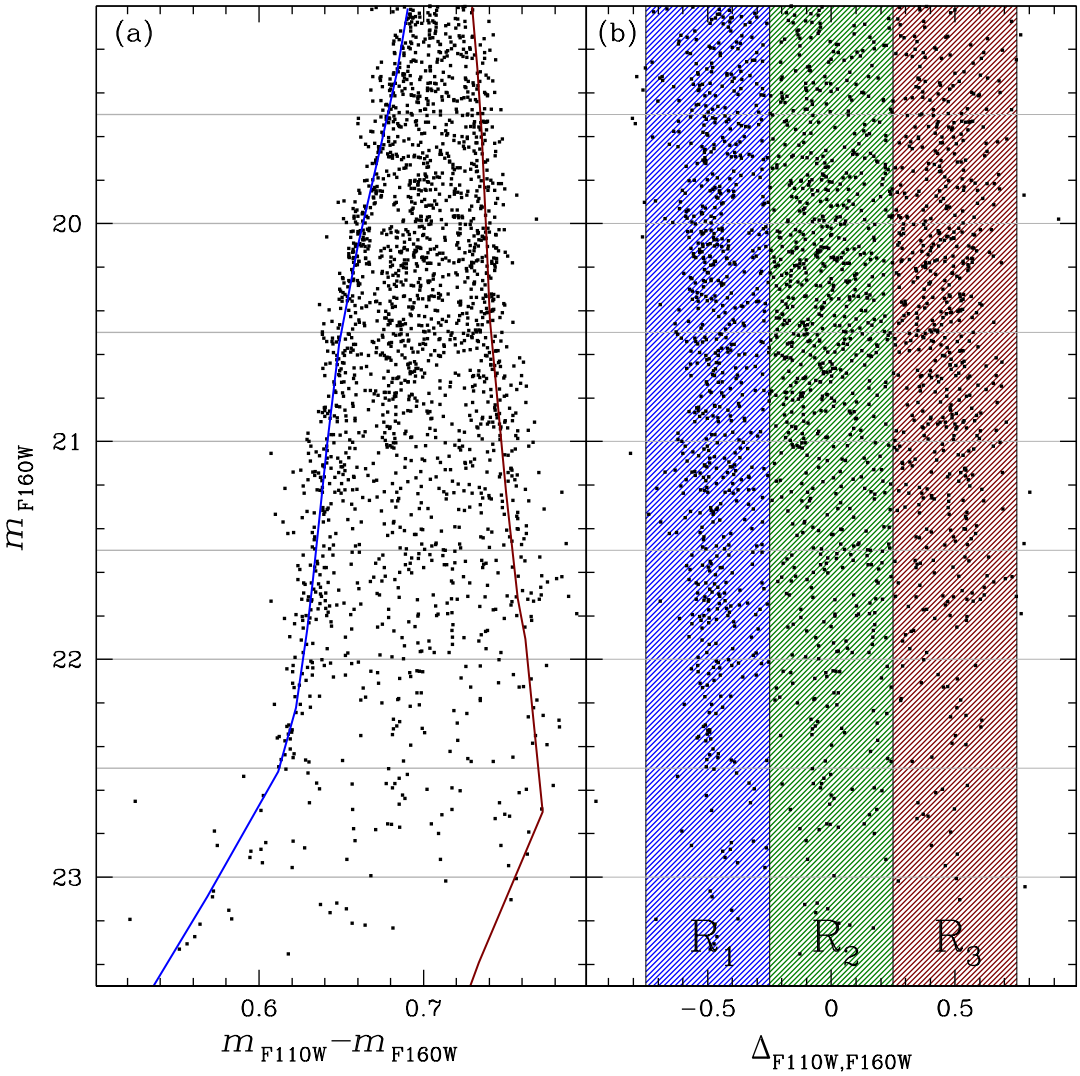

FIGURE 8.11: Procedure for estimating the LFs of MS-A, MS-B, and MS-C. (a) zoomed view of the $m_{\rm F160W}$ versus $m_{\rm F110W} - m_{\rm F160W}$ CMD, focusing on the region where the three MSs are distinctly identifiable. The bluest and reddest sequences are associated with MS-A and MS-C stars, respectively, while the middle sequence corresponds to MS-B stars. The blue and red lines represent the fiducials of MS-A and MS-C, respectively, and are utilised to construct the verticalized CMD shown in (b). (b) in the verticalized CMD, three distinct regions, denoted as R_1, R_2, and R_3, are defined, each corresponding to one of the three MS populations (MS-A, MS-B, and MS-C), distinguished by blue, green, and red colours, respectively.

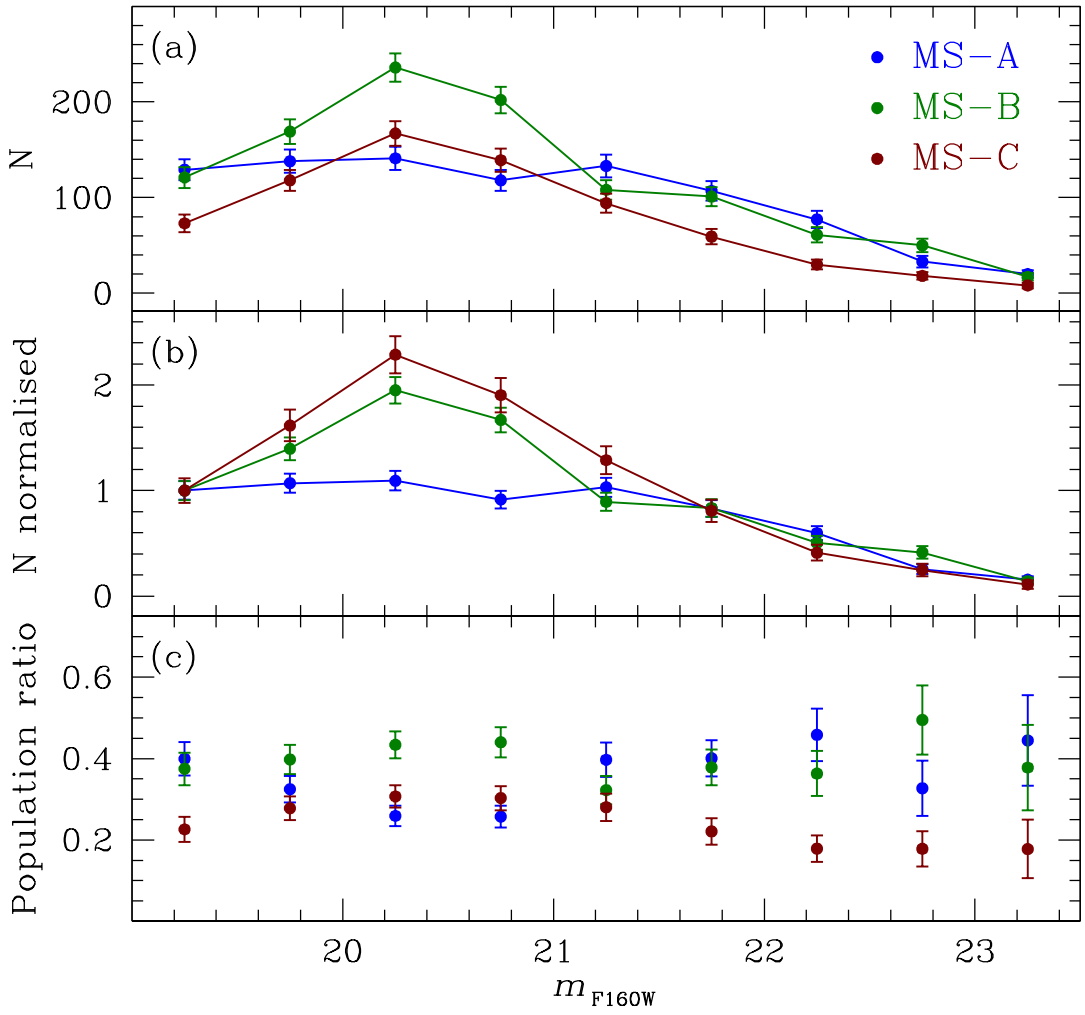

FIGURE 8.12: LFs estimated using regions in the verticalised CMD (see Fig. 10.5) (a) LFs for the three MSs. (b) LFs for the three MSs, normalised by the value of the first bin for each respective MS. (c) Number ratios for the three stellar populations with respect to the total, as a function of the $m_{\rm F160W}$ magnitude.

TABLE 8.4: Fractions of MS-A, MS-B, and MS-C stars relative to the total number of MS stars in nine m_{F160W} magnitude bins, obtained through the two different methods. Additionally, we provide the dispersions of the three best-fitting Gaussian functions ($\sigma_{MS-A,MS-B,MS-C}$). We also provide the weighted mean values of each fraction, with the uncertainties estimated as the ratio between the root mean square (rms) of the nine population-ratio measurements divided by the square root of 8.

Δm_{F160W}	Regions			Gaussian					
	N_A/N	N_B/N	N_C/N	N_A/N	N_B/N	N_C/N	σ_{MS-A}	σ_{MS-B}	σ_{MS-C}
19.0-19.5	0.40±0.04	0.37±0.04	0.23±0.03	0.39±0.04	0.21±0.03	0.40±0.05	0.13	0.08	0.22
19.5-20.0	0.32±0.03	0.40±0.04	0.28±0.03	0.27±0.03	0.43±0.04	0.30±0.03	0.09	0.18	0.14
20.0-20.5	0.26±0.02	0.43±0.03	0.31±0.03	0.18±0.02	0.53±0.04	0.29±0.03	0.06	0.21	0.11
20.5-21.0	0.26±0.03	0.44±0.04	0.30±0.03	0.21±0.03	0.47±0.04	0.32±0.03	0.07	0.17	0.12
21.0-21.5	0.40±0.04	0.32±0.03	0.28±0.03	0.30±0.04	0.52±0.06	0.18±0.03	0.09	0.29	0.10
21.5-22.0	0.40±0.04	0.38±0.04	0.22±0.03	0.23±0.04	0.70±0.08	0.07±0.02	0.05	0.35	0.10
22.0-22.5	0.46±0.06	0.36±0.06	0.18±0.03	0.35±0.07	0.49±0.08	0.16±0.04	0.04	0.24	0.10
22.5-23.0	0.33±0.07	0.49±0.09	0.18±0.04	0.31±0.08	0.38±0.10	0.31±0.08	0.11	0.08	0.14
23.0-23.5	0.44±0.11	0.38±0.11	0.18±0.07	0.43±0.17	0.25±0.12	0.32±0.14	0.04	0.06	0.31
	0.34±0.02	0.40±0.02	0.26±0.02	0.26±0.03	0.47±0.03	0.27±0.03			

8.4.2 Luminosity Function using a three-Gaussians fit

To assess the potential impact of intrinsic cross-contamination among the three stellar populations when evaluating their LFs, we employed an alternative method to derive the LFs of the three MSs. This method is based on the approach detailed in Milone et al. (2019).

Panels (a) and (b) of Fig. 8.13 represent the m_{F160W} versus $m_{F110W} - m_{F160W}$ CMD and the m_{F160W} versus $m_{F110W} - m_{F160W}$ verticalised CMD introduced in Fig. 10.5. Panels (c)-(m) of Fig. 8.13 show the $\Delta_{F110W,F160W}$ histogram distribution of stars in the nine magnitude intervals defined by the grey horizontal lines in panels (a) and (b) of Fig. 8.13. We estimated the best-fitting three-Gaussian function for each histogram in each magnitude bin and overlaid them on the histograms as grey continuous lines, with each component denoted by blue, green, and red colours.

In Milone et al. (2019), the estimation of the number of stars for each population was based on the areas beneath their corresponding Gaussians. However, upon closer examination of the three components of the three-Gaussian fit shown in panels (c)-(m) of Fig. 8.13, it becomes apparent that the Gaussian representing MS-A (in blue) provides a satisfactory fit to the histogram, while the Gaussian components of MS-B (in green) and MS-C (in red) do not adequately fit the data; for MS-C this is particularly true at fainter magnitude bins where the statistic for this component is very low. This discrepancy suggests that MS-B stars deviate from a Gaussian distribution. Consequently, a decision was made to estimate the number of stars in the MS-A and MS-C populations based on the areas beneath their respective Gaussians, and to calculate the number of stars in MS-B as the difference, in each bin, between the total number of stars and the sum of MS-A and MS-C populations. The resulting values (corrected for completeness) are represented in panel (a) of Fig. 8.14 and listed in Table 8.3. Notably, the LFs shown in this figure exhibit notable differences compared to those presented in Fig. 8.12 and estimated using the first procedure. Specifically, there is a reduction in the number of stars in MS-A, and an increase in

the number of stars in MS-B, while the number of MS-C stars has, on average, remained relatively constant. Within the magnitude interval $19 < m_{\rm F160W} < 21.25$, MS-B is the most populous, whereas MS-A and MS-C have approximately the same number of stars (albeit lower compared to MS-B).

The shape of the three LFs in Fig. 8.12 differs significantly, as highlighted in panel (b) of Fig. 8.14, where the LFs for individual MS populations are normalized by the value of the first bin for each respective MS. Specifically, the LF of MS-C now appears to resemble the LF of MS-A, in contrast to the results presented in Fig. 8.12 where it exhibited a trend similar to MS-B. We explain this change as due to the high degree of overlap between MS-B and MS-C distributions (as shown in panels (c)-(m) of Fig. 8.13), making it challenging to establish a precise boundary between these two populations. The observed similarity in panel (b) of Fig. 8.12 between the LFs of MS-B and MS-C may be attributed to cross-contamination of MS-B into the MS-C regions, which is particularly effective given the broad non-Gaussian distribution of MS-B and its larger population size compared to MS-C.

In essence, estimating the total fraction for MS-C proved to be the most challenging task. The most prudent approach appears to be estimating the number of MS-A using a Gaussian and determining the combined number of MS-B and MS-C as the difference between the total number of stars and the MS-A population. The LF for MS-A and the combined LF for MS-B and MS-C are illustrated in Fig. 8.15 for each magnitude bin. The values are reported in Table 8.5. It is evident that the LF of MS-B+MS-C stars exhibits a distinct shape compared to the LF of MS-A stars, providing evidence of a different LF between these two groups of stars.

Panel (c) of Fig. 8.14 shows the fractions of MS-A, MS-B, and MS-C stars relative to the total number of MS stars ($N_{\rm A}/N$, $N_{\rm B}/N$ and $N_{\rm C}/N$). The values, along with the dispersion of each Gaussian component ($\sigma_{\rm MS-A}$, $\sigma_{\rm MS-B}$ and $\sigma_{\rm MS-C}$), are listed in Table 8.4. While the ratios obtained in this study align with the values reported by Milone et al. (2019) within the magnitude range $19 < m_{\rm F160W} < 22$, there are differences present. These inconsistencies can be ascribed to two main differences in the data set used in our work compared to Milone et al. (2019). First, Milone et al. (2019) lacked access to proper motion data, and therefore, contamination from field objects was addressed using a statistical approach. Second, the new observations combined with the existing data were collected with different orientations and large offsets. While this has improved photometric accuracy, it has simultaneously led to a reduction in photometric precision, resulting in broader sequences.

By calculating weighted averages of the population ratios obtained in the nine magnitude intervals, we find that MS-A, MS-B, and MS-C encompass approximately 26±3%, 47±3%, and 27±3%, respectively, of the total number of MS stars. Notably, these values are consistent with the values reported in Milone et al. (2019) (26.3±1.4%, 46.9±1.3% and 26.8±2.0%, respectively), differing only by $0.09\,\sigma$, $0.03\,\sigma$ and $0.06\,\sigma$, respectively. Additionally, these ratios are in line with findings from studies on NGC 6752 encompassing a wider range of masses ($0.8 - 0.6$ M$_\odot$) and various radial distances (Milone et al., 2013; Nardiello et al., 2015b).

8.5 Mass Function of sub-populations

To determine the MF of NGC 6752 and its populations, we estimated the mass of each star below the MS knee by identifying the closest isomass line to the star's position on the CMD. The isomass lines for given initial stellar masses were determined

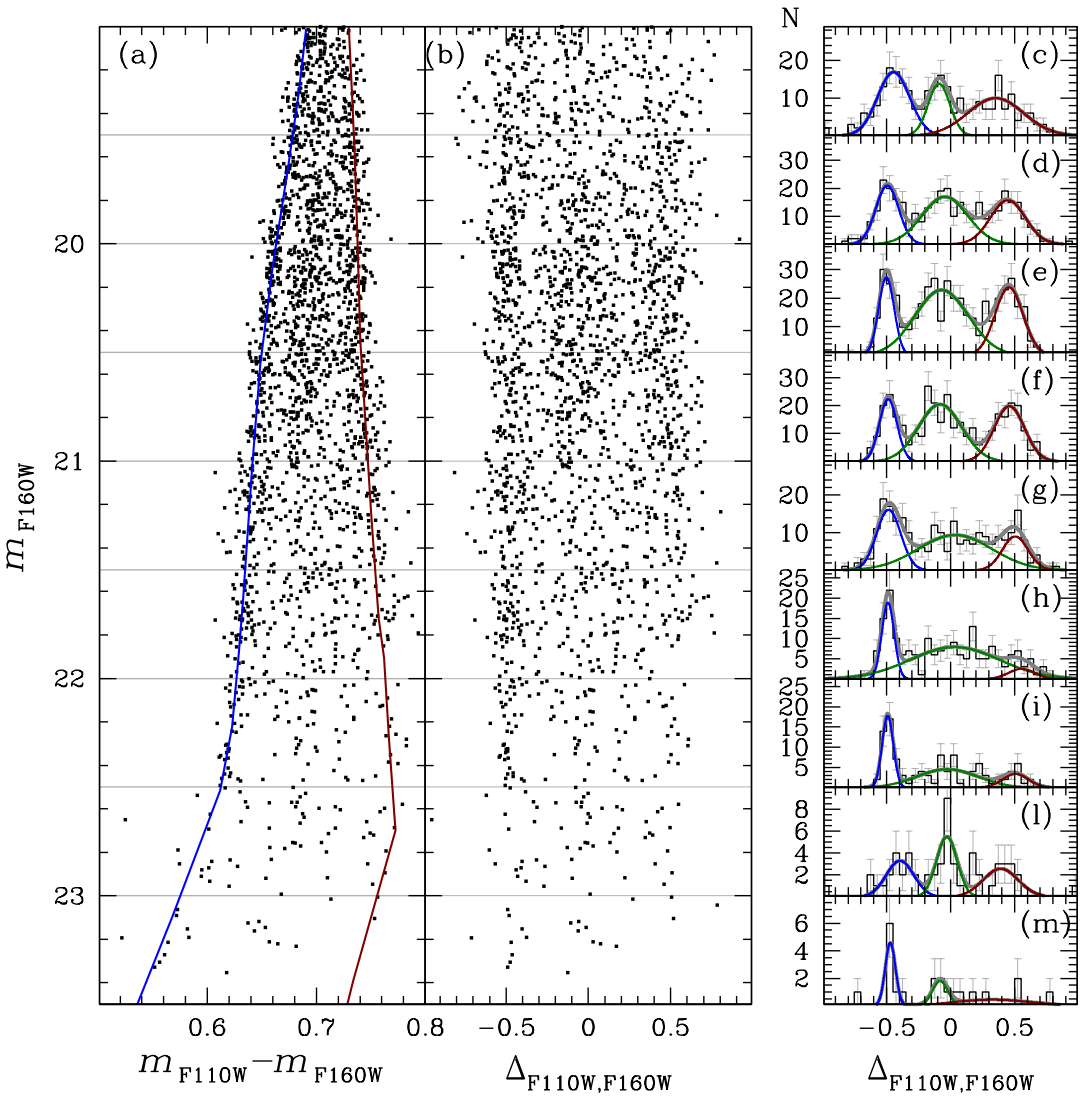

FIGURE 8.13: (a)-(b) Same as panels (a) and (b) of Fig. 10.5. (c)-(m) $\Delta_{F110W,F160W}$ histogram distribution of cluster stars in nine luminosity intervals, as indicated by the grey lines in (a) and (b). Overlaid on each histogram are the best-fitting three-Gaussian functions, visually represented by blue, green, and red lines.

TABLE 8.5: Number of stars in MS-A (N_A) and MS-B+MS-C together ($N_B + N_C$).

Δm_{F160W}		
	N_A	$N_B + N_C$
19.0-19.5	124±11	197±14
19.5-20.0	112±11	312±18
20.0-20.5	100±10	441±21
20.5-21.0	97±10	361±19
21.0-21.5	100±10	236±15
21.5-22.0	63±8	203±14
22.0-22.5	58±8	104±10
22.5-23.0	31±6	70±8
23.0-23.5	19±4	25±5

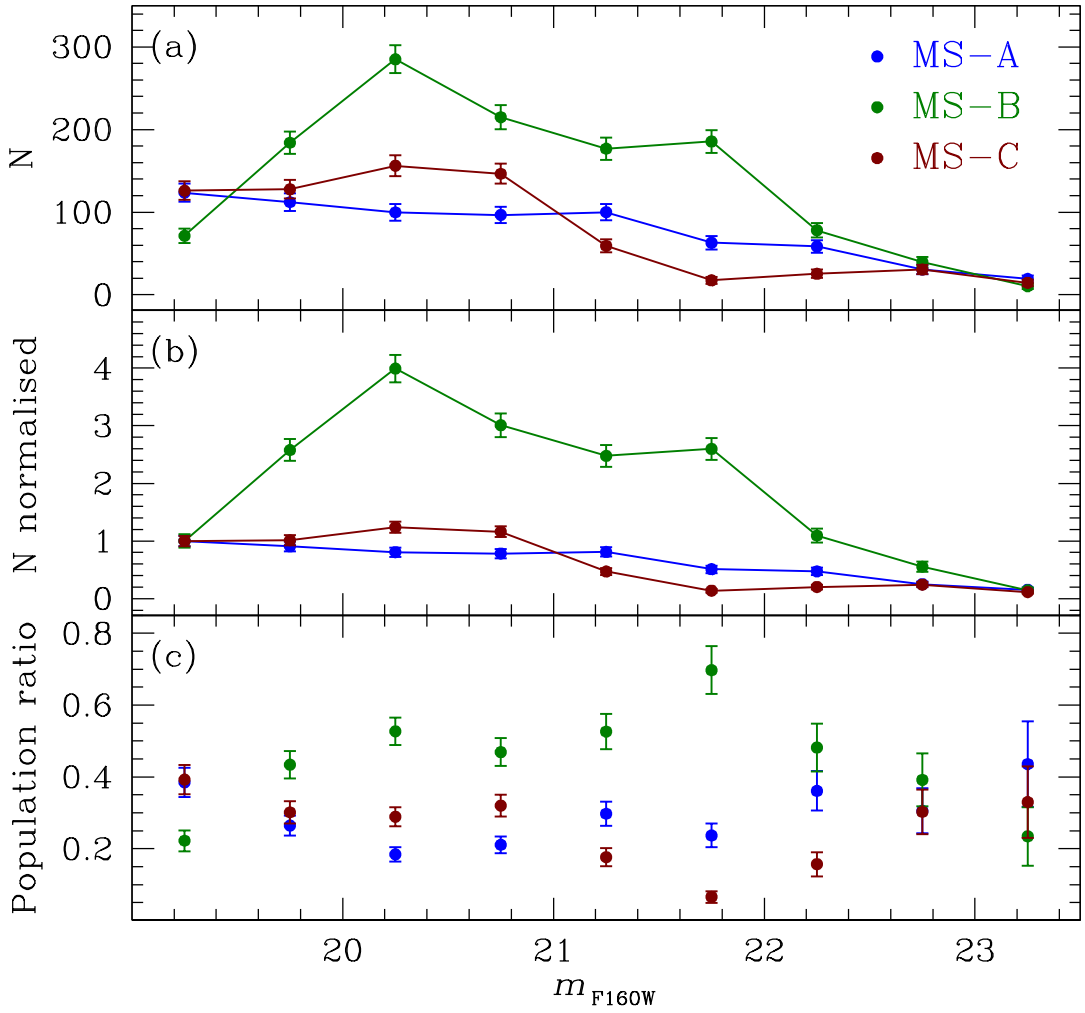

FIGURE 8.14: Same as Fig. 8.12 but using a three-Gaussians fit (see Fig. 8.13).

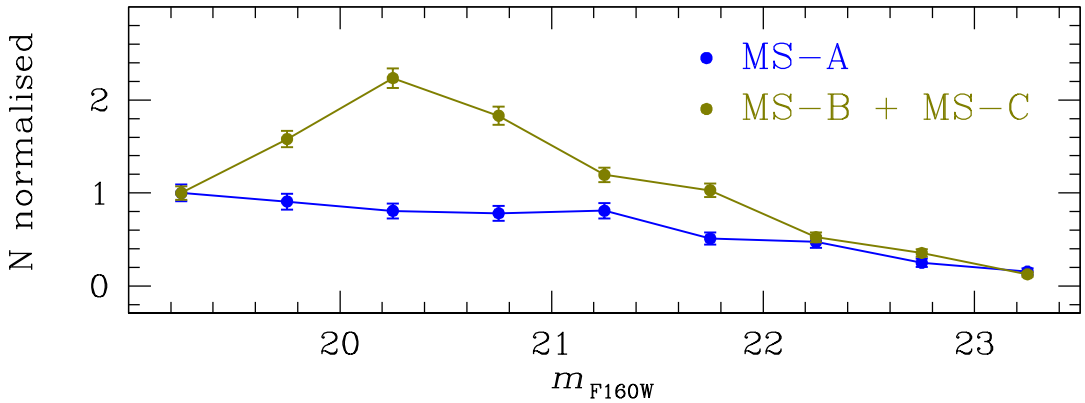

FIGURE 8.15: LFs for the MS-A and MS-B+MS-C together, normalised by the value of the first bin for each respective LF. See text for details.

by fitting parabolas to the isochrone points, corresponding to those masses. The obtained mass distribution was divided into 10 uniform bins, spanning the mass range from $\approx 0.091\,M_\odot$ to $0.44\,M_\odot$. The mass range was chosen to be as wide as possible while remaining within the magnitude bounds of Table 8.5 ($19 < m_{F160W} < 23.5$). The resulting histogram is shown in Fig. 8.16.

The star counts in each bin were corrected for the completeness estimates from Fig. 10.4. The displayed errors in each bin include the Poisson counting error and the statistical error due to incomplete sampling. The latter was calculated by drawing random magnitude measurements in each mass bin according to the observed magnitude distribution and carrying out synthetic observations, using the estimated completeness in Fig. 10.4 as the probability for each synthetic star to be observed. The final incomplete sampling error was taken as the standard deviation of the number of observed synthetic stars over 10^5 Monte Carlo trials.

The individual MF of MS-A and the combined MF of MS-B and MS-C were calculated by multiplying the total star count in each mass bin by the average population fraction within that bin, according to Table 8.5. The displayed errors for these two MFs in Fig. 8.16 include the statistical error in the total star count (Poisson and incomplete sampling), as well as the error in the estimated population fraction, all added in quadrature.

To determine whether the inferred MFs of MS-A and MS-B+C are statistically consistent, we evaluated the error-scaled absolute differences between the normalized star counts in each mass bin:

$$\Delta_i = \frac{\left|\Xi_i^A - \Xi_i^{B+C}\right|}{\sqrt{\mathrm{Var}(\Xi_i^A) + \mathrm{Var}(\Xi_i^{B+C})}} \tag{8.2}$$

where Ξ_i^A is the completeness-corrected normalized star count of MS-A in the i-th mass bin, Ξ_i^{B+C} is the completeness-corrected normalized combined star count of MS-B and MS-C in the i-th bin, Var represents the squared error of a given quantity. The normalization was chosen as $\sum_i \Xi_i^A = \sum_i \Xi_i^{B+C} = 1$. If the MFs of MS-A and MS-B+C are consistent, Δ_i is expected to approximately follow the standard half-normal distribution. We carried out a one-sample Kolmogorov-Smirnov test between the calculated values of Δ_i and the standard half-normal distribution. The resulting p-value of 0.027 suggests that the discrepancies between the MF of MS-A and the combined MF of MS-B+C cannot be explained by the measurement errors alone.

More in general, Fig. 8.16 shows that the MF of MS-A tends to be flatter than that of MS-B+C in most of the mass range ($0.2 - 0.45\,M_\odot$).

8.6 Summary and conclusions

In this chapter, we exploited NIR images of an external region of the GC NGC 6752, which were acquired by *HST* using the F110W and F160W filters of the WFC3/NIR camera at three distinct epochs (2018, 2019, and 2021). These filters are known for their sensitivity to stars with varying oxygen enhancement, making them ideal for investigating and differentiating mPOPs in the lower part of the MS.

The first epoch of this dataset was previously examined in an earlier publication within this series (Milone et al., 2019). In that study, it was revealed that the three distinct stellar populations within NGC 6752, originally observed in the brighter section of the CMD, exhibit three well-defined sequences extending from the MS knee down to $\sim 0.1\,M_\odot$.

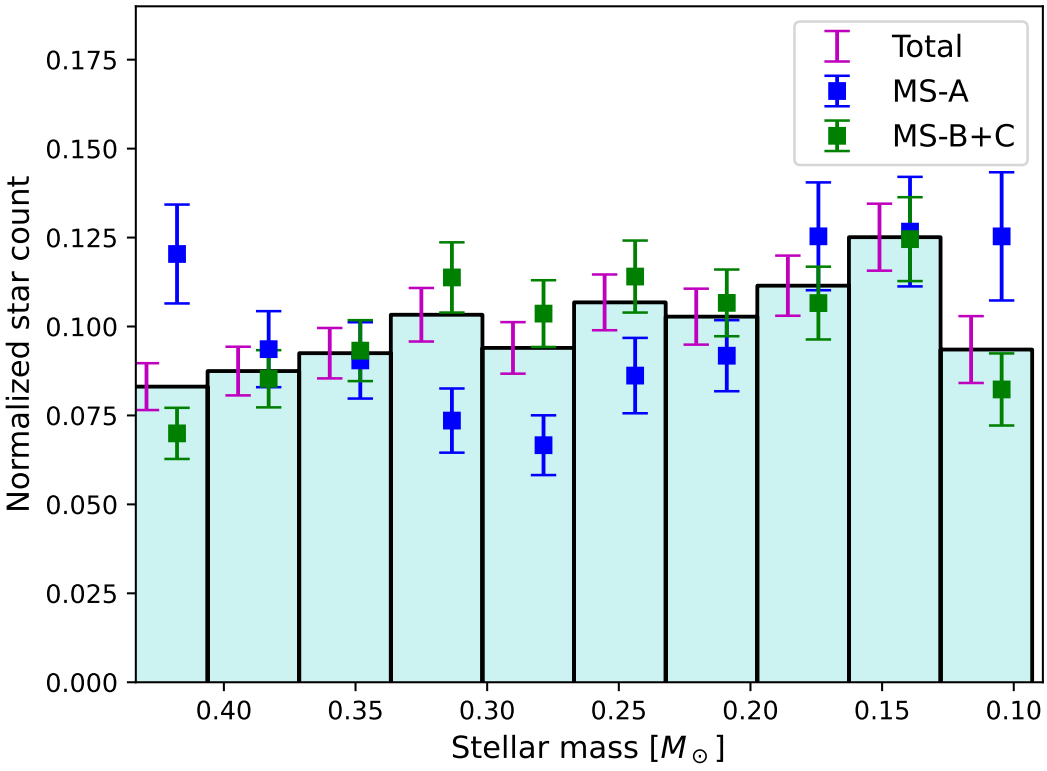

FIGURE 8.16: Estimated total mass function of NGC 6752 (cyan histogram bins with magenta error bars), sub-population MS-A (blue markers) and combination of the other two populations (green markers). The values are normalised such that the total star count is unity for all shown MFs. Each marker refers to the star count in the entire bin; small horizontal offsets in marker positions within the bins were added for clarity.

In this work, we presented a more detailed investigation of these observed multiple stellar sequences by incorporating additional observational epochs. The inclusion of new observational data has enabled us to make accurate distinctions between cluster members and background/foreground sources by using PM measurements. Furthermore, the number of available images has doubled compared to the previous work in Milone et al. (2019). This expanded photometric dataset enables us to conduct a more precise and comprehensive analysis of the three distinct stellar populations.

We presented the $m_{\rm F160W}$ versus $m_{\rm F110W} - m_{\rm F160W}$ CMD of the catalogue analysed in this study, which shows the triple sequence of stars extending from the MS knee to the lower end of the MS ($m_{\rm F160W} \sim 24$). We utilised this observed CMD to construct and fit three isochrones corresponding to the three distinct populations, employing the methodology outlined in Gerasimov et al. (2023). The isochrones are based on newly developed evolutionary models created with the `MESA` code and new model atmospheres calculated using `PHOENIX 15` and `BasicATLAS / ATLAS 9`.

We also introduced a representative 12.5 Gyr WD isochrone, computed using WD models developed by Salaris et al. (2022), which are specifically tailored for metal-poor progenitors. In the upper part of the WD isochrone, we identified three WDs that survived all the selection criteria. We utilised the WD isochrone to determine the $T_{\rm eff}$ and g values for the three surviving WDs.

Our research primarily focused on investigating the LFs and MFs in the lower part of the MS for the three stellar populations within NGC 6752. We utilised two methods to estimate the LFs of the three stellar populations. The first method involved the procedure introduced in Milone et al. (2012b). In the interval $19 < m_{\rm F160W} < 21.25$, MS-B has the most stars, with MS-A and MS-C having slightly fewer. In the interval $21.25 < m_{\rm F160W} < 23.5$, MS-B and MS-A have nearly the same number of stars, while MS-C has fewer. Within the magnitude range $19 < m_{\rm F160W} < 21.25$, the three populations show distinct trends, with MS-B and MS-C increasing significantly compared to MS-A. In the magnitude range $21.25 < m_{\rm F160W} < 23.5$, the three populations exhibit a more similar trend.

The second approach relies on the methodology outlined in Milone et al. (2019). The LFs obtained through this method exhibit significant disparities compared to those derived from the first method. Specifically, the LF of MS-C appears to resemble the LF of MS-B. This discrepancy is likely attributed to contamination, as the non-Gaussian distribution of MS-B stars may influence the observed LF of MS-C. Consequently, a decision was made to collectively consider MS-B and MS-C. The resulting LFs reveal a distinct shape for MS-B+MS-C in comparison to MS-A, indicating a difference in the LF between 1P and 2P stars.

To determine the MF of NGC 6752 and for its populations, the mass of each star below the MS knee was estimated by identifying the closest isomass line to its position on the CMD. The mass distribution was divided into 10 uniform bins, spanning a mass range from approximately $0.087\,{\rm M}_\odot$ to $0.47\,{\rm M}_\odot$. The individual MF of MS-A and the combined MF of MS-B and MS-C were calculated by multiplying the total star count in each mass bin by the average population fraction within that bin. Our analysis revealed that the MF of MS-A differs from the combined MF of MS-B+C. In particular for masses $0.2 - 0.45\,{\rm M}_\odot$ the MF of MS-A tends to be flatter than the MFs of MS-B+C

The present-day MF of stars in a globular cluster is determined by a combination of internal and external dynamical effects: two-body relaxations drive the segregation of massive stars towards the central regions and the outward migration of low-mass stars leading to a radial variation of the local MF with the distance from

the cluster centre. At the same time, stellar escape due to the effects of two-body relaxation and the external tidal field leads to the preferential loss of low-mass stars and the gradual flattening of the global MF (see e.g. Vesperini and Heggie 1997a).

A comprehensive analysis of the MF of NGC 6752 and its link with the cluster's dynamical history would require a complete radial coverage enabling the study of both the effects of mass segregation and those associated with stellar escape (see e.g. Webb and Vesperini, 2016). Our analysis is limited to the cluster's outer regions; the radial range covered by our data extends from about $2\,r_{\rm h}$ to about $3.4\,r_{\rm h}$ but most of the stars are between $2.5\,r_{\rm h}$ and $3\,r_{\rm h}$. Hence, a comprehensive investigation is beyond the scope of this chapter.

The presence of multiple populations in globular clusters differing not only in their chemical abundances but also in their dynamical properties has added another layer of complexity to the investigation of the MF and its link with the cluster's dynamical evolution. In particular, a number of theoretical studies of the formation of multiple populations (see e.g. D'Ercole et al. 2008b; Bekki 2010; Bekki 2011; Calura et al. 2019; Lacchin et al. 2022) predict that 2P stars formed more centrally concentrated than 1P stars and may be characterized by kinematic differences which are either imprinted at the time of the cluster's formation (see e.g. Bekki 2010; Bekki 2011; Hénault-Brunet et al. 2015; Lacchin et al. 2022) and/or produced during the cluster's evolution (see e.g. Tiongco, Vesperini, and Varri 2019; Vesperini et al. 2021; Sollima 2021).

A first investigation of the implications of the complex dynamical properties of multiple-population clusters for the evolution of the 1P and 2P MFs has been presented by Vesperini et al. (2018). Assuming the two populations formed with the same initial MF, even in cases when the global MF does not evolve significantly, significant differences may develop between the local MF of the 1P and the 2P. In particular, as shown in the N-body simulations of Vesperini et al. (2018), in a cluster's outer regions the local MF of the 2P tends to be steeper than the 1P MF. This is the consequence of the effects of mass segregation/low-mass star outward migration in a system in which the 2P was initially more centrally concentrated and populated the outer regions preferentially with low-mass stars (see Vesperini et al. 2018).

Although simulations specifically tailored to model the evolution of NGC 6752 would be required for a detailed comparison between simulations and observations, the general trend of the difference between the 1P and the 2P MFs in the cluster's outer regions found in Vesperini et al. (2018) is consistent with that revealed in our observational data.

Our observations thus provide possible evidence of one of the manifestations of the effects associated with the different dynamical histories of the different stellar populations.

Future observations, in particular with the *JWST*, would be essential to further extend the LF and MF analyses of NGC 6752 and its mPOPs, even into the brown dwarf regime. These observations in combination with a study of the structural and kinematic properties of multiple stellar populations will offer the information necessary to build a complete dynamical picture of this cluster and provide key constraints for theoretical studies of its formation and dynamical history.

Chapter 9

The *HST* large programme on NGC 6752 - The White Dwarf sequence

This chapter contains a study based on a dedicated HST large programme aimed at the study of the white dwarf cooling sequence (WD CS) in the globular cluster NGC 6752. The WD CS luminosity function (LF) is confirmed to peak at $m_{\rm F606W} \simeq 29.3 \pm 0.1$, consistent within uncertainties with what has been previously reported, and is now complete down to $m_{\rm F606W} \simeq 29.7$. We have performed robust and conclusive comparisons with model predictions that show how the theoretical LF for hydrogen envelope WD models closely follow the shape of the empirical LF. The magnitude of the peak of the observed LF is matched with ages between 12.7 and 13.5 Gyr, consistent with the cluster age derived from the main sequence turns off and subgiant branch. We also find that the impact of multiple populations within the cluster on the WD LF for $m_{\rm F606W}$ below 27.3 is negligible, and that the presence of a small fraction of helium envelope objects is consistent with the data. Our analysis reveals a possible hint of an underestimate of the cooling timescales of models in the magnitude range $28.1 < m_{\rm F606W} < 28.9$. Finally, we find that hydrogen envelope models calculated with a new tabulation of electron conduction opacities in the transition between moderate and strong degeneracy provide WD ages that are too small in comparison to the Main Sequence turnoff age. The material discussed in this Chapter has been published in Monthly Notices of the Royal Astronomical Society (MNRAS; Bedin et al. 2023).

9.1 Introduction

Located at a distance of about 4 kpc (Baumgardt and Vasiliev, 2021), NGC 6752 is one of the closest Milky Way globular clusters (GCs) to the Sun. With its proximity and low interstellar reddening, NGC 6752 was one of the first GCs to reveal the presence of white dwarfs (WDs) (Richer, 1978) before the advent of *Hubble Space Telescope (HST)*. A small sample of bright WDs in NGC 6752 observed with *HST* was employed by Renzini et al. (1996) to determine the cluster distance with a technique analogous to the main sequence fitting. More recently, Bedin et al. (2019b) using deeper *HST* observations, obtained a first, preliminary, WD luminosity function (LF) that reached the end of the cooling sequence of hydrogen envelope WDs. Thus, NGC 6752 belongs to an exclusive club of GCs for which the end of the WD cooling sequence has been observed, including NGC 6397 (Richer et al., 2006; Hansen et al., 2007), M 4 (Bedin et al., 2009b) and 47 Tuc (Hansen et al., 2013).

One peculiarity of NGC 6752 is the atypical horizontal branch (HB) morphology for its metallicity ([Fe/H]~ -1.6, Gratton et al. 2005). There are no RR Lyrae stars in

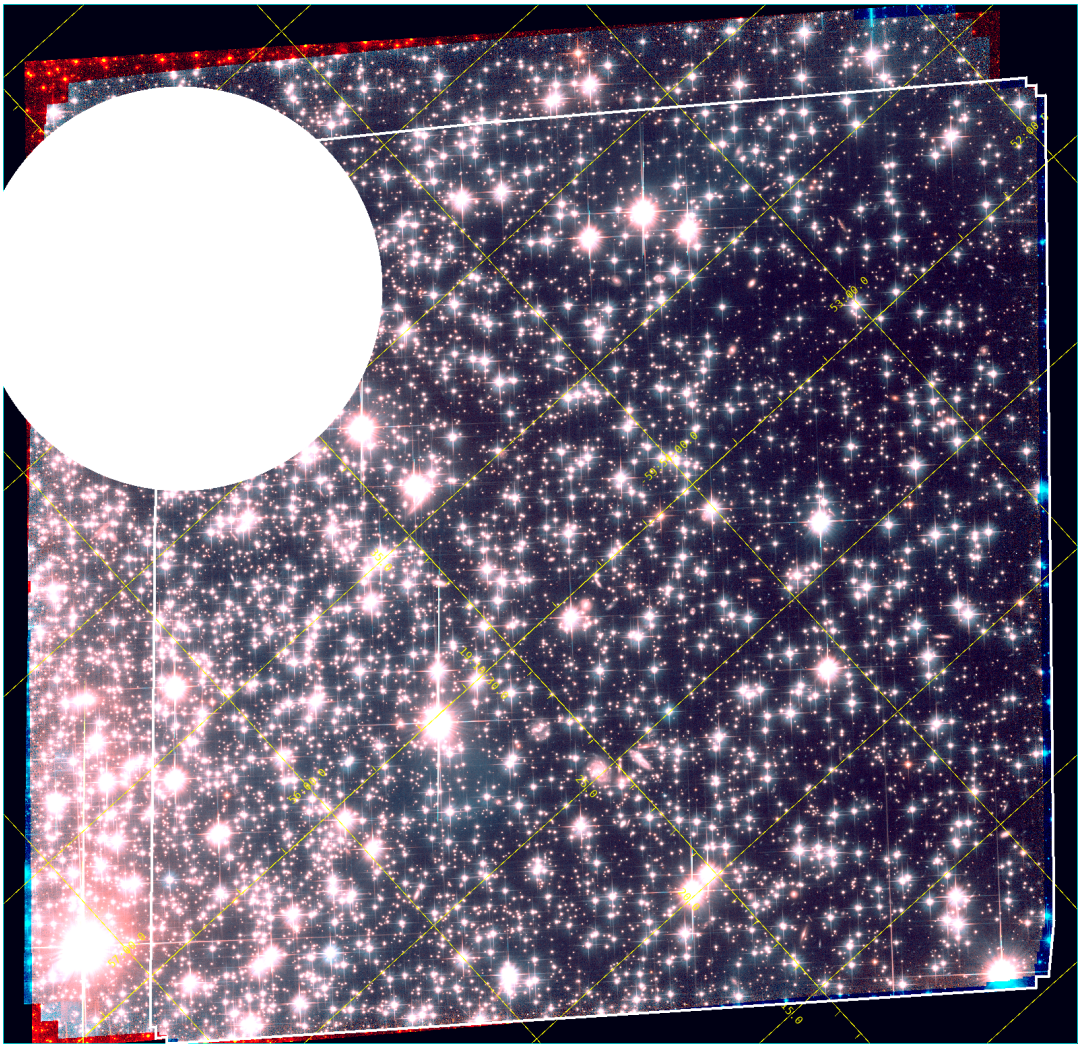

FIGURE 9.1: Tri-chromatic view of about 250″ × 250″ for the entire ACS/WFC data-set from *HST* programs GO-15096 & GO-15491. The white lines indicate the region observed at the first epoch. The circular white region is rejected from this work, as it used to mask out the *Bedin I* dwarf spheroidal galaxy in the background (Paper I). The yellow lines and labels indicate the *Gaia* DR3 reference frame.

its HB, which has a pronounced extension to the blue, related to the presence of multiple populations with different initial helium abundances (e.g., Bastian and Lardo, 2018a; Cassisi et al., 2014, and references therein). This blue morphology affects the bright part of the WD cooling sequence (CS), as shown very recently by Chen et al. (2022) based on near-UV imaging observations with *HST* Wide Field Camera 3. Using synthetic HB modelling by Cassisi et al. (2014) and theoretical results on WD progenitor evolution by Althaus et al. (2015), Chen et al. (2022) have shown that the bright part of the CS is populated by two types of WDs. A 'slow' – in terms of evolutionary speed – component supported by envelope hydrogen burning, and a 'canonical' component which is cooling without any substantial contribution from nuclear burning (more on this later).

This work is the fourth of a series of articles aimed at the scientific exploitation of an *HST* multi-cycle large program focused on the GC NGC 6752. The previous three publications were based on data from the first epoch of observations. Bedin et al. (2019c, Paper I) presented the discovery of a dwarf spheroidal galaxy that needs to be masked out in studies of the faint population of NGC 6752. Milone et al. (2019, Paper II) characterized the multiple stellar populations of NGC 6752; Finally, Bedin et al. (2019b, Paper III) reached, for the first time in NGC 6752, the end of the hydrogen envelope WD CS.

In this study, we have employed data for all epochs, which significantly improves the definition of the cluster WD CS and its LF, and allows us to perform a more robust and reliable investigation of the agreement between WD and main sequence turn off ages, the effect of the cluster multiple populations on the faint end of the CS, and the impact of helium envelope WDs on the LF. We have also been able to test two different treatments of the electron conduction opacities in the regime between moderate and strong degeneracy, which are crucial for the modelling of WD envelopes and have a major impact on the cooling times of the models (see Cassisi et al., 2021).

The Chapter is organized as follows: Section 9.2 presents the observations, while section 9.3 gives details for the data reduction. Section 9.4 provides a brief description of the artificial star tests. Section 9.5 describes the selection criteria used to obtain the cluster colour-magnitude diagram (CMD). Section 9.6 explains the decontamination of the cluster sample using proper motions. Section 9.7 presents the derived empirical WD LF. Section 9.8 compares the empirical LF with theory. Section 9.10 summarizes our results.

9.2 Observations

This study is based on images collected with the *Wide Field Channel* (WFC) of the *Advanced Camera for Surveys* (ACS) on board *HST* under the multi-cycle large program: *"The end of the White Dwarf Cooling Sequence of NGC 6752"*, programs: GO-15096 and GO-15491 (PI: Bedin). Paper III presented the first epoch of data obtained as part of program GO-15096, collected between September 7 and 18, 2018. These data consist of deep exposures of $\sim$1270 s each, 19 taken with the F814W filter and 56 taken with the F606W filter. Short exposures of $\sim$45 s each were also collected at the beginning of each orbit, 10 with the F814W filter and 27 with the F606W filter. Five of the planned 40 orbits failed (some only partially) because of poor guide-star acquisition and were repeated between August 1 and 15, 2019, resulting in an additional 5×45 s and 10×1270 s exposures with the F814W filter.

The second half of the data were collected between September 2 and 11, 2021 as a part of GO-15491. Due to changes in the *HST*-phase-II policies, deep exposures were on average shorter by ∼55 s to allow for more ease in the scheduling. We obtained long exposures of ∼1215 s each, 56 images with the F814W filter and 20 images with the F606W filter; and short exposures of ∼45 s, each 12 with the F814W filter and 28 images with the F606W filter. Two orbits were lost due to poor guiding, and these observations were repeated on February 14, 2022; with two short (45 s) and four deep (1209 s) exposures with the F814W filter. All images were collected between ∼2018.68 and ∼2022.12, resulting in four epochs over a time baseline of ∼3.5 yrs. In a forthcoming publication, we use these multi-epoch observations to conduct an astrometric analysis of stars bright enough to be detected in individual images ($V \lesssim 28$) to determine the absolute motions, parallax, and internal velocity dispersion of the cluster. Here, we analyze all of the images simultaneously to detect the faintest WD members of the cluster.

9.3 Data-reduction

The data reduction was essentially identical to that presented in Paper III but with about twice the number of images. We refer the interested reader to Paper III and previous publications for details on the procedures, and provide here a brief description.

We downloaded from the MAST archive[1] the `flc` images, which were pre-processed with *Space Telescope Science Institute (STScI)*'s pipeline. The `flc` images are corrected for dark current, bias, flat fielding, and charge-transfer efficiency (CTE) losses (following the Anderson and Bedin 2010 recipes for pixel-based correction) with the latest reference files, but with no re-sampling of the pixels.

We first conducted a *"first-pass"* analysis to derive optimized point-spread functions (PSFs) for all images, and to establish a common distortion-free reference frame. Fluxes and positions for relatively bright (down to ∼3.5 magnitudes below saturation), unsaturated stars were extracted from each `flc` image using software developed by J. Anderson, described in Anderson and King (2006). Each image was analyzed separately to create a tailored PSF in order to account for the particular breathing state of *HST*'s telescope tube, which affects both spatial and temporal variations relative to the library PSFs provided by Anderson (2006). This tailoring of PSFs was done with prescriptions introduced in Anderson and Bedin (2017) for WFC3/UVIS, and later extended to ACS/WFC by Bellini, Anderson, and Grogin (2018a). Next, both positions and fluxes are corrected for the geometric distortion of the detector by Anderson (2006),[2] which affects pixel areas and hence fluxes. These geometric corrections were used to produce a common, distortion-free reference frame –based on cluster members– to which all individual images are linked. Note that during the ∼3.5 years between the first and last epoch, cluster members are expected to have internal motions on the order of ∼1 mas; field objects will have much larger motions (more about motions in Sect. 9.6).

This *"first-pass"* analysis yields a distortion-free reference frame, with positions accurate to milli-arcsecond (mas) levels and magnitudes zero-pointed to milli-magnitude

[1] `mast.stsci.edu`

[2] Publicly available at `https://www.stsci.edu/~jayander/HST1PASS/LIB/GDCs/STDGCs/`

(mmag) precision levels. With these calibrations in hand, we performed a *"second-pass"* analysis in which all of the pixels from all of the images are analyzed simultaneously to search for the faintest sources in the field, in particular, those not detectable in individual images. This analysis was done using the most recent version of the code (KS2) developed by J. Anderson (first presented in Anderson et al. 2008), and applied in several other GC analyses (cf. Scalco et al. 2021 and references therein). The KS2 code goes through multiple iterations of finding, modelling, and subtracting point sources from the image, starting from the brightest sources and moving progressively to fainter sources in the subtraction residuals. The code solves for positions and fluxes, as well as other important diagnostic parameters such as the local sky noise (rmsSKY) which documents how noisy the investigated patch of sky is, and the RADXS parameter (introduced in Bedin et al. 2009b) which documents how well the source flux distribution resembles that of the PSF. The RADXS parameter is the most efficient diagnostic to eliminate faint unresolved galaxies, poorly measured stars perturbed by non-modellable neighbours, cosmic ray (CR) hits, PSF substructure, diffraction spikes, and other artefacts. Stars that are saturated in deep exposures have valid first-pass measurements from the short exposures and are linked to the deep-exposure-based master frame via common unsaturated stars.

Photometry was calibrated to the ACS/WFC Vega-mag system with the procedure given in Bedin et al. (2005b) using encircled energy and zero points available from STScI.[3] For the derived magnitudes in this photometric system, we adopt the symbols $m_{\rm F606W}$ and $m_{\rm F814W}$.

The KS2 code also produces stacked images for visual examination, which we release as part of the electronic material associated with this work. We combined these stacks for the two filters to produce a colour view of the studied region, shown in Fig. 9.1. [A tri-chromatic view was obtained using F606W & F814W for the blue & red channels, while using a wavelength-weighted mean of F606W and F814W for the green channel]. In the figure, we masked out a region centered on the dwarf spheroidal galaxy *Bedin I* (coordinates from Paper I) with a radius of 1000 pixels ($\sim 50''$). This region is completely excluded from our analysis, as it proved impossible to achieve a useful discrimination in the CMD between the location of the dwarf galaxy's stars and the WDs of NGC 6752.

The absolute astrometric registration to the International Celestial Reference System (ICRS) was achieved using sources in common with *Gaia* Early Data Release 3 (EDR3; Gaia Collaboration et al. 2021). Tabulated proper motions in *Gaia* EDR3 were transformed to the average Julian Day of images collected during the first epoch, following the procedures in Bedin and Fontanive (2018).
In the left panel of Fig. 9.2 we show a preliminary CMD for sources having $|\texttt{RADXS}| < 0.1$ in both F606W and F814W. In the next section, we will employ this CMD to define the fiducial line of the WD CS of NGC 6752. This fiducial will be used to generate artificial stars along it, which in turn will enable us to define the region within which to count the WDs of NGC 6752, and to carefully select well-measured stars (see Sect. 9.5).

9.4 Artificial Stars

When studying faint sources, artificial star tests (hereafter, ASTs) have several key roles, specifically: *(i)* ASTs are used to track and correct for systematic errors between input magnitude and recovered magnitudes (see Bedin et al. 2009b); *(ii)* ASTs are also

[3] www.stsci.edu/hst/acs/analysis/zeropoints

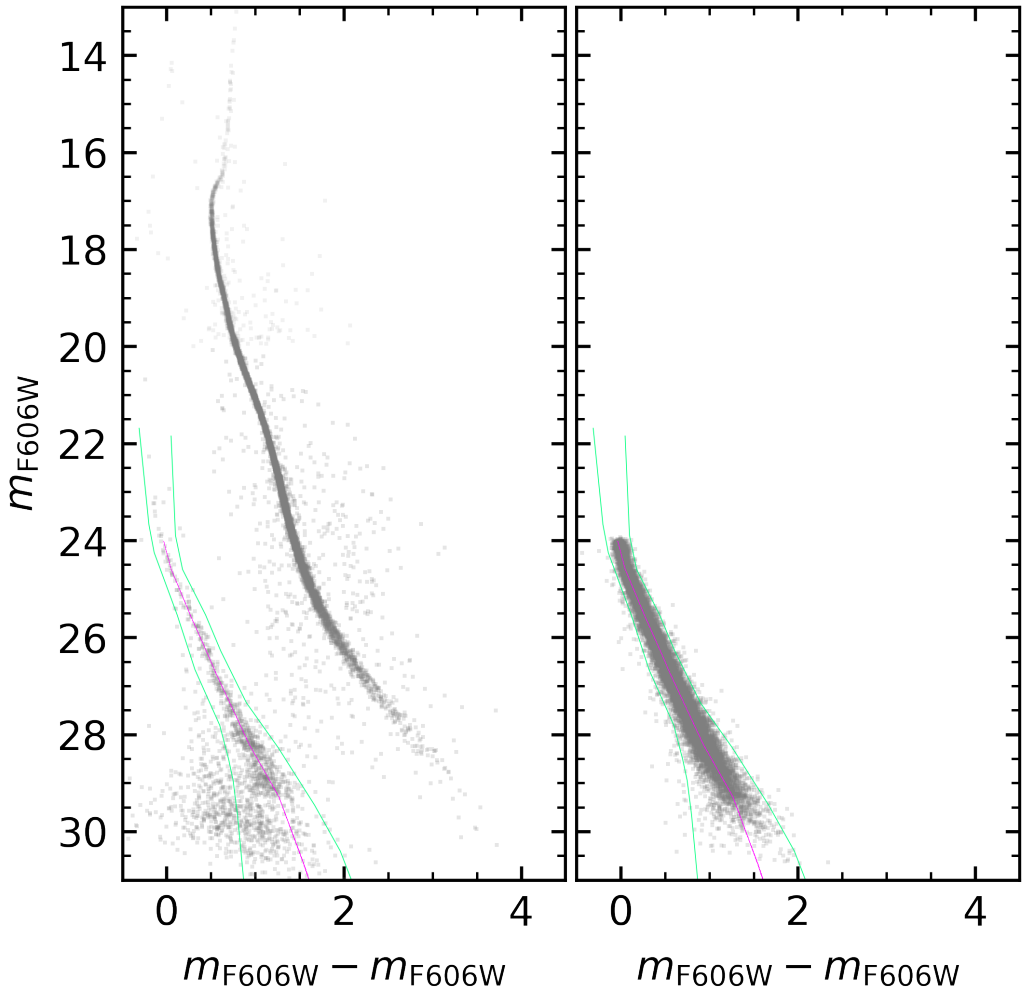

FIGURE 9.2: *(Left:)* Preliminary CMD for the sources within the studied field. Only sources with `RADXS` < 0.1 in both F606W and F814W are displayed. The line in magenta, obtained as described in Sect. 9.4, is the fiducial line for the WD CS of NGC 6752. The green lines define the region of the CMD within which we will count the WDs. *(Right:)* With the same scale, we show the CMD for artificial stars. The same magenta and green lines on the left panel are also displayed here. As can be seen, the lines in green define a region that is generous enough to include both the bulk of the observed real WDs in the left panel *and* the artificial stars added along the WD fiducial line recovered with large photometric errors. Note that the exact location of the magenta line does not affect the number of WDs counted within the region defined by the two green lines.

employed to estimate the random errors and therefore define which sources have a position on the CMD consistent with being WDs; *(iii)* ASTs are used to check and define the selections on the distribution of diagnostic parameters, such as `RADXS` or `rmsSKY`; and finally –and of fundamental importance– *(iv)* ASTs are used to assess the completeness of the sample.

In creating the ASTs, the first step is to choose where to add them in the CMD, and where to add them spatially across the field of view. Since we are studying the WD CS of NGC 6752, on the CMD we define a fiducial line, drawn by hand, along the bulk of the observed WDs down to where they seem to stop and extrapolate the fiducial to even fainter magnitudes in order to assess completeness. This fiducial line is shown in the left panel of Fig. 9.2 (in magenta, as in other figures of this Chapter).

With `KS2`, we added artificial stars along this fiducial line with a flat distribution in $m_{\rm F606W}$ between magnitudes 24 and 32, and with a homogeneous spatial distribution across the field of view. Therefore, this fiducial line was defined on the observed WD CS of NGC 6752. We did not use theoretical models, nor did we make assumptions about the WD CS location. We follow the prescriptions in Bedin et al. (2009b, section 2.3), and correct our magnitudes (both real and artificial) for input-output systematic errors, which are negligible at $m_{\rm F606W}$ $\sim$24, but become as large as $\sim$0.2 mag at the faintest magnitudes. In the following, our magnitudes –for both artificial and real sources– are corrected for these effects.

Unfortunately, ASTs cannot track down all the possible sources of photometric systematic errors, the most important being related to CTE effects. Indeed, in the case of real sources, their photo-released charge is bitten out by the electron traps encountered in the detector that are filled during the read-out process, all the way down to the amplifier (up to $\sim$2000 pixels). ASTs instead are just added values to the analyzed images, and their artificial charge was never subjected to all the electron traps which would lay along the read-out process.

The recent ISR by Anderson et al. (in preparation) use an observing strategy to self-calibrate these CTE-related photometric errors, which requires multiple observations of the same field to be collected at $\sim$90 degrees from each other. As our observations of NGC 6752 were not collected this way, a correction of this kind here is not possible. However, results in that work suggest that in the case of our data set, any *possible* systematic photometric error related to the CTE losses could amount to $\sim$0.1 mag which therefore in the following, we set as the limit of our photometric accuracy. We also note that F606W exposures have on average a 45% higher sky-background level than those in F814W ($\sim$136 vs. $\sim$94 photo-electrons) making photometry F606W less vulnerable to CTE losses, as many more electron traps are filled. Furthermore, the number of images in F606W is more than twice the number available in F814W (precisely 112 vs 53), making $m_{\rm F606W}$-magnitudes more robust measurements than those in F814W. For this reason, in the following, we will choose to analyze both the CMD and the LF in the $m_{\rm F606W}$-magnitudes.

To establish whether an inserted star was recovered or not, we assumed that if an artificial star is not recovered within 0.753 ($\sim -2.5\log 2$) magnitude (in both filters), and within 1 pixel from the inserted position (in both x and y detector coordinates), then the inserted artificial star was not recovered. The right panel of Fig. 9.2 shows artificial sources as inserted (in magenta) and how they were recovered (dots).

The panels of Fig. 9.2, together, are used to define the region within which we will count the WDs of NGC 6752. Specifically, this region is defined by two lines (in green) drawn by hand, which are a compromise between including the observed WDs of NGC 6752 with large photometric scatter, and excluding the vast majority of field objects. We allowed for photometric errors very large around the magenta line,

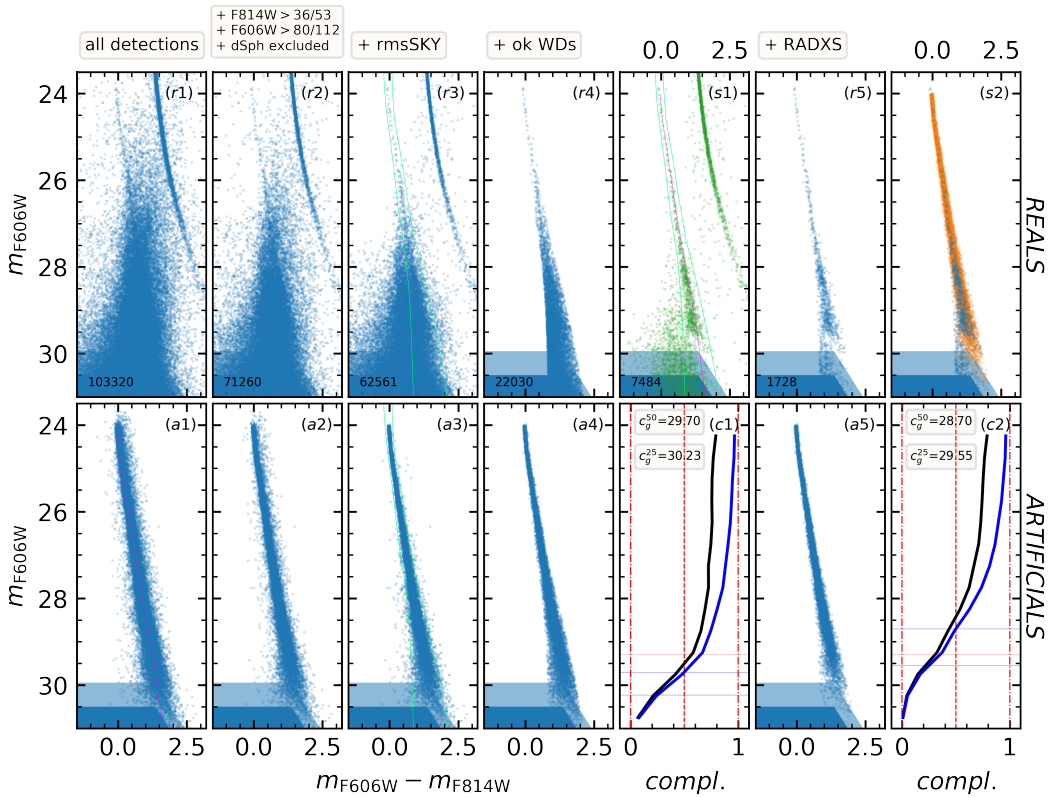

FIGURE 9.3: Panels show the progression of the cumulative selections adopted to obtain a sample of well-measured WDs along NGC 6752's WD CS. From left to right panels from (1) to (5) for real stars [top (r_i) panels] and artificial stars [bottom (a_i) panels]. A thin line in magenta in panel $(a1)$ show where artificial stars were added. Panels (c) show the obtained completeness, not including $(c1)$ or including $(c2)$ the selection on RADXS, which is by far the most effective parameter to select well-measured point sources. For clarity in panel $(s1)$ we "show" the effect of RADXS selection on stars also outside the WD region defined by the two green thin lines (see text). Finally, in panel $(s2)$ we show the direct comparison of real vs. artificial stars, clearly not showing a sharp drop in their number below $m_{F606W} \simeq 29.4$.

so that the bulk of the observed WDs (which might not follow exactly the magenta line), will still be included.

9.5 Colour-Magnitude Diagram and Selections

Following the approach of Paper III, in Fig. 9.3 we show the impact of our progressive selection criteria on artificial stars, and then apply the criteria identically to real sources. Each panel is labelled in the top-right corner with an (a) for ASTs, or with an (r) for real sources. The goal of these selections is to find the best compromise between keeping the largest sample of well-measured WD members of NGC 6752 and rejecting the detections that are most likely spurious, or poorly measured stars, or field objects in the foreground and background of the cluster – be they either stars or galaxies.

The KS2 code sets a detection threshold for potential sources to be any positive local maximum in an image that is above 1-σ of the local sky noise. Naturally, this

choice results in the inclusion of a large number of non-significant detections, but it has the value of showing where the floor level of the white noise is located. As in Paper III, we measured the background noise (1-σ) in the two filters for regions with average low background and transformed these values into magnitudes, associating to these peaks the value of the PSFs' central-pixel value (normalized to unity), and zero-pointing to the Vega-mag system. We show in panels (a) and (r) with shading the corresponding 5-σ (light-blue) and 3-σ (dark blue) regions. In the following, we will not consider as significantly detected any source below the 5-σ limits. Therefore, sources above these shaded regions could still be poorly measured objects or even artefacts, but nevertheless, they are solid detections.

Panel *(a1)* show all the artificial sources as inserted (in magenta) and as they were recovered (blue dots).

In panel *(a2)* we restricted our sources to those that fell in the part of the field that was observed in at least ∼70% of the F814W and F606W images. Given our large dither observing strategy, this leads to a significant reduction of the field of view which is used for this investigation.

Panel *(a3)* further restricts us to a region of the field where the `rmsSKY` was consistent with the noise within empty patches of sky, i.e., to regions that were not dominated by the bright halo of luminous stars. This selection has only a marginal effect in rejecting sources in noisy regions of the FoV, but it has a great significance in establishing which regions are suitable (*"good"*) for the detection of faint objects (thanks to the lower sky noise level). The computed completeness in *"good"* regions, is indicated by c_g, following Bedin et al. (2008).

In Panel *(a4)* we use the region enclosed within the two green lines in panel *(a3)* to reject all the ASTs recovered outside this region.

In the next panel, *(c1)*, instead of a CMD, we show the magnitude vs. completeness curve (i.e., the: number-of- recovered / number-of-inserted sources) with a black line, and the completeness limited to "good" regions (c_g) as a blue line for the surviving artificial stars. This panel shows that inserted sources that passed these selections are 50%-complete down to $m_{\rm F606W} \simeq 29.7$, and 25%-complete at $m_{\rm F606W} \simeq 30.2$. However, we can recognize that while 50%-completeness is well above the sky noise at 5-σ, the 25%-completeness is well below our 5-σ minimum threshold for significant sources. In the following, completeness corrections are assumed to be reliable only for magnitudes brighter than the 5-σ magnitude level expected for sky noise, even though we show some points below this.

In the next panel *(a5)*, we show the result after selection with our most effective diagnostic to reject non-stellar objects, i.e., the `RADXS` parameter. This parameter is able to reject most of the PSF artefacts, diffraction spikes, extended sources, and field objects that have moved significantly more than the cluster member stars (about 1 mas) during the ∼3.5 years between first and last epochs, causing a blur of the shape of stars that do not move as cluster members[4].

The bottom-right panel *(c2)* shows the completeness curves after the final selection on `RADXS` is also applied. Note that 25%-level of the c_g-completeness remains well above the 5-σ sky-level down to magnitudes $m_{\rm F606W} \simeq 29.55$, i.e., below the location of the WD CS LF's peaks as observed in Paper III.

In the top panels of Fig. 9.3, we have applied the very same selections defined for ASTs to the observed real sources. In panel *(r5)*, we show the final sample for

[4]Since cluster members are used to compute the transformations, they do not move within errors, especially toward faint magnitudes, where random errors dominate uncertainties.

NGC 6752's WD candidates. We also *show* the selection of two interesting real-star CMDs (labelled with *(s)*).

Panel *(s1)* shows the CMD for stars that passed all the selection criteria, but included sources falling outside the region between the two thin green lines defined in panel *(a3)*. This CMD includes non-WD candidates. Sources in this CMD are coloured in green and will be used in Sect. 9.6 to derive a model of the field contamination within the WD region in the CMD. Note also that the fiducial line defined in Sect. 9.4 (and shown in magenta) well represents the mean observed CMD location for WD CS of NGC 6752.

Panel *(s2)* shows a direct comparison of the CMDs for sources surviving all the selection criteria: ASTs (as selected in panel *(a5)*) are shown in orange, while real sources (as selected in panel *(r5)*) are shown in blue. From this CMD, it is evident that the observed real WD CS does not extend to magnitudes as faint as those of the recovered ASTs — a clear indication that we have reached and passed the peak of the WD CS LF of NGC 6752.

9.6 Proper-motion decontamination

We now check whether the proper motions (PMs) derived for the faintest stars can be of any help to discriminate between field objects falling within the WD region of the NGC 6752's CMD, and true cluster members. To this end, we combined the bulk of the first half of the data collected in ∼2018.7 and obtain averaged positions for the sources, which are then compared with their averaged positions as measured in the second half of the data collected in ∼2021.7. In the following analysis, we will consider only sources shown in green in panel *(s1)* of Fig. 9.3 (i.e., those surviving all the selection cuts described above, therefore considering sources outside the region of the WDs in the CMD), but for which it was possible to estimate a position at each of the two considered epochs.

Unfortunately, the absolute motion of NGC 6752 (relative to the field) is not very large: $(\mu_{\alpha\cos\delta};\mu_\delta) = (-3.155;-4.010) \pm (0.008;0.009)$ mas yr^{-1} (Libralato et al. 2022), resulting in a combined absolute motion of just 5.102 ± 0.012 mas yr^{-1}. With a time-baseline of just ∼3 yrs we can expect a separation of about ∼15 mas between the cluster members and the faintest extra-galactic unresolved field sources that sit in an absolute rest frame. Given the ACS/WFC pixel-size of 49.72 mas, this amounts to a displacement of about 0.3 pixel, which is an easily measurable quantity for the brightest stars, but it is smaller than the measurement errors for those extremely faint sources that become significant only when combining several dozen individual images of the same epoch.

We provide a quantitative illustration of this situation in Fig. 9.4. We colour-code in blue stars surviving the WD selection defined by the two thin green lines and in orange all other stars. In the top panels, we show vector-point diagrams of source displacements over the ∼3 years, in units of ACS/WFC pixels (of 49.72 mas) for 2D-displacements $(\Delta X, \Delta Y)$ between the two epochs (2018.7 vs. 2021.7). In the first, third and fourth bottom panels, we show CMDs. The second bottom panel from left shows the observed 1D-displacement (ΔR summing in quadrature the displacements in X and in the Y axes) as a function of the observed source $m_{\rm F606W}$-magnitude. Among bright stars, it is clear that there is a tight distribution in ΔR for cluster members, which remain distributed well below 0.1 pixel, and a broad tail toward higher ΔR, peaking between 0.2-0.4 pixels: these are field objects. However, at around magnitude $m_{\rm F606W} \simeq 28$, the random positional-measurement errors

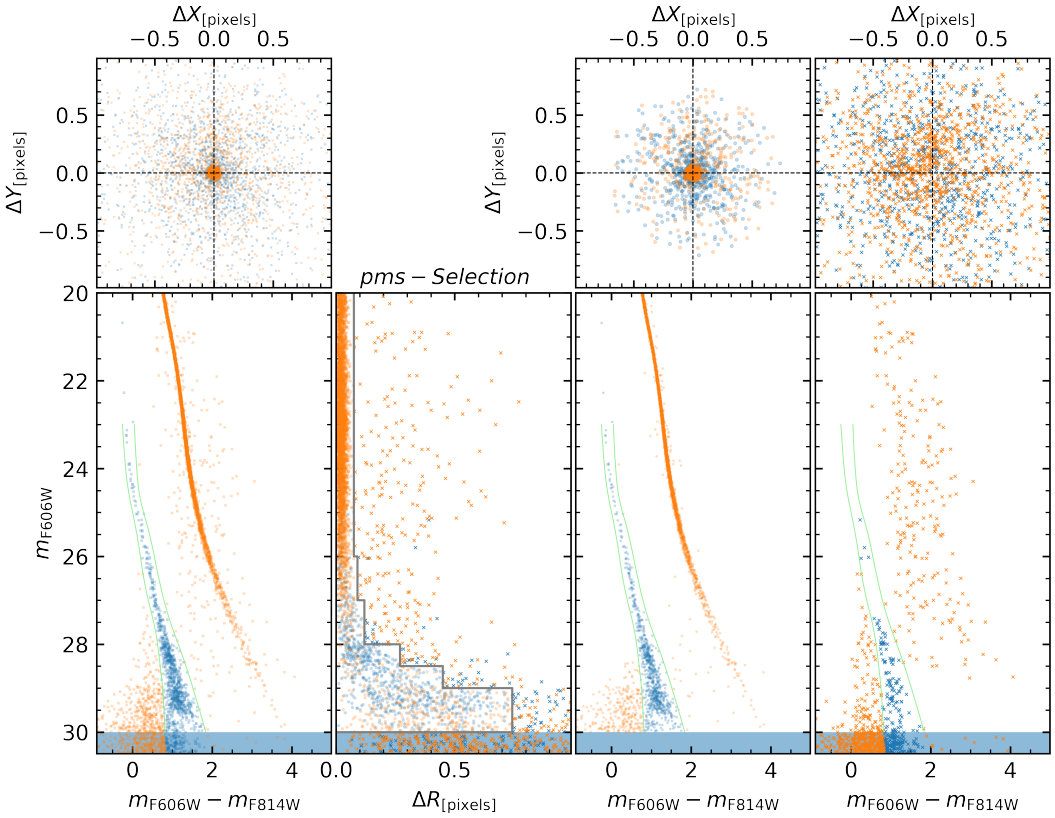

FIGURE 9.4: *(Bottom-left:)* CMD of the sources in panel (s1) of Fig. 9.3, here sources within the WD region (between the two green lines) are color-coded in blue and all the other sources in orange. Shading below $m_{\rm F606W} = 30$ marks the limit of significant detection for the sources of interest. *(Bottom-mid-left:)* 1-D displacements, ΔR, as function of $m_{\rm F606W}$. Bright stars (down to $m_{\rm F606W} \sim 28$) show a ΔR distribution with a tight dispersion (< 0.1 pixels) plus a tail with a much broader dispersion peaked around 0.3 pixels. We arbitrarily define two regions, indicated by the grey line, one that enclose the bulk of the ΔR at different magnitude bins (dots), and the other with objects of larger ΔR (small crosses). The next two bottom panels on the right show the CMDs for the stars within and beyond the grey line. Clearly, neither of the two CMDs are made only of members or only of field objects (see text). *(Top:)* 2-D vector point diagrams of the ∼3 yr-displacements for the samples shown in the corresponding panels below.

(which are summed in quadrature for the two epochs) explode for fainter stars. And at around magnitude $m_{\rm F606W} \simeq 28.5$, it clearly becomes impossible to disentangle members (with positional random errors around 0.4 pixels) from field objects (with a relative average displacement of $\sim$0.3 pixels).

With the observed bulk of stars at different magnitude intervals, we define the PM selections for objects consistent with the PM errors at the various magnitudes. This arbitrary selection is illustrated by the thick-grey line, Stars satisfying this selection (grey step-line) are indicated with circles, while stars not passing this selection or fainter than $m_{\rm F606W} \simeq 30$ are indicated with crosses. The panels on the right of this panel, show the vector-point diagram and the CMD for sources to the left or to the right of the gray-line criterion, keeping the blue colour code for WD candidates. The PM selection, while useful to reject outliers and objects with large PMs, is completely useless at separating WDs and field objects below $m_{\rm F606W} \simeq 28.5$, simply because the separation between field and members is much smaller than measurement errors below $m_{\rm F606W} \simeq 28.5$. In the next section, we introduce a work-around to properly define the WD CS LF of NGC 6752 down to its faintest magnitudes.

9.7 The corrected WD CS LF

As demonstrated in various *HST* studies, including those that made use of the *Hubble Ultra Deep Field* (e.g., **2010ApJ...708L..32B**; Bedin et al. 2008; Bedin et al. 2009b), the vast majority of contaminants in the CMD aligned with the cluster's WD CS are blue galaxies that are relatively easy to reject with shape parameters such as RADXS. However, at fainter magnitudes, unresolved blue galaxies become increasingly indistinguishable from stars. Although these faint unresolved blue point sources fall in a region just outside the WD CS (e.g., Bedin et al. 2009b and discussion, or Fig. 3 of Paper III), a number of blue stars in the Galactic field contaminate the LF. Unfortunately, this contamination appears far from negligible, and for a reliable study of the WD CS LF of NGC 6752 some correction of residual contaminants should be performed.

In this section, we develop a simple model to correct for field contamination. The process is illustrated in Fig. 9.5 and described in the following. In the first panel of this figure, from left-to-right, we show the CMD of sources defined in panel *(s1)* of Fig. 9.3, and use the two lines of Fig. 9.3 to define on the CMD what we will refer to as the *"WD-region"*. We then defined two other regions with the identical color-width at each magnitude of the CMD WD-region, but one at bluer colours (to the left of the WD-region), and one at redder colours (to the right of the WD-region). In the following, we refer to these as *"Blue-"* and *"Red-regions"*. Next, we counted the sources within each of these three regions and produced in the next panel to the right the luminosity functions (LFs) of each. We visualize the LF for those WD candidate objects observed within the WD region, and the Blue- and Red regions, with error bars that reflect statistical Poisson errors.

In the simplest model for the contaminant distribution on the CMD's WD-region, we assume that: *(i)* there are no WDs of NGC 6752 within the Blue- or Red-region; and *(ii)* the number of contaminants within the CMD WD-region is the average of the number of objects observed in the Blue- and in the Red-regions, at the various magnitudes. We show this model in Fig. 9.5, with corresponding errors estimated by linear propagation of Poisson noise.

In the third panel of Fig. 9.5, we compare the observed LF to the resulting WD LF corrected for the field-contamination model. The field-corrected LF is simply

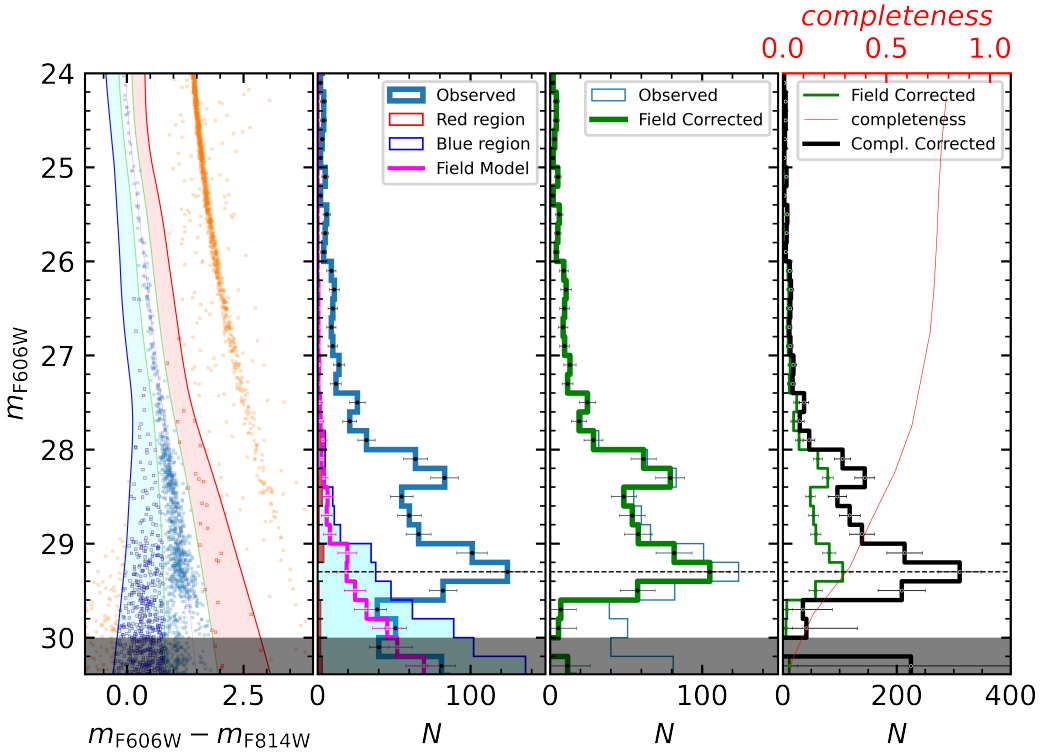

FIGURE 9.5: *(Left:)* The CMD where we define three regions along the WD CS. The shaded region in azure indicates sources passing the selections on the blue side of the WDs, the region shaded in red, the ones redder. Next panels are all WD CS LFs, where the histograms show the number of sources per magnitude interval, for observed stars within the WD region and for stars in the two shaded regions (see the legend). Our model for field distribution is the histogram in magenta. This is a simple average of the blue and red LF. This simple model is then subtracted from the observed LF, and shown in the third panel from left to right. Note how the faintest bins of the corrected WD CS LF are consistent with zero within the noise. Finally, the observed field-corrected WD CS's LF was corrected for completeness, and shown in black. Grey-shaded regions indicate levels where findings and completeness become unreliable (see text). Errors were linearly propagated and then corrected for compleness.

the observed LF minus the field model, with errors propagated linearly. Interestingly, in the faintest bins, $m_{\rm F606W}$ = 29.6 and 30, the field correction brings the observed WD CS LF to zero within the uncertainties. As this is what one would expect when the LF drops out –in spite of the naïve assumption for this distribution of contaminants– this is a rather reassuring feature of the goodness and validity of the model. Finally, in the last panel to the right, we show the completeness-corrected and field-corrected WD CS LF for NGC 6752 The errors on this LF were also corrected for completeness with a simple approximation, a linear propagation of the errors. As supplementary online material, we also release all data (completeness, observed LF, errors, CMD, photometric errors), to enable other groups to independently perform their own analyses. The WD LF in the right-panel of Fig. 9.5 is the one used in the next Section for the theoretical analyses.

9.8 Modelling the observed WD CS and LF

As in Paper III, a preliminary step to model theoretically the observed cooling sequence is to have estimates of the cluster parameters, such as distance and reddening. We employed here the same distance modulus $(m-M)_0$=13.10 and reddening $E(B-V)$=0.05 as in Paper III; this distance is consistent with the recent determination $(m-M)_0$=13.08±0.02 by Baumgardt and Vasiliev (2021), while the reddening is consistent with $E(B-V)$=0.046±0.005 determined by Gratton et al., 2005. We compared theoretical isochrones from the lower main sequence (MS) to the tip of the red giant branch (RGB), and a zero-age horizontal branch sequence (ZAHB), to the optical CMD of the cluster central regions from Nardiello et al. (2018, N18), merged with the deep photometry for the external field studied in this work, as shown in Fig. 9.6. These two photometries agree well, and the richer central field populates the post main sequence phases and the bright part of the WD CS. We employed α-enhanced ([α/Fe]=0.4) isochrones and ZAHB models by Pietrinferni et al. (2021) for [Fe/H]=−1.55 –consistent with [Fe/H]=$-1.55 \pm 0.01 \pm 0.06$ (random + systematic) determined by Gratton et al. (2005)– and an initial helium mass fraction Y=0.248. In this comparison with the observed CMD (and also for the modelling of the WD sequence) we applied extinction corrections to the $F606W$ and $F814W$ filters that depend on the model effective temperature, calculated as in Bedin et al. (2005b).

Figure 9.6 shows the overall good agreement between the theoretical models and the observed sequences on the MS, RGB and ZAHB. The plume of stars that departs from the ZAHB towards higher luminosities is made of objects coming from the blue tail of the HB, that are evolving towards the asymptotic giant branch (AGB). This comparison provides us with a MS turn-off (TO) age determination; isochrones with ages equal to 12.5 and 14.0 Gyr match the TO region of the CMD, and also bracket nicely the luminosity range of the subgiant branch that is very sensitive to age. We also display a 12.5 Gyr old isochrone with initial Y=0.275 (keeping the metal content fixed) to show the effect of the helium spread due to the presence of multiple populations in the cluster. Just as a reminder, the presence of multiple populations in a globular cluster is revealed by (anti)correlated variations of the abundances of C, N, O, Na (and sometimes Mg and Al), plus variations of the initial helium mass fraction Y (see, e.g., Renzini et al., 2015c) A typical globular cluster like NGC 6752 hosts a population of stars with 'normal' initial helium abundances and α-enhanced metal abundance patterns similar to those of field halo stars at the same [Fe/H] –we denote it as first population– together with a population of helium-enriched stars displaying a range of N, Na and He overabundance, coupled to C and O depletion

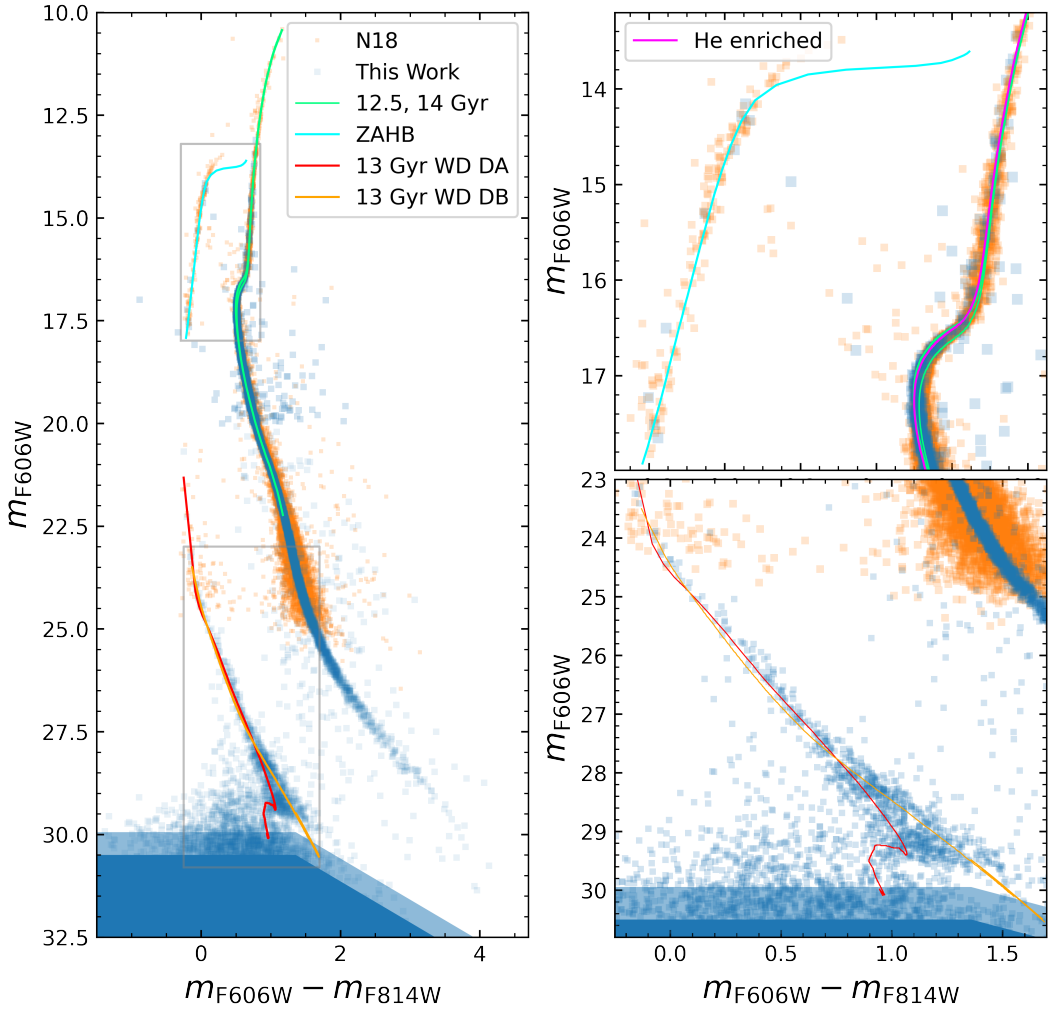

FIGURE 9.6: *(Left:)* Cluster CMD compared to theoretical isochrones. In orange, we display the catalogue from the central region of NGC 6752 by Nardiello et al. (2018, N18), in blue the deep photometry for the external field studied in this work. The two sets of data agree; the richer central field of N18 is based on much shallower observations of a much more crowded region, so they become incomplete at $m_{F606W} \sim 25$, but show well populated the bright and fast evolutionary phases, in particular: the RGB, the HB, and the bright part of the WD CS. The displayed ZAHB and theoretical isochrones are labelled. The 13 Gyr hydrogen envelope WD isochrone is denoted as DA, and the helium envelope counterpart is denoted as DB. *(Right:)* zoom-in of the gray-rectangular regions indicated in the CMD of the left panel. The *Top* panel shows the MS+HB+RGB region with also the He-enriched isochrone (in magenta). The *Bottom* panel focuses on the faint WD CS.

compared to field stars at the same [Fe/H] –we denote this as second population. When observing in optical filters and as long as the sum of the CNO abundances is the same in the first and second populations –as generally from spectroscopy– stellar models calculated with the standard helium and α-enhanced composition of the first population is appropriate to study observations of clusters' second populations (see the review by Cassisi and Salaris, 2020, and references therein).

In NGC 6752, the average difference ΔY among the cluster multiple populations is estimated to be small, $\sim 0.02 - 0.03$ (Nardiello et al., 2015a; Milone et al., 2018c; Cassisi et al., 2014), and the Y=0.275 isochrone well represents the cluster second population. We can clearly see that the effect of the enhanced He on the TO region of the isochrones is minor and does not appreciably affect the TO age estimates. Also, as discussed by Cassisi et al. (2014), the helium-rich second population is located towards the fainter blue end of the HB, a region where the corresponding helium rich ZAHB would overlap with the Y=0.248 ZAHB shown in Figure 9.6.

Moving now to the WD CS, Fig. 9.6 also shows a comparison between the observed CMD and two 13 Gyr WD isochrones, employing the same distance modulus and reddening as for the comparison to the MS, RGB and ZAHB CMD. The isochrones have been calculated from the carbon-oxygen core WD cooling tracks by Salaris et al. (2022); specifically, the models with hydrogen or helium envelopes and metal-poor progenitors (see Salaris et al., 2022, for details) computed with the Cassisi et al. (2007b) electron conduction opacities (see later for more details on this). We employed the same initial-final mass relation (IFMR) by Cummings et al. (2018) used to calculate the carbon/oxygen profiles of the WD models, and the progenitor lifetimes from Salaris et al. (2022) evolutionary tracks with the appropriate metallicity ([Fe/H]=-1.55). The helium envelope isochrone does not reach the faint end at this age, because of limitations of the input physics of the models. Due to these limitations, the calculations of WD models above $\sim 0.6 M_{\odot}$ could not reach cooling ages comparable with the ages of GCs. However, the fainter point along the helium envelope isochrone is still much fainter than the magnitude of the cut-off of the observed LF, because of the faster cooling times compared to hydrogen envelope models.

Figure 9.6 displays an overall good agreement between observations and isochrones from the bright to the faint end of the CS. Below $m_{\rm F606W} \sim 28$, the hydrogen envelope isochrone becomes increasingly offset towards bluer colours compared to observations, by up to $\sim$0.1. Given that hydrogen envelope WDs are present along the cluster CS (see, e.g. Renzini et al., 1996; Moehler et al., 2004; Chen et al., 2022) we believe that systematic offsets of this order are compatible with the residual uncertainties in the photometry of the faintest sources, that likely affect mostly the F814W filter (see end of Sect. 9.4).

Interestingly, the observed breadth of the faintest part of the WD CS is larger than that inferred from ASTs, but bracketed by the two shown isochrones. There also seems to be some structure with a possible hint of a gap around $m_{\rm F606W} \sim 28.8$; however, only data with better signal-to-noise would be able to investigate the exact shape of these putative features.

Our analysis of the WD LF focuses on isochrones from models with hydrogen envelopes, as current evidence indicates that at least the bright WDs in NGC 6752 and other GCs are generally found with hydrogen atmospheres (Moehler et al., 2004; Renzini et al., 1996; Davis et al., 2009; Chen et al., 2022). This assumption is reinforced by the fact that, as we describe below, the shape of the empirical LF agrees well with a population of WDs with hydrogen envelopes. We will briefly investigate the impact of the possible presence of WDs with helium envelopes in Sect. 9.9.1

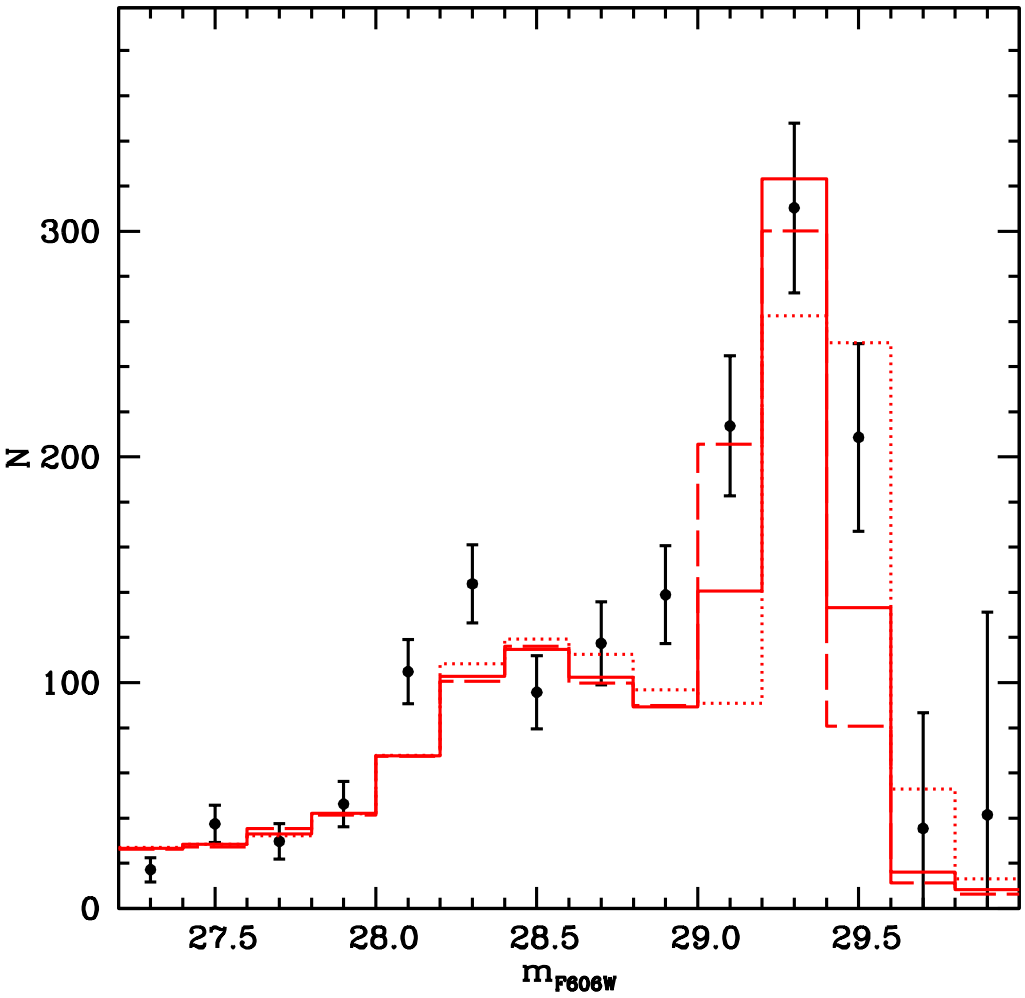

FIGURE 9.7: Observed WD LF compared to theoretical counterparts for ages equal to 12.7 Gyr (dashed line), 13.0 Gyr (solid line) and 13.5 Gyr (dotted line) respectively. The theoretical LFs have been calculated using for the progenitors' mass function a power law with exponent x=−2.3, and are normalized by matching the total number of stars of the empirical LF between $m_{\rm F606W}$=27.3 and 27.9 (see text for details).

To study in more detail the consistency of the ages from the CS and the MS TO, we need to model the WD LF. Before doing so, we need to consider the effect of the HB morphology of this cluster on the WD population.

As briefly discussed in the introduction, the HB of NGC 6752 shows a pronounced extension to the blue, with objects increasingly less massive when moving towards bluer colours, because of thinner hydrogen-rich envelopes around the helium core. Chen et al. (2022) have discussed in detail how the bluer HB stars have envelope masses too small to reach the asymptotic giant branch (AGB) after the end of core helium burning, hence they do not experience the thermal pulses and third dredge-up. These objects reach the WD stage with a residual hydrogen envelope thick enough to sustain stable thermonuclear burning (Althaus et al., 2015). For redder HB stars with masses above $\sim 0.56 M_{\odot}$ the post-HB evolution leads instead to the AGB phase and the thermal pulses. The resulting WDs have thinner outer hydrogen layers, of 'canonical' mass thickness equal to $\approx 10^{-4} M_{\rm WD}$ where $M_{\rm WD}$ is the total WD mass, not able to support efficient hydrogen burning (Althaus et al., 2015; Chen et al., 2021). As a consequence, the bright part of the cluster CS is populated by two different populations of WDs; a 'slower' population supported by envelope hydrogen burning, and a 'canonical' population which is cooling faster, without any substantial contribution from nuclear burning. The number ratio of these two populations is determined by the mass distribution of the HB stars which, in turn, is controlled by the distribution of initial helium abundances among the cluster's multiple populations, as studied by Cassisi et al. (2014). Down to $m_{\rm F606W}$ ∼25.1, the magnitude range studied by Chen et al. (2022), this number ratio 'slow'/'canonical' is equal to $\sim$ 70/30, a value that is expected to progressively decrease at fainter magnitudes because these WDs formed earlier in the life of the cluster, when stars along the HB were more massive and increasingly less blue. At $m_{\rm F606W} \sim 27.3$, corresponding to cooling times of 3.-3.5 Gyr, we expect to have only 'canonical' WDs because their HB progenitors all had masses above $0.56 M_{\odot}$ (see the discussion in Chen et al., 2022).

In our deep photometry, which covers the outer regions of the cluster, the bright part of the LF is not well populated because of the sparser density (necessary to study faint objects). Therefore, we will need to perform a comparison with model predictions considering $m_{\rm F606W} \geq$27.3, where the number of objects is at least 20 per bin. Coincidentally, this is also the magnitude range where only canonical DA WDs are expected to populate the CS.

We have calculated theoretical WD LFs starting from isochrones computed as described before, using as reference a Salpeter-like power law for the WD progenitor mass function with exponent x set to -2.3. The WD models we employ have negligible efficiency of Hydrogen burning in their envelopes (the mass thickness of the hydrogen envelope is equal to $10^{-4} M_{\rm WD}$). To properly include the photometric errors we followed a Monte Carlo approach; we have first randomly drawn progenitor masses according to the chosen mass function, and determined the magnitude and colour of the corresponding synthetic WD by interpolation along the isochrone, after applying the distance modulus and extinction. The magnitude and colour have then been perturbed by Gaussian random errors with $1\,\sigma$ values determined from the mean $1\,\sigma$ errors at the magnitude of the synthetic object, as obtained from the photometric analysis. We finally calculated the LF from the magnitude distribution of the resulting sample of synthetic WDs. For each LF calculation, we have drawn 100,000 synthetic stars, to minimize the statistical error in the star counts, and normalized the theoretical LFs matching the total number of objects in the empirical LF in the bins centred between $m_{\rm F606W}$=27.3 and 27.9 (130 objects).

Figure 9.7 shows theoretical LFs for the three ages that match the position of the

peak and subsequent drop of the star counts at the faint end of the empirical LF. As well known, the magnitude of this feature is a diagnostic for the total age (cooling age plus progenitor age) of a cluster's WD population. The fainter the magnitude, the older the WD population. The range of ages inferred from the theoretical LFs is between 12.7 and 13.5 Gyr, completely consistent with the cluster age derived from the MS TO and subgiant branch, as shown in Fig. 9.6.

The shape of the theoretical LFs follows closely the shape of the empirical counterpart. In the magnitude range used for the normalization, the theoretical LFs display a very mild increase of the number counts with increasing magnitude, as observed. There is a sharper increase of the number counts toward fainter magnitudes, with a roughly flat portion down to the bin centred at $m_{\rm F606W}$=28.9.

This magnitude range of the theoretical LF is populated by objects with mass – and progenitor mass– increasing only very slowly with magnitude, the average WD mass being around $0.56 M_{\odot}$, as shown in Fig. 9.8. The number of stars per magnitude bin will, therefore, be mainly determined by the local cooling speed, with a smaller contribution from the choice of the progenitor mass function. Starting from $m_{\rm F606W}$ $\sim$28.0 the cooling speed slows down because of the onset of crystallization, hence the local increase of the number counts.

Beyond $m_{\rm F606W}$=29.0 both theoretical and observed LFs display a steep increase of the number counts that peak at $m_{\rm F606W}$=29.3, followed by a sharp drop at fainter magnitudes. In this magnitude range the LF is populated by all other more massive WDs, originated from progenitors with initial mass above $\sim 1.5 M_{\odot}$, as shown in Fig. 9.8. These objects have reached fainter magnitudes because of their longer cooling times (shorter progenitor lifetimes). Their piling up in a relatively narrow magnitude range explains the appearance of the peak and cut-off in the LF at the bottom of the CS. As a consequence of this pile-up of WDs originated from progenitors with a large range of initial masses, a variation of the exponent of their mass function can have a major impact on the predicted WD number counts in this magnitude range.

As an aside, we note that Fig. 9.8 shows a non-monotonic relation between WD (and progenitor) mass and magnitude at the faint end of the theoretical LF. This is a consequence of the fact that at these luminosities the model cooling times do not increase monotonically with increasing WD mass. This is due to the interplay of the onset (in terms of luminosity) of crystallization that depends on the WD mass (higher masses start crystallizing earlier), and the associated time delays, which are in turn dependent on the WD mass (because of the different CO profiles) and luminosity (energy released at higher luminosities induce shorter time delays).

It is very important to notice also that the shape of the WD LF NGC 6752 is almost identical to the shape of the LF of the WD CS of M 4 (see Fig. 10 in Bedin et al., 2009b), despite the different metallicity and HB morphology (redder) of this more metal-rich cluster. In M 4 the WD LF also displays a very mild increase in the number counts toward fainter magnitudes, followed by a sharper increase and a roughly flat portion, before the pile up at the bottom end of the CS. These general trends can also be seen in the WD LFs of the metal-poor cluster NGC 6397 (with a blue HB morphology) and the red HB, metal rich cluster 47 Tuc (see Fig. 2 in Hansen et al., 2013) even though in this latter cluster the magnitude range spanned by the roughly flat portion of the LF is narrower, likely because of its younger age.

One important aspect to consider in the interpretation of the WD LF is the role of the progenitor mass function and the possible complexities associated with the effects of the cluster dynamical evolution on this mass function. In particular, as a

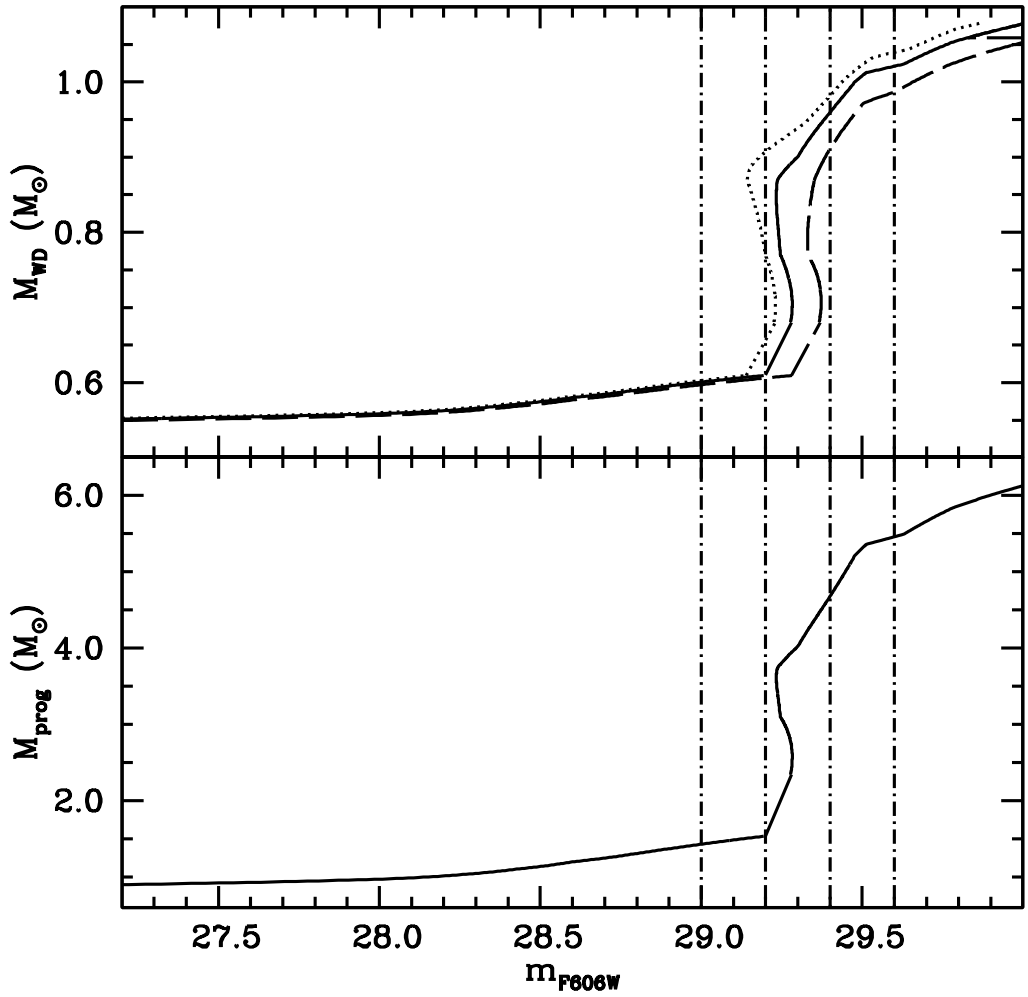

FIGURE 9.8: Distribution of the WD masses (in solar mass units – top panel) as a function of the $m_{\rm F606W}$ for the LFs displayed in Fig. 9.7 (keeping the same line-type code for the different ages). The bottom panel displays the corresponding distribution of the initial progenitor masses (in solar mass units) along the 13 Gyr LF. The dash-dotted vertical lines in the two panels mark the boundaries of the three magnitude bins that enclose the region of the peak and subsequent cut-off of the empirical LF.

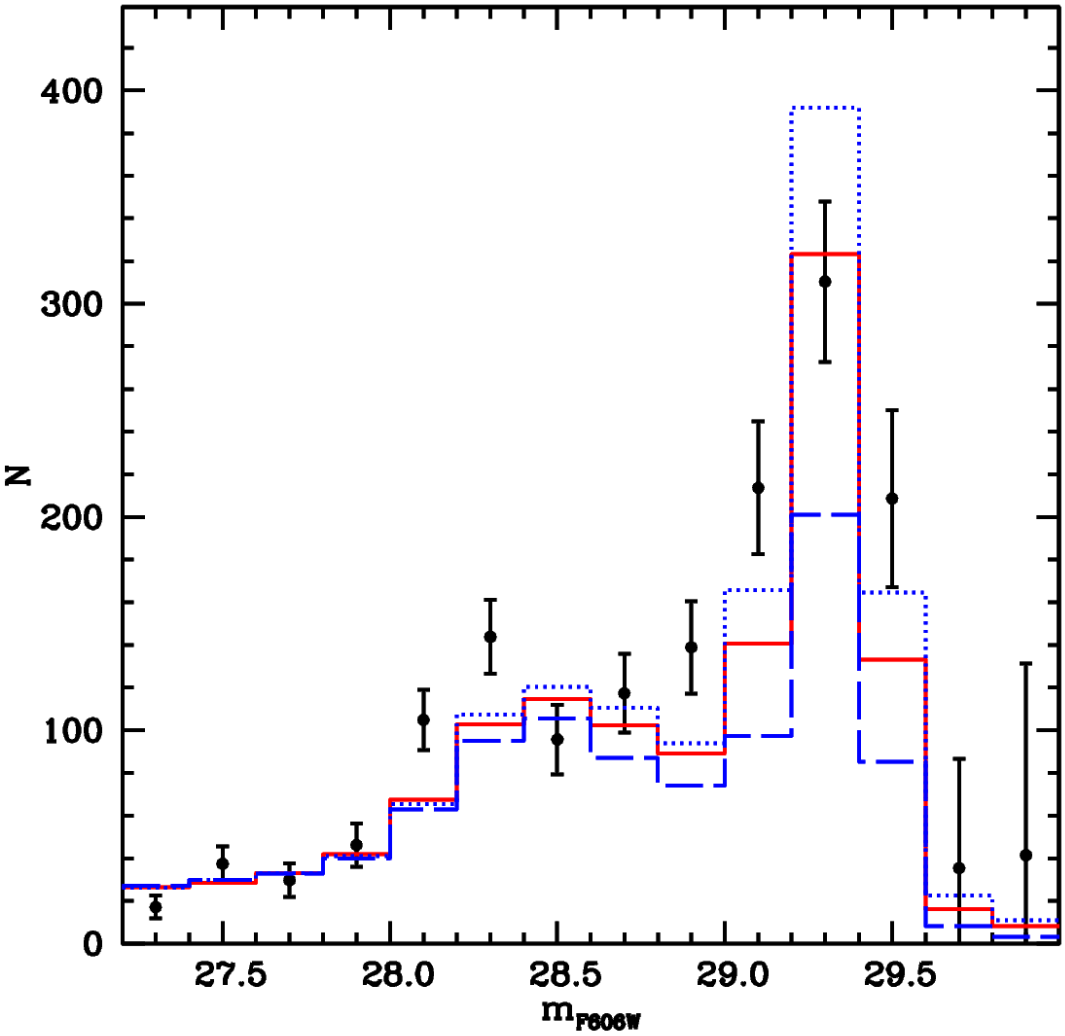

FIGURE 9.9: As Fig. 9.7, but showing three theoretical LFs for an age of 13 Gyr, calculated with exponents of the progenitor mass function equal to $x = -2.1$ (dotted line), -2.3 (solid line, the same LF of Fig. 9.7) and -2.8 (dashed line) respectively.

result of the interplay between internal dynamical processes and the external Galactic tidal field, globular clusters gradually lose stars that escape beyond the cluster's tidal radius. This mass loss preferentially affects low-mass stars and may significantly alter the cluster's global mass function (see, e.g., Vesperini and Heggie, 1997b; Baumgardt and Makino, 2003). This process may therefore play a role in determining the present-day mass distribution of WDs by altering the mass function of their progenitors before the WD formation and, more directly, by causing the preferential loss of low-mass WDs after their formation. In addition to these effects, it is important to consider the gradual segregation of massive stars towards the cluster's central regions and the outward migration of low-mass stars driven by the effects of two-body relaxation. Since observations do not typically cover the entire radial extension of a cluster, a detailed model of the WD mass distribution would also require proper consideration of the effects of segregation and local variations of their mass distribution. Modelling the combined effects of these processes is non-trivial and would require an extensive suite of simulations specifically aimed at reconstructing the dynamical history of the cluster, and exploring the implications for the mass distribution of its WD population. This is beyond the scope of this Chapter, but we emphasize that part of the discrepancies between the observed and the theoretical WD LFs shown below might be ascribed to the dynamical effects we have discussed.

9.8.1 The impacts of the cluster's stellar mass function and initial-final mass relation

In order to provide a general illustration of the dependence of the WD LF on the stellar MF, in Fig. 9.9 we show the effect of changing the exponent x of the progenitor's mass function in the calculation of the 13 Gyr LF. The magnitudes of peak and cut-off are not affected, but the number counts are. An exponent x=−2.15 matches better the observations compared to the x=−2.3 case. The total number of stars in the three bins centred at $m_{\rm F606W}$=29.1, 29.3 (the magnitude of the peak of the observed LF) and 29.5 of the empirical LF is 733±64, where the 1σ error has been calculated by propagating the 1σ errors on the number counts of the individual bins; the 13 Gyr theoretical LF calculated with x=−2.1 has 723 objects in this same magnitude range – consistent with the observations within less than 1σ– whilst only 600 objects populate the LF calculated with x=−2.3. In the range between $m_{\rm F606W}$=28.1 and 28.9 the empirical LF has 601±38 objects, whereas the theoretical counterpart calculated with x=−2.1 has 497 objects (477 objects in the LF calculated with x=−2.3), an underestimate of more than 2.5σ. This latter discrepancy might hint at some significant underestimate of the cooling timescales of models in this magnitude range; in fact, a qualitatively similar discrepancy along the flat part of the LF before the pile-up at the end of the CS can be seen in the comparison of theoretical LFs with observations in M 4 (see Fig. 13 in Bedin et al., 2009b).

In addition to the stellar mass function and its evolution driven by cluster dynamics, the IFMR may also play a key role in determining the WD LF. In Fig. 9.10 we display the results of another numerical experiment. It shows the 13 Gyr LF of Fig. 9.9 calculated with x=−2.1, plus a coeval LF computed by employing this time the linear IFMR by Salaris et al. (2009) and a progenitor mass function with exponent x=−1.95. The two theoretical LFs are almost identical, despite the different values of x and choice of IFMR. The number of objects around the peak of the observed LF is 707 for the LF calculated with the IFMR by Salaris et al. (2009), whilst in the range between $m_{\rm F606W}$=28.1 and 28.9 this LF contains 527 objects, a number that is within 2σ of the observations.

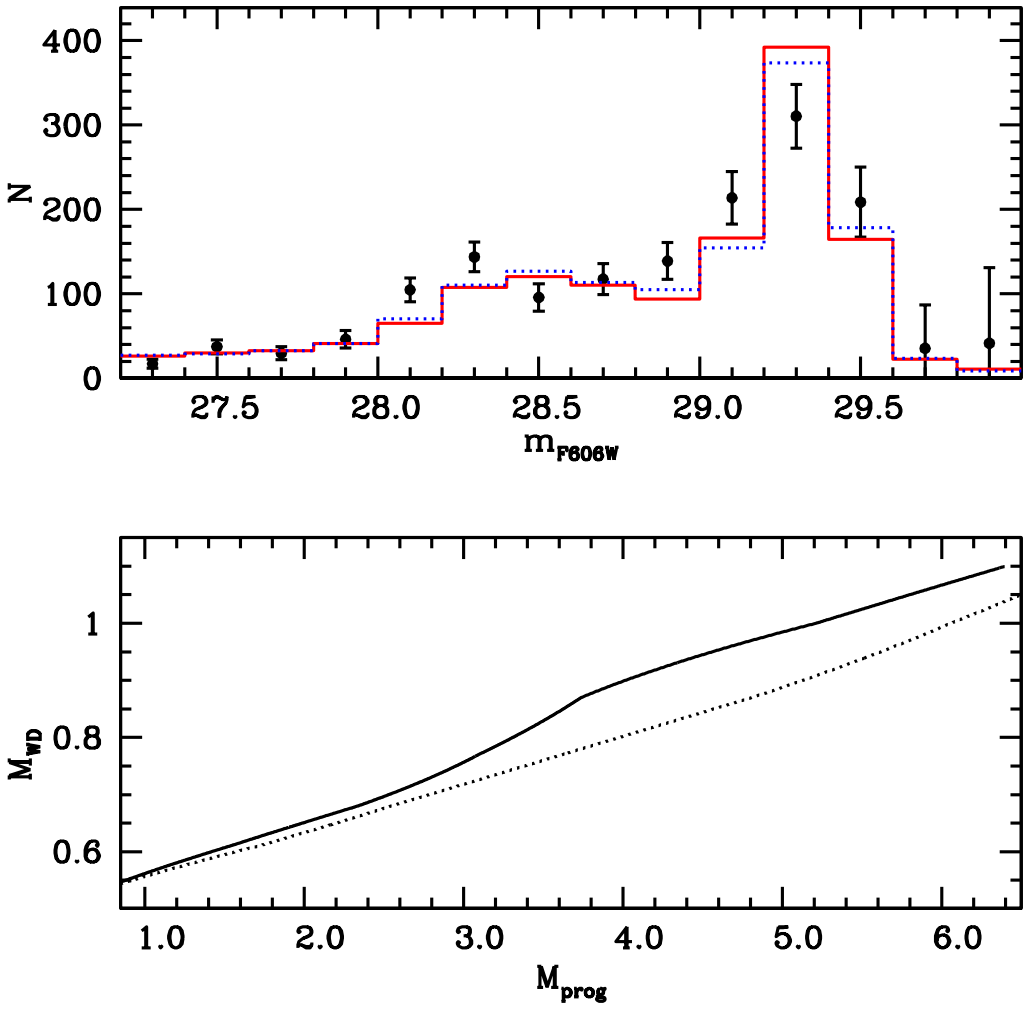

FIGURE 9.10: The top panel is as Fig 9.9 but showing the 13 Gyr theoretical LF calculated with $x = -2.1$ (solid line) plus a coeval one calculated using the Salaris et al. (2009) and x=−1.95 (dotted line). The bottom panel compares the IFMRs used in the calculation of the LFs in the top panel.

To summarize, the quality of the agreement between observed and theoretical star counts along the LF depend somehow on the choice of both the progenitor mass function and of the IFMR, but the magnitudes of the LF peak and cutoff are much more solid predictions of theory. This confirms that the consistency between MS TO and CS ages is robust.

9.8.2 The impact of the electron conduction opacities

The empirical WD LF allows us to test also WD models calculated with the recent electron conduction opacities by Blouin et al. (2020). These authors have published improved calculations for H and He compositions in the regime of moderate degeneracy, which they have combined with the Cassisi et al. (2007b) calculations to include the regime of strong degeneracy and cover the full parameter space necessary for stellar modelling. The opacities at the transition between moderate and strong degeneracy are still uncertain (see, e.g., Blouin et al., 2020; Cassisi et al., 2021), but they are crucial for modelling WD envelopes and predicting the correct cooling times. As investigated by Cassisi et al. (2021), different ways to model this transition region give a spectrum of values of the opacity that varies by up to a factor of $\sim$2.5 in the regime relevant to WD envelopes.

We have calculated WD isochrones and LFs as discussed before, this time employing the set of Salaris et al. (2022) WD models computed with the Blouin et al. (2020) conductive opacities. Figure 9.11 compares the observed LF with two of these new theoretical LFs for an age of 10.7 Gyr, computed with two different exponents of the progenitor mass function ($x = -1.8$ and $x = -2.3$, respectively). The age required to match the observed magnitude of the peak of the LF is now in disagreement with the age from the MS TO. Also, the number counts in the magnitude range between $m_{\rm F606W}$ $\sim$28 and $\sim$29, are largely underestimated, even for the LF calculated with x=$-$1.8, that compares well with the total number of objects around the peak of the empirical LF (721 objects in the theoretical LF). This is all consistent with the fact that, apart from the early stages of cooling, models calculated with Blouin et al. (2020) opacities evolve much faster than models computed with Cassisi et al. (2007b) opacities (Salaris et al., 2022).

9.9 The impact of the cluster's multiple populations

We have discussed already how the presence of multiple populations in the cluster impacts the bright part of the CS, because of the slowly cooling WDs supported by hydrogen burning in their envelopes, which are produced by the bluer HB progenitors (see Chen et al., 2022). In the magnitude range we are studying here, these are no longer present, but the existence of multiple populations can still potentially have an impact.

In this cluster, we have a $\sim$70% fraction of stars presently evolving in pre-WD phases with an initial value of Y larger by typically ΔY=0.02-0.03 compared to the remaining 30% of stars (Milone et al., 2017c; Milone et al., 2018c). When we assessed the impact of this second population on the MS TO ages, we calculated WD isochrones and LFs using progenitor lifetimes from Pietrinferni et al. (2021) models with initial Y=0.275. In the assumption that the IFMR is unaffected by this small variation of the initial He of the progenitors, we have verified with test calculations that the CO stratification of the WD models is also insensitive to such a small ΔY.

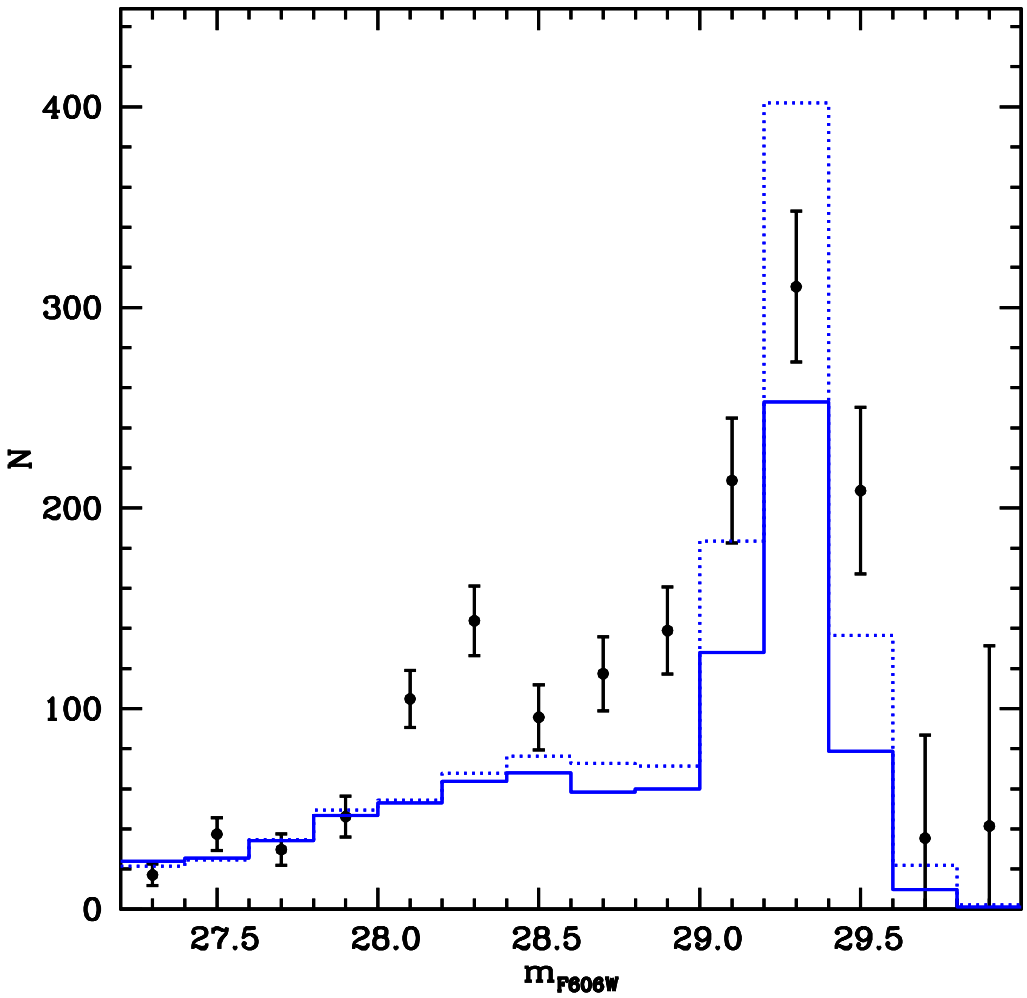

FIGURE 9.11: As Fig 9.7 but showing two 10.7 Gyr theoretical LFs calculated using the Blouin et al. (2020) electron conduction opacities, and exponents of the progenitor's mass function equal to -2.3 (solid line) and -1.8 (dotted line) respectively.

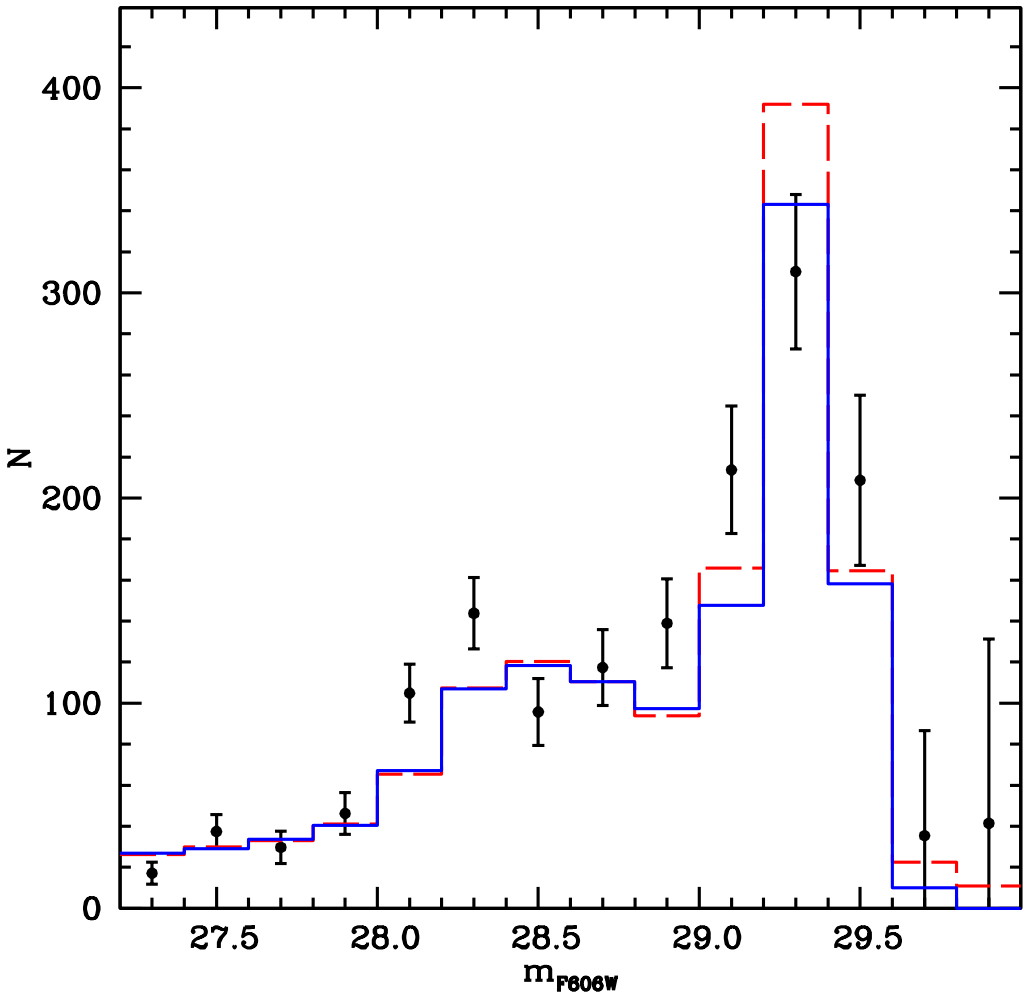

FIGURE 9.12: As Fig. 9.7, but showing two theoretical LFs for an age of 13 Gyr. The dashed line displays a LF calculated with helium-normal progenitors and mass function exponent equal to -2.1 (the same LF displayed as a solid line in Fig. 9.10), whilst the solid line shows a calculation with the same mass function but an initial Y=0.275 for the progenitors.

Figure 9.12 shows how such a small helium enhancement in the progenitors have a minor impact on the resulting WD LF. For a fixed age and exponent of the progenitor mass function, after normalization the second population WD LF is extremely similar to the LF of first population WDs. Differences are minimal around the peak of the LF, hence comparisons of the empirical LF with that of a composite population made of first and second-population WDs will give results essentially equivalent to the case of using models for just first population WDs.

9.9.1 The impact of helium envelope WDs

So far we have studied the WD LF using only models with hydrogen envelopes. The top panel of Fig. 9.13 compares with observations the 13 Gyr LF populated by hydrogen envelope models and progenitor mass function exponent $x = -2.1$ of Fig. 9.10, and a LF populated by helium envelope models. This latter LF had been computed as described before, using Salaris et al. (2022) models with pure helium envelopes. [5]

The shape of the LF populated by helium envelope models is very different from the observed one. It stays essentially flat from the magnitude range chosen for the normalization down to $m_{\rm F606W}$ ∼29.5, completely at odds with observations. Due to the generally faster cooling times of helium envelope models, in this magnitude range this LF is populated by objects with practically constant mass, around $0.55 M_{\odot}$, with progenitor initial masses in a relatively narrow mass range (the more massive objects appear at much fainter magnitudes). This also means that the number counts are insensitive to the choice of the exponent of the progenitor mass function.

The comparison shows clearly that the population of helium envelope objects must be a relatively small fraction of the total number of WDs observed, otherwise, the shape of the cluster LF would be very different from what is observed[6].

On the observational side, Moehler et al. (2004) have studied spectroscopically 5 objects along the cluster CS with $T_{\rm eff}$ between ∼20,000 K and ∼13,000 K (corresponding to $m_{\rm F606W}$ between ∼24 and 24.7 according to our isochrones) and found they all have hydrogen atmospheres. Renzini et al. (1996) found that in their sample of 21 bright cluster WDs with $T_{\rm eff}$ between ∼20,000 K and ∼10,000 K, the positions of two objects in the CMD is consistent with helium atmosphere WDs (∼10%).

We also note that the faint end of the observed CS in Fig. 9.6 has a width larger than what predicted by the artificial star analysis. This could be hinting at the presence of helium envelope WDs, that towards the faint end of the CS are expected to become increasingly redder than their hydrogen envelope counterpart, as shown in Fig. 9.6.

Assuming that the Renzini et al. (1996) result represents the true ratio between hydrogen and helium envelope WDs at birth (9:1), these WDs populate a magnitude range within the limits of =the Chen et al. (2022) study, where the number ratio 'slow'/'canonical' WDs is equal to ∼ 70/30. Our adopted WD models show that in the magnitude range of Chen et al. (2022) analysis the $0.54 M_{\odot}$ (a representative mass populating this temperature range) models with hydrogen and helium

[5] We notice that Bergeron et al. (2019) have shown how for WDs in the *Gaia* catalogue with helium-dominated atmospheres, the presence of a small percentage of hydrogen is required to determine more accurate stellar parameters.

[6] This is strictly true in the hypothesis that hydrogen envelope WDs do not transform into helium envelope objects during their cooling evolution, because of convective mixing with the underlying more massive helium layers (see, e.g., the discussion in Davis et al., 2009).

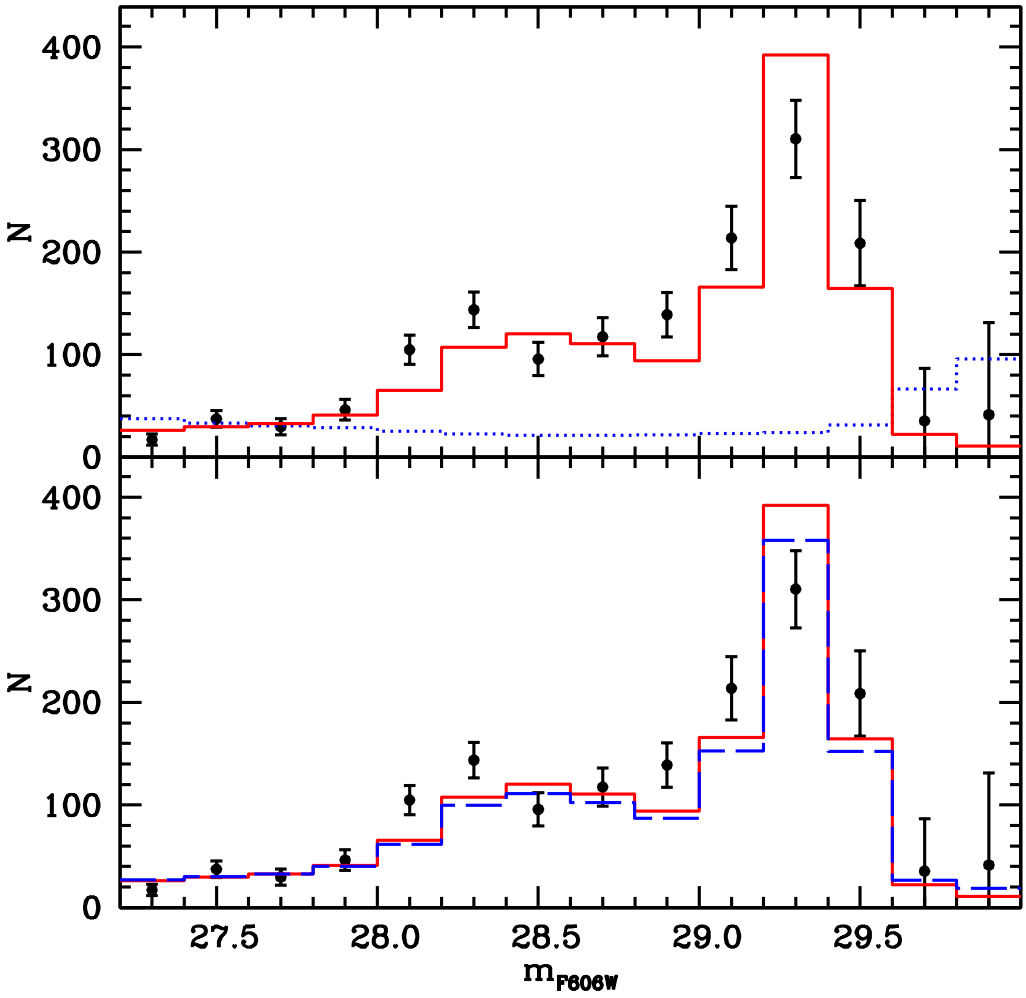

FIGURE 9.13: As Fig. 9.7, but showing in the top panel with a solid line, the same 13 Gyr LF plotted as a solid line in Fig. 9.10, populated by WDs with hydrogen envelopes and progenitor mass function with x=−2.1. The dotted line denotes a 13 Gyr LF calculated with the same IFMR and progenitor mass function but using WD models with helium envelopes (see text for details). The lower panel shows the same LF for hydrogen envelope WDs (solid line) and the LF for a composite population made of both hydrogen and helium envelope WDs (dashed line). The number ratio of hydrogen to helium envelope objects at formation is set to 90:10 at birth (see text for details).

envelopes have the same cooling times, implying that Chen et al. (2022) results obtained considering only hydrogen envelope models are unaffected if we include this small fraction (∼10% of the total) of helium envelope objects in the 30% of 'fast' WDs without hydrogen burning.

For our purposes, we have calculated a LF made of a composite population with 90% hydrogen envelope objects, and 10% helium envelope WDs at birth, both for an exponent of the progenitor mass function x=−2.1, assuming there is no transformation from hydrogen- to helium envelopes during the cooling. The lower panel of Fig. 9.13 replaces the LF of helium envelope models with this composite population in the magnitude range of interest to our analysis. Due to the generally faster cooling times of the helium envelope models, they make up only a few per cent of the total number of objects within the magnitude bins centred between $m_{\rm F606W} = 27.3$ and 29.5, and the composite LF is almost identical to the one calculated with just hydrogen envelope WDs.

9.10 Summary

This is our conclusive study on the WD CS of NGC 6752, which was the main goal of the multi-cycle *HST* large program GO-15096/15491. With respect to Paper III, which was based only on the first half of the data, we now doubled the total exposure time and extended our work taking advantage of all the data collected to better define the cluster CS and its LF. This has allowed us to perform robust and conclusive comparisons with theory; more specifically, the WD models by Salaris et al. (2022).

We found that the shape of cluster WD LF is very similar to its counterpart in the metal richer, redder horizontal branch GC M 4 (Bedin et al., 2009b), and that theoretical LFs for hydrogen envelope WD models calculated with the Cassisi et al. (2007b) electron conduction opacities follow closely the observed trend of star counts as a function of magnitude. The observed LF peaks at $m_{\rm F606W} \simeq 29.3 \pm 0.1$, consistent within uncertainties with what has been previously reported, and the magnitude of this peak is matched by WD isochrones with ages between 12.7 and 13.5 Gyr, consistent with the cluster age derived from the MS TO and subgiant branch. We confirm that the predicted magnitude of the LF peak and cutoff is unaffected by realistic variations of the adopted IFMR and the progenitor mass function. We also find that the impact of the cluster multiple populations on the WD LF for $m_{\rm F606W}$ larger than ∼27.3 is negligible.

Our analysis also reveals a possible hint of an underestimate of the cooling timescales of models in the magnitude range between $m_{\rm F606W}$=28.1 and 28.9. However, different choices of the IFMR can reduce the discrepancy between theoretical and empirical star counts in this magnitude range to below 2σ. A hint of a similar discrepancy can be found in the analysis of the WD LF in M 4 by Bedin et al. (2009b).

Renzini et al. (1996) photometry of a small sample of bright cluster WDs suggests the presence of a small fraction (∼10%) of WDs with helium envelopes. We find that this fraction of helium envelope objects has a negligible impact on the shape of the LF, and is potentially responsible for the colour width of the faint end of the observed CS.

Finally, we find that hydrogen envelope models calculated with the Blouin et al. (2020) electron conduction opacities provide WD ages in disagreement (they are too low) with the TO age.

Chapter 10

The *HST* Large Programme on NGC 6752 - Variability

We conducted a search for candidate variables and transits in an external field of NCG 6752 observed by the *Hubble Space Telescope* (*HST*) across four epochs. Our investigation aimed to identify variable stars and transits, but yielded only a few potential candidates, with just one potential transit detected. The limited number of findings can be attributed to the fact that the dataset utilized in this study was not specifically optimized for the discovery of variable stars and transits. However, during our analysis, we unexpectedly discovered a supernova within a background galaxy in our observed field. The light curve of the supernova indicates a subtle, nearly constant decrease in luminosity, suggesting that the peak luminosity of the supernova has likely already occurred.

10.1 Introduction

The detection of periodic variables in globular clusters (GCs) provides valuable insights into stellar evolution, binary systems, and the dynamical processes at play within these dense stellar environments. Furthermore, the identification of planetary transits within such clusters contributes to our understanding of exoplanetary systems in extreme environments.

NGC 6752 is one of the closest GCs and is known to host different stellar populations, making it one of the best targets for photometric investigations. In this chapter, we present an analysis of *Hubble Space Telescope* (*HST*) data focused on the discovery of periodic variables and planetary transits within this globular cluster.

This study is based on the analysis of images acquired using the Wide-Field Channel (WFC) of the Advanced Camera for Surveys (ACS) aboard *HST* as part of the multi-cycle large program titled *The end of the White Dwarf Cooling Sequence of NGC 6752*, with program IDs GO-15096 and GO-15491 (PI: Bedin), aimed at observing an external region of the cluster.

Our approach involves carefully studying light curves created from the *HST* data, looking for periodic changes in brightness that indicate the presence of periodic variables. Additionally, we expand our investigation to search for planetary transits, looking for minor brightness reduction caused by orbiting exoplanets passing in front of their host stars.

The chapter is organised as follows: Section 10.2 outlines the data set utilized and the corresponding data reduction process. Section 10.3 details the extraction of light curves, while Sections 10.4 and 10.5 concentrate on the identification of candidate variables and transits, respectively. Section 10.6 is dedicated to the study of a supernova discovered in the background within our images.

10.2 Data analysis

The image data were collected using two filters, F606W and F814W, during four distinct epochs (2018, 2019, 2021, and 2022), spanning from 2018 to 2022, resulting in an observational period of ≈3.5 years. The F814W filter was employed in all epochs, while the F606W filter was utilized only in the first and third epochs. During each orbit, the HST acquired one short exposure and two long exposures. For this analysis, we specifically utilized the long exposures, as they provide the depth required for precise light curve extraction. Each epoch covers an observational duration of approximately 1 to 10 days, with a cadence ranging from approximately 3 to 18 images per day. Although this dataset was not explicitly designed for investigating stellar variabilities, we have nonetheless extracted light curves to explore the possibility of identifying variable stars. For a comprehensive description of the dataset, please refer to Bedin et al. (2019a) and Bedin et al. (2023, hereafter Paper III and Paper IV).

The data reduction process closely followed the procedures outlined in Scalco et al. (2021). Data reduction involved the modelling of an effective Point Spread Function (ePSF, Anderson and King, 2000; Anderson and King, 2006) tailored to each individual frame. This PSF tailoring was executed using the techniques introduced in Anderson and Bedin (2017) for WFC3/UVIS and subsequently extended to ACS/WFC by Bellini, Anderson, and Grogin (2018b). The resulting tailored PSFs were employed to extract stellar magnitudes and positions from each image. These distortion-corrected positions from all images were then transformed into a common distortion-corrected reference frame.

To ensure the accuracy of our analysis and prevent spurious detections resulting from star spikes and blending, we pre-processed the images by effectively removing these artefacts through the application of specially designed masks. The removal of star spikes and blending was done by using the software tool `acswfc_mask_spikes.F`, which was developed by Jay Anderson. It's important to note that in this study, we exclusively utilized the deblended images.

10.3 Light curves

We began by creating an initial input list, by selecting a sample of well-measured and cluster member stars based on a set of quality parameters produced during our reduction stage, in the analogy of what was done in Scalco et al. (2021), and based on their position in the vector-point diagram (VPD). Our initial input list comprised a total of 11,334 stars.

To extract the light curves we followed the procedure presented in Nardiello et al. (2015c) using a specifically designed `FORTRAN` software. In brief, the software takes the input catalogue, PSFs and transformation files defined in the previous section, and extracts the raw fluxes of all the selected sources present in the input catalogue using both PSF and aperture photometry. In addition to the PSF and aperture magnitudes, the software also generates several quality parameters as output, including the `QFIT` parameter, which assesses the precision of the PSF fitting process. In the subsequent analysis, we will exclusively utilize the light curves obtained through PSF photometry, as they provide the most accurate photometric data, with the light curves obtained from aperture photometry serving solely as a point of comparison.

10.3.1 Detrending of light curves

To remove residual systematic errors from the light curves derived in the previous section, we followed the procedure described in detail by Nascimbeni et al. (2014) and Nardiello et al. (2015c). In summary, the correction of light curves involved three distinct methods: the global zero-point correction (GZP), local zero-point correction (LZP), and a weighted local zero-point correction (WZP).

Our first step was to identify a set of reference stars, which would serve to define the photometric zero-point of each target star in all the individual images. The list of candidate reference stars is selected by discarding all the stars with a photometric rms of the raw light curves 2.5σ larger than the median rms at a given magnitude and a `QFIT` value 3σ larger than the median QFIT value at a given magnitude. We also require these stars to be bright, non-saturated ($-13.5 < m_{\mathrm{F814W}} < -6$) and that they be detected and measured at least on 70% of the frames, as a reasonable compromise between completeness and FOV coverage.

For the kth target star, the jth reference star, and the ith epoch where both stars are detected, the GZP correction, denoted as τ_i, can be expressed as:

$$m'_{i,k} = m_{i,k} - \tau_i = m_{i,k} - \langle m_{i,j} - \langle m_{i,j} \rangle_i \rangle_j \tag{10.1}$$

where $\langle x \rangle_j$ denotes the averaging of quantity x over the index y. The outcome of the GZP method yields a conventional, unweighted differential photometry, where all reference stars carry equal weight.

The LZP and WZP corrections are computed with an expression equivalent to τ. For LZP, we considered the $N = 35$ closest reference stars in position to the target stars, while for WZP, we evaluated the correction using the weighted mean of magnitudes for our reference star set, instead of an unweighted median. The weights for this computation, are defined with an analytical function that depends on the relative sky position distance and magnitude distance between the reference star and the target star and was determined using equations 2, 3, and 4 from Nascimbeni et al. (2014).

Panel (a) of Fig. 10.1 compares the scatter of the light curves corrected using the GZP (red), LZP (green) and WZP (blue) detrending algorithms, for the PSF-fitting photometry, for the F814W filter (a similar plot can be obtained for the F606W filter). As a comparison, we also show in panel (b) the same plot for the light curves obtained with the aperture photometry. The improvement obtained with the correction is evident, especially on the bright, non-saturated side of the sample, where the improvement is around 20-40%. For the PSF photometry, the GZP correction gives a lower improvement with respect to the other two, as expected. The LZP correction seems to be the one that gives the highest improvements, while the WZP correction is in the middle. For this reason, only the LZP light curves are analysed in the next sections.

10.4 Variable finding

We utilized the Lomb–Scargle (LS) periodogram (Lomb, 1976; Scargle, 1982) to identify potential variable stars within our dataset of LZP-corrected light curves. The analysis was carried out using the `VARTOOLS V1.40` code developed by Hartman et al. (2008) and publicly available[1]. The LS algorithm is very effective at detecting sinusoidal or pseudo-sinusoidal periodic variables and provides a formal false alarm

[1] https://www.astro.princeton.edu/ jhartman/vartools.html.

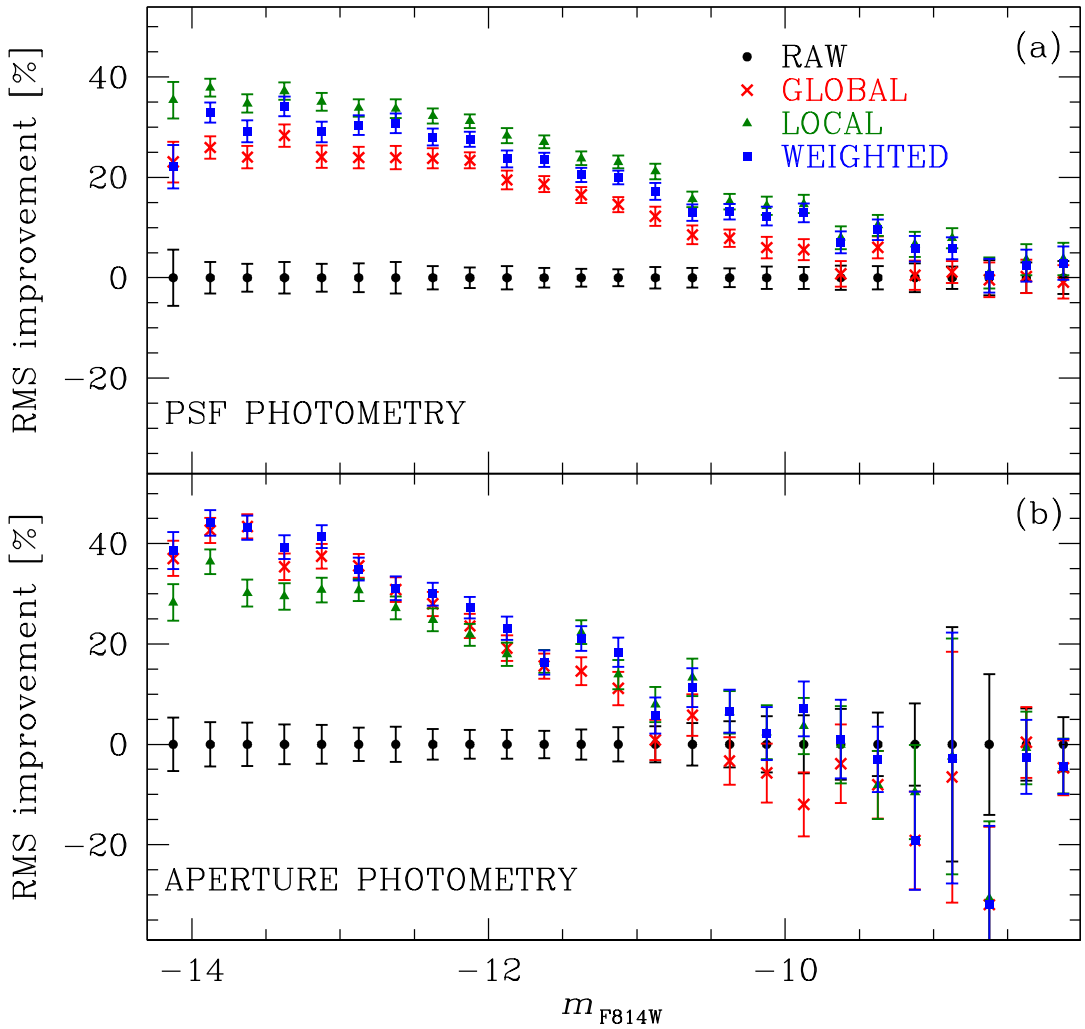

FIGURE 10.1: Percentage improvement, as a function of the F814W magnitude, on the photometric rms (i.e. the per cent reduction of rms compared to raw light curves, averaged on 0.25 mag bins.) of the GZP (red), LZP (green) and WZP (blue) detrending algorithms, for both the PSF-fitting photometry (panel (a)) and the aperture photometry (panel (b)).

probability (FAP) as a quantitative metric for selecting stars with the highest likelihood of being genuine variables. To enhance candidate selection, we also employed the 'signal-to-pink noise' (SNR) diagnostic parameter as defined by Hartman et al. (2009).

Initially, we filtered the light curves by excluding all detections with a QFIT value greater than 1. Variability analysis was conducted on light curves containing at least 26 detections for the F814W filter and 55 detections for the F606W filter, corresponding to 50% of the total epochs. Additionally, we considered light curves with a photometric rms of the LZP-corrected curve less than 1, resulting in 4,784 light curves for the F814W filter and 4,414 light curves for the F606W filter.

Our search was divided into various period ranges: 0.05-0.1, 0.1-1, 1-10, 10-100, and 100-1000 days, with each set analyzed independently. Panels (a) and (b) of Fig. 10.2 illustrate FAP and SNR values as functions of the detected period for all light curves within the 0.1-1 day period interval and the F814W filter. Similar plots can be generated for other period intervals and the F606W filter. It's noteworthy that most stars cluster around FAP $\sim$ 0 and SNR $\sim$ 5, indicating non-variable stars, while a few stars exhibit lower FAP values and higher SNR values, suggesting they are candidate variables.

To identify candidate variables and estimate our analysis's completeness, we followed this procedure: for each period interval and filter, we generated synthetic light curves sampled at the same epochs as real data, with magnitudes randomly drawn from a Gaussian distribution centred around the median magnitude of the light curve. The rms was determined by the median rms value at a given magnitude. We then subjected these synthetic curves to the same analysis as the real data. This approach preserved noise and sampling cadence while breaking phase coherence, simulating the expected output when no intrinsic signal is present. For comparison, we created another set of light curves by injecting a periodic signal into the previously generated synthetic curves. The periodic signal had a random period (within the considered period interval), random amplitude (between 0 and 3 times the median rms at a given magnitude), and random phase (between 0 and 1). We then analyzed these generated curves in the same manner as real data, representing the expected output when an intrinsic signal is present.

Completeness was assessed by determining the ratio of correctly recovered periods. A period was considered correctly recovered when the difference between the recovered period and the injected period was less than 5 times the average error on the recovered period. This yielded completeness values ranging from $\approx$40% to $\approx$10%, depending on the interval period and filter.

Panels (c) and (d) of Fig. 8.4 display FAP and SNR values as functions of the detected period for synthetically generated curves (green dots) and curves with injected periodic signals (blue dots) within the 0.1-1 day period interval and the F814W filter. In this figure, only points where the period in the injected light curves was successfully recovered are shown. Similar plots are obtainable for other period intervals and the F606W filter. As expected, the blue dots, representing light curves with no periodic signal, exhibit FAP and SNR values close to zero, reflecting background noise. Conversely, the green dots, representing light curves with an injected periodic signal, have higher SNR values and lower FAP values. To distinguish the presence of a periodic signal from its absence, we divided the distribution of blue dots into 10-period bins and evaluated the 95th percentile of FAP and SNR values for each bin. These values are depicted as red lines in Fig. 8.4. We employed these defined lines as thresholds to differentiate candidate variables from non-candidate variables in the real light curves (red lines in Fig. 10.2). All data points above both

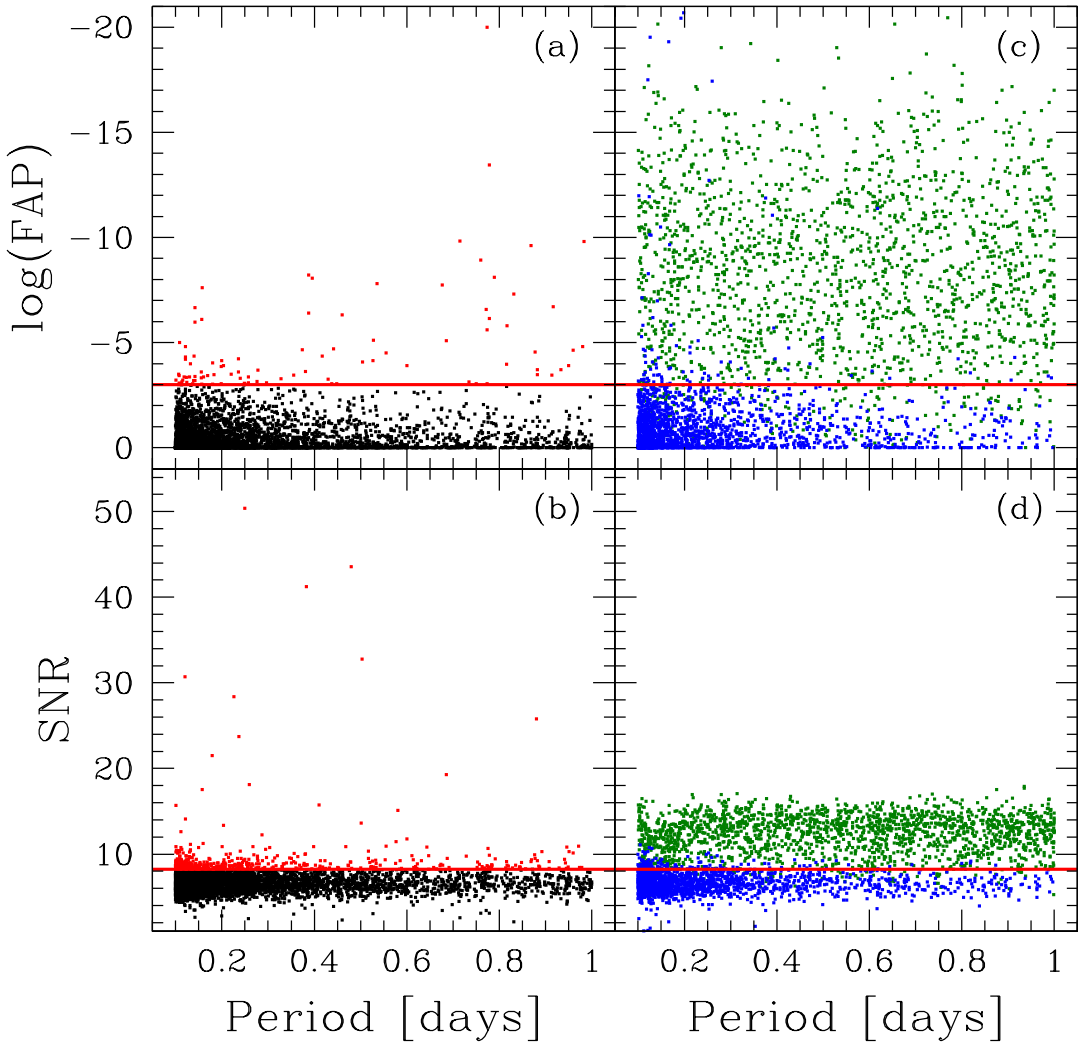

FIGURE 10.2: (a)-(b) FAP and SNR as a function of the detected period within the 0.1-1 day range for the F814W filter. Non-candidate variables are depicted as black dots, while candidate variables are highlighted in red. (c)-(d) Same as (a) and (b) but for the synthetic light curves (blue dots) and the synthetic light curves with an injected period (green dots). In all panels, the red lines serve as demarcations, indicating the thresholds distinguishing between candidate and non-candidate variables. Similar plots can be generated for different period intervals and the F606W filter.

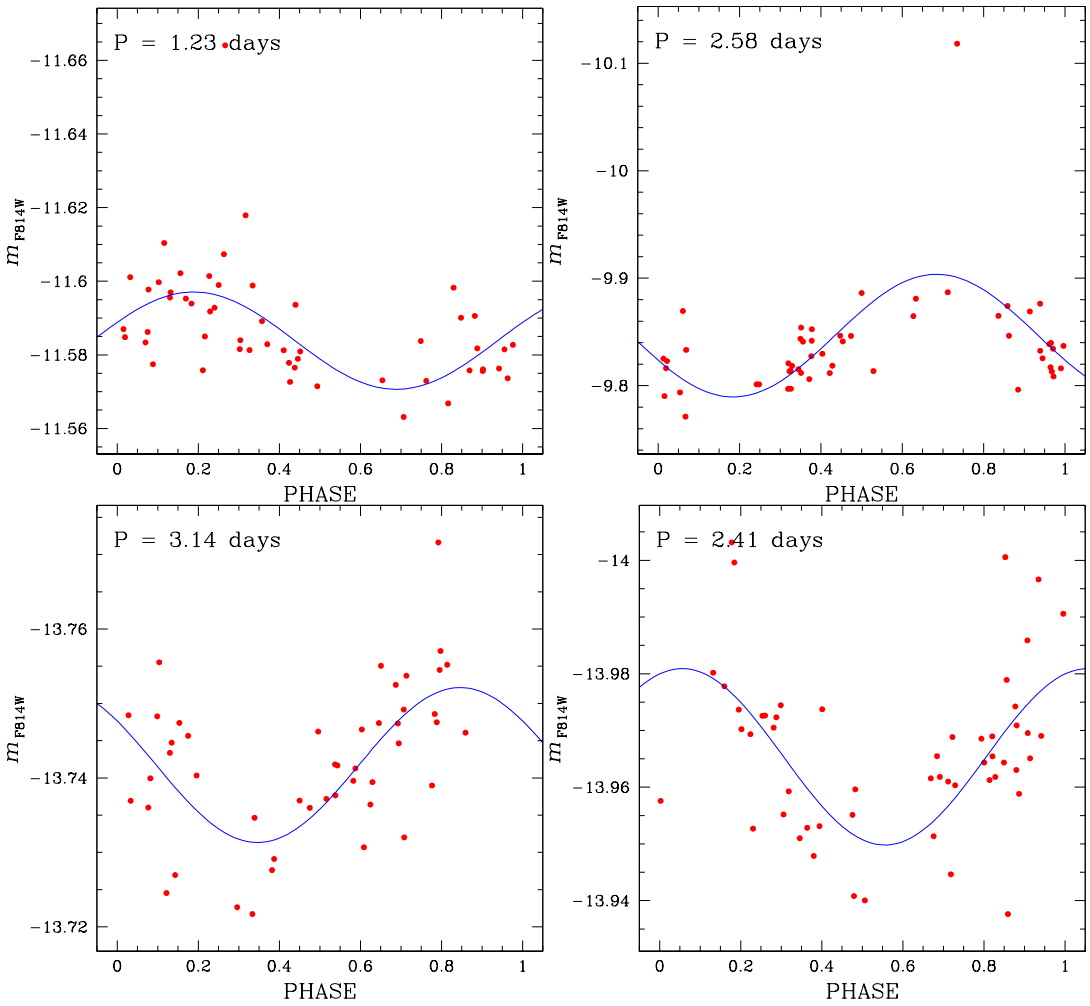

FIGURE 10.3: Light curves of a sample of candidate variables.

red lines in both panels were considered candidate variables and are represented as red dots.

We conducted a visual examination of the candidate variables identified through the method explained above. Fig. 10.3 provides an example of folded light curves (depicted as red data points) along with their respective best-fit sinusoidal functions (represented by a blue line) of four stars from our selected sample of candidate variables. However, it is important to note that the dataset utilized in this study was not specifically tailored for the discovery of variable stars. Consequently, the absence of clearly discernible variable stars in our observations is both expected and justified.

10.5 Transit finding

To identify potential transit within our dataset, we ran the Box-Least Squares (BLS) transit search algorithm (Kovács, Zucker, and Mazeh, 2002) from the `VARTOOLS V1.40` code to the same sample of selected light curves used in the previous section. To select the candidate transit we used a few quality parameters provided by the BLS algorithm, such as the SNR.

We followed a similar procedure to the procedure adopted in the previous section. Our search was divided into various period ranges: 0.1-0.5, 0.5-2, 2-10, 10-85, and 85-730 days, with each set analyzed independently. Panels(a) of Fig. 10.4 display

the SNR values as functions of the detected period for our sample of light curves. It's noteworthy that most stars cluster around SNR $\sim$ 5, indicating non-variable stars, while a few stars exhibit higher SNR values, suggesting they are candidate variables.

We studied the detection efficiency of the BLS algorithm on our sample of light curves by injecting transit signals of planets having radii R_P^{inj} in the synthetic curves generated in the previous section, by using the routine `INJECTTRANSIT` implemented in `VARTOOLS V1.40`. To inject the transit signals in each light curve, we roughly estimated the stellar radius and mass of each star analysed in this work by using their m_{F606W} versus $m_{F606W} - m_{F814W}$ colour-magnitude diagram (CMD). We converted magnitudes into stellar masses and radii via isochrone fitting, for which we used isochrones from the Dartmouth Stellar Evolution Database (Dotter et al., 2008) for the stars along the main sequence and isochrones from Salaris et al. (2022) for the stars along the white dwarf (WD) cooling sequence (CS). We adopted cluster metallicities [Fe/H] from Harris (1996) and Harris (2010) and assumed primordial helium abundance (Y = 0.246). We assumed [α/Fe] = +0.2 (Dotter et al., 2010) and adopted age, distance modulus and reddening that best fit the data.

By following the prescriptions of Nardiello et al. (2021), we considered 3 different cases in which R_P^{inj} randomly vary between a given minimum and maximum: (i) we first injected (super-)Earth-size planets having radii $0.85 \leq R_P^{inj} \leq 3.9 R_{Earth}$; (ii) the second case we considered was for (super-)Neptune planets having radii $3.9 < R_P^{inj} \leq 11.2 R_{Earth} \sim 1 R_J$; finally, we considered giant planets with radii $1.0 < R_P^{inj} \leq 2.5 R_J$. The detection efficiency was determined by determining the ratio of correctly recovered transit periods. A period was considered correctly recovered when the difference between the recovered period and the injected period was less than 5 times the average error on the recovered period. The average completeness of our sample is relatively low, ranging from values of $\sim 5 - 10\%$ for periods of 0.1-0.5 days, $\sim$ 5% for periods of 0.5-2 days, $\sim$ 1% for periods of 2-10 days and $\approx$ 0% for longer periods. These low values are to be conducted to the cadence of our dataset which is not well suited to conduct this kind of investigation. Given the small values of the completeness for periods larger than 2 days, we opted to focus our investigation on only transit periods less than 2 days.

Panels (b) of Fig. 10.4 display the SNR values as functions of the detected period for synthetically generated curves (green dots), for which the period has been recovered, and curves with injected transit signals (blue dots) within the 0.1-5 day period interval and radii $0.85 \leq R_P^{inj} \leq 3.9 R_{Earth}$, in the F814W filter. Similar plots are obtainable for other period intervals, radii and the F606W filter. As can be seen, the blue dots, reflecting background noise, exhibit smaller values with respect to the green dots, and there is a clear separation between the two. To distinguish the presence of transit from its absence, we defined a threshold at SNR=10 to separate candidate transit from non-candidate transit and applied the same selection to real stars (red lines in both panels of Fig. 10.4). All data points above the red line in panel (a) of Fig. 10.4 were considered candidate transits and are represented as red dots.

We performed a detailed visual inspection of both light curves and images for all stars that met the previously outlined criteria. Our examination of the images revealed various features in many candidate stars, such as intersecting spikes or the proximity of very bright stars. both of which could impact significantly the photometry of our candidate star. Based on these observations, it is highly probable that these stars represent false detections. Only one star exhibits characteristics suggesting it could be a valid and reliable candidate. The corresponding light curve

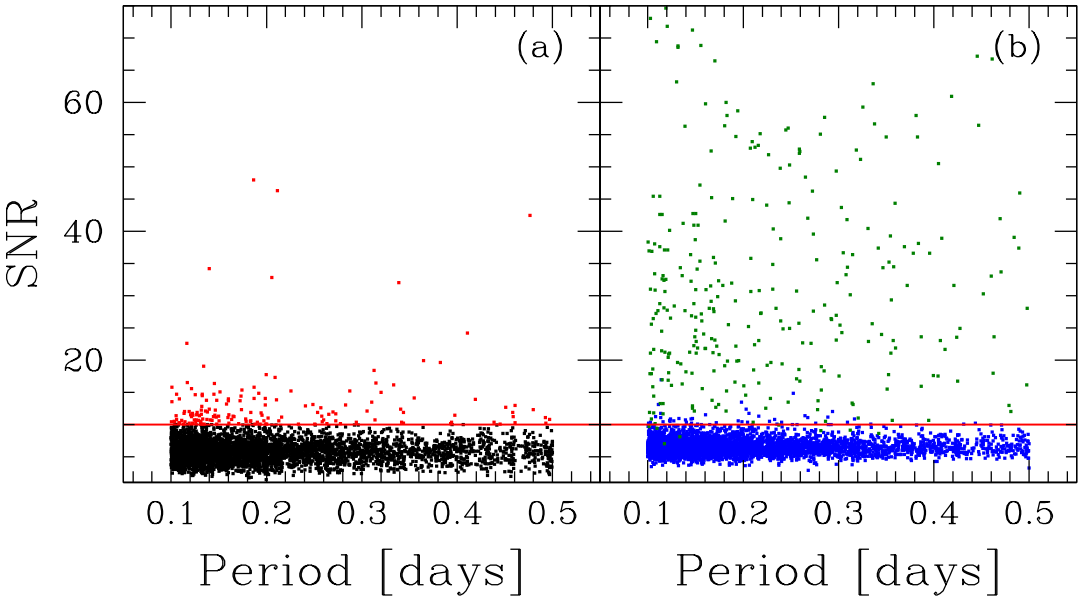

FIGURE 10.4: (a) SNR as a function of the detected period within the 0.1-5 day range for the F814W filter. Black dots represent non-candidate transits while red dots represent candidate transits. (b) Same as panels (a) but for the synthetic light curves (blue dots) and the synthetic light curves with an injected transit (green dots) of a planet having radii $0.85 \leq R_{\rm P}^{\rm inj} \leq 3.9 R_{\rm Earth}$. Similar plots can be generated for different period intervals, radii intervals and for the F606W filter. In both plots, the red lines distinguish between candidate variables and non-candidate variables.

is presented in Fig. 10.5. Panels (a) and (b) depict the star's positions in the $m_{\rm F606W}$ versus $m_{\rm F606W} - m_{\rm F814W}$ CMD and VPD, respectively. To mitigate the risk of false detections due to artefacts, we employed the centroid positions of the candidate star in each image extracted during the light curve extraction as a discriminating factor, as illustrated in panel (c). Most points are centrally located, with a few outliers situated at a distance from the centre. We identified and flagged points outside a defined limit (indicated by a red circle in panel (c)) as poorly measured and suspicious. Panel (d) shows the light curve of the candidate star, with the red line indicating the transit model, while panel (e) displays the difference between the transit model and the observed points. Tag numbers in panel (d) indicate the image number of each point. In panels (c), (d), and (e), points outside the red circle in (c) are displayed in grey, while others are in black.

A mosaic of images centered on the candidate transit is displayed in Fig.,10.6. The number of each image is highlighted in red within each piece of the mosaic.

10.6 Discovery of a supernova in the background

One of the outcomes generated by our reduction software comprises stacked images, in both filters, of the observed field. During our analysis of one such stacked image, we detected a supernova (SN) within a background galaxy in our observed field. This supernova is prominently visible in the initial epoch of our data collection but subsequently becomes undetectable in subsequent epochs. Fig. 10.7 shows the image

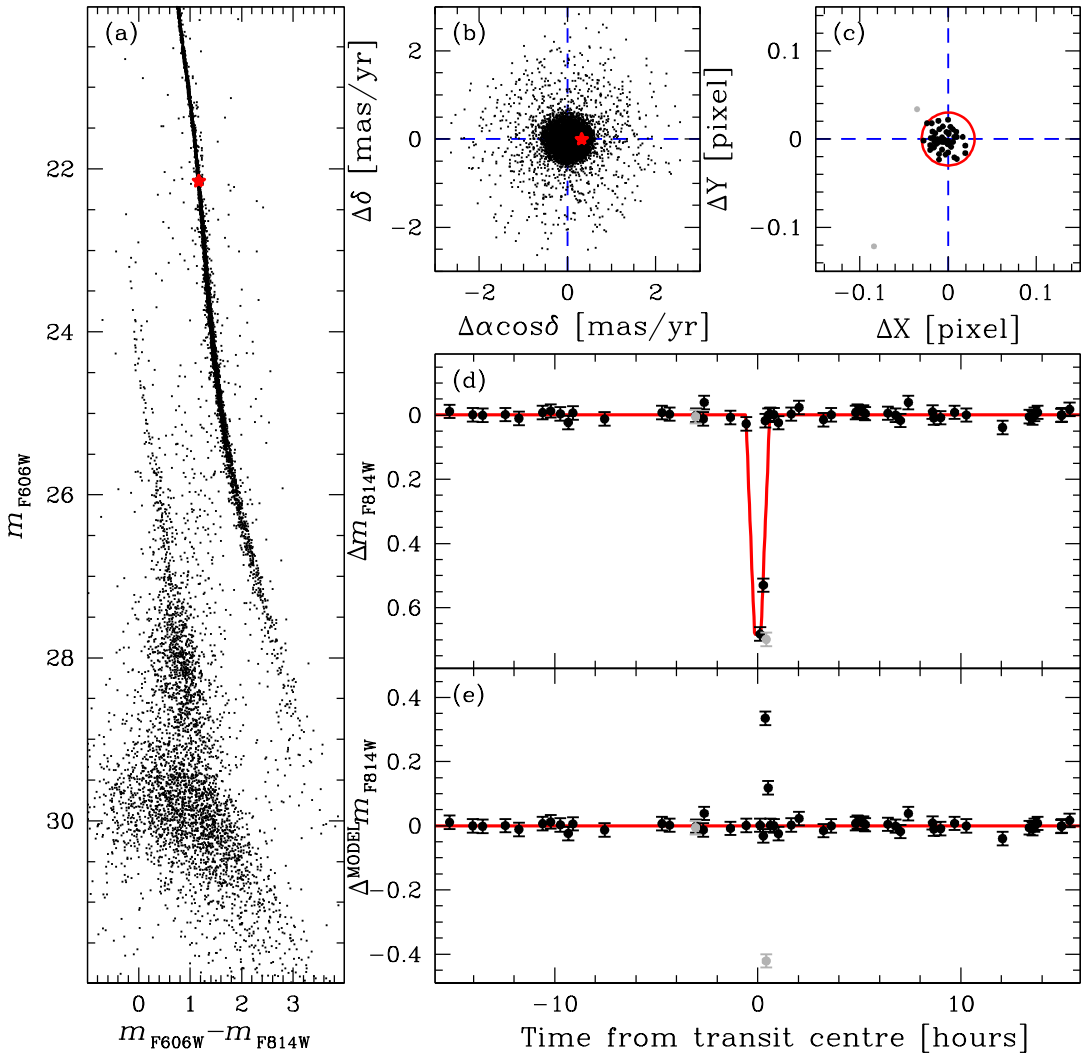

FIGURE 10.5: Overview of a candidate transit. (a)-(b) m_{F606W} versus $m_{F606W} - m_{F814W}$ CMD and VPD, respectively, for stars in our sample (black dots). The candidate star is denoted by a red star in both panels. The blue dashed lines in (b) indicate the VPD centre. (c) In-/out-of-transit difference centroid of the candidate star across all images used for light curve extraction. Points located outside the red circle are flagged as suspicious and excluded from the light curve analysis. (d) Folded light curve of the candidate star, with the transit model represented by the red line. (e) Difference between observed points and the transit model. In panels (c), (d), and (e), points outside the red circle in (c) are displayed in grey, while others are in black.

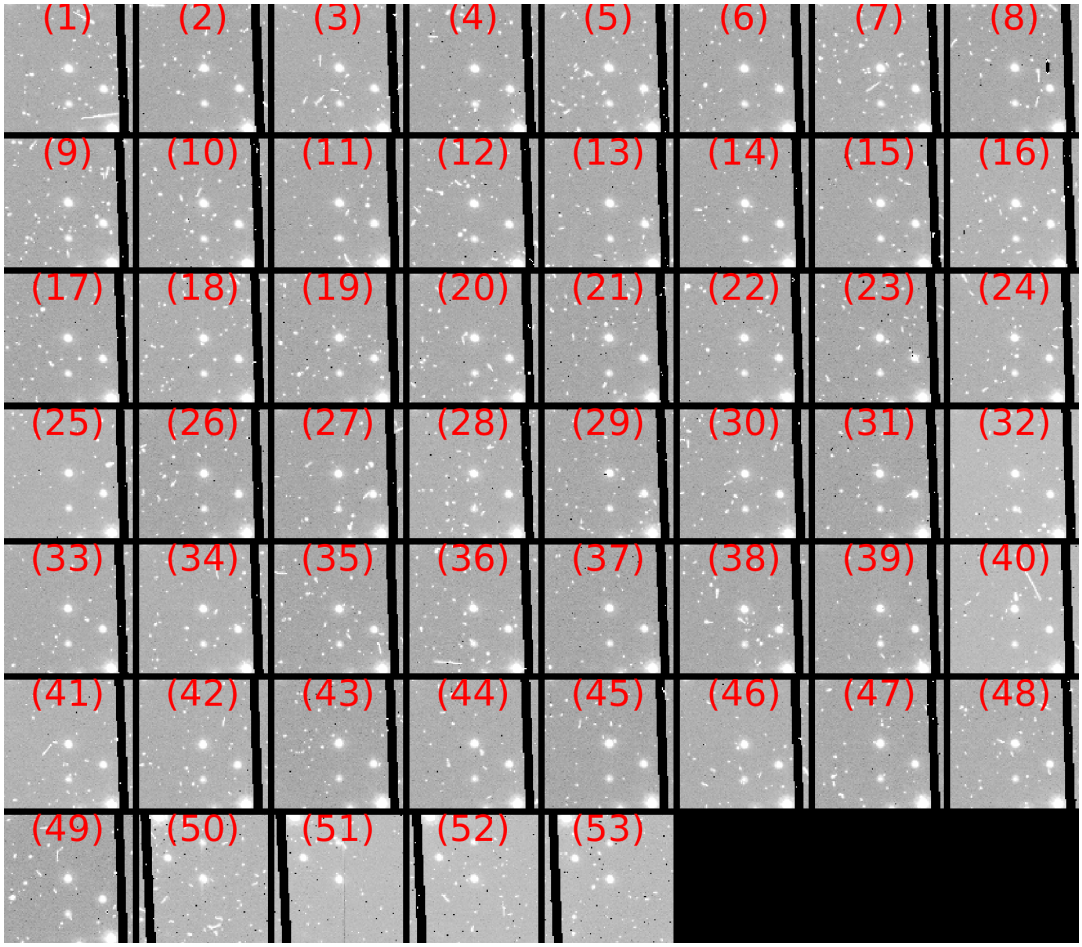

FIGURE 10.6: Mosaic of images centred on the candidate transit star in F814W.

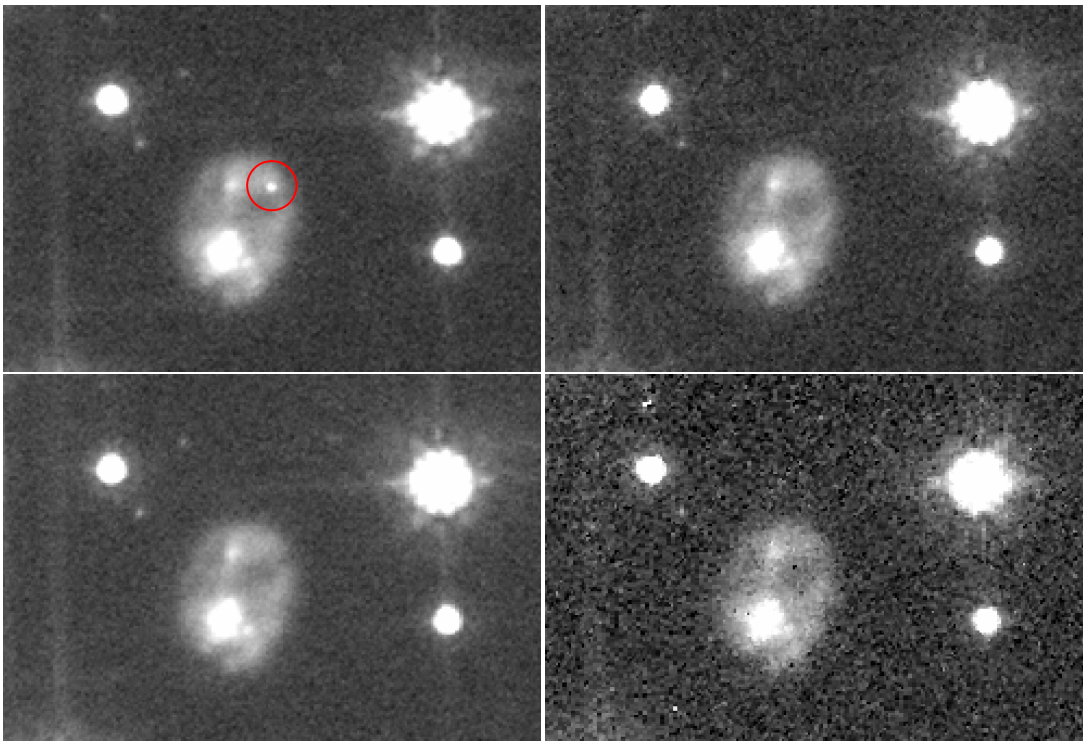

FIGURE 10.7: Stacked images obtained using the F814W filter showing the SN and its host galaxy. In the first epoch (top-left panel), the SN (centred in the red circle) is conspicuously prominent. However, its brightness significantly diminishes in the second epoch (top-right panel), eventually fading away entirely in the third (bottom-left panel) and fourth epochs (bottom-right panel).

of the SN and its host galaxy captured using the F814W filter across four different epochs.

To effectively isolate the SN from its host galaxy, we created a series of images by subtracting the stack from the third epoch (where the SN is not visible, thus serving as our reference) from the images collected during the other epochs. We combined these subtracted images using the same methodology employed to produce the stacked images shown in Fig. 10.7. Fig. 10.8 shows the resultant subtracted stacked images, with the notable observation that the SN is exclusively prominent in the subtracted stacked image from the first epoch. Fig. 10.9 shows the stacked images from the first and third epochs, using the F606W filter, to depict the SN and its host galaxy. Notably, the SN appears less visible in the F606W filter compared to the F814W filter. The right panel of Fig. 10.9 presents images produced by subtracting the stacked image from the third epoch from those captured during the first epoch. For the purpose of analyzing the light curve of this SN, we utilized the images from the first epoch where it is prominently visible, by following the same procedures as described earlier. The magnitude of the SN as a function of time is illustrated in Fig. 10.10, for the F814W (black dots) and F606w (red dots) filters. It is worth noting that the SN's light curve exhibits a subtle, though nearly constant, decrease in luminosity, suggesting that we have likely passed the peak luminosity of the SN.

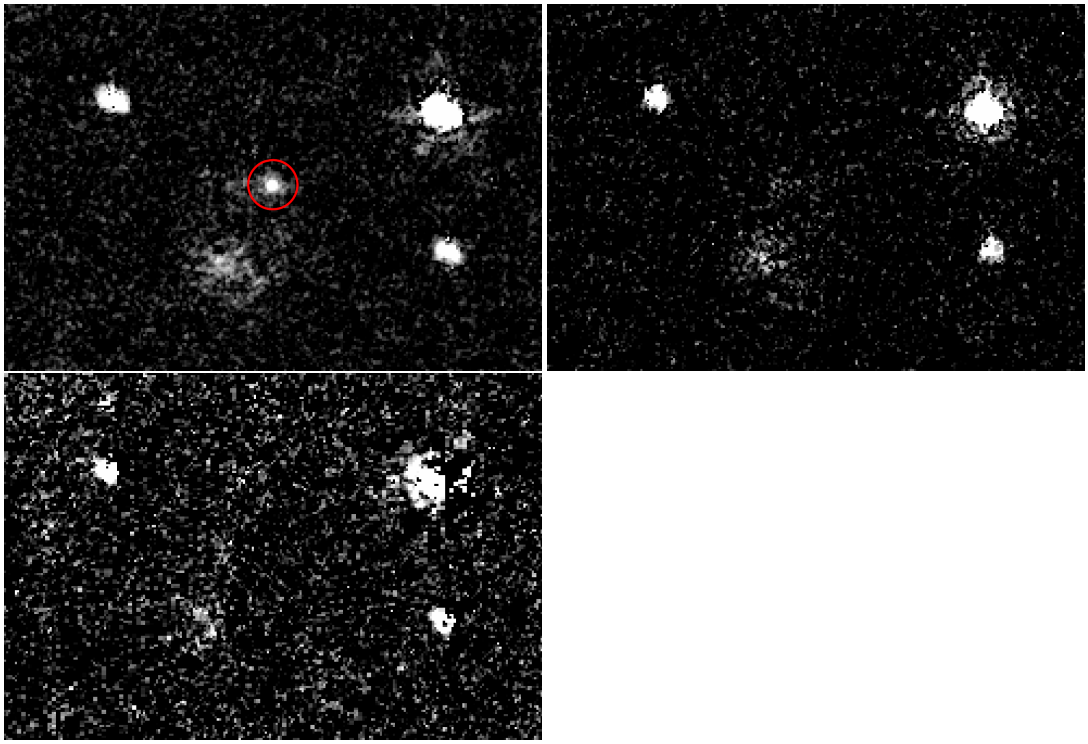

FIGURE 10.8: Composite images generated by subtracting the stack from the third epoch from that of the first (left panel), second (middle panel), and fourth (right panel) epoch. It's worth noting that the SN is distinctly visible only in the left panel.

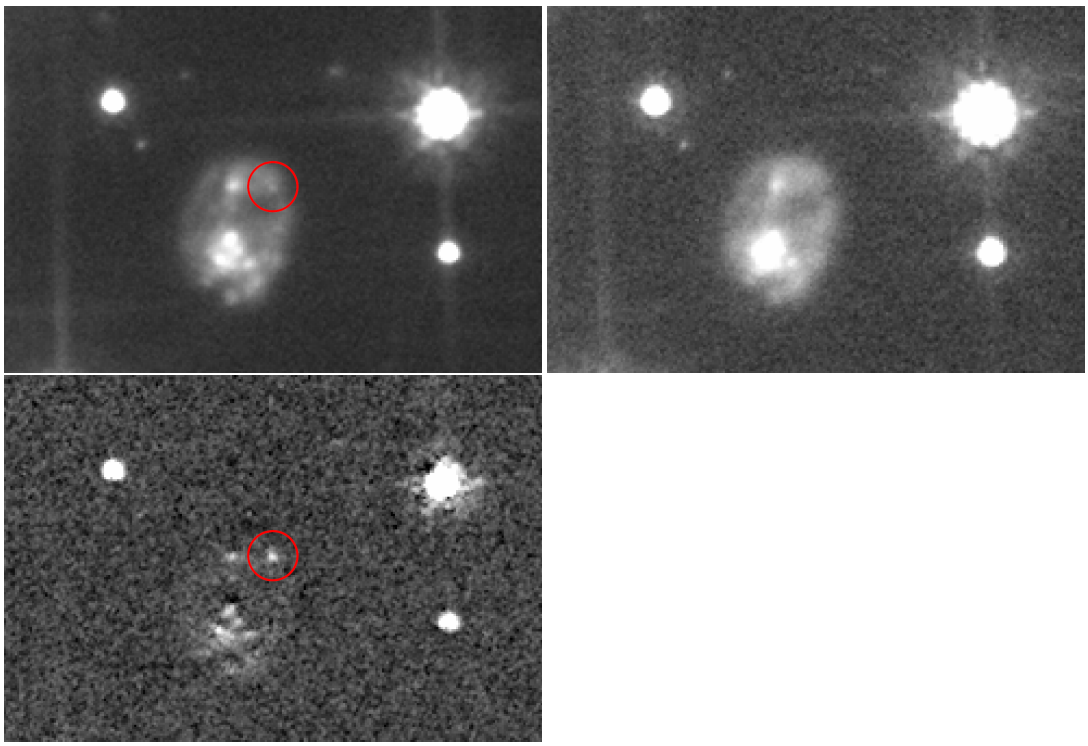

FIGURE 10.9: Similar to Fig. 10.7 and 10.8 but for the F606W filter. The left and middle panels display stacked images from the first and third epochs, respectively. The right panel presents the image resulting from the subtraction of the third epoch stacked image from those of the first epoch.

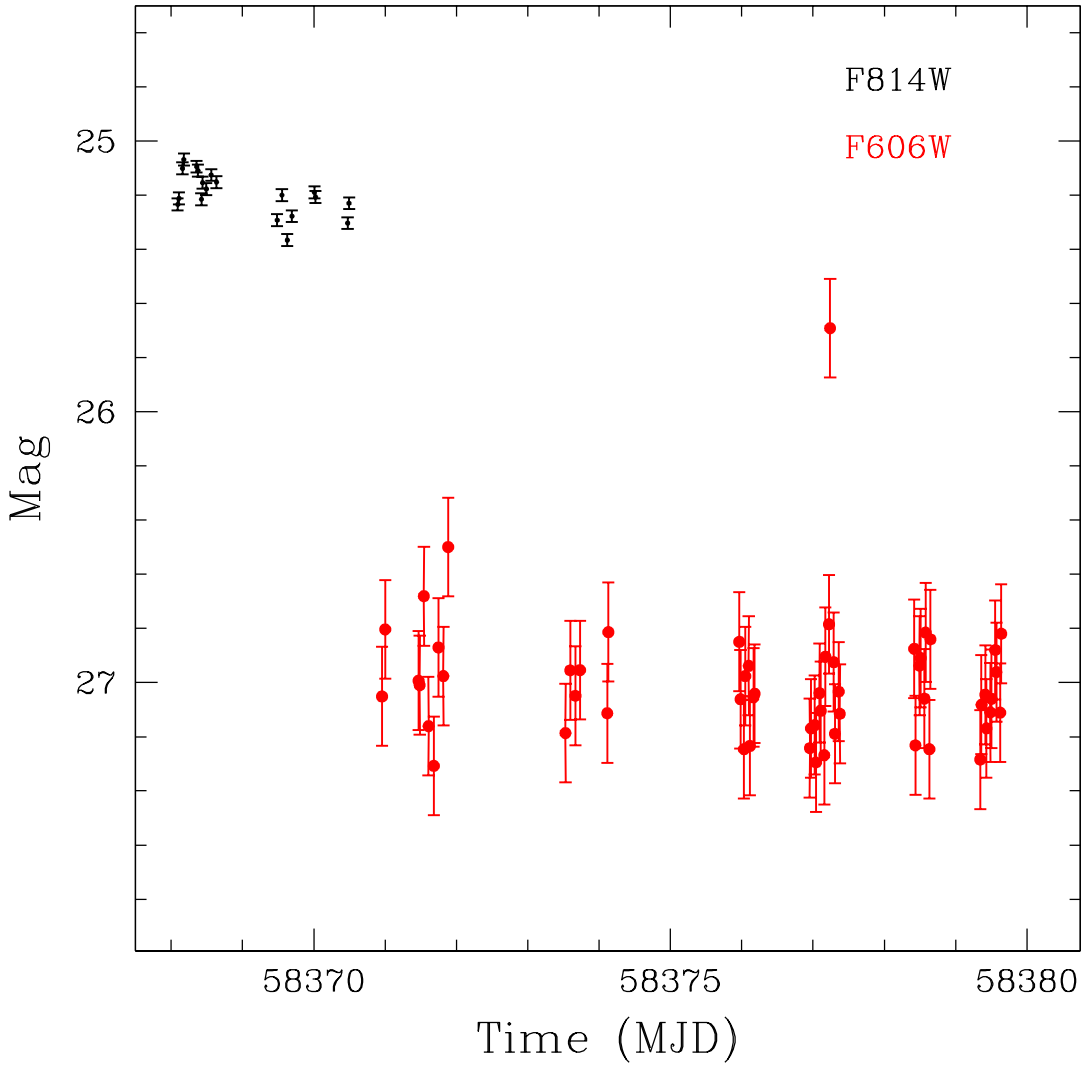

FIGURE 10.10: Light curve of the SN in the first epoch using images from both filters.

10.7 Conclusion

In this chapter, we conducted a search for candidate variables and transits in an external field of NCG 6752 as observed by the *Hubble Space Telescope* (*HST*) across four epochs.

We started by defining an initial input list of stars based on quality parameters from our reduction process and considering the stars' positions in the VPD. To derive the light curves, we followed the method outlined by Nardiello et al. (2015c) using a specifically designed `FORTRAN` software. This software utilized input catalogues, ePSFs, and transformation files from earlier stages, extracting raw fluxes via both PSF and aperture photometry.

We employed a methodology detailed by Nascimbeni et al. (2014) and Nardiello et al. (2015c) to detrend the light curves, involving three distinct correction methods: GZP, LZP, and WZP. A comparison of scatter in light curves after correction using GZP, LZP, and WZP algorithms revealed significant improvement, particularly for bright, non-saturated stars. LZP correction yielded the highest improvements, followed by WZP, while GZP showed comparatively lower enhancement, especially in PSF photometry. Hence, we proceeded to analyze only LZP-corrected light curves in subsequent sections.

We employed the LS periodogram to detect potential variable stars within our dataset of LZP-corrected light curves. This analysis was conducted using the `VARTOOLS V1.40` code. The search was divided into period ranges, with each set analyzed independently. To identify candidates and estimate analysis completeness, we generated synthetic light curves matching real data epochs and subjected them to the same analysis. We also created a set of light curves by injecting periodic signals, assessing completeness by comparing recovered periods with injected ones, yielding completeness values ranging from ≈40% to ≈10%. We used the FAP and SNR parameters to identify candidate variables. We visually examined promising candidates and presented folded light curves and their best-fit sinusoidal functions for the top four candidates.

To detect potential transits within our dataset, we utilized the BLS transit search algorithm from the `VARTOOLS V1.40` code on the same set of selected light curves used in the variable analysis. We evaluated the BLS algorithm's detection efficiency by injecting transit signals into synthetic curves generated based on our previous analysis. We estimated stellar radius and mass using the m_{F606W} versus $m_{\mathrm{F606W}} - m_{\mathrm{F814W}}$ CMD and isochrone fitting. The detection efficiency varied depending on the planet's size and period, with completeness ranging from $\sim 5-10\%$ for shorter periods to $\approx$ 0% for longer ones. We used the SNR parameter to find candidate transit. We visually inspected light curves and images for stars meeting with SNR larger than 10. Most candidate stars exhibited features suggesting they were false detections, except for one potential candidate.

Our search to identify variable stars and transits yielded only a handful of potential candidates, with just one potential transit identified. The limited number of discoveries is not unexpected. It is important to note that the dataset utilized in this study was not specifically tailored for the discovery of variable stars. Consequently, the absence of clearly discernible variable stars in our observations is both expected and justified.

Finally, during our analysis of stacked images obtained from our reduction software, we made an unexpected discovery: SN within a background galaxy in our observed field. This SN was prominently visible in the initial epoch but became undetectable in subsequent epochs. For further analysis of the SN's light curve, we

focused on the images from the first epoch where it was prominently visible. We followed the same procedures as described earlier to analyze the SN's magnitude as a function of time. The light curve of the SN exhibits a subtle, nearly constant decrease in luminosity, suggesting that the peak luminosity of the SN has likely passed.

Chapter 11

Conclusion

In this thesis we made use of data from various instruments, such as the space telescopes Hubble Space Telescope and Gaia, to provide a detailed study of two Galactic globular clusters (GCs)r: NGC 5139 (Omega Centauri, or ω Cen) and NGC 6752. As ancillary science we have also presented a study on the rotation of GCs as a function of the stellar mass and a photometric study of the galactic bulge. All the results presented in this work will be extremely helpful to investigate the origin of Globular clusters and in particular their multiple stellar populations by comparing the observation with theoretical models. Here I provide a summary of my work.

11.1 Summary

While GCs are have always been assumed to be the best representation of simple stellar populations, i.e., composed of stars with the same age and chemical composition, we now know that those objects are characterized by multiple sequences of stars with different chemical compositions. Spectroscopic and photometric studies made in the past 20 years have revealed that substantially all GCs present different stellar populations, with the number of stellar populations ranging from two (as in the case of NGC 6397, Milone et al. 2012a) to more than fifteen (ω Cen, Bellini et al. 2017d).
Multiple populations (mPOPs) in globular clusters (GCs) exhibit distinct patterns. However, mPOPs can be categorized into two main groups: the first generation (1G) and the second generation (2G). 1G stars have a composition similar to the interstellar matter from which they formed, while 2G stars show significant variations in helium and light elements such as carbon, nitrogen, oxygen, sodium, magnesium, aluminum, and silicon among the cluster members.
The occurrence and complexity of mPOPs in GCs increase with the mass of the cluster. More massive GCs have larger variations in helium and a higher fraction of 2G stars. Some clusters exhibit a strong helium enhancement in their 2G populations, while others show smaller differences. The 1G and 2G stars display anti-correlations in their light element abundances, with the 2G stars depleted in carbon and oxygen but enhanced in nitrogen and sodium. Heavy elements, including iron and *s*-process elements, also exhibit internal variations in some massive clusters.
Various scenarios have been proposed to explain the formation of mPOPs in GCs. Some suggest multiple bursts of star formation, where 2G stars form from material polluted by previously evolved, more massive 1G stars. Other scenarios propose coeval formation of mPOPs, with 2G stars resulting from gas accretion onto protostars. Supermassive stars, massive interacting binaries, fast-rotating massive stars, and asymptotic giant branch (AGB) stars may eject materials with compositions similar to 2G stars, but these scenarios face many difficulties.

Understanding the chemical and dynamical properties of mPOPs is crucial for constraining models related to the formation and evolution of GCs in the early Universe. It has implications for various areas such as star formation, the dynamics of stellar systems, the origin of exotic objects like binary black holes emitting gravitational waves, the assembly of the Galactic halo, and the role of GCs in the re-ionization of the early Universe.
Hubble Space Telescope (HST) has been a fundamental instrument in studying multiple stellar populations in globular clusters (GCs). By combining ultraviolet and optical filters, HST is able to efficently separate different stellar populations. In particular, the combination of UVIS/WFC3 F275W, F336W, and F438W filters is commonly used to identify multiple populations in GCs. These filters include molecular bands related to oxygen, nitrogen, carbon, and other elements.
Studies based on HST photometry have shown that plotting F814W magnitude against F275W-F814W color or a pseudo-color ($C_{F275W,F336W,F438W}$) efficiently identifies multiple stellar populations. Two-color diagrams, known as chromosomic maps (ChMs), derived from photometry in different filters sensitive to specific chemical compositions, provide detailed analysis of multiple populations in Milky Way GCs. The most commonly used ChM is the two-pseudo-color diagram ($C_{F275W,F336W,F438W}$) versus F275W-F814W, which maximizes separation between stellar populations along the main sequence and the red giant branch.
The F110W and F160W filters of the WFC3/IR camera on HST are widely used to characterize multiple populations of M-dwarfs in GCs. Indeed, the F160W band is heavily affected by absorption from various molecules that contain oxygen, including H_2O, while F110W photometry is almost unaffected by the oxygen abundance. As a consequence, 2G stars, which are depleted in oxygen with respect to the 1G, have brighter F160W magnitudes and redder F110W−F160W colors than the 1G. M-dwarfs in GCs have shown multiple sequences with different chemical compositions, including helium and light element variations. The presence of these populations in fully-convective M-dwarfs indicates that their chemical composition is not solely a result of stellar evolution.
Different GCs, such as NGC 2808, M4, NGC 6752, and ω Cen, exhibit varying degrees of complexity in their multiple stellar populations, including different oxygen abundances among M-dwarfs. The relative numbers of stars in these populations and their chemical abundances provide constraints for theoretical studies on the formation of multiple populations in GCs.
In this thesis, we particularly focus our attenction on two globular clusters, NGC 6752 and ω Cen. The results presented in this work will serve as an important benchmark for the understanding of the origin of multiple-stellar populations in GCs.

11.1.1 External fields in ω Cen

As a part of our investigation on the multiple stellar populations in ω Cen we presented the reduction of four external field of the cluster observed with HST programs GO-14118 + GO-14662 (PI: Bedin, L. R.) and GO-16247 (P.I. Scalco). For each of the four fields we presented the state-of-the-art catalogue and atlases.
Each field was reduced following the procedure described in Scalco et al. (2021). The first-pass photometry involves measuring the positions and fluxes of stars in each exposure using the `hst1pass` software. This code employs a single pass of source finding without neighbor subtraction, using time-averaged empirical Point Spread Function (PSF) libraries. Perturbations are applied to the PSF to obtain the best spatially variable PSF for each image.

A common reference coordinate system is defined for each field based on a WFC3/UVIS F814W single-exposure catalogue. Linear transformations are derived using bright, unsaturated, and well-measured stars in each filter to transform stellar positions from individual exposures onto the common reference frame. The photometry of preliminary catalogues is zero-pointed to the first long exposure taken in each filter/epoch.
The second-pass photometry used the `KS2` software package. This software simultaneously finds and measures stars in all individual exposures and filters. It employs multiple passes of finding, gradually moving from brighter to fainter stars. The star-finding process involves constructing weighted masks around bright stars, subtracting them, and iteratively identifying fainter stars that meet relaxed search criteria. The photometric measurements are performed using different approaches depending on the brightness and crowding of stars. Finally. the photometry has been zero-pointed into the Vega magnitude system by following the recipe of Bedin et al. (2005a), Bellini et al. (2017b) and Nardiello et al. (2018).
We cross-reference the stars in our catalogue with the stars in the Gaia early Data Release 3 (Gaia eDR3; Gaia Collaboration et al. 2021). We used the proper motions (PMs) calculation technique developed by Bellini et al. (2014) and improved upon by Bellini et al. (2018) and Libralato et al. (2018b) to compute the PMs. This technique follows an iterative procedure involving two main steps. First, it transforms the stellar positions from each exposure into a common reference frame using a six-parameter linear transformation. Second, it fits these transformed positions as a function of the epoch with a least-square straight line. The slope of this line, obtained after multiple outlier-rejection stages, provides a direct measurement of the PM. Systematic errors in the PMs were corrected following the prescription of Bellini et al. (2014) and Bellini et al. (2018) i.e. locally correcting the PM of each star according to the 2.5σ-clipped median value of the closest likely cluster members.
The final catalog comprises several files, including an astrometric file and multiple photometric files. Together with the photometry, we provide other diagnostic parameters such as the RMS of the individual-exposure photometry measurements, the quality-of-fit (QFIT) parameter (that informs about the accuracy of the PSF-fitting during the measurements of the position and the flux of a star), the "o" parameter (defined as the initial ratio of the light within the fitting radius due to nearby neighbors to the light of the star), the RADXS parameter (a shape parameter that measures how much the deviation of the PSF shape is from the predictions; see Bedin et al. 2008). Finally, we report the number of images in which a star was found (N_f), and the number of good measurements of the star used to compute its average position and flux (N_g).
Together with the PMs also provide for a series of PM diagnostic as described in Bellini et al. (2014). We also provide, for each source, an estimate of the membership probability by followint the method based on PMs and described by Balaguer-Núnez, Tian, and Zhao (1998), Bellini et al. (2009) and Nardiello et al. (2018).
Finally, we also release for each of the two fields the atlases, i.e., a view of the field through stacked images, in two versions: sampled at $1\times$- and at $2\times$-supersampled pixels.

11.1.2 Brown dwarfs population in ω Centauri

Brown dwarfs are substellar objects with masses below the threshold required for sustaining hydrogen fusion, ($\sim 0.08 M_\odot$). Unlike stars, brown dwarfs do not reach

energy equilibrium and instead cool down gradually, causing a decrease in their effective temperature and luminosity. These objects have low effective temperatures, which enable complex molecular chemistry and the formation of various cloud compositions in their atmospheres. Due to their sensitivity to elemental abundances in their spectra and their continuous cooling process, brown dwarfs offer an important tool for studying the evolutionary history of the Milky Way.
However, observing brown dwarfs is challenging due to their faint luminosity and low temperatures, limiting their studies to the closest and youngest objects in our galaxy. As a result, research on brown dwarfs has primarily focused on isolated sources with near-solar metallicities and chemical compositions that do not fully represent the early evolutionary stages of our galaxy, lacking secondary indicators of their origins and physical properties.
To address these limitations, the study presented in Gerasimov et al. (2022b) is focus to brown dwarfs in globular clusters. Globular clusters consist of tens of thousands of coeval members with similar ages and chemical compositions that can be inferred photometrically from the color-magnitude diagram (CMD). Importantly, unlike field stars in the solar neighborhood, globular cluster members exhibit chemical abundances characteristic of the early metal-poor phases of Milky Way formation. Therefore, globular clusters offer unique opportunities for studying brown dwarfs with non-solar abundances and old ages, allowing for independent constraints on various parameters through the analysis of the overall cluster population.
In the context of globular clusters, a recent study by Gennaro et al. (2022) introduced new models for analyzing the interior and atmosphere of brown dwarfs in Omega Centauri, which is the most massive globular cluster in the Milky Way. By comparing synthetic color-magnitude diagrams generated from these models with new observations obtained by the Hubble Space Telescope (HST) of the low-mass main sequence in Omega Centauri, Gennaro et al. (2022) were able to determine more accurate physical properties of the cluster and account for interstellar reddening. Moreover, these models were extended to the substellar regime, allowing predictions of the expected colors, magnitudes, and densities of brown dwarfs in Omega Centauri, even at extremely low effective temperatures of approximately 1000 K.
We presented the data reduction and analysis of one external field of Omega Centauri. The data presented were used to calculate new interior and atmosphere models and determine the physical properties of the cluster members to make predictions for brown dwarfs in the cluster (see Gerasimov et al. 2022b).
The observations were conducted in a field located approximately 3 half-light radii ($\sim$ 7 arcminutes) southwest of the cluster center. This field represents the deepest observed region of ω Cen for which both optical and near-infrared HST data are available.
The data reduction process followed a procedure similar to previous studies on other ω Cen fields. Point spread function (PSF) fitting software called KS2 was used to extract positions, fluxes, and quality parameters of the sources. The photometric zero-point was determined using the approach described by Bedin et al. (2005). The data were filtered based on quality parameters such as photometric error, correlation with the model PSF, and flux outside the core compared to the PSF prediction.
Relative proper motions of the sources in the observed region were used to separate field stars from cluster members. Proper motions were obtained by comparing the positions of stars measured in the earliest and latest HST programs, providing a baseline of up to 15 years. Systematic photometric offsets and differential reddening corrections were applied to the photometry in each filter.
To measure the luminosity function (LF), the completeness of sources as a function

of color and magnitude was quantified. Artificial stars with random positions were generated, and their magnitudes were distributed along the approximate ridgeline of the main sequence in various color-magnitude spaces. The artificial stars were introduced into each exposure and measured individually to avoid overcrowding. A star was considered recovered if the difference between the generated and measured positions was within a certain threshold, and the magnitude difference was below a certain limit. The photometric errors and completeness for each half-magnitude bin were computed.
The study provides an astro-photometric catalog of measured sources in the HST imaged fields, including right ascensions, declinations, VEGAMAG magnitudes in different filters before zero-pointing and differential reddening corrections. The catalog also contains flags to differentiate unsaturated and saturated stars and a proper motion-based flag to distinguish between field stars and cluster members.
Additionally, there are four additional catalog files that contain differential reddening-corrected and zero-pointed color-magnitude diagrams in different observational planes. Each file corresponds to a specific color-color or color-magnitude combination.
Finally, for each filter, separate files are provided that contain estimated photometric errors and completeness values computed in each half-magnitude bin.

11.1.3 The white dwarf sequence of NGC 6752

NGC 6752 is a nearby Galactic globular cluster (GC), located approximately at 4 kpc from the Sun. It has been extensively studied due to its proximity and low interstellar reddening. NGC 6752 was one of the first GCs to reveal the presence of white dwarfs (WDs) even before the Hubble Space Telescope (HST) era. The cluster's distance has been determined using WD observations with HST, and a preliminary WD luminosity function (LF) has been obtained, reaching the end of the cooling sequence.
One distinctive feature of NGC 6752 is its unusual horizontal branch (HB) morphology, characterized by a lack of RR Lyrae stars and an extended blue region. This peculiar HB morphology is attributed to the presence of multiple populations with different initial helium abundances. Recent observations with the Wide Field Camera 3 (WFC3) onboard of HST have shown that this blue morphology affects the bright part of the WD cooling sequence.
This study is part of a series of pubblications based on the analysis of data from HST multi-cycle large program focused on NGC 6752. Previous publications in this series have reported the discovery of a dwarf spheroidal galaxy, the characterization of the multiple stellar populations and the reaching of the end of the hydrogen envelope WD cooling sequence in NGC 6752.
In this particular study, data from all epochs were utilized to improve the definition of the cluster's WD cooling sequence and its LF. The aim was to investigate the agreement between WD and main sequence turn-off ages, the impact of multiple populations on the faint end of the cooling sequence, and the influence of helium envelope WDs on the LF. Different treatments of electron conduction opacities were also tested, as they play a crucial role in modeling WD envelopes and affect the cooling times of the models.
The study reveals that the shape of the cluster's WD LF closely resembles that of the metal-rich and redder horizontal branch globular cluster M4. The observed LF follows the theoretical predictions for hydrogen envelope WD models calculated using electron conduction opacities. The LF peak occurs at an approximate magnitude of $m_{F606W} \simeq 29.3 \pm 0.1$, consistent with previous studies. The magnitude of the peak

corresponds to WD isochrones with ages between 12.7 and 13.5 Gyr, in agreement with the cluster's age estimated from the main sequence turn-off (TO) and subgiant branch.
The analysis confirms that variations in the initial-final mass relation (IFMR) and progenitor mass function do not significantly affect the predicted magnitude of the LF peak and cutoff. The influence of multiple populations within the cluster on the WD LF is found to be negligible for magnitudes larger than approximately $m_{F606W} \sim 27.3$.
The study also identifies a potential discrepancy between theoretical models and empirical star counts in the magnitude range between $m_{F606W=28.1}$ and 28.9. However, different choices of the IFMR can reduce this discrepancy to a level below 2σ. A similar discrepancy is observed in the analysis of the WD LF in M4.
Previous photometry by Renzini & Buzzoni (1986) indicates the presence of a small fraction (around 10%) of WDs in the cluster with helium envelopes. However, it is determined that this fraction of helium envelope objects has a minimal impact on the shape of the LF and is potentially responsible for the color spread at the faint end of the observed CS.
Finally, we highlighted that hydrogen envelope models calculated using electron conduction opacities from Blouin et al. (2018) yield WD ages that conflict with the TO age, as they are lower than expected.

11.1.4 Relation between globular clusters' internal rotation and stellar masses

Using data from the Gaia telescope, we provided the observational evidence of a relation between globular clusters' internal rotation and stellar masses.
Contrary to the traditional picture of globular clusters (GCs) as isotropic and non-rotating systems, recent observational studies have demonstrated the presence of internal rotation in many GCs. Theoretical investigations have explored the dynamics of rotating clusters and the influence of various dynamical processes on their internal rotation. One prediction from these studies is that as GCs evolve, the internal rotational velocity becomes dependent on stellar mass, with more massive stars rotating faster around the cluster's center than lower-mass stars.
We examined the theoretical predictions obtained by Livernois et al. (2022) and used data from the Gaia Data Release 3 catalog to analyze the rotational properties of three GCs (47 Tuc, ω Cen, and M 5) with the aim of validate the predicted relationship between internal rotation and stellar mass.
For each of the clusters analyzed in our study, we retrieved all sources from the *Gaia* DR3 archive that are located within a given radius from the nominal cluster center and pass a series of astrometric and photometric parameters. We than used a procedure based on stellar PMs, π and positions in the colour-magnitude diagram (CMD) to select a sample of cluster members.
Our study reveals that 47 Tuc and M 5 exhibit a correlation between rotation and stellar mass, where the rotational velocity increases with increasing stellar mass. This provides the first observational evidence supporting the predicted rotation-mass relation. In the case of ω Cen, the observed trend between rotational velocity and mass can be attributed to the combined effects of mass segregation and radial variation in rotational velocity. ω Cen is a relatively young cluster, and the absence of a significant $\mu_{\rm TAN}$-mass trend (or the presence of a weaker trend undetected in our analysis) is consistent with the expected development of this relationship during a cluster's long-term evolution.

Due to the limited sensitivity of Gaia, our analysis focuses only on nearby and rapidly rotating GCs, ensuring an adequate mass range and rotation signal to accurately characterize the $\mu_{\rm TAN}/\sigma_0$-mass slope. Future observational investigations can expand the mass range to lower masses than currently available and extend observations to the tidal radius. These efforts would significantly enhance the exploration of the $\mu_{\rm TAN}/\sigma_0$-mass relationship, allowing for a comprehensive investigation of this trend and exploration of its dependence on other dynamical properties and evolutionary history of clusters.

11.1.5 The kinematics of NGC 6752

N-body simulations suggest that the distinct kinematic properties observed in the 1G and 2G stars within globular clusters are a result of their different initial conditions. By studying the internal prpper motions of these multiple stellar populations, including rotation, velocity dispersion, and radial profile of anisotropy, we can gain insights into the formation and evolution of globular clusters and distinguish between different formation scenarios. The Gaia mission has provided high-precision proper motion data, revitalizing the investigation of internal kinematic properties of globular clusters. However, due to Gaia's limitations in crowded and faint environments, these studies have focused only on bright stars outside the inner regions. The high resolving power of the Hubble Space Telescope (HST) offers a powerful tool to study the proper motions of stars in crowded and faint regions inaccessible to Gaia. NGC 6752 is a cluster known to host different stellar populations, as indicated by its complex color-magnitude diagrams derived from optical and ultraviolet photometry. The cluster contains three distinct stellar populations referred to as A, B, and C. Population A consists of stars with a primordial helium abundance (Y $\approx$ 0.246), while populations B and C have enhanced helium abundances of approximately 0.01 and 0.03, respectively. These stellar populations have been identified and separated across the entire color-magnitude diagram, spanning from the red giant branch to the main sequence and M-dwarf regime. Spectroscopic studies have revealed that population C stars exhibit enhancements in nitrogen, aluminum, silicon, and sodium, and depletions in carbon, oxygen, and magnesium compared to population A. Population B stars exhibit intermediate chemical compositions.
In this chapter, a comprehensive kinematic study of the globular cluster NGC 6752 was presented. The study used data from various sources including Hubble Space Telescope (HST), Gaia, and ESO/VLT-Keck. The kinematics of NGC 6752 were investigated along with the luminosity function (LF) and mass function (MF) of the cluster.
The absolute proper motion and parallax of NGC 6752 were estimated using data from the Gaia space telescope. A sample of well-measured sources was selected based on specific criteria, and a membership criterion combining position and proper motions was applied to identify cluster members. The color-magnitude diagram was then used to further refine the selection. The absolute proper motion and parallax were determined by evaluating the median values of proper motion and parallax in magnitude bins. The obtained values were in agreement with previous studies.
The absolute radial velocity of NGC 6752 was estimated using the radial velocities catalog of the cluster. Outliers were initially removed based on membership probability, and the color-magnitude diagram was used for further refinement. The median values of line-of-sight velocity in magnitude bins were used to determine the absolute radial velocity of the cluster. The obtained value was consistent with previous studies.

Membership probabilities were derived using a method based on proper motions and parallax. The absolute proper motion and parallax of the cluster were then re-estimated using the selected sample of stars. The new values obtained were similar to the previous estimates.
Structural parameters of the cluster, such as ellipticity and position angle, were determined using data from Gaia. The 2D binned kernel density of selected stars was calculated, and elliptical contours were fitted to the density contours. The weighted means of ellipticity and position angle were evaluated for each bin. The final estimate of the ellipticity and position angle of the cluster were obtained by evaluating the weighted mean of the bins.
The rotation of NGC 6752 in the plane of the sky was studied using a specific method presented in Scalco et al. (2023). A sample of stars with reliable photometry and astrometry was selected, and a procedure based on stellar proper motions, parallax, and positions in the color-magnitude diagram was applied to identify probable cluster members. The rotation profile obtained in this study was consistent with previous findings.
The velocity dispersion profile of NGC 6752 was examined using a combination of Gaia and HST data. The profile was analyzed both globally and for the three different stellar populations within the cluster. The chromosomic map technique was employed to separate the populations in the main sequence and study their velocity dispersion profiles separately. No significant differences in kinematics were found among the three populations.
The equipartition profile of NGC 6752 was investigated using the provided proper motion catalog. The sample was divided into radial bins, and the velocity dispersion of stars in each mass bin was calculated. The equipartition value was evaluated in each radial bin by fitting the velocity dispersion as a function of stellar mass. The obtained equipartition profile agreed with previous studies.
The kinematics of M-dwarf stars in NGC 6752 were studied using an infrared HST field. The three stellar populations were identified in the lower part of the color-magnitude diagram, and their velocity dispersion profiles were examined. No significant differences in kinematics were observed among the three populations, similar to the main sequence and RGB stars.
The LOS velocity catalog was used to study the velocity dispersion in the line-of-sight direction. The central dispersion value was determined and found to be consistent with previous studies.
Finally, the HST catalogue was utilized to investigate the mass function (MF) of NGC 6752, both overall and for its three distinct stellar populations, at various radial distances from the cluster center. To determine the completeness level of the analyzed sample, artificial stars (ASs) were employed. Initially, the mass function of the central field of NGC 6752 was examined without differentiating between the three stellar populations. The resulting total MF is shown in Figure 7.33. Next, the $m_{F275W} - m_{F814W}$ vs. $C_{F275W,F336W,F438W}$ chromosomal map was employed to separate the three stellar populations on the main sequence (MS) and study their respective mass functions. Notably, population A exhibited a considerably steeper mass function slope, $\alpha_A = 2.338 \pm 0.269$, compared to populations B and C ($\alpha_B = 1.805 \pm 0.267$ and $\alpha_C = 0.91 \pm 0.206$, respectively). This procedure was then repeated for fields F1 and F2. Multiple stellar populations are identifiable in the low MS for field F1 and in the mass function for field F2. Since these two fields are situated at similar radial distances from the cluster center, their information was combined to obtain an extended mass function for the three stellar populations. Figure 7.39 illustrates the mass function for the three stellar populations identified in fields F1 and F2.

The lower mass range ($0.1<M/M_{\odot}<0.5$) corresponds to field F1, while the upper range ($0.55<M/M_{\odot}<0.75$) is provided by field F2. Figures 7.40 and 7.41 display the mass functions for the three stellar populations separately in fields F1 and F2, along with their respective slope represented by a dashed line. The slope values of the mass function for the three stellar populations in field F1 are $\alpha_A = -0.523 \pm 0.098$, $\alpha_B = -0.327 \pm 0.164$, and $\alpha_C = -0.404 \pm 0.027$, respectively. In field F2, the corresponding slope values are $\alpha_A = -2.504 \pm 3.177$, $\alpha_B = -1.763 \pm 1.435$, and $\alpha_C = -2.835 \pm 1.423$.

11.1.6 Hα emitters in ω Cen

Globular clusters (GCs) are highly efficient environments for the formation of exotic objects such as low-mass X-ray binaries (LMXBs), cataclysmic variables (CVs), millisecond pulsars (MSPs), and blue straggler stars (BSSs). These objects originate from binary systems and interactions within the dense cores of GCs, providing insights into the dynamical evolution of these clusters.
Following a method proposed by De Marchi et al. (2010) to identify stars with Hα excess emission in star-forming regions, we conducted an Hα survey of main-sequence stars in ω Cen using archival Hubble Space Telescope observations. The method combines broad-band F435W and F625W photometry with narrow-band Hα imaging to measure the EW(Hα) of stars exhibiting Hα excess emission. This enables the identification and characterization of accreting stars in this GC. To assess the photometric continuum, we used the $m_{\rm F435W} - m_{\rm F625W}$ vs. $m_{\rm F625W} - m_{\rm F658N}$ color-color diagram. Subsequently, we identified sources that displayed a $m_{\rm F625W} - m_{\rm F658N}$ color difference from the photometric continuum, which was at least five times larger than the intrinsic photometric error of the source. Among these, we determined the Hα emission width pEW and selected sources with a pEW>20. In total, we identified 38 sources meeting these criteria.

11.1.7 Variability in NGC 6752

The detection of periodic variables in GCs offers crucial insights into stellar evolution, binary systems, and the dynamic processes within these dense stellar environments. Additionally, identifying planetary transits within GCs enhances our understanding of exoplanetary systems in extreme conditions.
NGC 6752, being one of the closest GCs and hosting diverse stellar populations, presents an ideal target for photometric studies.
We conducted a thorough search for candidate variable stars and transits within an external field of NGC 6752 observed by the Hubble Space Telescope across four epochs.
We initiated the search by selecting stars based on quality parameters and positional information. Light curves were then derived using a dedicated FORTRAN software following a method outlined in previous studies. Three correction methods (GZP, LZP, and WZP) were applied to detrend the light curves, with LZP correction showing the most significant improvement, particularly for bright, non-saturated stars. Hence, only LZP-corrected light curves were analyzed further.
Variable stars were identified using the LS periodogram, with the analysis divided into period ranges. Synthetic light curves were generated to estimate analysis completeness, revealing values ranging from approximately 40% to 10%. Candidate variables were identified using FAP and SNR parameters, and the top candidates were visually examined, with folded light curves presented for the top four.

Transit searches were conducted using the BLS algorithm, with transit signal injection used to assess detection efficiency. Despite a thorough search, only one potential transit candidate was identified, highlighting the challenges in detecting such phenomena in this dataset.
Unexpectedly, a supernova within a background galaxy was discovered during the analysis of stacked images. Although the SN was visible in the initial epoch, it became undetectable in subsequent epochs. The SN's light curve showed a subtle, nearly constant decrease in luminosity, indicating that its peak luminosity had likely passed.
Overall, while the search yielded only a handful of potential candidates, including one potential transit and the discovery of a supernova, the limited number of discoveries was expected given the dataset's design and purpose.

Bibliography

Allard, F., D. Homeier, and B. Freytag (Dec. 2011). "Model Atmospheres From Very Low Mass Stars to Brown Dwarfs". In: *Cool Stars 16*. Vol. 448, p. 91. DOI: 10.48550/arXiv.1011.5405. arXiv: 1011.5405 [astro-ph.SR].

— (June 2012). "Models of very-low-mass stars, brown dwarfs and exoplanets". In: *Philosophical Transactions of the Royal Society of London Series A* 370.1968, pp. 2765–2777. DOI: 10.1098/rsta.2011.0269. arXiv: 1112.3591 [astro-ph.SR].

Allard, France and Peter H. Hauschildt (May 1995). "Model Atmospheres for M (Sub)Dwarf Stars. I. The Base Model Grid". In: *ApJ* 445, p. 433. DOI: 10.1086/175708. arXiv: astro-ph/9601150 [astro-ph].

Althaus, Leandro G. et al. (Apr. 2015). "White dwarf evolutionary sequences for low-metallicity progenitors: The impact of third dredge-up". In: *A&A* 576, A9, A9. DOI: 10.1051/0004-6361/201424922. arXiv: 1502.03882 [astro-ph.SR].

Anderson, J. (Jan. 2006). "Empirical PSFs and Distortion in the WFC Camera". In: *The 2005 HST Calibration Workshop: Hubble After the Transition to Two-Gyro Mode*. Ed. by Anton M. Koekemoer, Paul Goudfrooij, and Linda Lou Dressel, p. 11.

Anderson, J. and L. R. Bedin (Sept. 2017). "The M 4 Core Project with HST - V. Characterizing the PSFs of WFC3/UVIS by focus". In: *MNRAS* 470.1, pp. 948–963. DOI: 10.1093/mnras/stx1278. arXiv: 1706.00386 [astro-ph.IM].

Anderson, Jay (1997). In: *Ph.D. thesis, Univ. California, Berkeley*.

Anderson, Jay (Mar. 2016). *Empirical Models for the WFC3/IR PSF*. Instrument Science Report WFC3 2016-12, 42 pages.

Anderson, Jay and Luigi R. Bedin (Sept. 2010). "An Empirical Pixel-Based Correction for Imperfect CTE. I. HST's Advanced Camera for Surveys". In: *PASP* 122.895, p. 1035. DOI: 10.1086/656399. arXiv: 1007.3987 [astro-ph.IM].

Anderson, Jay and Ivan R. King (Oct. 2000). "Toward High-Precision Astrometry with WFPC2. I. Deriving an Accurate Point-Spread Function". In: *PASP* 112.776, pp. 1360–1382. DOI: 10.1086/316632. arXiv: astro-ph/0006325 [astro-ph].

— (Feb. 2006). *PSFs, Photometry, and Astronomy for the ACS/WFC*. Instrument Science Report ACS 2006-01, 34 pages.

Anderson, Jay et al. (June 2008). "The Acs Survey of Globular Clusters. V. Generating a Comprehensive Star Catalog for each Cluster". In: *AJ* 135.6, pp. 2055–2073. DOI: 10.1088/0004-6256/135/6/2055. arXiv: 0804.2025 [astro-ph].

Andrievsky, S. M. et al. (Apr. 2008). "NLTE determination of the aluminium abundance in a homogeneous sample of extremely metal-poor stars". In: *A&A* 481.2, pp. 481–487. DOI: 10.1051/0004-6361:20078837. arXiv: 0802.1519 [astro-ph].

Balaguer-Núnez, L., K. P. Tian, and J. L. Zhao (Dec. 1998). "Determination of proper motions and membership of the open clusters NGC 1817 and NGC 1807". In: *A&AS* 133, pp. 387–394. DOI: 10.1051/aas:1998324.

Bastian, N. and C. Lardo (Sept. 2018a). "Multiple Stellar Populations in Globular Clusters". In: *ARAA* 56, pp. 83–136. DOI: 10.1146/annurev-astro-081817-051839. arXiv: 1712.01286 [astro-ph.SR].

Bastian, N. et al. (Dec. 2013). "Early disc accretion as the origin of abundance anomalies in globular clusters". In: *MNRAS* 436.3, pp. 2398–2411. DOI: 10.1093/mnras/stt1745. arXiv: 1309.3566 [astro-ph.GA].

Bastian, Nate and Carmela Lardo (Sept. 2018b). "Multiple Stellar Populations in Globular Clusters". In: *ARA&A* 56, pp. 83–136. DOI: 10.1146/annurev-astro-081817-051839. arXiv: 1712.01286 [astro-ph.SR].

Baumgardt, H. and M. Hilker (Aug. 2018). "A catalogue of masses, structural parameters, and velocity dispersion profiles of 112 Milky Way globular clusters". In: *MNRAS* 478.2, pp. 1520–1557. DOI: 10.1093/mnras/sty1057. arXiv: 1804.08359 [astro-ph.GA].

Baumgardt, H. and E. Vasiliev (Aug. 2021). "Accurate distances to Galactic globular clusters through a combination of Gaia EDR3, HST, and literature data". In: *MNRAS* 505.4, pp. 5957–5977. DOI: 10.1093/mnras/stab1474. arXiv: 2105.09526 [astro-ph.GA].

Baumgardt, H. et al. (Feb. 2019). "Mean proper motions, space orbits, and velocity dispersion profiles of Galactic globular clusters derived from Gaia DR2 data". In: *MNRAS* 482.4, pp. 5138–5155. DOI: 10.1093/mnras/sty2997. arXiv: 1811.01507 [astro-ph.GA].

Baumgardt, Holger and Junichiro Makino (Mar. 2003). "Dynamical evolution of star clusters in tidal fields". In: *MNRAS* 340.1, pp. 227–246. DOI: 10.1046/j.1365-8711.2003.06286.x. arXiv: astro-ph/0211471 [astro-ph].

Beccari, G. et al. (Jan. 2014). "Hα photometry of low-mass stars in 47 Tucanae: chromospheric activity and exotica". In: *MNRAS* 437.3, pp. 2621–2631. DOI: 10.1093/mnras/stt2074. arXiv: 1310.6673 [astro-ph.SR].

Bedin, L. R. and C. Fontanive (Dec. 2018). "Extending Gaia DR2 with HST narrow-field astrometry: the WISE J154151.65-225024.9 test case". In: *MNRAS* 481.4, pp. 5339–5349. DOI: 10.1093/mnras/sty2626. arXiv: 1809.09181 [astro-ph.SR].

Bedin, L. R. et al. (Sept. 2019a). "The HST large programme on NGC 6752 - III. Detection of the peak of the white dwarf luminosity function". In: *MNRAS* 488.3, pp. 3857–3865. DOI: 10.1093/mnras/stz1968. arXiv: 1907.06300 [astro-ph.SR].

— (Sept. 2019b). "The HST large programme on NGC 6752 - III. Detection of the peak of the white dwarf luminosity function". In: *MNRAS* 488.3, pp. 3857–3865. DOI: 10.1093/mnras/stz1968. arXiv: 1907.06300 [astro-ph.SR].

Bedin, L. R. et al. (Mar. 2019c). "The HST Large Programme on NGC 6752. I. Serendipitous discovery of a dwarf Galaxy in background". In: *MNRAS* 484.1, pp. L54–L58. DOI: 10.1093/mnrasl/slz004. arXiv: 1902.00271 [astro-ph.GA].

Bedin, L. R. et al. (Jan. 2023). "The HST large programme on NGC 6752 - IV. The White Dwarf sequence". In: *MNRAS* 518.3, pp. 3722–3736. DOI: 10.1093/mnras/stac3219. arXiv: 2211.02391 [astro-ph.SR].

Bedin, Luigi R. et al. (Apr. 2004). "ω Centauri: The Population Puzzle Goes Deeper". In: *ApJl* 605.2, pp. L125–L128. DOI: 10.1086/420847. arXiv: astro-ph/0403112 [astro-ph].

Bedin, Luigi R. et al. (Mar. 2005a). "Transforming observational data and theoretical isochrones into the ACS/WFC Vega-mag system". In: *MNRAS* 357.3, pp. 1038–1048. DOI: 10.1111/j.1365-2966.2005.08735.x. arXiv: astro-ph/0412328 [astro-ph].

— (Mar. 2005b). "Transforming observational data and theoretical isochrones into the ACS/WFC Vega-mag system". In: *MNRAS* 357.3, pp. 1038–1048. DOI: 10.1111/j.1365-2966.2005.08735.x. arXiv: astro-ph/0412328 [astro-ph].

Bedin, Luigi R. et al. (May 2008). "Reaching the End of the White Dwarf Cooling Sequence in NGC 6791". In: *ApJ* 678.2, pp. 1279–1291. DOI: 10.1086/529370. arXiv: 0801.1346 [astro-ph].

Bedin, Luigi R. et al. (June 2009a). "The End of the White Dwarf Cooling Sequence in M4: An Efficient Approach". In: *ApJ* 697.2, pp. 965–979. DOI: 10.1088/0004-637X/697/2/965. arXiv: 0903.2839 [astro-ph.GA].

— (June 2009b). "The End of the White Dwarf Cooling Sequence in M4: An Efficient Approach". In: *ApJ* 697.2, pp. 965–979. DOI: 10.1088/0004-637X/697/2/965. arXiv: 0903.2839 [astro-ph.GA].

Bekki, K. and K. C. Freeman (Dec. 2003). "Formation of ω Centauri from an ancient nucleated dwarf galaxy in the young Galactic disc". In: *MNRAS* 346.2, pp. L11–L15. DOI: 10.1046/j.1365-2966.2003.07275.x. arXiv: astro-ph/0310348 [astro-ph].

Bekki, Kenji (Nov. 2010). "Rotation and Multiple Stellar Population in Globular Clusters". In: *ApJl* 724.1, pp. L99–L103. DOI: 10.1088/2041-8205/724/1/L99. arXiv: 1010.3841 [astro-ph.CO].

— (Apr. 2011). "Secondary star formation within massive star clusters: origin of multiple stellar populations in globular clusters". In: *MNRAS* 412.4, pp. 2241–2259. DOI: 10.1111/j.1365-2966.2010.18047.x. arXiv: 1011.5956 [astro-ph.GA].

Bekki, Kenji and John E. Norris (Feb. 2006). "The Origin of the Double Main Sequence in ω Centauri: Helium Enrichment due to Gas Fueling from Its Ancient Host Galaxy?" In: *ApJl* 637.2, pp. L109–L112. DOI: 10.1086/500413. arXiv: astro-ph/0512385 [astro-ph].

Bekki, Kenji and Takuji Tsujimoto (Dec. 2019). "A New Formation Model for ω Centauri: A Complex Interplay of Astrophysical Processes". In: *ApJ* 886.2, 121, p. 121. DOI: 10.3847/1538-4357/ab464d. arXiv: 1909.11295 [astro-ph.GA].

Bellini, A., J. Anderson, and L. R. Bedin (May 2011). "Astrometry and Photometry with HST WFC3. II. Improved Geometric-Distortion Corrections for 10 Filters of the UVIS Channel". In: *PASP* 123.903, p. 622. DOI: 10.1086/659878. arXiv: 1102.5218 [astro-ph.IM].

Bellini, A. et al. (Jan. 2009). "Ground-based CCD astrometry with wide field imagers. III. WFI@2.2m proper-motion catalog of the globular cluster ω Centauri". In: *A&A* 493.3, pp. 959–978. DOI: 10.1051/0004-6361:200810880. arXiv: 0810.1914 [astro-ph].

Bellini, A. et al. (Aug. 2010). "New Hubble Space Telescope WFC3/UVIS Observations Augment the Stellar-population Complexity of ω Centauri". In: *AJ* 140.2, pp. 631–641. DOI: 10.1088/0004-6256/140/2/631. arXiv: 1006.4157 [astro-ph.GA].

Bellini, A. et al. (June 2013). "A Double White-dwarf Cooling Sequence in ω Centauri". In: *ApJl* 769.2, L32, p. L32. DOI: 10.1088/2041-8205/769/2/L32. arXiv: 1305.0265 [astro-ph.GA].

Bellini, A. et al. (Dec. 2014). "Hubble Space Telescope Proper Motion (HSTPROMO) Catalogs of Galactic Globular Clusters. I. Sample Selection, Data Reduction, and NGC 7078 Results". In: *ApJ* 797.2, 115, p. 115. DOI: 10.1088/0004-637X/797/2/115. arXiv: 1410.5820 [astro-ph.SR].

Bellini, A. et al. (Sept. 2015). "The Hubble Space Telescope UV Legacy Survey of Galactic Globular Clusters: The Internal Kinematics of the Multiple Stellar Populations in NGC 2808". In: *ApJl* 810.1, L13, p. L13. DOI: 10.1088/2041-8205/810/1/L13. arXiv: 1508.01804 [astro-ph.GA].

Bellini, A. et al. (Aug. 2017a). "Hubble Space Telescope Proper Motion (HSTPROMO) Catalogs of Galactic Globular Clusters. V. The Rapid Rotation of 47 Tuc Traced

and Modeled in Three Dimensions". In: *ApJ* 844.2, 167, p. 167. DOI: 10.3847/1538-4357/aa7c5f. arXiv: 1706.08974 [astro-ph.GA].

Bellini, A. et al. (June 2017b). "The State-of-the-art HST Astro-photometric Analysis of the Core of ω Centauri. I. The Catalog". In: *ApJ* 842.1, 6, p. 6. DOI: 10.3847/1538-4357/aa7059. arXiv: 1704.07425 [astro-ph.SR].

Bellini, A. et al. (June 2017c). "The State-of-the-art HST Astro-photometric Analysis of the Core of ω Centauri. II. Differential-reddening Map". In: *ApJ* 842.1, 7, p. 7. DOI: 10.3847/1538-4357/aa705f. arXiv: 1705.01951 [astro-ph.SR].

Bellini, A. et al. (Aug. 2017d). "The State-of-the-art HST Astro-photometric Analysis of the Core of ω Centauri. III. The Main Sequence's Multiple Populations Galore". In: *ApJ* 844.2, 164, p. 164. DOI: 10.3847/1538-4357/aa7b7e. arXiv: 1706.07063 [astro-ph.SR].

Bellini, Andrea, Jay Anderson, and Norman A. Grogin (Nov. 2018a). *Focus-diverse, empirical PSF models for the ACS/WFC*. Instrument Science Report ACS 2018-8.

— (Nov. 2018b). *Focus-diverse, empirical PSF models for the ACS/WFC*. Instrument Science Report ACS 2018-8.

Bellini, Andrea et al. (Jan. 2018). "The HST Large Programme on ω Centauri. II. Internal Kinematics". In: *ApJ* 853.1, 86, p. 86. DOI: 10.3847/1538-4357/aaa3ec. arXiv: 1801.01504 [astro-ph.GA].

Bergeron, P. et al. (May 2019). "On the Measurement of Fundamental Parameters of White Dwarfs in the Gaia Era". In: *ApJ* 876.1, 67, p. 67. DOI: 10.3847/1538-4357/ab153a. arXiv: 1904.02022 [astro-ph.SR].

Bessell, M. S., F. Castelli, and B. Plez (May 1998). "Model atmospheres broad-band colors, bolometric corrections and temperature calibrations for O - M stars". In: *A&A* 333, pp. 231–250.

Bianchini, P. et al. (Dec. 2018). "The internal rotation of globular clusters revealed by Gaia DR2". In: *MNRAS* 481.2, pp. 2125–2139. DOI: 10.1093/mnras/sty2365. arXiv: 1806.02580 [astro-ph.GA].

Blouin, Simon et al. (Aug. 2020). "New Conductive Opacities for White Dwarf Envelopes". In: *ApJ* 899.1, 46, p. 46. DOI: 10.3847/1538-4357/ab9e75. arXiv: 2006.16390 [astro-ph.SR].

Brown, Jeffery A. and George Wallerstein (July 1993). "High Resolution CCD Spectra of Stars in Globular Clusters. VIII. The Self -Enrichment History of Omega Centauri". In: *AJ* 106, p. 133. DOI: 10.1086/116623.

Cadelano, Mario et al. (Oct. 2023). "JWST uncovers helium and water abundance variations in the bulge globular cluster NGC 6440". In: *arXiv e-prints*, arXiv:2310.13056, arXiv:2310.13056. DOI: 10.48550/arXiv.2310.13056. arXiv: 2310.13056 [astro-ph.GA].

Caffau, E. et al. (May 2010). "The solar photospheric abundance of carbon. Analysis of atomic carbon lines with the CO5BOLD solar model". In: *A&A* 514, A92, A92. DOI: 10.1051/0004-6361/200912227. arXiv: 1002.2628 [astro-ph.SR].

Calura, F. et al. (Nov. 2019). "Formation of second-generation stars in globular clusters". In: *MNRAS* 489.3, pp. 3269–3284. DOI: 10.1093/mnras/stz2055. arXiv: 1906.09137 [astro-ph.SR].

Carretta, E. et al. (Oct. 2009). "Na-O anticorrelation and HB. VII. The chemical composition of first and second-generation stars in 15 globular clusters from GIRAFFE spectra". In: *A&A* 505.1, pp. 117–138. DOI: 10.1051/0004-6361/200912096. arXiv: 0909.2938 [astro-ph.GA].

Casagrande, L. and Don A. VandenBerg (Sept. 2018). "On the use of Gaia magnitudes and new tables of bolometric corrections". In: *MNRAS* 479.1, pp. L102–L107. DOI: 10.1093/mnrasl/sly104. arXiv: 1806.01953 [astro-ph.SR].

Cassisi, S. et al. (June 2007a). "Updated Electron-Conduction Opacities: The Impact on Low-Mass Stellar Models". In: *ApJ* 661.2, pp. 1094–1104. DOI: 10.1086/516819. arXiv: astro-ph/0703011 [astro-ph].

— (June 2007b). "Updated Electron-Conduction Opacities: The Impact on Low-Mass Stellar Models". In: *ApJ* 661.2, pp. 1094–1104. DOI: 10.1086/516819. arXiv: astro-ph/0703011 [astro-ph].

Cassisi, Santi and Maurizio Salaris (July 2020). "Multiple populations in massive star clusters under the magnifying glass of photometry: theory and tools". In: *AAPR* 28.1, 5, p. 5. DOI: 10.1007/s00159-020-00127-y. arXiv: 2006.13172 [astro-ph.SR].

Cassisi, Santi et al. (Nov. 2014). "On the missing second generation AGB stars in NGC 6752". In: *A&A* 571, A81, A81. DOI: 10.1051/0004-6361/201424540. arXiv: 1410.3599 [astro-ph.SR].

Cassisi, Santi et al. (Oct. 2021). "Electron conduction opacities at the transition between moderate and strong degeneracy: Uncertainties and impacts on stellar models". In: *A&A* 654, A149, A149. DOI: 10.1051/0004-6361/202141425. arXiv: 2108.11653 [astro-ph.SR].

Chen, J. et al. (June 2022). "Slowly cooling white dwarfs in NGC 6752". In: *arXiv e-prints*, arXiv:2206.10039, arXiv:2206.10039. arXiv: 2206.10039 [astro-ph.SR].

Chen, Jianxing et al. (Sept. 2021). "Slowly cooling white dwarfs in M13 from stable hydrogen burning". In: *Nature Astronomy* 5, pp. 1170–1177. DOI: 10.1038/s41550-021-01445-6. arXiv: 2109.02306 [astro-ph.GA].

Cool, Adrienne M. et al. (Feb. 2013). "HST/ACS Imaging of Omega Centauri: Optical Counterparts of Chandra X-Ray Sources". In: *ApJ* 763.2, 126, p. 126. DOI: 10.1088/0004-637X/763/2/126. arXiv: 1212.2646 [astro-ph.SR].

Cordero, M. J. et al. (Jan. 2014). "Detailed Abundances for a Large Sample of Giant Stars in the Globular Cluster 47 Tucanae (NGC 104)". In: *ApJ* 780.1, 94, p. 94. DOI: 10.1088/0004-637X/780/1/94. arXiv: 1311.1541 [astro-ph.SR].

Cordero, M. J. et al. (Mar. 2017). "Differences in the rotational properties of multiple stellar populations in M13: a faster rotation for the 'extreme' chemical subpopulation". In: *MNRAS* 465.3, pp. 3515–3535. DOI: 10.1093/mnras/stw2812. arXiv: 1610.09374 [astro-ph.GA].

Cordoni, G. et al. (Aug. 2020a). "Gaia and Hubble Unveil the Kinematics of Stellar Populations in the Type II Globular Clusters ω Centauri and M22". In: *ApJ* 898.2, 147, p. 147. DOI: 10.3847/1538-4357/aba04b. arXiv: 2006.16355 [astro-ph.SR].

Cordoni, G. et al. (Jan. 2020b). "Three-component Kinematics of Multiple Stellar Populations in Globular Clusters with Gaia and VLT". In: *ApJ* 889.1, 18, p. 18. DOI: 10.3847/1538-4357/ab5aee. arXiv: 1905.09908 [astro-ph.SR].

Cummings, Jeffrey D. et al. (Oct. 2018). "The White Dwarf Initial-Final Mass Relation for Progenitor Stars from 0.85 to 7.5 $M_\odot$". In: *ApJ* 866.1, 21, p. 21. DOI: 10.3847/1538-4357/aadfd6. arXiv: 1809.01673 [astro-ph.SR].

Dalessandro, E. et al. (Sept. 2018). "The Unexpected Kinematics of Multiple Populations in NGC 6362: Do Binaries Play a Role?" In: *ApJ* 864.1, 33, p. 33. DOI: 10.3847/1538-4357/aad4b3. arXiv: 1807.07918 [astro-ph.GA].

Dalessandro, Emanuele et al. (Sept. 2021). "3D core kinematics of NGC 6362: central rotation in a dynamically evolved globular cluster". In: *MNRAS* 506.1, pp. 813–823. DOI: 10.1093/mnras/stab1257. arXiv: 2105.02246 [astro-ph.GA].

D'Antona, F. et al. (May 2016). "A single model for the variety of multiple-population formation(s) in globular clusters: a temporal sequence". In: *MNRAS* 458.2, pp. 2122–2139. DOI: 10.1093/mnras/stw387. arXiv: 1602.05412 [astro-ph.GA].

D'Antona, Francesca and Vittoria Caloi (Aug. 2004). "The Early Evolution of Globular Clusters: The Case of NGC 2808". In: *ApJ* 611.2, pp. 871–880. DOI: 10.1086/422334. arXiv: astro-ph/0405016 [astro-ph].

Davis, D. Saul et al. (Nov. 2009). "The Spectral Types of White Dwarfs in Messier 4". In: *ApJ* 705.1, pp. 398–407. DOI: 10.1088/0004-637X/705/1/398. arXiv: 0909.2254 [astro-ph.SR].

De Marchi, Guido, Nino Panagia, and Martino Romaniello (May 2010). "Photometric Determination of the Mass Accretion Rates of Pre-main-sequence Stars. I. Method and Application to the SN 1987A Field". In: *ApJ* 715.1, pp. 1–17. DOI: 10.1088/0004-637X/715/1/1. arXiv: 1002.4864 [astro-ph.GA].

de Mink, S. E. et al. (Nov. 2009). "Massive binaries as the source of abundance anomalies in globular clusters". In: *A&A* 507.1, pp. L1–L4. DOI: 10.1051/0004-6361/200913205. arXiv: 0910.1086 [astro-ph.SR].

Decressin, T., C. Charbonnel, and G. Meynet (Dec. 2007). "Origin of the abundance patterns in Galactic globular clusters: constraints on dynamical and chemical properties of globular clusters". In: *A&A* 475.3, pp. 859–873. DOI: 10.1051/0004-6361:20078425. arXiv: 0709.4160 [astro-ph].

Decressin, T. et al. (Mar. 2007). "Fast rotating massive stars and the origin of the abundance patterns in galactic globular clusters". In: *A&A* 464.3, pp. 1029–1044. DOI: 10.1051/0004-6361:20066013. arXiv: astro-ph/0611379 [astro-ph].

Denissenkov, P. A. and F. D. A. Hartwick (Jan. 2014). "Supermassive stars as a source of abundance anomalies of proton-capture elements in globular clusters". In: *MNRAS* 437.1, pp. L21–L25. DOI: 10.1093/mnrasl/slt133. arXiv: 1305.5975 [astro-ph.SR].

D'Ercole, Annibale et al. (Dec. 2008a). "Formation and dynamical evolution of multiple stellar generations in globular clusters". In: *MNRAS* 391.2, pp. 825–843. DOI: 10.1111/j.1365-2966.2008.13915.x. arXiv: 0809.1438 [astro-ph].

— (Dec. 2008b). "Formation and dynamical evolution of multiple stellar generations in globular clusters". In: *MNRAS* 391.2, pp. 825–843. DOI: 10.1111/j.1365-2966.2008.13915.x. arXiv: 0809.1438 [astro-ph].

D'Ercole, Annibale et al. (Sept. 2010). "Abundance patterns of multiple populations in globular clusters: a chemical evolution model based on yields from AGB ejecta". In: *MNRAS* 407.2, pp. 854–869. DOI: 10.1111/j.1365-2966.2010.16996.x. arXiv: 1005.1892 [astro-ph.GA].

Dondoglio, E. et al. (Jan. 2021). "Multiple Stellar Populations along the Red Horizontal Branch and Red Clump of Globular Clusters". In: *ApJ* 906.2, 76, p. 76. DOI: 10.3847/1538-4357/abc882. arXiv: 2011.03283 [astro-ph.GA].

Dondoglio, E. et al. (Mar. 2022). "Survey of Multiple Populations in Globular Clusters among Very-low-mass Stars". In: *ApJ* 927.2, 207, p. 207. DOI: 10.3847/1538-4357/ac5046. arXiv: 2201.08631 [astro-ph.SR].

Dotter, Aaron et al. (Sept. 2008). "The Dartmouth Stellar Evolution Database". In: *ApJs* 178.1, pp. 89–101. DOI: 10.1086/589654. arXiv: 0804.4473 [astro-ph].

Dotter, Aaron et al. (Jan. 2010). "The ACS Survey of Galactic Globular Clusters. IX. Horizontal Branch Morphology and the Second Parameter Phenomenon". In: *ApJ* 708.1, pp. 698–716. DOI: 10.1088/0004-637X/708/1/698. arXiv: 0911.2469 [astro-ph.SR].

Dotter, Aaron et al. (Jan. 2015). "Stellar models of multiple populations in globular clusters - I. The main sequence of NGC 6752". In: *MNRAS* 446.2, pp. 1641–1656. DOI: 10.1093/mnras/stu2170. arXiv: 1410.4570 [astro-ph.SR].

Einsel, Christian and Rainer Spurzem (Jan. 1999). "Dynamical evolution of rotating stellar systems - I. Pre-collapse, equal-mass system". In: *MNRAS* 302.1, pp. 81–95. DOI: 10.1046/j.1365-8711.1999.02083.x.

Ernst, A. et al. (May 2007). "N-body models of rotating globular clusters". In: *MNRAS* 377.2, pp. 465–479. DOI: 10.1111/j.1365-2966.2007.11602.x. arXiv: astro-ph/0702206 [astro-ph].

Fabricius, C. et al. (May 2021). "Gaia Early Data Release 3. Catalogue validation". In: *A&A* 649, A5, A5. DOI: 10.1051/0004-6361/202039834. arXiv: 2012.06242 [astro-ph.GA].

Ferraro, F. R. et al. (June 2018). "MIKiS: The Multi-instrument Kinematic Survey of Galactic Globular Clusters. I. Velocity Dispersion Profiles and Rotation Signals of 11 Globular Clusters". In: *ApJ* 860.1, 50, p. 50. DOI: 10.3847/1538-4357/aabe2f. arXiv: 1804.08618 [astro-ph.GA].

Gaia Collaboration et al. (Nov. 2016). "Gaia Data Release 1. Summary of the astrometric, photometric, and survey properties". In: *A&A* 595, A2, A2. DOI: 10.1051/0004-6361/201629512. arXiv: 1609.04172 [astro-ph.IM].

Gaia Collaboration et al. (Aug. 2018). "Gaia Data Release 2. Kinematics of globular clusters and dwarf galaxies around the Milky Way". In: *A&A* 616, A12, A12. DOI: 10.1051/0004-6361/201832698. arXiv: 1804.09381 [astro-ph.GA].

Gaia Collaboration et al. (May 2021). "Gaia Early Data Release 3. Summary of the contents and survey properties". In: *A&A* 649, A1, A1. DOI: 10.1051/0004-6361/202039657. arXiv: 2012.01533 [astro-ph.GA].

Gaia Collaboration et al. (June 2023). "Gaia Data Release 3. Summary of the content and survey properties". In: *A&A* 674, A1, A1. DOI: 10.1051/0004-6361/202243940. arXiv: 2208.00211 [astro-ph.GA].

Gerasimov, Roman et al. (Dec. 2020). "A New Grid of Model Atmospheres for Metal-poor Ultracool Brown Dwarfs". In: *Research Notes of the American Astronomical Society* 4.12, 214, p. 214. DOI: 10.3847/2515-5172/abcf2c.

Gerasimov, Roman et al. (May 2022a). "The HST Large Program on ω Centauri. V. Exploring the Ultracool Dwarf Population with Stellar Atmosphere and Evolutionary Modeling". In: *ApJ* 930.1, 24, p. 24. DOI: 10.3847/1538-4357/ac61e5. arXiv: 2111.10063 [astro-ph.SR].

— (May 2022b). "The HST Large Program on ω Centauri. V. Exploring the Ultracool Dwarf Population with Stellar Atmosphere and Evolutionary Modeling". In: *ApJ* 930.1, 24, p. 24. DOI: 10.3847/1538-4357/ac61e5. arXiv: 2111.10063 [astro-ph.SR].

Gerasimov, Roman et al. (Oct. 2023). "Exploring the Chemistry and Mass Function of the Globular Cluster 47 Tucanae with New Theoretical Color-Magnitude Diagrams". In: *arXiv e-prints*, arXiv:2310.11800, arXiv:2310.11800. arXiv: 2310.11800 [astro-ph.SR].

Gieles, Mark et al. (Aug. 2018). "Concurrent formation of supermassive stars and globular clusters: implications for early self-enrichment". In: *MNRAS* 478.2, pp. 2461–2479. DOI: 10.1093/mnras/sty1059. arXiv: 1804.04682 [astro-ph.GA].

Glantz, S. A. and B. K Slinker (1990). In: *Primer of Applied Regression and Analysis of Variance (New York: McGraw-Hill)*.

Goldsbury, Ryan et al. (Dec. 2010). "The ACS Survey of Galactic Globular Clusters. X. New Determinations of Centers for 65 Clusters". In: *AJ* 140.6, pp. 1830–1837. DOI: 10.1088/0004-6256/140/6/1830. arXiv: 1008.2755 [astro-ph.GA].

Gratton, R. G. et al. (Sept. 2005). "Precise reddening and metallicity of NGC 6752 from FLAMES spectra". In: *A&A* 440.3, pp. 901–908. DOI: 10.1051/0004-6361:20053019. arXiv: astro-ph/0505201 [astro-ph].

Gratton, Raffaele et al. (Nov. 2019). "What is a globular cluster? An observational perspective". In: *A&AR* 27.1, 8, p. 8. DOI: 10.1007/s00159-019-0119-3. arXiv: 1911.02835 [astro-ph.SR].

Griggio, M. and L. R. Bedin (Apr. 2022). "Astrometric star-cluster membership probability: application to the case of M 37 with Gaia EDR3". In: *MNRAS* 511.4, pp. 4702–4709. DOI: 10.1093/mnras/stac391. arXiv: 2202.07942 [astro-ph.GA].

Halir, Radim and Jan Flusser. In: *Proc. of the 6th Int. Conf. in Central Europe on Computer Graphics and Visualization, 125* ().

Hansen, B. M. S. et al. (Aug. 2013). "An age difference of two billion years between a metal-rich and a metal-poor globular cluster". In: *Nature* 500.7460, pp. 51–53. DOI: 10.1038/nature12334. arXiv: 1308.0032 [astro-ph.SR].

Hansen, Brad M. S. et al. (Dec. 2007). "The White Dwarf Cooling Sequence of NGC 6397". In: *ApJ* 671.1, pp. 380–401. DOI: 10.1086/522567. arXiv: astro-ph/0701738 [astro-ph].

Harris, William E. (Oct. 1996). "A Catalog of Parameters for Globular Clusters in the Milky Way". In: *AJ* 112, p. 1487. DOI: 10.1086/118116.

— (Dec. 2010). "A New Catalog of Globular Clusters in the Milky Way". In: *arXiv e-prints*, arXiv:1012.3224, arXiv:1012.3224. DOI: 10.48550/arXiv.1012.3224. arXiv: 1012.3224 [astro-ph.GA].

Hartman, J. D. et al. (Mar. 2008). "Deep MMT Transit Survey of the Open Cluster M37. II. Variable Stars". In: *ApJ* 675.2, pp. 1254–1277. DOI: 10.1086/527460. arXiv: 0709.3484 [astro-ph].

Hartman, J. D. et al. (Apr. 2009). "Deep MMT Transit Survey of the Open Cluster M37 IV: Limit on the Fraction of Stars with Planets as Small as $0.3R_J$". In: *ApJ* 695.1, pp. 336–356. DOI: 10.1088/0004-637X/695/1/336. arXiv: 0809.3807 [astro-ph].

Hauschildt, Peter H., E. Baron, and France Allard (July 1997). "Parallel Implementation of the PHOENIX Generalized Stellar Atmosphere Program". In: *ApJ* 483.1, pp. 390–398. DOI: 10.1086/304233. arXiv: astro-ph/9607087 [astro-ph].

Hénault-Brunet, V. et al. (June 2015). "Multiple populations in globular clusters: the distinct kinematic imprints of different formation scenarios". In: *MNRAS* 450.2, pp. 1164–1198. DOI: 10.1093/mnras/stv675. arXiv: 1503.07532 [astro-ph.GA].

Hong, Jongsuk et al. (Apr. 2013). "Comparative study between N-body and Fokker-Planck simulations for rotating star clusters - II. Two-component models". In: *MNRAS* 430.4, pp. 2960–2972. DOI: 10.1093/mnras/stt099. arXiv: 1211.6527 [astro-ph.SR].

Jindal, Abhinav, Jeremy J. Webb, and Jo Bovy (Aug. 2019). "The orbital anisotropy profiles of nearby globular clusters from Gaia Data Release 2". In: *MNRAS* 487.3, pp. 3693–3701. DOI: 10.1093/mnras/stz1586. arXiv: 1903.11070 [astro-ph.GA].

Johnson, Christian I. and Catherine A. Pilachowski (Oct. 2010). "Chemical Abundances for 855 Giants in the Globular Cluster Omega Centauri (NGC 5139)". In: *ApJ* 722.2, pp. 1373–1410. DOI: 10.1088/0004-637X/722/2/1373. arXiv: 1008.2232 [astro-ph.SR].

— (Aug. 2012). "Oxygen and Sodium Abundances in M13 (NGC 6205) Giants: Linking Globular Cluster Formation Scenarios, Deep Mixing, and Post-RGB Evolution". In: *ApJl* 754.2, L38, p. L38. DOI: 10.1088/2041-8205/754/2/L38. arXiv: 1207.1919 [astro-ph.SR].

Johnson, Christian I. et al. (Aug. 2015). "A Spectroscopic Analysis of the Galactic Globular Cluster NGC 6273 (M19)". In: *AJ* 150.2, 63, p. 63. DOI: 10.1088/0004-6256/150/2/63. arXiv: 1507.00756 [astro-ph.SR].

Jurcsik, Johanna (Oct. 1998). "Spatial Metallicity Asymmetry in ω Centauri". In: *ApJl* 506.2, pp. L113–L116. DOI: 10.1086/311648. arXiv: astro-ph/9808327 [astro-ph].

Kamann, S. et al. (Oct. 2018). "Cluster kinematics and stellar rotation in NGC 419 with MUSE and adaptive optics". In: *MNRAS* 480.2, pp. 1689–1695. DOI: 10.1093/mnras/sty1958. arXiv: 1807.10612 [astro-ph.GA].

Kamann, S. et al. (Feb. 2020). "How stellar rotation shapes the colour-magnitude diagram of the massive intermediate-age star cluster NGC 1846". In: *MNRAS* 492.2, pp. 2177–2192. DOI: 10.1093/mnras/stz3583. arXiv: 2001.01731 [astro-ph.SR].

Kamlah, A. W. H. et al. (Nov. 2022). "The impact of stellar evolution on rotating star clusters: the gravothermal-gravogyro catastrophe and the formation of a bar of black holes". In: *MNRAS* 516.3, pp. 3266–3283. DOI: 10.1093/mnras/stac2281. arXiv: 2205.04470 [astro-ph.GA].

Kim, Eunhyeuk, Hyung Mok Lee, and Rainer Spurzem (June 2004). "Dynamical evolution of rotating stellar systems - III. The effect of the mass spectrum". In: *MNRAS* 351.1, pp. 220–236. DOI: 10.1111/j.1365-2966.2004.07776.x. arXiv: astro-ph/0402478 [astro-ph].

King, I. R. et al. (July 2012). "Hubble Space Telescope Observations of an Outer Field in Omega Centauri: A Definitive Helium Abundance". In: *AJ* 144.1, 5, p. 5. DOI: 10.1088/0004-6256/144/1/5. arXiv: 1205.3760 [astro-ph.GA].

Kovács, G., S. Zucker, and T. Mazeh (Aug. 2002). "A box-fitting algorithm in the search for periodic transits". In: *A&A* 391, pp. 369–377. DOI: 10.1051/0004-6361:20020802. arXiv: astro-ph/0206099 [astro-ph].

Krause, M. et al. (Apr. 2013). "Superbubble dynamics in globular cluster infancy. II. Consequences for secondary star formation in the context of self-enrichment via fast-rotating massive stars". In: *A&A* 552, A121, A121. DOI: 10.1051/0004-6361/201220694. arXiv: 1302.2494 [astro-ph.GA].

Kurucz, R. L. (1970). "Atlas: a Computer Program for Calculating Model Stellar Atmospheres". In: *SAO Special Report* 309.

Kurucz, Robert L. (2005). "ATLAS12, SYNTHE, ATLAS9, WIDTH9, et cetera". In: *Memorie della Societa Astronomica Italiana Supplementi* 8, p. 14.

— (2014). "Model Atmosphere Codes: ATLAS12 and ATLAS9". In: *Determination of Atmospheric Parameters of B-, A-, F- and G-Type Stars*. Springer International Publishing, pp. 39–51. DOI: 10.1007/978-3-319-06956-2_4.

Lacchin, E., F. Calura, and E. Vesperini (Oct. 2021). "On the role of Type Ia supernovae in the second-generation star formation in globular clusters". In: *MNRAS* 506.4, pp. 5951–5968. DOI: 10.1093/mnras/stab2061. arXiv: 2107.07962 [astro-ph.GA].

Lacchin, E. et al. (Nov. 2022). "The role of rotation on the formation of second generation stars in globular clusters". In: *MNRAS* 517.1, pp. 1171–1188. DOI: 10.1093/mnras/stac2328. arXiv: 2209.05178 [astro-ph.GA].

Lane, Richard R. et al. (Aug. 2010). "Halo globular clusters observed with AAOmega: dark matter content, metallicity and tidal heating". In: *MNRAS* 406.4, pp. 2732–2742. DOI: 10.1111/j.1365-2966.2010.16874.x. arXiv: 1004.4696 [astro-ph.GA].

Lanzoni, B. et al. (July 2018). "The Strong Rotation of M5 (NGC 5904) as Seen from the MIKiS Survey of Galactic Globular Clusters". In: *ApJ* 861.1, 16, p. 16. DOI: 10.3847/1538-4357/aac26a. arXiv: 1804.10509 [astro-ph.GA].

Lardo, C. et al. (Jan. 2011). "Mining SDSS in search of multiple populations in globular clusters". In: *A&A* 525, A114, A114. DOI: 10.1051/0004-6361/201015662. arXiv: 1010.4697 [astro-ph.GA].

Lardo, C. et al. (Jan. 2015). "The Gaia-ESO Survey: Kinematics of seven Galactic globular clusters". In: *A&A* 573, A115, A115. DOI: 10.1051/0004-6361/201425036. arXiv: 1411.4886 [astro-ph.GA].

Larkin, Mikaela M., Roman Gerasimov, and Adam J. Burgasser (Jan. 2023). "Characterization of Population III Stars with Stellar Atmosphere and Evolutionary Modeling and Predictions of their Observability with the JWST". In: *AJ* 165.1, 2, p. 2. DOI: 10.3847/1538-3881/ac9b43. arXiv: 2210.09185 [astro-ph.SR].

Lee, Jae-Woo (July 2017). "Multiple Stellar Populations of Globular Clusters from Homogeneous Ca-CN Photometry. II. M5 (NGC 5904) and a New Filter System". In: *ApJ* 844.1, 77, p. 77. DOI: 10.3847/1538-4357/aa7b8c. arXiv: 1706.07969 [astro-ph.GA].

Libralato, Mattia et al. (July 2018a). "Hubble Space Telescope Proper Motion (HST-PROMO) Catalogs of Galactic Globular Cluster. VI. Improved Data Reduction and Internal-kinematic Analysis of NGC 362". In: *ApJ* 861.2, 99, p. 99. DOI: 10.3847/1538-4357/aac6c0. arXiv: 1805.05332 [astro-ph.SR].

Libralato, Mattia et al. (Feb. 2018b). "The HST Large Programme on ω Centauri. III. Absolute Proper Motion". In: *ApJ* 854.1, 45, p. 45. DOI: 10.3847/1538-4357/aaa59e. arXiv: 1801.01502 [astro-ph.GA].

Libralato, Mattia et al. (Mar. 2019). "The Hubble Space Telescope UV Legacy Survey of Galactic Globular Clusters. XVIII. Proper-motion Kinematics of Multiple Stellar Populations in the Core Regions of NGC 6352". In: *ApJ* 873.2, 109, p. 109. DOI: 10.3847/1538-4357/ab0551. arXiv: 1902.02787 [astro-ph.SR].

Libralato, Mattia et al. (Aug. 2022). "The Hubble Space Telescope UV Legacy Survey of Galactic Globular Clusters. XXIII. Proper-motion Catalogs and Internal Kinematics". In: *ApJ* 934.2, 150, p. 150. DOI: 10.3847/1538-4357/ac7727. arXiv: 2206.09924 [astro-ph.GA].

Libralato, Mattia et al. (Feb. 2023). "The Hubble Space Telescope UV Legacy Survey of Galactic Globular Clusters. XXIV. Differences in Internal Kinematics of Multiple Stellar Populations". In: *ApJ* 944.1, 58, p. 58. DOI: 10.3847/1538-4357/acaec6. arXiv: 2301.04148 [astro-ph.GA].

Lindegren, L. et al. (May 2021). "Gaia Early Data Release 3. The astrometric solution". In: *A&A* 649, A2, A2. DOI: 10.1051/0004-6361/202039709. arXiv: 2012.03380 [astro-ph.IM].

Linsky, Jeffrey L. (June 1969). "On the Pressure-Induced Opacity of Molecular Hydrogen in Late-Type Stars". In: *ApJ* 156, p. 989. DOI: 10.1086/150030.

Livernois, Alexander et al. (Oct. 2021). "Early dynamics and violent relaxation of multimass rotating star clusters". In: *MNRAS* 506.4, pp. 5781–5801. DOI: 10.1093/mnras/stab2119. arXiv: 2107.11394 [astro-ph.GA].

Livernois, Alexander R. et al. (May 2022). "Long-term evolution of multimass rotating star clusters". In: *MNRAS* 512.2, pp. 2584–2593. DOI: 10.1093/mnras/stac651. arXiv: 2204.06578 [astro-ph.GA].

Lomb, N. R. (Feb. 1976). "Least-Squares Frequency Analysis of Unequally Spaced Data". In: *Ap&SS* 39.2, pp. 447–462. DOI: 10.1007/BF00648343.

Marino, A. F. et al. (Nov. 2008). "Spectroscopic and photometric evidence of two stellar populations in the Galactic globular cluster NGC 6121 (M 4)". In: *A&A* 490.2, pp. 625–640. DOI: 10.1051/0004-6361:200810389. arXiv: 0808.1414 [astro-ph].

Marino, A. F. et al. (Apr. 2010). "Chemical composition of stellar populations in ω Centauri". In: *Light Elements in the Universe*. Ed. by Corinne Charbonnel et al. Vol. 268, pp. 183–184. DOI: 10.1017/S1743921310004096. arXiv: 1001.1500 [astro-ph.SR].

Marino, A. F. et al. (Apr. 2011). "Sodium-Oxygen Anticorrelation and Neutron-capture Elements in Omega Centauri Stellar Populations". In: *ApJ* 731.1, 64, p. 64. DOI: 10.1088/0004-637X/731/1/64. arXiv: 1102.1653 [astro-ph.SR].

Marino, A. F. et al. (Feb. 2012). "The C+N+O Abundance of ω Centauri Giant Stars: Implications for the Chemical-enrichment Scenario and the Relative Ages of Different Stellar Populations". In: *ApJ* 746.1, 14, p. 14. DOI: 10.1088/0004-637X/746/1/14. arXiv: 1111.1891 [astro-ph.SR].

Marino, A. F. et al. (June 2015). "Iron and s-elements abundance variations in NGC 5286: comparison with 'anomalous' globular clusters and Milky Way satellites". In: *MNRAS* 450.1, pp. 815–845. DOI: 10.1093/mnras/stv420. arXiv: 1502.07438 [astro-ph.SR].

Marino, A. F. et al. (Aug. 2019). "The Hubble Space Telescope UV Legacy Survey of Galactic Globular Clusters - XIX. A chemical tagging of the multiple stellar populations over the chromosome maps". In: *MNRAS* 487.3, pp. 3815–3844. DOI: 10.1093/mnras/stz1415. arXiv: 1904.05180 [astro-ph.SR].

Mastrobuono-Battisti, Alessandra and Hagai B. Perets (Dec. 2013). "Evolution of Second-generation Stars in Stellar Disks of Globular and Nuclear Clusters: ω Centauri as a Test Case". In: *ApJ* 779.1, 85, p. 85. DOI: 10.1088/0004-637X/779/1/85. arXiv: 1304.6086 [astro-ph.GA].

— (May 2016). "Second-generation Stellar Disks in Dense Star Clusters and Cluster Ellipticities". In: *ApJ* 823.1, 61, p. 61. DOI: 10.3847/0004-637X/823/1/61. arXiv: 1506.08198 [astro-ph.GA].

McKenzie, Madeleine and Kenji Bekki (Jan. 2021). "Simulations of globular clusters within their parent galaxies: multiple stellar populations and internal kinematics". In: *MNRAS* 500.4, pp. 4578–4596. DOI: 10.1093/mnras/staa3376. arXiv: 2101.02348 [astro-ph.GA].

Milone, A. P. et al. (Feb. 2010). "Multiple Stellar Populations in the Galactic Globular Cluster NGC 6752". In: *ApJ* 709.2, pp. 1183–1194. DOI: 10.1088/0004-637X/709/2/1183. arXiv: 0912.2055 [astro-ph.SR].

Milone, A. P. et al. (Jan. 2012a). "A Double Main Sequence in the Globular Cluster NGC 6397". In: *ApJ* 745.1, 27, p. 27. DOI: 10.1088/0004-637X/745/1/27. arXiv: 1110.1077 [astro-ph.SR].

Milone, A. P. et al. (Jan. 2012b). "Luminosity and mass functions of the three main sequences of the globular cluster NGC 2808". In: *A&A* 537, A77, A77. DOI: 10.1051/0004-6361/201116539. arXiv: 1108.2391 [astro-ph.SR].

Milone, A. P. et al. (Jan. 2012c). "Multiple Stellar Populations in 47 Tucanae". In: *ApJ* 744.1, 58, p. 58. DOI: 10.1088/0004-637X/744/1/5810.1086/141918. arXiv: 1109.0900 [astro-ph.SR].

Milone, A. P. et al. (Apr. 2012d). "The ACS survey of Galactic globular clusters. XII. Photometric binaries along the main sequence". In: *A&A* 540, A16, A16. DOI: 10.1051/0004-6361/201016384. arXiv: 1111.0552 [astro-ph.SR].

Milone, A. P. et al. (Aug. 2012e). "The Infrared Eye of the Wide-Field Camera 3 on the Hubble Space Telescope Reveals Multiple Main Sequences of Very Low Mass Stars in NGC 2808". In: *ApJL* 754.2, L34, p. L34. DOI: 10.1088/2041-8205/754/2/L34. arXiv: 1206.5529 [astro-ph.SR].

Milone, A. P. et al. (Apr. 2013). "A WFC3/HST View of the Three Stellar Populations in the Globular Cluster NGC 6752". In: *ApJ* 767.2, 120, p. 120. DOI: 10.1088/0004-637X/767/2/120. arXiv: 1301.7044 [astro-ph.SR].

Milone, A. P. et al. (Apr. 2014). "The M 4 Core Project with HST - II. Multiple stellar populations at the bottom of the main sequence". In: *MNRAS* 439.2, pp. 1588–1595. DOI: 10.1093/mnras/stu030. arXiv: 1401.1091 [astro-ph.SR].

Milone, A. P. et al. (Feb. 2015a). "The Hubble Space Telescope UV Legacy Survey of galactic globular clusters - II. The seven stellar populations of NGC 7089 (M2)⋆". In: *MNRAS* 447.1, pp. 927–938. DOI: 10.1093/mnras/stu2446. arXiv: 1411.5043 [astro-ph.SR].

Milone, A. P. et al. (July 2015b). "The Hubble Space Telescope UV Legacy Survey of Galactic Globular Clusters. III. A Quintuple Stellar Population in NGC 2808". In: *ApJ* 808.1, 51, p. 51. DOI: 10.1088/0004-637X/808/1/51. arXiv: 1505.05934 [astro-ph.SR].

Milone, A. P. et al. (July 2017a). "The HST large programme on ω Centauri - I. Multiple stellar populations at the bottom of the main sequence probed in NIR-Optical". In: *MNRAS* 469.1, pp. 800–812. DOI: 10.1093/mnras/stx836. arXiv: 1704.00418 [astro-ph.SR].

Milone, A. P. et al. (Jan. 2017b). "The Hubble Space Telescope UV Legacy Survey of Galactic globular clusters - IX. The Atlas of multiple stellar populations". In: *MNRAS* 464.3, pp. 3636–3656. DOI: 10.1093/mnras/stw2531. arXiv: 1610.00451 [astro-ph.SR].

— (Jan. 2017c). "The Hubble Space Telescope UV Legacy Survey of Galactic globular clusters - IX. The Atlas of multiple stellar populations". In: *MNRAS* 464.3, pp. 3636–3656. DOI: 10.1093/mnras/stw2531. arXiv: 1610.00451 [astro-ph.SR].

Milone, A. P. et al. (Oct. 2018a). "Gaia unveils the kinematics of multiple stellar populations in 47 Tucanae". In: *MNRAS* 479.4, pp. 5005–5011. DOI: 10.1093/mnras/sty1873. arXiv: 1807.03511 [astro-ph.SR].

Milone, A. P. et al. (Dec. 2018b). "The Hubble Space Telescope UV legacy survey of galactic globular clusters - XVI. The helium abundance of multiple populations". In: *MNRAS* 481.4, pp. 5098–5122. DOI: 10.1093/mnras/sty2573. arXiv: 1809.05006 [astro-ph.SR].

— (Dec. 2018c). "The Hubble Space Telescope UV legacy survey of galactic globular clusters - XVI. The helium abundance of multiple populations". In: *MNRAS* 481.4, pp. 5098–5122. DOI: 10.1093/mnras/sty2573. arXiv: 1809.05006 [astro-ph.SR].

Milone, A. P. et al. (Apr. 2019). "The HST Large Programme on NGC 6752 - II. Multiple populations at the bottom of the main sequence probed in NIR". In: *MNRAS* 484.3, pp. 4046–4053. DOI: 10.1093/mnras/stz277. arXiv: 1901.07230 [astro-ph.SR].

Milone, A. P. et al. (Sept. 2020). "A chromosome map to unveil stellar populations with different magnesium abundances. The case of ω Centauri". In: *MNRAS* 497.3, pp. 3846–3859. DOI: 10.1093/mnras/staa2119. arXiv: 2006.13101 [astro-ph.SR].

Milone, A. P. et al. (June 2023). "Multiple stellar populations in globular clusters with JWST: an NIRCam view of 47 Tucanae". In: *MNRAS* 522.2, pp. 2429–2447. DOI: 10.1093/mnras/stad1041. arXiv: 2301.10889 [astro-ph.SR].

Moehler, S. et al. (June 2004). "Spectral types and masses of white dwarfs in globular clusters". In: *A&A* 420, pp. 515–525. DOI: 10.1051/0004-6361:20035819. arXiv: astro-ph/0403245 [astro-ph].

Mould, J. R. and A. R. Hyland (Sept. 1976). "Infrared observations and the structure of the lower main sequence." In: *ApJ* 208, pp. 399–413. DOI: 10.1086/154620.

Nardiello, D. et al. (Jan. 2015a). "Observing multiple stellar populations with VLT/FORS2. Main sequence photometry in outer regions of NGC 6752, NGC 6397, and NGC 6121 (M 4)". In: *A&A* 573, A70, A70. DOI: 10.1051/0004-6361/201424117. arXiv: 1410.7503 [astro-ph.SR].

— (Jan. 2015b). "Observing multiple stellar populations with VLT/FORS2. Main sequence photometry in outer regions of NGC 6752, NGC 6397, and NGC 6121

(M 4)". In: *A&A* 573, A70, A70. DOI: 10.1051/0004-6361/201424117. arXiv: 1410.7503 [astro-ph.SR].

Nardiello, D. et al. (Mar. 2015c). "Variable stars in two open clusters within the Kepler/K2-Campaign-0 field: M35 and NGC 2158". In: *MNRAS* 447.4, pp. 3536–3547. DOI: 10.1093/mnras/stu2697. arXiv: 1412.5688 [astro-ph.SR].

Nardiello, D. et al. (Dec. 2018). "The Hubble Space Telescope UV Legacy Survey of Galactic Globular Clusters - XVII. Public Catalogue Release". In: *MNRAS* 481.3, pp. 3382–3393. DOI: 10.1093/mnras/sty2515. arXiv: 1809.04300 [astro-ph.SR].

Nardiello, D. et al. (Aug. 2021). "A PSF-based Approach to TESS High quality data Of Stellar clusters (PATHOS) - IV. Candidate exoplanets around stars in open clusters: frequency and age-planetary radius distribution". In: *MNRAS* 505.3, pp. 3767–3784. DOI: 10.1093/mnras/stab1497. arXiv: 2105.09952 [astro-ph.EP].

Nardiello, D. et al. (Nov. 2022). "Photometry and astrometry with JWST - I. NIRCam point spread functions and the first JWST colour-magnitude diagrams of a globular cluster". In: *MNRAS* 517.1, pp. 484–497. DOI: 10.1093/mnras/stac2659. arXiv: 2209.06547 [astro-ph.SR].

Nardiello, D. et al. (Oct. 2023). "Photometry and astrometry with JWST - III. A NIRCam-Gaia DR3 analysis of the open cluster NGC 2506". In: *MNRAS* 525.2, pp. 2585–2604. DOI: 10.1093/mnras/stad2445. arXiv: 2308.10575 [astro-ph.SR].

Nascimbeni, V. et al. (Aug. 2014). "The M 4 Core Project with HST - III. Search for variable stars in the primary field". In: *MNRAS* 442.3, pp. 2381–2391. DOI: 10.1093/mnras/stu930. arXiv: 1405.1626 [astro-ph.SR].

Norris, John E. (Sept. 2004). "The Helium Abundances of ω Centauri". In: *ApJl* 612.1, pp. L25–L28. DOI: 10.1086/423986.

Norris, John E. and G. S. Da Costa (July 1995). "The Giant Branch of omega Centauri. IV. Abundance Patterns Based on Echelle Spectra of 40 Red Giants". In: *ApJ* 447, p. 680. DOI: 10.1086/175909.

Norris, John E. et al. (Oct. 1997). "The Giant Branch of ω Centauri: The Dependence of Kinematics on Abundance". In: *ApJl* 487.2, pp. L187–L190. DOI: 10.1086/310895.

Pallanca, C. et al. (Aug. 2013). "The Optical Counterpart to the X-Ray Transient IGR J1824-24525 in the Globular Cluster M28". In: *ApJ* 773.2, 122, p. 122. DOI: 10.1088/0004-637X/773/2/122. arXiv: 1306.6416 [astro-ph.SR].

Pallanca, Cristina et al. (Aug. 2017). "A Complete Census of Hα Emitters in NGC 6397". In: *ApJ* 845.1, 4, p. 4. DOI: 10.3847/1538-4357/aa7ca6. arXiv: 1706.09435 [astro-ph.SR].

Pancino, E. et al. (Apr. 2002). "High-Resolution Spectroscopy of Metal-rich Giants in ω Centauri: First Indication of Type Ia Supernova Enrichment". In: *ApJl* 568.2, pp. L101–L105. DOI: 10.1086/340378. arXiv: astro-ph/0202397 [astro-ph].

Pancino, Elena et al. (May 2000). "New Evidence for the Complex Structure of the Red Giant Branch in ω Centauri". In: *ApJl* 534.1, pp. L83–L87. DOI: 10.1086/312658. arXiv: astro-ph/0003222 [astro-ph].

Paxton, Bill et al. (Jan. 2011). "Modules for Experiments in Stellar Astrophysics (MESA)". In: *ApJs* 192.1, 3, p. 3. DOI: 10.1088/0067-0049/192/1/3. arXiv: 1009.1622 [astro-ph.SR].

Paxton, Bill et al. (Sept. 2013). "Modules for Experiments in Stellar Astrophysics (MESA): Planets, Oscillations, Rotation, and Massive Stars". In: *ApJs* 208.1, 4, p. 4. DOI: 10.1088/0067-0049/208/1/4. arXiv: 1301.0319 [astro-ph.SR].

Paxton, Bill et al. (Sept. 2015). "Modules for Experiments in Stellar Astrophysics (MESA): Binaries, Pulsations, and Explosions". In: *ApJs* 220.1, 15, p. 15. DOI: 10.1088/0067-0049/220/1/15. arXiv: 1506.03146 [astro-ph.SR].

Paxton, Bill et al. (Feb. 2018). "Modules for Experiments in Stellar Astrophysics (MESA): Convective Boundaries, Element Diffusion, and Massive Star Explosions". In: *ApJs* 234.2, 34, p. 34. DOI: 10.3847/1538-4365/aaa5a8. arXiv: 1710.08424 [astro-ph.SR].

Paxton, Bill et al. (July 2019). "Modules for Experiments in Stellar Astrophysics (MESA): Pulsating Variable Stars, Rotation, Convective Boundaries, and Energy Conservation". In: *ApJs* 243.1, 10, p. 10. DOI: 10.3847/1538-4365/ab2241. arXiv: 1903.01426 [astro-ph.SR].

Pietrinferni, Adriano et al. (Feb. 2021). "Updated BaSTI Stellar Evolution Models and Isochrones. II. α-enhanced Calculations". In: *ApJ* 908.1, 102, p. 102. DOI: 10.3847/1538-4357/abd4d5. arXiv: 2012.10085 [astro-ph.SR].

Piotto, G. et al. (May 2007). "A Triple Main Sequence in the Globular Cluster NGC 2808". In: *ApJl* 661.1, pp. L53–L56. DOI: 10.1086/518503. arXiv: astro-ph/0703767 [astro-ph].

Piotto, G. et al. (Mar. 2015). "The Hubble Space Telescope UV Legacy Survey of Galactic Globular Clusters. I. Overview of the Project and Detection of Multiple Stellar Populations". In: *AJ* 149.3, 91, p. 91. DOI: 10.1088/0004-6256/149/3/91. arXiv: 1410.4564 [astro-ph.SR].

Piotto, Giampaolo et al. (Mar. 2005). "Metallicities on the Double Main Sequence of ω Centauri Imply Large Helium Enhancement". In: *ApJ* 621.2, pp. 777–784. DOI: 10.1086/427796. arXiv: astro-ph/0412016 [astro-ph].

Plummer, H. C. (Mar. 1911). "On the problem of distribution in globular star clusters". In: *MNRAS* 71, pp. 460–470. DOI: 10.1093/mnras/71.5.460.

Prantzos, N. and C. Charbonnel (Oct. 2006). "On the self-enrichment scenario of galactic globular clusters: constraints on the IMF". In: *A&A* 458.1, pp. 135–149. DOI: 10.1051/0004-6361:20065374. arXiv: astro-ph/0606112 [astro-ph].

Renzini, A. et al. (Dec. 2015a). "The Hubble Space Telescope UV Legacy Survey of Galactic Globular Clusters - V. Constraints on formation scenarios". In: *MNRAS* 454.4, pp. 4197–4207. DOI: 10.1093/mnras/stv2268. arXiv: 1510.01468 [astro-ph.GA].

— (Dec. 2015b). "The Hubble Space Telescope UV Legacy Survey of Galactic Globular Clusters - V. Constraints on formation scenarios". In: *MNRAS* 454.4, pp. 4197–4207. DOI: 10.1093/mnras/stv2268. arXiv: 1510.01468 [astro-ph.GA].

— (Dec. 2015c). "The Hubble Space Telescope UV Legacy Survey of Galactic Globular Clusters - V. Constraints on formation scenarios". In: *MNRAS* 454.4, pp. 4197–4207. DOI: 10.1093/mnras/stv2268. arXiv: 1510.01468 [astro-ph.GA].

Renzini, Alvio (Oct. 2023). "A transient overcooling in the early Universe? Clues from globular clusters formation". In: *MNRAS* 525.1, pp. L117–L120. DOI: 10.1093/mnrasl/slad091. arXiv: 2305.14476 [astro-ph.GA].

Renzini, Alvio, Anna F. Marino, and Antonino P. Milone (June 2022). "The formation of globular clusters as a case of overcooling". In: *MNRAS* 513.2, pp. 2111–2117. DOI: 10.1093/mnras/stac973. arXiv: 2203.03002 [astro-ph.GA].

Renzini, Alvio et al. (July 1996). "The White Dwarf Distance to the Globular Cluster NGC 6752 (and Its Age) with the Hubble Space Telescope". In: *ApJL* 465, p. L23. DOI: 10.1086/310128.

Richer, H. B. (Aug. 1978). "Evidence for white dwarfs in the globular cluster NGC 6752." In: *ApJL* 224, pp. L9–L13. DOI: 10.1086/182747.

Richer, Harvey B. et al. (Aug. 2006). "Probing the Faintest Stars in a Globular Star Cluster". In: *Science* 313.5789, pp. 936–940. DOI: 10.1126/science.1130691. arXiv: astro-ph/0702209 [astro-ph].

Richer, Harvey B. et al. (July 2013). "A Dynamical Signature of Multiple Stellar Populations in 47 Tucanae". In: *ApJl* 771.1, L15, p. L15. DOI: 10.1088/2041-8205/771/1/L15. arXiv: 1306.1226 [astro-ph.SR].

Riello, M. et al. (May 2021). "Gaia Early Data Release 3. Photometric content and validation". In: *A&A* 649, A3, A3. DOI: 10.1051/0004-6361/202039587. arXiv: 2012.01916 [astro-ph.IM].

Salaris, Maurizio et al. (Feb. 2009). "Semi-empirical White Dwarf Initial-Final Mass Relationships: A Thorough Analysis of Systematic Uncertainties Due to Stellar Evolution Models". In: *ApJ* 692.2, pp. 1013–1032. DOI: 10.1088/0004-637X/692/2/1013. arXiv: 0807.3567 [astro-ph].

Salaris, Maurizio et al. (Feb. 2022). "The updated BASTI stellar evolution models and isochrones - III. White dwarfs". In: *MNRAS* 509.4, pp. 5197–5208. DOI: 10.1093/mnras/stab3359. arXiv: 2111.09285 [astro-ph.SR].

Sarajedini, Ata et al. (Apr. 2007). "The ACS Survey of Galactic Globular Clusters. I. Overview and Clusters without Previous Hubble Space Telescope Photometry". In: *AJ* 133.4, pp. 1658–1672. DOI: 10.1086/511979. arXiv: astro-ph/0612598 [astro-ph].

Scalco, M. et al. (Aug. 2021). "The HST large programme on ω Centauri - IV. Catalogue of two external fields". In: *MNRAS* 505.3, pp. 3549–3561. DOI: 10.1093/mnras/stab1476. arXiv: 2107.08726 [astro-ph.SR].

Scalco, M. et al. (June 2023). "First observational evidence of a relation between globular clusters' internal rotation and stellar masses". In: *MNRAS* 522.1, pp. L61–L65. DOI: 10.1093/mnrasl/slad042. arXiv: 2303.15253 [astro-ph.GA].

Scargle, J. D. (Dec. 1982). "Studies in astronomical time series analysis. II. Statistical aspects of spectral analysis of unevenly spaced data." In: *ApJ* 263, pp. 835–853. DOI: 10.1086/160554.

Simioni, M. et al. (Nov. 2016). "The Hubble Space Telescope UV Legacy Survey of Galactic globular clusters - X. The radial distribution of stellar populations in NGC 2808". In: *MNRAS* 463.1, pp. 449–458. DOI: 10.1093/mnras/stw2003. arXiv: 1608.03124 [astro-ph.SR].

Smith, Graeme H. (Feb. 1987). "The chemical inhomegeneity of globular clusters." In: *PASP* 99, pp. 67–90. DOI: 10.1086/131958.

Sollima, A. (Apr. 2021). "Monte Carlo simulations of multiple populations in globular clusters: constraints on the cooling flow versus accretion scenario using million bodies simulations". In: *MNRAS* 502.2, pp. 1974–1989. DOI: 10.1093/mnras/stab154. arXiv: 2102.01707 [astro-ph.GA].

Sollima, A. et al. (Jan. 2007). "Deep FORS1 Observations of the Double Main Sequence of ω Centauri". In: *ApJ* 654.2, pp. 915–922. DOI: 10.1086/509711. arXiv: astro-ph/0609650 [astro-ph].

Soltis, John, Stefano Casertano, and Adam G. Riess (Feb. 2021). "The Parallax of ω Centauri Measured from Gaia EDR3 and a Direct, Geometric Calibration of the Tip of the Red Giant Branch and the Hubble Constant". In: *ApJL* 908.1, L5, p. L5. DOI: 10.3847/2041-8213/abdbad. arXiv: 2012.09196 [astro-ph.GA].

Souza, S. O. et al. (Feb. 2020). "Self-consistent Analysis of Stellar Clusters: An Application to HST Data of the Halo Globular Cluster NGC 6752". In: *ApJ* 890.1, 38, p. 38. DOI: 10.3847/1538-4357/ab6a0f. arXiv: 2001.02697 [astro-ph.SR].

Stanford, Laura M., G. S. Da Costa, and John E. Norris (May 2010). "Abundances of C, N, Sr, and Ba on the Red Giant Branch of ω Centauri". In: *ApJ* 714.2, pp. 1001–1014. DOI: 10.1088/0004-637X/714/2/1001. arXiv: 1003.4661 [astro-ph.SR].

Szölgyén, Ákos, Yohai Meiron, and Bence Kocsis (Dec. 2019). "Anisotropic Mass Segregation in Rotating Globular Clusters". In: *ApJ* 887.2, 123, p. 123. DOI: 10.3847/1538-4357/ab50bb. arXiv: 1903.11610 [astro-ph.GA].

Tiongco, Maria, Angela Collier, and Anna Lisa Varri (Sept. 2021). "Central dynamics of multimass rotating star clusters". In: *MNRAS* 506.3, pp. 4488–4498. DOI: 10.1093/mnras/stab1968. arXiv: 2107.03396 [astro-ph.GA].

Tiongco, Maria A., Enrico Vesperini, and Anna Lisa Varri (2016). In: *MNRAS* 455, 3693T.

Tiongco, Maria A., Enrico Vesperini, and Anna Lisa Varri (July 2017). "Kinematical evolution of tidally limited star clusters: rotational properties". In: *MNRAS* 469.1, pp. 683–692. DOI: 10.1093/mnras/stx853. arXiv: 1704.05918 [astro-ph.GA].

— (Mar. 2018). "The complex kinematics of rotating star clusters in a tidal field". In: *MNRAS* 475.1, pp. L86–L90. DOI: 10.1093/mnrasl/sly009. arXiv: 1801.06236 [astro-ph.GA].

Tiongco, Maria A., Enrico Vesperini, and Anna Lisa Varri (2019). In: *MNRAS* 487, 5535T.

Tiongco, Maria A., Enrico Vesperini, and Anna Lisa Varri (May 2022). "Early dynamical evolution of rotating star clusters in a tidal field". In: *MNRAS* 512.2, pp. 1584–1597. DOI: 10.1093/mnras/stac643. arXiv: 2203.04330 [astro-ph.GA].

Trenti, M., G. Bertin, and T. S. van Albada (Apr. 2005). "A family of models of partially relaxed stellar systems. II. Comparison with the products of collisionless collapse". In: *A&A* 433.1, pp. 57–72. DOI: 10.1051/0004-6361:20041705. arXiv: astro-ph/0411541 [astro-ph].

Trenti, Michele and Roeland van der Marel (Nov. 2013). "No energy equipartition in globular clusters". In: *MNRAS* 435.4, pp. 3272–3282. DOI: 10.1093/mnras/stt1521. arXiv: 1302.2152 [astro-ph.GA].

Vasiliev, Eugene and Holger Baumgardt (Aug. 2021). "Gaia EDR3 view on galactic globular clusters". In: *MNRAS* 505.4, pp. 5978–6002. DOI: 10.1093/mnras/stab1475. arXiv: 2102.09568 [astro-ph.GA].

Ventura, Paolo et al. (Mar. 2001). "Predictions for Self-Pollution in Globular Cluster Stars". In: *ApJl* 550.1, pp. L65–L69. DOI: 10.1086/319496. arXiv: astro-ph/0103337 [astro-ph].

Vesperini, E. and D. C. Heggie (Aug. 1997a). "On the effects of dynamical evolution on the initial mass function of globular clusters". In: *MNRAS* 289.4, pp. 898–920. DOI: 10.1093/mnras/289.4.898. arXiv: astro-ph/9705073 [astro-ph].

— (Aug. 1997b). "On the effects of dynamical evolution on the initial mass function of globular clusters". In: *MNRAS* 289.4, pp. 898–920. DOI: 10.1093/mnras/289.4.898. arXiv: astro-ph/9705073 [astro-ph].

Vesperini, E. et al. (Sept. 2014). "Kinematical fingerprints of star cluster early dynamical evolution." In: *MNRAS* 443, pp. L79–L83. DOI: 10.1093/mnrasl/slu088. arXiv: 1406.3634 [astro-ph.GA].

Vesperini, Enrico et al. (Mar. 2013). "Dynamical evolution and spatial mixing of multiple population globular clusters". In: *MNRAS* 429.3, pp. 1913–1921. DOI: 10.1093/mnras/sts434. arXiv: 1212.2651 [astro-ph.GA].

Vesperini, Enrico et al. (May 2018). "Evolution of the stellar mass function in multiple-population globular clusters". In: *MNRAS* 476.2, pp. 2731–2742. DOI: 10.1093/mnras/sty407. arXiv: 1803.02381 [astro-ph.GA].

Vesperini, Enrico et al. (Apr. 2021). "Dynamical evolution of multiple-population globular clusters". In: *MNRAS* 502.3, pp. 4290–4304. DOI: 10.1093/mnras/stab223. arXiv: 2102.01717 [astro-ph.GA].

Villanova, S. et al. (July 2007). "The Multiplicity of the Subgiant Branch of ω Centauri: Evidence for Prolonged Star Formation". In: *ApJ* 663.1, pp. 296–314. DOI: 10.1086/517905. arXiv: astro-ph/0703208 [astro-ph].

Wang, Long et al. (Jan. 2020). "The possible role of stellar mergers for the formation of multiple stellar populations in globular clusters". In: *MNRAS* 491.1, pp. 440–454. DOI: 10.1093/mnras/stz3033. arXiv: 1910.14040 [astro-ph.SR].

Watkins, Laura L. et al. (Apr. 2015). "Hubble Space Telescope Proper Motion (HST-PROMO) Catalogs of Galactic Globular Cluster. II. Kinematic Profiles and Maps". In: *ApJ* 803.1, 29, p. 29. DOI: 10.1088/0004-637X/803/1/29. arXiv: 1502.00005 [astro-ph.GA].

Watkins, Laura L. et al. (Sept. 2022). "Hubble Space Telescope Proper Motion (HST-PROMO) Catalogs of Galactic Globular Clusters. VII. Energy Equipartition". In: *ApJ* 936.2, 154, p. 154. DOI: 10.3847/1538-4357/ac77f7. arXiv: 2206.05300 [astro-ph.GA].

Webb, Jeremy J. and Enrico Vesperini (Dec. 2016). "Radial variation in the stellar mass functions of star clusters". In: *MNRAS* 463.3, pp. 2383–2393. DOI: 10.1093/mnras/stw2186. arXiv: 1608.07293 [astro-ph.GA].

Winter, Andrew J. and Cathie J. Clarke (May 2023). "Accretion of substellar companions as the origin of chemical abundance inhomogeneities in globular clusters". In: *MNRAS* 521.2, pp. 1646–1673. DOI: 10.1093/mnras/stad312. arXiv: 2301.11412 [astro-ph.GA].

Yong, D. et al. (Aug. 2005). "Abundances in giant stars of the globular cluster NGC 6752". In: *A&A* 438.3, pp. 875–888. DOI: 10.1051/0004-6361:20052916. arXiv: astro-ph/0504283 [astro-ph].

Yong, David et al. (Sept. 2008). "Nitrogen Abundances in Giant Stars of the Globular Cluster NGC 6752". In: *ApJ* 684.2, pp. 1159–1169. DOI: 10.1086/590658. arXiv: 0806.0187 [astro-ph].

Ziliotto, Tuila et al. (Aug. 2023). "Multiple Stellar Populations in Metal-poor Globular Clusters with JWST: A NIRCam View of M92". In: *ApJ* 953.1, 62, p. 62. DOI: 10.3847/1538-4357/acde76. arXiv: 2304.06026 [astro-ph.SR].

Università degli Studi di Ferrara

Sezioni

Dottorati di ricerca

Il tuo indirizzo e-mail

michele.scalco@unife.it

Oggetto:

Dichiarazione di conformità della tesi di Dottorato

Io sottoscritto Dott. (Cognome e Nome)

Scalco Michele

Nato a:

Thiene

Provincia:

Vicenza

Il giorno:

29/08/1995

Avendo frequentato il Dottorato di Ricerca in:

Physics

Ciclo di Dottorato

35

Titolo della tesi:

Multiple stellar populations in globular clusters

Titolo della tesi (traduzione):

Popolazioni stellari multiple in ammassi globulari

Tutore: Prof. (Cognome e Nome)

Rosati Piero

Settore Scientifico Disciplinare (S.S.D.)

FIS/05

Parole chiave della tesi (max 10):

photometry, astrometry, globular clusters

Consapevole, dichiara

CONSAPEVOLE: (1) del fatto che in caso di dichiarazioni mendaci, oltre alle sanzioni previste dal codice penale e dalle Leggi speciali per l'ipotesi di falsità in atti ed uso di atti falsi, decade fin dall'inizio e senza necessità di alcuna formalità dai benefici conseguenti al provvedimento emanato sulla base di tali dichiarazioni; (2) dell'obbligo per l'Università di provvedere al deposito di legge delle tesi di dottorato al fine di assicurarne la conservazione e la consultabilità da parte di terzi; (3) della procedura adottata dall'Università di Ferrara ove si richiede che la tesi sia consegnata dal dottorando in 1 originale cartaceo e 1 in formato PDF/A caricata sulla procedura informatica Esse3 secondo le istruzioni pubblicate sul sito: http://www.unife.it/studenti/dottorato alla voce ESAME FINALE – disposizioni e modulistica; (4) del fatto che l'Università, sulla base dei dati forniti, archivierà e renderà consultabile in rete il testo completo della tesi di dottorato di cui alla presente dichiarazione attraverso la pubblicazione ad accesso aperto nell'Archivio Istituzionale dei Prodotti della Ricerca IRIS-UNIFE (www.iris.unife.it) oltre che attraverso i Cataloghi delle Biblioteche Nazionali Centrali di Roma e Firenze; DICHIARO SOTTO LA MIA RESPONSABILITA': (1) che la copia della tesi depositata presso l'Università di Ferrara in formato cartaceo è del tutto identica a quella caricata in formato PDF/A sulla procedura informatica Esse3, a quelle da inviare ai Commissari di esame finale e alla copia che produrrò in seduta d'esame finale. Di

conseguenza va esclusa qualsiasi responsabilità dell'Ateneo stesso per quanto riguarda eventuali errori, imprecisioni o omissioni nei contenuti della tesi; (2) di prendere atto che la tesi in formato cartaceo è l'unica alla quale farà riferimento l'Università per rilasciare, a mia richiesta, la dichiarazione di conformità di eventuali copie; (3) che il contenuto e l'organizzazione della tesi è opera originale da me realizzata e non compromette in alcun modo i diritti di terzi, ivi compresi quelli relativi alla sicurezza dei dati personali; che pertanto l'Università è in ogni caso esente da responsabilità di qualsivoglia natura civile, amministrativa o penale e sarà da me tenuta indenne da qualsiasi richiesta o rivendicazione da parte di terzi; (4) che la tesi di dottorato non è il risultato di attività rientranti nella normativa sulla proprietà industriale, non è stata prodotta nell'ambito di progetti finanziati da soggetti pubblici o privati con vincoli alla divulgazione dei risultati, non è oggetto di eventuali registrazioni di tipo brevettale o di tutela. PER ACCETTAZIONE DI QUANTO SOPRA RIPORTATO

Firma del dottorando

Ferrara, li 30/07/2024 Firma del Dottorando Michele Scalco

Firma del Tutore

Visto: Il Tutore Si approva Firma del Tutore